Alteration Spatially Associated with the Phoenix Unconformity-Related Uranium Deposit, Athabasca Basin, Saskatchewan, Canada.

Jack Dann MGeol (Hons)

Thesis submitted to the

in partial fulfilment of the requirements for the

M.Sc degree in Earth Sciences

Ottawa-Carleton Geoscience Centre

Department of Earth and Environmental Sciences

Faculty of Science

University of Ottawa

Abstract

Unconformity-related uranium deposits in the Athabasca Basin represent a significant global resource of uranium. One such deposit, the Phoenix Deposit, discovered in 2007 on Denison Mine's Wheeler River property, shares similarities with other deposits in the Basin. The Phoenix Deposit is located at the apex between a basement shear structure, and the unconformity between the crystalline basement and overlying sandstones. The shear structure extends into the sandstones, this structure controls the distribution of alteration minerals in the basement and early alteration phases in sandstones. The shear structure extending to sandstones is not spatially associated with late alteration phases associated with the uranium deposit, suggesting that the structure was not important for uranium mineralisation.

Bulk rock compositions of sandstones show chimney-like distribution of elements above the uranium deposit. The most notable ones are the distribution of yttrium, and boron. Rare earth elements and yttrium are not soluble in aqueous fluids at low temperatures and they are enriched in uranium ore. Therefore, the chimney-like distribution of elements are attributed to uraniferous hydrothermal activity in sandstones.

Petrographic and chemical analysis of alteration associated with the Phoenix Deposit shows two types of tourmaline, a pre-ore (Tur 1) in the basement, which is likely a metamorphic product (Tur1) and a syn-ore magnesiofoitite (Tur 2) in the basement and the sandstones. Three generations of chlorite are identified within the alteration halo of the Phoenix Deposit; an early Fe-rich clinochlore (C1) in the basement and sandstones, the second generation, Mg-rich sudoitic chlorite (C2) in the basement, and a late, sudoitic chlorite (C3) in the basement and sandstones. Illite shows three types; an early and late M1 and a late M2. M1 is found as two polytypes, 1Mc and 1Mt, in the basement and sandstones, with the 1Mt having a spatial relationship with the uranium deposit. Late M2 illite is coarse-grained and occurs in the basement and sandstones.

Near Infrared (NIR) spectra of sandstones overlying the deposit shows absorption features between 600 and 700 nm. It is considered that these absorption features appear to have been produced during late hydrothermal activity and may have a temporal as well as spatial relationship with uranium mineralisation.

Acknowledgements

First and foremost, I would like to thank Prof. Kéiko Hattori for offering, providing and supporting me through this body of work and its various trials, tribulations and delays. Her knowledge, patience and experience have added greatly to this work.

I would like to acknowledge the Research Affiliate Program bursary I received from Natural Resources Canada. This project was funded by Targeted Geoscience Initiative 4 Uranium Ore Systems program at Natural Resources Canada through a research grant to Kéiko Hattori, and I thank Dr Eric Potter at the Geological Survey of Canada for providing support. The Society of Economic Geologists is appreciatively acknowledged for a Graduate Student Fellowship Award that I received in 2012. Denison Mines and associated staff are thanked for providing extensive logistical support.

I also thank those who have helped me complete this work, Mr Michael Power, for continuing support, refreshing opinions and sampling assistance. Dr Jeanne Percival of the Geological Survey of Canada for assisting with XRD interpretation and the provision of unpublished SWIR spectra of common alteration minerals and their mixtures forum in the Athabasca Basin. Dr Tara Kell of uOttawa for assisting with XRD Analysis. The late Dr Eion Cameron is also thanked for his contribution. The input of reviewers, Prof. Ingrid Kjarsgaard, Prof. Mark Hannington and Prof Fred Gaides has been gratefully received, and is acknowledged.

Of note are people from both sides of the Atlantic, my family (and associated dogs), Sarah Walker, Adam Sookdeo, Stacey Wetmore, Erin Adalakha, Fritz Griffith, Dave Lowe, Fabio Stern, Chris Fry, Nathan and Michelle Harrison, Hayley Jenkins, Dr Rick Smith and all those at FWS Consultants. This experience has not been without its highs, lows and extensions, but I hope to have emerged as a professional geoscientist ready to find my place in today's modern geoscience industry.

Statement of Originality

The work presented in this thesis and appendices was conducted by myself at the University of Ottawa. Sample collection and petrographic analytical work (detailed below) was carried out by myself at the University of Ottawa and the Geological Survey of Canada (Ottawa), clay fractions were produced by the Geological Survey of Canada and petrographic thin sections were prepared in-house at the University of Ottawa. The whole rock geochemical analysis of samples was carried out by Saskatchewan Research Council laboratory in Saskatoon, Saskatchewan, for Denison Mines Corp.

I collected 299 samples used in this study between 2011 and 2012. The majority of basement samples and some sandstone samples (JD1A-JD4A, DPX1-DPX88 and the WS Shear and Sandstone Extension to the WS

Shear samples) were collected in early September 2011, while the second, sandstone dominated samples (DPX100 to DPX299) were collected August 2012. Where necessary, samples were split into subsamples based on their composition, texture and features. I produced all powdered XRD, clay concentrate samples for XRD analysis, and analysed all samples at the University of Ottawa, I also analysed, spliced, pre-processed and identified all SWIR spectra of samples.

I undertook a petrographic analysis of all 63 thin sections used in this study, analysed selected samples SEM and Electron Microprobe and calculated all mineral formulas. Furthermore, I prepared all statistical and geospatial analysis present in Geological Survey of Canada Open File Report 7463 (Appendix 1.1), creating interpolated raster maps from geochemical data in the sandstones.

List of Contents

Abstract ii
Acknowledgements iii
Statement of Originality iii
List of Contents v
List of Tables. viii
List of Figures. ix
List of Plates x
List of Appendices. xi
1. INTRODUCTION 1
1.1 Objectives. 1
1.2 Rationale for Study and Outline of the thesis 1
1.3 Previous Work 3
1.3.1 Past Work Undertaken on the Alteration of the Phoenix Unconformity-Related Uranium Deposit. 3
1.3.2 Basement Shears Associated with Unconformity-Related Uranium Deposits 3
1.3.3 Tourmaline Mineral Chemistry 4
1.3.4 Alteration Mineralogy of Previous Studies. 4
1.3.5 Contribution to Knowledge 5
1.4 Regional Geology 6
1.4.1 Basement Geology 6
1.4.2 Regional Structural Geology 8
1.4.3 Sandstone Geology 10
1.5 Athabascan Unconformity-Related Uranium Deposits. 11
1.5.2 Egress Type Deposits 11
1.5.2 Ingress-Type Deposits 12
1.6 Wheeler River Property Geology 12
1.6.1 Alteration on the Wheeler River Property 13
1.6.2 Wheeler River Property Structural Geology 14
1.6.3 The Phoenix Uranium Deposit 15
2 METHODS 17
2.1 Sampling 17
2.1.1 Sample Details 17
2.1.2 Targeted Drill Cores 17
2.1.3 Geochemical Analysis 19
2.2 Preparation of Samples 19

2.2.1 Short Wave Infrared Samples 19
2.2.2 Clay Concentrates 19
2.2.3 Clay Fractions 20
2.3 Laboratory Analytical Methods 20
2.3.1 Scanning Electron Microscopy (SEM) 20
2.4.1.1 High Vacuum mode 20
2.4.1.2 Low Vacuum mode. 20
2.3.2 Electron Probe Micro Analyser 20
2.3.3 XRD Analysis 21
2.3.4 Clay Fractions 21
2.3.5 Clay Concentrates 21
2.4 Short Wave Infrared Analysis 22
2.4.1 Identification of Sample Mineralogy 23
2.4.2 Specific Absorption Features of Chlorites 24
2.4.3 Illite crystallinity as determined by the Kübler and m-Kübler values 25
2.4.4 Illite Polytypes 26
2.5 Identification of Mineral Phases 28
2.5.1 Tourmaline 28
2.5.2 Illite 28
2.5.3 Chlorite 28
2.6 Temporal Relationships Between Mineral Phases 28
2.6.1 Basement 28
2.6.2 Sandstones 29
2.7 Whole Rock Geochemistry 29
2.7.1 Chemical Analysis Method 29
2.7.2 Geographical Information Systems Technical Method 30
3 RESULTS 31
3.1 Alteration types, their Distribution and Petrology 31
3.1.1 Petrographic Analysis 34
3.1.2 Back Scattered Electron Imagery 41
3.2 Other Phases 44
3.2.1 Iron oxide and oxyhydroxides 44
3.2.2 Titanium Oxides and Sulphides 44
3.2.3 Kaolin Group Minerals 45
3.2.4 Quartz 45
3.3 Paragenesis of Alteration Mineralogy at the Phoenix Deposit. 46
3.4 Mineral Chemistry 48
3.4.1 Tourmaline 48
3.2.1.2 Occurrences 48
3.4.2 Illite 54

3.4.3 Chemical Composition of Illite 55
3.4.4 Chlorite 57
3.4.5 Chlorite Composition 58
3.5 Illite Crystallinity 61
3.5.1 Kübler value in Clay Fractions 61
3.5.2 M-Kübler in Clay Concentrates 62
3.6 Illite Polytypes 66
3.6.1 Clay Fractions 66
3.6.2 Clay Concentrates 70
3.7 Near Infrared Spectra Surrounding the Phoenix Deposit 75
3.7.1 Petrographic Analysis 82
3.7.2 Illite Polytypes and Features in the NIR 83
3.8 Whole Rock Geochemistry 84
3.8.1 Boron 84
3.8.2. Magnesium Oxide 85
3.8.3. Potassium Oxide 86
3.8.4.Yttrium 87
4 DISCUSSION 88
4.1 Nature and Sequence of the Alteration Associated with the Phoenix Deposit. 88
4.1.1 Tourmalines 88
4.1.2 Illite Polytypes 90
4.1.3 Chlorite Polytypes and Chemistry. 92
4.2 Whole Rock Geochemistry 92
4.3 Near Infrared Spectroscopy of the Alteration Sequence above the Phoenix Deposit. 93
4.4 Role of The Sandstone Extension to the WS Shear to Hydrothermal Activity in the Athabasca Sandstones 95
5 CONCLUSIONS 97
5.1.1 The Identification and Description of Key Alteration Minerals Surrounding the Phoenix Deposit and their Chemistry, Distribution and Timing of Their Crystallisation. 97
5.1.2 Evaluation of the Role of the WS Shear and the Sandstone Extension to the WS Shear and their Association with the Distribution of Alteration Mineralogy Surrounding the Phoenix Deposit. 97
5.1.3 Evaluation of The Polytypes and Crystallinity of Illite in the Alteration Halo Surrounding the Phoenix Deposit. 98
5.1.4 Determination and Evaluation of Behaviour and Source of NIR Variation Observed Above the Phoenix Deposit. 98
5.1.5 Whole Rock Geochemistry Overlying the Phoenix Deposit 98
5.1.6 Application of Techniques to Exploration 99
6 REFERENCES 100

List of Tables.

Title	Page Number
Table 1: Summary of the Manitou Falls and Read Formations on the Wheeler River Property.	10
Table 2: XRD analysis carried out on samples from the alteration halo of the Phoenix Deposit.	21
Table 3: Technical specification of Terraspec device used in this study.	23
Table 4: Absorption features used in the identification of minerals using SWIR.	24
Table 5: Absorption features of various species of chlorite.	24
Table 6: Positions of calculated d values (Å) and intensity of polytypes of illite observed in this study.	27
Table 7: Tur1 composition	49
Table 8: Basement Tur2 composition	50
Table 9: Sandstone Tur2 composition	50
Table 10: Basement M1 composition	55
Table 11: Sandstone M1 composition	55
Table 12: C1 chlorite	58
Table 13: C2 early sudoite	58
Table 14: C3 late sudoite	59
Table 15: Illite polytypes from Clay Fraction analysis identified in the Sandstone Extension to the WS Shear structure samples and non WS-Shear Structure samples	67
Table 16: Illite polytypes in DDH WR277	69
Table 17: Illite polytypes in DDH WR286.	69
Table 18: Illite polytypes in DDH WR380.	69
Table 19: Illite polytypes in WS Shear samples.	70
Table 20: Illite polytypes from elsewhere in the Manitou Falls Sandstones.	70
Table 21 Illite polytypes present in basement samples.	70
Table 22: Illite polytypes from vein samples overlying the Phoenix Deposit.	72
Table 23: Illitic polytypes and the position of the NIR absorption features.	81
Table 24: Review of magnesiofoitite and uranium mineralisation paragenesis	87
Table 25: Differences in samples from the WS Shear and Samples away from the WS Shear	94

List of Figures.

Title	Page Number
Figure 1: The Phoenix Deposit within the Athabasca Basin	6
Figure 2: Bedrock geology of sub-Athabasca basement rocks.	8
Figure 3: Distribution of basement faults in the south-east of the Athabasca Basin	9
Figure 4: Geological sketch map of Athabasca Basin showing outlines of the seven deposystems and the location of Phoenix in the south-east of the basin.	11
Figure 5: Generalised geological settings of monometallic and poly-metallic unconformity-associated uranium deposits in the eastern Athabasca Basin.	12
Figure 6: Regional clay alteration phases in the south eastern Athabasca Basin.	13
Figure 7: Stratigraphic schematic of the Phoenix Deposit	14
Figure 8: Schematic cross-section of the Phoenix Deposit	16
Figure 9: Location of samples collected during sandstone dominated systematic Diamond Drill Core sampling.	18
Figure 10: Typical absorption patterns for common minerals noted in the alteration package of Phoenix	24
Figure 11: Position of the Full Width at Half Maximum (FWHM) on an illite-rich XRD diffractogram displaying both 2θ and d spacing (Å).	26
Figure 12: Schematic of chlorite and Illite distribution around the Phoenix Deposit.	32
Figure 13: General mineral paragenesis for the basement rocks of the Phoenix Deposit.	46
Figure 14: General mineral paragenesis for the Read and Manitou Falls Members overlying the Phoenix Deposit.	47
Figure 15: Calculated Total vs. X site vacancy in tourmalines from the alteration halo of the Phoenix Deposit.	49
Figure 16: Ternary plots of tourmaline compositions from the Phoenix Deposit.	51
Figure 17: Binary plot of x-site vacancy vs $Al_Y/(Al_Y+Mg+Fe)$.	52
Figure 18: Binary plot of x-site vacancy vs Y-site Mg/(Mg+Fe) ratio.	52
Figure 19: Binary plot of x-site vacancy vs F.	53
Figure 20: Molar proportion Al-Si-Fe ternary diagram of white mica compositions in the alteration halo of the Phoenix Deposit.	56
Figure 21: C1 chlorite composition on basis of 14 oxygens.	57
Figure 22: An Al-Mg-Fe ternary diagram for chlorites around the Phoenix Deposit.	59
Figure 23: Clay fraction 10 Å Full Width at Half Maximum (FWHM) vs sample depth	60
Figure 24: Clay concentrates 10Å Full Width at Half Maximum (FWHM) vs sample depth	61
Figure 25: m-Kübler values of clay concentrate from samples in the Athabasca Sandstones surrounding the Phoenix Deposit.	63
Figure 26: Kübler values of clay fractions from samples in the Athabasca Sandstones surrounding the Phoenix Deposit.	64

Title	Page Number
Figure 27: XRD diffractogram of clay fraction separates from non-shear samples collected from the alteration halo surrounding the Phoenix Deposit.	65
Figure 28: XRD diffractogram of clay fraction of shear samples collected from the alteration halo surrounding the Phoenix Deposit.	66
Figure 29: Distribution of illite polytypes and chlorite phases determined with XRD through the alteration halo of the Phoenix Deposit from clay fractions.	68
Figure 30: Distribution of illite polytypes and chlorite phases determined with XRD through the alteration halo of the Phoenix Deposit from clay concentrates.	71
Figure 31: Clay fraction Kübler Value of illite polytypes determined via XRD from Athabasca sandstone units overlying the Phoenix Deposit.	72
Figure 32: Clay concentrates m-Kübler Value of illite polytypes determined via XRD from Athabasca sandstone units overlying Phoenix deposit.	73
Figure 33: Example spectra for samples illustrating the NIR absorption features.	74
Figure 34: Approximate location of NIR absorption features.	75
Figure 35: Fe_2O_3 (total) abundance in DDH WR277, WR286 and WR380.	76
Figure 36: Example Spectra for samples illustrating the NIR absorption features.	77
Figure 37: Distribution of the location of the NIR absorption features around the Phoenix Deposit's alteration halo.	78
Figure 38: Classified distribution of the location of NIR features around the Phoenix Deposit alteration halo	79
Figure 39: Phase relationships of samples which exhibit low NIR absorption features analysed via SWIR	80
Figure 40: Whole rock interpolations of B (fusion) through the sandstones.	82
Figure 41: Whole rock interpolations of MgO through the sandstones.	83
Figure 42: Whole rock interpolations of K_2O through the sandstones.	84
Figure 43: Whole rock interpolations of Y through the Sandstones.	85
Figure 44: Paragenetic sequence of alteration products and the role of the Sandstone Extension to the WS Shear	94

List of Plates

	Title	Page Number
Plate P1	Photomicrograph Imagery	34
Plate P2	Photomicrograph Imagery	35
Plate P3	Photomicrograph Imagery	36
Plate P4	Photomicrograph Imagery	38
Plate P5	Photomicrograph Imagery	39
Plate S1	Back Scattered Electron	41
Plate S2	Imagery	42-43

List of Appendices.

Appendix 1	**Geological Survey of Canada Open File Report**
1.1	Geological Survey of Canada, Open File Report 7463
Appendix 2	**Sample Locations**
2.1	Drill core collar locations
2.2	Thin section and SEM sample locations
Appendix 3	**Electron Microprobe Results**
3.1	Tourmaline raw EPMA Data
3.2	Chlorite raw EPMA Data
3.3	Illite raw EPMA Data
Appendix 4	**Short Wave Infrared Spectroscopy (SWIR) Analysis**
4.1	Shortwave Infrared spectra of samples collected
4.2	Mineral identification using the Spectral Geologist Software
Appendix 5	**X Ray Diffraction (XRD) Analysis**
5.1	Whole rock powder sample diffractograms
5.2	Clay concentrate sample diffractograms
5.3	Clay fraction XRD Analysis of clays from the study area.

1. INTRODUCTION

1.1 Objectives.

This study took a holistic approach to identifying and characterising the alteration minerals surrounding the Phoenix Deposit and to develop tools potentially useful in exploration for concealed uranium deposits. The objectives of this study were to:

- Identify key alteration minerals surrounding the Phoenix Deposit and describe their chemistry, distribution and timing of their crystallisation.
- Evaluate the role of the WS Shear and the Sandstone Extension to the WS Shear and their association with the distribution of alteration mineralogy surrounding the Phoenix Deposit.
- Determine the crystallinity and polytypes of illite in the alteration halo surrounding the Phoenix Deposit.
- Determine and evaluate the behaviour and source of NIR variation observed above the Phoenix Deposit.

1.2 Rationale for Study and Outline of the thesis

Exploration targets for Athabascan type unconformity uranium deposits are commonly elongate highly reflective geophysical features spatially associated with graphitic conductors. The small size of deposits, but exceptionally high grade and discrete, spatially limited distribution of tracer elements make exploration for such deposits a challenge.

Two years before the discovery of the Phoenix Deposit a drill core was drilled directly over the deposit but terminated on drilling conditions associated with intense alteration (Kerr, 2010). This foreshadowing of the discovery of the Phoenix Deposit has acted as a driver for this study to identify tools which could have aided in identifying the underlying prospectivity.

This thesis contains three main sections:

The first section introduces Athabascan unconformity-related deposits and their location, alteration mineralogy and morphology. The Phoenix unconformity uranium deposit, including the WS Shear structure, is introduced.

The second section - The methods and results, details the sampling protocol and the location of samples collected at the Phoenix Deposit, the methods employed to analyse those samples and the results.

Finally, the results are discussed in relation to the nature and sequence of alteration in the sandstones and basement and the role the WS Shear and the Sandstone Extension to the WS Shear structures had in the alteration sequence, the anytical techniques outlined in the second section are reviewed as exploration tools.

1.3 Previous Work

1.3.1 Past Work Undertaken on the Alteration of the Phoenix Unconformity-Related Uranium Deposit.

Since its discovery in 2007, various studies have looked at aspects of the Phoenix Deposit; O'Connel (2015) studied tourmalines from samples overlying the Phoenix Deposit, and found them to be similar to those from other Athabascan uranium deposits. Kerr (2010) presented the first description of the alteration on the Phoenix Deposit alongside its structural setting and the exploration history of the property and the discovery of the Phoenix Deposit. Four technical reports, resource estimates, and most recently, a Preliminary Economic Statement (Arseneau and Revering, 2010; Roscoe, 2014; Roscoe and Mathisen, 2015, Repais, 2016, respectively) have mentioned the alteration and the morphology of the orebody and considered the role of the WS Shear in the basement and the Sandstone Extension to the WS Shear as a potential fluid conduit.

Multielement statistical analysis has been performed in the sandstones overlying Phoenix (Chen et al. 2017). Also, a recent paper by Li et al. (2017), modelled the fluid flow from the WS Shear structure but offered no comment on alteration mineralogy or chemistry. Power (2014) surveyed surficial deposits overlying the deposit, which was initiated in conjunction with this study.

1.3.2 Basement Shears Associated with Unconformity-Related Uranium Deposits

The majority of unconformity-related uranium deposits in the Athabasca Basin are hosted at, near or within basement hosted shear zones (Jefferson et al. 2007), which are interpreted to have acted as fluid pathways prior, during, and after uranium mineralisation (Fayek and Kyser 1993). At the Phoenix Deposit, this manifests itself in the basement as the WS Shear structure.

The WS Shear structure is known to have been active during the deposition of the Read Formation resulting in 10 m of displacement across the unconformity (Kerr, 2010). Upwards into the sandstone, this is thought to have caused fracturing in a loosely defined area of brecciation termed the 'Sandstone Extension to the WS Shear'.

There is prior evidence of elemental migration up the Sandstone Extension to the WS Shear (Power, 2014). Li et al. (2017), modelled the pathways of mineralising fluids around Phoenix and the basement hosted, Gryphon Deposit, 5 km to the east. At the Phoenix Deposit, Li et al. (2017) identified the WS Shear Structure in the basement as a fluid pathway, with a presumed continuation of the fluid pathway into the overlying sandstones.

1.3.3 Tourmaline Mineral Chemistry

Tourmaline group minerals varied chemistry, and a relative ease of identification has led them to become important petrological tools in identifying geological environments and fluid regimes during their formation (e.g., Jolliff et al. 1987; Dyar et al. 1999; Novák et al. 1999 and Adlakha and Hattori 2016).

Tourmaline is an indicator mineral for uranium exploration in the Athabasca basin (Hoeve and Sibbald 1978, Alexandre et al. 2005 and Rosenberg and Foit 2006), principally because it is ubiquitous in proximity to Athabascan uranium deposits. Studies on tourmaline within Athabascan uranium deposits (Hoeve and Sibbald 1978, Alexandre et al. 2005, Cloutier et al. 2009, Mercadier et al. 2012. Adlakha et al. 2013 and Adlakha et al. 2017) have mainly concentrated on deducing its relationship to uranium mineralisation and the composition of the mineralising fluids. Such studies have determined that the late, alkali-deficient magnesiofoitite in the vicinity of Athabascan deposits is synchronous with uranium mineralisation (Hoeve and Sibbald 1978, Kotzer and Kyser 1995, Fayek and Kyser 1997, Derome et al. 2005, Adlakha, 2015 and Adlakha et al. 2017), and represents the mixing of a reducing ore fluid and an oxidising basal fluid (Kotzer and Kyser, 1990 and Ng et al. 2013b).

1.3.4 Alteration Mineralogy of Previous Studies.

The Kübler index has been used to identify illite crystallinity surrounding the Cigar Lake Athabascan uranium deposit (Percival et al. 1993), along structural trends in the Thelon basin (Rigeler et al. 2014 and Beyer et al. 2010) and in prospecting for unconformity-related uranium deposits in the Australian Alligator Rivers Uranium field (Polito et al. 2011). The results have been used in generating temperature estimates for illitisation. In illite and muscovite polytypes occur due to changes in the chemical composition or organisation of the layered silicate structure of the mineral, as a result of an increasing temperature.

Polytypes of illites associated with unconformity-related uranium deposits have been studied at the Shear Creek deposit (Laverret et al. 2006), K-Zone in the Wheeler River property (Cloutier et al. 2010), and the P2 zone associated with the McArthur River deposit (Adlakha et al. 2013). The majority of studies found illites to be similar in composition but crystallinity, grain size and texture differ.

Chlorite is common in the Athabasca basin and it is considered to be associated with uranium mineralisation (Voultsidis et al. 1982). Chlorites at the K-Zone (Cloutier et al. 2010), P2 zone (Adlakha et al. 2013), McArthur River, Dawn and Rabbit Lake deposits (Alexandre et al. 2005) are similar to those identified in the alteration halo of the Phoenix Deposit.

Short Wave InfraRed (SWIR) is commonly used to determine the alteration mineralogy (Hauff 2008). Various studies have applied the technique, including automated systems for core logging (Mathieu et al. 2017), the orebody of the McArthur River uranium deposit (Adlakha et al. 2013), for quantitative analysis (Zhang et al. 2001) and for regional surveying (Bosman et al. 2012).

1.3.5 Contribution to Knowledge

I have published two Open-File Reports with the Geological Survey of Canada (Open Files 7463 and 7366), these are provided in Appendix 1. I have produced abstracts and given presentations at the Society of Economic Geologists Minerals Colloquium, Toronto in 2012 and 2013, and the Saskatchewan Geological Survey Open House in 2011 and 2012. I also presented at the Joint Annual Meeting of the Geological Association of Canada and Mineralogical Association of Canada in St Johns, 2012.

1.4 Regional Geology

The Athabasca Basin is in the northern part of the provinces of Saskatchewan and Alberta, between 57° and 59° north, and 104° and 111° east. Tectonically, it lies within the transition of the Archean to Paleoproterozoic metamorphic terranes of the Canadian shield. It is one of a series of Proterozoic basins in northern Canada, including the Thelon, Hornby Bay, Elu and Dessert Lake Basins.

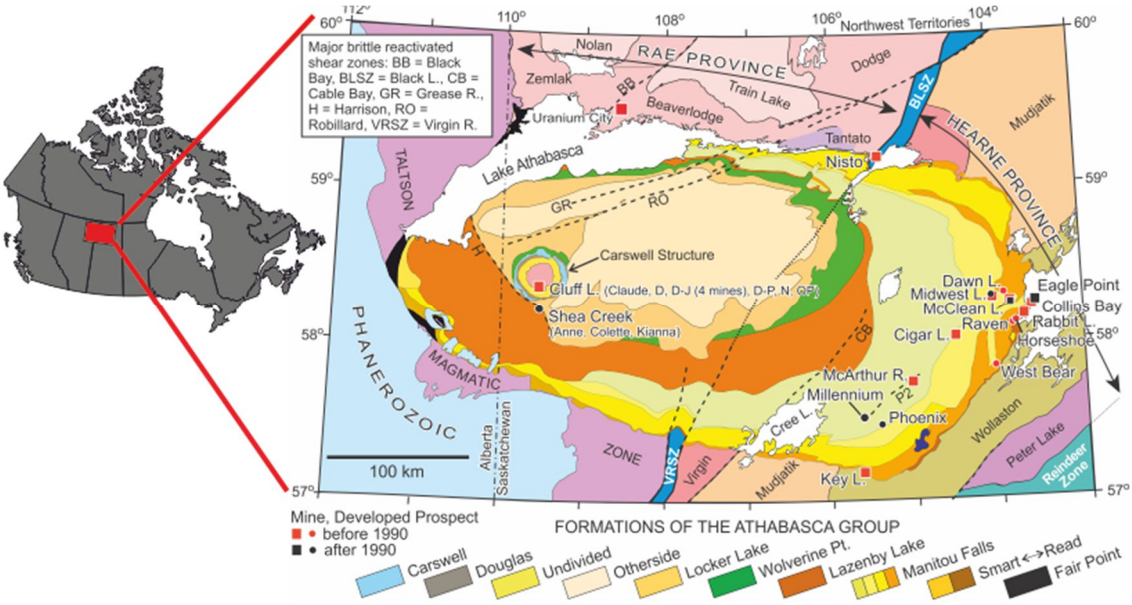

Figure 1: The Phoenix Deposit within the Athabasca Basin, from Jefferson et al. (2007). The Phoenix Deposit is located in the south-eastern corner of the basin to the south of McArthur River deposit and the east of Millennium deposit.

1.4.1 Basement Geology

The majority of the producing and past-producing uranium deposits in the Athabasca basin overlie the transition zone between the Wollaston and Mudjatik domains of the Hearne Province (Annesley et al. 2005), as illustrated in Figure 1. Phoenix, McArthur River, Millennium and Cigar Lake deposits lie within this transitional zone. The transition zone comprises pelitic, quartzose and arkosic paragneissic units that are isoclinally folded and interleaved with Paleoproterozoic orthogneiss and abundant pegmatitic intrusions (Jefferson et al. 2007). Graphitic pelites and paragneisses comprise 70 to 85% of the metasedimentary sequence of the Hearne Province, which is similar in basement geology to many of the unconformity-related deposits in the basin (Annesley et al. 2005 and Jefferson et al. 2007). Recent exploration successes have yielded discoveries at Patterson Lake South and Arrow in the south-west of the basin.

The Athabasca Basin was formed between 1760-1550 Ma as a series of north-east to south-west sub-basins controlled by major Hudsonian age faults in the underlying basement rocks (Ramaekers

et al. 2007 and Alexandre et al. 2009), with the youngest sediments in the basin being dated to 1541 ± 13 Ma (Creaser and Stasiuk 2007). These Hudsonian age faults have been interpreted to have played a significant role in localising uranium-bearing fluids in the basement during uranium mineralisation (Jefferson et al. 2007) and as such have represented narrow targets for exploration. The dominantly quartzose Athabasca Group is subdivided into ten formations, which include four fluvial, unconformity-bound sequences (Ramaekers et al. 2007).

In the East, the Mudjatik domain is a northeast-trending, shearbounded belt consisting mainly of felsic gneisses with subordinate metasediments, of which the protoliths vary in depositional age from between 2.1 to ca. 1.85 Ga (Tran et al. 2008). The lowest sequence consists of quartzite, amphibolite, and rare banded iron formation units (Harper et al. 2005). The western Mudjatik Domain is highly metamorphosed, consisting of psammitic to pelitic gneiss, which represents 70–80% of the metasedimentary rocks occurring in the Wollaston Domain (Annesley et al. 2005). Also present are garnet, cordierite, sillimanite, titanium-rich biotite, and perhaps most significant to models of Athabascan type deposits - local enrichments in graphite.

To the west, the Wollaston domain is a north-east trending fold and thrust belt composed of Paleoproterozoic Wollaston Group metasediments, of pelitic, quartzose and arkosic paragneissic units isoclinally folded and interleaved with Paleoproterozoic orthogneiss and abundant pegmatitic intrusions (Jefferson et al. 2007). Graphitic pelites and paragneisses compose 70 to 85% of the metasedimentary sequence of the Hearne Province (Annesley et al. 2005 and Jefferson et al. 2007).

The magnetic low identified through total magnetic intensity maps (Figure 3) hosts the majority of discovered deposits in the southeastern Athabasca basin. The regional basement geology is presented in Figure 2.

Location of the Phoenix Deposit in Relation to Regional Basement Geology of the Athabasca Basin and Alteration Corridors

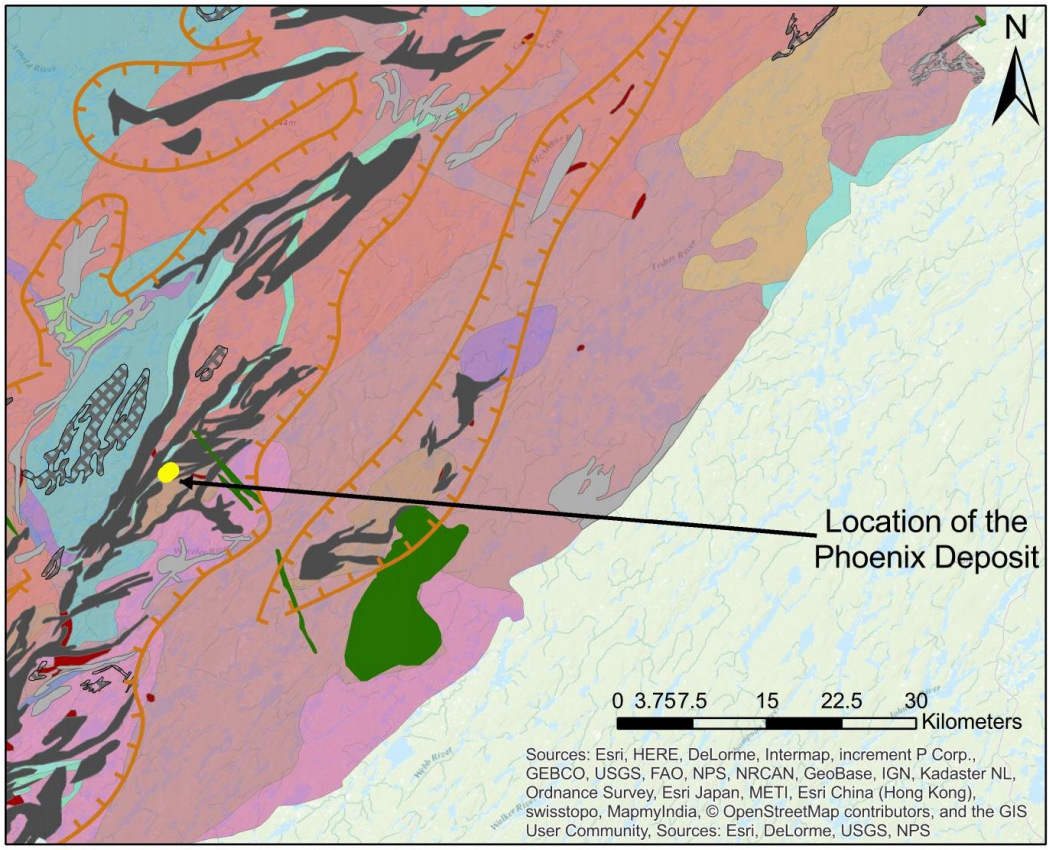

Modified from: Card,C.D. and Heath,P .(2015):Bedrock geology of sub-Athabasca basement rocks (NT S74H); Saskatchewan Geological Survey, Saskatchewan.Ministry of the Economy ,Geoscience Map 2015-1.

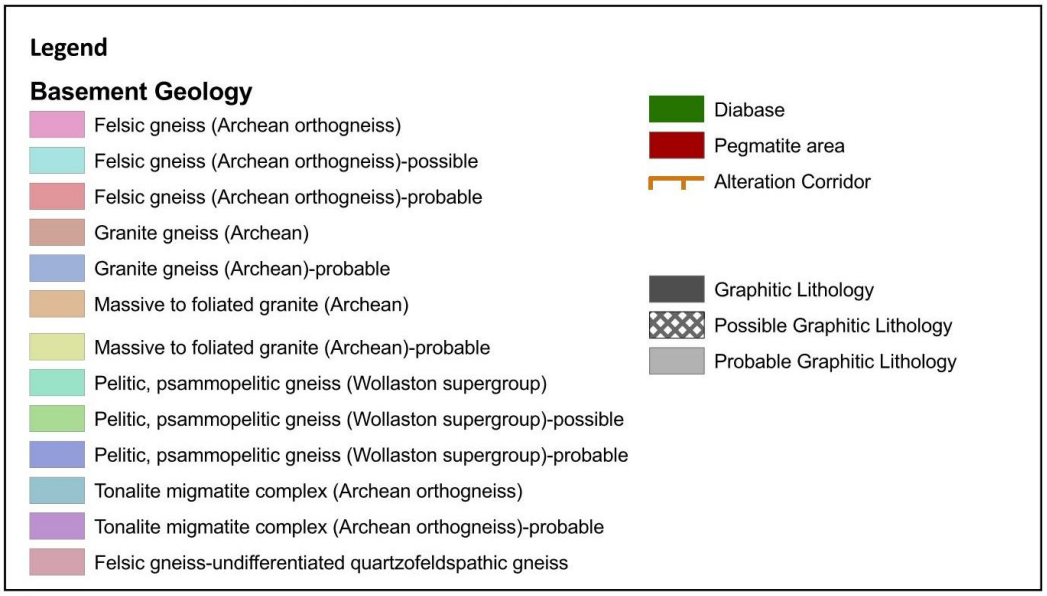

Figure 2: Modified from Card and Heath. (2015). Geology of basement rocks. The location of the Phoenix Deposit is denoted by the Yellow circle overlying graphitic lithologies.

1.4.2 Regional Structural Geology

Athabascan unconformity-related uranium deposits are for the most part situated at, or very close to the apex of large fault structures in the basement of the Athabasca Basin (Kyser and Cuney, 2008). The location of high-grade deposits is attributed to the interaction between oxidising

basinal fluids and reducing fluids derived from either the basement (Wilson and Kyser, 1987; Kotzer and Kyser, 1995 and Fayek and Kyser, 1997) or from the ingress of basinal fluids into the reducing basement and conversion into reducing fluids (Hoeve and Sibbald, 1978, Komninou and Sverjensky, 1996, Alexandre et al. 2005). The structure of the Athabasca Basin is dominated by multiple late, brittle faults, which offset the unconformity and overlying sediments. These are interpreted to represent the reactivation of basement shear zones and structures (Hoeve and Sibbald 1978, Hoeve et al.,1980, McGill et al. 1993, Card et al. 2007, Jefferson et al. 2007 and Tourigny et al. 2007). As with the Phoenix Deposit, these faults are present in sheared graphitic lithologies, which have experienced substantial offsets. The close relationship between reactivated basement faults hosted in graphitic lithologies and uranium deposits is a major target of exploration in the basin via geophysical methods (Jefferson et al. 2007).

The regional tectonic and structural setting of the Phoenix Deposit (Figure 3) is defined by three main sets of faults, a north-east trending group (white lines on Figure 3), follow the micro and macrostructure of the Wollaston and Mudjatik domains, inferring that this set of faults, which includes the WS Shear, represent reactivated Hudsonian structures (Annesley et al. 2005). The northwest (black lines on Figure 3) trending faults are not a major structural feature of Phoenix, but are shown to cut across the WS Shear and pelitic basement units (Arseneau and Revering 2010), While north-northwest (blue lines on Figure 3) faults are thought to be the youngest, and represent part of the Tabbernor fault system (Annesly et al. 2005).

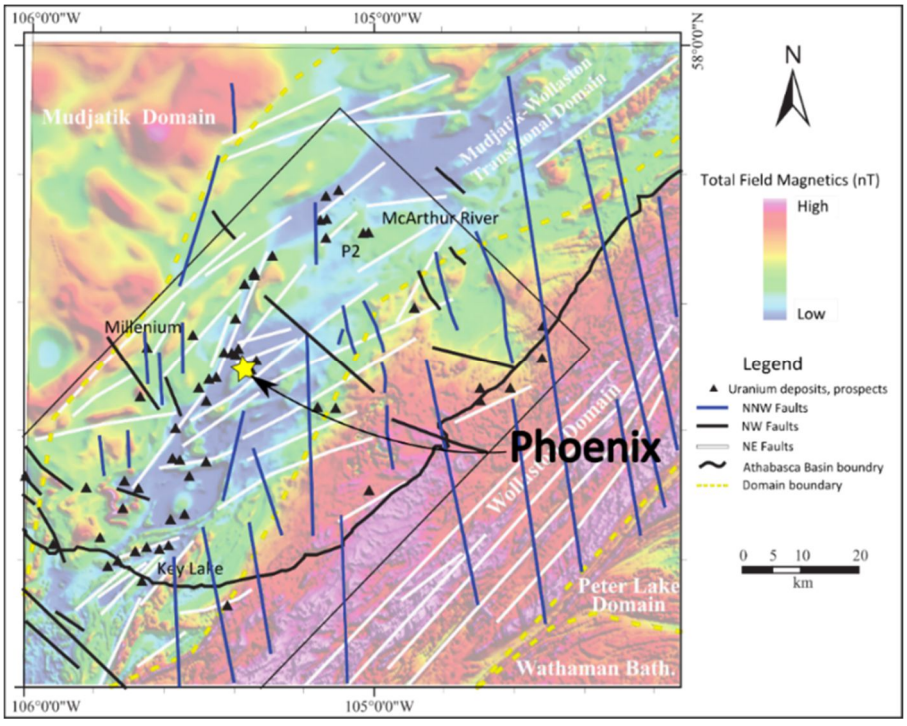

Figure 3: Modified from Li et al. (2015) Distribution of basement faults in the south-east of the Athabasca Basin, interpreted from aeromagnetic maps from Card et al. (2007). The Phoenix Deposit is indicated by a yellow star, blue lines are north north-west trending faults, grey lines are north-west trending faults, and

white lines are north east trending faults. Uranium deposits generally occur within proximity to north east tending fault structures.

1.4.3 Sandstone Geology

On a basin scale, the sedimentary units within the Athabasca Basin are split into five mainly paleoflow defined 'deposystems', which from west to east are the 'Bourassa', 'McLeod', 'Karras' (in the south), 'Moosonees' (in the north) and the 'Ahenakew' (Yeo et al. 2002). The Phoenix Deposit is in the Ahenakew deposystem (Figure 4.). The eastern deposystems (Karras, Akenakew and Moosonees) yield generally western paleoflow directions and sediments are subdivided into the Manitou Falls Formation (three Members) and the Read Formation. While the western deposystems (Fidler, McLeod and Bourassa) yield generally north and western paleoflow directions, and are subdivided into the Wolverine Point, Lazenby Carswell, Douglas, Otherside and Locker Lake formations. In the Ahenakew deposystem, the three members of the Manitou Falls Formation and the Read Formation are present, overlying the Phoenix deposit. These are summarised in Table 1.

Table 1: Summary of the Manitou Falls and Read Formations on the Wheeler River Property.

Unit Name	Description
Dunlop Member (MFd)	This member is a medium- to fine-grained quartz arenite with >1% mudstone, commonly an aggregate of clay intraclasts (claystone and mudstone, rarely siltstone or very fine quartz arenite) (Raemakers et al. 2007)
Collins Member (MFc)	This member is a quartz arenite containing 2 cm thick with >30% clasts of granule size and larger quartz. (Ramaekers et al., 2002) Throughout the eastern Athabasca Basin the Collins Member is also known to contain abundant 2–4 mm granules and sparse pebbles (Jefferson et al. 2001).
Bird member (MFb)	This member is at least 2% conglomerate, defined as beds thicker than 2 cm with at least 30% conglomeratic clasts. Geochemical data suggest that the MFb originally ranged from sublithic to subarkosic. Clay matrix is minor, commonly 1–3%; clay intraclasts are sporadic in quartz arenite and conglomerate beds (Ramaekers et al. 2002).
Read Formation (RF)	This member is laterally and vertically heterogeneous succession of low-angle crossbedded quartz arenite, quartz pebble conglomerate, and red silty mudstone (Ramaekers et al. 2007).

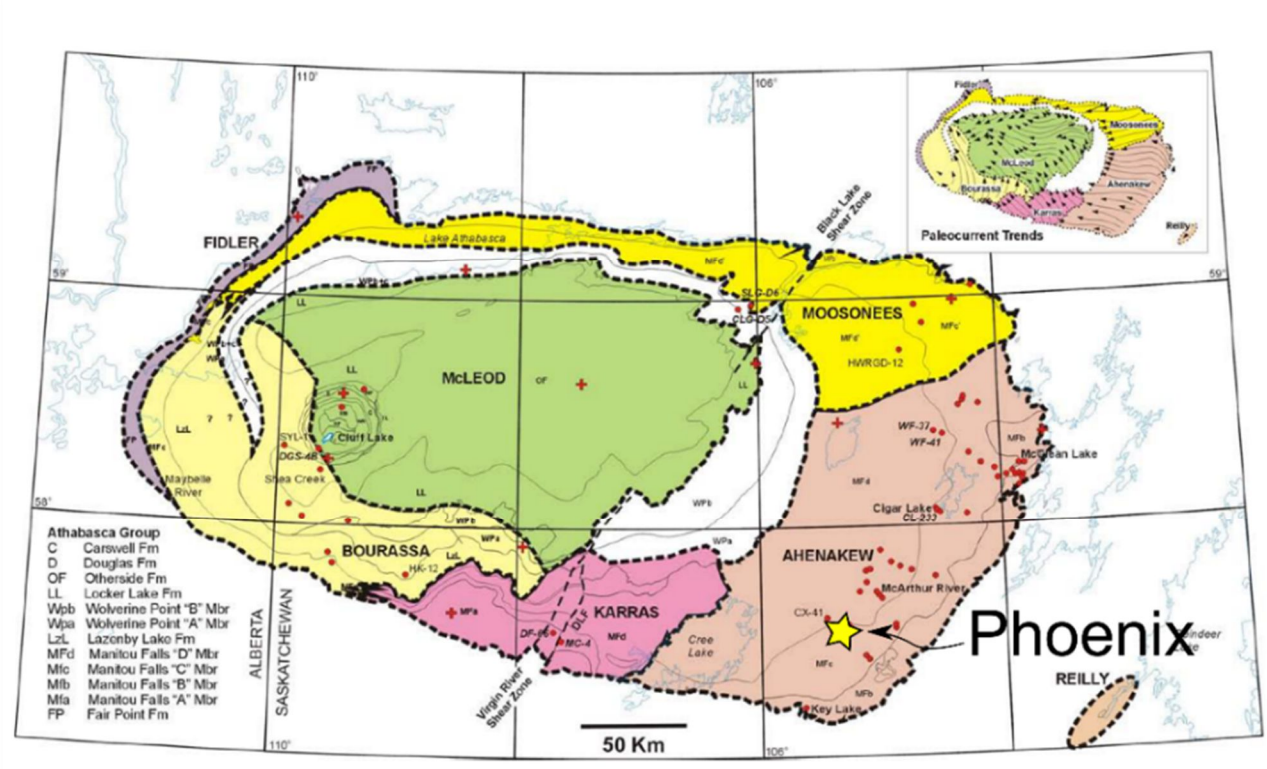

Figure 4: Modified from Yeo et al. (2003) Geological sketch map of Athabasca Basin showing outlines of the seven deposystems and the location of the Phoenix Deposit in the south-east of the basin.

1.5 Athabascan Unconformity-Related Uranium Deposits.

Unconformity-related uranium deposits are spatially and genetically linked to major faults in the basement, which transect the paleo-weathered basement rocks. The overlying lithologies, which are dominantly sandstone with some siltstones are collectively termed the Athabasca Group sandstones. Unconformity-related uranium deposits are grouped into two types, based on the hypothesised fluid flow/inflow from the basement and the location of the majority of orebody in relation to the unconformity. These are 'Egress' type deposits in sandstone and 'ingress'-type basement-hosted deposits (Jefferson et al. 2007).

1.5.2 Egress Type Deposits

'Egress' deposits occur either along the unconformity, straddling both the Athabasca Group sandstones and the upper basement lithologies or occur entirely within the Athabasca Group sandstones, as pods or 'stringers'. These deposits include Cigar Lake, Maurice Bay, and minor perched uranium mineralisation at Centennial (Reid et al. 2010). Such deposits are typically 'polymetallic', containing uraninite as the principal uranium-bearing ore mineral with complex assemblages of sulphide minerals containing lead, nickel, cobalt, arsenic, zinc and molybdenum

(Jefferson et al.,2007). Alteration surrounding these deposits is extensive and forms illite – kaolinite – chlorite alteration haloes within the Athabascan Group sandstones along the deep crustal faults.

1.5.2 Ingress-Type Deposits

'Ingress' deposits, such as Sue Zone C, Millennium, Eagle Point, basement uranium mineralisation at Centennial and McArthur River Zone 2, are entirely basement hosted and typically within or proximal to faults and shears (Andrade 1989, Marlatt et al. 1992, Tourigny et al. 2001, Cloutier et al. 2009 and Alexandre et al. 2012). Alteration surrounding these deposits is considerably more narrow than in egress-type deposits and shows a zoning from illite ± sudoite alteration, followed by a sudoite ± illite and finally a zone of Fe-Mg chlorite ± sudoite (Quirt 2003 and Jefferson et al. 2007).

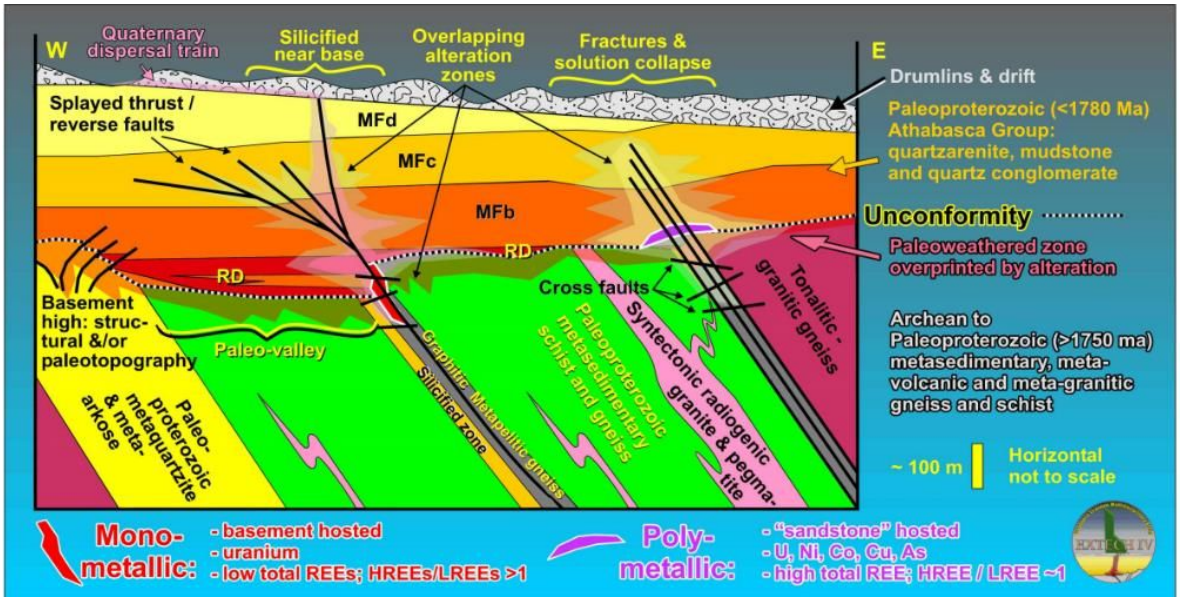

Figure 5: Generalized geological settings of monometallic and poly-metallic unconformity-associated uranium deposits in the eastern Athabasca Basin. In ascending stratigraphic order, from Jefferson et al. (2007).

1.6 Wheeler River Property Geology

In the vicinity of the Phoenix Deposit, and throughout the Wheeler River Property, the Athabasca Sandstone is composed of a 170 to 560 m thick sequence dominated by the Manitou Falls Formation quartz arenite. The Formation is grouped into three members, the Bird (MFb), Collins (MFc) and the Dunlop (MFd) members, which can be differentiated based on conglomeratic and interclast material (Ramaekers et al. 2007). Below the Manitou Falls Formation, the Read Formation (RF) is composed of a lower pebble-cobble conglomeratic unit overlain by an upper unit of well-sorted sandstone to pebbly sandstone. The formation varies in thickness, from over 200 m west of the quartzite ridge, to absent above quartzite ridge (Arseneau and Revering. 2011). The

MFb is similar to the RF but features at least 1.2% conglomeratic material in beds thicker than 2cm. It is occasionally absent above the quartzite ridge (Arseneau and Revering 2011).

1.6.1 Alteration on the Wheeler River Property

The principal regional clay phase in the sandstones of the Athabasca Basin is diagenetic dickite (Jefferson et al. 2007), however, at the Phoenix Deposit, excluding one localised sample, this is largely absent. The Wheeler River property, and thus the Phoenix Deposit lies within a broad illite anomaly that trends northeast from Key Lake to McArthur River (Earle and Sopuck 1989) as shown in Figure 6. Chlorite and 'dravite' are also present locally (Arseneau and Revering 2011), with a chlorite band running from the west of the Phoenix Deposit to 40 km south of Cigar Lake. Further east, running from McArthur River to the north of Key Lake a dravite anomaly is also present, although this is not in the vicinity of the Phoenix Deposit (Jefferson et al. 2007). Alteration within both the sandstones and the basement underlying the deposit is principally illite dominated, with kaolinite, tourmaline and chlorite (Arseneau and Revering 2012).

The basement rocks are composed of metasedimentary rocks belonging to the Wollaston and the Mudjatik domain and include graphitic and non-graphitic pelitic and semi-pelitic gneisses, quartzite and rare calc-silicate rocks together with felsic and quartz-feldspathic granitoid gneisses (Arseneau and Revering 2011). Granitic pegmatites are common, with coarse-grained K-feldspar, quartz and micas. Metasediments were metamorphosed to upper amphibolite metamorphic grade, with some facies metamorphosed to granulite facies in the Wollaston Group metasediments (Annesley et al. 2005). To the west of the Phoenix Deposit, a quartzite ridge, which is a major topographic feature

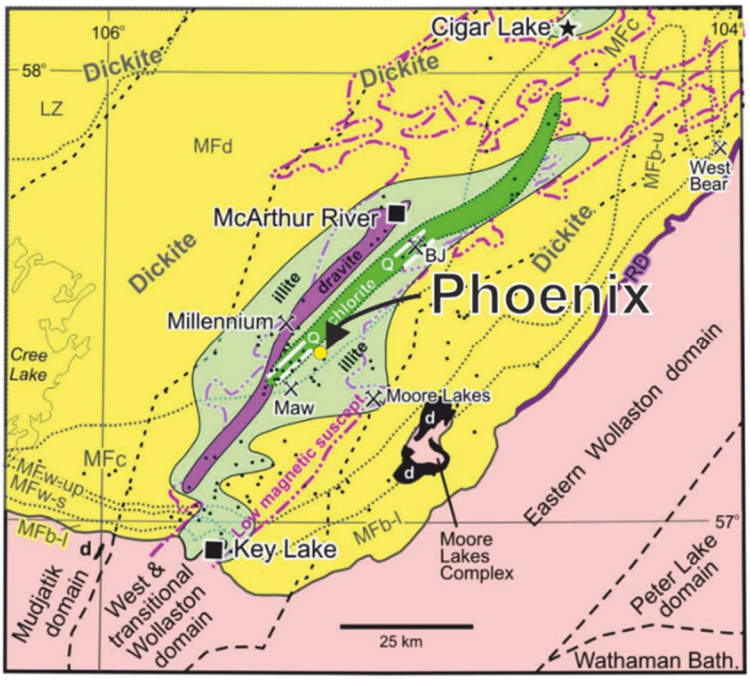

Figure 6: Modified from Jefferson et al. (2007). Regional clay alteration phases in the south-eastern Athabasca Basin. The Phoenix Deposit is located to the east of the regional chlorite trend in an area of regional illite dominated alteration.

at the unconformity and an interpreted impermeable and structural barrier (Arseneau and Revering 2010), dips between 45°-75° to the south-east, with an undulating azimuth of around 55°. Tallus deposits overly the north-west flank of the quartzite ridge and consist of angular fragments of quartzite, which in some areas of the property display associations with uranium mineralisation (Kerr, 2010).

1.6.2 Wheeler River Property Structural Geology

At the Phoenix Deposit, and within this study, the 'WS Shear' refers to the well-defined fault structure within the basement, while the 'Sandstone Extension to the WS Shear' refers to the poorly defined Extension to the basement fault into the overlying sandstones. Fault systems associated with unconformity-related deposits, (i.e. the Sandstone Extension to the WS Shear) above the Phoenix Deposit have been suggested as transit routes for metals to surface (Power 2014).

Various structural models have been proposed for the Wheeler River property. With the simplest being the property located to the east of an anticline (Kerr 2010). At Wheeler River, as with other properties, the juxtaposition of the mechanically competent quartzite and granitoid gneiss units alongside many kilometres of relatively incompetent graphitic pelite have provided favourable geology for the development of extensive thrust and strike-slip and/or wrench faults. These are juxtaposed alongside later normal faults, at the interface between competent/incompetent units.

Locally at the Phoenix Deposit, the quartzite unit appears to have acted as a 'backstop' for the thrusting and reverse faulting. To the westward side of the quartzite ridge (i.e. the opposite side to uranium mineralisation at the Phoenix Deposit) a small brittle fault zone occurs as a southeasterly

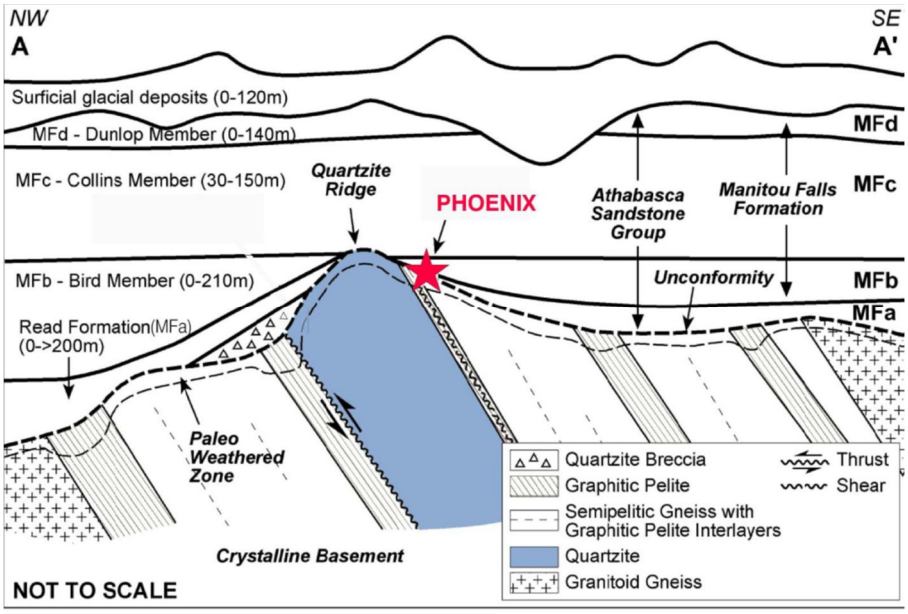

Figure 7: Stratigraphic schematic of the Phoenix Deposit, from Arseneau and Revering (2012). The Phoenix Deposit is located to the south-east of the quartzite ridge (blue) at the apex of a shear zone (termed the 'WS Shear') and the unconformity.

dipping thrust along the footwall of the quartzite. This structure was active during the deposition of the Read Formation and possibly during the MFc (Kerr 2010).

1.6.3 The Phoenix Uranium Deposit

The Phoenix Deposit, discovered in 2008 on the Wheeler River Property, is operated by Denison Mines Corporation (90%), and co-owned by JCU (10%). The total indicated mineral resource of 63,000,000 pounds of U_3O_8 is based on 232,000 tonnes of uranium at an average grade of 12.30% U_3O_8. In addition, the total inferred mineral resource is 1,100,000 pounds of U_3O_8 based on 7,800 tonnes of uranium with an average grade of 6.27% U_3O_8 (Repais and Mathisen 2018). Uranium mineralisation occurs mainly as pitchblende, with high levels of Cu (up to 3200 ppm) and Pb up to (2.25 wt %), and minor Ni, Co, As, Zn and Ag in the A and B orebodies (Arseneau and Revering 2011).

Uranium mineralisation at the Phoenix Deposit occurs in the form of uraninite/pitchblende (UO_2), with high-grade uranium present along the unconformity in flattened profiles and on the hanging and foot walls of the WS reverse fault (Kerr 2010). Uranium mineralisation along the WS Shear occurs as steeply dipping, thin (1-3m wide) parallel to sub-parallel bands for up to 20 m below the unconformity. Uranium mineralisation in the lowest 15 m of the Read Formation appears to be related to the Sandstone Extension to the WS Shear and hanging wall splays, indicating reactivation occurred along these faults after the deposition of the Read Formation and MFb member. Despite mineralisation extending into the basement, Phoenix is classified as a sandstone-hosted egress-type model (Roscoe et al, 2012).

This study uses a projection of the ore body produced by Denison Mines Corporation in 2011, at a cut-off grade of 0.1% U_3O_8 It is recognised that the actual area of uranium mineralisation extends beyond this, although with a lower grade and thickness (grade in % U_3O_8 x thickness in metres) of between 0.601 to 0.01.

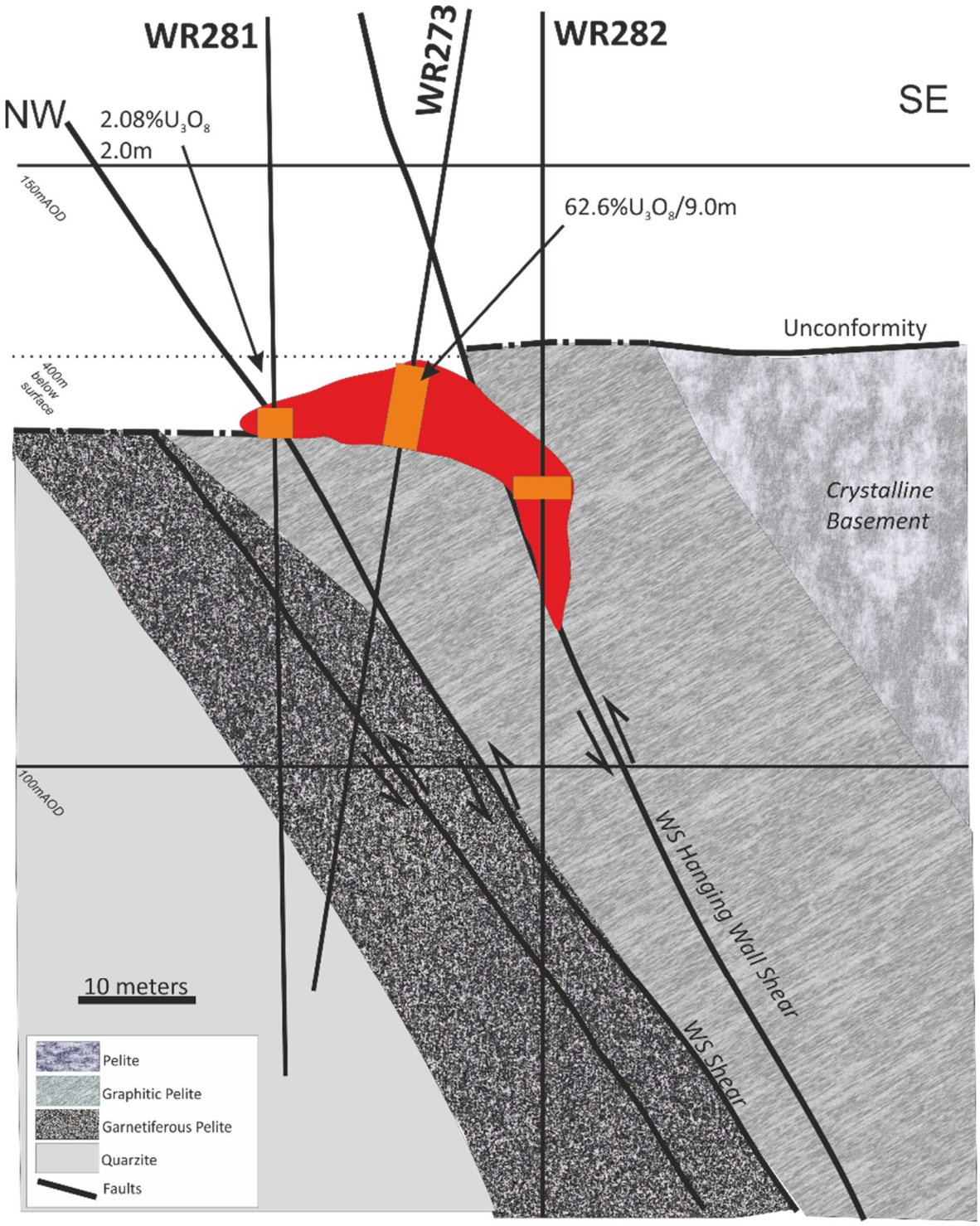

Figure 8: Schematic cross-section of the Phoenix Deposit. Uranium mineralisation is proximal to the unconformity between the early Paleoproterozoic crystalline basement rocks and the overlying Read Formation and Manitou Falls Formation units, the deposit is located approximately 400 m beneath the present-day surface. The WS Shear and associated Hanging Wall Shear (heavy dark lines) are major structural features associated with these deposits. The WS Shear is a north-east to south-west trending (055° azimuth) reverse fault that dips 55° to the SE at the base of the graphitic pelite along the footwall of the quartzite ridge, it continues into the sandstones, where it becomes poorly defined, both the WS Shear and the associated Hanging Wall Shear splay and become diffused. Red colouration represents inferred resource, orange is intercepts of mineralised material. (Modified from Gamelin et al. 2010).

2 METHODS

2.1 Sampling

2.1.1 Sample Details

A total of 299 samples were collected from 28 drill cores located directly above, below, around and up to 1.8 km from the Phoenix Deposit A and B zones, including 97 basement samples and 202 sandstone samples. Basement samples were variably hydrothermally altered metasedimentary rocks, pegmatite and quartzite, while the sandstone samples collected were variably altered, silicified and fractured. No samples were collected from the ore zone due to restrictions on taking radioactive material off-site.

Samples have been collected over two periods, the majority of basement samples and some sandstone samples (JD1A-JD4A, DPX1-DPX88 and the WS Shear and the Sandstone Extension to the WS Shear) were collected in early September 2011, while the second, sandstone dominated samples (DPX100+) were collected in August 2012. Where necessary, samples were split into subsamples based on their composition, texture and features. Detailed locations are provided in Appendix 2.1. Of particular interest in this study is the role of the WS Shear in the alteration of basement rocks and the sandstones overlying the Phoenix Deposit. Sampling and subsequent analysis was focussed on providing a comparison away from and within the WS Shear and the Sandstone Extension to the WS Shear. In the basement, samples were collected in the pelitic lithologies below the uranium mineralisation and along the unconformity to offer a comparison to the samples collected from the WS Shear. In the sandstones, similar reasoning was employed- samples were collected to determine the alteration phases along strike of the Sandstone Extension to the WS Shear, above and to the northeast and southwest of the Phoenix Deposit.

During sampling, special attention was also paid to the preferential collection of fractured and vein samples. Sampling in the sandstones centred on six drill cores spread along the graphitic conductor and associated uranium mineralisation, which had been drilled by Denison Mines Corporation and partners in the five years before 2012. Figure 9 illustrates their geographic spread.

2.1.2 Targeted Drill Cores

Drill core from six drill cores (outlined below and Figure 9) was targeted based on whole rock geochemistry of samples collected by Denison Mines Corp from the drill cores to aid in the collection of samples which were intensely altered or were high in elements which are considered

as geochemical tracers for uranium deposits. The leach and analytical method quoted below is presented in Section 2.1.3 Geochemical Analysis.

- WR 277 – To the north of the orebody, an area of elevated uranium (up to 2.4 ppm), arsenic (up to 1.74 ppm), lead (up to 4.35 ppm) values which extend through the sandstone. This is an area of extended uranium values, but not considered economic uranium mineralisation away from the WS Shear structure along the unconformity.
- WR 286 – To the north of the orebody – as a comparison to WR 277. Featured many of the same anomalous results as WR 277, however, is vertical and intersects the unconformity away from uranium mineralisation.
- WR291 – Directly over the 'B' orebody and a 'chimney' of high anomalous values of arsenic (up to 3.89 ppm), boron (up to 1840 ppm total via fusion), uranium (5.06 ppm), iron oxide(1.92 ppm) and thorium (21.2 ppm) alongside intense alteration.
- WR321- Centre area, between the 'A' and 'B' orebodies, area of a 'chimney' of anomalous values of arsenic (up to 1.26 ppm), boron (up to 2290), uranium (3.77 ppm), thorium (27.6 ppm) intermittently throughout the sequence.
- WR353- The southern extremity of the 'B' orebody.
- WR380- Located 1.8 m south of WR 353, to provide a baseline of samples not overlaying uranium mineralisation, and act as 'regional' samples overlying similar structures (geophysically and structurally) to the Phoenix Deposit, and to act as a control to observations from directly over the deposit.

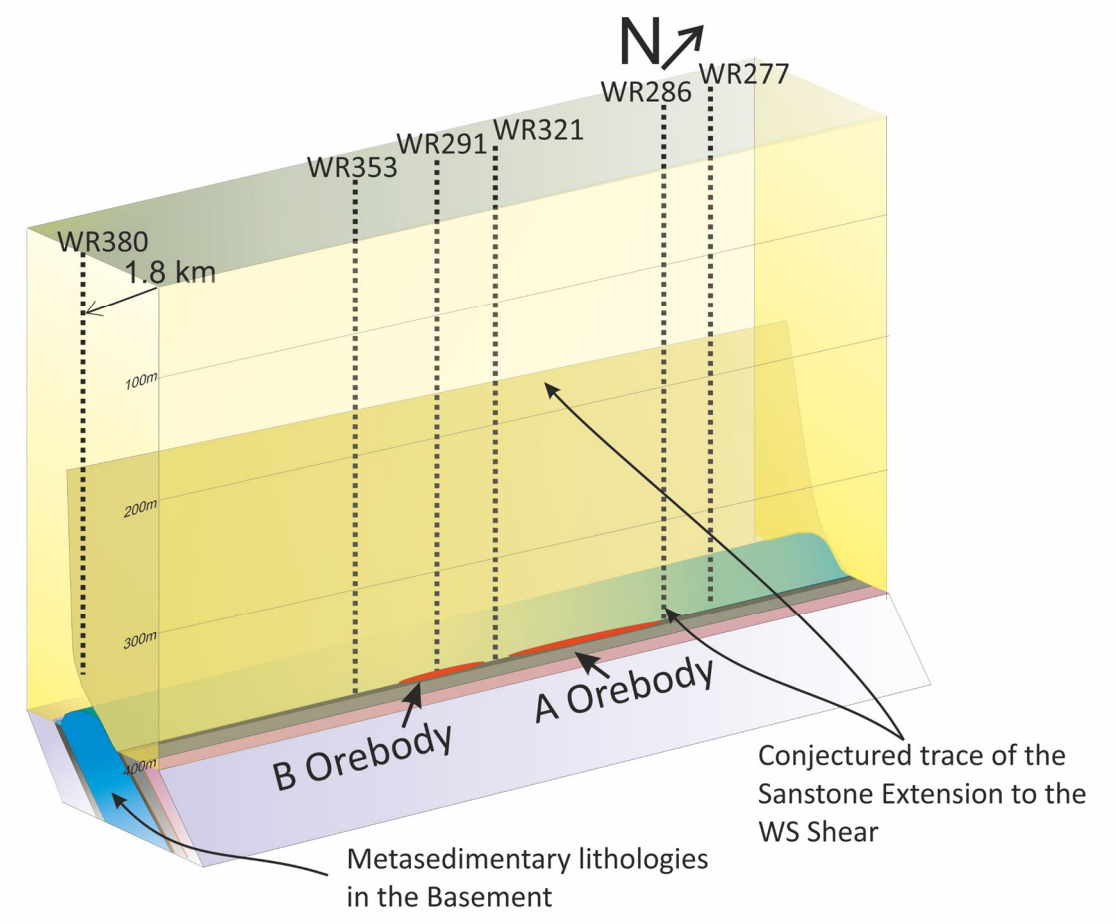

Figure 9: Location of samples collected during core sampling, drill core WR380 is 1.8 km to the south-west of the deposits. The A and B orebodies are based on internal Denison Mines Corp. reports and diagrams. Basement colours denote the metasedimentary lithologies in the basement; garnetiferous perlites (purple), graphitic schists (grey), quartzite (blue). The conjectured trace of the Sandstone Extension to the WS Shear is also denoted.

2.1.3 Geochemical Analysis

All the geochemical data quoted in Section 2.1.2 and below were produced at the Saskatchewan Research Council Geoanalytical Labs in Saskatoon, Canada for Denison Mines Corporation. Analyses which are indicated to be derived from the partial leach method (for arsenic, cobalt, copper, molybdenum, nickel, lead, uranium, vanadium and thorium) where produced by an aliquot of pulp was digested in a hot aqua regia bath for approximately 1 hour. Then diluted to 15ml using de-ionised water, followed by Inductively Coupled Plasma Mass Spectrometry (ICP-MS) or Inductively Coupled Plasma - Optical Emission Spectrometry (ICPOES).

For analysis, which were derived from total digestion (aluminium, iron, potassium, magnesium, phosphorus, lithium, tungsten, ytterbium, cerium, thorium), aliquots of pulp were digested in a hot mixture of concentrated acids of HF, HNO_3, and $HClO_4$. The residue was then dissolved in 15 ml of 5% HNO_3 and made to volume using de-ionised water before analysis. For boron, an aliquot of pulp was fused in a mixture of NaO_2/$NaCO_3$ in a muffle oven. The fused melt was then dissolved in de-ionised water and analysed by ICP-OES.

2.2 Preparation of Samples

2.2.1 Short Wave Infrared Samples

Whole rock samples for SWIR analysis were cut to produce a flat, clean surface using a band saw then air dried for a period of 1 - 4 hours before analysis at room temperature. Clay fraction and clay concentrate samples were produced via the methods described below and placed in plastic trays before analysis but thick enough to ensure no reflectance of the container.

2.2.2 Clay Concentrates

Clay concentrates were produced from sandstones to improve the detection of minor phases – such as clays (typically <5 wt%) within whole rock samples. This method was also utilised to provide coarse illite samples to determine polytypes.

Seventy-four clay concentrates were produced in-house at the University of Ottawa, these have been used to identify illite polytypes and crystallinity in the coarser grained illites. They were produced by grinding at least 100 grams of dry samples to <64 µm. Ground powder was placed into a 15 ml centrifuge tube up to the 10 ml level (around 15-20 grams of powder) to which water was added up to 15 ml. Samples were then agitated for 10 minutes, then subjected to whirlpool agitation for 5 minutes. After this time, samples were placed in a centrifuge and spun for 15 minutes at 2500 rpm. Clays and fine particles were removed from the top of the centrifuge tubes, the processes was repeated to enhance recovery and samples were dried at room temperature

(~20°C). Samples typically formed a very fine-grained clay-rich powder. Quartz was intentionally retained in samples to act as calibration for the diffractogram, recovery rates for clay within the sandstones ranged from 5% to up to 60%.

2.2.3 Clay Fractions

Clay fractions of samples were prepared by staff of the Geological Survey of Canada, under the supervision and direction of Dr Jeanne Percival. Samples were prepared by separating the <2 µm fraction via ultrasonic agitation in distilled water, shaking and centrifugation. Size fractions other than <2 µm (e.g. 2-16 µm) were obtained by varying the centrifuge speed and time. Clay was extracted by removing a 20 ml aliquot of the final clay suspension and freeze-drying to dryness.

2.3 Laboratory Analytical Methods

Petrographic analysis was undertaken on 52 thin sections using a petrographic microscope with transmitted and reflected light sources, the results of which form Plates 1, 2,3 and 4.

2.3.1 Scanning Electron Microscopy (SEM)

2.4.1.1 High Vacuum mode

Selected samples were examined using a JEOL 6610LV Scanning Electron Microscope at the University of Ottawa on carbon-coated samples in high vacuum mode. Images of Back Scattered Electron (BSE) are presented in Plate S2.

2.4.1.2 Low Vacuum mode.

Selected fragments of drill core were examined as non-coated samples in low vacuum. BSE images are presented in Plate S1.

2.3.2 Electron Probe Micro Analyser

Nine selected samples were also analysed for mineral chemistries using a JEOL 8230 Electron Probe Micro- Analyzer (EPMA) at an accelerating voltage of 15 kV, and with a beam current of 20 nA and focused to 5-10 µm in diameter depending on grain size. Data collection times and total background times were 20 s for all elements except for K and Si (10 s), and F and Cl (50 s). The standards were sanidine (Si$K\alpha$, Al$K\alpha$,K$K\alpha$), rutile (Ti$K\alpha$), hematite (Fe$K\alpha$), tephroite (Mn$K\alpha$), sphalerite (Zn$L\alpha$), diopside (Mg$K\alpha$, Ca$K\alpha$), albite (Na$K\alpha$), tugtupite (Cl$K\alpha$), sanbornite (Ba$L\alpha$), fluorite (F$K\alpha$), and celestine (Sr$L\alpha$) Data reduction was carried out using a ZAF routine.

2.3.3 XRD Analysis

Samples were anlysed on a Philips PW 3020 X'Pert Diffractometer at the University of Ottawa's X-ray Core Facility. XRD Anlaysis occurred at a 45 kV accelerating voltage, 40 mA current, with exact measurement parameters varying per a sample.

Mineral identification and estimation of modal abundances were performed by pattern matching using the MDI JADE, PANalytical HighScore software and reference patterns from the ICDD database (2006) and manual analysis. Table 2 presents the number of samples produced and utilised as part of this study.

Table 2: XRD analysis carried out on samples from the Phoenix Deposit. * clay fractions were analysed three times on a Zero-Background Holder (ZBH) - once as a smear, once glycated and once heated to 550C.

Sample Type	Numbers of Samples
Whole Rock	98
Clay Concentrates	74
Clay Fractions (total number of samples) *	24

2.3.4 Clay Fractions

Clay fraction samples were produced by pipetting a small drop of water and ground powder onto Zero Background Holder (ZBH) and allowing to air dry for four to 24 hours at 10-22°C. Samples used in this study were also subjected to glycolation by placing ethylene glycol within a desiccation vessel, adding the prepared clay fraction slides on a desiccator shelf within the vessel and leaving for 6-8 hours, then reanalysed. Samples were exposed to ethylene glycol to cause any smectite or montmorillonite present within the samples to expand, resulting in a shift of the 17Å peak.

Following glycolation, samples were also exposed to sustained heating at 550°C to cause collapse or destruction of peaks applicable to smectite, montmorillonite or Interstratified illite montmorillonite / vermiculite. Appendix 5.4 presents data.

2.3.5 Clay Concentrates

Clay concentrate samples were produced from sandstones, as such, they are not purely clay, and contain a significant amount of quartz. Samples were scanned between 2° and 85° with a step size of 0.02°. Samples were analysed as random powders which were lightly pressed into sample mounts and analysed between 3° and 30° with a step size of 0.02° per sec, a scan speed of 0.02 and time per step of 1.00 s.

Whole rock samples were analysed as random powders which were lightly pressed into sample mounts and analysed between 5° and 85° with a step size of 0.02° - 0.05°, scan speed of 0.02° per sec.

2.4 Short Wave Infrared Analysis

Infrared spectroscopy is used to characterise minerals including phyllosilicates and iron oxi-hydroxides (Hunt et al. 1971) and determine the approximate compositions of Fe- vs Mg-chlorite (McLeod et al. 1987 and Doublier et al. 2012).

Infrared spectra were acquired using an ASD TerraSpec® spectrometer. Technical details are recorded in Table 3. This spectral device measures the radiation reflected by minerals in the wavelength range between 350 and 2500 nm, to achieve this, three detectors are used, one covering the Visible to Near InfraRed wavelengths ('VNIR' 350–1000 nm) and two covering ShortWave-InfraRed (SWIR 1000–2500 nm). Principally due to the multiple detectors used, the spectral resolution was 3 nm between 350 and 1000 nm, 6 nm between 1000 and 1800 nm, and 7 nm between 1800 and 2500 nm.

Samples DPX1 – DPX89 and shear samples (WR256A to WR404) were analysed in one session, and samples DPX100-DPX341 were analysed in a separate session. Clean reference plates (Spectralon TM panel) were used every ten samples to minimise sample deviation, and care was taken to avoid contamination of samples by detritus on the light source, and it was cleaned after each powdered sample and wiped down every ten samples with de-ionised water.

Data were acquired using Indico® Pro acquisition software and spliced using ASD ViewSpec™ Pro for post-processing. Conditions and instrument were kept the same for both sets of analyses, as suggested by Zhang et al. (2001).

Table 3: Technical details of Terraspec 4 used for analysis samples used in this study.

Wavelength Range	350-2500 nm
Resolution	3 nm @ 700 nm and 10 nm @ 1400/2100 nm
Scanning time	10,000 milliseconds per analysis
Signal-to-noise ratio	VNIR: 9,000:1 @ 700 nm SWIR 1: 9,000:1 @ 1400 nm SWIR 2: 4,000:1 @ 2100 nm
Photometric noise	VNIR: 48 nAU @ 700 nm SWIR 1: 48 nAU @ 1400 nm SWIR 2: 110 nAU @ 2100 nm
Stray light	VNIR: 5000:1 (0.02%) NIR: 10,000:1 (0.01%)
Wavelength reproducibility	0.1 nm
Wavelength accuracy	0.5 nm
Channels	2151
VNIR detector	(350-1000 nm) 512 element silicon array
SWIR 1 & 2 detectors	(1001-1800 nm) & (1801-2500 nm) Graded Index InGaAs Photodiode, TE Cooled

2.4.1 Identification of Sample Mineralogy

Select samples were analysed using 'The Spectral Geologist' (The Spectral Geologist 2012) the results of which are presented in Appendix 4.2. The remainder of the samples were processed manually using comparisons to published literature. Table 4 and 5 below illustrates the specific wavelengths which were used for the identification of minerals. Figure 10 illustrates typical absorption patterns used in the identification of alteration minerals surrounding the Phoenix Deposit. A total of 383 SWIR spectra were generated from 299 samples to identify the mineralogy of samples from the sandstones and basement around the Phoenix Deposit. All samples were also processed manually with the results compared to the output from TSG software, details of the selected data used for TSG output and manual identification and the full output from the TSG are in Appendix 4.2.

Table 1: Absorption features used in the identification of minerals in this study.

Mineral / Family	Indicative absorption features and relative size and location (nm).
Illite	1400 (large, sharp), 1412 (medium), 1414 (major, large), 1842 (small broad), 1900 (broad, deep), 1944 (broad, large), 1989 (large step), 2014 (small), 2110 (small), 2198 and 2200 (major, sharp), 2210 (major), 2345 (medium), 2360 (large), 2436 (minor), 2440 (medium and broad)
Tourmaline	2200 (large), 2210 (major doublet), 2244 (major doublet), 2300 (medium), tourmaline has an indicative sequence of absorption features between 2300-2500 (see Figure 12)
Chlorite	1390 (sharp, medium), 1441 (medium, chlorite), 1855 (small, sharp), 1990 (large broad), 2001 (broad deep), 2246 (large sharp), 2296 (chlorite), 2300 (Mg-OH), 2320 (major, occ. Broad)
Kaolinite	1364 (small), 1392 (large, sharp), 1395 (major doublet), 1397 (major doublet), 1400 (large, doublet), 1409 (major doublet), 1416 (doublet), 1900-1915 (large), 2160 (large), 2166 (major doublet), 2200 (large), 2290 -2300 (broad small)

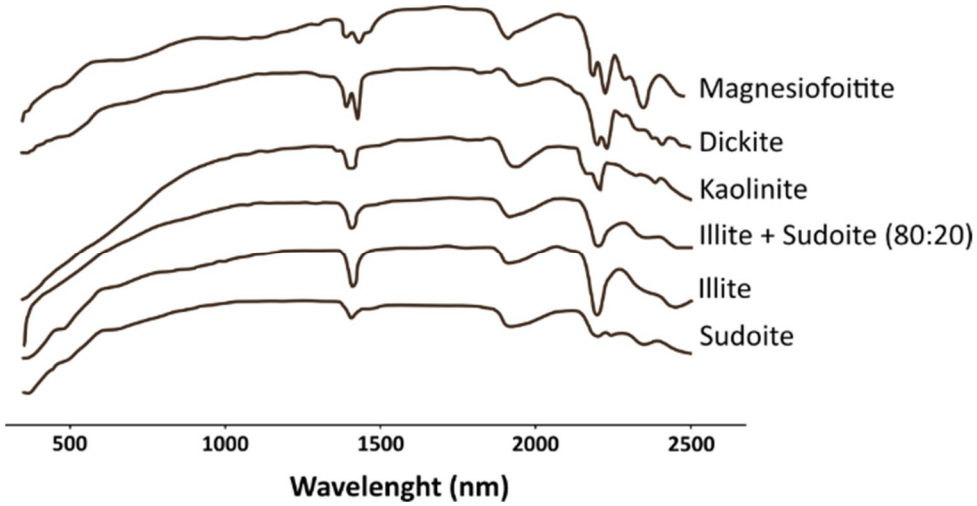

Figure 10: Typical absorption patterns for common minerals noted in the alteration package of the Phoenix Deposit, derived from standards from the Athabasca Basin (J. Percival, personal communication 2012).

2.4.2 Specific Absorption Features of Chlorites

Specific absorption wavelengths can correspond to specific species of chlorite and have been used in the identification of chlorite in this study. They are presented below in Table 4.

Table 4: Absorption features of Mg and intermediate (Fe-Mg) chlorite. Modified from AusSpec International (2008).

	FeOH Wavelength	MgOH Wavelength
Mg chlorite	2240-2249 nm	2320 – 2329 nm
Intermediate chlorite (Fe-Mg chlorite)	2250 – 2256 mm	2330 – 2348 nm

2.4.3 Illite crystallinity as determined by the Kübler and m-Kübler values

Kübler analysis, also called the illite 'crystallinity' index, is a well-established tool first used for determining the metamorphic grade in low-grade pelitic rocks (Kübler 1964). It has since been used for the depth of burial in sandstone reservoirs (Enrenberg and Nadeau 1989), the crystallinity of illite in porphyry copper deposits (Eaton and Setterfield 1993) and as a tool in regional-scale exploration for epigenetic Cu deposits (Duba and Jones 1983). The Kübler index measures changes in the 'Full Width at Half Maximum' (FWHM) of the first basal reflection (001) of dioctahedral illite at a spacing of approximately 10 Å, as demonstrated in Figure 11.

The method was introduced by Kübler (1964) as a tool to identify the differences between diagenetic sequences and low-grade metamorphism in pelitic sequences. The smaller the Kübler value, the greater the size of the crystals. This study has used traditional Kübler analysis and a modified version also described by Kübler (1967) using the coarser grained 'clay concentrate' powders described above. The results from samples of the coarse-grained powders are termed 'm-Kübler values. Due to the larger crystal size of the clay concentrate m-Kübler samples coarse-grained illite yielded an artificially increased FWHM of the illite 001 peak, and therefore an artificially decreased crystallinity.

Although values cannot be compared between the two methods, comment and analysis can be given between the m-Kübler values within the alteration halo of the Phoenix Deposit and the along trend, regional drill core (WR380). Due to the expected larger grain size of the clay concentrate samples, the m-Kübler method allows for the evaluation of the relative crystallinity for coarser grained crystals of illite.

Expandable layered phyllosilicates, such as smectite, broaden the XRD peaks, resulting in wider Kübler values, (Eberl and Velde 1989; Jaboyedoff et al. 2001). Clay fraction samples from the Phoenix Deposit have been examined for the presence of smectite in the XRD spectra, but it was not identified (Appendix 6.4).

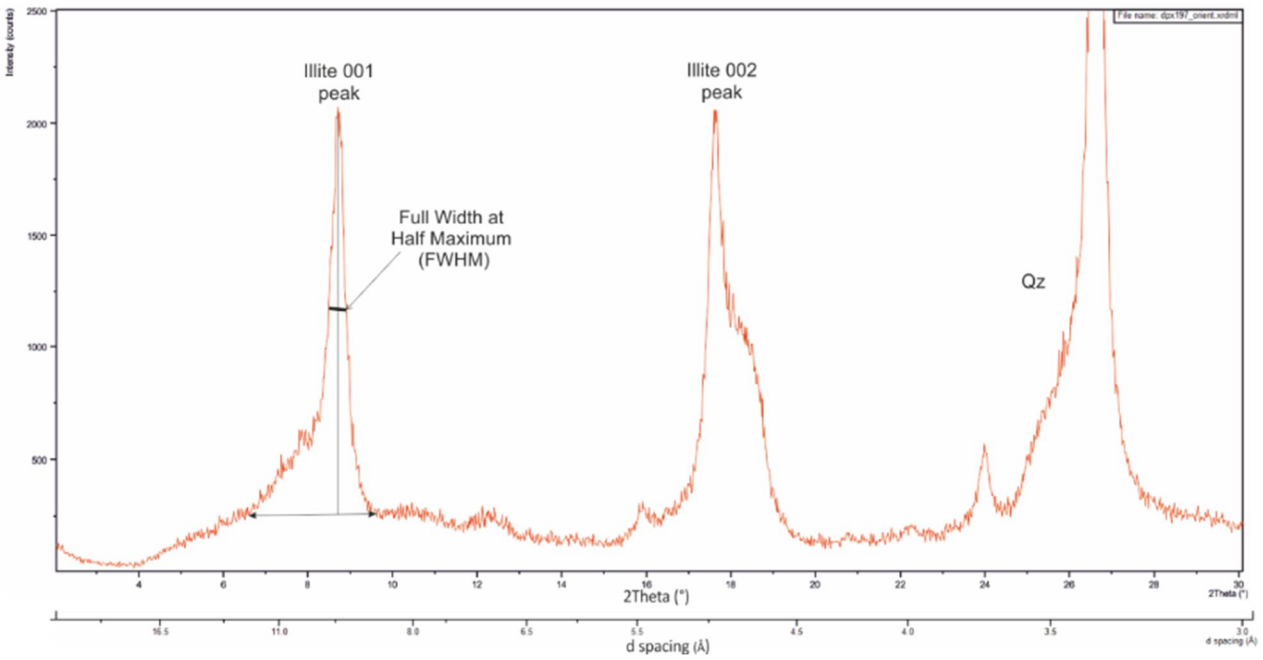

Figure 11: Position of the Full Width at Half Maximum (FWHM) on an illite-rich XRD diffractogram. Diffractogram is generated using Cu Ka. This diffractogram is from sample DPX 197, which was collected from DDH286, 211.4 m downcore and shows a highly crystalline sample of illite.

This study uses two methods to examine the illite crystallinity of differing size fractions to allow for the identification and analysis of phases >2 µm observed in SEM imagery (Plate S1-1). This study presents a 'modified Kübler index', which is referred to as 'm-Kübler' and is used to allow analysis of more coarser grained samples. Powdered samples have successfully been used for illite crystallinity studies before (Gunthrie et al. 1986; Laverret et al. 2006), and as such are valid.

2.4.4 Illite Polytypes

In order to identify of illite polytypes in samples, patterns of XRD of clay fraction samples have been compared to calculated and published spectra from other Athabascan deposits documented by Drits et al. (1993) and Laverret et al. (2006). Three common polytypes of illites exist, the one-layer monoclinic (1M), two-layer monoclinic (2M) and three-layer trigonal (3T) polytypes. Each of the layers (i.e. 1M vs 2M) refers to the number of repeats of the two-layer stacking within a unit.

1Mc illite has vacant *cis*-octahedra forming one of two symmetrically independent point Systems - the other *cis*-octahedra as well as the trans-octahedra are occupied, while 1Mt illite has a one-layer monoclinic structure with vacant *trans*-sites (Drits et al. 1993). The classification of 1Mt as the third generation of illite in the alteration halo but not numbered as such (i.e. 3T or 3M) as per normal nomenclature, is due to uncertainty of the paragenetic relationship between 1Mc and 1Mt, and to allow for comparison to other studies elsewhere in the Athabasca basin, such as Laverret et al. (2006).

Each species of polytype can be identified from each other through XRD, as the variations in the structure and differing vacant trans-sites or the position with the repeating unit diffract X-rays along differing crystal planes, resulting in variations in the d-spacing (Å). The d-spacing, their respective 2 theta (with Cukα) values and intensity of the 1Mc, 1Mt and 2M illite polytypes are shown on Table 6.

Compositionally the M1 illite identified within this study is fine grained in nature. However, the early, fine-grained illite identified at other deposits is termed 'illite' by other workers (Drits et al. 1993; Kotzer and Kyuser 1997 and Laverret et al. 2006), and this study follows suit.

Table 6: Positions of calculated d values (Å) and intensity of polytypes of illite observed in this study. Modified from Drits et al. (1993). Diagnostic peaks for each polytype are highlighted in bold.

1Mc illite polytype			**1Mt illite polytype**			**2M illite polytype**		
Calculated d values (Å)	2 theta (with Cukα)	Relative Intensity	Calculated d values (Å)	2 theta (with Cukα)	Relative Intensity	Calculated d values (Å)	2 theta (with Cukα)	Relative Intensity
4.5	19.713°	10	4.5	19.713°	100	4.48	19.8°	55
4.47	19.844°	100	4.44	19.979	10	4.46	19.891°	65
4.309	**20.593°**	**20**	**4.351**	**20.394**	**45**	4.109	21.609°	14
4.106	21.624°	15	4.107	21.624°	20	**3.973**	**22.358°**	**12**
3.885	**22.872°**	**35**	**3.655**	**24.332°**	**65**	**3.889**	**22.848°**	**37**
3.591	24.999°	25	3.338	26.346°	100	3.735	23.803°	32
3.338	26.346°	100	3.35	26.586°	20	**3.5**	**25.424°**	**44**
3.348	26.603°	50	**3.073**	**29.003°**	**55**	3.351	26.578°	100
3.126	**28.53°**	**30**	**2.927**	**30.516°**	**15**	**3.208**	**27.786°**	**70**
2.873	**31.104°**	**30**				**2.999**	**29.858°**	**47**
						2.87	**31.170°**	**35**

2.5 Identification of Mineral Phases

Full discussion into the methodology behind individual phases is presented in Section 2.6.

2.5.1 Tourmaline

Crystals texture and paragenetic relationships have been used to identify Tur1 and Tur2, paragenetic relationships to other phases are based on sample descriptions and imagery from Rosenberg and Foit (2006), Mercadier et al. (2012) Ng et al. (2012) Adlakha et al. (2013), O'Connel (2015) and Adlakha and Hattori (2016).

2.5.2 Illite

The texture has been used to identify M1 and M2, while XRD analysis has been used to determine the 1Mc and 1Mt and 2M polytypes. XRD diffractograms (clay fraction and clay concentrates) from the Phoenix Deposit are compared to published work from uranium deposits in the Athabasca Basin. Table 6 lists the locations or peaks of the 1Mc, 1Mt and 2M polytype used in this study following the patterns documented by Drits et al. (1993), Laverret et al. (2006), Kister et al. (2006) and Cloutier et al. (2010).

2.5.3 Chlorite

Petrographic analysis has been used to identify the three generations of chlorite found at the Phoenix Deposit (C1, C2 and C3) and their respective paragenetic relationships to other phases. XRD diffractograms of samples of whole rock and clay concentrates have been compared to published data for sudoitic chlorites (Percival and Kodama 1989 and Billaut et al. 2002). To determine the presence of Fe-Mg chlorite, SWIR spectra were compared to published data for sudoitic and Fe-Mg chlorites (Tables 3 and 4).

2.6 Temporal Relationships Between Mineral Phases

2.6.1 Basement

In the vicinity of the WS Shear Structure, Tur1 is present as euhedral-subhedral crystals which are brown and pleochroic in Plain Polarised Light (PPL) and light blue-green in Cross Polarised Light (XPL). Generally, Tur1 replaces earlier metamorphic phases (Plate P1/D). In BSE Tur1 is shown to have a thin darker rim (Plate S2/5). Tur1 is shown to be cross cut and replaced by graphite and C1 which pseudomorphs earlier biotite.

Elsewhere in the basement, away from the WS Shear, C1 is present as pervasive, often fine-grained phase filling the space produced by dissolution of quartz (Plate P1/C), C1 is replaced by dark olive green C2 which forms fine-grained aggregates in association with M1 fine-grained illite. M2 illite is present as a coarse-grained, second order interference colours phase, which occasionally replaces C1. M2 illite is shown to replace M1 illite (Plate P5/D).

In the vicinity of the WS Shear, Tur2 is fine-grained and forms spherical to radial aggregates along grain boundaries and veinlets (Plates S2/7, S2/8), elsewhere in the basement, Tur2 forms 'spars' of the 1st order birefringence and along grain boundaries of Tur2 crystals (Plate P1/A).

Despite a varied protolith lithology, pervasive alteration is evident in all pelitic samples, The quartzite ridge to the north-west of the deposit has been largely unaffected by the alteration in the pelitic lithologies and retains garnet, tourmaline (Tur0), pyrite and microcline feldspar (Plate P1/G).

2.6.2 Sandstones

In the sandstones, 1M illite is recognised as a widespread, pervasive, fine-grained alteration phase, which infills fractures and pores created by dissolution of detrital quartz in the Athabasca Sandstone and is associated with an early phase of Fe oxides (Plate P5/D) and in the sandstone C1. 2M illite in the Athabasca Sandstones is a coarse-grained, 2nd-order birefringence phase which occasionally forms acicular masses (Plates P5/D, P4/F). The temporal relationship of coarse-grained, dark green sudoite in the sandstone is less well defined that the basement sudoite, but it is seen to be later than 1M.

Tur2 is present as acicular crystals up to 100µm in size, which are light brown in PPL, paler at the end of the crystals and have 1st to 2nd order birefringence in samples of the whole thickness of the slide, and occasional 3rd to 4th order birefringence in thinner samples. Tur2 'spars' grow off quartz grains and replace earlier M2 (Plates P3/D, P4/F and P5/F).

2.7 Whole Rock Geochemistry

2.7.1 Chemical Analysis Method

As part of this study, interpolation of whole rock geochemistry in the sandstones overlying the Phoenix Deposit was undertaken and is presented in Dann et al. (2014) in Appendix 1.1. This section reports on the compositional variation of MgO, K_2O and B, using the analytical method described in Section 2.1, Sampling. The data of MgO and K_2O for 23 drill cores from DDH WR 190A to WR 269 were determined using ICP-OES whereas the data for 111 drill cores from DDH WR 270 to WR 384 were obtained using ICP-MS. For boron, an aliquot of pulp was fused in a mixture of

$NaO_2/NaCO_3$ in a muffle oven. The fused melt was then dissolved in de-ionised water and analysed by ICP-OES. The majority of data used for both interpolations and statistical analysis had values well above detection limits, which are reported in Table 2 in Dann et al. (2014) and the entire Open-File Report appears in Appendix 1.1.

2.7.2 Geographical Information Systems Technical Method

The data was projected to seven horizontal planes 50 m apart, and then they were projected on one pseudo-vertical section. Inclined drill core data were subjected to basic trigonometric functions, allowing the calculation of true depth and placement within a 3D framework, relative to its declination, azimuth, elevation and location.

Interpolation was performed using ESRI's ArcGIS 10.0 ArcMap software equipped with the Spatial Analysis toolbox. The drill core locations are spread along a 2.4km strike of the WS shear, but only span 200m across the shear structure and with an irregular distribution in a 3D space. As a result, the interpolation results are significantly varied due to different densities of data points and resulted in the spatial analysis being performed with an Inverse Distance Weighting (IDW) algorithm under a power of 2, attempting to mitigate any undue bias in the distribution of the data. By using IDW, an algorithm calculates the weighted mean of known values inside a moving spatial window that is calculated and assigned to the pixel in the centre, with all interpolated values between the minimum and maximum observed values (Bartier and Keller 1996). This is achieved by running an element by - element interpolation inside of a defined polygon that surrounds the drill core locations. One barrier was used to maintain consistency during interpolation. To minimise undue interpolation surrounding the data points a rectangular barrier was drawn as close as possible to all points. Points which fell outside the barrier were excluded. The locations of the drill cores and respective barriers are described in (Figure 3 in Dann et al. 2014, Appendix 1.1).

3 RESULTS

3.1 Alteration types, their Distribution and Petrology

The Phoenix Deposit is accompanied by alteration similar to that observed in other Athabasca Basin unconformity-associated deposits. Sandstones display varying degrees of silicification and desilicification, as well as tourmaline alteration, chloritisation, and illitisation. As shown in Dann et al. (2014) tourmaline alteration, is present in a well-defined chimney structure originating 50 m above the deposit to within 50 m of the surface (total height of 250 m). Sandstones also display intense illite alteration. The distribution of illite within the sandstones of the Phoenix Deposit can be seen in the distribution of K_2O since illite is the only host of K (Dann et al. 2014) (Figure 30).

In the sandstones, chlorite forms two distinct phases, Fe-Mg chlorite and sudoite. Fe-Mg chlorite is present in the Read Formation and in the MFb and MFd up to a depth of 200 m downcore (around 200 m from the unconformity) and within 50 m of the surface (around 350 m from the unconformity). Later sudoite is restricted to the deeper part of the MFb member and the Read Formation.

Hematite and druzy quartz are present in all members of the Manitou Falls / Read Formation overlying the Phoenix Deposit. In both the basement and the sandstones, the Sandstone Extension to the WS Shear and associated splays act as foci for alteration, which is not thought to be restricted to within 100 m of the shear structure (Repais 2016). Alteration associated with the Sandstone Extension to the WS Shear is paragentically and compositionally similar to alteration elsewhere in the sandstones, albeit more pervasive. The basement in the northeast part of the Phoenix Deposit is much more extensively bleached and clay altered than that to the southwest (Roscoe 2014).

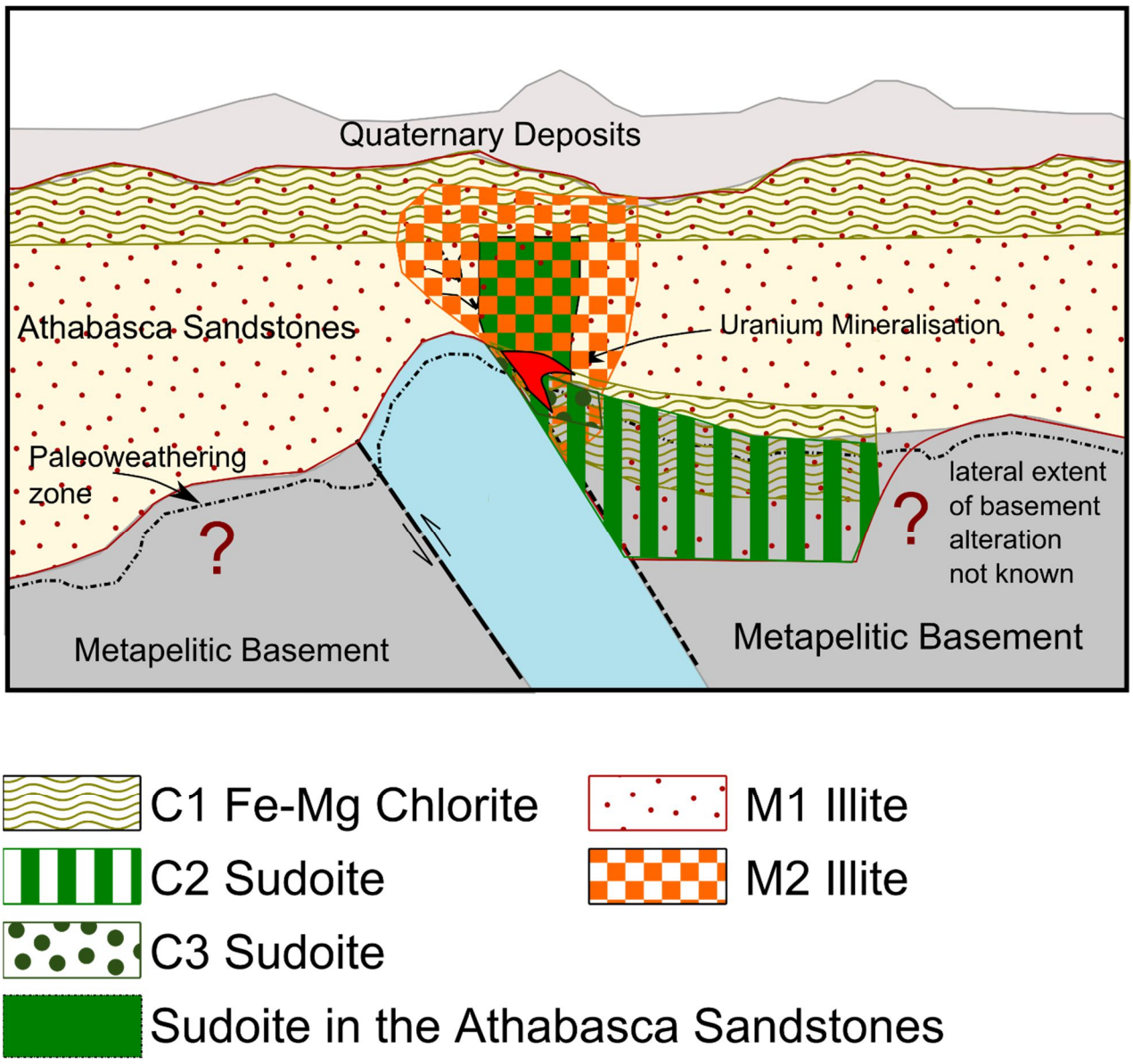

Figure 12: Schematic of chlorite and illite distribution around the Phoenix Deposit. Based on findings of this study and other studies (Kerr et al. 2010, Arseneau, and Revering 2010, and Roscoe 2012). Regionally, M1 illite is present throughout the sandstones and analysed samples within the basement, while later, more localised M2 is present overlying and immediately surrounding the Phoenix Deposit. Early C1 is found within the deep (Read Formation) and shallow (MFc/MFd) C2 sudoite in the sandstones is present overlying mineralisation, in a more discrete chimney to M2. In the basement, C1 and C2 are widely present, with C2 sudoite being found deeper. C3 sudoite is found close (< 50 m) to the orebodies of the Phoenix Deposit.

3.1.1 Petrographic Analysis

Plate: 1 Petrographic Micrographs: P1/A (DPX 89; WR257, 250.5 m - Sandstones). Early illite M1 intergrown with C2 and magnesiofoitite (Tur2) and associated Fe oxides (FeOx) P1/B (DPX 20; WR332; 442.5 m – Basement). Replacement of garnet by early FeOx and early illite (M1) and C1, *A indicates the replacement of former micaceous strain shadows around garnet porphyroblast. P1/C (DPX 5; WR383; 453.25 m– Basement). C1 undergoing replacement by C2 and M1, which in turn fills partially dissolved/recrystallised quartz (Qz1), M1 + FeOx and Qz2 appears to replace C2. P1/D (281B; WR281; 412.7 m – Basement Shear). Dravite (Tur1) following metamorphic foliation with C1 (pseudomorphing biotite) following an early metamorphic foliation, with remobilised graphite (Gr) crosscutting C1. P1/E (DPX51; WR282; 415 m – Basement) Basement: M1 and C2 replacing early C1, close to the unconformity. P1/F (DPX13; WR376; 442.3 m – Basement) TS/PPL: All three generations of alteration chlorite observed at the Phoenix Deposit. Replacement of fine-grained C1 by fine-grained C2 and M1, C3 is seen to fill space produced through dissolution of quartz (Qz) and earlier phases (*A.) Early pyrite replaces C1 but fails to interact with other phases. P1/G (DPX63; WR358 403.1 m - Basement) M2 lllite pseduomorphing and early fabric of titanium oxide (M2 + An).

Plate: 2 Petrographic Micrographs: P2/A (DPX170; WR277 187.1 m). Magnesiofoitite (Tur2) and associated FeOx replacing mudstone clast in partially silicified sandstone. P2/B (DPX171; WR379; 403.7 m – Sandstone) Silifcation of quartz in Athabasca sandstone; associated with FeOX. Detrital quartz (QzD) fused with silicified quartz (QzS) and associated FeOx. Quartz intergrowth shows the same extinction as the grain, indicating a growth of the crystal structure. P2/C (DPX12; WR376; 447.4 m – Basement). M1 associated with pyrite (Py), with C1 replaced by M1/C2. P2/D (DPX103; WR367; 425.7 m – Basement). Unaltered Garnet (Gnt), with metamorphic/detrital tourmaline (Tur0) and metamorphic pyrite (Py). P2/E (DPX81; WR293; 288 m – Sandstones) Late magnesiofoitite (Mgf) crosscutting annealed quartz (Qz) and microcline (Mc)grains (*A), this sample is from within an area of extensive boron enrichment. P2/F (WR404; 323.3 m – Sandstone Extension to the WS Shear). RL, PPL / TS, XPL: Replacement of detrital magnetite (Mag) by bladed hematite (Hem) and later FeOx alteration associated. M1 illite is present infilling pore space. P2/G (DPX35; WR282; 421.4 m – Basement Shear). Late Pyrite cross-cutting C3 + M2 P2/H (DPX282B; WR282; 398.9 m – Basement Shear) RL, PPL: C2 pseudomorphing earlier biotite, following a metamorphic foliation with Graphite (Gr). Pyrite (Py) and chalcopyrite (Ccp) are cut by C3.

Plate: 3 Petrographic Micrographs: P3/A (DPX70; WR329; 399 m- Sandstones). Vuggy Quartz (Qz2) intergrown with FeOx infilling pore spaces in detrital Quartz (QzD) P3/B (DPX 19; WR332; 442.8 m - Basement). Detrital/diagenetic tourmaline (Tur0) and annealed quartz, Tur0 is cut by bladed quartz overgrowth (*A) P3/C (DPX60; WR358; 403.6 m – Basement). Late C3 pseudomorphing biotite and replacing C2+M1. P3/D (DPX149; WR277; 282m Sandstones) Replacement of M2 by magnesiofoitite (Tur2). This sample has a NIR absorption feature at 674 nm.P3/E (DPX63; WR358; 403.1m Basement) Two generations of quartz dissolution along a fracture, Qz1 is colourless in PPL and light grey in in XPL, white Qz2 is darker, with FeOx and infills/replaces Qz1. Dashed lines in ppl indicate line of QzO/Qz1 boundary. P3/F (WR293B; WR293; 251m Sandstone Extension to the WS Shear). Detrital hematite replaced by magnetite along crystal planes, which is then partially replaced by late pyrite. Suggesting a late-stage change in fs_2. Unaffected Bladed Hematite (Hem2) is present in close proximity. Magnesiofoitite (Tur2) is also shown to be in close proximity (in XPL transmitted light). P3/F (WR293B; WR293; 251m Sandstone Extension to the WS Shear). Replacement of M2 by magnesiofoitite (Tur2).

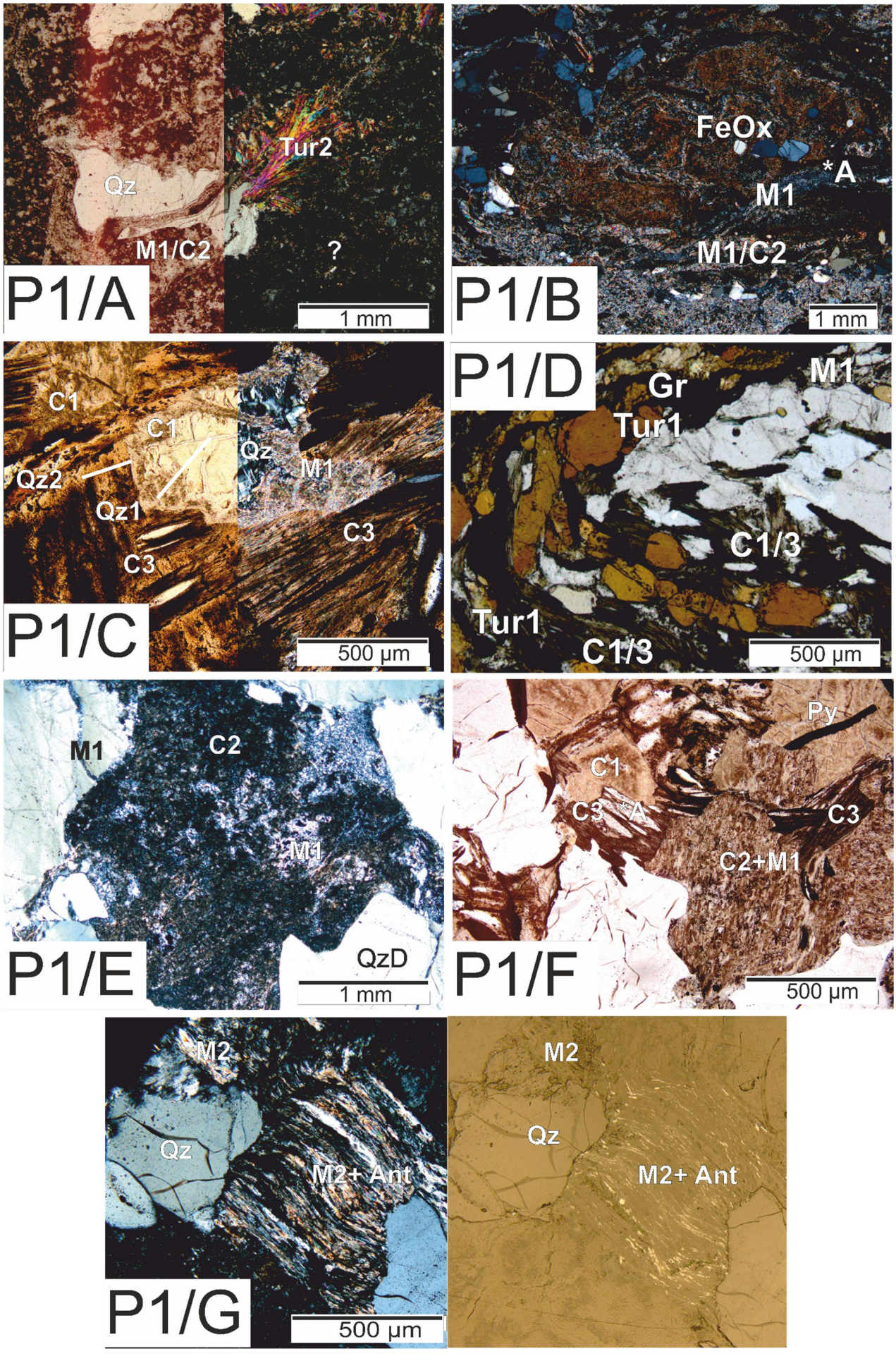
P1/A
Qz
Tur2
M1/C2
?
1 mm
P1/B
FeOx
*A
M1
M1/C2
1 mm
P1/C
C1
C1
Qz2
Qz1
Qz
M1
C3
C3
500 µm
P1/D
Gr
M1
Tur1
C1/3
Tur1
C1/3
500 µm
P1/E
M1
C2
M1
QzD
1 mm
P1/F
Py
C1
C3
*A
C3
C2+M1
500 µm
P1/G
M2
Qz
M2+ Ant
500 µm
M2
Qz
M2+ Ant

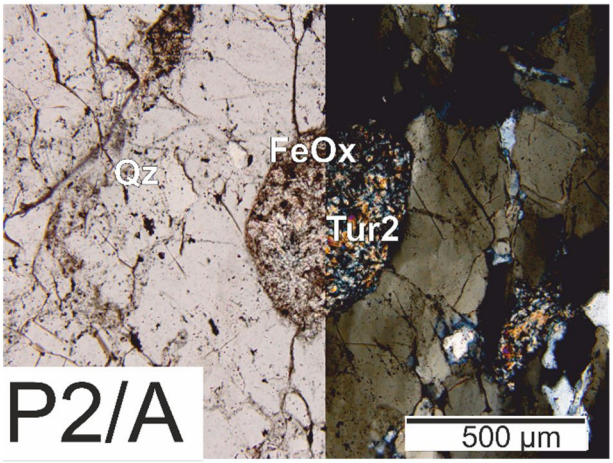

P2/A

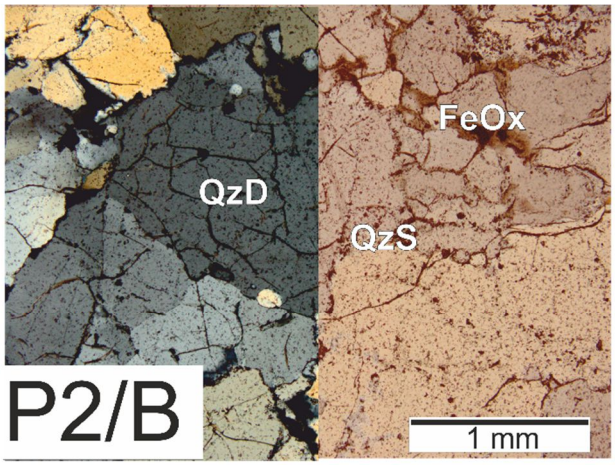

P2/B

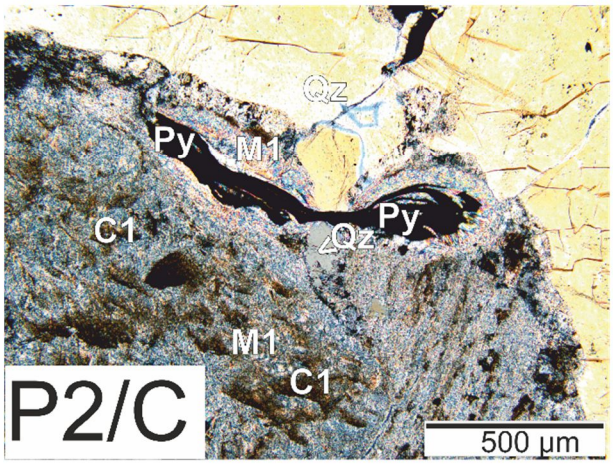

P2/C

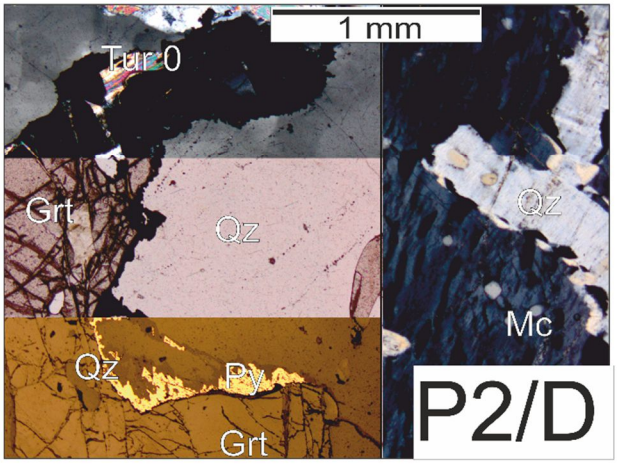

P2/D

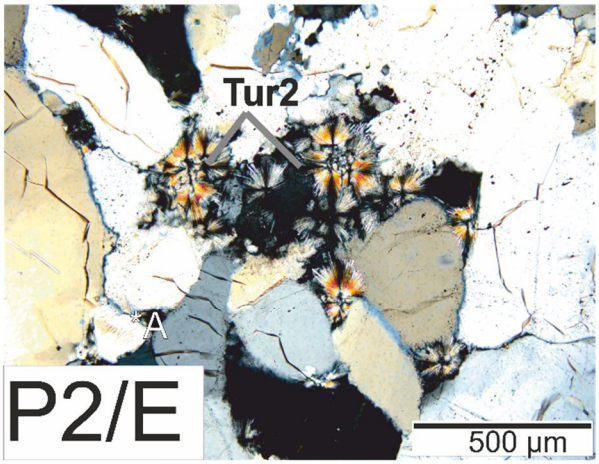

P2/E

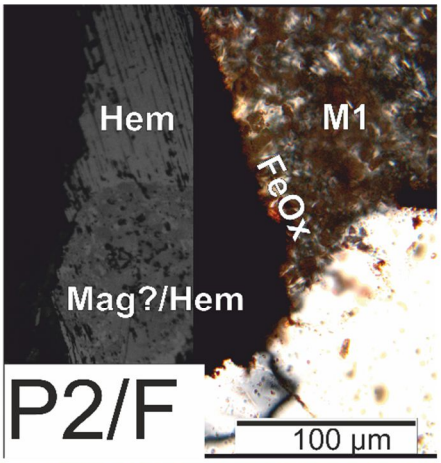

P2/F

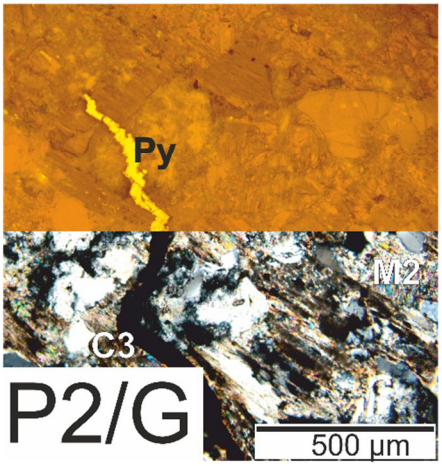

P2/G

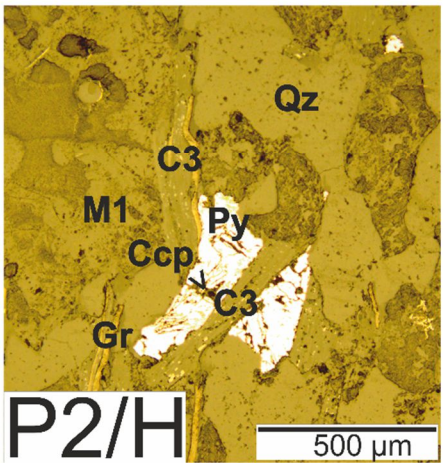

P2/H

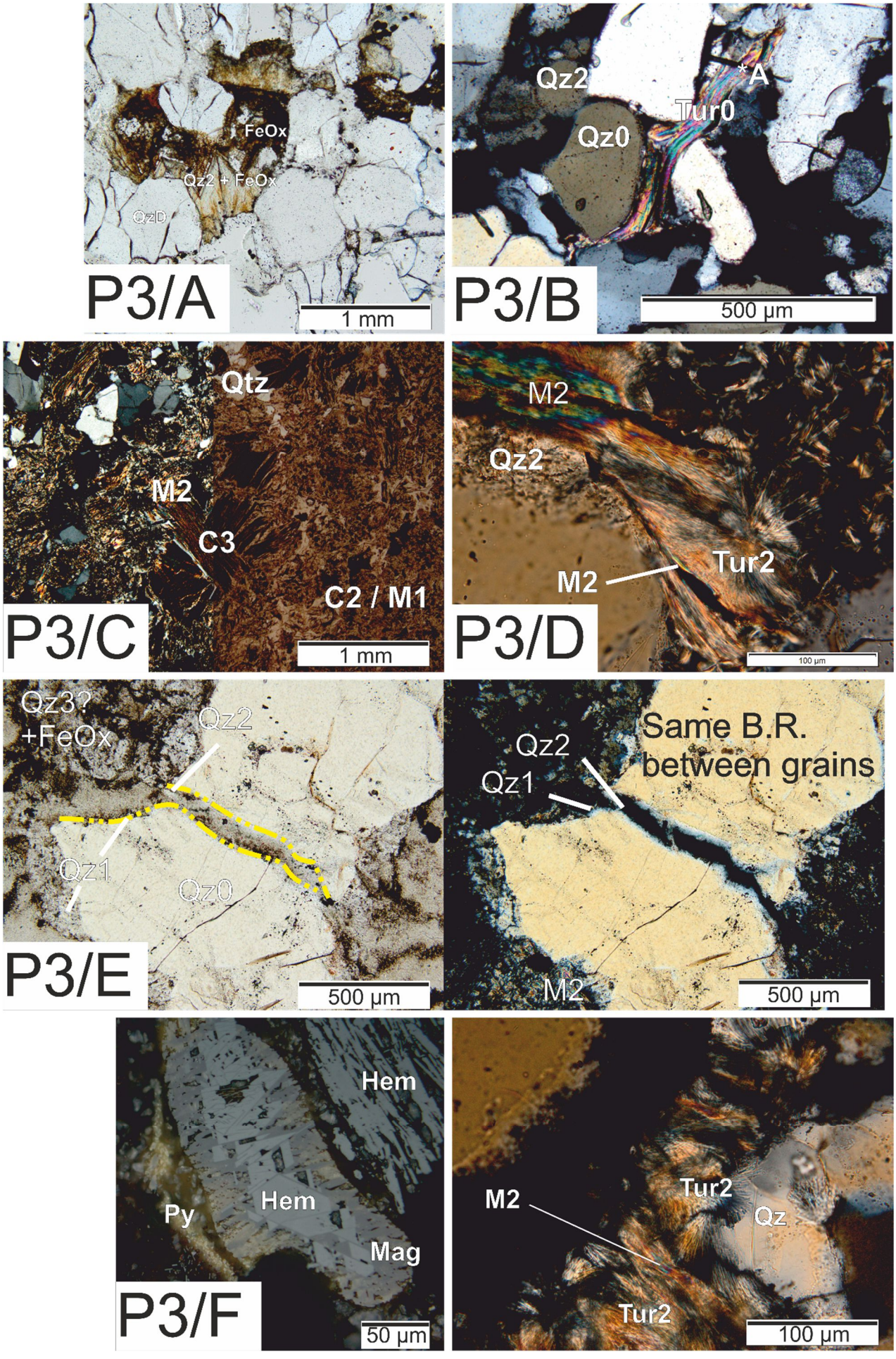
FeOx
Qz2 + FeOx
QzD
P3/A
1 mm
Qz2
*A
Tur0
Qz0
P3/B
500 µm
Qtz
M2
C3
C2 / M1
P3/C
1 mm
M2
Qz2
Tur2
M2
P3/D
100 µm
Qz3?
+FeOx
Qz2
Qz1
Qz0
P3/E
500 µm
Qz2
Qz1
Same B.R.
between grains
M2
500 µm
Hem
Py
Hem
Mag
P3/F
50 µm
Tur2
M2
Qz
Tur2
100 µm

Plate: 4 Petrographic Micrographs: P4/A (282A –WR282; 399m Basement). Early M1 illite, replacing fine-grained quartz, with late C3 pseudomorphing after biotite (Bt). P4/B (DPX176; WR 286; 28.1 m Sandstone). Kaolinite vein from the top of the MFd; with possible chlorite and illite P4/C (DPX 209 – WR321; 94.2 m Sandstone). Partially annealed quartz in the Athabasca Sandstones. P4/D (WR256A; WR256; 190.7 m Sandstone Extension to the WS Shear). M1 and C1(?) filling pore spaces with the Sandstone Extension to the WS Shear, with annealed Qz2. P4/E (DPX67; WR408; 400.1 m Basement). Apatite (App) vein cross-cutting C2+M1, with C1 and preserved early garnet. P4/F: (DPX170; 187.1m). Replacement of 'etched' detrital quartz QzO with mid pyrite (Py2). P4/G (DPX103, WR367 425.7m Basement). Tur0 and garnet (Gnt) in an unaltered sample of quartzite, chlorite (Chl) after biotite rings garnet.

Plate: 5 P5/A (DPX138; WR380; 268.8 m Sandstone, 1.8 km south of the Phoenix Deposit). Bladed hematite (Hem2) has grown on rim of detrital grains. P5/B (WR409A, WR409, 317.7m Sandstone shear). Bladed hematite (Hem2) with associated magnesiofoitite (Tur2) crosscutting M1 and M2 illite. P5/C (WR301A, WR301 315m Sandstone shear.) Fe oxides appear coeval to M2 illite or magnesiofoitite (Tur2). P5/D (DPX51, WR282, 414.98 m). Basement M1 illite being replaced by M2 illite (dashed line denotes boundary). P5/E (DPX170; 187.1m). M2 illite being replaced by Tur2. P5/G (DPX138, WR380, 268.6m Sandstone). Replacement of hematite by magnetite. Note the cross-cutting of bladed hematite by magnetite at '*A' in the zoomed in section (right).

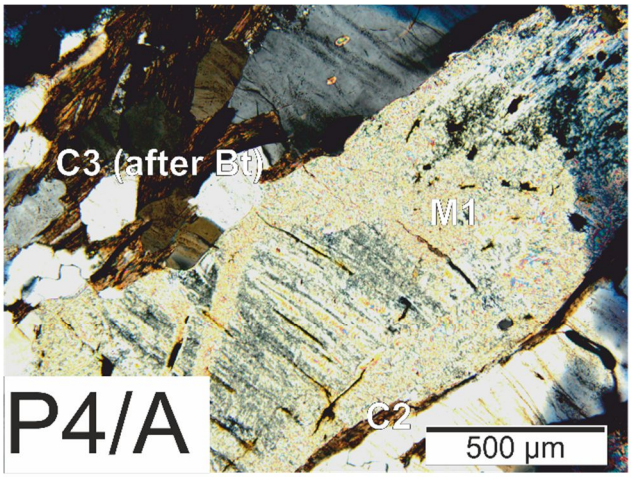

P4/A

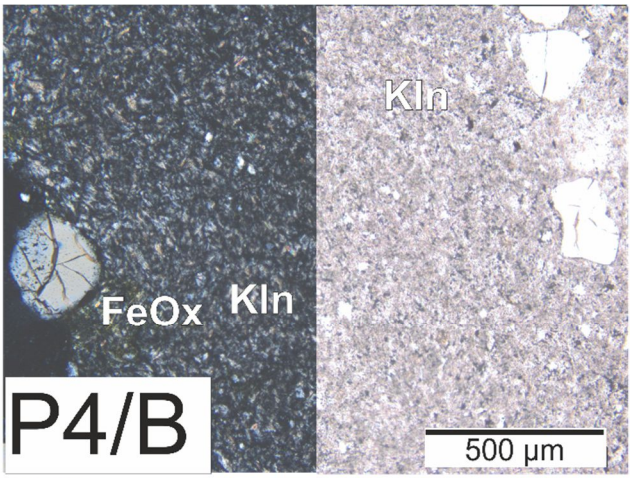

P4/B

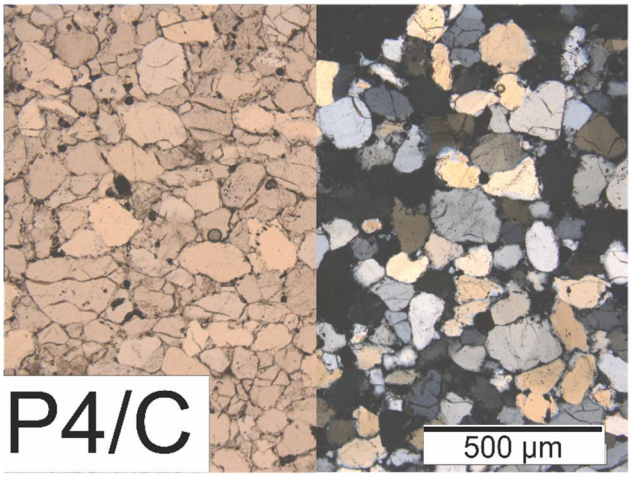

P4/C

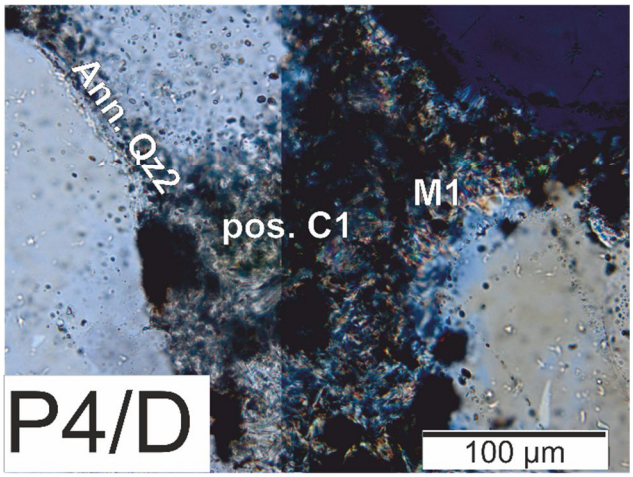

P4/D

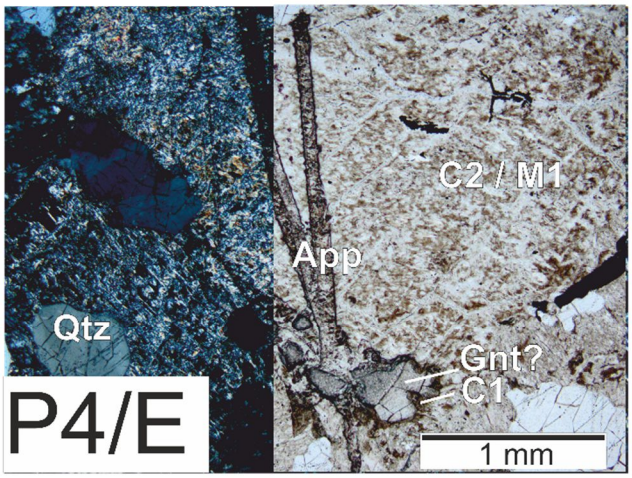

P4/E

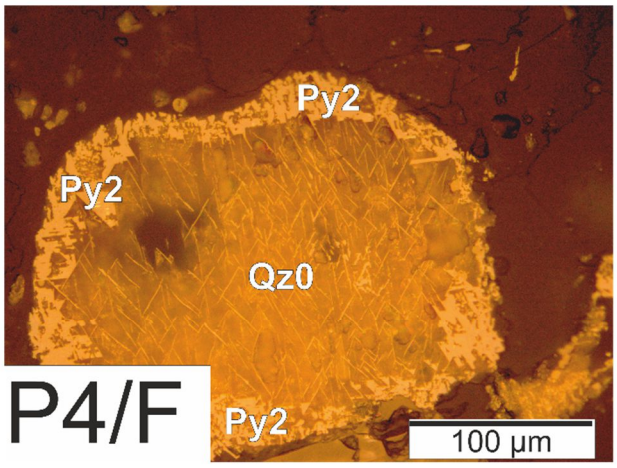

P4/F

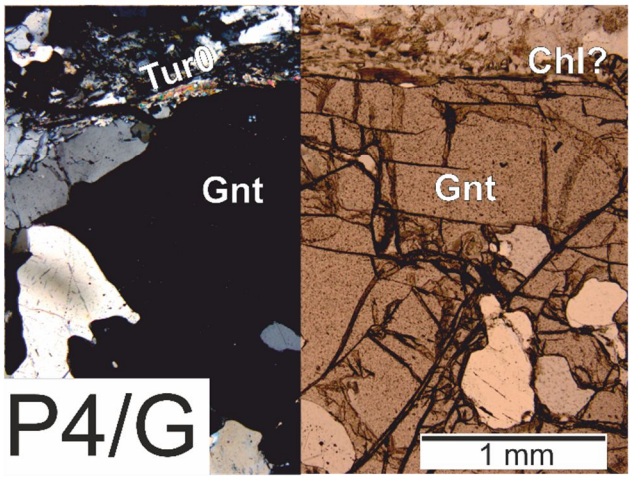

P4/G

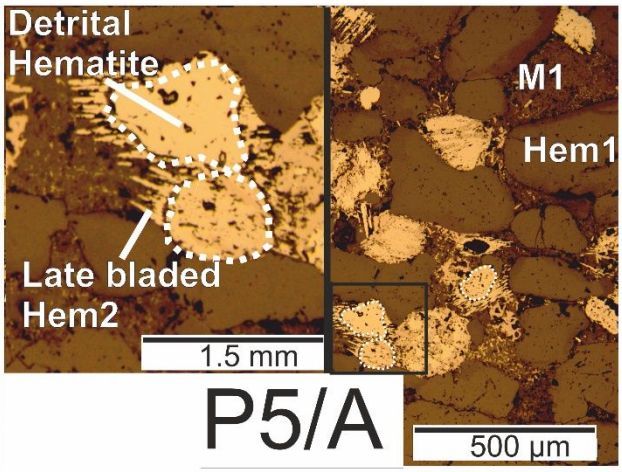
Detrital Hematite
Late bladed Hem2
1.5 mm
M1
Hem1
500 µm
P5/A

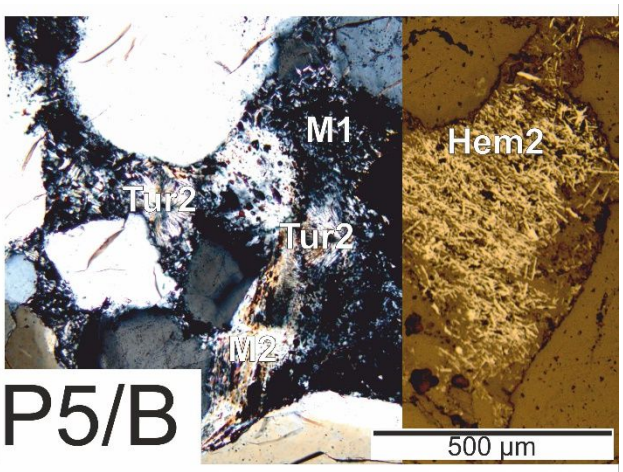
M1
Tur2
Tur2
M2
Hem2
500 µm
P5/B

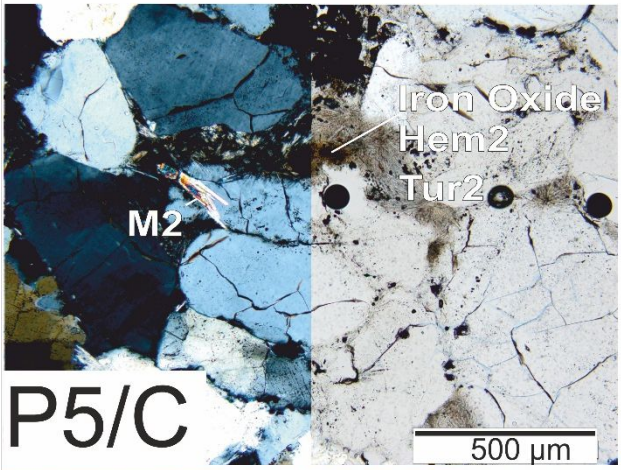
M2
Iron Oxide
Hem2
Tur2
500 µm
P5/C

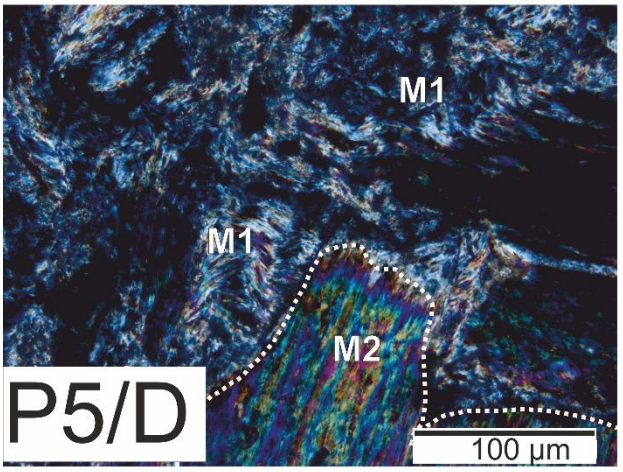
M1
M1
M2
100 µm
P5/D

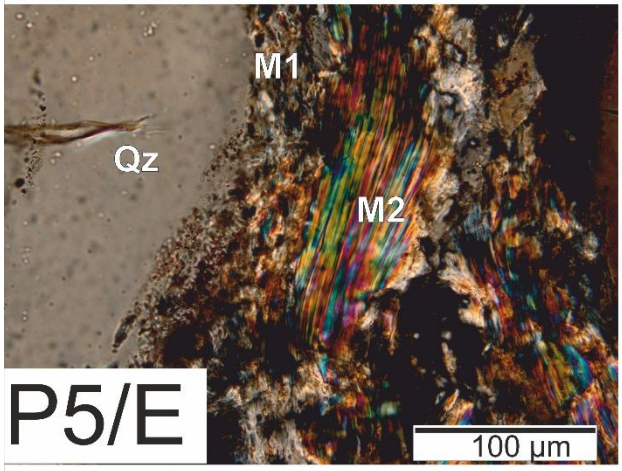
M1
Qz
M2
100 µm
P5/E

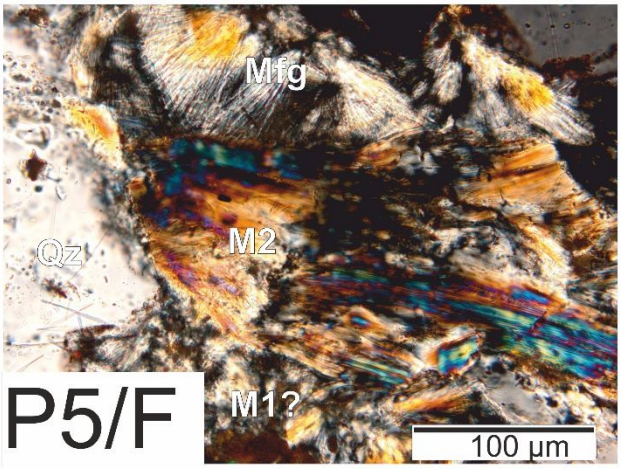
Mfg
M2
Qz
M1?
100 µm
P5/F

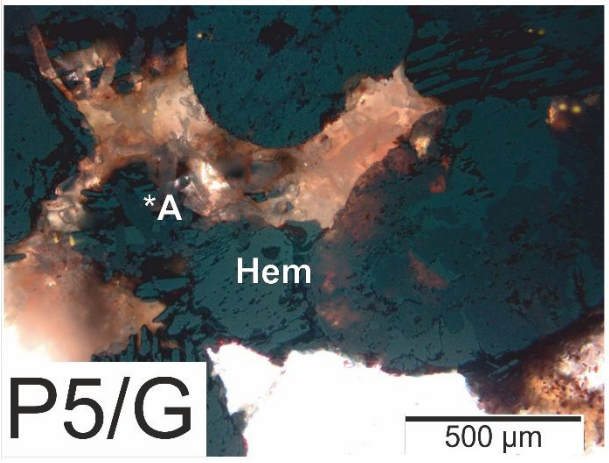
*A
Hem
500 µm
P5/G

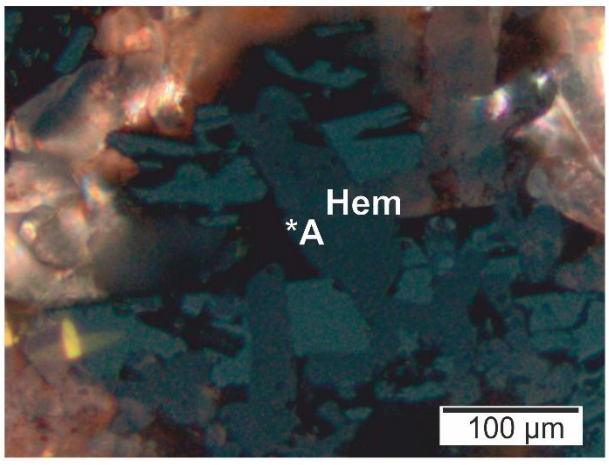
Hem
*A
100 µm

3.1.2 Back Scattered Electron Imagery

Plate: 'S1' Back Scattered Electron Imagery: S1/1 (WR301B – WR301; 319 m; Sandstone Extension to the WS Shear) Magnesiofoitite (Tur2) flakes on quartz. S1/2 (WR293A – WR293; 244.9 m; Sandstone Extension to the WS Shear). M1 flakes on quartz. S1/3 (DPX74 – WR329 360.7 m Sandstone). Kaolinite flakes with sudoite (Sud) and U-Zn-S-Ox mineral (identified via EPMA). S1/4 (DPX16; WR332; 445.7 m Basement). MLC = Mixed Layered Clay. M1/C2, with graphite (Gr) and late sudoite (Sud).

Plate: 'S2' Back Scattered Electron Imagery: S2/1 (DPX62; WR358; 407.7 m Basement). Sudoite with titanium oxide pseudomorphing earlier biotite. S2/2 (WR409A; WR409; 319.9 m Sandstone) Early diagenetic tourmaline (tur0) within an M1 illite groundmass amid partially annealed quartz, minor magnesiofoitite is present as 'spars'. S2/3 (DPX70; WR329; 400 m Basement). Multiple generations of hematite and Fe oxides (FeOx); including a diagenetic overgrowth of Hem1 over quartz, and a detrital Hem0 with later Hem3 bladed overgrowth (*A). Hem 3 is shown to replace M1 (*B). The polytypes 1Mt and 1Mc are shown to be present in this sample, with the late 1Mt illitic polytype cross-cutting late hydrothermal hematite (Hem 3) denoted by *C. It can be distinguished from the 'Mgf' in S2/2 by its lower relief and more bounded, less 'spary' nature. S2/4 (WR409A; WR409; 317.3 m – Sandstone Extension to the WS Shear). Interstitial 1Mt and 1Mc present in a sample utilised for XRD-based illite polytype analysis. S2/5 (WR281B; WR281; 417.4 m – Basement WS Shear). Tur1 and Tur1.1 rimming larger grains. With partially remobilised graphite and sudoite. Pyrite is common and appears coeval with sudoite. S2/6 (WR358; 403 m –Basement) Late C3 reacting biotite and partially replacing M1. S2/7 (WR281B; WR281; 417.4 m – Basement WS Shear). From a well-defined infilled fracture; Tur2 growing within a fracture surface replacing Tur1. S2/8 (WR281B; WR281; 417.4 m – Basement WS Shear). Tur2 growing off Tur1 with graphite and sudoite.

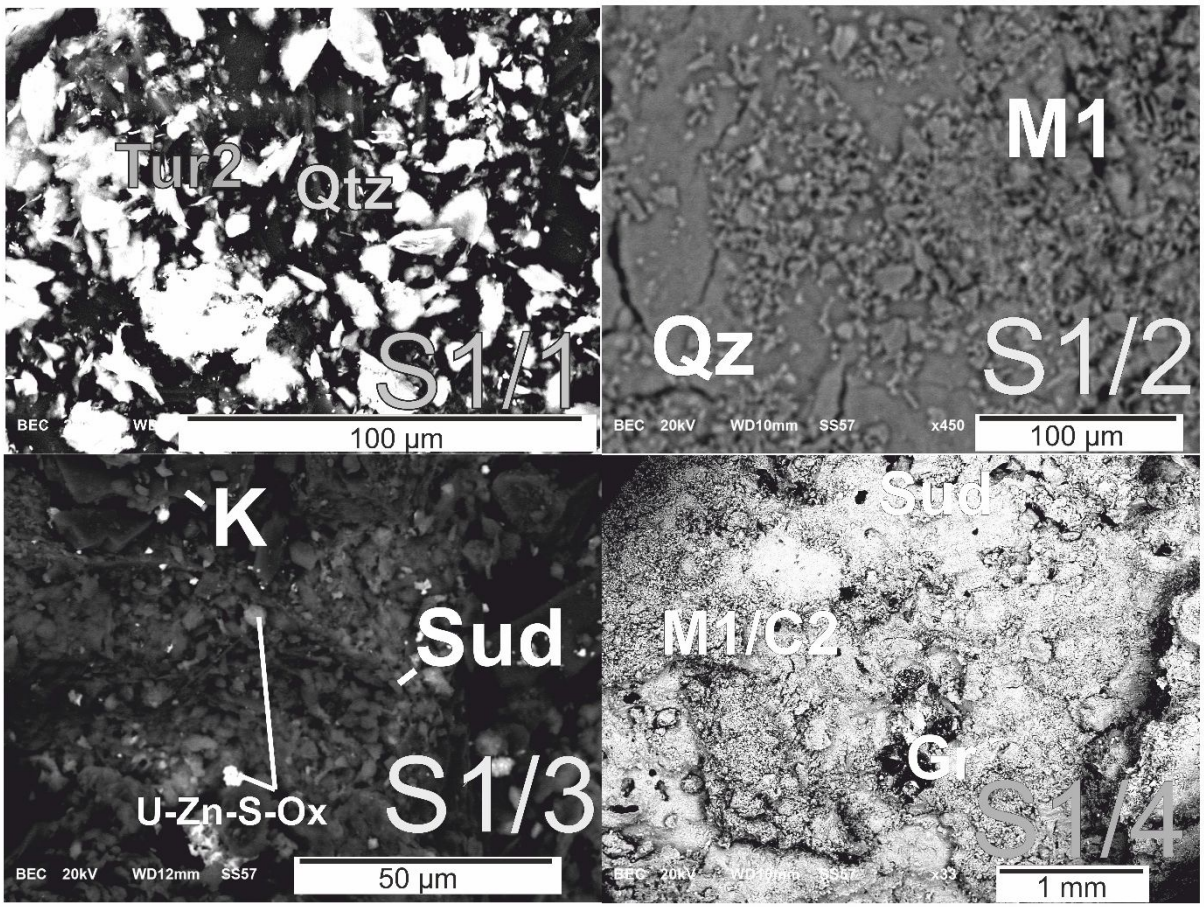

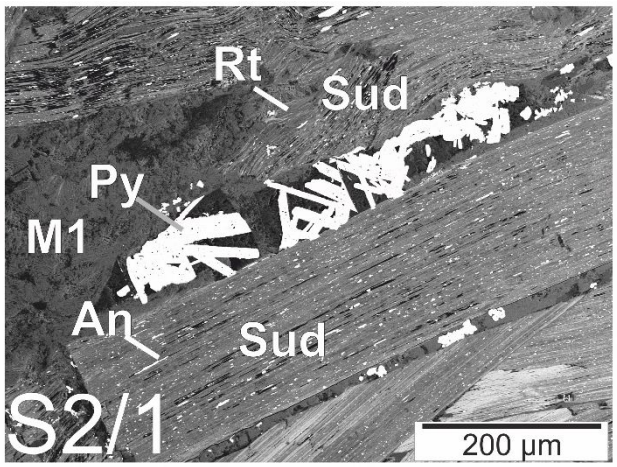
Rt
Sud
Py
M1
An
Sud
S2/1
200 µm

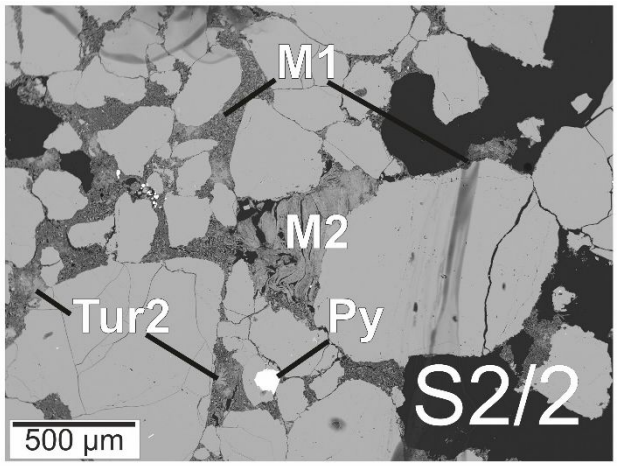
M1
M2
Tur2
Py
S2/2
500 µm

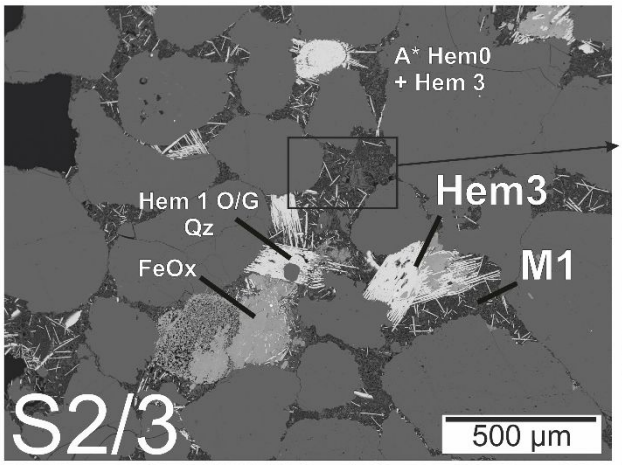
A* Hem0
+ Hem 3
Hem3
Hem 1 O/G
Qz
FeOx
M1
S2/3
500 µm

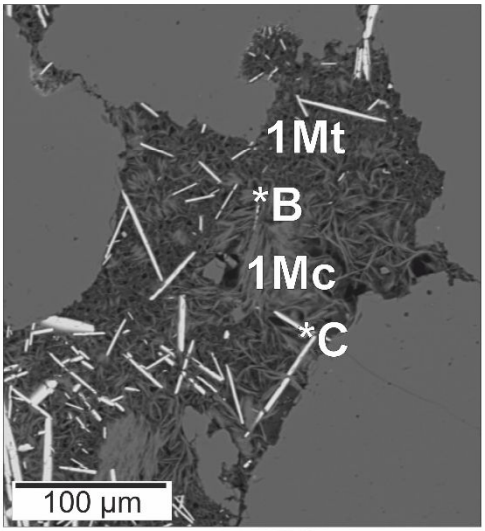
1Mt
*B
1Mc
*C
100 µm

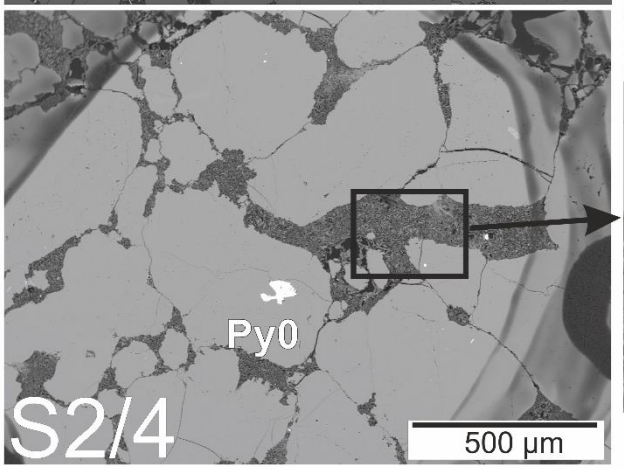
Py0
S2/4
500 µm

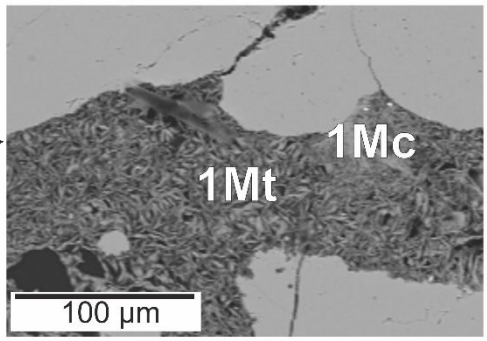
1Mc
1Mt
100 µm

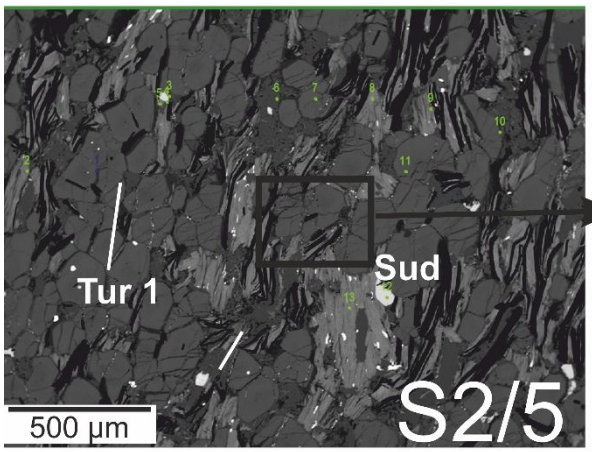
Tur 1
Sud
500 µm
S2/5

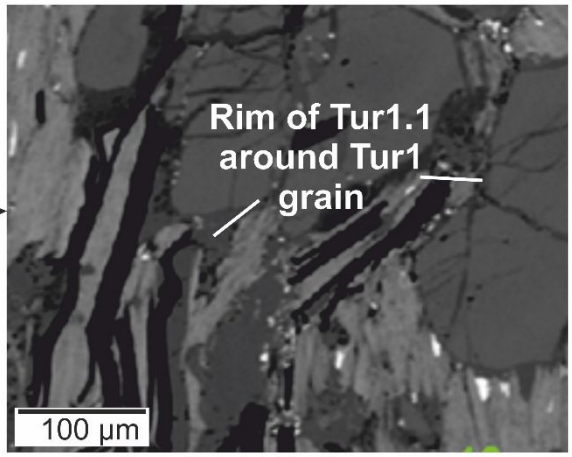
Rim of Tur1.1
around Tur1
grain
100 µm

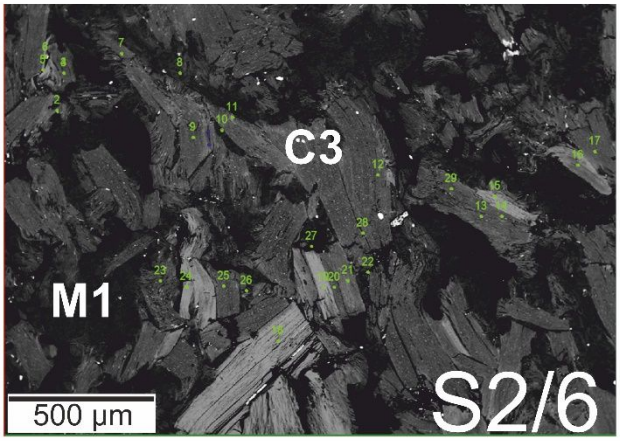
C3
M1
500 µm
S2/6

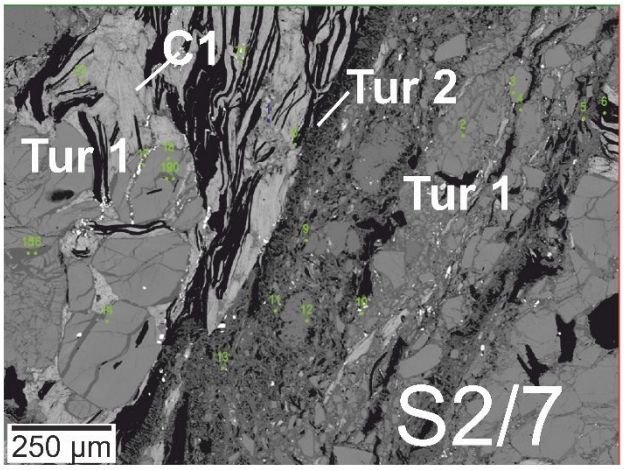
C1
Tur 2
Tur 1
Tur 1
250 µm
S2/7

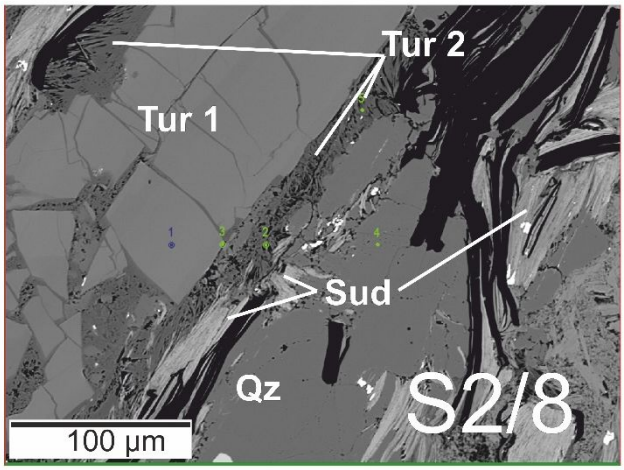
Tur 2
Tur 1
Sud
Qz
100 µm
S2/8

3.2 Other Phases

3.2.1 Iron oxide and oxyhydroxides

Detrital hematite, Hem0, is identified as rounded to subrounded grains in the sandstone and are noted being replaced by later alteration phases, such as M1 (Plate P2/F, S2/3) and pyrite (Plate P3/F). Detrital hematite is also reported from Key Lake (Ramaekers and Dunn 1977) and elsewhere in the Athabasca Group sandstones (Ramaekers 1990). In this study 'Fe oxides' are used to denote phases which are not opaque in transmitted light or have similar colouration to hematite, are rich in Fe, non-crystalline and likely a Fe-oxy-hydroxide. A final, late Fe oxide alteration event may also resulted in the crystallisation of magnetite as shown in Plate P3/F.

The first of the three generations of Fe oxide (FeOx) replacements are considered to be coeval with M1. Although, M1 is seen to crosscut Hem1 in Plate S2/3, elsewhere in the sandstones M1 is shown to be coeval with FeOx1 (Plate P2/F). The second Fe oxide generation is inferred from the coeval growth of C2 and FeOx2 in the sandstones (Plates P1/A and P1/F), and the final third generation is inferred from coeval growth with Qz3 quartz , shown in Plate P3/A).

Although three generations of Fe oxides have been identified, the mineralogy of Fe oxide minerals that replace earlier phases is not fully established. Based on thin-section evidence (Plate P1/B) Fe oxide replaces garnets in the pelitic and graphitic basement units and is common with M1 and C1. Quartz overgrowths appear to have occurred with the crystallisation of Fe oxides, including within the vuggy quartz (Qz2) in the sandstones (Plate P3/A). The growth of late hematite (Hem2) in proximity to Tur2 is shown in Plate P5/B and is clearly later than M1 as shown in Plate S2/3, and as it has not been affected by the earlier magnetite and hematite, it is considered late in the alteration sequence. Bladed late Hem2 is identified growing from detrital hematite (Plate P5/A).

3.2.2 Titanium Oxides and Sulphides

Present within M2 illite and late C3 which has pseudomorphed biotite, titanium oxide is common, forming small acicular crystals (20-80µm) and elongated lozenge-shaped crystals between the 'Plates' in illite and chlorites (1-5µm). Titanium oxide is interpreted to be derived from early biotite which later M2 illites have pseudomorphed, as M2 illite have been observed without titanium oxide (Plate P1/F). Sulphites are present overlying the Phoenix Deposit, principally as pyrite (although minor chalcopyrite and rare covellite have been observed in the sandstones), pyrite is observed to be late in both the basement and the sandstones.

3.2.3 Kaolin Group Minerals

Occasionally observed in thin section kaolin group minerals are noted in some cases in XRD throughout the alteration package- Dickite was only identified in one sample (via SWIR), and its relationship to kaolinite is unclear.

3.2.4 Quartz

Quartz overgrowths and lamellar structures are common throughout the overlying sandstones and observed within the basement samples. In the sandstone overlying the Phoenix Deposit, overgrowths are present as silicified 'bell' (Qz1) and as a vuggy variety (Qz2). Due to a coeval relationship with M1 illite in the sandstones, sandstone Qz1 is considered early and occurs alongside Fe oxide overgrowth and the replacement of detrital hematite. Qz2 is present as vuggy quartz in the sandstones, and overgrowths in the basement, occur alongside Fe oxides, and in the sandstone form occasional trigonal overgrowths filling pore spaces (Plate P3/A). In the basement, Qz1 is present as 'dusty' quartz with C1, while Qz2 is present as 'clean' overgrowths. The relationship between Qz1 and Qz2 in either basement or sandstones has not established.

3.3 Paragenesis of Alteration Mineralogy at the Phoenix Deposit.

Mineral paragenesis is based on textural relationships of alteration minerals (early and late hydrothermal alteration and possible late alteration). The order of paragenesis of alteration for the basement and the sandstones is presented in Figure 13 and Figure 14, respectively.

The detrital mineralogy of the Manitou Falls Formation overlying the Phoenix Deposit consists predominantly of subangular - rounded, sand to cobble-sized detrital quartz particles. Remnants of detrital hematite (Hem0) with later hematite growth are observed in the sandstones (Plate P5/A).

The basement geology in the vicinity of the Phoenix Deposit is composed of pelites, graphitic pelites, pegmatites and quartzite. Which would have contained (and evidence is noted for) quartz, microcline feldspar, biotite (with abundant Ti oxide as shown in Plate P1/G), garnet and early tourmaline (Tur0) in Plate H1/G, graphite is present along the WS Shear (Plate P1/D).

Restricted to samples along the WS Shear, Tur1 (dravite) is noted as being cross-cut by remobilised graphite and has Tur2 (magnesiofoitite) growing from crystal edges (Plate S2/8). C2 is seen to replace the rim of Tur1 (Plate S2/5), suggesting C2 postdates Tur 1. Due to the presence of Tur2 in the sandstones, but the absence of Tur1 in the sandstones, it is suggested that Tur1 was crystallised within the basement in the vicinity of the WS Shear Structure before the deposition of the Read and Manitou Falls Formations.

In the sandstones, the diagenetic alteration is characterised by an initial growth of Fe oxide (FeOx1) overgrowths (Plate P4/C). Following this was a secondary quartz overgrowth (Qtz2) throughout the Athabasca sandstones, with pore filling and replacement of Qtz1 (Plate P3/E), this was followed by regional scale illite crystallisation (M1).

Early hydrothermal alteration in the basal units involved regional scale illite crystallisation (M1) and C2 crystallisation, followed by M2 replacing M1 illite in the sandstones (Plates P5/D and P5/E), C2 is fine-grained and grows alongside M1 (Plates P3/C, P1/E and P4/E). M2 acted to pseudomorph biotite in the basement (Plate P1/G), and elsewhere C3 replaced C1 and M1 (Plate P1/C). M2 is replaced by magnesiofoitite in the sandstones (Plate P4/F) and appears to have a similar temporal relationship with magnesiofoitite in the basement (Plate P3/D).

This study has not had access to uranium-rich core, and as such generating a paragenetic sequence featuring uranium mineralisation is not possible. Based on the work of other studies (Ng et al. 2012 and Adlakha et al. 2015), uranium mineralisation is considered to have occurred prior to or coeval with late Tur2 in the sandstones and roughly coeval with C3 crystallisation in the basement. This sequence places uranium mineralisation as also being coeval with vuggy quartz (Qz3) growth in the

sandstones (Plate P3/A) and with graphite remobilisation (a potential reductant) in the basement, replacing C2 (Plate P1/D). C3 also is seen to replace M2 and as pseudomorphs of earlier biotite (Plates P3/C, P4/A, S2/1, S2/5 and XC), with late pyrite crosscutting all observed phases.

In the sandstones, the final stage is characterised by small (20-50 µm) needles of Tur2 replacing M2 (Plates P2/A, P2/E, P3/G, P4/F), quartz and M2+C2. Although sudoite has been identified through XRD and SWIR based mineralogical analysis in the sandstones, it is not clear which generation (C2 or C3) it belongs to.

Late stage conversion of hematite into magnetite within a reducing environment alongside pyrite is evident in Plate P3/F. This event is considered coeval with uranium mineralisation in the basement and is accompanied by late C3 in the deep sandstones. Finally, the post uranium mineralisation phase of alteration around the Phoenix Deposit is kaolinite in fractures (Plate P4/B) and late 1Mt illite. 1Mt illite is seen replacing 1Mc illite (Plates S2/3 and S2/4) and therefore in lieu of other temporal information it is presumed to be post 1Mc and may share relationships with 1Mt observed elsewhere, which found material similar to 1Mt to be post uranium mineralisation (Laverret et al. 2006).

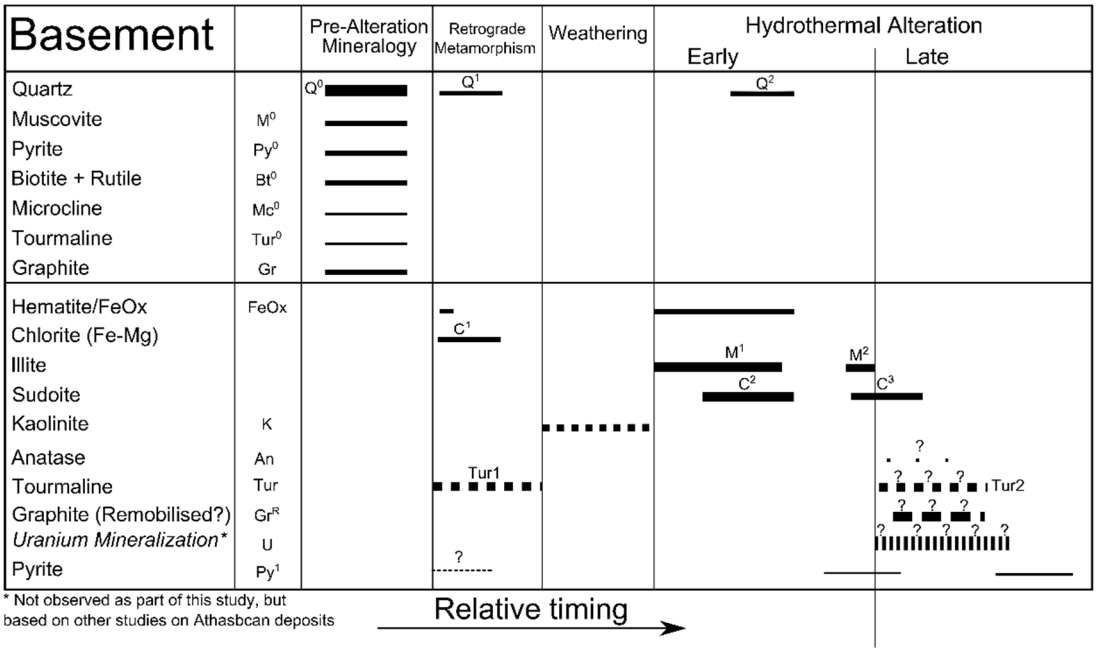

Figure 13: General mineral paragenesis for the basement rocks of the Phoenix Deposit. With five main observable alteration stages: metamorphism, weathering, early and late hydrothermal alteration. The thickness of lines indicates abundance in thin section and hand sample, dashed lines and question marks (?) indicate uncertainty. Other than the presence of dravitic tourmaline there is no notable difference in the paragenesis between basement units away from or in close proximity to the WS Shear.

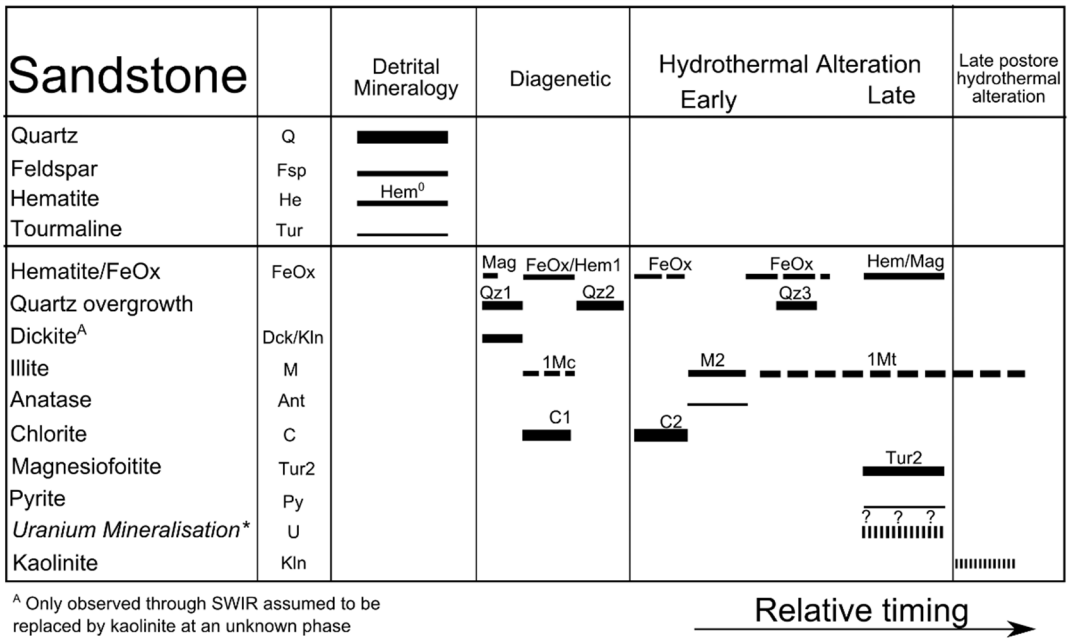

Figure 14: General mineral paragenesis for the Read and Manitou Falls Formations overlying the Phoenix Deposit. Four main observable alteration stages have been established: diagenetic, early and late hydrothermal alteration and postore alteration. The thickness of lines indicates abundance in thin section and hand sample; dashed lines indicate uncertainty. There is no notable difference in the paragenesis between the sandstone units and the WS Shear.

3.4 Mineral Chemistry

3.4.1 Tourmaline

3.2.1.2 Occurrences

Two main generations of tourmaline alterations were noted within this study area. An early tourmaline (Tur1) is dravatic in compsosion, present only in the basement and in proximity to the WS Shear structure (Sample WR281B) or areas of intense hydrothermal alteration (Sample DPX 62). Within the graphitic pelite, Tur1 is brecciated edged with a very thin material, which appears darker in BSE (as shown in Plate S2/5). Limited chemical analysis has been carried out on the darker material, but it shows no significant differences in composition to the core of the Tur1 grains. In crossed polars Tur1 is present as straw yellow to dark orange crystals following an earlier metamorphic foliation (P1/D)

The later tourmaline, Tur2 (magnesiofoitite), is associated with the WS shear in the basement and more widely within the sandstones; In the basement, Tur2 is acicular and replaces Tur1, graphite and chlorite (Plates S2/4 and S2/5) In the sandstones, Tur2 is more prevalent, and found in the Sandstone Extension to the WS Shear, and non-sheared sandstones 100 m above the unconformity. Tur2 in sandstones forms prismatic to slightly acicular aggregates of crystals within a matrix of M1 illite and chlorite.

3.2.1.2 Mineral Chemistry and Chemical Composition of Tourmaline

The chemical formula of tourmaline was calculated based on the ideal formula $XY_3Z_6(T_6O_{18})(BO_3)_3V_3W$, which assumes 3 B in the B-site, 6 Si + Al forming the T-site and 3 OH in the V-site. As suggested by Rosenberg and Foit (2006), the stoichiometric proportions of tourmaline were normalised to 15 cations (Y + Z + T sites). For cation site assignment, the T-site was filled first with Si^{4+}, then Al^{3+} to sum 6 cations. The Z-site was occupied by Al^{3+} and the remaining Al^{3+} was assigned to the Y-site. The Y-site was filled by Ti^{+}, Fe^{2+} and Mg^{2+}. All Ca^{2+}, K^{+} (where present, and not thought to be derived from contamination) and Na^{+} were assigned to the X-site. The W-site accommodates F^{-}, OH^{-} and O_2^{-}. The fractions of OH^{-} and O_2^{-} were calculated to compensate excess cation charges. All Fe was assumed to be Fe^{2+} for tourmalines. The assignment of Fe^{2+} into Tur1 is supported by the following evidence; Firstly, the *f*O2 is expected to be low in metapelites due to the buffer by abundant graphite. Secondly, any Fe^{3+}, if present, is preferentially incorporated into co-existing illite and biotite over tourmaline (Dyar et al. 2002). For Tur2, the cation charges were in excess when Fe^{3+} was used over Fe^{2+} within stoichiometric calculations. All chemical analysis was carried out using EPMA and is presented in Appendix 3.

Note on Low Totals

Totals from the EPMA carried out on the majority of samples of tourmaline were lower than the ideal values of 82-85%. Lithium is often identified as a potential source of low totals (Clark, 2007). However, no lithium bearing tourmalines have been identified within the Athabasca basin, and fluid inclusion studies from tourmalines have failed to yield lithium as being present in the mineralising brine (Richard et al.,2011). Figure 15 presents the calculated total vs X site vacancy in tourmalines analysed in this study, and demonstrates the positive relationship between X site vacancy and the calculated total (Figure 15). This suggests that the low totals are not related to vacancies of the calculated structure of the samples analysed and are derived from either missing elements or analytical errors. Therefore, the low totals are attributed to the surface condition of areas for analysis.

All samples with totals of <80% were excluded from compositional analysis.

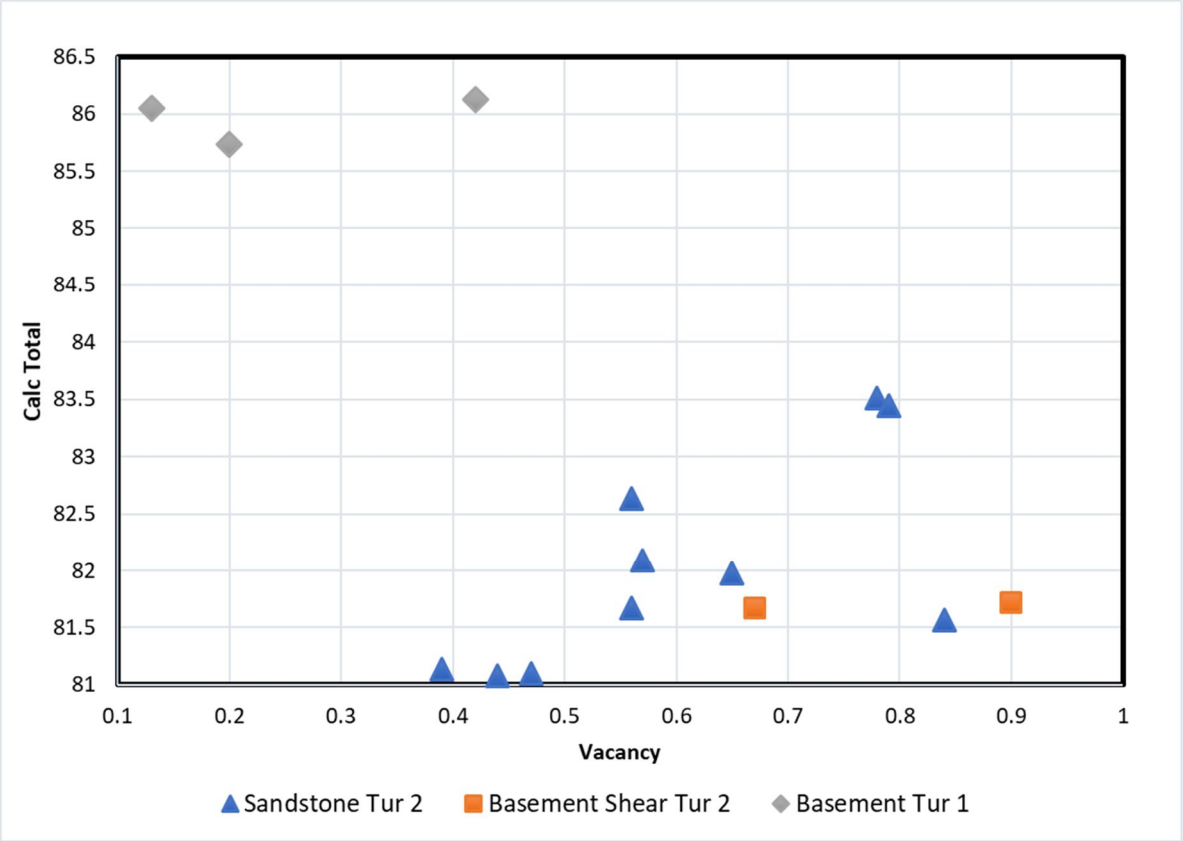

Figure 15: Calculated Total vs. X site vacancy in tourmlaines from the alteration halo of the Phoenix Deposit. The vacancy of sandstone Tur2 increases with the calculated total of the sample. In the basement, Tur 1 appears to have no correlation with calculated totals and vacancy.

Tur1-Basement

Tur1 is Mg-rich, Fe-poor with an average formula of $(\square_{0.18}Ca_{0.32}Na_{0.5})(Mg_{1.9}Fe^{ii}_{0.71}Al_{0.23}Ti_{0.11})Al_6(Si_{5.86}Al_{0.14}O_{18})(BO_3)_3OH_3(F_{0.31}OH_{3.69})$ based on the analysis of 9 locations in 4 grains in one sample. It is a dravitic tourmaline and has low Na and vacancy (Table 7). Samples also show a slight variation in the Y site in Al (0.12-0.28), Fe (0.72-0.78) and Mg (1.83-1.93). Samples show considerable variation in composition, with samples closer to veins or cracks being Na-enriched relative to those in the cores of grains.

Table 7: Basic statistics of Tur1 composition, units per formula. From 4 grains (9 spots) in sample WR281B. For composition and formulae calculations, please see Appendix 4.3.

	Mg	Al	Fe	Na
Average	1.87	0.23	0.74	0.49
Std Dev	0.03	0.05	0.02	0.05
Max	1.93	0.28	0.78	0.62
Min	1.83	0.12	0.72	0.45
n =	9	9	9	9

Tur2 -Basement

Tur 2 in the basement has an average composition of $(\square_{0.74}Na_{0.25})(Mg_{1.94}Al_{0.66}Fe^{iii}_{0.21})Al_6(Si_{6.03}O_{18})(BO_3)_3OH_3(F_{0.07}OH_{3.93})$ based on the compositional analysis of two grains which both had totals of 81.7%. The two samples analysed had compositions in Y site of Al of 0.484 and 0.96, Mg 1.931 and 1.984 and in Fe of 0.06 – 0.46. In the X site the vacancies were 0.44 to 0.85, (Table 8). It is a magnesiofoitite tourmaline.

Table 8: Tur2 Basement composition of 2 grains in the basement, units per formula (sample number WR281B). For composition and formulae calculations, please see Appendix 3.3.

Vacancy	Mg	Al	Fe	Na
0.84	1.929	0.96	0.06	0.15
0.44	1.931	0.433	0.46	0.32

Tur2 -Sandstone

Tur2 in the sandstones has an average composition of $(\square_{0.81}Na_{0.19})(Mg_{1.78}Al_{1.37}Fe^{iii}_{0.11})Al_6(Si_{5.72}Al_{0.28}O_{18})(BO_3)_3OH_3(F_{0.04}OH_{3.95})$ from analysis of 16 grains in one sample in the Read Formation. Table 9 shows a large variation in Fe (0.11 – 1.2) and variation in Mg (1.65 – 1.89) and Al (1.03 – 1.89) in the Y site between samples in close proximity to each other. X site vacancies range from 0.76 to 0.82. It is a magnesiofoitite tourmaline.

Table 9: Tur2 Sandstone composition of 16 grains (sample DPX81), units per formula. For composition and formulae calculations, please see Appendix 3.3.

	Vacancy	Mg	Al	Fe	Na
Average	0.78	1.78	1.08	0.11	0.19
Std Dev	0.02	0.07	0.29	0.41	0.04
Max	0.82	1.89	1.89	1.2	0.22
Min	0.76	1.65	1.03	0.11	0.09
N =	16	16	16	16	16

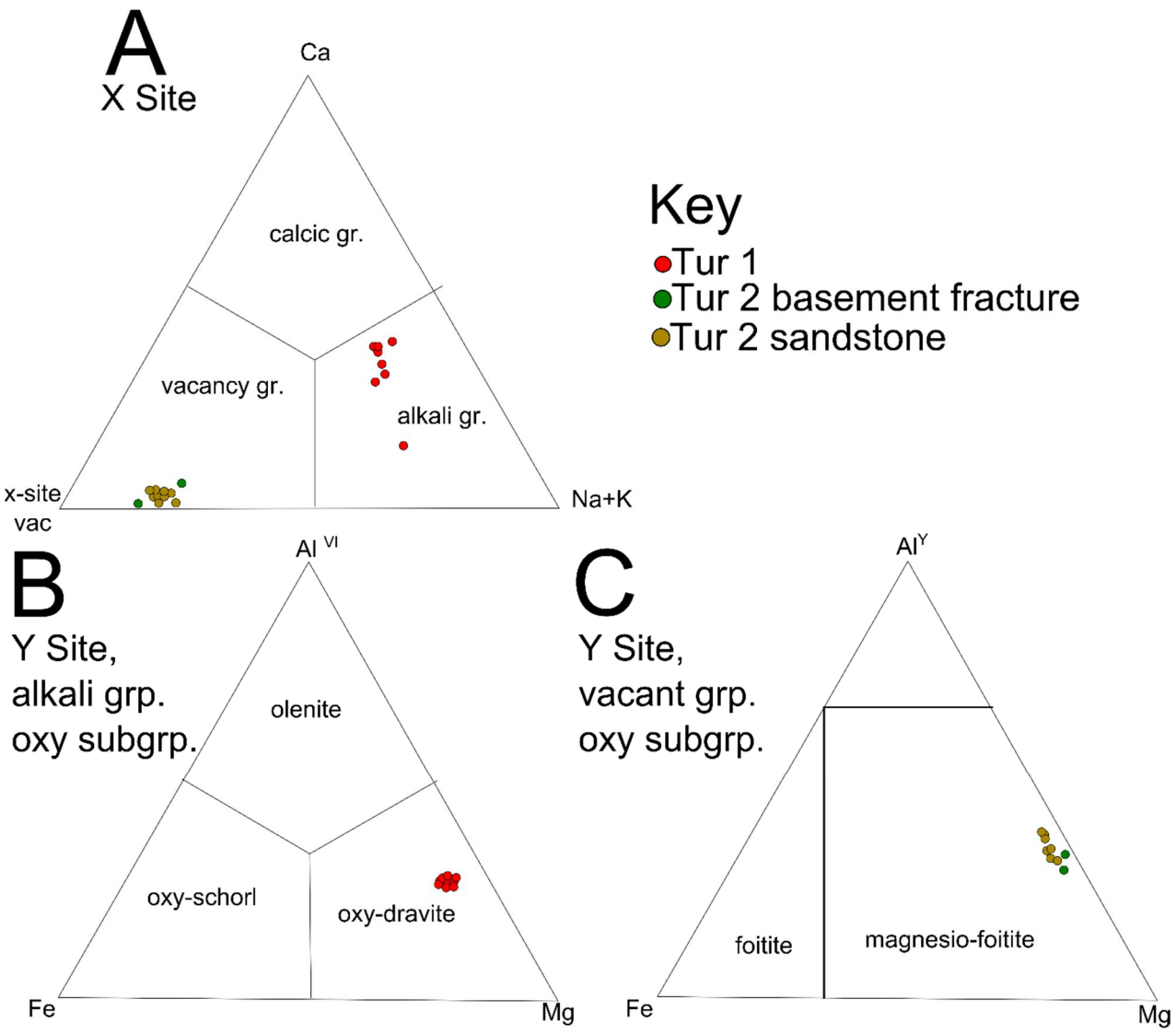

Figure 16: Ternary plots of tourmaline compositions from the areas surrounding the Phoenix Deposit (modified from Henry et al. 2011). A) X-Site occupancy, B) Y-Site occupancy for oxy-species and C) Y-site occupancy for the X-site vacant group.

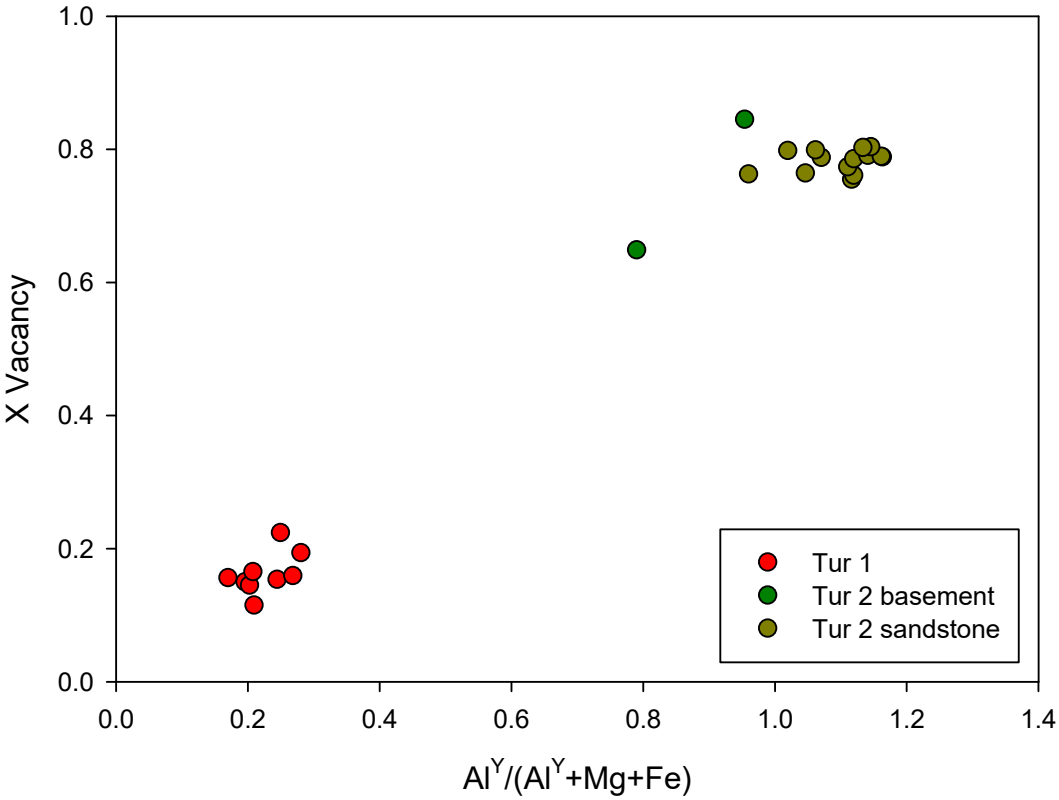

Figure 17: Binary plot of x-site vacancy vs $Al^{Y}/(Al^{Y}+Mg+Fe)$

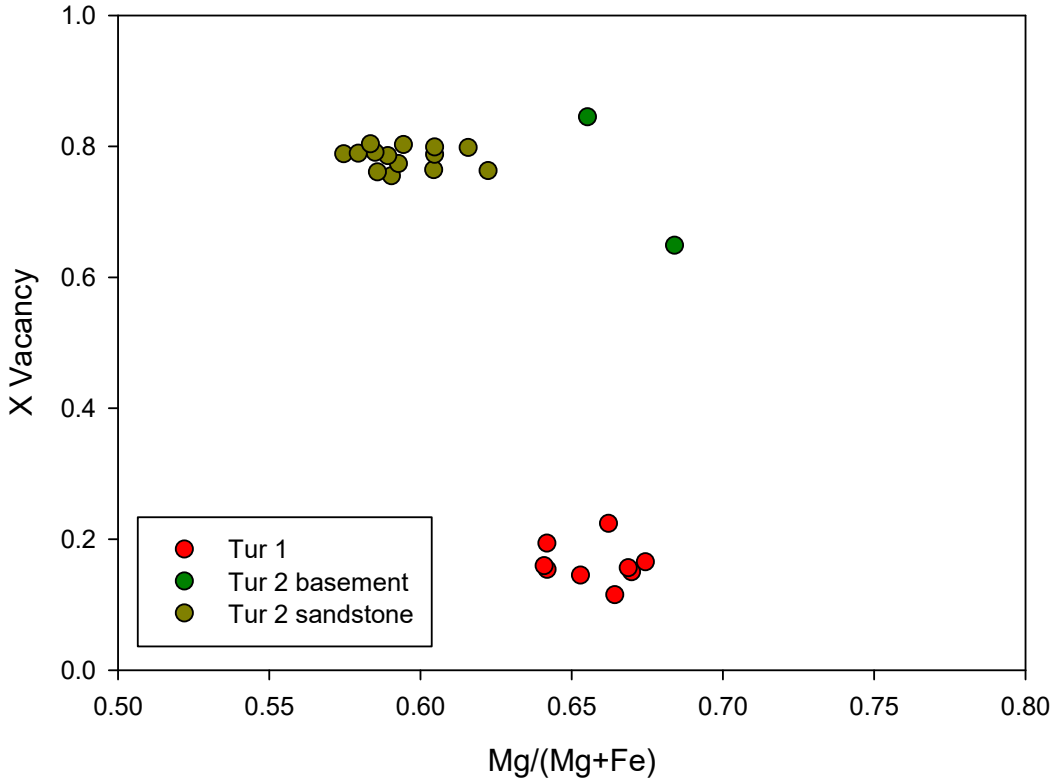

Figure 18: Binary plot of x-site vacancy vs Y-site Mg/(Mg+Fe) ratio

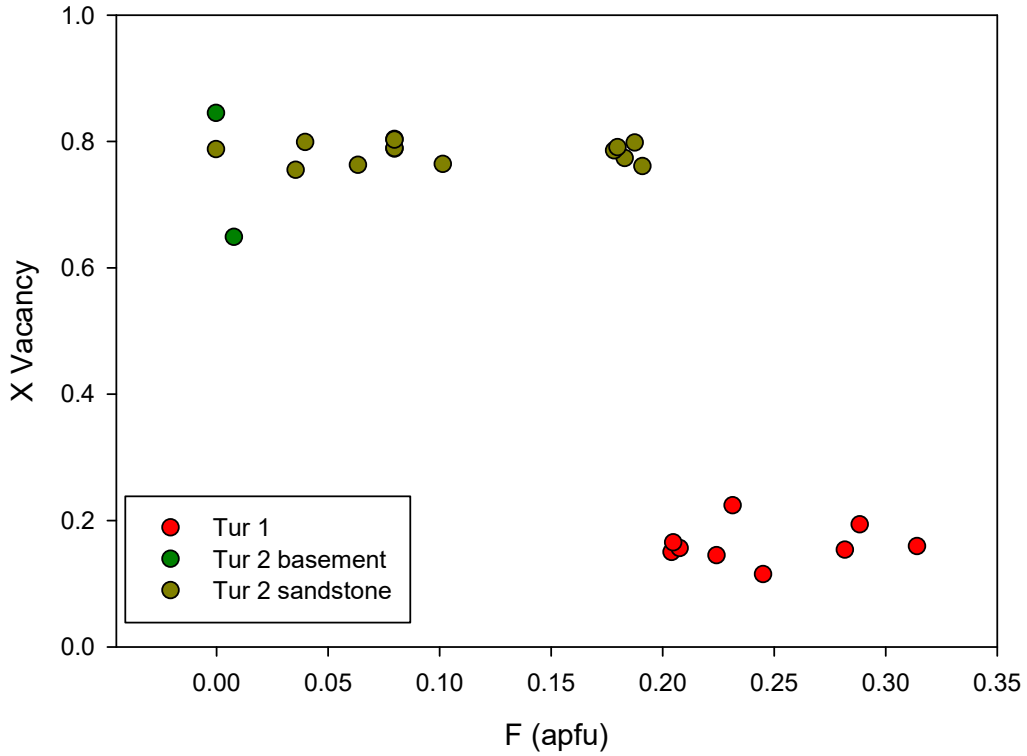

Figure 19: Binary plot of x-site vacancy vs F apfu.

3.4.2 Illite

3.6.2.1 Occurrences

Textural analysis of the thin section and BSE imagery reveals three different forms of white mica. The 1Mc illite identified in this study is interpreted to be an early phase, and is shown to be equivalent to the c-1M polytype identified elsewhere in the Athabasca Basin (Drits et al. 1993; Laverret et al. 2006).

At the Phoenix Deposit, the early M1 (1Mc) is coeval with C1 in the sandstones, and C2 in the basement, and crosscut by later mid alteration sequence M2 illite. A third, late polytype, 1Mt, is equivalent to the t-1M polytype identified elsewhere in the Athabasca Basin (Drits et al. 1993) and has been suggested as a late paleoflow indicator phase which may have associations with the uranium mineralisation (Laverret et al. 2006).

Eight illite-containing samples were analysed for their composition using EPMA, five in the basement and three in the sandstones. All calculations were based on 14 oxygens. Based on phase relationships all Fe was assumed to be Fe^{2+} as substitution of Fe^{3+} for Fe^{2+} is not a readily available mechanism for the Fe-poor M1 illites in this study (Murad and Wagner 1994).

3.2.3.2 1Mc and 1Mt Illite

In the basement M1 is a fine-grained (<1µm), Fe-poor spongiform, very fine-grained illite, which is pervasive overprinting quartz (Plate 1/C), Fe oxides which have pseudomorphed garnet (Plate 1/B) and earlier metamorphic minerals.

Within the sandstones, M1 illite is a ubiquitous alteration phase. In the lower sandstone units and basement, M1 shares an association with C2 commonly interspersed with Fe oxides, but elsewhere, in the upper sandstones, it commonly occurs without an association with Fe oxides. Occasionally, such as within the Sandstone Extension to the WS Shear, XRD analysis has indicated the presence of 1Mc and 1Mt polytypes within the sandstone alteration package. The distinction between the 1Mc and 1Mt polytypes cannot be readily made in thin section; both polytypes are observable through SEM (Plates S2/3 and S2/4). The 1Mc polytype comprises the vast majority of the M1 interstitial material overlying the Phoenix Deposit and is formed of fine acicular crystals filling pore space and replacing quartz (Plates P2/C and P4/D).

3.2.3.3 M2 Illite

In the sandstones, M2 is coarser grained with crystals between 100µm and 200µm with a high birefringence (Plates P3/C, P5/D and P5/E) and replaces quartz, M1 and C2. Unlike M1, M2 is relatively uncommon throughout the sandstones but is present within the WS Shear. In the basement, M2 is coarser grained (up to 5 mm, suggesting, at least textually, it may be muscovite) and occasionally containing Ti-bearing phases (Plate P1/G). M2 replaces M1 and pseudomorphs biotite and replaces earlier alteration derived chlorite.

3.4.3 Chemical Composition of Illite

The majority of illite overlying the Phoenix Deposit is the 1Mc polytype, which is the early 'regional' illite based on the observation in WR 380. Later M2 and very late 1Mt are present above and around the orebodies as shown on Figure 29 and Figure 30.

XRD derived polytype analysis has not been carried out in the basement samples due to difficulty to obtain clay fraction and clay concentrates. However, thin section petrographic analysis (Plates 1 to 5) has indicates the presence of both M1 and M2 of illite in the sandstone, and M1 is considerably more widespread.

Chemically, the Illite identified at the Phoenix Deposit is closer to true muscovite than to illite, as demonstrated in Figure 20. However, in line with other studies which share a similar composition of illite (e.g. Hoeve and Sibbald 1978, Kotzer and Kyser 1995, Fayek and Kyser 1997) the micaceous material identified in the alteration halo of the Phoenix Deposit is termed as 'illite' in order to maintain a comparable nomenclature with other works.

3.6.3.1 Mineral Chemistry

The basement hosted 1Mc is K rich, but relatively Mg and Fe-poor, with a formula of $K_{0.85}Mg_{0.22}Fe^{(II)}_{0.09}Al_{1.66}(Si_{3.54}Al_{0.46}O_{10})(OH_{1.99}F_{0.01})$ as shown in Table 10. Samples show a considerable variation in K (0.52 – 0.97 in apfu) and significant variation for Mg (0.083- 0.77 in apfu) and Fe (0.05 - 0.64 in apfu), as shown in below in Table 10 and compared to the sandstone-hosted M1 and chlorites identified in this study in Figure 20.

Table 10: Basement hosted M1 illite, units per formula based on 14 oxygen.

	X Site	Y Site			Z Site	
	K^+	Mg^{2+}	Fe^{2+}	Al^{3+}	Si^{4+}	Al^{3-}
Average	0.839	0.251	0.108	0.652	3.522	0.478
Std Dev	0.09	0.15	0.1	0.02	0.13	0.13
Max	0.967	0.775	0.641	0.668	3.71	0.795
Min	0.522	0.099	0.05	0.589	3.205	0.29
n	37	37	37	37	37	37

Like the basement hosted M1, the sandstone-hosted M1 is K rich, but relatively Mg and Fe-poor, with a formulae of $K_{0.75}Mg_{0.34}Fe^{(II)}_{0.06}Al_{1.68}(Si_{3.42}Al_{0.58}O_{10})(OH_{1.99}F_{0.01})$. Table 11 illustrates that basement hosted M1 samples show variation in K (0.52 – 0.94) and quite an extreme variation for Mg (0.01- 0.94) and Fe is variable (0.05 - 0.87) with the sandstone M1 depleted in Fe. Comparison to the basement-hosted M1 and chlorites identified in this study is presented in Figure 20.

Table 11: Sandstone -hosted M1 illite, units per formula based on 14 oxygen.

	X Site	Y Site			Z Site	
	K^+	Mg^{2+}	Fe^{2+}	Al^{3+}	Si^{4+}	Al^{3-}
Average	0.751	0.337	0.059	0.663	3.419	0.581
Std Dev	0.196	0.272	0.015	0.007	0.153	0.153
Max	0.942	0.943	0.089	0.672	3.599	0.904
Min	0.262	0.08	0.037	0.642	3.096	0.401
n	18	18	18	18	18	18

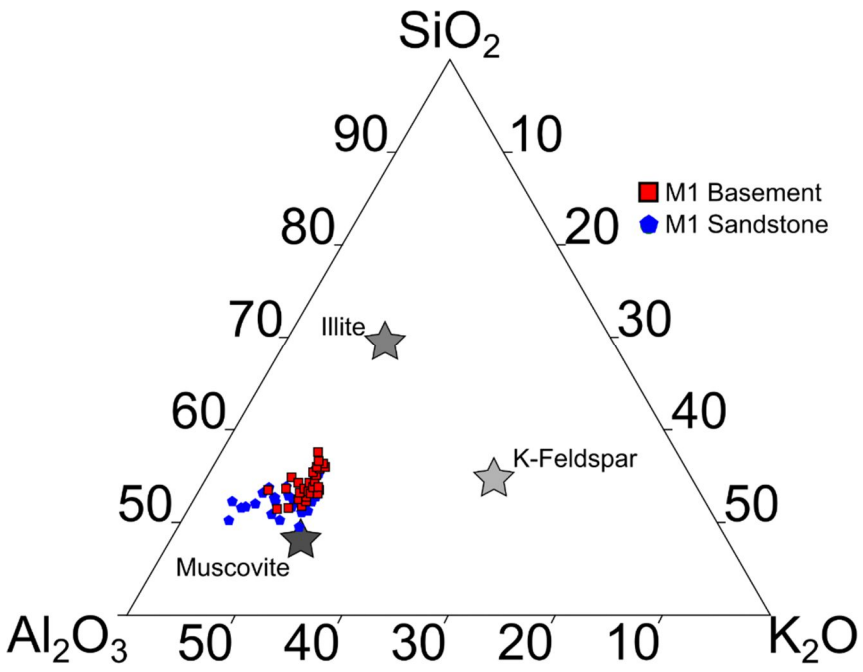

Figure 20: Molar proportion Al-Si-Fe ternary diagram of white mica compositions in the alteration halo of the Phoenix Deposit and ideal composition of, K-feldspar, illite and muscovite (modified from Cloutier et al., 2009).

3.4.4 Chlorite

Occurrences and distribution of different types of chlorite

Occurring as a very fine-grained, olive green in XPL and translucent in (PPL) in the basement samples and associated with early Quartz overgrowth (Qtz0), C1 is largely replaced by M1/C2 (Plate P2/C) and in C3 (Plate P1/F).

C2 is present as a fine-grained, light green – orangey green crystals in thin sections, often in close spatial relationship with M1, it occurs in both the basement and the Athabasca sandstone samples. Both C2 and M1 are fine-grained, due to their roughly coeval growth in the sandstones and basement they are observed forming intergrowths shown in (Plates P3/C, P1/F, P4/E, BSE images S1/4). Late C3 occurs as coarser grained phase, often pseudo-morphing biotite (Plate P4/G), and pervasively replacing C1 and C2+M1 throughout the basement (Plate P3/C).

Based on observations from XRD diffractograms of whole rock and clay concentrates alongside SWIR spectra analysed as part of this study, Fe-Mg chlorite (C1) is present at three locations of the Athabasca Sandstones, in the topmost sandstones in MFd, accompanying a bleached zone of kaolinite and tourmaline, and in a broad zone running along the unconformity. C2 sudoite is limited to the deep Athabascan sandstones (Read Formation), generally within 50 m of the orebodies of the Phoenix Deposit.

Seven basement chlorite grains were analysed for their composition by EPMA as part of this study. Sandstone samples of chlorite returned low totals and were excluded from the data set, the low totals are considered to be due to errors in the locations chosen for analysis, the suite of elements analysed for were appropriate in comparison to other studies on Athabascan type uranium deposits. All formulae are calculated based on 14 oxygens assuming all Fe as Fe^{3+}.

3.4.5 Chlorite Composition

The analysis in the basement has been undertaken on three texturally distinct generations of chlorite. The results are compiled on an Al-Mg-Fe ternary diagram (Figure 22).

C1 Basement Chlorite

The first generation, basement chlorite C1 has an average structural formula of $(Mg_{2.65}Fe_{1.9}Al_{1.45})(Si_{2.71}Al_{1.29})O_{10}(OH_{7.95}F_{0.05})$ (Table 12). Analytical results with of elevated Ti were excluded from the data because of the concern that they were mixed with rutile. As shown in Figure 21 C1 chlorites plot within the ripidolite subgroup of clinochlore.

Table 12: C1 chlorite. Units per formula based on 14 oxygen.

	Mg^{2+}	Fe^{3+}	Al^{3+}	Si^{4+}	Al^{IV}	F^-	Cl^-
Average	2.543	1.827	1.239	2.608	1.392	0.051	0
Std Dev	0.293	0.318	0.114	0.064	0.064	0.029	0
Max	3.081	2.178	1.533	2.697	1.549	0.1	0
Min	2.247	1.383	1.02	2.451	1.303	0.01	0
n	12	12	12	12	12	12	12

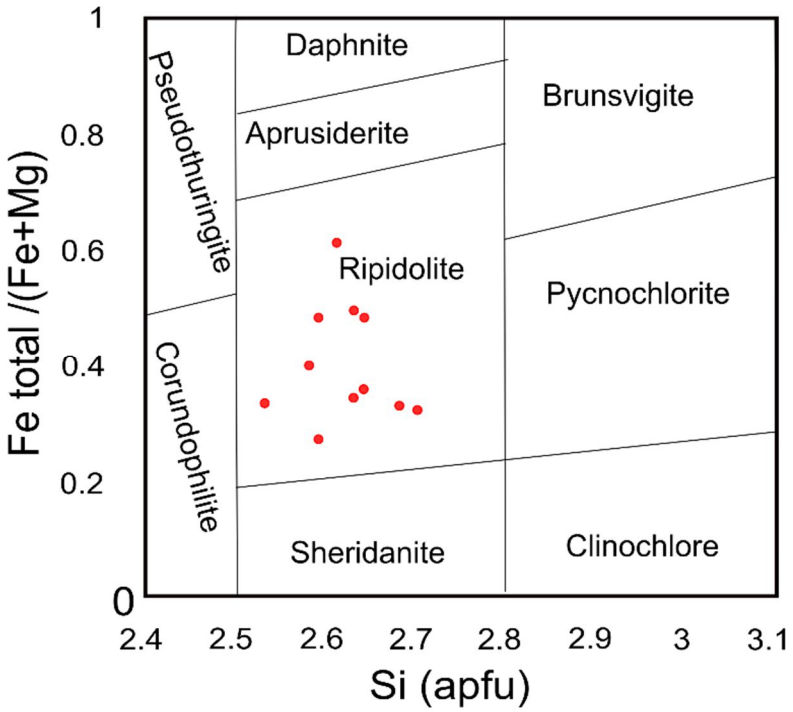

Figure 21: Modified from Hey (1954), C1 chlorite composition on basis of 14 oxygens. Red circles represent the composition of basement C1 chlorites within this study.

3.2.6.2 C2 Basement Chlorite

The second generation of basement chlorite, C2 has an average structural formula of $(Mg_2Fe_{0.39}Al_{2.56})(Si_{3.19}Al_{0.81})O_{10}(OH_{7.95}Cl_{0.01}F_{0.04})$. Table 13 presents results.

Table 13: C2 early Sudoite. Units per formula based on 14 oxygens.

	Mg^{2+}	Fe^{3+}	Al^{3+}	Si^{4+}	Al^{IV}	F^-	Cl^-
Average	2.002	0.399	2.554	3.189	0.811	0.039	0
Std Dev	0.121	0.318	0.213	0.088	0.088	0.012	0
Max	2.143	0.79	2.809	3.281	0.991	0.06	0
Min	1.76	0.046	2.231	3.009	0.719	0.02	0
n	9	9	9	9	9	9	9

3.2.6.3 C3 Basement Chlorite

Late chlorite, C3 has a structural formula $(Mg_{1.97}Fe_{0.23}Al_{2.65})(Si_{3.29}Al_{0.71})O_{10}(OH_{7.95}Cl_{0.01}F_{0.04})$, and shows roughly a similar chemistry to C2, the other sudoitic chlorite. Table 14 presents results.

Table 14: C3 late Sudoite. units per formula based on 14 oxygens.

	Mg^{2+}	Fe^{3+}	Al^{3+}	Si^{4+}	Al^{IV}	F^-	Cl^-
Average	1.971	0.236	2.65	3.29	0.71	0.042	0
Std Dev	0.417	0.218	0.354	0.189	0.189	0.023	0
Max	2.586	0.609	3.275	3.673	1.079	0.1	0
Min	1.116	0.038	2.103	2.921	0.327	0	0
n	21	21	21	21	21	21	21

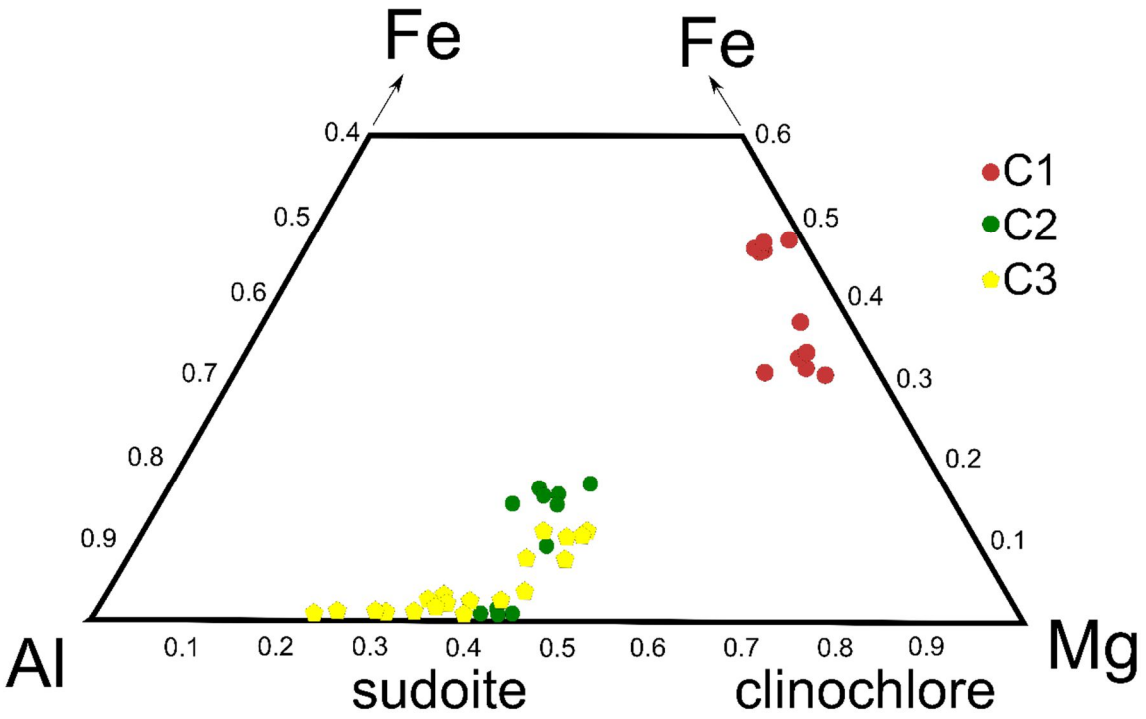

Figure 22: Modified from Cloutier et al. 2010: An Al-Mg-Fe ternary diagram for chlorites around the Phoenix Deposit. C1 (red solid circles), C2 (green solid circles) and C3 (yellow solid circles) plotted as a function of cation proportions. Also shown is the ideal composition of clinochlore and sudoite.

3.5 Illite Crystallinity

3.5.1 Kübler value in Clay Fractions

As shown in Figure 23, Samples from the Athabasca Sandstones show a slight inverse correlation between crystallinity and depth (illite crystallinity is inverse to the 10 Å FWHM), suggesting shallower samples are more crystalline than those deeper, and closer, to the deposit. Samples from the Sandstone Extension to the WS Shear structure show a great variety of Kübler values, between 0.34 and 0.52. These values straddle the diagenetic and anchizones, with one shallow sample within the higher temperature epizone. Between 320 and 340 m downcore there is a large variation in results, with no significant correlations. No units are used when expressing Kübler values.

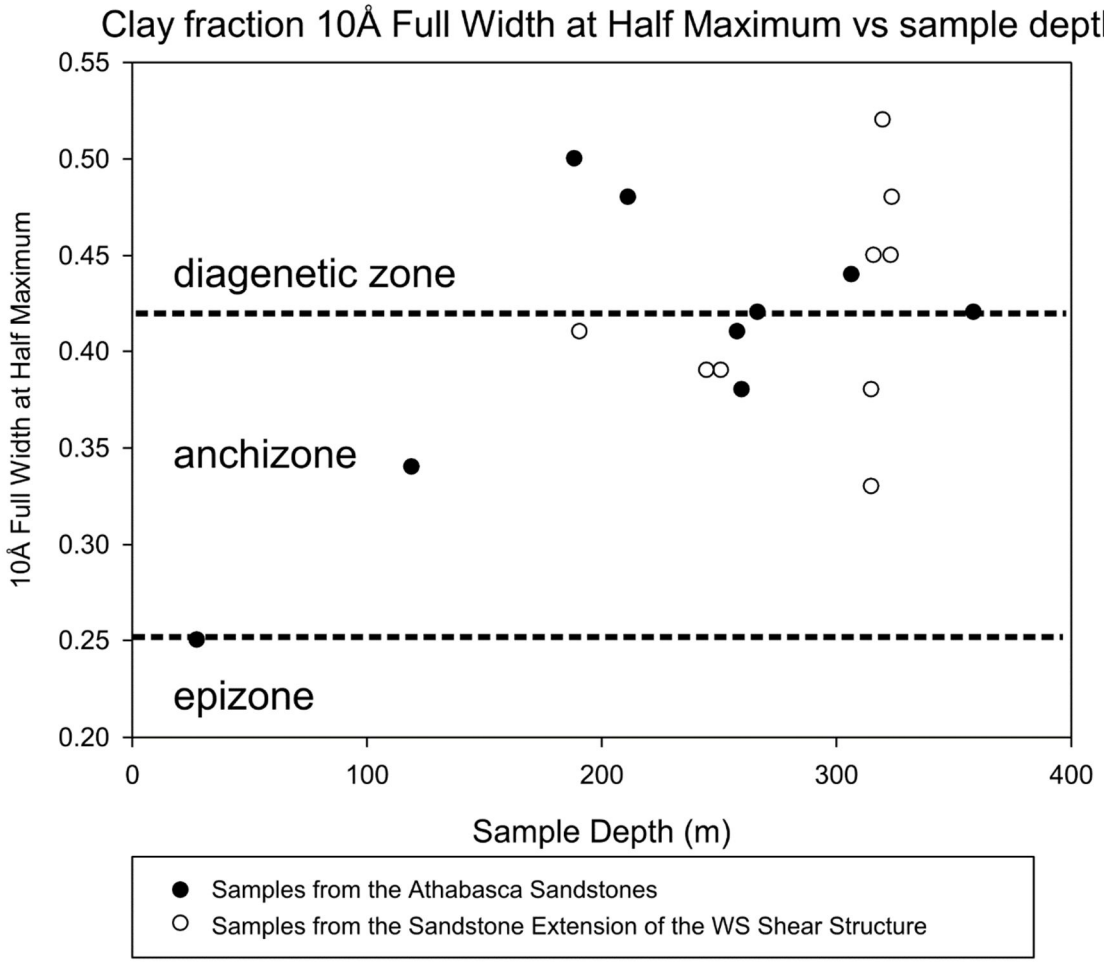

Figure 23: Clay fraction 10A Full Width at Half Maximum vs sample depth. There is a broad inverse correlation between the two. The fields for epizone, diagenetic and anchizone metamorphic domains are after Kubler (1967). The majority of samples plot within the diagenetic and anchizone metamorphic domains with one shallow sample within the higher temperature epizone.

3.5.2 M-Kübler in Clay Concentrates

As shown in Figure 24, Samples from the Sandstone Extension to the WS Shear show a slight positive correlation with an m-Kübler value (as described in Section: 3.7.2; M-Kübler in Clay Concentrates) of 0.18 to 0.32 between 225 m and 325 m downcore. Athabascan sandstone samples are more diverse, samples from WR380, around 1.8 km from the Phoenix Deposit have values between 0.23 and 0.36 between similar depths. Samples from WR277 from north of the Phoenix orebodies have a broadly inverse correlation from 0.43 at 25 m below ground level to 0.27 at 235 m downcore. In Figure 23, samples from the Sandstone Extension to the WS Shear show a positive correlation with depth, with these results being significantly less crystalline closer to the uranium mineralisation and become lower (so more crystalline) as one moves away from uranium mineralisation. The crystallinity of illite elsewhere in the alteration package is comparable to that noted in the shallower (<250 m downcore) samples retrieved from the Sandstone Extension to the WS Shear.

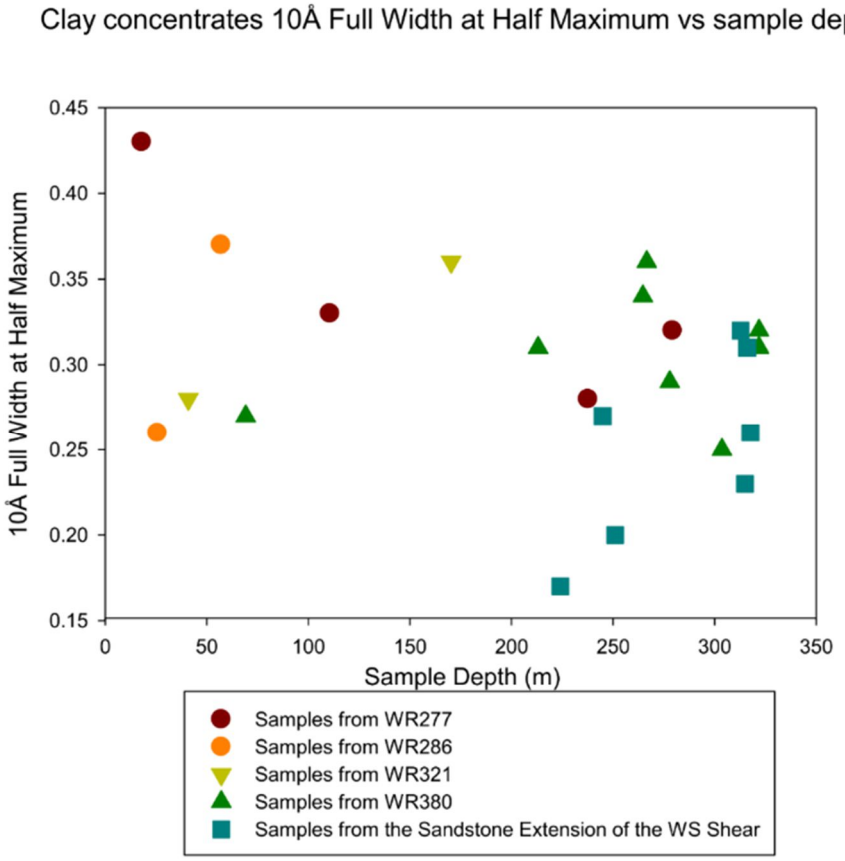

Figure 24: Clay concentrates 10A Full Width at Half Maximum (FWHM) vs sample depth. There is a slight positive correlation between samples from the Sandstone Extension to the WS Shear and WR321 and depth. While there is a broadly inverse correlation with depth for WR277 and no trend for WR380.

The distribution of crystallinity samples in Figure 25 shows in the vicinity of the deposit, and along the Sandstone Extension to the WS Shear m-Kübler values are generally low (i.e. crystalline). These low values are between 0.2 and 0.33, and further points of lower crystallinity close to the unconformity, including in a sample of elevated radioactivity. There is one elevated value in the Sandstone Extension to the WS Shear at around 290 m below surface. There appears to be a 'halo' of higher crystalline illite surrounding the Phoenix Deposit and along the Sandstone Extension to the WS Shear, bounded by less crystalline samples in WR380 to the south and WR277 to the north.

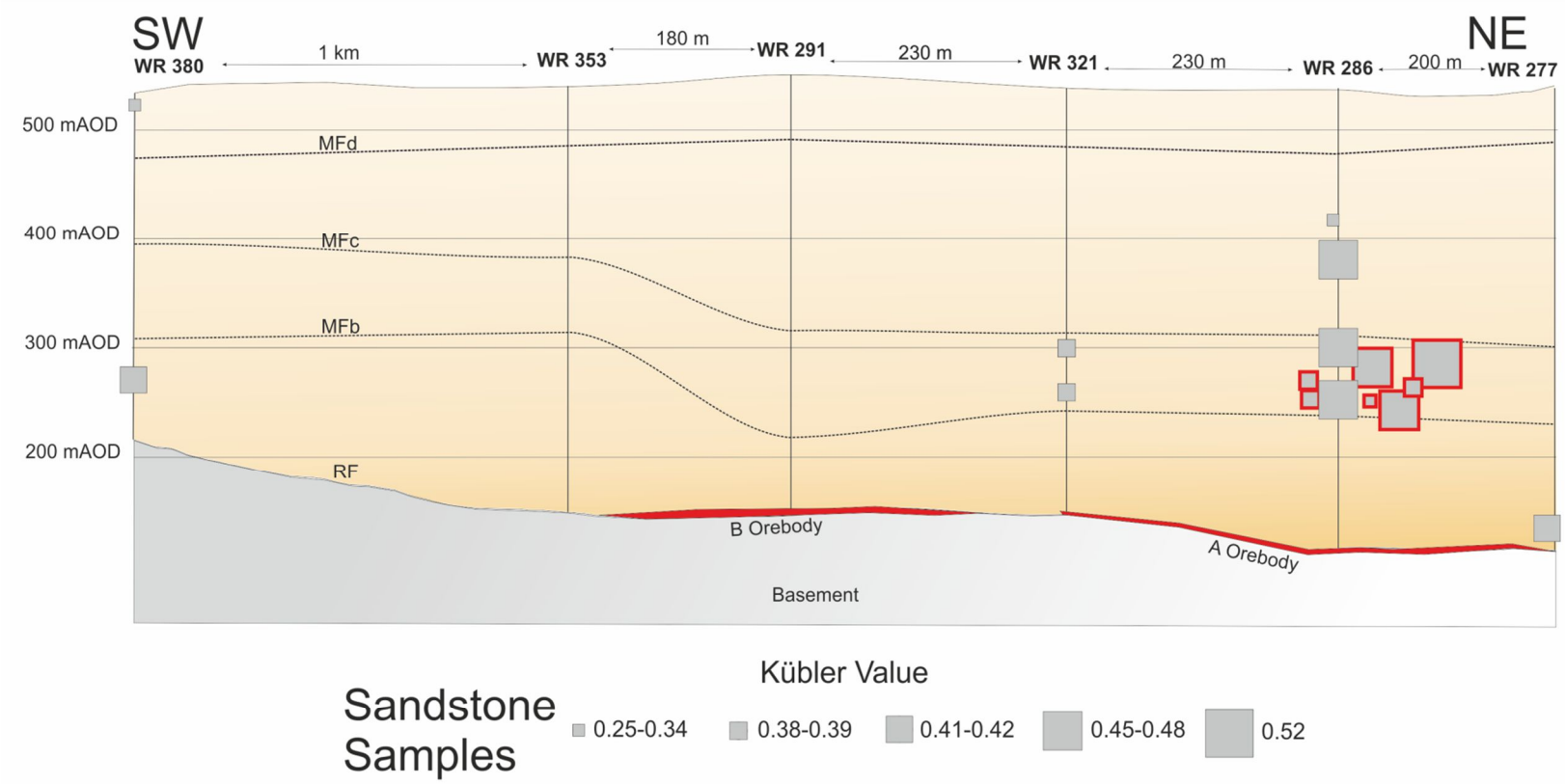

Figure 25: Kübler values of clay fractions from samples in the Athabasca Sandstones overlying the Phoenix Deposit. Crystalline samples occur at the periphery to the 'A' orebody, and in shallow sandstones over the 'A' orebody; however the majority of samples in the sandstones above the 'A' orebody deposit are poorly crystalline. Samples from the Sandstone extension to the WS Shear are variable, with both highly crystalline and poorly crystalline samples in close proximity.

The regional drill core (WR380) and drill core to the north of the orebodies have low - moderately crystalline samples (i.e. high values).

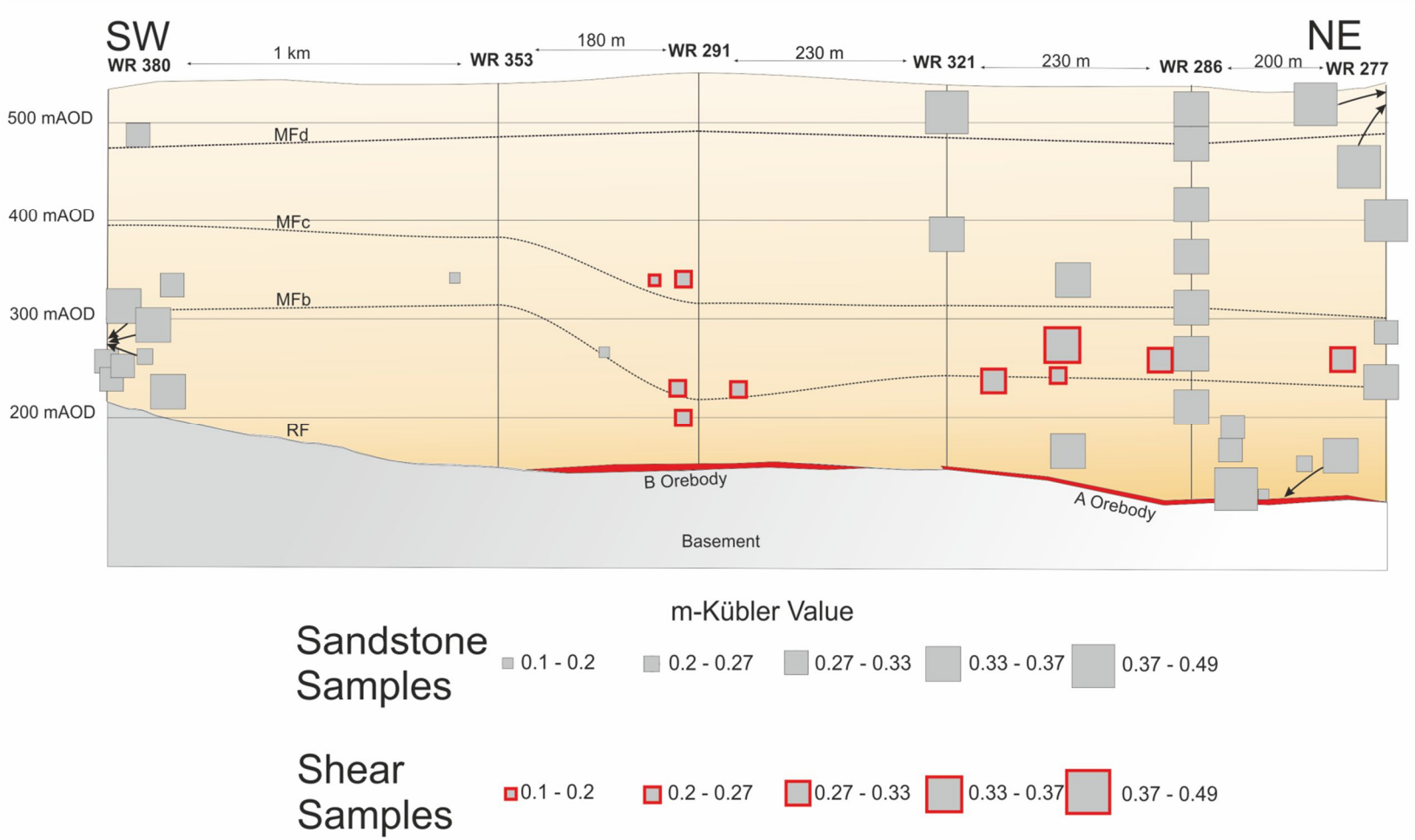

Figure 26: m-Kübler values of clay concentrate from samples in the Athabasca Sandstones surrounding the Phoenix Deposit. In contrast to the Kübler presented in Figure 25.

Poorly crystalline samples are present from surface to the unconformity overlying the 'A' orebody, with occasional crystalline samples within the Sandstone extension to the WS Shear. In contrast, samples overlying the 'B' orebody from both the Sandstone extension to the WS Shear and the Athabasca sandstones are shown to be highly crystalline. Samples from the regional WR 380 drill core are variable, but generally comparative to the crystallinities recorded overlying the 'A' orebody.

3.6 Illite Polytypes

3.6.1 Clay Fractions

Clay fractions have been used to determine illite polytypes overlying the Phoenix Deposit, Figure 27 and Figure 28 present the results of XRD analysis on clay fraction smears.

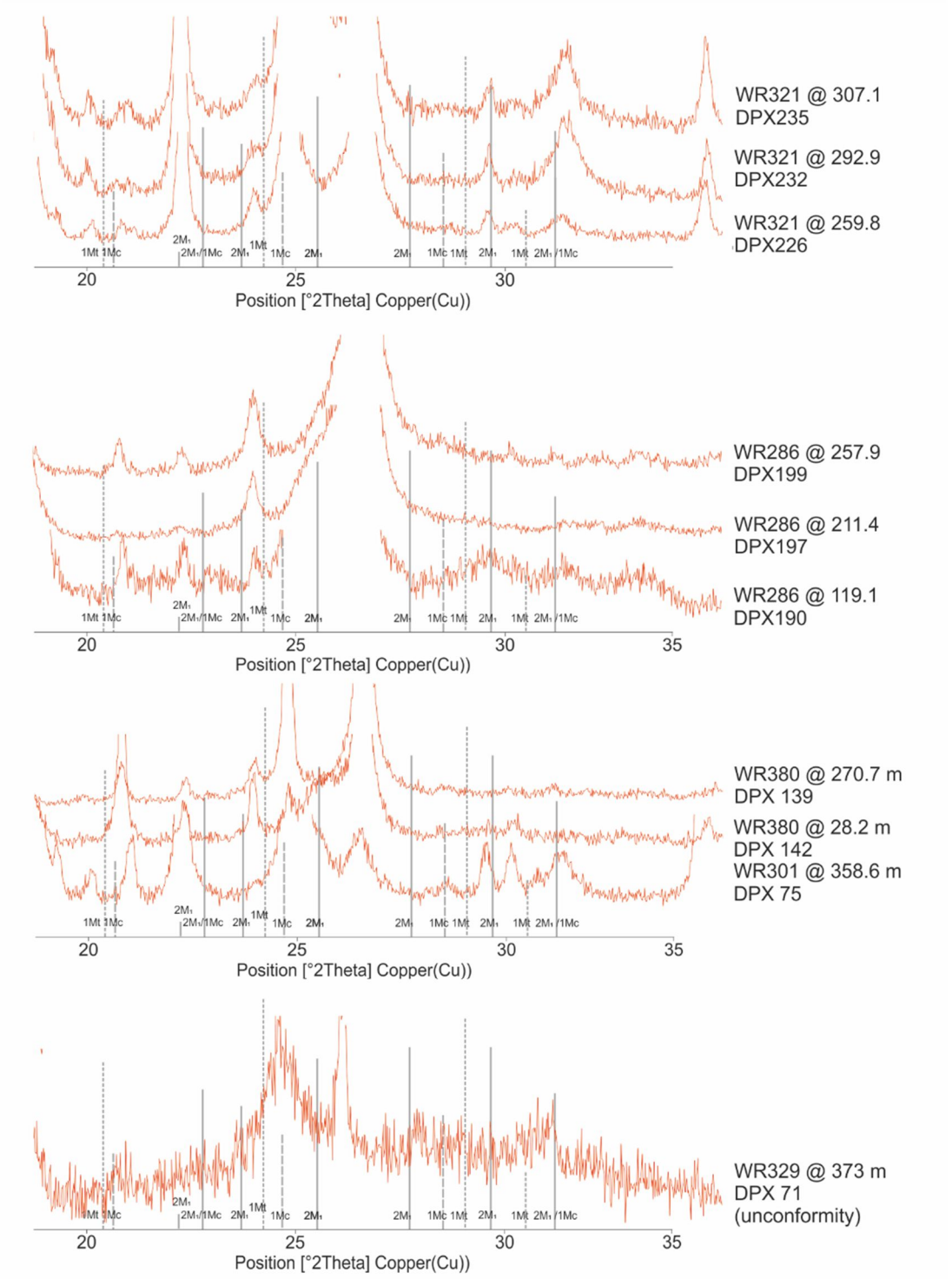

Figure 27 XRD profiles of <2µm clay fraction separates from samples collected from the alteration halo surrounding the Phoenix Deposit. Sample locations are shown in Appendix 3. Major peak positions for 1Mc, 1Mt and 2M illite polytypes are from Drits et al. (1993), Peaks of dravitic tourmaline are shown with D, those for sudoite with S values for tourmaline and sudoite are taken from Laverret et al. (2006)

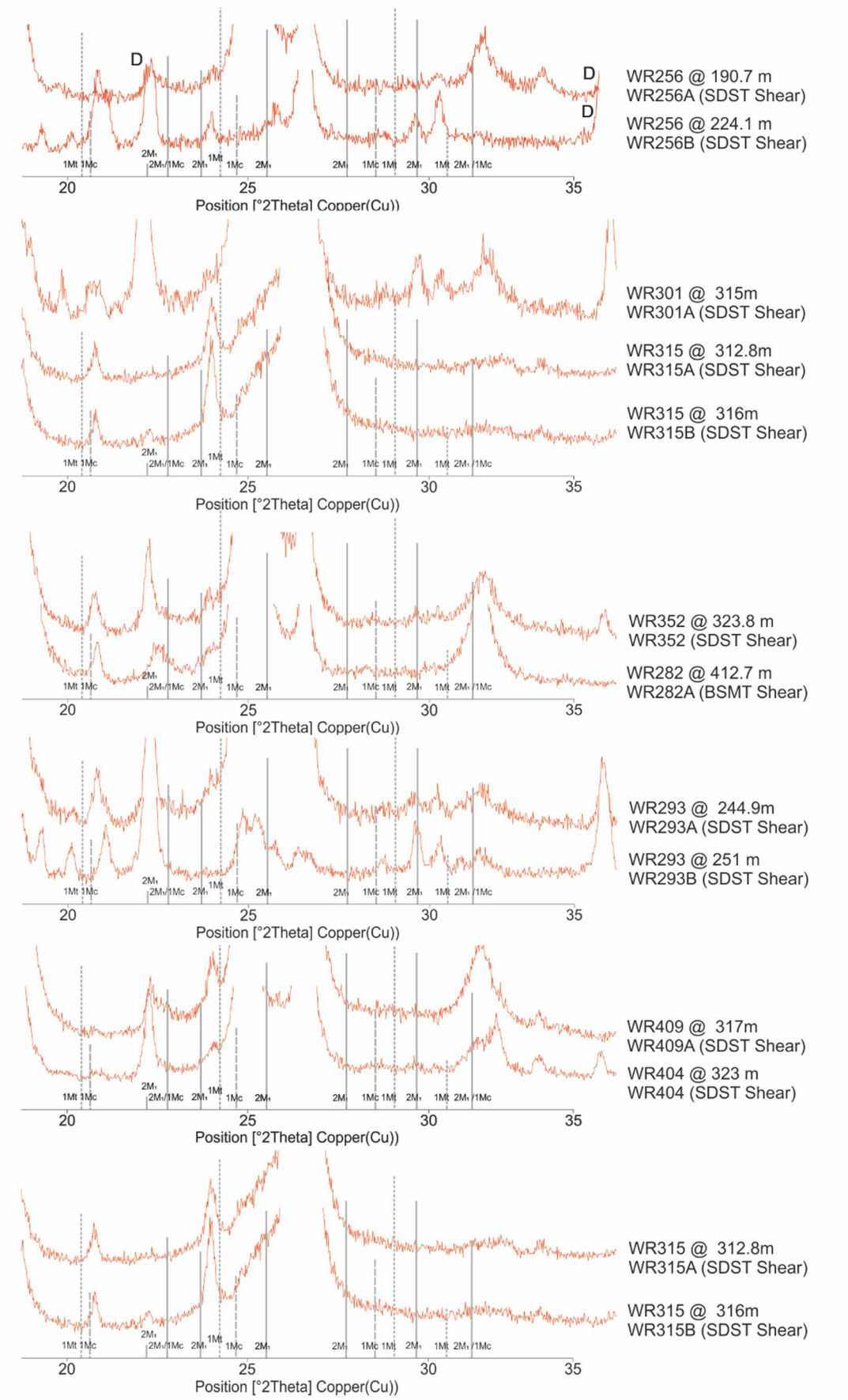

Figure 28: XRD profiles of <2µm clay fraction of samples collected from the Sandstone Extension to the WS Shear Structure. Sample locations are shown in Appendix 3. Major peak positions for 1Mc, 1Mt and 2M illite polytypes are from Drits et al. (1993), Peaks of dravitic tourmaline are shown with D, those for sudoite with S values for tourmaline and sudoite are taken from Laverret et al. (2006).

As shown in Table 15 illites from the basement WS Shear up to 31 meters below the unconformity are the 1Mt polytype. While in the sandstones samples from the Sandstone Extension to the WS Shear, the 1Mc polytype is prevalent. The 1Mt polytype is largely absent overlying the Phoenix Deposit, only present in a sample from the WS Shear (WR293 251 m downcore). The late 2M polytype is identified in only two areas of the sandstones, to the south of the 'A' orebody in WR321 (293 and 307 m downcore) and possibly alongside a sample containing 1Mt collected from along the unconformity, in an area of weakly uraniferous material.

Figures 27 and 28 illustrate the presence of illite polytypes throughout the alteration package. Magnesiofoitite is also widely noted and appears to be present in samples from tourmaline-rich areas noted through other methods.

Table 15: Illite polytypes from clay fraction analysis identified in the Sandstone Extension to the WS Shear samples and samples from away from the Sandstone Extension to the WS Shear. Sandstone Extension to the WS Shear samples contained both 1Mc and 1Mt, while those away from the shear (with the exception of a sample at the unconformity) contained no 1Mt, and only 1Mc and 2M.

Sandstone Extension to the WS Shear Samples			**Samples from away from the Sandstone Extension to the WS Shear**		
DDH	Depth (m)	Illite Polytypes	DDH	Depth (m)	Illite Polytypes
WR256	190.7	1Mc	WR380	28.2	1Mc
WR256	224.1	1Mc	WR286	119.2	1Mc
WR293	224.9	1Mc	WR286	211.4	n/i
WR293	251	1Mt	WR286	257.9	1Mc
WR315	312.8	1Mc	WR321	259.8	n/i
WR315	316	1Mc	WR380	270.7	1Mc
WR301	315	1Mc	WR321	292.9	2M?
WR409	317.7	1Mc	WR321	307.1	2M
WR404	323.3	1Mc	WR301	358.6	1Mc
WR352	323.8	1Mc	WR329	373.0 (unconformity)	1Mt, 2M?
WR282	412.7 (basement)	1Mt			

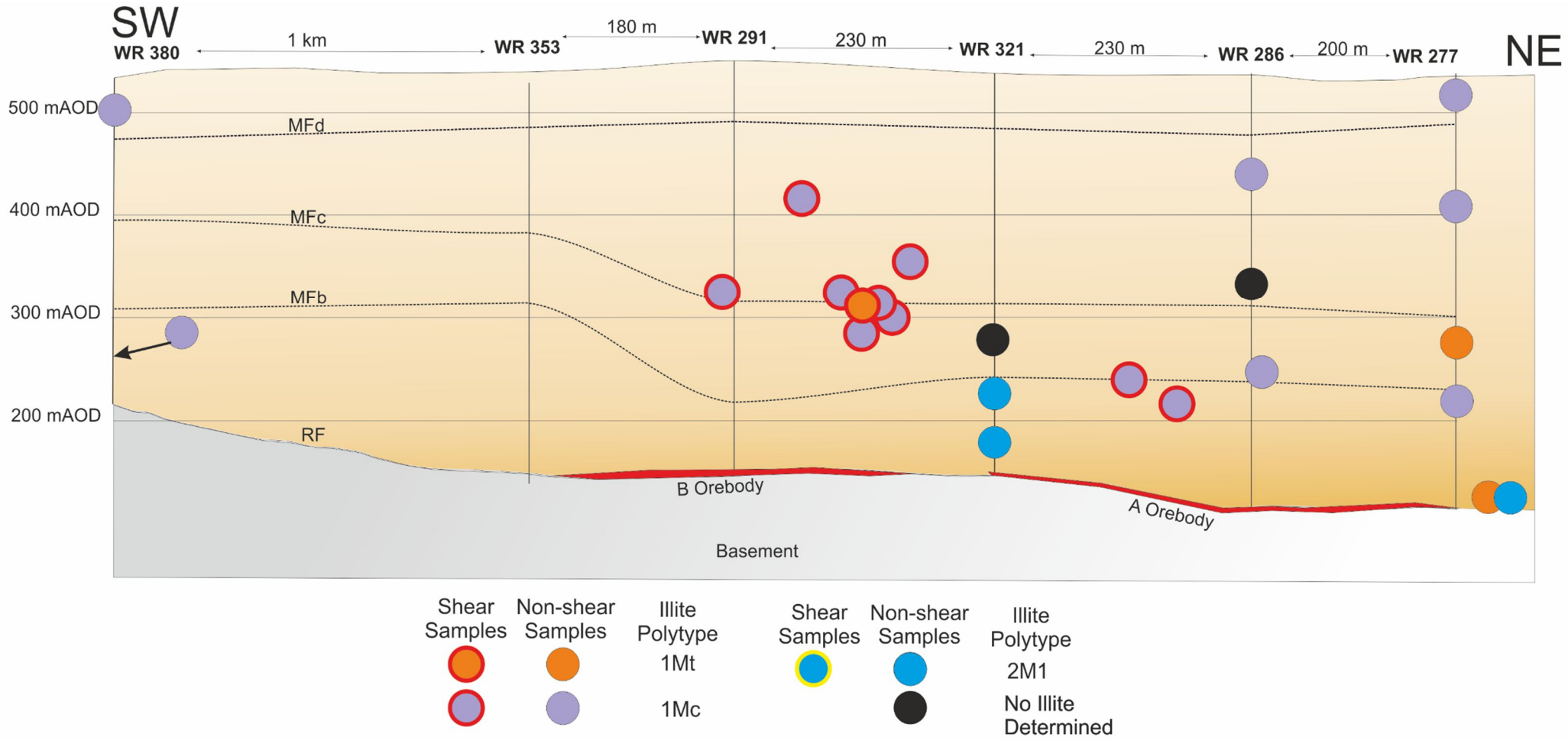

Figure 29: Distribution of illite polytypes determined with XRD through the alteration halo of the Phoenix Deposit from clay fractions. Drill core WR380 is 1.8 km south east of the orebodies down strike of the WS Shear and acts as a 'regional' comparison to the samples analysed from closer to the deposit.

3.6.2 Clay Concentrates

Over three times more data has been produced by this study from 'Clay Concentrates' than from 'Clay Fractions' (Table 4), and as such, they offer a considerably wider dataset for analysis of illite polytypes across the alteration system of the Phoenix Deposit. Drits et al. (1993) successfully used randomly orientated powders in the identification of illite polytypes in comparison to clay fractions from the Shear Creek uranium deposit, prepared in a very similar method to the clay concentrates used in this study. These analyses offer mineralogical information regarding the coarser grained illite phase in addition to that acquired from the clay fraction.

Table 16 to 21 below gives the results of this analysis, where relative abundances are given as 1 (lowest) to 2 (highest). Appendix 6.3 illustrates the XRD spectra and analysis undertaken.

Table 16: Illite polytypes from clay concentrate samples identified in DDH WR277

Sample Name	DDH	Depth (m)	1Mt	1Mc	2M
DPX 155	277	29.9		1	
DPX 153	277	18.1		2	
DPX 161	277	111.7		1	
DPX 150	277	240	1	1	
DPX 149	277	282		2	

Table 17: Illite polytypes from clay concentrate samples identified in DDH WR286.

Sample Name	DDH	Depth (m)	1Mt	1Mc	2M
DPX 198	286	22.6	1	1	
DPX 181	286	57			2
DPX 189	286	125.5		1	
DPX 193	286	156.6	2		
DPX 194	286	188.5			1

Table 18: Illite polytypes from clay concentrate samples identified in DDH WR380. Samples DPX 137 and DPX 134 were composed of competent sandstones and the infill from small vein structures.

Sample Name	DDH	Depth (m)	1Mt	1Mc	2M
DPX 138	380	268.8		1	
DPX 139	380	270.7		1	
DPX 137 sandstone sample	380	282.2		1	
DPX 137 vein infill sample	380	282.2		1	
DPX 134 vein infill sample	380	308.3		2	
DPX 134 sandstone sample.	380	308.3	n/i		
DPX 136	380	320.2		1	

Table 19: Illite polytypes from clay concentrate samples identified in intersections in the Sandstone Extension to the WS Shear.

Sample Name	DDH	Depth (m)	1Mt	1Mc	2M
WR256A	256	190.7	1?	2	
WR256B	256	224.1	2	1	
WR315B	315	316		1	
WR409A	409	317.7	0.5	1	
WR301B	301	319		1	

Table 20: Illite polytypes from clay concentrate samples identified from elsewhere in the Manitou Falls Formation Sandstones.

Sample Name	DDH	Depth (m)	1Mt	1Mc	2M
DPX 280	353	23.55		1	
DPX 205	321	40.9		1	
DPX 221	321	170.3	2	1	
DPX079	256	303.45		1	
DPX074	329	360.7		1	

Table 21 Illite polytypes from clay concentrate samples identified present in basement samples.

Sample Name	DDH	Depth	1Mt	1Mc	2M
DPX 256	373	397.5	2		1?
DPX 64	358	402.89	1	2	1
DPX 105	317	407.4		1	
DPX 30	282	428.62	1		
DPX 23	332	439.7	2		

From the analysis presented in Figures 25 and 26 and summarised in Table 15, Figure 30 (overleaf) can be generated. From the coarser grained clay concentrate samples from Table 16 to 21 and presented in Appendix 6.3 Figure 30 can be generated.

As shown in Table 15, illite from the basement to within 31 meters below the unconformity are the mainly the 1Mt polytype, with minor 1Mc and 2M. While in the sandstones, samples from the Sandstone Extension to the WS Shear, the 1Mc polytype is prevalent, with five of the eight samples containing of 1Mc, and three containing 1Mt.

Of the twenty one clay concentrates containing illite from the non-shear sandstones overlying the Phoenix Deposit, nineteen contained 1Mc, while only four contained 1Mt, and two 2M. Of the four 1Mt samples, three were directly overlying the orebody (WR286, 22.6 m and 157 m downcore, WR321 170 m downcore) and one was slightly to the north of uranium mineralisation (WR277, 240 m downcore). The two 2M samples were identified directly over the deposit, in WR286 at 57 m and 189 m downcore.

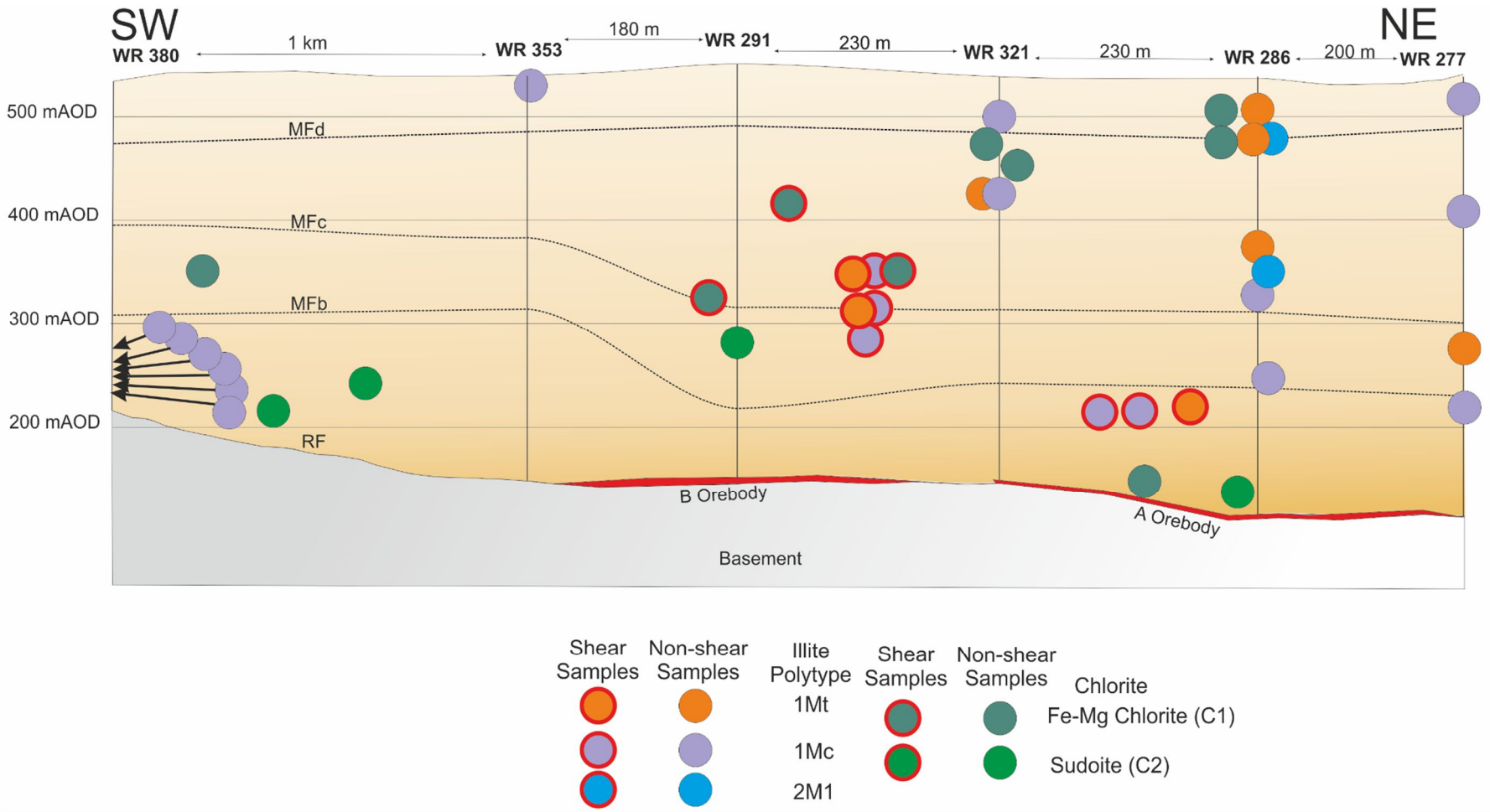

Figure 30: Distribution of illite polytypes determined with XRD through the alteration halo of the Phoenix Deposit from clay concentrates. The location of chlorite polytype samples deduced via XRD are also presented. Drill core WR380 is 1.8 km south-east of the orebodies down strike of the WS Shear and acts as a 'regional' comparison to the samples analysed from closer to the deposit.

Desilicification, veining of quartz and fracturing are noted overlying unconformity-related deposits in the Athabasca Basin, with the Phoenix Deposit being no exception. As part of this study, vein samples which contained significant clay material were separated and analysed to determine illite polytypes. Data is dominated by samples from the 'regional' WR380 drill core, which does not overly uranium mineralisation and is 1 km to the south eest of the Phoenix Deposit. WR380 had only the 1Mc polytype in both vein and non-vein samples. In the vicinity of uranium mineralisation, a vein sample containing the 2M polytype is present overlying uranium mineralisation in WR286 at 57 m downcore (Table 22).

Table 22: Illite polytypes from vein samples overlying the Phoenix Deposit. Relative abundances are given as 1 (lowest) to 2 (highest). 'n/I' indicates no illite was identified in this sample.

Sample Name	DDH	Depth (m)	1Mt	1Mc	2M1
DPX 181 vein sample	WR286	57			2
DPX 137 sandstone	WR380	282.2		1	
DPX 137 vein sample	WR380	282.2		1	
DPX 134 vein sample	WR380	308.3		2	
DPX 134 sandstone	WR380	308.3	n/i		

3.8.1 Illite crystallinity and polytypes

Figure 31 and Figure 32 illustrate the lack of relationship between the illite polytypes(s) present in a sample and its Kübler or m-Külber index. There is no clear relationship with polytype, depth or Kübler index, even amongst those samples containing multiple polytypes.

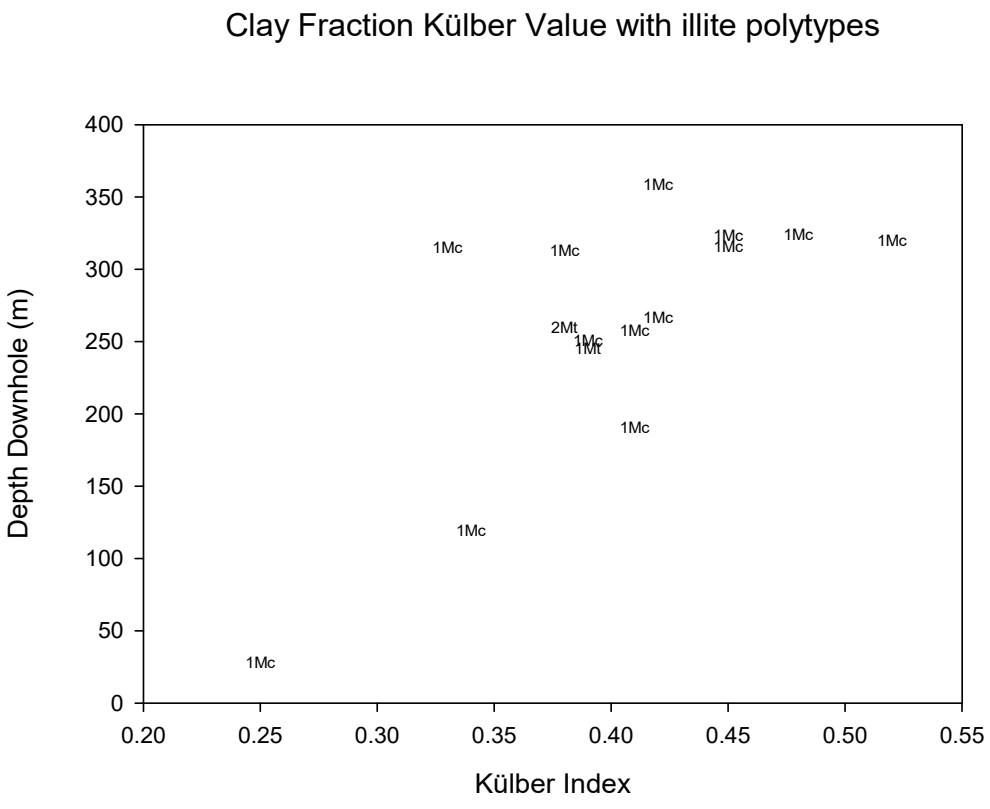

Figure 31: Clay Fraction Külber Value with illite polytypes determined via XRD from Athabasca sandstone units overlying the Phoenix Deposit. There is no relationship between Kübler Value and polytype.

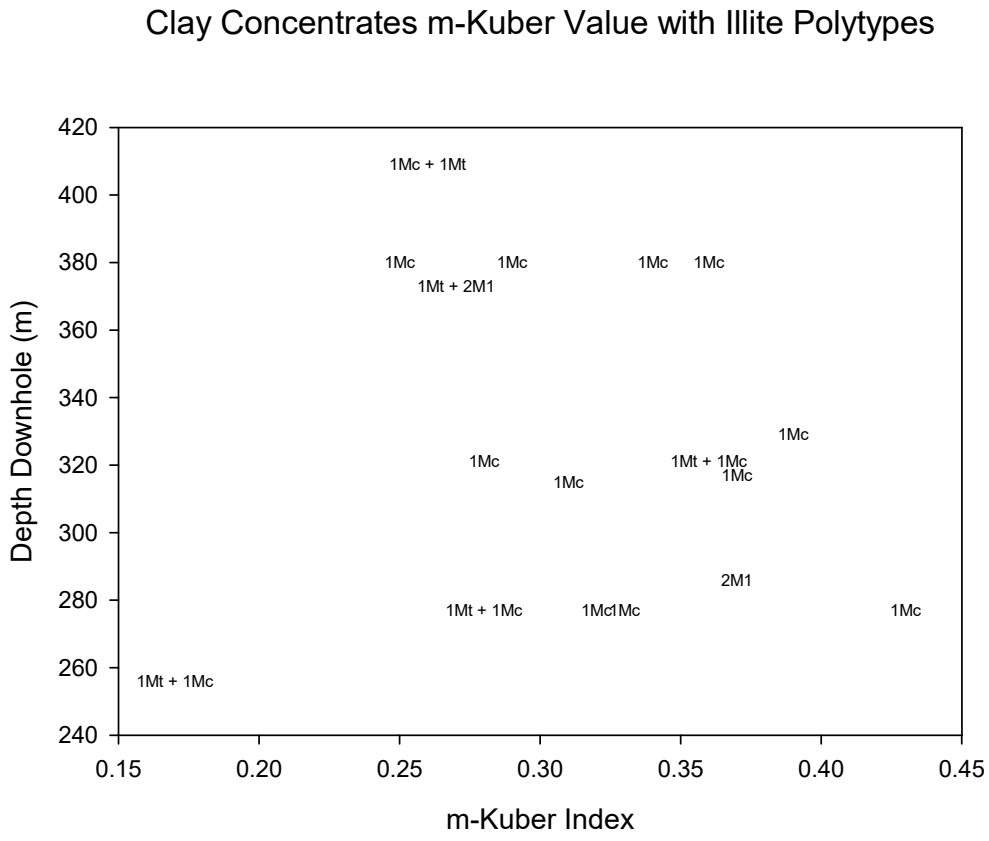

Figure 32: Clay Concentrates m-Kübler value with illite polytypes determined via XRD from Athabasca sandstone units overlying the Phoenix Deposit. There is no relationship between m-Kübler value and polytype.

3.7 Near Infrared Spectra Surrounding the Phoenix Deposit

Absorption features in the NIR appear to have two main absorption features between 500 to 700 and 845 to 905 nm, indicated in Figure 34. From the total dataset of samples, absorption features between 400 to 600 nm make up less than 10% of samples. With the majority of samples having absorption features between two bands: 600 nm to 700 nm and 845 nm to 900 mm. The higher of these ranges are noted to correlate with hematite, which is shown to have strong absorption features between 850 to 900 nm by Hauff (2000).

The absorption features are identified in 129 of the 229 sandstone samples analysed (56%). The two NIR absorption features observed at the Phoenix Deposit and the hematite NIR mineral signature are illustrated in Figure 34. Based on Portable Infrared Mineral Analyser (PIMA) data provided by Denison Mines Corp to characterise the clay mineralogy of the Phoenix Deposit, PIMA is limited to spectra between 1300nm and 2500 nm, excluding the features described within this study. Example spectra are displayed in Figure 36. For ease of discussion features discussed herein are grouped into two groupings, a 'low' (between 600 and 700 nm) and 'high' (between 900 and 1nm) group, as demonstrated in Figure 33.

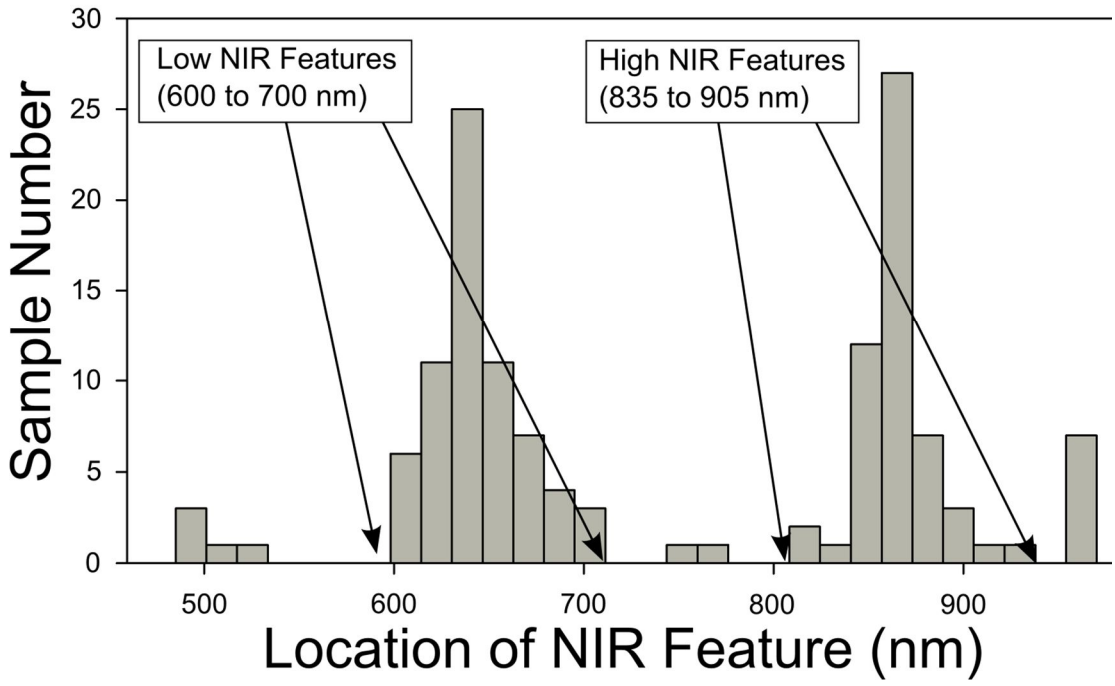

Figure 33: Distribution of NIR features in the sandstones overlying the Phoenix Deposit, where two features are present in one sample, both are included within the histrogram.

There is a clear bimodal distribution of values between 700 nm and 835 nm. As identified in this study; 'Low' NIR features are between 600 and 700 nm and 'High' NIR features are between 835 and 905 nm.

Sandstone drill cores with samples which yield low (i.e. 600-700 nm) NIR absorption features are: WR321, WR293, WR291, shallow basement samples of WR329, most samples of WR353 and basement WS Shear samples. Those containing higher NIR values include WR380, 1.8 km to the south of the orebodies in an area without uranium mineralisation, the shallow Sandstone Extension to the WS Shear, shallow competent sandstone samples in WR286 and deep basement samples in WR353 and WR329.

Sandstone samples of WR286 display principally high (i.e. 835 – 905 nm) NIR absorption features and basement samples of the same core show low NIR absorption features, while WR277 yielded both low and high NIR absorption in similar samples. Drill cores WR277, WR286 and WR380 have similar abundances of Fe_2O_3 (total) (Figure 35) suggesting that the amount of (total) Fe in the sandstones has no significant impact on the NIR spectra generated.

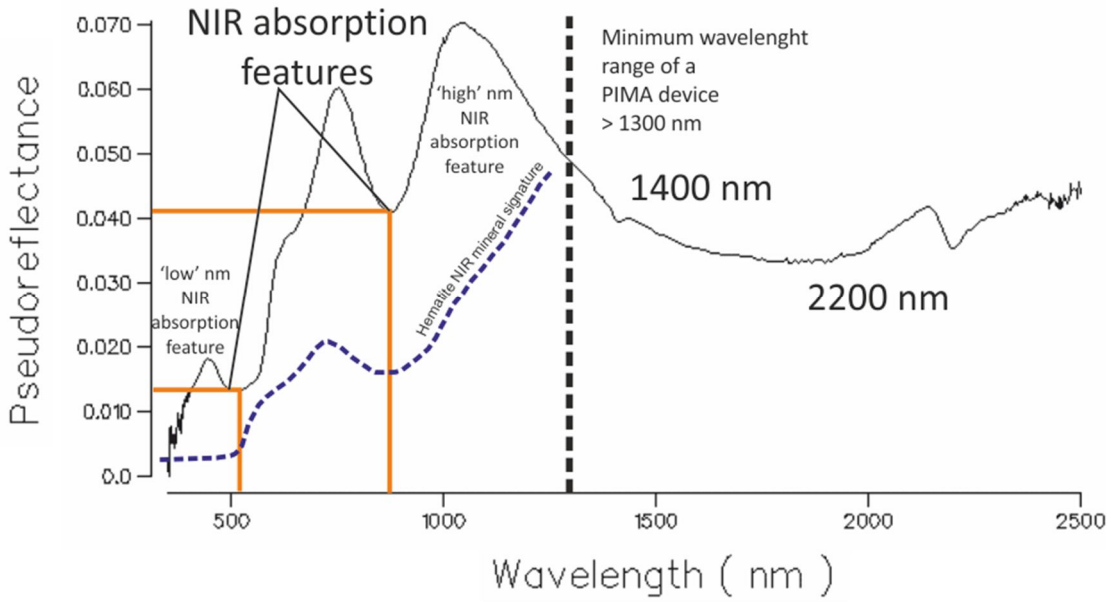

Figure 34: Approximate Location of NIR absorption features, an example spectrum of pure hematite for reference, amongst other diagnostic mineralogical absorption features and the higher minimum wavelength range of a PIMA device (<1300 µm). Above is an example spectrum from this study, with both absorption features, the 'low' feature is anomalously low (530 nm) (DPX 138, WR380 from 2688 m downcore).

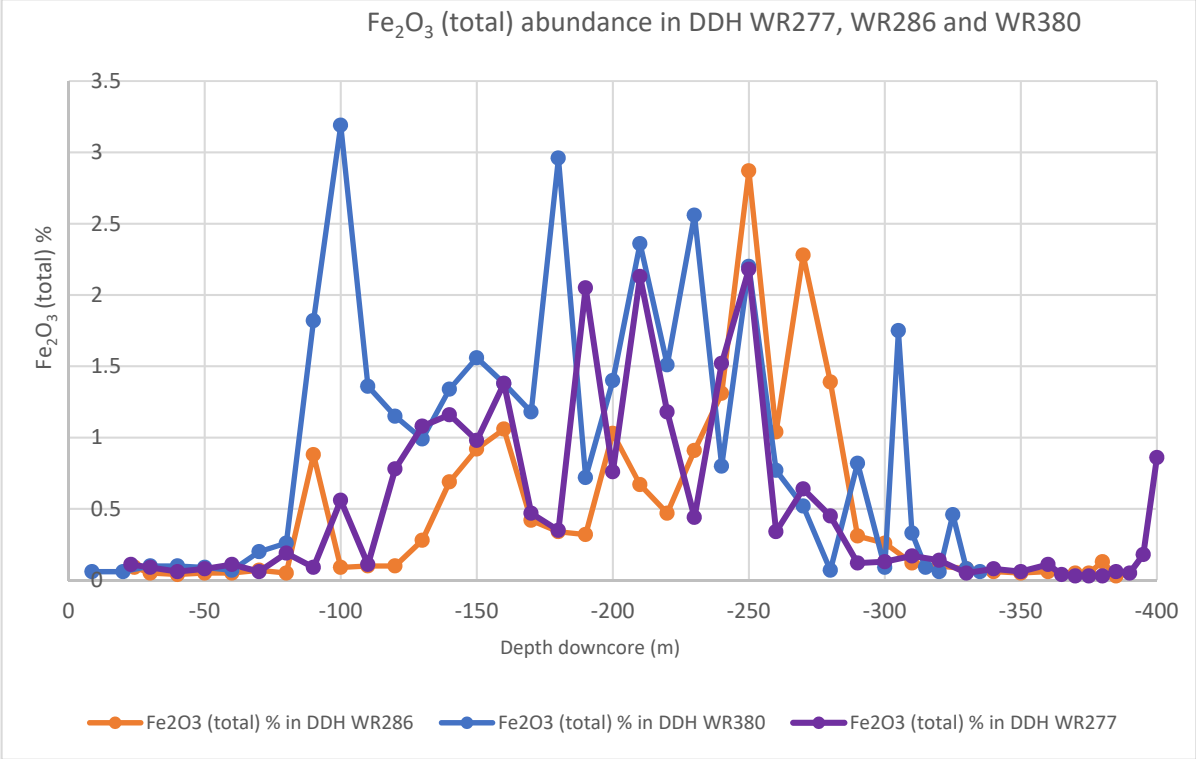

Figure 35: Fe_2O_3 (total) abundance in DDH WR277, WR286 and WR380. This data was derived from analysis performed by SRC (outlined in Section 2 and in Dann et al.,2014). There is no relationship between the abundance of total Fe_2O_3 and the location of the NIR absorption features in the alteration halo of the Phoenix Deposit as shown in Figures 37 and 38.

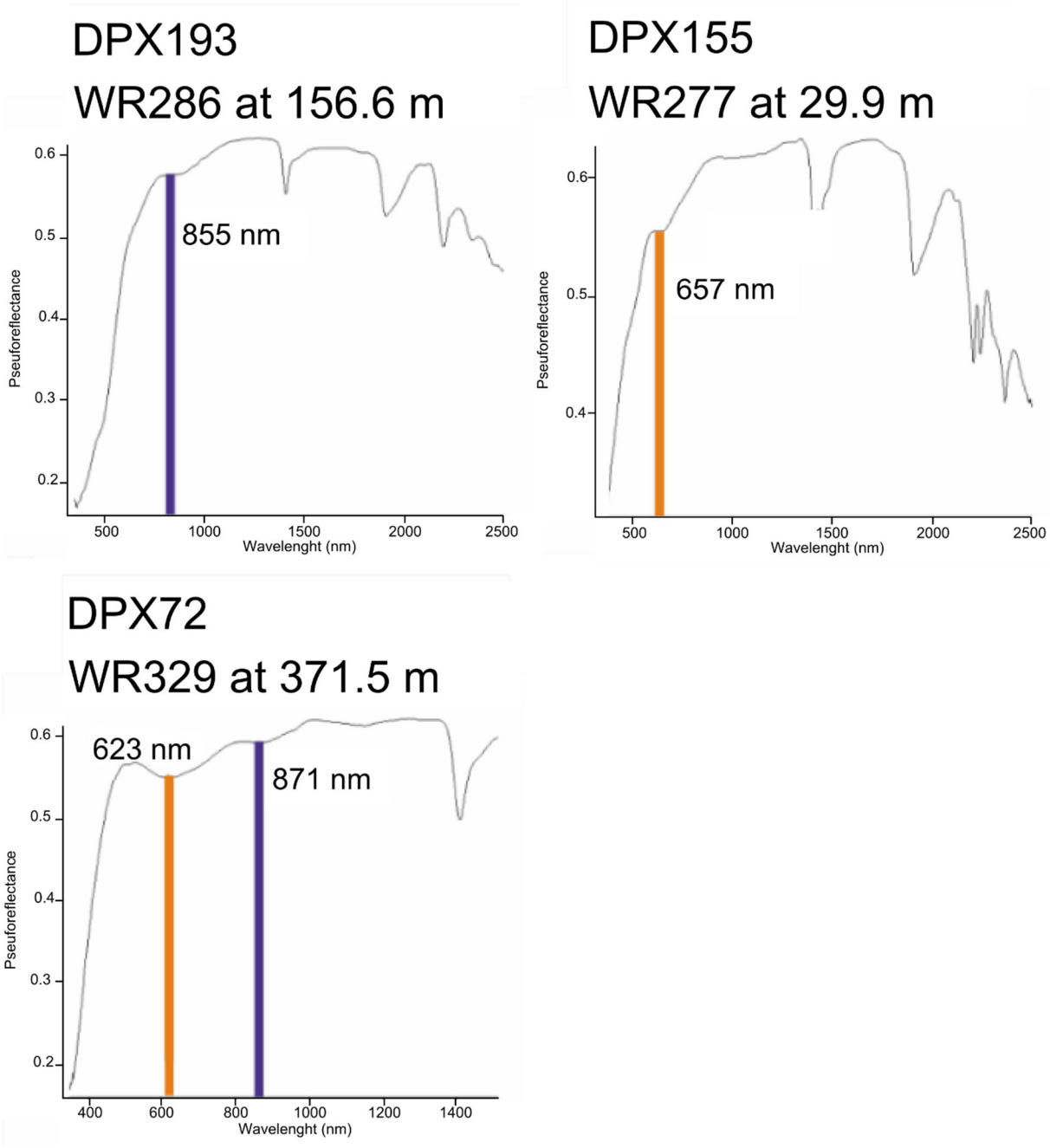

Figure 36: Example spectra for samples illustrating the location of their respective NIR absorption features in the SWIR spectra of each sample. The colours are those used on Figure 37. The features described in this study are generally an absorption feature of between 5- 20 nm

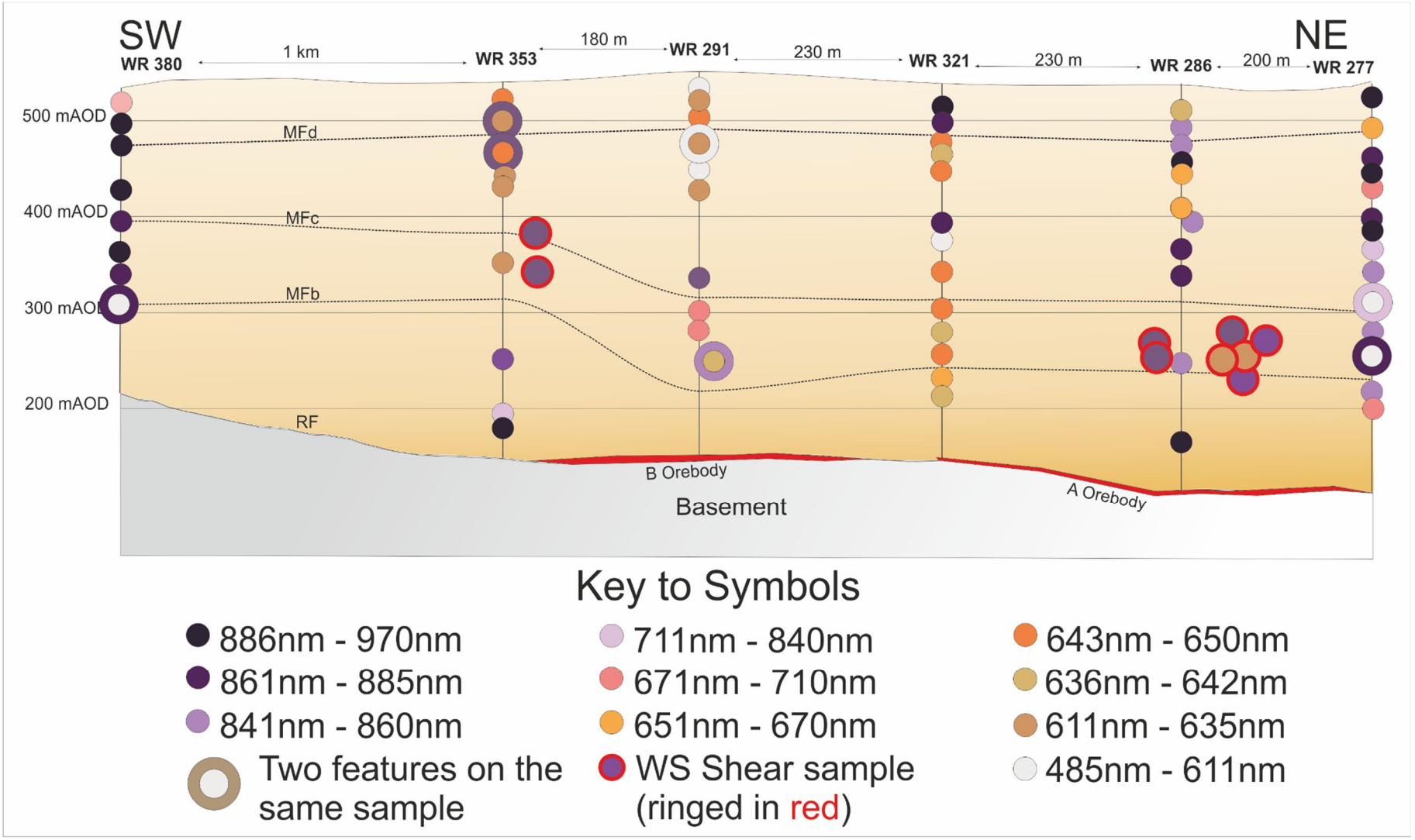

Figure 37: Distribution of the location of the NIR absorption features around the Phoenix Deposit alteration halo. 'Two features in the same sample' refers to those which show both a lower and high NIR absorption features were noted in the NIR.

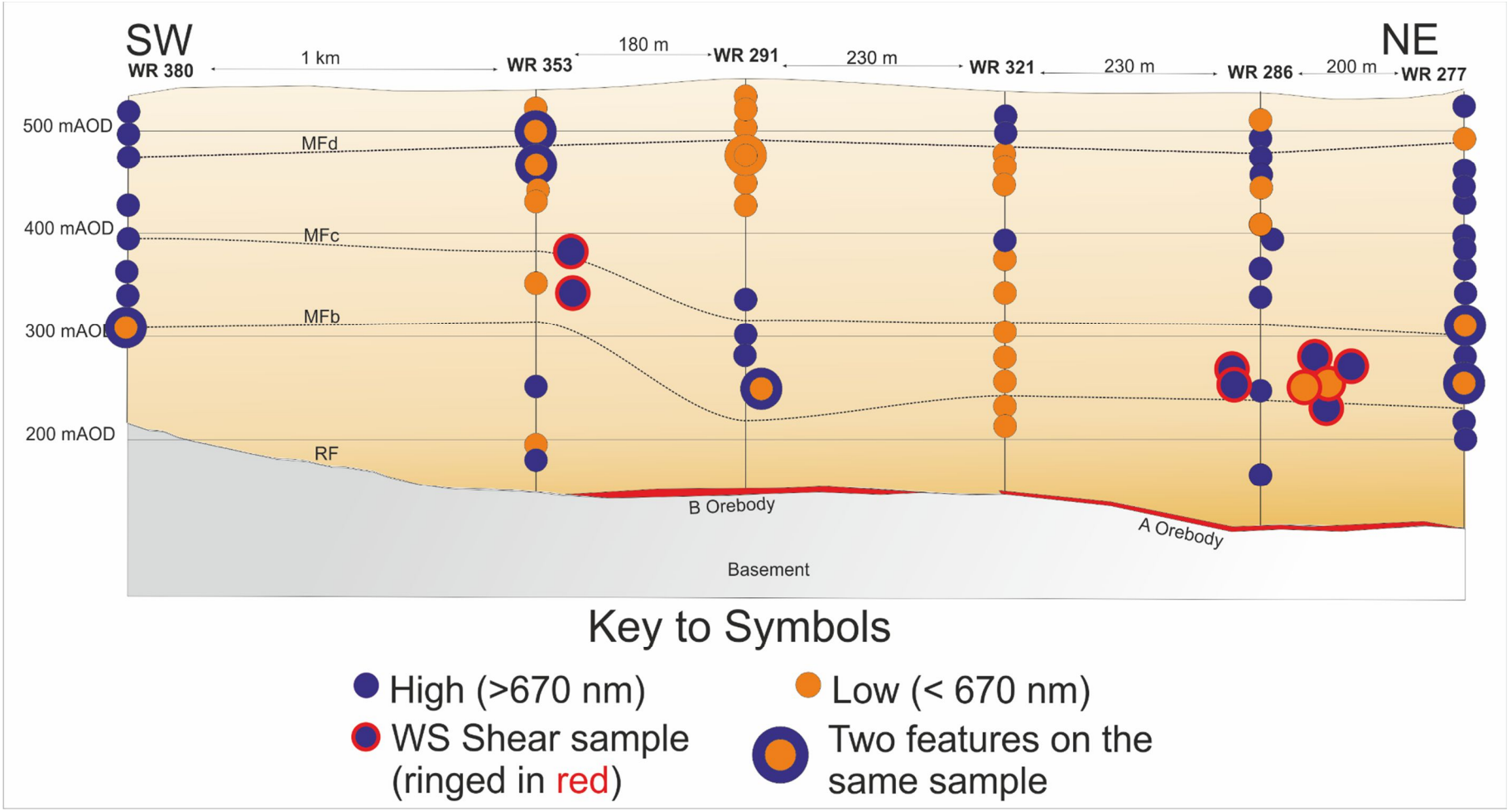

Figure 38: Classified distribution of the location of NIR features around the Phoenix Deposit. Exclusively low features are present in the sandstones overlying the deposit, and common to shallow depths in drill cores in the vicinity of mineralisation; elsewhere, 1.8 km to the south-west in drill core WR380 almost exclusively 'high' features are recorded. Samples from the Sandstone Extension to the WS Shear record both low and high features.

3.7.1 Petrographic Analysis

Petrographic analysis has been undertaken of samples overlying the Phoenix Deposit, which has included some of the samples analysed via NIR (Figure 39) these are displayed in Plates 1 to 5. (pages 34 to 39)

Sample Name	NIR Signature nm	Phase Relationships	Thin Section Imagery (Heading: Petrographic Analysis; Plates 1 to 5)
WR301a	630	M2 illite or magnesiofoitite with possible coeval Fe oxides	P4/G
WR256a	858	M1 illite associated with fine-grained hematite.	P4/D
WR404	865	M1 illite with fine-grained Fe oxides	P2/F
DPX138	860	Bladed hematite has grown on rim of detrital grains of Fe oxides	P5/B, P5/H
DPX166	872	M2 illite with fine-grained hematite.	P2/A
DPX70	843	Vuggy quartz (Qz^2) and Fe oxide infilling pores.	P3/A, S2/3
DPX81	676	Late magnesiofoitite crosscutting quartz grains	P2/E

Figure 39: Phase relationships present in thin section samples which exhibit NIR absorption features analysed via SWIR.

3.7.2 Illite Polytypes and Features in the NIR

Illite polytypes are compared to NIR absorption features, which is shown in Table 23. The majority of 1Mt and 2M1 are within samples which show (800-900 nm) in the NIR. However, eight samples (greyed out) from a variety of depths (29.9 m to 317.5m) host illite and have a lower 600-700 nm NIR absorption feature. Of those, all contain 1Mc, and two additional samples (overlying uranium mineralisation) contain the 1Mt polytype.

Table 23: Illitic polytypes and the position of the NIR absorption features. Samples with a NIR related absorption features below 700 nm are noted in grey. The relative abundances of illite are given as 1 (lowest) to 2 (highest). A primary feature is the dominant absorption feature within the NIR spectra, which displays the deepest trough, the secondary feature is less prominent. Pseudo-reflectance is the measure of reflectance in a specific part of the spectrum, when compared against the total amount of light reflected from the substance. High values (0.7 – 0.9) of pseudo-reflectance indicate shallow absorption features, while low values (0.1-0.4) indicate deep absorption features.

Sample Details						**Primary Feature**		**Secondary Feature**	
Sample Name	*Core*	*Depth*	*Illite polytypes*			*NIR absorption feature (nm)*	*Pseudo-reflectance*	*NIR absorption feature (nm)*	*Pseudo-reflectance*
		(m)	*1Mt*	*1Mc*	*2M1*				
Sandstone Samples									
DPX 149	*277*	*282*		*2*		***694***	***0.46***		
DPX 150	*277*	*240*	*1*	*1*		872	0.18		
DPX 153	*277*	*18.1*		*2*		970	0.36		
DPX 155	*277*	*29.9*		*1*		***657***	***0.54***		
DPX 193	*286*	*156.6*	*2*			*855*	*0.27*		
DPX 194	*286*	*188.5*			*1*	*847*	*0.62*	***525***	***0.15***
DPX 201	*286*	*283.5*		*1*	*2*	*962*	*0.49*		
DPX 138	*380*	*268.8*		*1*		*860*	*0.28*	***516***	***0.23***
DPX 139	*380*	*270.7*		*1*		*848*	*0.6*		
WR256A	*256*	*190.7*	*1?*	*2*		*858*	*0.89*		
WR256B	*256*	*224.1*	*2*	*1*		*857*	*0.72*		
WR315B	*315*	*316*		*1*		*857*	*0.33*		
WR301B	*301*	*319*		*1*		***630***	***0.9***		
DPX 280	*353*	*23.55*		*1*		***651***	***0.69***		
DPX 205	*321*	*40.9*		*1*		*958*	*0.49*		
DPX 221	*321*	*170.3*	*2*	*1*		***639***	***0.24***		
DPX079	*256*	*303.45*		*1*		*878*	*0.46*		
DPX074	*329*	*360.7*		*1*		***632***	***0.47***		
DPX072	*329*	*371.46*	*2*	*2*		***639***	***0.65***	871	*0.75*
Basement Samples									
DPX 256	*373*	*397.5*	*2*		*1?*	*959*	*0.67*		
DPX064	*358*	*402.89*	*1*	*2*	*1*				
DPX 105	*317*	*407.4*		*1*					
DPX030	*282*	*428.62*	*1*						
DPX023	*332*	*439.7*	*2*			***624***	***0.54***		

3.8 Whole Rock Geochemistry

The distribution of B, MgO, K_2O and Y in the Athabasca Sandstones, the diagrams presented below have been produced through the methodology outlined above in Section 2.3.1.

3.8.1 Boron

Boron concentration displays a chimney-like distribution of elevated values rising from the vicinity of the two ore bodies and which extend above the 450 msl plane (Fig. 40). The most notable area of greatly elevated values are directly above the northern terminus of the 'B' ore body and the southern terminus of 'A' ore body, with two smaller minor multipoint areas of elevated values rising from the north of the 'A' ore zone. At 200 msl, boron values are lower (relative to the rest of the slice) directly above the ore zones.

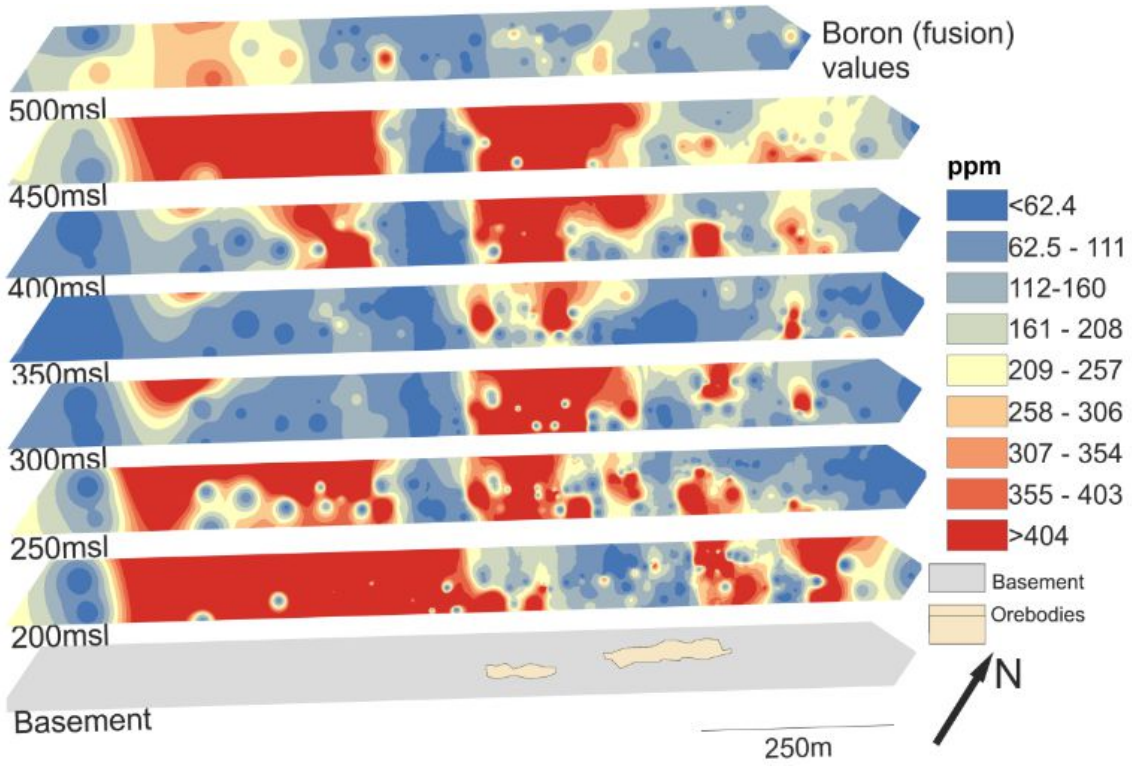

Figure 40: Whole rock interpolations of B through the sandstones. WR321 and WR291 plot within the elevated B values between both orebodies. The locations of WR321 and 291 are shown in Figure 9.

3.8.2. Magnesium Oxide

Elevated MgO values appear to form broad 'chimneys' to the north and south of the ore bodies that are considerably higher when compared to the regional datasets (presented in Dann et al, 2014; Appendix 1.1). Between 300 and 350 msl, elevated, values do occur over the B ore body and appear to link with elevated points in the 400 and 450 msl plane (Fig. 41).

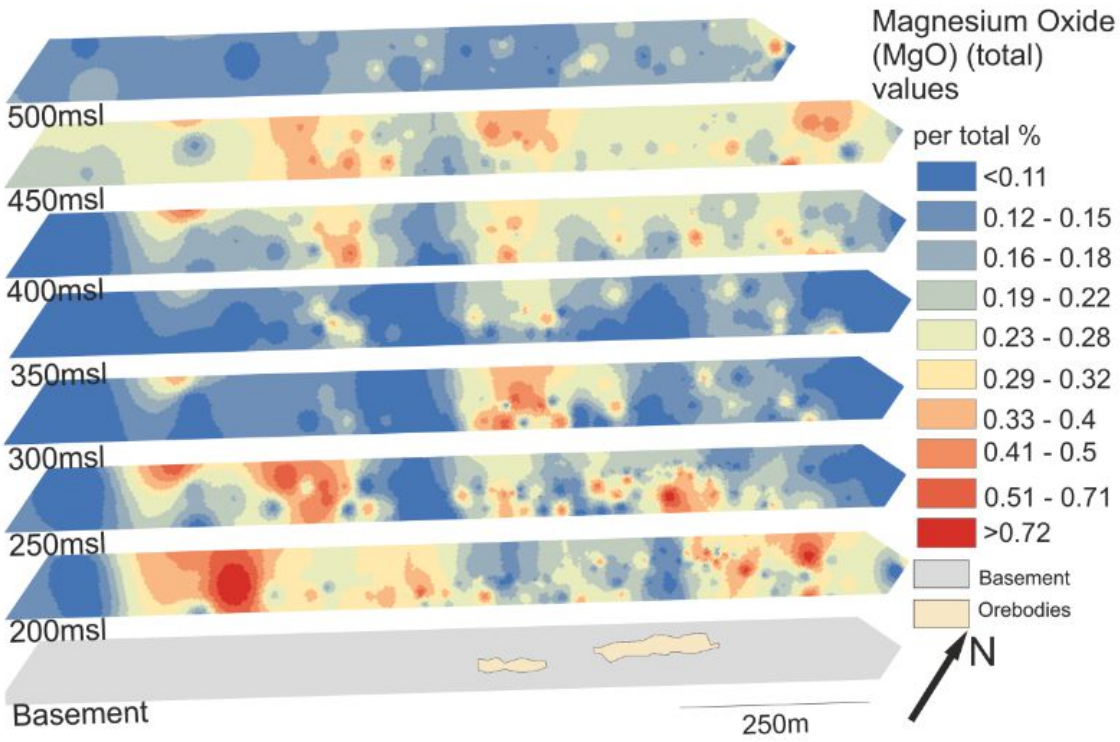

Figure 41: Whole rock interpolations of MgO through the sandstones. WR321 and WR291 plot within the elevated MgO values between both orebodies. The locations of WR321 and WR291 are shown in Fig. 9

3.8.3. Potassium Oxide

K_2O concentrations of bulk rocks, determined by total digestion method, display highly elevated values in the 250, 300 and 350 msl slices, as shown in Figure 42. Overall the high values of K_2O in the sandstones match the observed the distribution of illite in the sandstones (Figures 12, 29 and 30) and as such, K2O contents are considered as a proxy for illite. A vertical chimney-like distribution of low values overlies the ore zones, extending from the basement (approximately 450 to 500 m bgl) to the 400 msl slice (approximately 100 m.

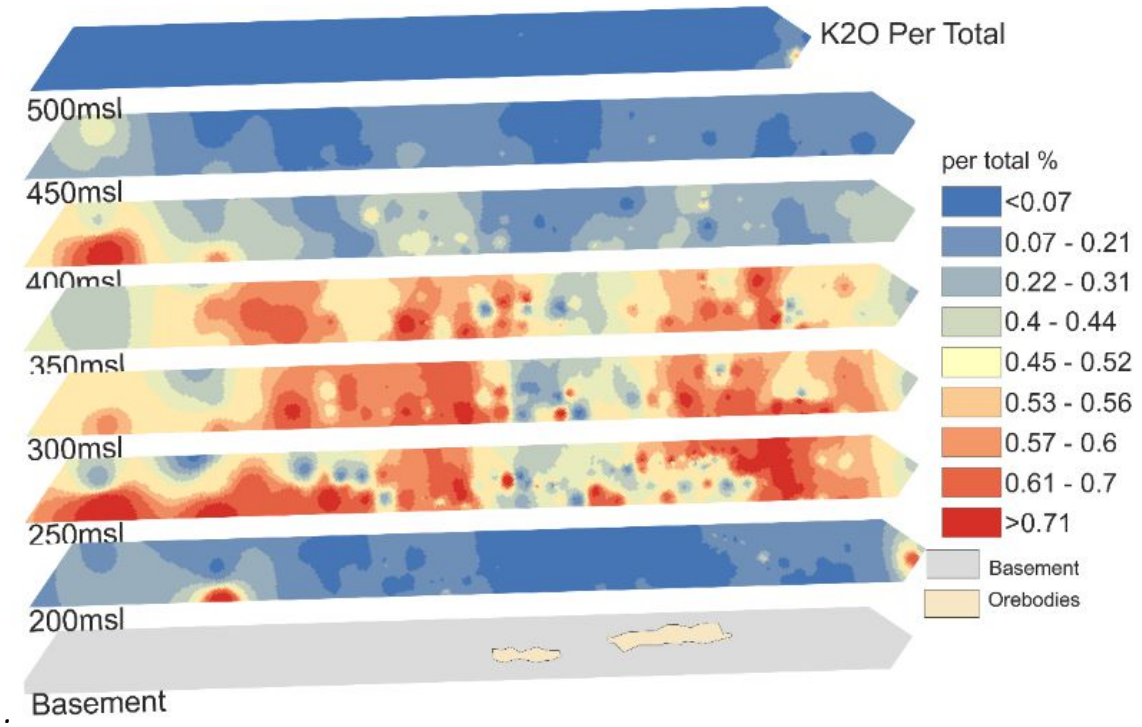

Figure 42: Whole rock interpolations of K_2O through the sandstones. WR321 and WR291 plot within the elevated K_2O values between both orebodies.

3.8.4.Yttrium

Total digestion yttrium values exhibit three, multipoint vertical areas of elevated values that extend from directly above the ore bodies to the upper sandstone, as shown in Figure 43; below.

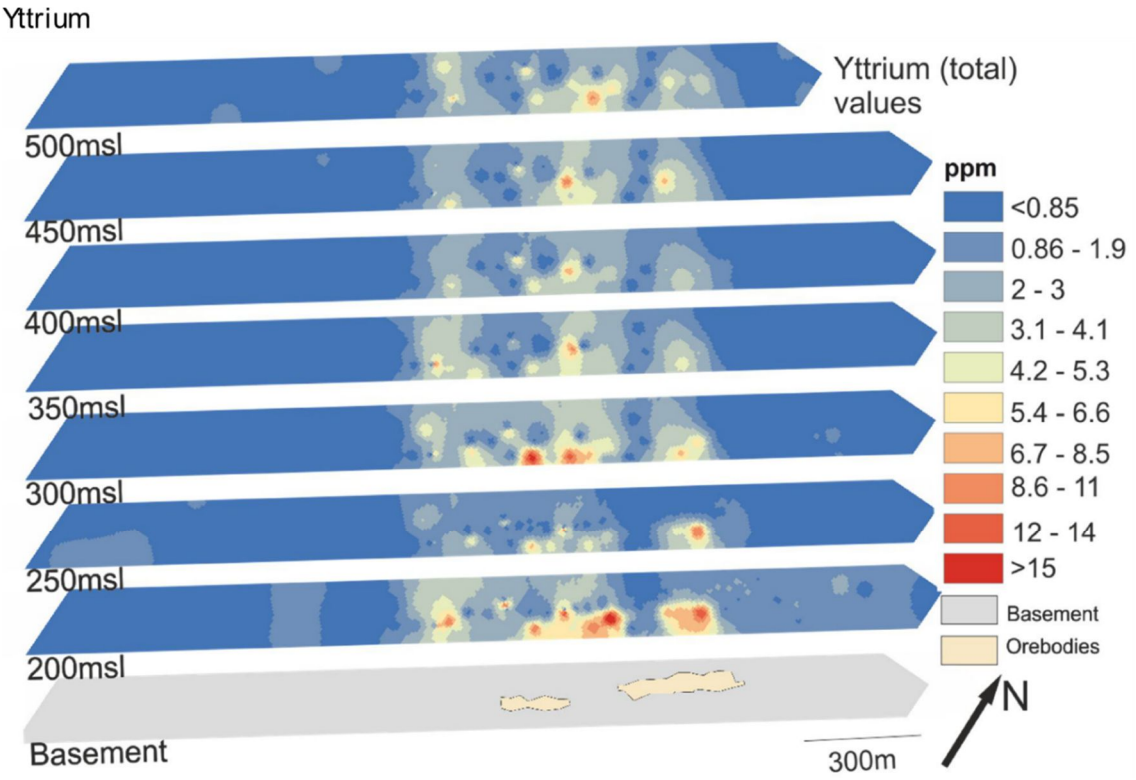

Figure 43: Whole rock interpolations of Y concentrations in total digestion data through the sandstones.

4 DISCUSSION

4.1 Nature and Sequence of the Alteration Associated with the Phoenix Deposit.

4.1.1 Tourmalines

Coarse-grained tourmalines of dravitic composition similar to that noted in this study have been reported in the basement elsewhere in the Athabasca basin (Rosenberg and Foit 2006, Mercadier et al.,2012 and Adlakha and Hattori, 2016). The Tur1 from the Phoenix Deposit is Mg rich and present only within pelitic lithologies along or very close to the WS Shear in intensely altered basement samples. Card (2012, 2014) suggested the crystallisation of Tur1 prior to the deposition of the Athabascan sandstones after peak metamorphism. Tur1's very restricted position along the WS Shear and absence elsewhere in less altered metapelites suggests that its generation may be linked to a late metamorphic fluid utilising the WS Shear and other faults as a fluid pathway for three reasons:

i. Tur1 is noted to wrap around quartz and follow a metamorphic foliation with limited evidence of later shearing and fracturing, at least on a micro-scale, suggesting it replaced biotite and illite, as opposed to being derived from an earlier igneous melt.
ii. Tur1 is also only noted from two spatially restricted samples, from a sample within the WS Shear (WR281A) and a sample proximal, from a related area of intense hydrothermal alteration and brecciation (DPX62). In the event Tur1 was derived from a partial melt, it is expected that its spatial distribution would be much greater within the basement.
iii. No Tur1 is observed within the Athabasca sandstones, despite Tur2 and other alteration phases being present in both the basement and sandstones. Thus Tur1's formation must predate the deposition of these units.

The crystallisation of tourmaline, from an event prior to the deposition of the Athabasca sandstones but after peak metamorphism is known (Card 2012). At the McArthur River uranium deposit, this event was attributed to dravitic tourmaline, pyrite and quartz crystallisation in the basement (Adlakha and Hattori 2016). The late metamorphic hydrothermal fluids have been proposed as sources for the quartzite ridges in proximity to major basement faults, such as the WS Shear (Card 2014). Similar temporal and spatial relationships appear to exist at the Phoenix Deposit

(Figure 13). The Tur1 from this study is identified to be similar in composition to the Oxy-dravite 'Tur2' from P2 (Adlkha and Hattori, 2016).

Magnesiofoitite is reported from multiple unconformity-related deposits, the composition of magnesiofoitite in this study shares some similarities to reported results from elsewhere such as: McArthur River P2, Second Link Lake, Key Lake, Rabbit Lake (Kotzer 1993, Rosenberg and Foit 2006, Mercadier et al. 2012, Ng et al. 2012 and Adlakha and Hattori 2016) and previous studies on the Phoenix Deposit, Gryphon and the MAW zone (O'Connel 2015; Chen et al. 2017).

Samples of Tur 2 identified in the basement and sandstone at the Phoenix Deposit are similar in composition and texture to the tourmaline related to ore formation at P2; (Adlakha and Hattori 2016 and Adlakha et al. 2017) suggesting Tur2 in the basement to be related to uranium mineralisation.

There is a general consensus that magnesiofoitite (identified as Tur2 in this study at the Phoenix Deposit) has some temporal relationship to uranium mineralisation elsewhere in the basin, and various ages for the generation of magnesiofoitite have been suggested from other deposits, for summary and references see Table 24. In lieu of samples available to this study, and based on the evidence from other deposits it is considered that magnesiofoitite from the Phoenix Deposit is coeval with uranium mineralisation. This is consistent with the association of boron with uranium in sandstones above the Phoenix Deposit (Chen et al. 2017).

Table 24: Review of magnesiofoitite and uranium mineralisation paragenesis with reference to other studies undertaken on Athabascan Deposits

Relationship to uranium mineralisation	Evidence of magnesiofoitite crystallisation at that point in the alteration sequence	Reference
Pre-Mineralisation	➢ Overprinted by ore-related chlorite	Ng et al. 2013a
Synchronous with Ore Formation	➢ Occurs in the matrix of ore-hosting breccias ➢ Close spatial association with ore ➢ δD and δ18O values of magnesiofoitite suggest it formed from the mixing of basinal (groundwater and minor marine inputs) and basement fluids when the mineralisation took place	Hoeve and Sibbald 1978, Kotzer and Kyser 1995, Fayek and Kyser 1997, Derome et al. 2005, Adlakha et al. 2015 and Adlakha et al. 2017.
Post-Mineralisation	➢ Post ore occurrence in voids "created by pre-ore alteration but not filled with uraninite." ➢ Overprints pre-ore and syn-ore alteration assemblages	Alexandre et al. 2005 and Cloutier et al. 2009

4.1.2 Illite Polytypes

Illite is a significant component in alteration halos surrounding unconformity-related uranium deposits, with the Phoenix Deposit being no exception. At the Phoenix Deposit, there are three generations of illite, which are defined by their differing chemistries (M1 and M2) and subtly different petrological and textual relationships (1Mc and 1Mt). 1Mc and 1Mt are the 'diagenetic' regional illite, and illite interpreted to be related to later post uranium mineralisation alteration, respectively.

Laverret et al. (2006) identified that the 1Mc and 1Mt polytypes in uranium mineralised areas (such as the Phoenix Deposit) is related to the infiltration of fluids formed after interaction with the basement rocks. This observation is partly supported by the illite polytypes overlying the Phoenix deposit. Both the 1Mc and 1Mt polytypes have been identified in the basement, however the 1Mt polytype is not common in the sandstones. It is found only in one clay fraction sample of in the Sandstone Extension to the WS Shear (Table 15) and six clay concentrate samples in the Sandstone Extension to the WS Shear and the non-sheared sandstones. In contrast, the majority of samples in the sandstone contain 1Mc illitic polytype. Through SEM imagery (S2/3) the paragenesis of the 1Mc and 1Mt illite examined in this study appear to be similar to those at other deposits. At Millennium the 1Mt illite polytype is observed growing from the edge of the 1Mc illite (Cloutier et al. 2009), as observed at the Phoenix Deposit (Plate S2/3). Illite of differing polytypes is present within minor fractures overlying the Phoenix Deposit, as described in Table 22.

Late 2M illite occurs peripheral to the A ore body close to the basement, but it is absent along the Sandstone Extension to the WS Shear. The evidence indicates that hydrothermal fluids responsible for 2M illite did not utilise the the Sandstone Extension to the WS Shear as fluid their pathway. This suggests that major faults hosted in sandstones do not act as structural controls for the crystallisation of illite, in contrast to early suggestions (Hoeve and Quirt 1984). Fractures which were present prior to 2M crystallisation were utilised by the fluid forming the 2M illite, (which the vein sample presented in Table 17 supports). The absence of the 2M polytype from the uranium mineralised unconformity sample (DPX72) implies that 2M illite crystallisation and potential fluid movement along the unconformity was limited.

The m-Kübler index utilised by this study has allowed analysis of coarser grained samples which represent coarse-grained fraction of illitic alteration. It should be noted that m-Kübler does not utilise clay fractions, and, as such, the larger crystal lattice available for diffraction via XRD would cause results which are lower (i.e. artificially more crystalline) than true 'Kübler' analysis. Results and discussion are therefore centred on the relative relationships between samples in the sandstones above the deposit, and are incompatible with studies on other deposits via other

methods. Sandstone Extension to the WS Shear samples present a slight positive correlation between 200 and 317m downcore, ranging from 0.17 to 0.32, this is more crystalline than samples noted from the regionally altered 'WR380' (implying greater crystallinity). This is in contrast to the expected hypothesis that crystallinity should decrease as one moves away from the deposit, while the evidence here indicates the opposite is true. Overlying the deposit, there is no clear correlation of crystallinity with depth, as such, this implies there is a limited relationship between the two.

The majority of illite samples in the sandstones above the A orebody are poorly crystalline. Samples from the Sandstone Extension to the WS Shear are variable in crystallinity, with both highly crystalline and poorly crystalline samples in close distances. Two samples to the south of the 'A' orebody are highly crystalline, while those from the 'regional' WR 380 drillcore have low - moderately crystalline samples, showing high Kubler values.

Illite samples overlying the 'B' orebody, in both the Sandstone Extension to the WS Shear Structure and the Athabasca Sandstones are highly crystalline, in contrast to those over the 'A' orebody; which are generally moderately to poorly crystalline. Illite samples from the 'regional' WR 380 drillcore show variable crystallinity, but generally more crystalline than those overlying the 'A' orebody, but less crystalline than those overlying the 'B' orebody.

Kubler values can be only obtained from clay fraction samples (Figure 23). The data presented in this study are used to calculate temperatures of illite crystallisation following Merriman and Frey (1999) and Figure 3 in Verdel et al (2012). Illites overlying the Phoenix Deposit have Kübler values of between 0.25 and 0.52, which corresponds to ~270°C to ~170-190°C (Verdel et al. 2012), a similar temperature to that determined for diagenetic fluids based on fluid inclusion studies by Pagel (1975), for quartz overgrowths from other Athabascan deposits based on fluid inclusions (Kotzer and Kyser, 1990) and from illites in the nearby K-Zone based on Kübler anlaysis (Cloutier et al, 2009). Illite samples from the Sandstone Extension to the WS Shear have m Kübler values which suggest temperatures ranged from to ~260°C to ~170-190°C. Of the samples analysed there is a general average of 0.4, which, after Verdel et al. (2012) suggests a formation temperature of 200°C. Kübler indexes reported as part of this study are generally comparable to those from other studies from mineralised areas (Ng. 2012) and plot largely within the diagenetic to anchizones. The polytypes of samples could present a reason for the differences in crystallinity and illite crystallinity. However, Figure 31 illustrates the lack of relationship between the Kübler values of polytypes from the Phoenix Deposit, observations which are shared by the m-Kübler analysis (Figure 32).

4.1.3 Chlorite Polytypes and Chemistry.

Chlorite is a significant component in alteration halos surrounding unconformity-related uranium deposits, with the Phoenix Deposit being no exception. In the basement, there are three generations, C1 to C3, and two in the sandstones, where chlorite C1 is noted in the shallow sandstones, and sudoitic C3 chlorite overlying uranium mineralisation. The early C1 is shown to plot within the Ripidolite subgroup (Figure 21), but contain less Al and more Fe than uranium mineralisation chlorite identified in basement-hosted deposits (Figure 22).

In the basement, pre-ore C2 is coeval with M1 illitisation (as demonstrated by the intergrowth of M1 illite and C2 in Plates P1/F and P4/E). C2 chlorite and is classified as a sudoite by composition. Although multiple samples plot towards a more clinochlore composition they lack the necessary Mg and are instead Fe and Al dominant. Late C3 chlorite is similar in composition and generation to C2, coeval with M2 crystallisation and sharing the same compositional trend towards clinochlore, but, again, lacks the necessary magnesium. Based on petrogenic relationships C3 is interpreted to be of a similar age to uranium mineralisation, an observation which is noted in other Athabascan type deposits (Adlakha and Hattori 2016).

4.2 Whole Rock Geochemistry

Bulk rock geochemical data shows 'chimneys' of elevated values in Y, B and Mg directly overlying the orebodies, and a depletion of K_2O concentrations.

The values of K_2O above the ore bodies are generally elevated in comparison to regional data (Dann et al., 2014) Close examination of the data from the sandstones overlying the Phoenix Deposit reveals an area of low K_2O values in the sandstones between the 'A' and 'B' ore bodies, suggesting replacement of K_2O in this area. Values of MgO are similar to that of B and form broad 'chimneys' to the north and south of the ore bodies.

Despite the well-defined chimney structures observed in Y, mean Y values above the Phoenix Deposit are lower than regional Athabasca Sandstone DDH and outcrop mean values (Dann et al, 2014) suggests depletion and localised enrichment of Y overlying the Phoenix Deposit forming the hydrothermally derived chimney structures. Low values of elements associated with alteration, such as B, MgO, and K_2O, directly above the deposits are interpreted to reflect intense silicification in the sandstones. The lateral extent of the chimneys (i.e. normal to the orebodies and trace of the WS Shear) is not known.

4.3 Near Infrared Spectroscopy of the Alteration Sequence above the Phoenix Deposit.

SWIR spectra are commonly used in the Athabasca basin to identify mineralogy and establish potential vectors to ore (Zhang et al. 2001). During the analysis of the drill core collected from the Phoenix Deposit, two types of absorption features are present (Figure 33). The low NIR feature (as shown in Figure 37 and Figure 38) appears unrelated to the distribution of illite or chlorite polytypes analysed as part of this study, as there is no significant spatial relationship between the two populations of data. In illite rich samples, the majority of samples yielding 1Mc illite polytypes also share a high NIR signature (Table 15 and Table 23) suggesting that illitic alteration, be it the initial regional, or diagenetic K-bearing, later M2 or 1Mt is not the causation behind the low NIR features. There appears to be no relationship between the 'low' NIR features and whole rock abundances of K_2O (Figure 42).

Fe oxides are a widespread diagenetic and alteration derived phase overlying the Phoenix Deposit, and Fe oxides are well known to have absorption features in the NIR (Hauff 2008). Fe oxides are also present in sufficient abundances to affect the spectra of the sandstone overlying the Phoenix Deposit. However, the abundance of total Fe within the sandstones also does not have any spatial relationships with low absorption features in the NIR as shown in Figure 35, suggesting the abundance of Fe does not control the observed shift seen in the absorption features.

With reference to the features observed at the Phoenix Deposit, a strong absorption edge between 400 and 600 nm may result from paired excitations between magnetically coupled ferric cations (Sherman and Waite 1985) and absorption bands related to the energy level changes in the valence electrons, known as crystal field transitions. Three such bands are known to be expressed in ferric (Fe^{3+}) Fe -bearing minerals: Located at a broad band between 750 and 950 nm associated with the 6A1 g _ 4T1 g transition; another band that commonly appears between 550 and 650 nm related to the 6A1 g _ 4T2 g transition; and a narrower band near 450 nm caused by the 6A1 g _ 4A1 g, 4Eg transitions (Hunt & Ashley 1979; Burns 1993).

Similarly, ferrous (Fe^{2+}) Fe also allows for crystal field transitions, although at different wavelengths to those observed in ferric Fe. Most common are broad absorption bands in the 900 to 1100 nm wavelength range related to spin-allowed transitions between the Eg and T2 g levels created by the splitting of the D ground state of ferrous Fe in an octahedral crystal field (Hunt and Ashley 1979, Burns 1993). Thus, the oxidation state of Fe could provide a source for the observed shifts in absorption features in the NIR.

Changes in the oxidation state of Fe within alteration minerals have been proposed as a reductant source by Komninou and Sverjensky (1996) and Ng et al. (2013b). However, chlorites overlying the Phoenix Deposit are not present in the same samples which have 'low' NIR features. M1 illite identified through this study has insufficient Fe (<5%) to allow for the substitution of Fe^{3+} for Fe^{2} (Murad and Wagner 1994). The reduction of Fe within chlorites can also be discounted as there is a limited spatial relationship between the 'low' NIR features and chlorites in the sandstones overlying the Phoenix Deposit. Therefore, neither illites or chlorites are considered to be the source behind the observed features in the NIR. Magnesiofoitite does not have absorption features within the NIR, and therefore is not the causation behind the features.

This study has observed a relationship between the NIR absorption features and the Tur2 phase, principally in the distribution of boron overlying the deposit, as shown in Figure 40. Drill cores, WR321 and WR291, both of which overly the deposit, are noted as having extensive Magnesiofoitite (Tur2) and both have considerably more samples that show the lower NIR absorption feature rather than the higher NIR absorption feature. This is contrast to other drill cores, where the reverse is generally true (Figure 37).

Whole rock geochemistry interpolations of B and Mg (Figure 40 and Figure 41) indicate an abundance of B and Mg within drill cores WR321 and WR291. These elements form a continuous elevated feature from 50 m above the unconformity to surface, terminating before the higher value NIR samples in WR321. Petrographic analysis of 'low' NIR samples, such as DPX81 (Plate P2/E), reveals well-formed magnesiofoitite filling pores formed through dissolusion of quartz with no other alteration minerals observed. In WR380, which is notable for having high (800-950 mm) NIR absorption features, the whole rock geochemistry results of B and Mg (Figure 40 and Figure 41) are both anomalously low. This observation suggests the source for the low NIR feature is spatially related to tourmaline, unrelated to other alteration phases and restricted to the vicinity of the deposit. Tourmaline, however, lacks any absorption features in the NIR, suggesting another mechanism.

Magnesiofoitite (Tur2 in this study) is often proposed as being coeval with uranium mineralisation (Hoeve and Sibbald 1978, Kotzer and Kyser 1995, Fayek and Kyser 1997, Derome et al. 2005, Kotzer and Kyser 1995, Adlakha et al. 2015 and Adlakha et al. 2017). Similar relationships are considered to have been present at the Phoenix Deposit, suggesting there may be a temporal relationship between the features in the NIR and U mineralisation. However, with no alteration minerals having a suitable NIR signature, and as no single mineralogical component has been identified, the mechanism behind the 'low' and 'high' NIR features is unknown.

4.4 Role of The Sandstone Extension to the WS Shear to Hydrothermal Activity in the Athabasca Sandstones

The Sandstone Extension to the WS Shear and similar faults in the Athabasca sandstones overlying uranium deposits have been considered to have acted as fluid conduits, with the potential for fluid flow from the deposits to the surface established in surficial geochemical surveys over the Phoenix Deposit (Power et al. 2014). However, this study indicates that the Sandstone Extension to the WS Shear's role as a fluid conduit above 100 - 150 m from the unconformity was limited. This is principally due to the similarity between the absorption features in the NIR, illite polytype and whole rock geochemistry in the shear and non-shear samples. Visually, alteration in the Sandstone Extension to the WS Shear is more intense than in non-sheared sandstones, but with no unique attributes.

M2 illite is observed within the WS Shear and the Sandstone Extension to the WS Shear through thin section, and only via polytype analysis through the rest of the sandstones. This suggests a potassium-bearing M2 generating fluid may have utilised the Sandstone Extension to the WS Shear alongside moving through the sandstones via other means, or at least been present for a sufficiently long period of time to allow for the growth of 4-5 mm wide crystals. Clay fractions of illite record the Sandstone Extension to the WS Shear being of a similar diagenetic zone to the Athabasca Sandstone (Figure 23), while the coarser clay concentrates show a slight increase in crystallinity between the Sandstone Extension to the WS Shear and depth (Figure 24). There is no evidence of increased radioactivity along the WS Shear, as scintillation counter readings of samples from the Sandstone Extension to the WS Shear and comparable depth samples show no difference.

Re-activation of basement faults in the Athabasca basin has been suggested as a driver for fluid flow in the basement, such as along the P2 fault associated with McArthur River (Ng et al. 2013a). This is interpreted to have generated conditions suitable for the mixing of reducing fluids and oxidising uraniferous fluids to interact, allowing for the generation of these deposits. Basement faults would have acted as conduits and areas regions of enhanced permeability and porosity as demonstrated by Li et al. (2017) enabling diagenetic and later, alteration causing fluids to circulate in the basement rocks. Such faults could be vital to the generation of these deposits. However, the evidence indicates that the Sandstone Extension to the WS Shear within the sandstones is simply a relic of early, pre-alteration structure with some role in the early alteration of the sandstones above the Phoenix Deposit, but no role as a significant fluid conduit later than M2 (Figure 44).

Table 25: Differences in mineralogy from samples from the WS Shear and samples away from the WS Shear.

Study	**Difference in Samples from Sandstone Extension to the WS Shear to surrounding sandstones**
Illite crystallinity	Minor, and inconclusive, samples from the Sandstone Extension to the WS Shear show a comparable m- Kübler value than samples elsewhere in the alteration package. There is a slight difference between Sandstone Extension to the WS Shear and those in WR380, suggesting some proximal control. For clay fraction samples: The Sandstone Extension to the WS Shear displays a mixed range of crystallinity values, however, there is a lack of suitable samples from the sandstone for comparison
Illite polytypes	No significant difference in shear or sandstone samples.
NIR feature	No significant difference. samples from the Sandstone Extension to the WS Shear samples exhibit both the higher and lower NIR absorption signatures.
Petrology	Considerably more alteration noted in the lower Sandstone Extension to the WS Shear samples, M2 illite present in Sandstone Extension to the WS Shear and sandstones.

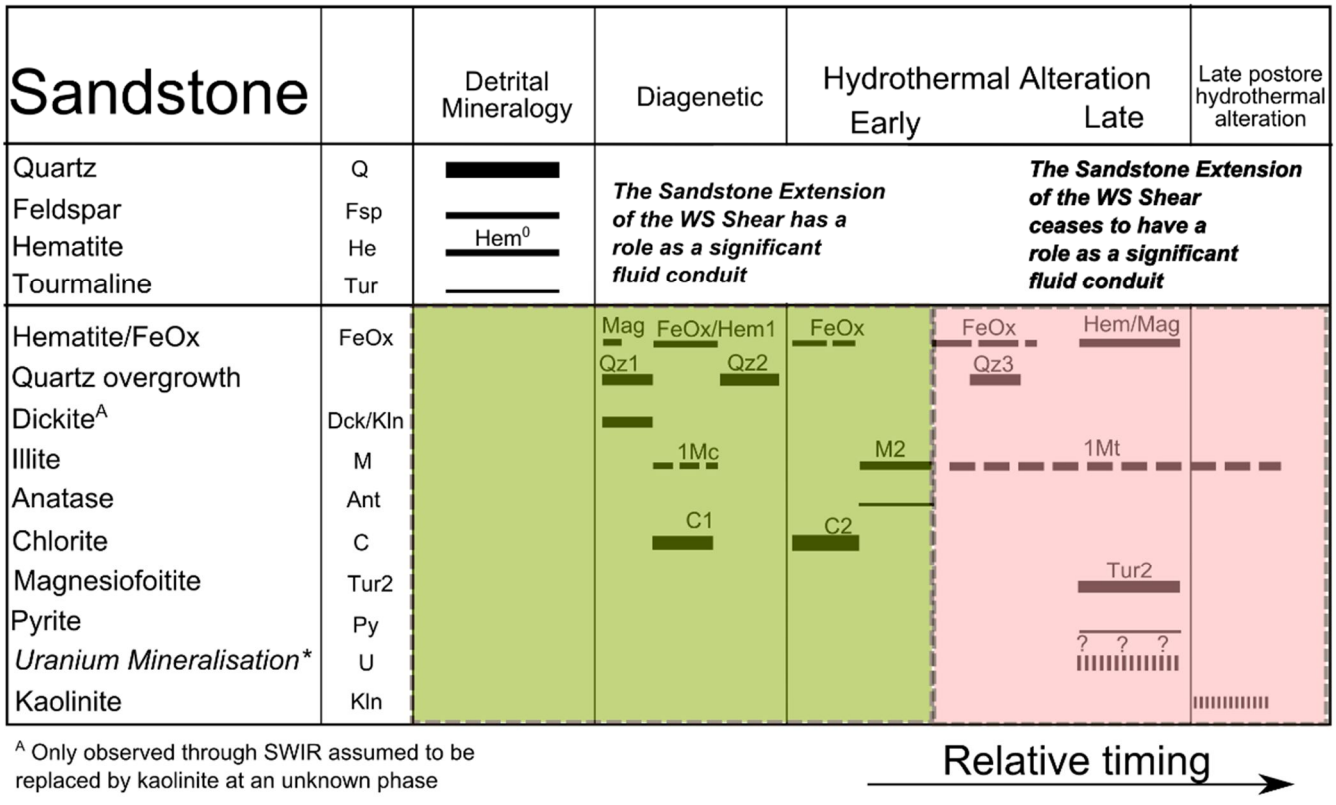

Figure 44: Paragenetic sequence of alteration products and the role of the Sandstone Extension to the WS Shear

5 CONCLUSIONS

The broad aim of this study was to identify and characterise the alteration minerals surrounding the Phoenix Deposit and to develop tools useful in exploration for concealed uranium deposits, as set out in the objectives.

5.1.1 The Identification and Description of Key Alteration Minerals Surrounding the Phoenix Deposit and their Chemistry, Distribution and Timing of Their Crystallisation.

This study has determined the paragenetic sequence of alteration minerals in metapelitc basement lithologies and overlying sandstones.

Three generations of chlorite are identified, an early Fe-Mg chlorite C1 – related to metamorphism, mid and late sudoitic C2 and C3 in basement rocks, whereas in the sandstones, C1 during the diagenesis and C2 from later hydrothermal alteration.

Early regional 1M illite is a ubiquitous alteration phase in the basement it has been identified to be coeval with C2. In the sandstones, 1M illite is identified to be coeval to C1. The late M2 illite is identified in both the basement and within the sandstone forming a chimney-like structure overlying the deposit it is of similar temporal age to C3 in the basement and postdates C2 in the sandstones. None of the generations of illite identified in this study are considered to be related to ore formation. However, C3 chlorite does share a slight temporal and spatial relationship.

Dravitic tourmaline has been identified as a product of metamorphic fluids along the WS Shear within the basement by previous workers. No dravitic tourmaline is identified in the sandstones in this study. Magnesiofoitite is often cited as syn-uranium mineralisation product and is found within the basement WS Shear Structure, the Sandstone Extension to the WS Shear and the non-shear sandstones. Chemical data from the basement WS Shear and the non-shear sandstones suggests there are no major differences between the two types of magnesiofoitite identified at the Phoenix Deposit, and samples analysed by this study are similar to that from other deposits.

5.1.2 Evaluation of the Role of the WS Shear and the Sandstone Extension to the WS Shear and their Association with the Distribution of Alteration Mineralogy Surrounding the Phoenix Deposit.

One of the major aims of this study was to evaluate the role of the Extension to the WS Shear in Sandstones in the alteration surrounding the Phoenix Deposit. Based on the results presented above, the Sandstone Extension to the WS Shear's role appears to be limited after the second generation of illite (M2) and although there is some evidence of late fluid movement along the fault, as demonstrated by the presence of magnesiofoitite. The Sandstone Extension to the WS Shear's only significant difference with the rest of the sandstone units is more M2 illitic intense alteration. Therefore it is not considered to be a preferential fluid conduit during the later

alteration and ultimately the uranium mineralisation. Furthermore, it is not considered to have a role as a pathway for late 'pathfinder elements' from the deposit to the surface.

5.1.3 Evaluation of The Polytypes and Crystallinity of Illite in the Alteration Halo Surrounding the Phoenix Deposit.

Illitic alteration at the Phoenix Deposit is unrelated to uranium mineralisation, preceding as two main (one regional, one local to the mineralisation) events. A third later minor local event (1Mt) is also documented, of which the temporal relationships are unclear.

As part of this study, illite polytypes are used to demonstrate the multiple generations of illite overlying the Phoenix Deposit. Three generations of illite polytypism are identified, and a slight spatial relationship between the 1Mt and 2M polytypes and U mineralisation is determined.

There is a no significant relationship of the illite crystallinity through either the m-Kübler or Kübler methods and proximity to the uranium orebodies. A minor increase in crystallinity is observed in the Sandstone Extension to the WS Shear, yet this is unlikely to be related to uranium mineralisation due to the different temporal differences between illite crystallisation and uranium mineralisation stages demonstrated in this study. The temperature of formation of illites at the Phoenix Deposit corresponds to ~170-190°C to ~270°C, which matches the regional formation temperature data from illite reported elsewhere in the Athabasca Basin, there is no relationship between illite crystallinity/temperature of crystallisation and polytype.

5.1.4 Determination and Evaluation of Behaviour and Source of NIR Variation Observed Above the Phoenix Deposit.

Near InfraRed spectroscopy shows variations in the spectral features from samples directly overlying the Phoenix Deposit between ≈ 835-905 nm to ≈ 600-700. Petrographic analysis established that samples with low NIR spectral features contain potentially syn ore magnesiofoitite and have a similar distribution to extensive boron 'chimneys' overlying the deposit.

The presence of a NIR absorption feature in the near infrared at 600-700 nm spatially associated with high boron (identified to be magnesiofoitite) values could be used as a vector towards uranium mineralisation.

5.1.5 Whole Rock Geochemistry Overlying the Phoenix Deposit

This study identified that Y exhibits a well-defined 'chimney' directly above mineralisation, but with values below the regional sandstone data far from any uranium deposits and outcrop values (reported in Dann et al., 2014). The low values on both side of the "chimney" are likely due to depletion of Y by hydrothermal activity. B also features a well-defined 'chimney' overlying the deposit, as a result of crystallisation of magnesiofoitite

5.1.6 Application of Techniques to Exploration

Techniques identified within this study are of direct relevance to ongoing exploration;

Although studying illite polytypes and crystallinity is impractical in a field setting, it could be carried out alongside chemical and petrological analysis of samples in a controlled environment.

This study identified elevated chimneys in the sandstones of Y and B overlying mineralisation which could offer a powerful exploration tool.

The identification of features in the NIR which may be coeval with mineralisation, offer a tool for U exploration not just in the Athabasca Basin, but also in Roll-Front U deposits elsewhere. Similar equipment is already in use on exploration campaigns in the region, and elsewhere, and thus can be rapidly and cheaply implemented into future exploration campaigns.

6 REFERENCES

Adlakha, E.E., Hattori, K., Zaluski, G., Kotzer, T., Potter, E.G, 2015. Mineralogy of a fertile fluid conduit related to unconformity-type uranium deposits in the Athabasca Basin, Saskatchewan. Geological Survey of Canada Open File Report 7791, pp 74-82. Doi:10.4095/295776.

Adlakha, E.E., Hattori, K., Davis, W.J. Boucher, B., 2017. Characterizing fluids associated with the McArthur River U deposit, Canada, based on tourmaline trace element and stable (B, H) isotope compositions. Chemical Geology, vol 466 p 417-435.

Adlakha, E.E., Hattori, K., 2016. Petrogenesis and composition of tourmaline-types along the P2 fault and McArthur River uranium deposit, Athabasca Basin, Canada. Canadian Mineralogist, vol. 54, pp. 661-679.

Alexandre, P., Kyser, K., Jiricka, D., Witt, G., 2012. Formation and evolution of the Centennial unconformity-related uranium deposit in the south-central Athabasca Basin, Canada. Economic Geology 107, pp. 385–400.

Alexandre, P., Kyser, K., Polito, P., Thomas, D., 2005. Alteration mineralogy and stable isotope geochemistry of Paleoproterozoic basement-hosted unconformity-type uranium deposits in the Athabasca Basin, Canada. Economic Geology 100, pp. 1547–1563.

Alexandre, P., Kyser, K., Thomas, D., Polito, P., Marlat, J., 2009. Geochronology of unconformity-related uranium deposits in the Athabasca Basin, Saskatchewan, Canada and their integration in the evolution of the basin. Mineralium Deposita 44, pp. 41–59.

Andrade, N., 1989. The Eagle Point uranium deposits, northern Saskatchewan, Canada (No. IAEA-TECDOC--500).

Annesley, I.R., Madore, C., Portella, P., 2005. Geology and thermotectonic evolution of the western margin of the Trans-Hudson Orogen: evidence from the eastern sub- Athabasca basement, Saskatchewan. Canadian Journal of Earth Sciences 42, pp. 573–597.

Arseneau, G., Revering, C., 2010. Technical report on the Phoenix deposit (Zones A and B)-Wheeler River project, eastern Athabasca Basin, Northern Saskatchewan, Canada. Denison Mines Corporation, NI 43-101 Technical Report. (96 pp.).

AusSpec International. (2010). AusSpec Workshop Manual for CD. Australia: AusSpec International Ltd (http://www.ausspec.com/).

Bartier, P.M. Kelley, C.P., 1996. Multivariate interpolation to incorporate thematic surface data using inverse distance weighting (IDW), Computers and Geosciences, v.22, p. 795-799.

Beyer, S.R., Hiatt, E.E., Kyser, K., Dalrymple, R.W. Pettman, C., 2011. Hydrogeology, sequence stratigraphy and diagenesis in the Paleoproterozoic western Thelon Basin: Influences on unconformity-related uranium mineralization. Precambrian Research, 187(3), pp.293-312.

Billault, V., Beaufort, D., Patrier, P. Petit, S., 2002. Crystal Chemistry of Fe-sudoites from Uranium Deposts in the Athabasca Basin (Saskatchewan, Canada). Clays and Clay Minerals, 50(1), pp.70-81.

Burns, R.G., 1993. Mineralogical applications of crystal field theory (Vol. 5). Cambridge University Press.

Card, C.D., 2012. The origins of anomalously graphitic rocks and quartzite ridges in the basement to the southeastern Athabasca Basin. Summary of Investigations, 2, pp.2012-4.

Card, C. D. 2014. Altered Pelitic Gneisses and Associated “Quartzite Ridges” Beneath the Southeastern Athabasca Basin: Alteration Facies and their Relationship to Uranium Deposits along the Wollaston-Mudjatik Transition. in Summary of Investigations 2013, Volume 2, Saskatchewan Ministry of the Economy, Miscellaneous Report 2013-4.2, Paper A-4, 23pp.

Card, C.D. Heath, P. 2015. Bedrock geology of sub-Athabasca basement rocks (NTS 74H). Saskatchewan Geological Survey, Saskatchewan Ministry of the Economy, Geoscience Map 2015-1, map and GIS shapefile data package.

Card, C.D., Pana, D., Portella, P., Thomas, D.J. Annesley, I.R., 2007. Basement rocks to the Athabasca Basin, Saskatchewan and Alberta. Bulletin of the Geological Survey of Canada, 588, pp.69.

Chen, S., Hattori, K. Grunsky, E.C., 2017. Multielement statistical evidence for uraniferous hydrothermal activity in sandstones overlying the Phoenix uranium deposit, Athabasca Basin, Canada. Mineralium Deposita, pp.1-16.

Clark, C.M., 2007. Tourmaline: Structural formula calculations. The Canadian Mineralogist, 45(2), pp. 229-237.

Cloutier, J., Kyser, K., Olivo, G.R., Alexandre, P., 2010. Contrasting patterns of alteration at the Wheeler River area, Athabasca Basin, Saskatchewan, Canada: insights into the apparently uranium-barren Zone K alteration system. Economic Geology 105, .pp 303–324.

Cloutier, J., Kyser, K., Olivo, G.R., Alexandre, P., Halaburda, J., 2009. The Millenium uranium deposit, Athabasca Basin, Saskatchewan, Canada: an atypical basement hosted unconformity-related uranium deposit. Economic Geology 104, pp 815–840.

Creaser, R , A Stasiuk, L D., 2007, Depositional age of the Douglas Formation, northern Saskatchewan, determined by Re-Os geochronology, In: EXTECH IV: Geology and Uranium EXploration TECHnology of the Proterozoic Athabasca Basin, Saskatchewan and Alberta; by Jefferson, C W (ed.); Delaney, G (ed.); Geological Survey of Canada, Bulletin no. 588, 2007; pp. 341-346; 1 CD-ROM

Dann, J., Hattori, K., Potter, E.G., Sorba, C., 2014. Discrimination of Elemental Assemblages in the Alteration Halo of the Phoenix Deposit, Saskatchewan, Through Applied GIS. Geological Survey of Canada Open File.

Doublier, M.P., Roache, T., Potel, S., Lukamp, C., 2012. Short-wavelength infrared spectroscopy of chlorite can be used to determine very low metamorphic grades. European Journal of Mineralogy. 24, pp 891–902.

Drits, V.A., Weber, F., Salyn, A.L. Tsipursky, S.I., 1993. X-ray identification of one-layer illite varieties: Application to the study of illites around uranium deposits of Canada. Clays and Clay Minerals, 41, pp.389-389.

Duba, D., Jones, A. E. W., 1983. The application of illite crystallinity, organic matter reflectance, and isotopic techniques to mineral exploration; a case study in southwestern Gaspe, Quebec, Economic Geology, 78(7) pp. 1350-1363.

Dyar, M.D., Lowe, E.W., Guidotti, C.V. Delaney, J.S., 2002. Fe3+ and Fe2+ partitioning among silicates in metapelites: A synchrotron micro-XANES study. American Mineralogist, 87(4), pp.514-522.

Earle, S., Sopuck, V., 1989, Regional lithogeochemistry of the eastern part of the Athabasca basin uranium province, Saskatchewan: International Atomic Energy Agency, Technical document TECHDOC-500,pp. 263−269.

Eaton, P.C. Setterfield, T.N., 1993. The relationship between epithermal and porphyry hydrothermal systems within the Tavua Caldera, Fiji. Economic Geology, 88(5), pp.1053-1083.

Eberl, D. D., B. Velde. 1989. "Beyond the Kübler index." Clay minerals 24, no. 4: pp. 571-577.

Ehrenberg, S.N. Nadeau, P.H., 1989. Formation of diagenetic illite in sandstones of the Garn Formation, Haltenbanken area, mid-Norwegian continental shelf. Clay Minerals, 24(2), pp.233-253.

Fayek, M., Kyser, T.K., 1997. Characterization of multiple fluid-flowevents and rare-earth element mobility associated with formation of unconformity-type uranium deposits in the Athabasca Basin, Saskatchewan. The Canadian Mineralogist 35,pp. 627–658.

Gamelin, C., Sorba, C., Kerr, W. 2010. The discovery of the Phoenix deposit: A new high-grade, Athabasca Basin unconformity-type uranium deposit, Saskatchewan, Canada. In: Saskatchewan Geological Survey Open House 2010 Abstract Volume, 17, 10.

Hauff, P., 2008. An overview of VIS-NIR-SWIR field spectroscopy as applied to precious metals exploration. Spectral International Inc, 80001, pp.303-403.

Henry, D.J., Novák, M., Hawthorne, F.C., Ertl, A., Dutrow, B.L., Uher, P. Pezzotta, F., 2011. Nomenclature of the tourmaline-supergroup minerals. American Mineralogist, 96(5-6), pp.895-913.

Hey, M.H., 1954. A new review of the chlorites. Mineralogical Magazine 224, 277–292.

Hoeve, J., Sibbald, T.I.I., 1978, On the genesis of Rabbit Lake and other unconformity-type uranium deposits in northern Saskatchewan, Canada: Economic Geology, v. 73,pp. 1450−1473.

Hunt, G.R. Ashley, R.P., 1979. Spectra of altered rocks in the visible and near infrared. Economic Geology, 74(7), pp.1613-1629.

Hunt, G.R., Salisbury J.W., Lenhof J., 1971. Visible and near-infrared spectra of minerals and rocks, III. Oxides and hydroxides, Modern Geology., 2, pp. 191-205.

Jaboyedoff, M., F. Bussy, B. Kübler, Ph Thelin. 2001. "Illite “crystallinity” revisited." Clays and clay minerals 49, no. 2: pp. 156-167.

Jefferson, C., Percival, J.B., Bernier, S., Cutts, C., Drever, G., Jiricka, D., Long, D., McHardy, S., Quirt, D., Ramaekers, P. Wasyliuk, K., 2001. Lithostratigraphy and mineralogy in the Eastern Athabasca Basin, northern Saskatchewan—progress in year 2 of EXTECH IV. Summary of investigations, 2(Part B), pp.2001-4.

Jefferson, C.W., Thomas, D.J., Gandhi, S.S., Ramaekers, P., Delaney, G., Brisbin, D., Cutts, C., Quirt, D., Portella, P., Olson, R.A., 2007. Unconformity-associated uranium deposits of the Athabasca Basin, Saskatchewan and Alberta. In: Jefferson, C.W., Delaney, G. (Eds.), EXTECH IV: Geology and Uranium EXploration TECHnology of the Proterozoic Athabasca Basin, Saskatchewan and Alberta: Geological Survey of Canada, Bulletin, 588, pp. 23–67.

Jolliff, B.L., Papike, J.J. Laul, J.C., 1987. Mineral recorders of pegmatite internal evolution: REE contents of tourmaline from the Bob Ingersoll pegmatite, South Dakota. Geochimica et Cosmochimica Acta, 51(8), pp.2225-2232.

Kerr, W.C., 2010. The discovery of the Phoenix deposit: a new high-grade, Athabasca Basin unconformity-type uranium deposit, Saskatchewan, Canada. In: Goldfarb, R.J., Marsh, E.E., Monecke, T. (Eds.), The Challenge of Finding New Mineral Resources: Global Metallogeny, Innovative Exploration, and New Discoveries: Society of Economic Geologists, Special Publication, Vol. 2 (15): Zinc–Lead, Nickel–Copper–PGE, and Uranium, pp. 703–728.

Kister, P., Laverret, E., Quirt, D., Cuney, M., Mas, P.P., Beaufort, D. Bruneton, P., 2006. Mineralogy and geochemistry of the host-rock alterations associated with the Shea Creek unconformity-type uranium deposits (Athabasca Basin, Saskatchewan, Canada). Part 2. Regional-scale spatial distribution of the Athabasca Group sandstone matrix minerals. Clays and Clay Minerals, 54(3), pp.295-313.

Komninou, A., Sverjensky, D.A., 1996. Geochemical modelling of the formation of an unconformity-type uranium deposit. Economic Geology 91, pp. 590–606.

Kotzer, T.G. 1993. Fluid history of the Proterozoic Athabasca Basin; Ph D. thesis, University of Saskatchewan, Saskatoon, Saskatchewan.

Kotzer, T.G., Kyser, T.K., 1995. Petrogenesis of the Proterozoic Athabasca Basin, northern Saskatchewan, Canada, and its relation to diagenesis, hydrothermal uranium mineralization and Paleohydrogeology. Chemical Geology 120,pp. 45–89

Kübler, B., 1964. Les argiles, indicateurs de métamorphisme. Rev. Inst. Fr. Pétrole, 19, pp.1093-1112.

Kübler, B., 1967. La cristallinité de l'illite et les zones tout à fait supérieures du métamorphisme. Etages tectoniques, pp.105-121.

Kyser, K., Cuney, M., 2008. Geochemical characteristics of uranium and analytical methodologies. In: Cuney, M., Kyser, K. (Eds.), Recent and Not-so-recent Developments in Uranium Deposits and Implications for Exploration: Mineralogical Association of Canada, Short Course, vol. 39, pp. 23–56.

Laverret, E., Mas, P.P., Beaufort, D., Kister, P., Quirt, D., Bruneton, P., Norbert, C., 2006, Mineralogy and geochemistry of the host-rock alterations associated with the Shea Creek unconformity-type uranium deposits (Athabasca basin, Saskatchewan, Canada). Part. 1. Spatial variation of illite properties: Clays and Clay Minerals, v. 54,pp. 275−294.

Li, Z., Bethune, K.M., Chi, G., Bosman, S.A. Card, C.D., 2015. Topographic features of the sub-Athabasca Group unconformity surface in the southeastern Athabasca Basin and their relationship to uranium ore deposits. Canadian Journal of Earth Sciences, 52(10), pp.903-920.

Li, Z., Chi, G., Bethune, K.M., Eldursi, K., Thomas, D., Quirt, D. Ledru, P., 2017. Synchronous egress and ingress fluid flow related to compressional reactivation of basement faults: the Phoenix and Gryphon uranium deposits, southeastern Athabasca Basin, Saskatchewan, Canada. Mineralium Deposita, pp.1-16.

Marlatt, J., McGill, B., Matthews, R., Sopuck, V. Pollock, G. 1992. The discovery of the McArthur River uranium deposit, Saskatchewan, Canada (No. IAEA-TECDOC--650).

Mathieu, M., Roy, R., Launeau, P., Cathelineau, M. Quirt, D. 2017. Alteration mapping on drill cores using a HySpex SWIR-320m hyperspectral camera: Application to the exploration of an unconformity-related uranium deposit (Saskatchewan, Canada). Journal of Geochemical Exploration, 172, pp.71-88.

McLeod, R.L., Gabell, A.R., Green, A.A., Gardavsky, V., 1987. Chlorite infrared spectral data as proximity indicators of volcanogenic massive sulphide mineralization, in Proceedings, Pacific Rim Congress 87, Gold Coast, Queensland, Australia, Australasian Institute of Mining and Metallurgy, pp. 321–324.

Mercadier, J., Richard, A. Cathelineau, M., 2012. Boron-and magnesium-rich marine brines at the origin of giant unconformity-related uranium deposits: δ11B evidence from Mg-tourmalines. Geology, 40(3), pp.231-234.

Merriman, R.J. Frey, M., 1999. Patterns of very low-grade metamorphism in metapelitic rocks. In: Frey, M. & Rovertseon D. (eds) Low-grade metamorphism, Blackwell Science, Oxford, pp.61-108.

Murad, E. Wagner, U., 1994. The Mössbauer spectrum of illite. Clay Minerals, 29(1), pp.1-10.

Ng, R. 2012. Geochemical and mineralogical evolution of the McArthur River Zone 4 unconformity-related uranium ore body and application of iron oxidation state in clay alteration as indicator of uranium mineralization. Unpublished M.Sc. thesis, Queen's University, Kingston, Ontario, Canada, pp. 207.

Ng, R., Alexandre, P. Kyser, K., 2013a. Mineralogical and geochemical evolution of the unconformity-related McArthur River Zone 4 orebody in the Athabasca Basin, Canada: implications of a silicified zone. Economic Geology, 108(7), pp.1657-1689.

Ng, R., Alexandre, P., Kyser, K., Cloutier, J., Abdu, Y.A. Hawthorne, F.C., 2013b. Oxidation state of iron in alteration minerals associated with sandstone-hosted unconformity-related uranium deposits and apparently barren alteration systems in the Athabasca Basin, Canada: Implications for exploration. Journal of Geochemical Exploration, 130, pp.22-43.

Novák, M., Povondra, P. Julie, B., 2004. Schorl-oxy-schorl to dravite-oxy-dravite tourmaline from granitic pegmatites; examples from the Moldanubicum, Czech Republic. European Journal of Mineralogy, 16(2), pp.323-333.

O'Connel, I, 2015, Characterization of Tourmaline from the Maw Zone, Gryphon Zone and Sandstone above the Phoenix Uranium Deposits, Athabasca Basin, Saskatchewan Canada, Unpublished Bsc (Honours) Thesis, University of Ottawa.

Pacquet, A. Weber, F., 1993. Petrography and mineralogy of alteration halos around the Cigar Lake deposit and their relation to the mineralization. Canadian Journal of Earth Sciences, 30(4), pp.674-688.

Percival, J.B. Kodama, H., 1989. Sudoite from Cigar Lake, Saskatchewan. The Canadian Mineralogist, 27(4), pp.633-641.

Polito, P.A., Kyser, T.K., Alexandre, P., Hiatt, E.E. Stanley, C.R., 2011. Advances in understanding the Kombolgie Subgroup and unconformity-related uranium deposits in the Alligator Rivers Uranium Field and how to explore for them using lithogeochemical principles. Australian Journal of Earth Sciences, 58(5), pp. 453-474.

Power, M.J., 2014, Geochemical surface expression of the Phoenix and Millennium uranium deposits, Athabasca Basin, Saskechewan. Unpublished Masters Thesis, University of Ottawa

Quirt, D.H.2003, Athabasca unconformity-type uranium deposits: One deposit type with many variations: Uranium Geochemistry 2003, International Conference, Nancy, France, April 13−16, 2003, Proceedings, pp. 309−312.

Ramaekers, P. 1990: Geology of the Athabasca Group (Helikian) in northern Saskatchewan. Saskatchewan Energy and Mines, Miscellaneous Report 195, pp. 49.

Ramaekers, P., Jefferson, C.W., Yeo, G.M., Collier, B., Long, D.G.F., Drever, G., McHardy, S., Jiricka, D., Cutts, C., Wheatley, K., Catuneanu, O., Bernier, S., Kupsch, B., Post, R.T., 2007. Revised geological map and stratigraphy of the Athabasca Group, Saskatchewan and Alberta. In: Jefferson, C.W., Delaney, G. (Eds.), EXTECH IV: Geology and Uranium EXploration TECHnology of the Proterozoic Athabasca Basin, Saskatchewan and Alberta: Geological Survey of Canada, Bulletin, 588, pp. 155–191.

Ramaekers, P., Yeo, G. Jefferson, C., 2001. Preliminary overview of regional stratigraphy in the Late Paleoproterozoic Athabasca Basin, Saskatchewan and Alberta. Summary of Investigations, 2, pp. 2001-2004.

Reid, K., Ansdell, K., Jiricka, D., Witt, G. Card, C., 2010. Regional setting and general characteristics of the Centennial unconformity-related uranium deposit, Athabasca Basin, Saskatchewan.

Repais, K. 2016. Preliminary Economic Assessment for the Wheeler River Uranium Project, Saskatchewan, Canada. SRK Consulting (Canada)

Repais, K., Mathisen. M., 2018. Technical Report with an Updated Mineral Resource Estimate for the Wheeler River Property, Northern Saskatchewan, Canada . SRK Consulting (Canada) & Canada, Roscoe Postle Associates Consultants Ltd.

Richard, A., Pettke, T., Cathelineau, M., Boiron, M.C., Mercadier, J., Cuney, M. Derome, D., 2010. Brine–rock interaction in the Athabasca basement (McArthur River U deposit, Canada): consequences for fluid chemistry and uranium uptake. Terra Nova, 22(4), pp.303-308.

Roscoe, W. E., 2014. Technical Report on a Mineral Resource Estimate For The Wheeler River Property, Eastern Athabasca Basin, Northern Saskatchewan, Canada, Roscoe Postle Associates Consultants Ltd.

Rosenberg, P.E. Foit, F.F., 2006. Magnesiofoitite from the uranium deposits of the Athabasca Basin, Saskatchewan, Canada. The Canadian Mineralogist, 44(4), pp.959-965.

Sherman, D.M., Waite, T.D., 1985. Electronic spectra of Fe^{3+} oxides and oxide hydroxides in the near IR to near UV. American Mineralogist, 70(11-12), pp. 1262-1269.

Tourigny, G., Wilson, S., Breton, G. Portella, P., 2001. Structural controls and emplacement of uranium mineralization at the Sue C deposit, McClean Lake operation, northern Saskatchewan. Saskatchewan Energy and Mines Miscellaneous Report, 4, pp. 334-352.

Tran, H.T., Ansdell, K.M., Bethune, K.M., Ashton, K. Hamilton, M.A., 2008. Provenance and tectonic setting of Paleoproterozoic metasedimentary rocks along the eastern margin of Hearne craton: Constraints from SHRIMP geochronology, Wollaston Group, Saskatchewan, Canada. Precambrian Research, 167(1), pp.171-185.

Velde, B., Hower, J., 1963. Petrological Significance of Illite Polymorphism in Paleozoic Sedimintary Rocks. American Mineralogist, 48(11-2), pp.1239.

Verdel, C., van der Pluijm, B.A. Niemi, N., 2012. Variation of illite/muscovite 40Ar/39Ar age spectra during progressive low-grade metamorphism: an example from the US Cordillera. Contributions to Mineralogy and Petrology, 164(3), pp.521-536.

Voultsidis, V., von Pechmann, E., Classen, D., 1982, Petrography, mineralogy and genesis of the U-Ni deposits, Key Lake, Saskatchewan, Canada, in Amstutz, G.C., El Goresy, A., Frenzel, G., Kluth, C, Moh, G., Wauschkuhn, A. & Zimmermann, R.A. ed., Ore genesis - the state of the art: Springer Verlag, Berlin, pp. 469-490.

Weaver, C.E., Wampler, J.M. Pecuil, T.E., 1967. Mössbauer analysis of iron in clay minerals. Science, 156(3774), pp.504-508.

Wilson, M.R., Kyser, T.K., 1987. Stable isotope geochemistry of alteration associated with the Key Lake uranium deposit, Canada. Economic Geology 82, pp. 1540–1557

Yeo, G., Jefferson, C.W., Ramaekers, P., 2002. A preliminary comparison of Mantiou Falls Formation stratigraphy in Four Athabasca Basin Deposystems. Summary of Investigations, 2, pp.2002-4.

Zhang, G., Wasyliuk, K. Pan, Y., 2001. The characterization and quantitative analysis of clay minerals in the Athabasca Basin, Saskatchewan: Application of shortwave infrared reflectance spectroscopy. The Canadian Mineralogist, 39(5), pp.1347-1363

Appendix to accompany:

Alteration Spatially Associated with the Phoenix Unconformity-Related Uranium Deposit, Athabasca Basin, Saskatchewan, Canada.

Thesis submitted to the
Faculty of Graduate and Postdoctoral Studies
in partial fulfilment of the requirements for the
M.Sc degree in Earth Sciences

Jack Dann, Ottawa, Ontario, 2019.

Appendix 1	Open File Reports	Page Number
1.1	Geological Survey of Canada, Open File Report 7463	109
Appendix 2	Sample Locations	
2.1	Whole Drillcore Sample Locations	176
2.2	Thin section and SEM sample locations	183
Appendix 3	Electron Microprobe Results	
3.1	Tourmaline raw EMPA Data	185
3.2	Chlorite raw EMPA Data	186
3.3	Illite raw EMPA Data	191
Appendix 4	Short Wave Infrared Spectroscopy (SWIR) Analysis	
4.1	Short Wave Infrared Spectra of samples collected	194
4.2	Samples identified through The Spectral Geologist Software	326
Appendix 5	X Ray Diffraction (XRD) Analysis	
5.1	Whole Rock Powder Sample Diffractograms	331
5.2	Clay Concentrate Sample Diffractograms	357
5.3	Clay Fraction XRD Analysis of Clays from the Alteration Halo of the Phoenix Deposit.	379

Appendix 1	Open File Reports	Page Number
1.1	Geological Survey of Canada, Open File Report 7463	109

GEOLOGICAL SURVEY OF CANADA
OPEN FILE 7463

Discrimination of Elemental Assemblages in the Alteration Halo of the Phoenix Deposit, Saskatchewan, Through Applied GIS

J. Dann, K. Hattori, E.G. Potter and C. Sorba

2014

Natural Resources Canada Ressources naturelles Canada

Canada

GEOLOGICAL SURVEY OF CANADA
OPEN FILE 7463

Discrimination of Elemental Assemblages in the Alteration Halo of the Phoenix Deposit, Saskatchewan, Through Applied GIS

J. Dann[1], K. Hattori[1], E.G. Potter[2] and C. Sorba[3]

[1]-Department of Earth Sciences, University of Ottawa, Ottawa, ON K1N 6N5
[2]- Geological Survey of Canada, 601 Booth St, Ottawa, ON K1A 0E9
[3]- Denison Mines Corp., Suite 200-230 22nd St. East, Saskatoon, SK S7K 0E9

2014

doi:10.4095/293122

This publication is available for free download through GEOSCAN (http://geoscan.ess.nrcan.gc.ca/).

Recommended citation
Dann, J., Hattori, K., Potter, E.G., and Sorba, C., 2014. Discrimination of Elemental Assemblages in the Alteration Halo of the Phoenix Deposit, Saskatchewan, Through Applied GIS; Geological Survey of Canada, Open File 7463. doi:10.4095/293122

Publications in this series have not been edited; they are released as submitted by the author.

Abstract
This study was initiated as part of the TGI-4 uranium ore systems project to evaluate the dispersion of ore-related elements that could be used to increase exploration effectiveness for deeply buried, unconformity-related uranium mineralization. The Phoenix deposit, located in the Athabasca Basin, currently has indicated resources of approximately 52.3 million lbs U_3O_8. The mineralization consists of four pods termed the A, B, C and D ore zones at ca. 400 meters depth. The pods occur both at the unconformity and within the basement as steeply dipping zones associated with a fault zone termed the WS shear.

The siliciclastic sandstones of the Athabasca Group overlying the Phoenix deposit are characterized by elevated enrichments in the elements Y, W, B, Mg, As, Pb, B, Co and Cu. Preliminary geochemical analyses of sandstone samples from the Manitou Falls Formation indicate a clear migration of Y and W in vertical columns while B, MgO and As data reveal zones of elevated values that extend from the ore zones to upwards of 350m above the deposit and 2.4 km along strike. Away from these chimneys, values of MgO, B, and As are comparable to that of regional outcrop and drillhole data, suggesting localized, well-defined enrichment of these elements in the vicinity of Phoenix. The abundance of other elements elevated in the orebody, such as Ni, Li and V, show little spatial relationship to mineralization in the overlying sandstones. These preliminary results illustrate that certain elements can play a guiding role in the exploration of unconformity-related uranium deposits.

Introduction

Currently, all of Canada's uranium production is from unconformity-related deposits situated in the Athabasca Basin, Saskatchewan. With recent exploration successes at increasing depths in the basin, new efficient means of targeting these deeply buried deposits are required. Under the Targeted Geoscience Initiative Four (TGI-4) program, this study is examining the movement of elements from deep-seated ore deposits to the near surface environment. This subject is of intense interest not only for exploration but also for environmental studies and mine site remediation.

In this study, we discuss the spatial relationship of elevated metals concentrations within sandstones overlying the Phoenix Deposit, located on the Wheeler River Property. As a means of tracking elemental distribution in the sandstones overlying the Phoenix Deposit, interpolations of whole rock lithogeochemistry at 50m intervals have been performed for elements associated with mineralization, recognized pathfinder elements and major elements. A major shear zone (WS shear) is associated with the Phoenix deposit and has been proposed as a potential conduit for pre-, syn- and post-ore fluids (Kerr, 2010; Arseneau and Revering, 2010; this study). Its role in the migration and distribution of elements is discussed herein.

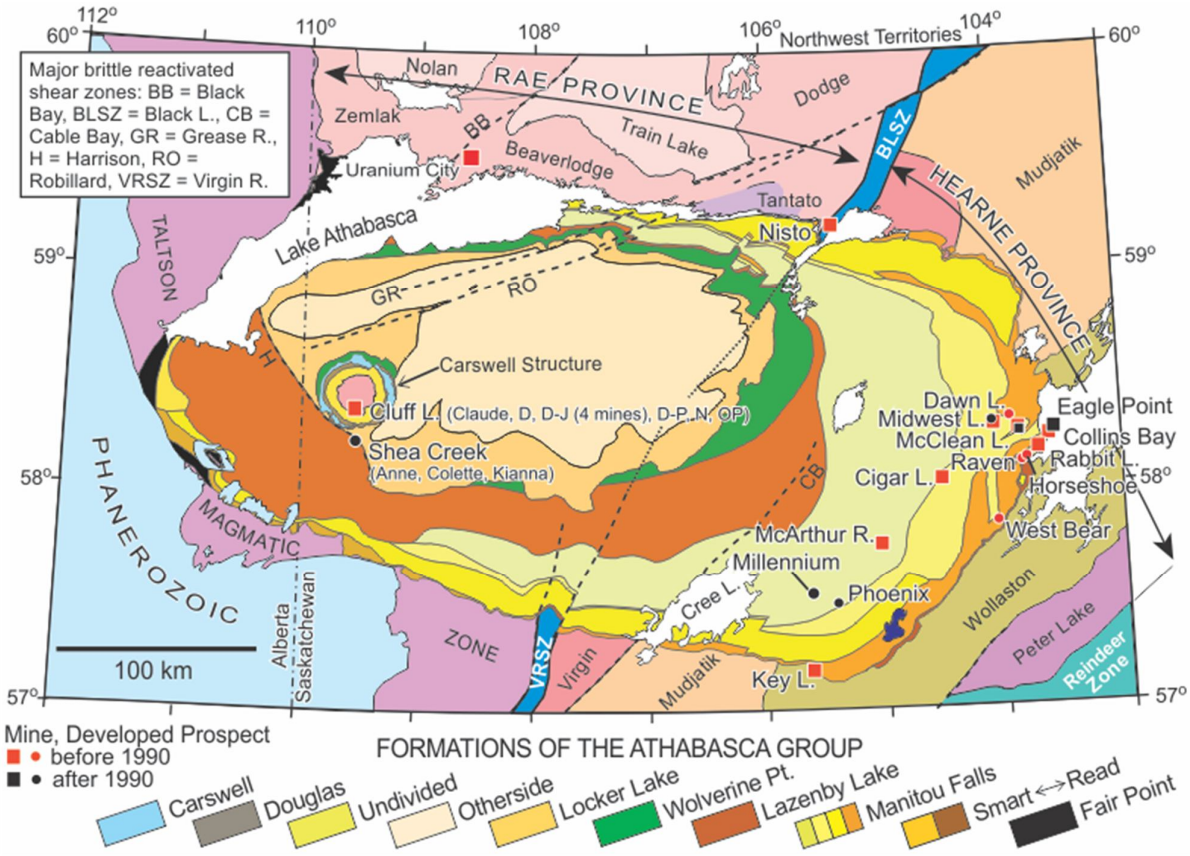

Figure 1: Geologic map of the Athabasca Basin, northern Saskatchewan, Canada. The Phoenix deposit is located in the southeast margin of the Athabasca Basin. Modified from Jefferson et al., (2007).

Regional Geology

The majority of the producing, past-producing and active uranium prospects in the Athabasca Basin overly the basement transition between the Wollaston and Mudjatik domains of the Hearne Province (Annesley et al., 2005). The transition zone comprises pelitic, quartzose and arkosic paragneissic lithologies that are isoclinally folded and interleaved with Paleoproterozoic orthogneiss and abundant pegmatitic intrusions (Jefferson et al., 2007). Graphitic pelites and paragneiss compose 70 to 85% of the metasedimentary sequence (Annesley et al., 2005).

The Athabasca Basin was formed between 1760-1500 Ma as a series of northeast-southwest sub basins controlled by major Hudsonian age faults in the underlying basement rocks (Ramaekers et al., 2007). These faults have been interpreted to have had played a significant role in localizing uranium-bearing fluids during deposit formation (Jefferson et al., 2007). The dominantly quartzose Athabasca Group is subdivided into ten Formations, which constitute four fluvial, unconformity-bound sequences (Ramaekers et al., 2007; Yeo et al., 2007).

Local Geology

Within the Wheeler River Property, the Athabasca sandstone is composed of a 170 to 560 m thick sequence dominated by the Manitou Falls Formation quartz arenite. At the Phoenix deposit, three members overlie the basal Read Formation (RD; historically termed the MFa): the Bird (MFb), Collins (MFc) and the Dunlop (MFd) members, which can be differentiated based on conglomeratic and interclast material (Ramaekers et al., 2007). The RD is composed of a lower unit of pebble-cobble conglomeratic rocks overlain by an upper unit of well sorted sandstone to pebbly sandstone. The RD varies in thickness, from over 200m west of a basement quartzite ridge, to absent directly above this paleotopographic high (Bosman and Korness, 2007; Kerr, 2010). The MFb is similar to the RD, although it is differentiated by greater than 1.2% conglomeratic material in beds thicker than 2 cm (Ramaekers et al., 2007) and is also absent above the quartzite ridge (Bosman and Korness, 2007; Kerr, 2010). The 30 to 150 m thick MFc is a relatively clean sandstone, with locally scattered pebbles or granules and minor pebble layers interpreted to be pebble lag deposits. The MFd member is characterized by the presence of at least 0.6% clay intraclasts (Jefferson et al., 2007).

The dominant regional diagenetic clay phase in the sandstones of the Athabasca Basin is dickite. The Phoenix deposit also lies within a broad regional illite and chlorite anomaly present in surficial material and outcrops of Athabasca Group sandstone that trends northeast from Key Lake to McArthur River (Earle and Sopuck, 1989; Jefferson et al., 2007). The authors also recognized a tourmaline (dravite) anomaly associated with this trend, but this zone lies west of the Phoenix deposit.

The basement rocks are composed of metasedimentary rocks belonging to the Wollaston Supergroup and Mudjatik domain. These include graphitic and non-graphitic pelitic and semipelitic gneisses, quartzite, and rare calc-silicate rocks together with felsic and quartz feldspathic granitoid gneisses (Arseneau and Revering, 2010). Granitic pegmatites are common, with coarse-grained K-feldspar, quartz and micas. Garnet, cordierite and sillimanite occur in the metapelites, indicating upper amphibolite metamorphic grade (Arseneau and Revering, 2010). The quartzite ridge, a major paleotopographic high at the unconformity and an interpreted impermeable and structural barrier (Arseneau and Revering, 2010) dips between 45° – 75° to the southeast, with an undulating azimuth of around 055°.

Geology of the Phoenix deposit

Discovered in 2008, the Phoenix deposit is operated by Denison Mines Corporation (60%) and co-owned by Cameco Corporation (30%) and JCU Exploration Company Limited (10%). By late 2012, drilling defined four mineralized zones; two which have been subject to extensive drilling (A

and B) and contain 43-101 compliant resource estimates. The remaining two zones (C and D) are still undergoing exploration and resource delineation. The A and B zones contain indicated resources of 52.34 million pounds of U_3O_8 (Arseneau and Revering, 2010; Roscoe, 2012). Uranium mineralization occurs mainly as uraninite, with high levels of Cu (up to 3200 ppm) and Pb up to 2.25 wt %), and minor Ni, Co, As, Zn and Ag in the A and B zones (Arseneau and Revering, 2010).

The Phoenix deposit is situated along the northeast-trending reverse structure of WS Shear which dips to the southeast and is rooted in either the base of the graphitic pelite or along the western edge of the quartzite ridge (Arseneau and Revering, 2010). Mineralization along the WS Shear occurs as steeply dipping, thin (1-3m wide) parallel to sub-parallel bands for up to 20 m below the unconformity. Mineralization in the lowest 15 m of the RD appears to be related to extension of the WS Shear and hanging wall splays, indicating reactivation occurred along these faults after deposition of the RD and MFb (Kerr, 2010).

This study uses a projection of the ore body produced by Denison Mines Corporation in 2011, at a cut-off grade of 0.1% U_3O_8. It is recognized that the actual area of mineralization extends beyond this, although with a lower grade and thickness (grade in wt% U_3O_8*m) of between 0.601 to 0.01.

Athabasca Sandstones above the Phoenix Deposits

Geochemical interpolations were performed along slices at 50m intervals. Where slices pass through more than one lithological unit, stratigraphic boundaries were derived from core logging performed by Denison Mines Corp., staff using the parameters outlined in Ramaekers et al., (2007). The regional data from Card et al., (2011) and Bosman and Card, (2012) followed the same logging parameters.

Table 1: Division of the Athabasca Group in relation to the slices analysed as part of this study.

Depth (msl)	Member/Formation
500	MFd
450	MFc
400	MFc
350	MFc/MFb
300	MFb/MFc
250	MFb
200	MFb/RD

Methods

Geochemical Data

All the geochemical data were produced at the Saskatchewan Research Council Geoanalytical Labs in Saskatoon, Canada for Denison Mines Corporation. Samples were subjected to partial leach method whereby an aliquot of pulp was digested in a hot aqua regia bath for approximately 1 hour, then diluted to 15ml using de-ionized water, followed by Inductively Coupled Plasma Mass Spectrometry (ICP-MS) or Inductively Coupled Plasma - Optical Emission Spectrometry (ICP-OES). Where partial leach data are not available, total digestion values have been used, in which aliquots of pulp were digested in a hot mixture of concentrated acids of HF, HNO_3, and $HClO_4$. The residue was then dissolved in 15 ml of 5% HNO_3 and made to volume using de-ionized water prior to analysis. For boron, an aliquot of pulp was fused in a mixture of $NaO_2/NaCO_3$ in a muffle oven. The fused melt was then dissolved in de-ionized Water and analysed by ICP-OES.

This study uses two populations of data: data from DDH WR 190A to WR 269 (number of DDH =23) were derived from ICP-OES whereas DDH WR 270 to WR 384 (number of DDH =111) used ICP-MS. The majority of data used for both interpolations and statistical analysis had values well above detection limits (Table 2), and any values at detection limits were not manipulated and retained for median value calculation. Due to the low variance of tungsten, which had a large number of samples at detection limit, tungsten was excluded from statistical analysis and comparison to regional data. All the geochemical data are summarized in Appendix A.

Table 2: Working Detection limits of elements for both analytical methods applied in this study, compared to the population of each dataset.

Leach Method	Partial Digestion								Total Digestion									
	As	Co	Cu	Mo	Ni	Pb	U	V	Al_2O_3	Fe_2O_3	K_2O	MgO	P_2O_5	Li	W	Y	Ce	B
MFb	**Working Detection Limits from ICP-OES**																	
Lowest Value Sample	0.1	0.1	0.2	0.1	0.1	0.2	0.3	0.4	1.4	0.11	0	0.03	0.02	1	0.5	1	21	1
Number of Samples at Lowest Value	13	59	18	163	1	1	153	3	1	1	1	1	2	2	168	2	1	1
% of Population	7.4	34	10	93	0.6	0.6	87	1.7	0.57	0.57	0.6	0.57	1.14	1.1	95.5	1.1	0.6	0.6
Working Detection Limits from ICP-MS																		
Lowest Value Sample	0.2	0	0.1	0	0.2	0.4	0.1	0.1	0.04	0.05	0	0.01	0.02	0.5	0.1	0.3	0.5	20
Number of Samples at Lowest Value	1	1	1	7	1	1	1	1	1	1	1	1	1	2	726	3	1	1
% of Population	0.1	0.1	0.1	0.9	0.1	0.1	0.1	0.1	0.13	0.13	0.1	0.13	0.13	0.3	95.9	0.4	0.1	0.1

Leach Method	Partial Digestion								Total Digestion									
	As	Co	Cu	Mo	Ni	Pb	U	V	Al_2O_3	Fe_2O_3	K_2O	MgO	P_2O_5	Li	W	Y	Ce	B
MFc	**Working Detection Limits from ICP-OES**																	
Lowest Value Sample	0.1	0.1	0.1	0.1	0.2	0.2	0.3	0.2	0.36	0.03	0	0.03	0.01	1	0.5	1	15	6
Number of Samples at Lowest Value	156	113	3	299	3	1	317	9	1	4	1	1	1	8	313	2	1	1
% of Population	46	33	0.9	87	0.9	0.3	92	2.6	0.29	1.17	0.3	0.29	0.29	2.3	91.3	0.6	0.3	0.3
Working Detection Limits from ICP-MS																		
Lowest Value Sample	0.1	0	0.1	0	0.1	0.2	0.1	0.1	0.48	0.04	0	0.03	0.01	1	0.1	0.1	18	10
Number of Samples at Lowest Value	1	3	1	1	1	1	1	15	1	28	1	1	2	14	1048	3	1	1
% of Population	0.1	0.3	0.1	0.1	0.1	0.1	0.1	1.4	0.09	2.64	0.1	0.09	0.19	0.1	98.9	0.3	0.1	0.1

Table 2: continued.

Leach Method	Partial Digestion								Total Digestion									
	As	Co	Cu	Mo	Ni	Pb	U	V	Al_2O_3	$Fe_2O_3(t)$	K_2O	MgO	P_2O_5	Li	W	Y	Ce	B
MFd	**Working Detection Limits from ICP-OES**								**Working Detection Limits from ICP-OES**									
Lowest Value Sample	0.08	0.05	0.54	0.02	0.4	0.33	0.24	0.2	0.6	0.03	0.02	0.08	0.01	1	0.1	0.4	16	34
Number of Samples at Lowest Value	1	9	1	5	1	1	1	1	1	5	2	1	2	2	67	1	1	1
% of Population	0.29	2.62	0.29	1.46	0.29	0.29	0.29	0.29	0.29	1.46	0.58	0.29	0.58	2.2	19.5	0.29	0.29	0.29
	Working Detection Limits from ICP-MS								**Working Detection Limits from ICP-MS**									
Lowest Value Sample	0.07	0.04	0.33	0.02	0.2	0.2	0.14	0.1	0.45	0.03	0.02	0.06	0.01	2	0.1	0.27	16	13
Number of Samples at Lowest Value	2	7	1	17	1	1	1	10	2	33	1	1	6	53	134	1	7	1
% of Population	0.58	2.04	0.29	4.96	0.29	0.29	0.29	2.92	0.58	9.62	0.29	0.29	1.75	24	39.1	0.29	2.04	0.29

Note: Total Fe expressed as $Fe_2O_3(t)$;

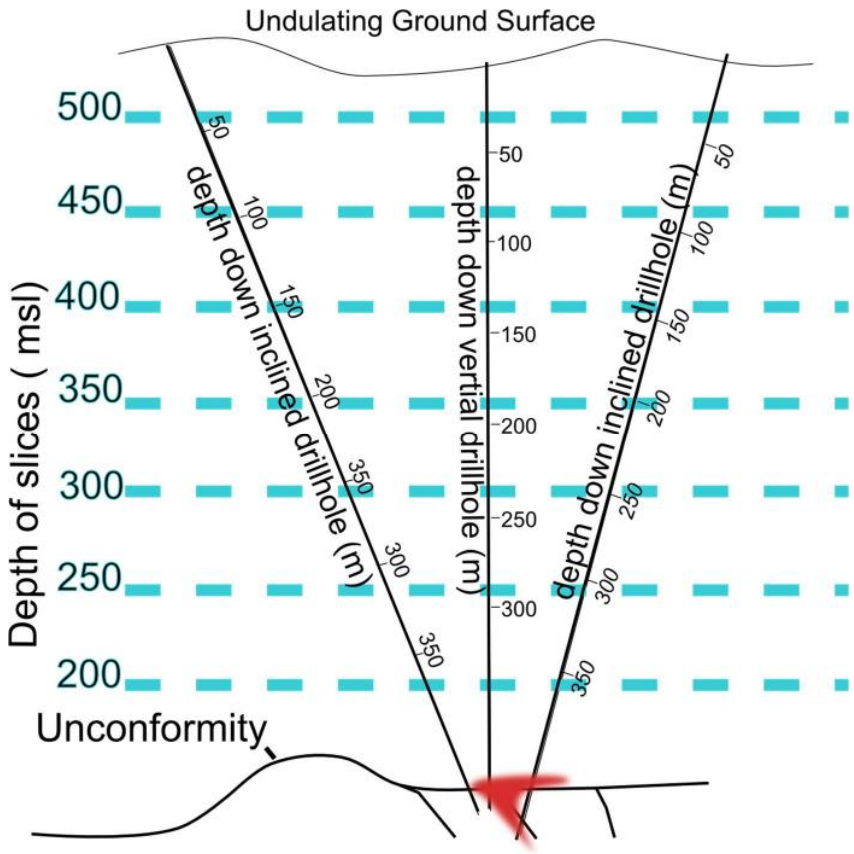

Figure 2: Schematic diagram illustrating organization of diamond drill holes (DDH) and the interpolated slices through the sandstone package. This method allows for inclined DDH on the undulating surface to be laterally compared at the same level as vertical DDH.

Interpolation and Construction of 3D Model

In order to account for inclination of diamond drill holes (DDH) and different elevations of the drill sites, a basic three-dimensional (3D) model was constructed to interpret the data along flat planes through the sandstone. Inclined DDH data were subjected to basic trigonometric functions, allowing the calculation of true depth and placement within a 3D framework, relative to its declination, azimuth, elevation and location (Figure 2).

True depth of each data point is presented relative to meters above mean sea level (msl). The unconformity varies from 94 msl to 195 msl, hence the interpolation of slices of the bulk rock geochemistry above 200 msl were chosen to discuss the compositions of sandstones. The number of data points used were as follows: 200 msl (n= 162), 250 msl (n= 137), 300 msl; (n=90), 350 msl; (n=95), 400 msl; (n=93), 450 msl; (n=90), 500 msl; (n=77). Since drilling was carried out to define an ore body along a linear trend (WS Shear fault), points are primarily focused along this axis.

Maps of the points and limits of interpolation for each slice are provided in Figure 3. Any values quoted in the text are directly from the whole rock lithogeochemistry and not from interpolated

values. The Inverse Distance Weighted (IDW) method was used to interpolate geochemical values. Although more commonly applied to soil data (Kane et al, 1982; Zhang et al, 2008; Grunsky 2010), it allows for visualization of the distribution of elements in a multidimensional space, making it suitable for this study.

Interpolation was performed using ESRI's ArcGIS 10.0 ArcMap software equipped with the Spatial Analysis toolbox. The DDH locations are spread along a 2.4km strike of the WS shear, but only span 200m across the shear structure and with an inconsistent distribution in a 3D space. As a result, the interpolation results are often significantly varied between individual dense points and resulted in the spatial analysis being performed with an IDW algorithm under a power of 2, attempting to mitigate any undue bias of the spatial arrangement of the data. By using IDW, an algorithm calculates the weighted mean of known values inside a moving spatial window that is calculated and assigned to the pixel in the centre, with all interpolated values between minimum and maximum observed values (Bartier and Keller, 1996). This is achieved by running an element-by-element interpolation inside of a defined polygon that surrounds the DDH locations. One barrier was used to maintain consistency through the interpolations. To minimize undue interpolation surrounding the data points, a rectangular barrier was drawn as close as possible to all points. Points which fell outside the barrier and resulted in unwarranted interpolation were excluded. The locations of the DDH and respective barriers are described in Figure 3.

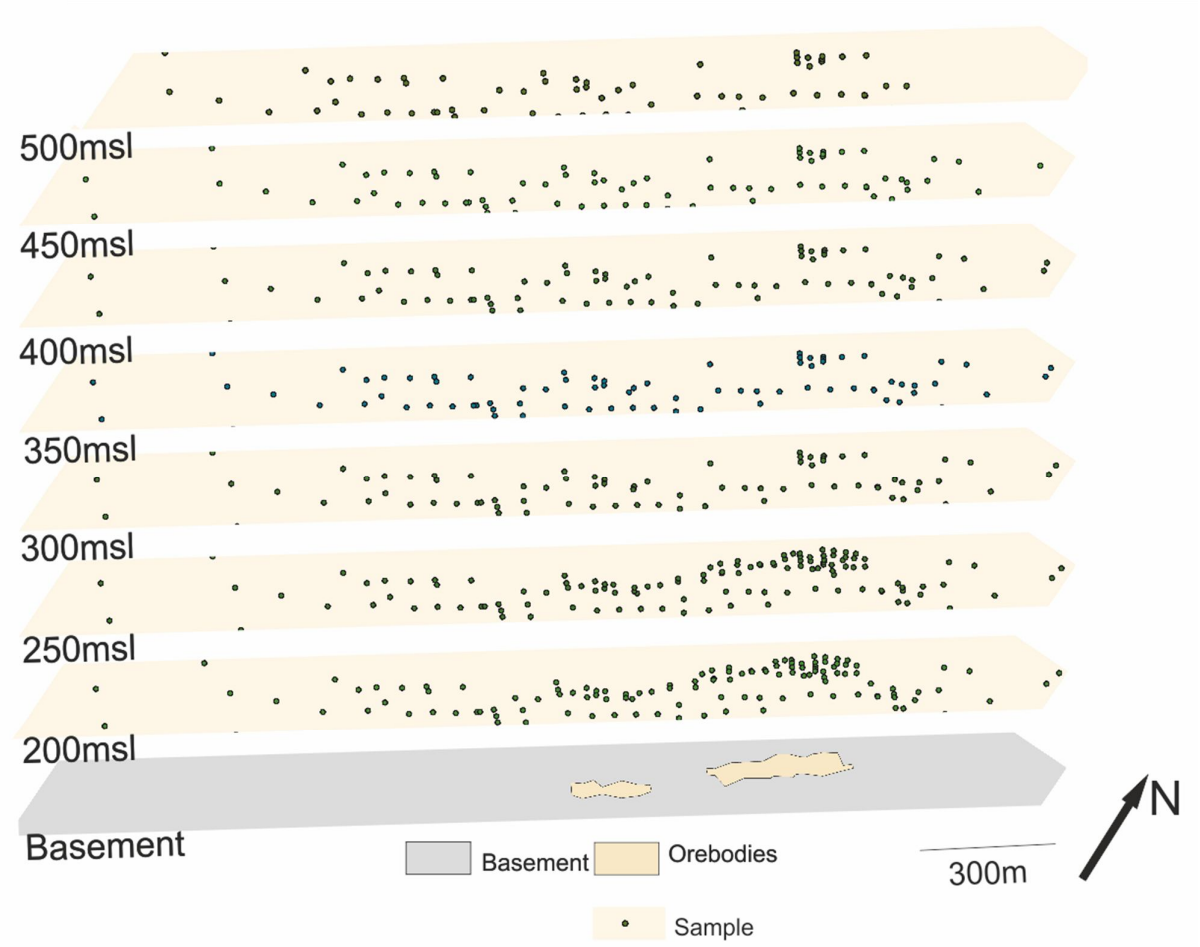

Figure 3: Distribution of points used for interpolation, the boundaries of interpolations and location of the orebodies .

Observations

Spatial Elemental Variation

Interpolations are displayed as pseudo 3D models produced with an isometric viewpoint in Corel Draw 16. This allows for a clear observation of elemental behaviour throughout the sequence. For reference, the locations of the A (northernmost) and B (southern) zone are shown.

Histograms and quantile-quantile (Q-Q) plots are used to compare the data to regional Athabasca Basin outcrop data from Card et al., (2011) and regional DDH data from Bosman and Card (2012). Q-Q plots are a graphical means of comparing a frequency distribution with respect to an expected frequency distribution, which is usually a normal distribution in unaltered systems. These plots are generated by calculating quantile values for the normal frequency distribution (value of the normal frequency distribution over the range of probability, 0.0–1.0) and then plotting these against the ordered observed data. If a frequency distribution is normally distributed, the resulting

plot will be a straight line. If the frequency distribution of the population is skewed or the population is polymodal, the plot will be curved or discontinuous (Grunsky, 2010). The comparative data used in this study also used the Sandstone Exploration Package from Saskatchewan Research Council Geoanalytical Labs.

Insufficient regional data from the Read Formation does not allow comparison with the data from Phoenix and therefore no analysis has been carried out. Read Formation values from Phoenix were simply excluded and have not been used in the statistical analysis of this study. All data obtained during this study are presented in Appendix A.

Uranium

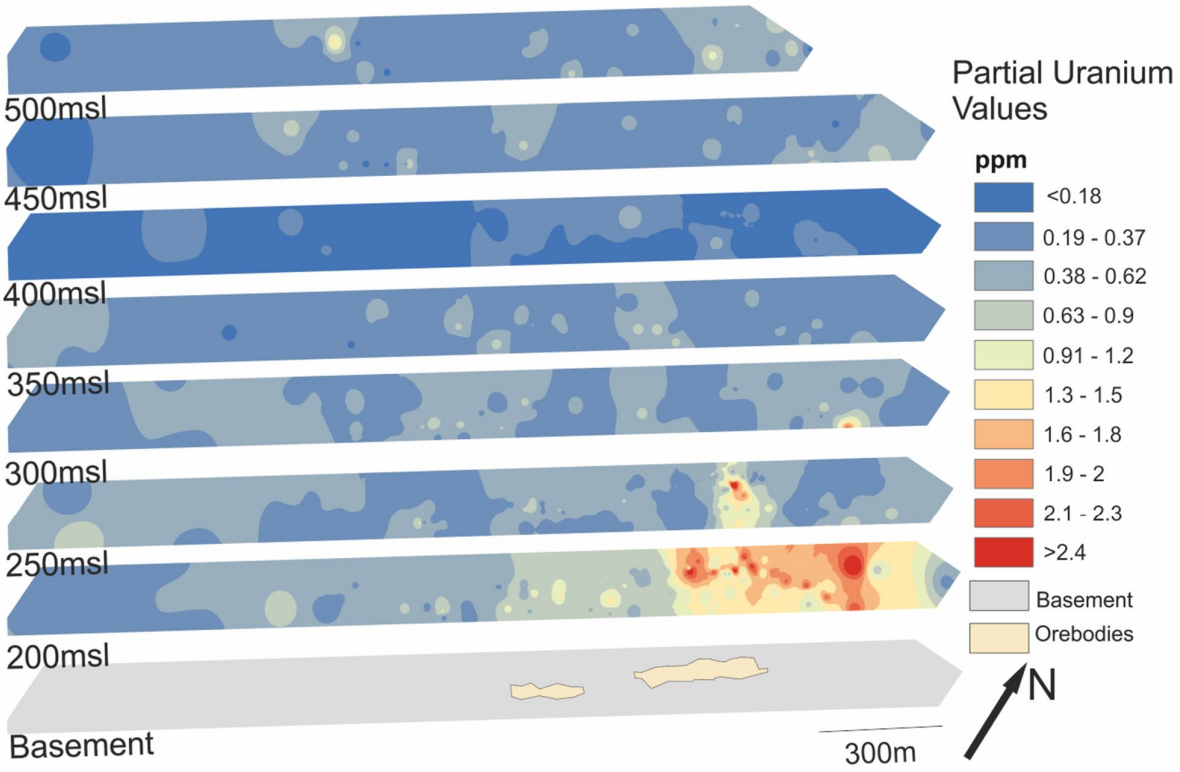

Figure 4: Partial leach uranium values from sandstone overlying the Phoenix deposit. Detection Limit of 0.01ppm U.

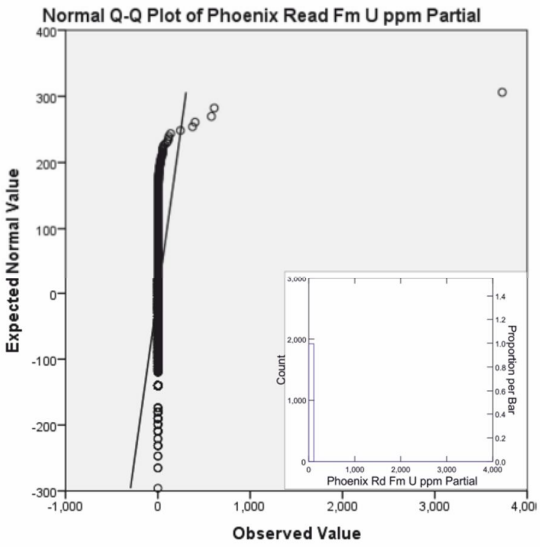
Normal Q-Q Plot of Phoenix Read Fm U ppm Partial
Expected Normal Value
Observed Value
Count
Proportion per Bar
Phoenix Rd Fm U ppm Partial

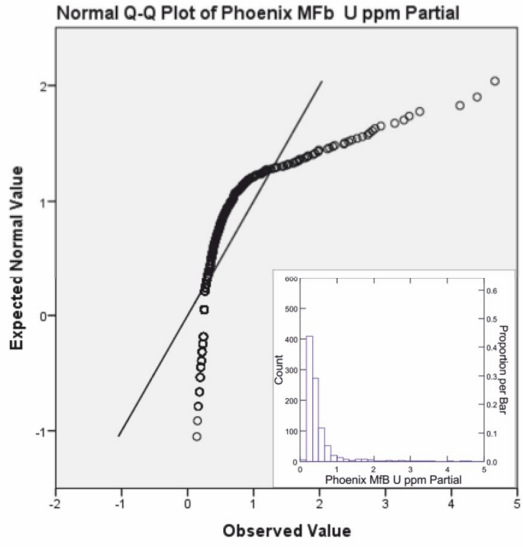
Normal Q-Q Plot of Phoenix MFb U ppm Partial
Expected Normal Value
Observed Value
Count
Proportion per Bar
Phoenix MfB U ppm Partial

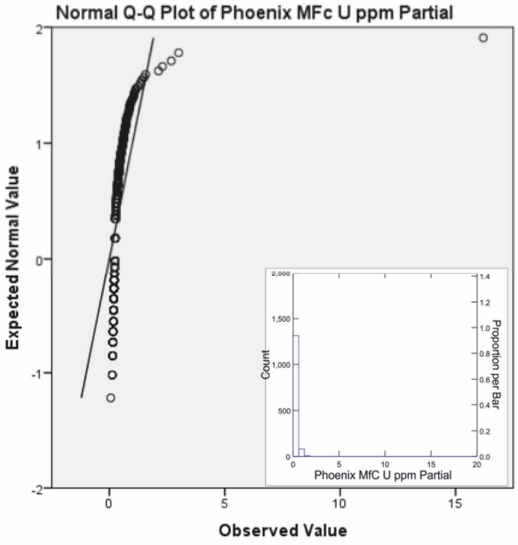
Normal Q-Q Plot of Phoenix MFc U ppm Partial
Expected Normal Value
Observed Value
Count
Proportion per Bar
Phoenix MfC U ppm Partial

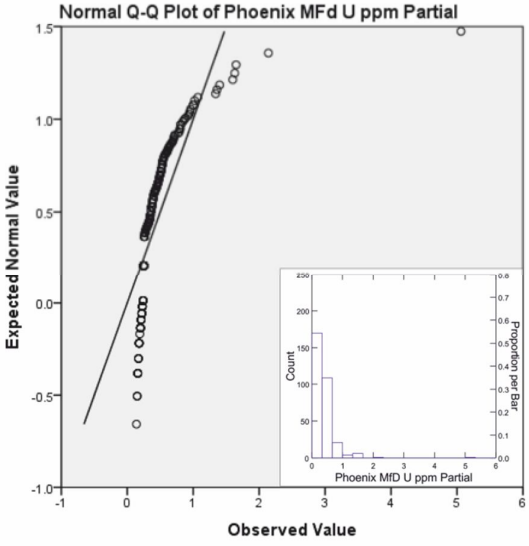
Normal Q-Q Plot of Phoenix MFd U ppm Partial
Expected Normal Value
Observed Value
Count
Proportion per Bar
Phoenix MfD U ppm Partial

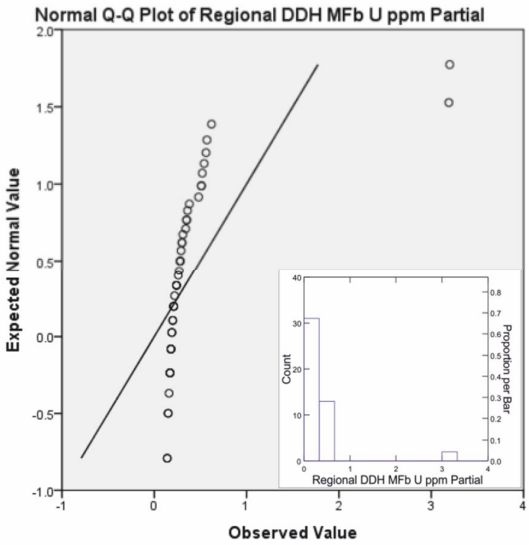
Normal Q-Q Plot of Regional DDH MFb U ppm Partial
Expected Normal Value
Observed Value
Count
Proportion per Bar
Regional DDH MFb U ppm Partial

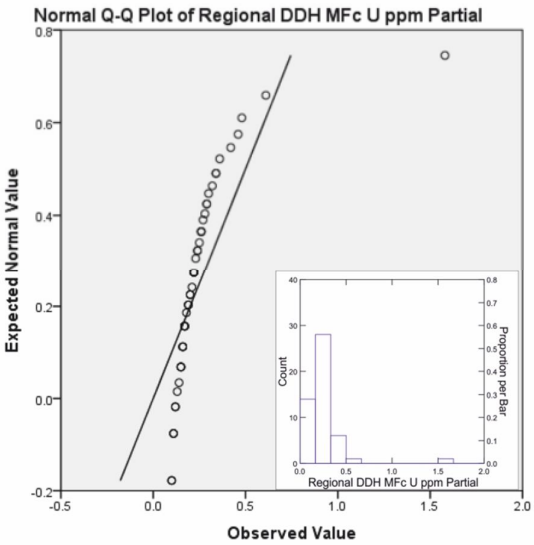
Normal Q-Q Plot of Regional DDH MFc U ppm Partial
Expected Normal Value
Observed Value
Count
Proportion per Bar
Regional DDH MFc U ppm Partial

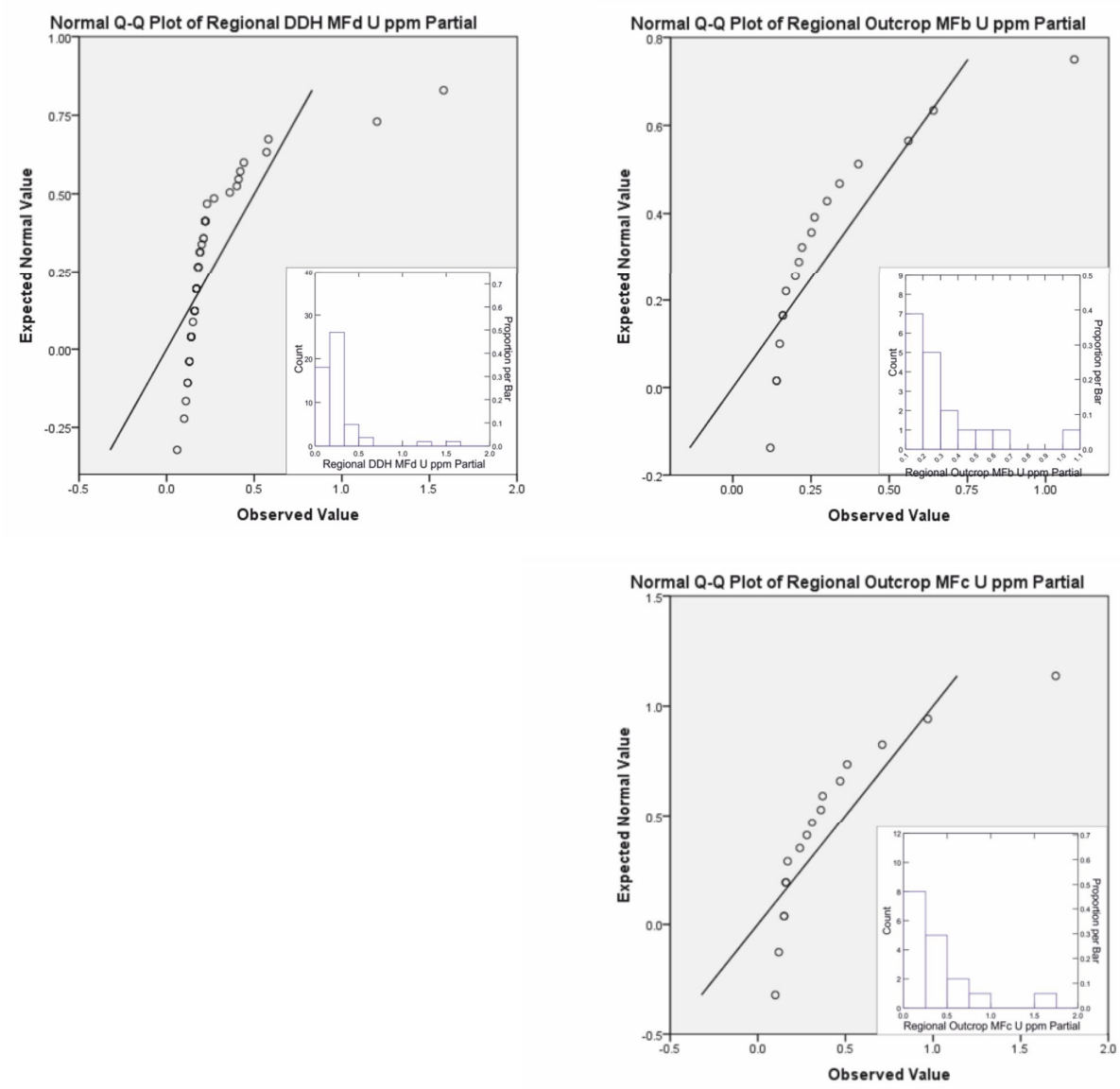

Figure 5: Q-Q and histogram (insets) plots of partial leach uranium values from regional outcrop, regional DDH and sandstones overlying the Phoenix deposit

Arsenic

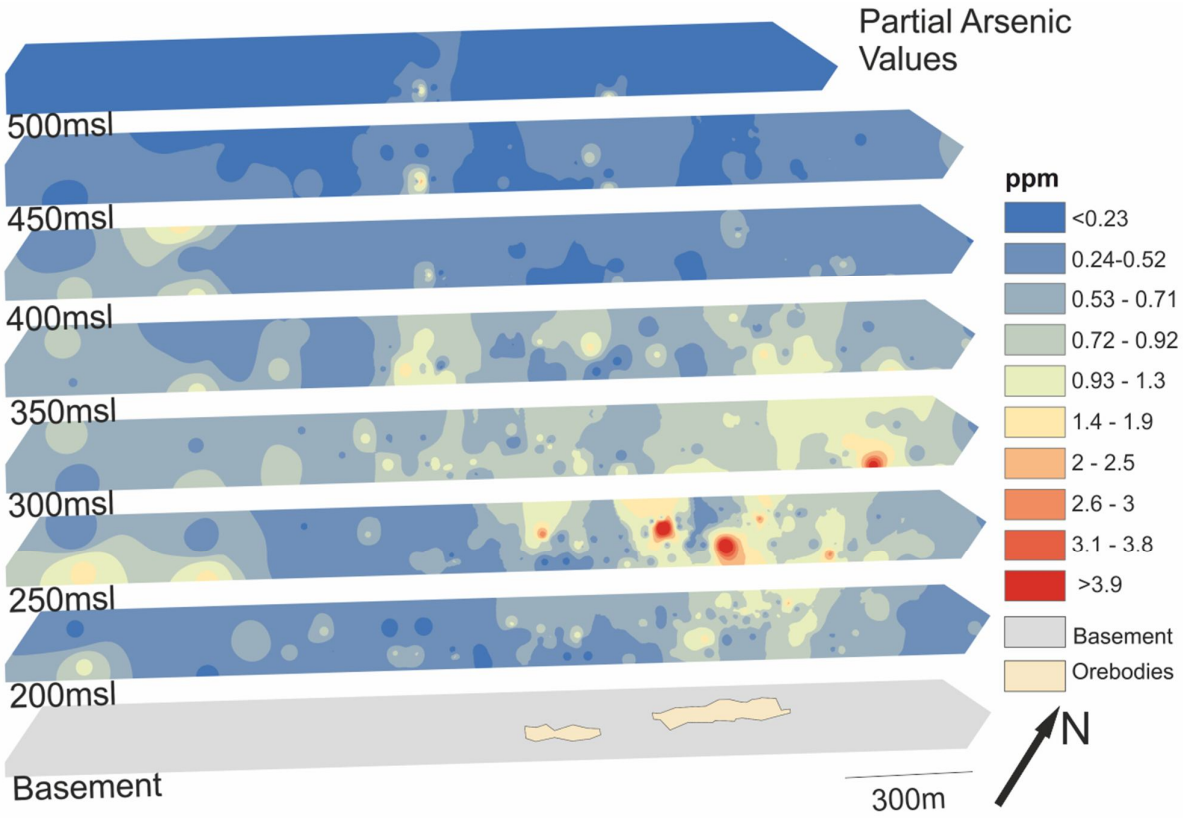

Figure 6: Partial leach As values from sandstone overlying the Phoenix deposit. Detection Limit of 0.01ppm As.

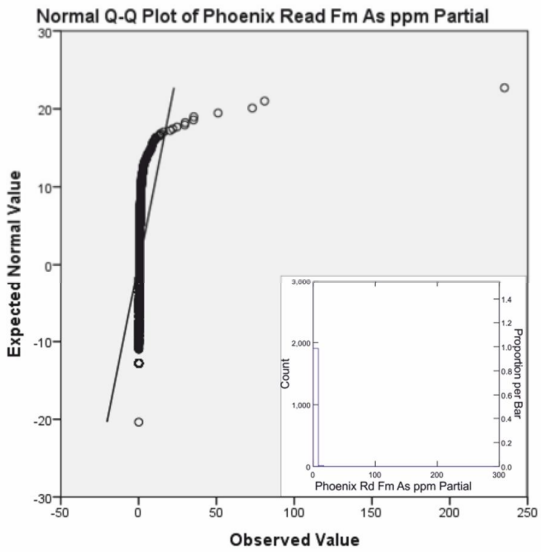
Normal Q-Q Plot of Phoenix Read Fm As ppm Partial
Expected Normal Value
Observed Value
Count
Proportion per Bar
Phoenix Rd Fm As ppm Partial

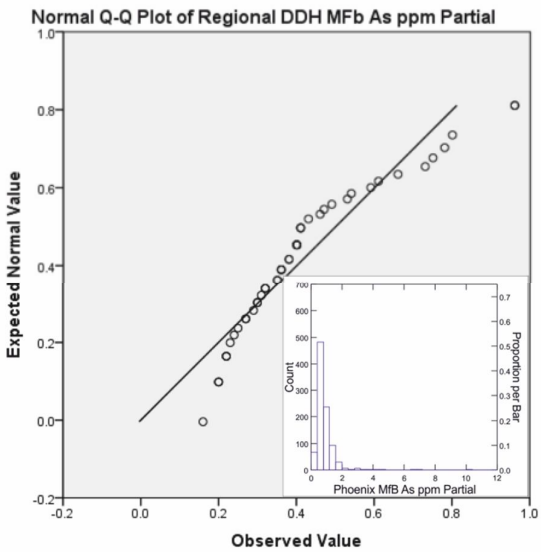
Normal Q-Q Plot of Regional DDH MFb As ppm Partial
Expected Normal Value
Observed Value
Count
Proportion per Bar
Phoenix MfB As ppm Partial

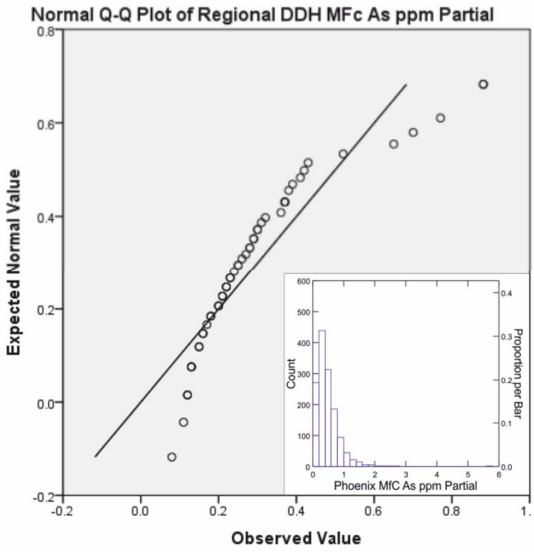
Normal Q-Q Plot of Regional DDH MFc As ppm Partial
Expected Normal Value
Observed Value
Count
Proportion per Bar
Phoenix MfC As ppm Partial

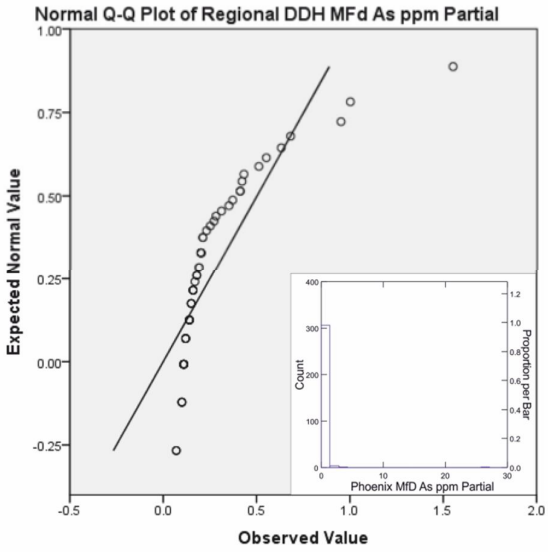
Normal Q-Q Plot of Regional DDH MFd As ppm Partial
Expected Normal Value
Observed Value
Count
Proportion per Bar
Phoenix MfD As ppm Partial

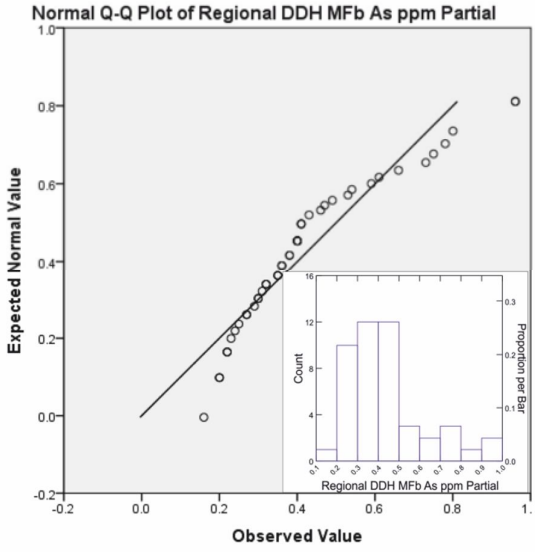
Normal Q-Q Plot of Regional DDH MFb As ppm Partial
Expected Normal Value
Observed Value
Count
Proportion per Bar
Regional DDH MFb As ppm Partial

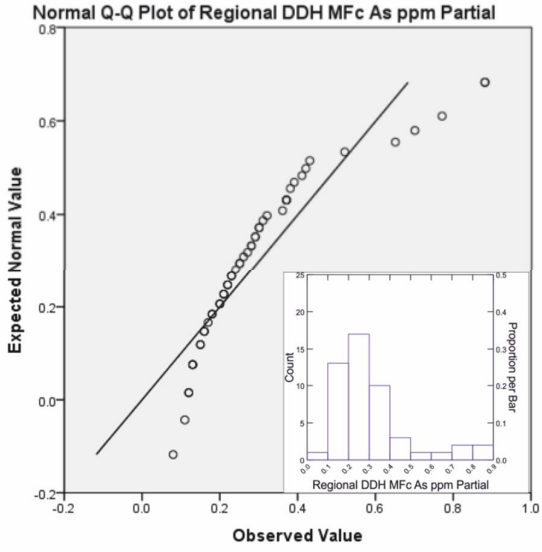
Normal Q-Q Plot of Regional DDH MFc As ppm Partial
Expected Normal Value
Observed Value
Count
Proportion per Bar
Regional DDH MFc As ppm Partial

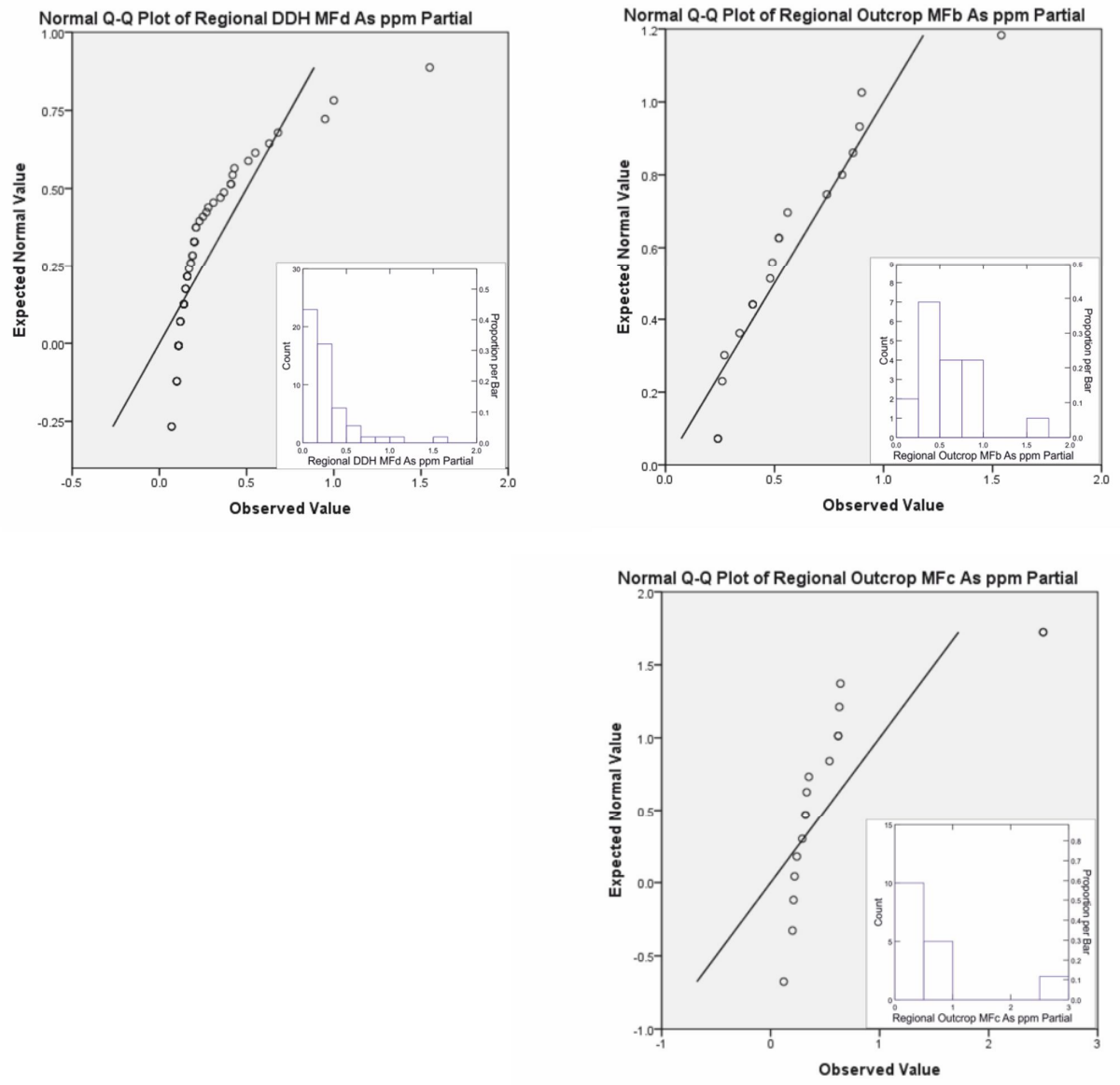

Figure 7: Q-Q and histogram (insets) plots of partial arsenic values from regional outcrop, regional DDH and sandstones overlying the Phoenix

Cobalt

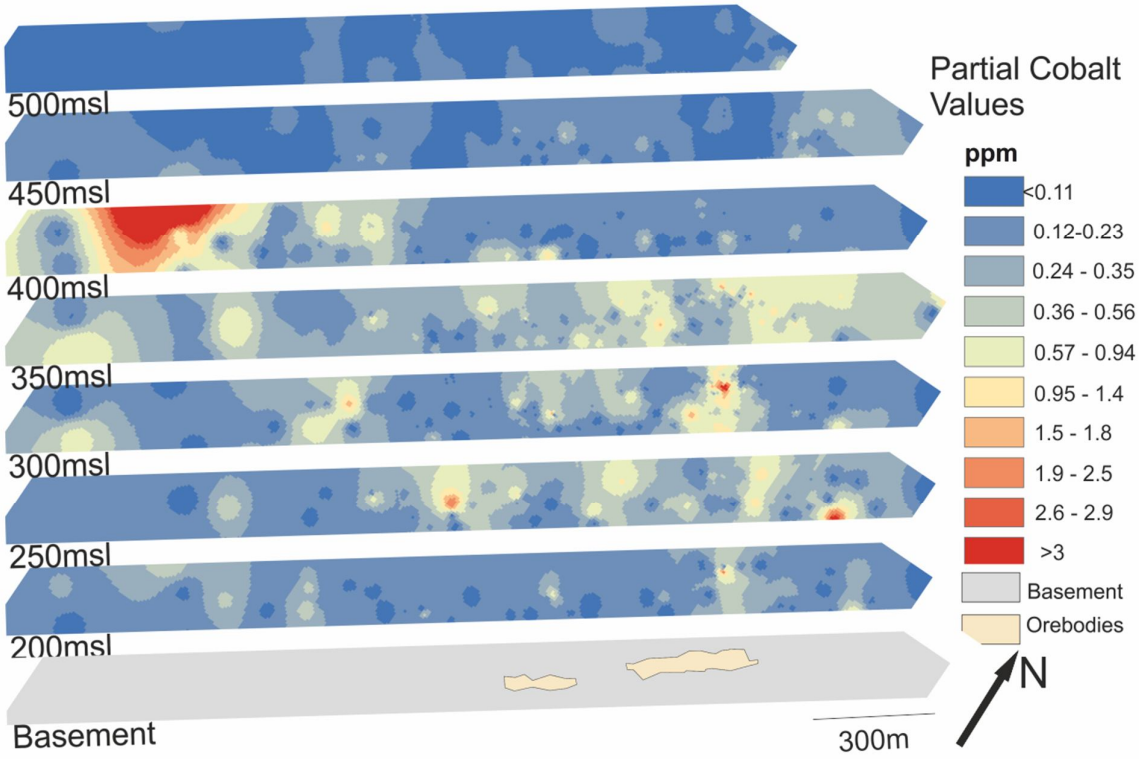

Figure 8: Partial leach cobalt values from sandstone overlying the Phoenix deposit. Detection Limit of 0.01ppm Co.

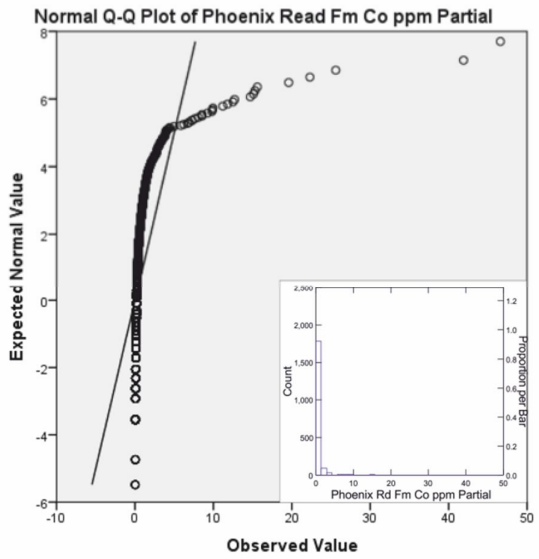
Normal Q-Q Plot of Phoenix Read Fm Co ppm Partial
Expected Normal Value
Observed Value
Count
Proportion per Bar
Phoenix Rd Fm Co ppm Partial

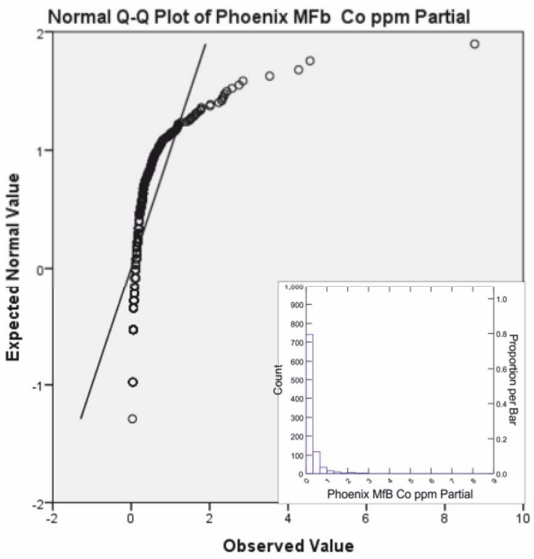
Normal Q-Q Plot of Phoenix MFb Co ppm Partial
Expected Normal Value
Observed Value
Count
Proportion per Bar
Phoenix MfB Co ppm Partial

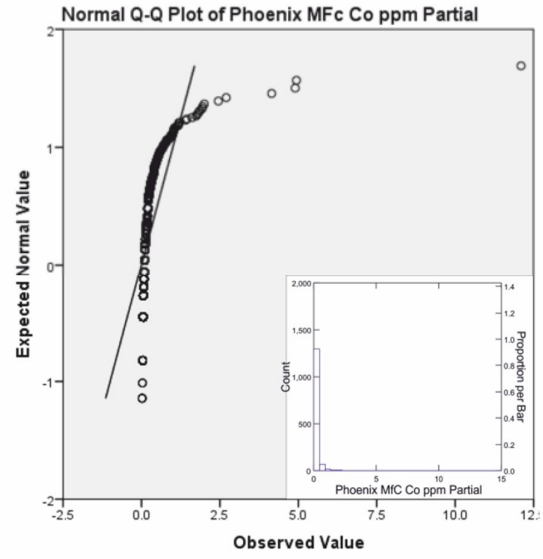
Normal Q-Q Plot of Phoenix MFc Co ppm Partial
Expected Normal Value
Observed Value
Count
Proportion per Bar
Phoenix MfC Co ppm Partial

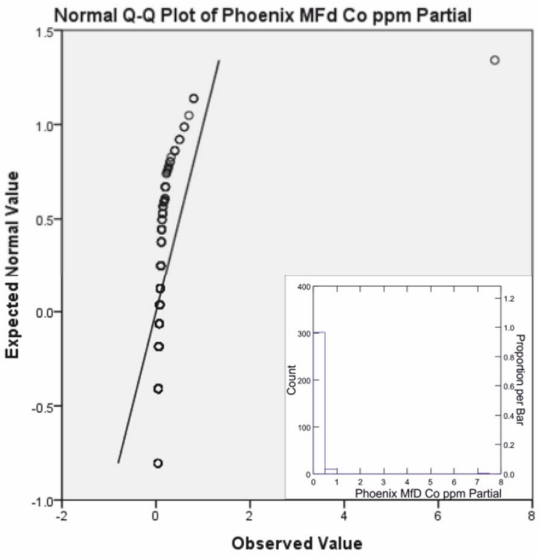
Normal Q-Q Plot of Phoenix MFd Co ppm Partial
Expected Normal Value
Observed Value
Count
Proportion per Bar
Phoenix MfD Co ppm Partial

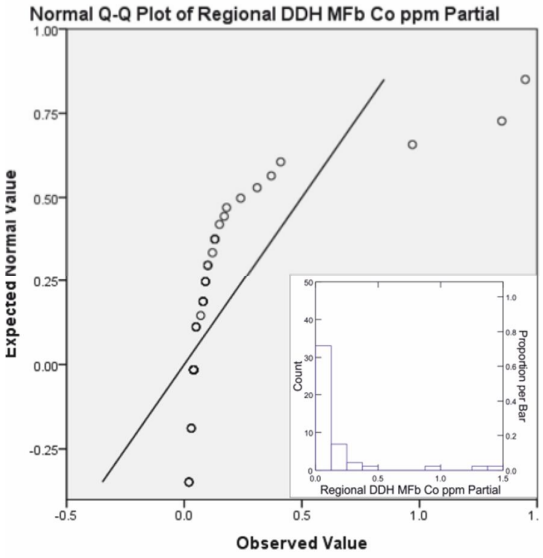
Normal Q-Q Plot of Regional DDH MFb Co ppm Partial
Expected Normal Value
Observed Value
Count
Proportion per Bar
Regional DDH MFb Co ppm Partial

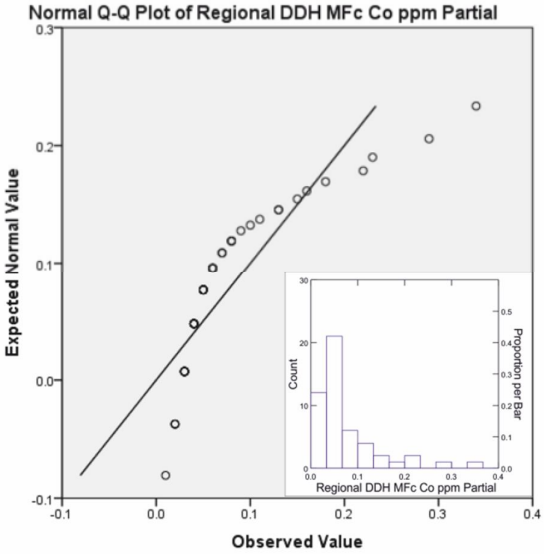
Normal Q-Q Plot of Regional DDH MFc Co ppm Partial
Expected Normal Value
Observed Value
Count
Proportion per Bar
Regional DDH MFc Co ppm Partial

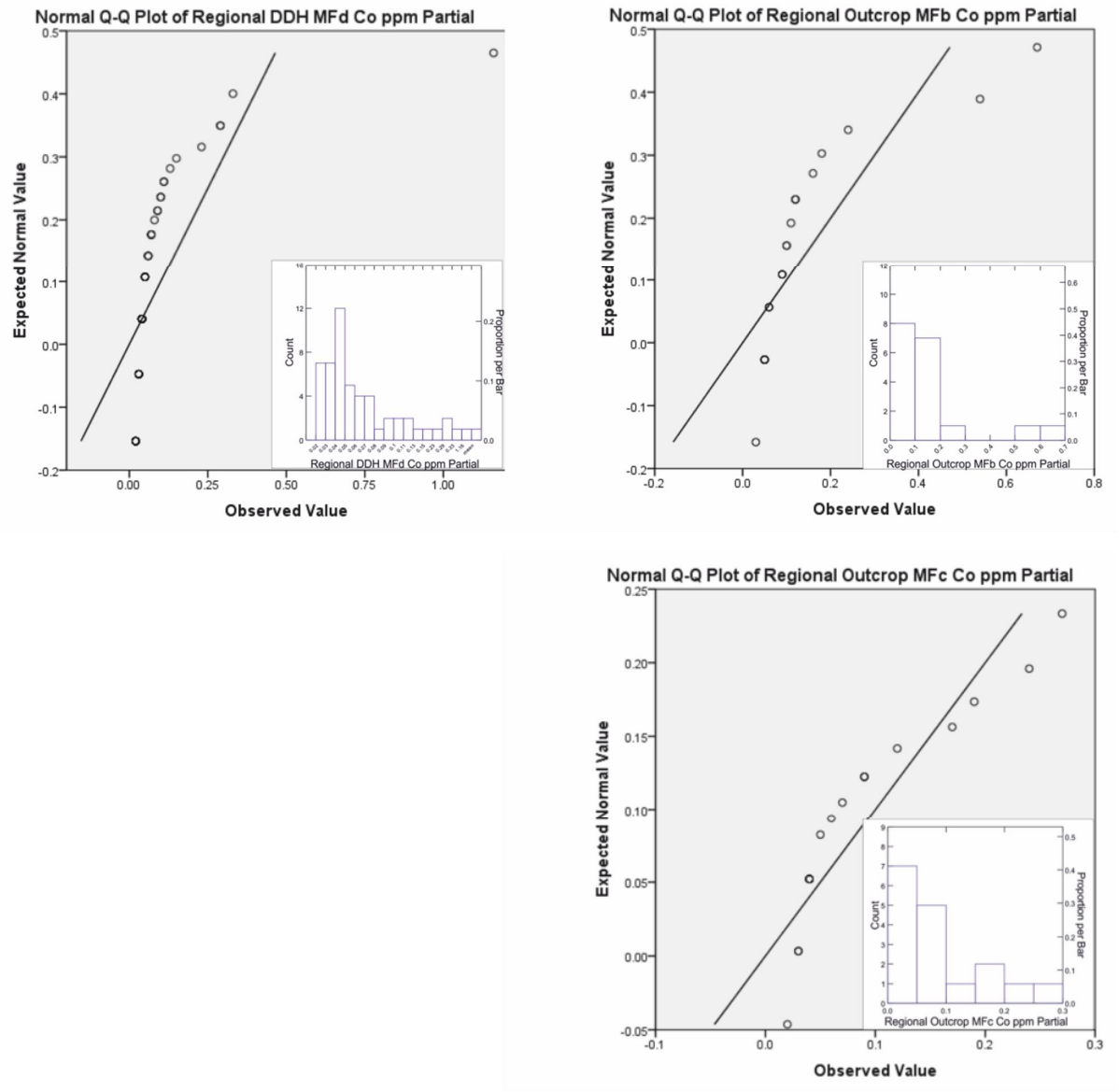

Figure 9: Q-Q and histogram (insets) plots of partial leach cobalt values from regional outcrop, regional DDH and sandstones overlying the Phoenix deposit.

Copper

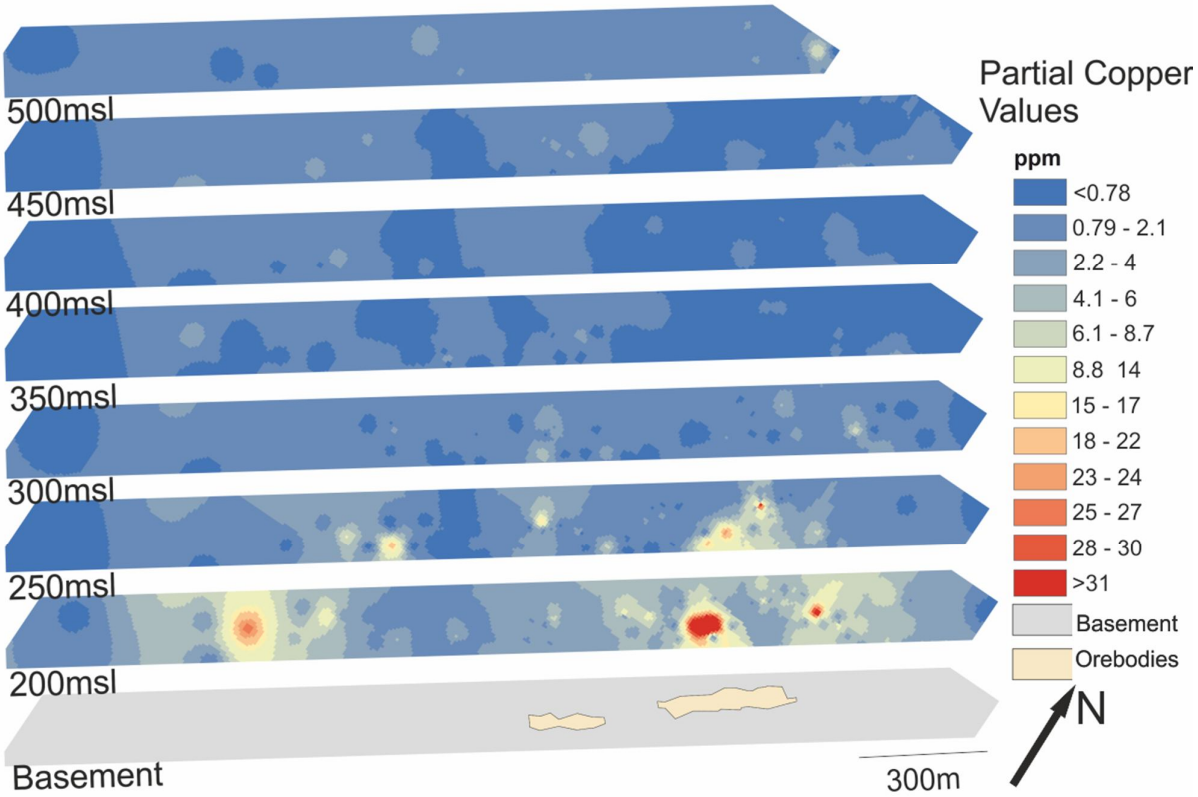

Figure 10: Partial leach copper values from sandstone overlying the Phoenix deposit. Detection Limit of 0.01ppm Cu.

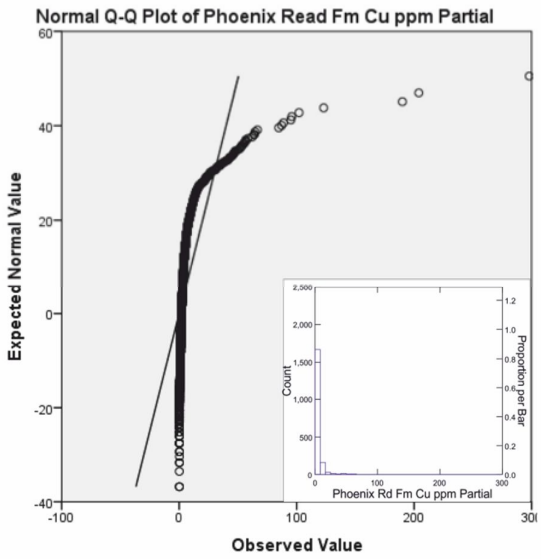
Normal Q-Q Plot of Phoenix Read Fm Cu ppm Partial
Expected Normal Value
Observed Value
Count
Proportion per Bar
Phoenix Rd Fm Cu ppm Partial

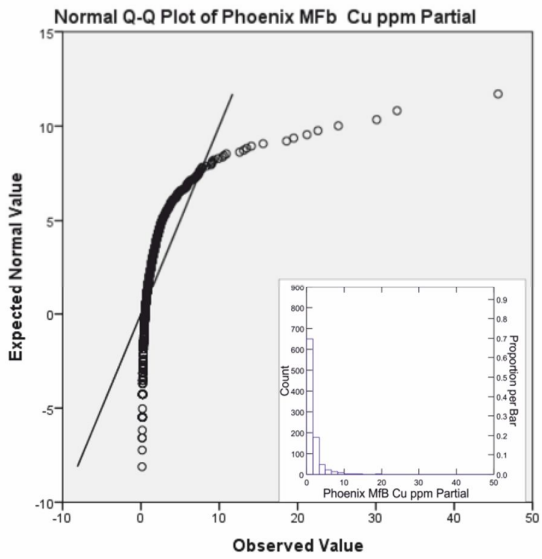
Normal Q-Q Plot of Phoenix MFb Cu ppm Partial
Expected Normal Value
Observed Value
Count
Proportion per Bar
Phoenix MfB Cu ppm Partial

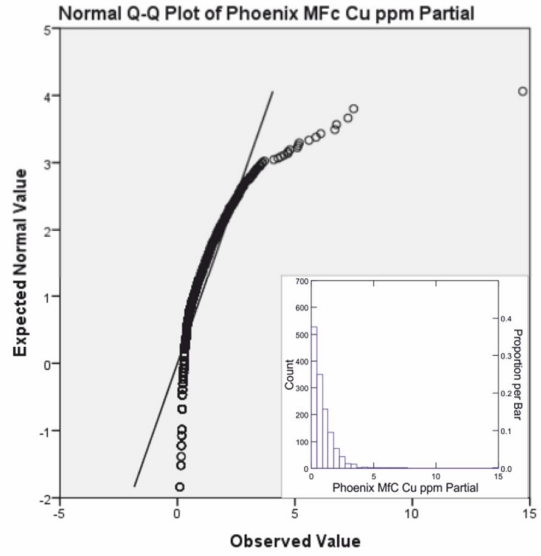
Normal Q-Q Plot of Phoenix MFc Cu ppm Partial
Expected Normal Value
Observed Value
Count
Proportion per Bar
Phoenix MfC Cu ppm Partial

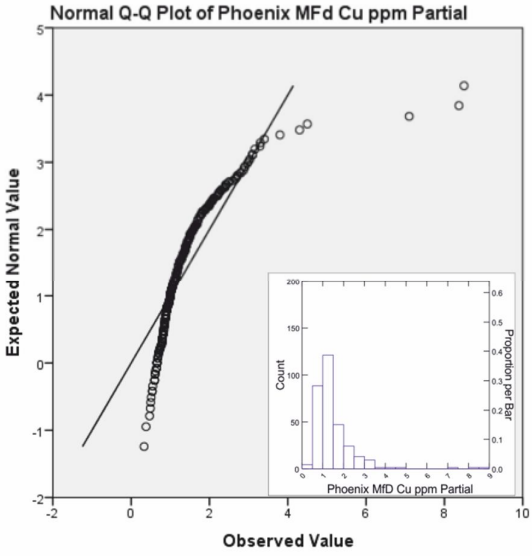
Normal Q-Q Plot of Phoenix MFd Cu ppm Partial
Expected Normal Value
Observed Value
Count
Proportion per Bar
Phoenix MfD Cu ppm Partial

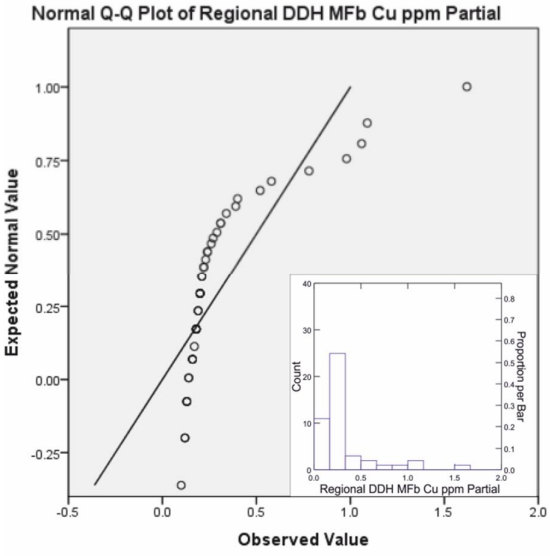
Normal Q-Q Plot of Regional DDH MFb Cu ppm Partial
Expected Normal Value
Observed Value
Count
Proportion per Bar
Regional DDH MFb Cu ppm Partial

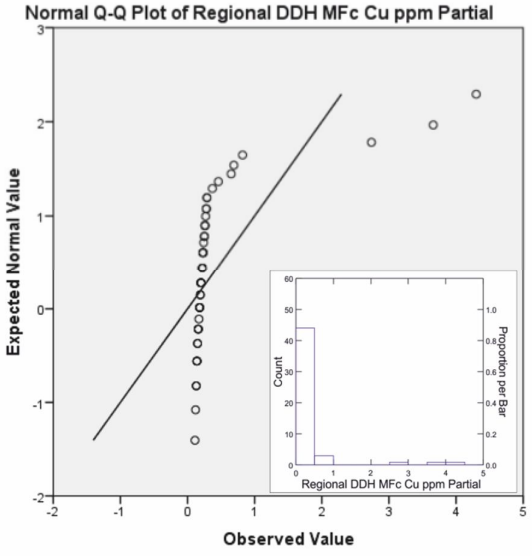
Normal Q-Q Plot of Regional DDH MFc Cu ppm Partial
Expected Normal Value
Observed Value
Count
Proportion per Bar
Regional DDH MFc Cu ppm Partial

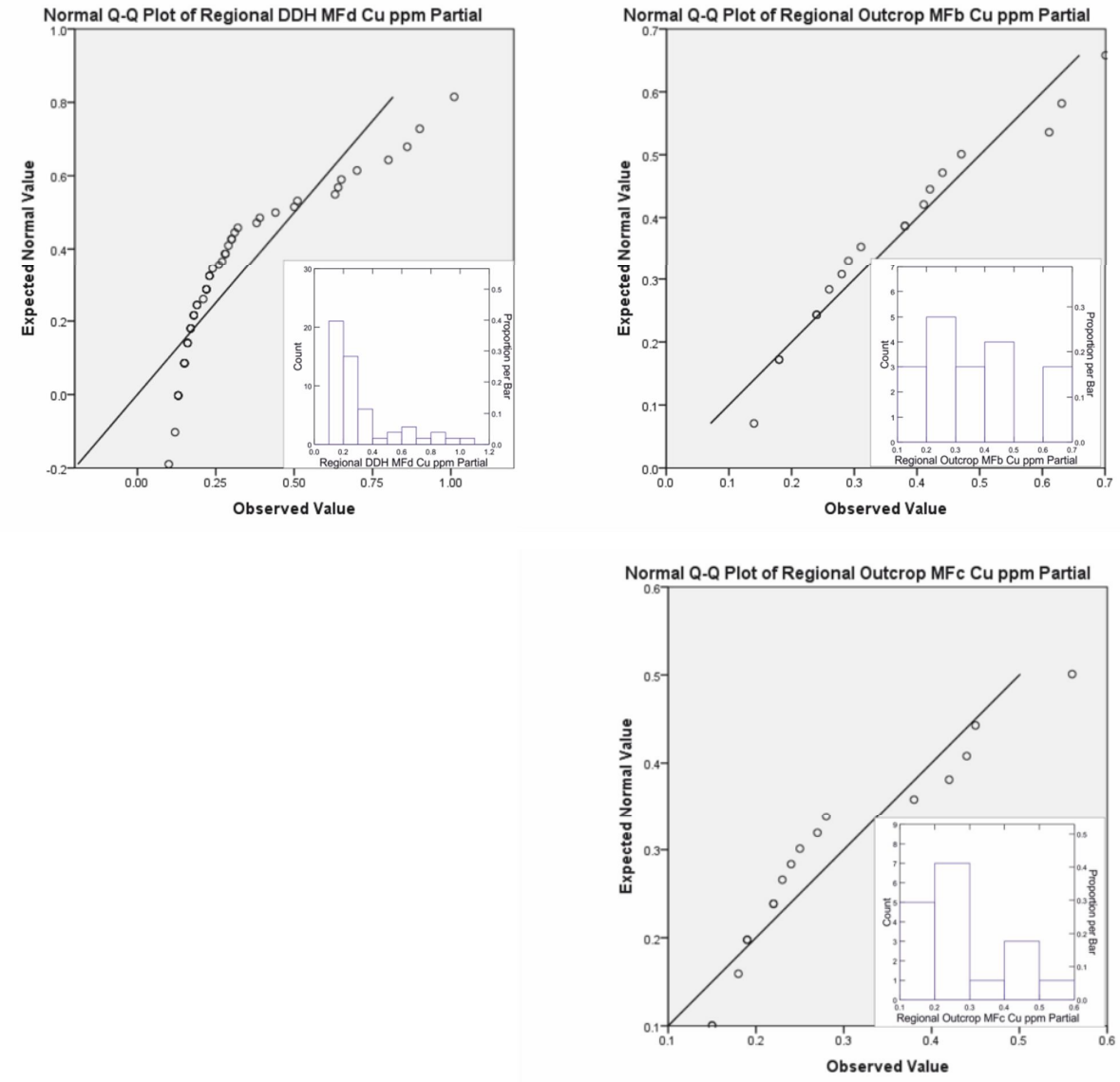

Figure 11: Q-Q and histogram (insets) plots of partial leach copper values from regional outcrop, regional DDH and sandstones overlying the Phoenix deposit.

Molybdenum

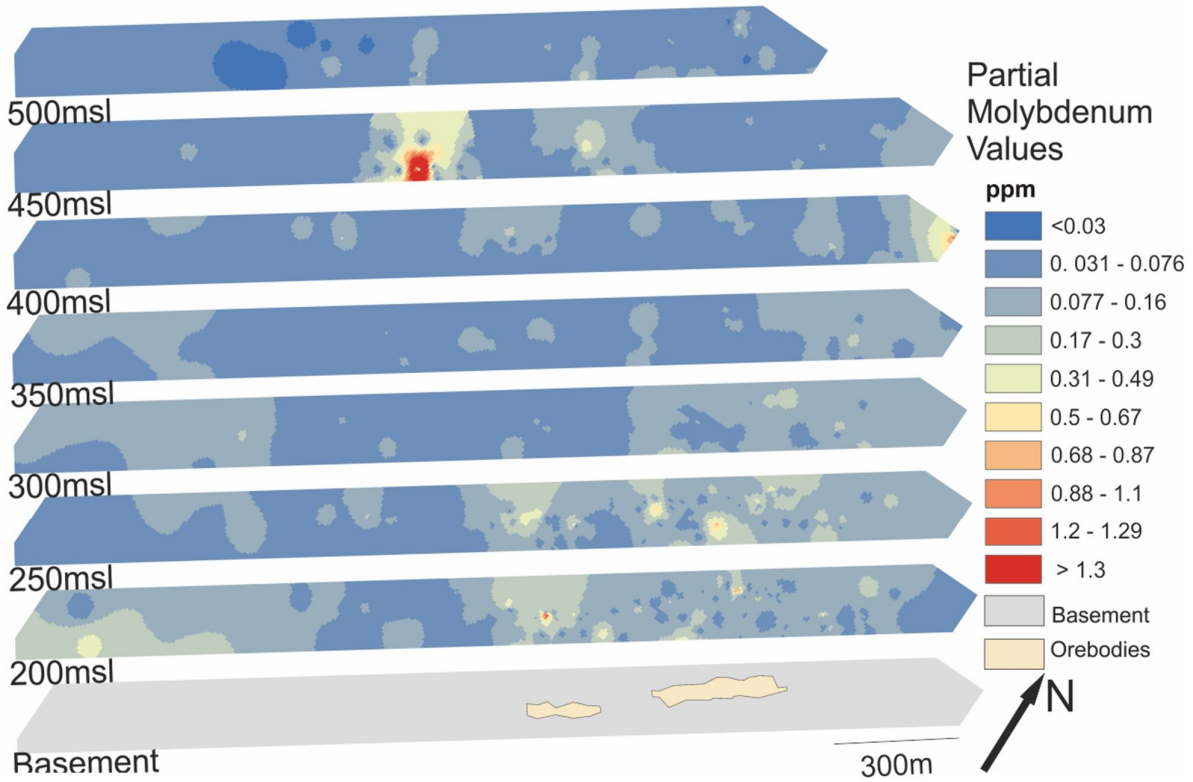

Figure 12: Partial leach molybdenum values from sandstone overlying the Phoenix deposit. Detection Limit of 0.01ppm Mo

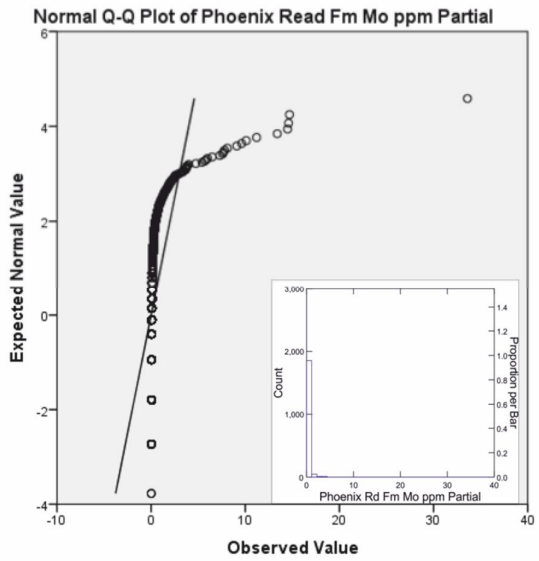
Normal Q-Q Plot of Phoenix Read Fm Mo ppm Partial
Expected Normal Value
Observed Value
Count
Proportion per Bar
Phoenix Rd Fm Mo ppm Partial

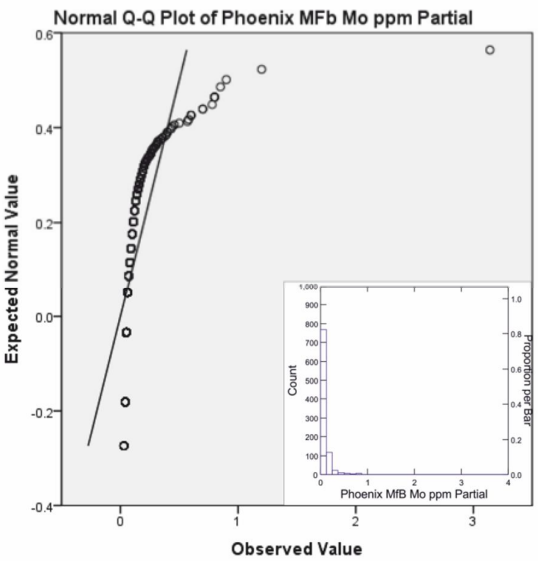
Normal Q-Q Plot of Phoenix MFb Mo ppm Partial
Expected Normal Value
Observed Value
Count
Proportion per Bar
Phoenix MfB Mo ppm Partial

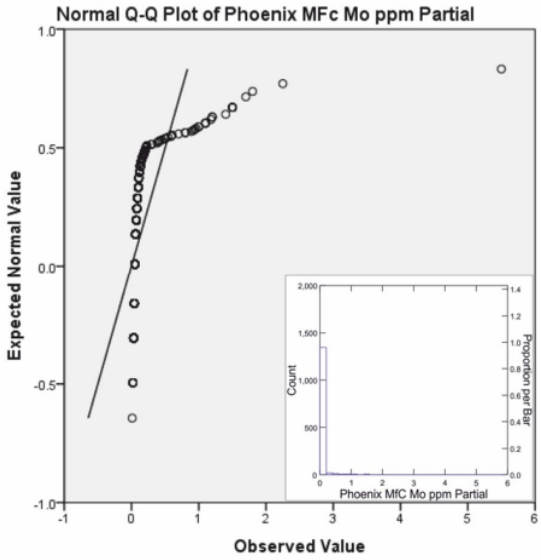
Normal Q-Q Plot of Phoenix MFc Mo ppm Partial
Expected Normal Value
Observed Value
Count
Proportion per Bar
Phoenix MfC Mo ppm Partial

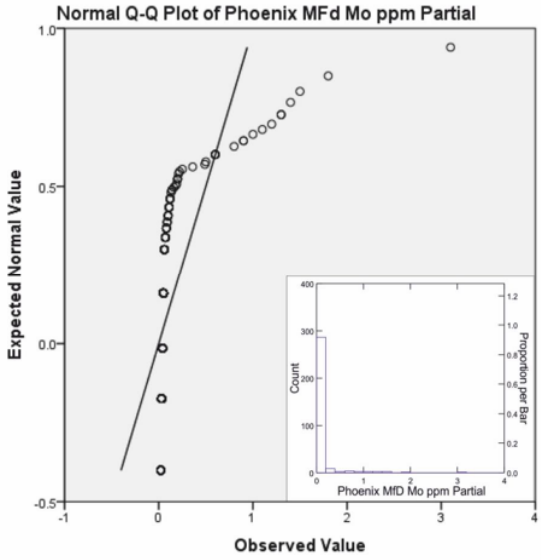
Normal Q-Q Plot of Phoenix MFd Mo ppm Partial
Expected Normal Value
Observed Value
Count
Proportion per Bar
Phoenix MfD Mo ppm Partial

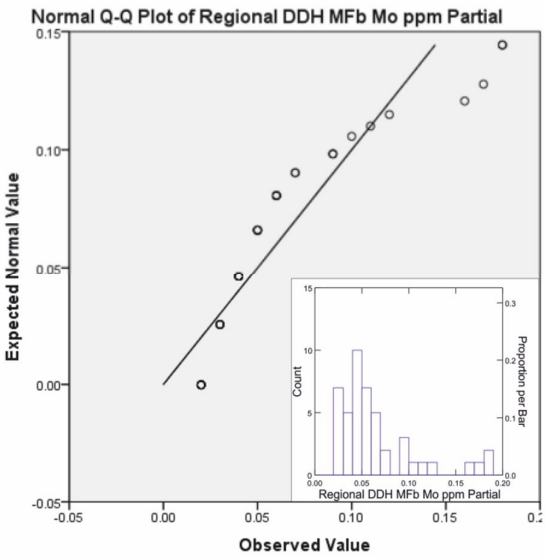
Normal Q-Q Plot of Regional DDH MFb Mo ppm Partial
Expected Normal Value
Observed Value
Count
Proportion per Bar
Regional DDH MFb Mo ppm Partial

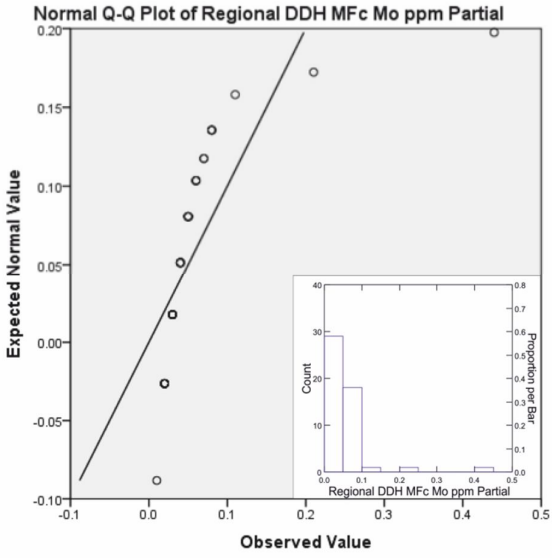
Normal Q-Q Plot of Regional DDH MFc Mo ppm Partial
Expected Normal Value
Observed Value
Count
Proportion per Bar
Regional DDH MFc Mo ppm Partial

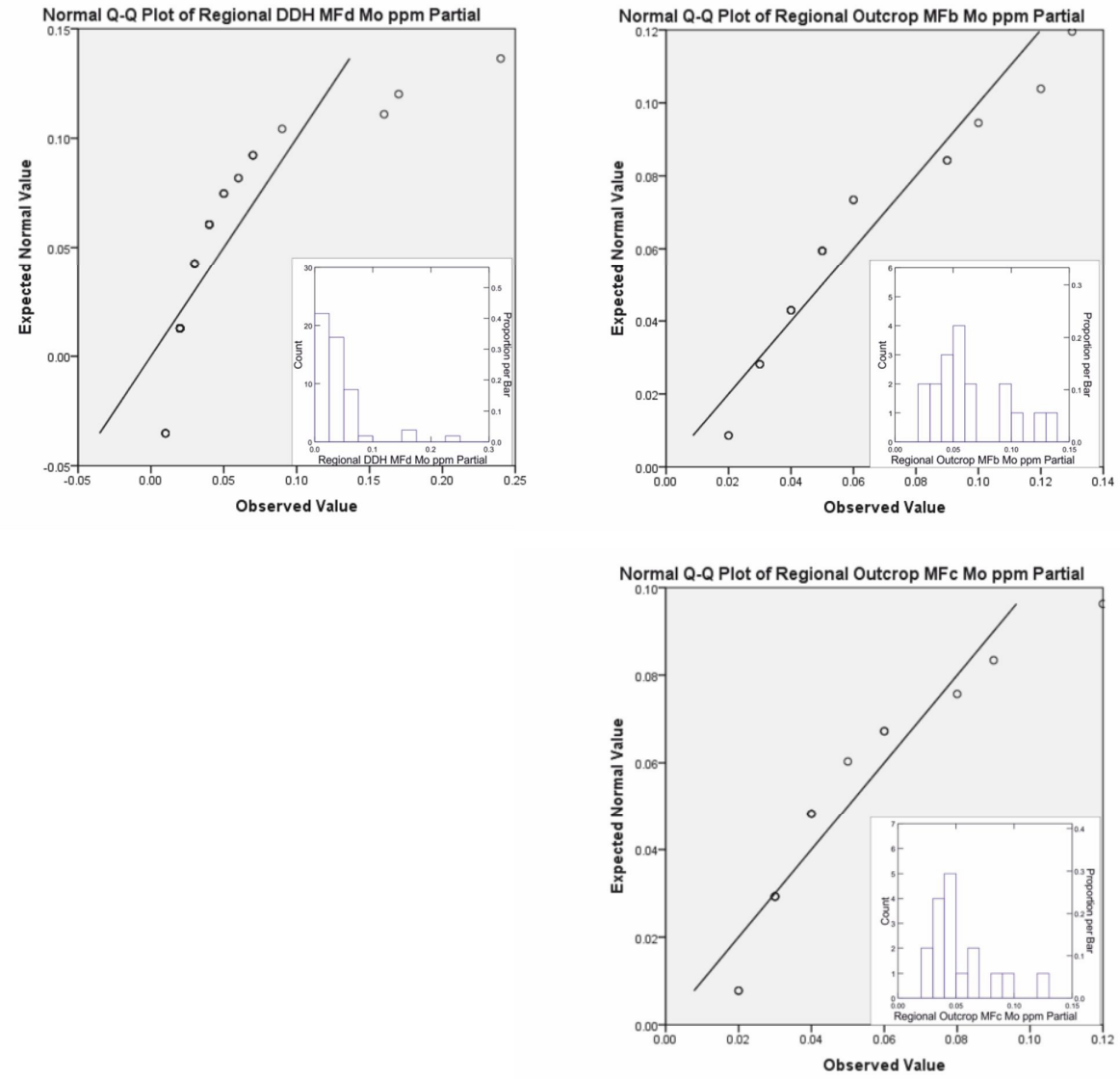

Figure 13: Q-Q and histogram (insets) plots of partial leach molybdenum values from regional outcrop, regional DDH and sandstones overlying the Phoenix deposit.

Nickel

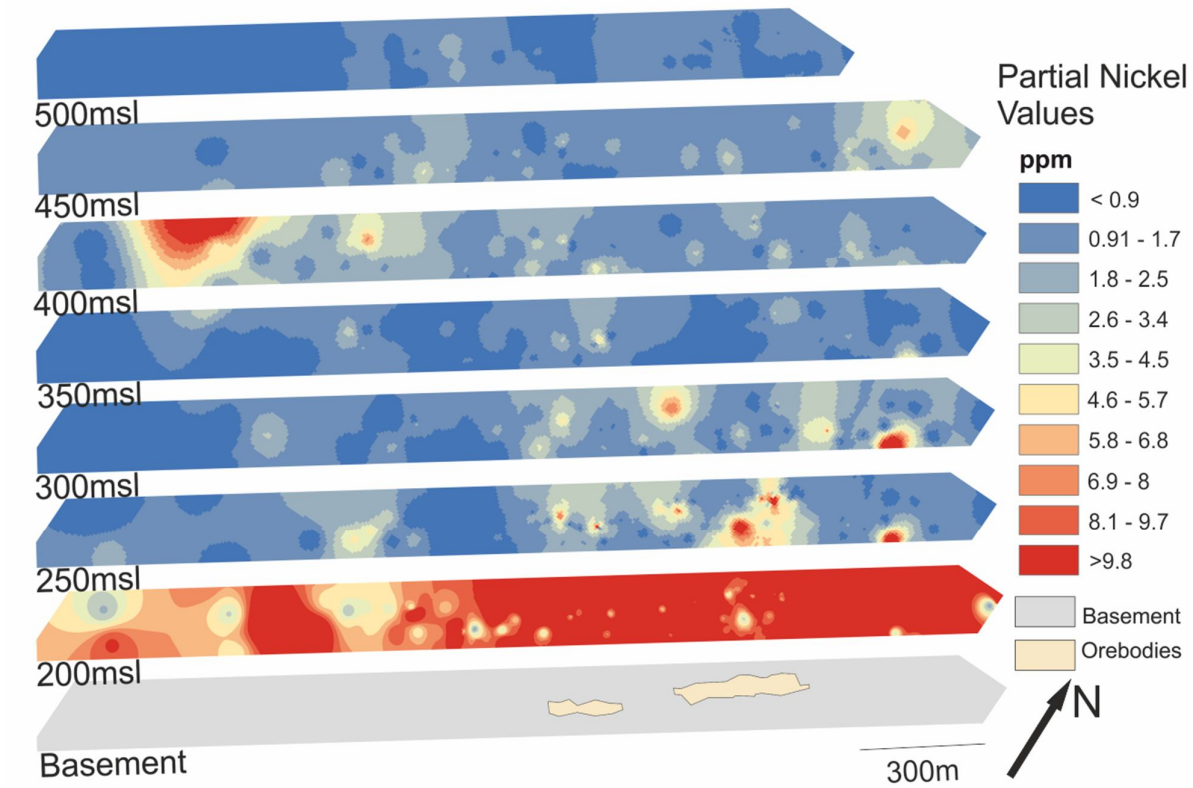

Figure 14: Partial leach nickel values from sandstone overlying the Phoenix deposit. Detection Limit of 0.01ppm Ni.

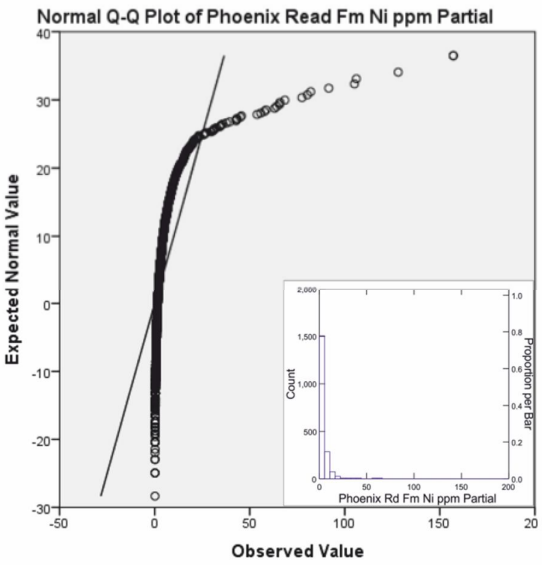
Normal Q-Q Plot of Phoenix Read Fm Ni ppm Partial
Expected Normal Value
Observed Value
Phoenix Rd Fm Ni ppm Partial
Count
Proportion per Bar

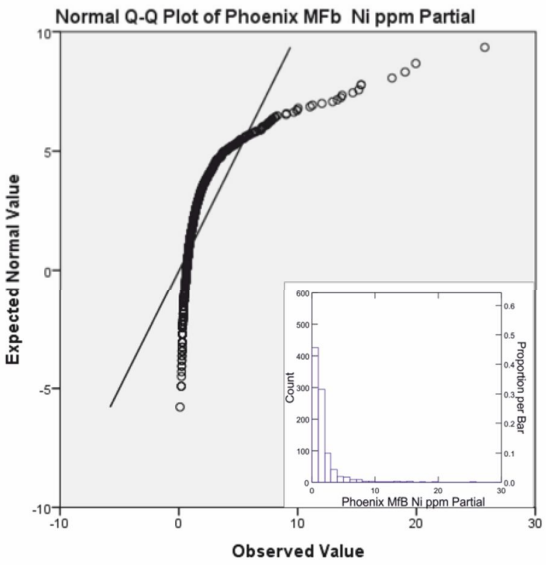
Normal Q-Q Plot of Phoenix MFb Ni ppm Partial
Expected Normal Value
Observed Value
Phoenix MfB Ni ppm Partial
Count
Proportion per Bar

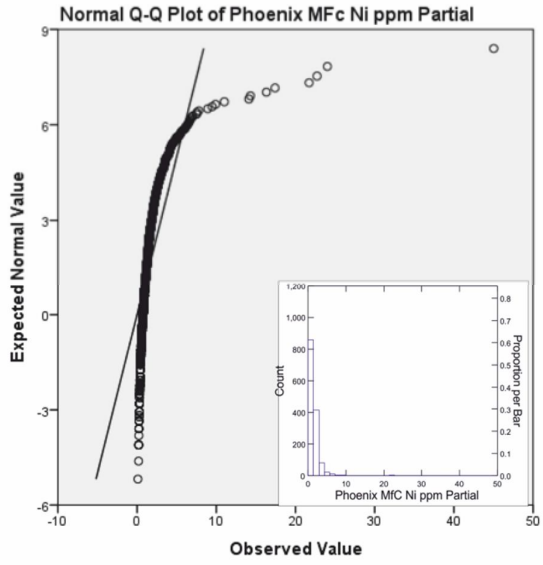
Normal Q-Q Plot of Phoenix MFc Ni ppm Partial
Expected Normal Value
Observed Value
Phoenix MfC Ni ppm Partial
Count
Proportion per Bar

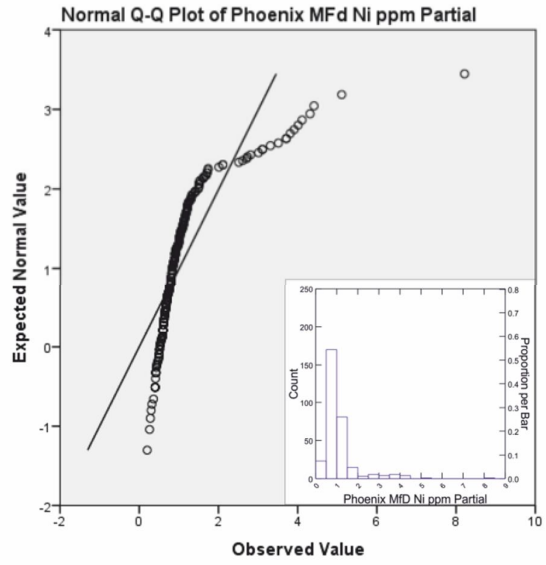
Normal Q-Q Plot of Phoenix MFd Ni ppm Partial
Expected Normal Value
Observed Value
Phoenix MfD Ni ppm Partial
Count
Proportion per Bar

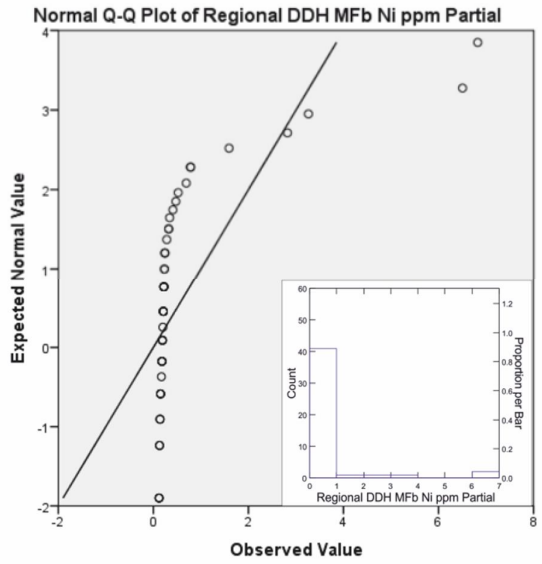
Normal Q-Q Plot of Regional DDH MFb Ni ppm Partial
Expected Normal Value
Observed Value
Regional DDH MFb Ni ppm Partial
Count
Proportion per Bar

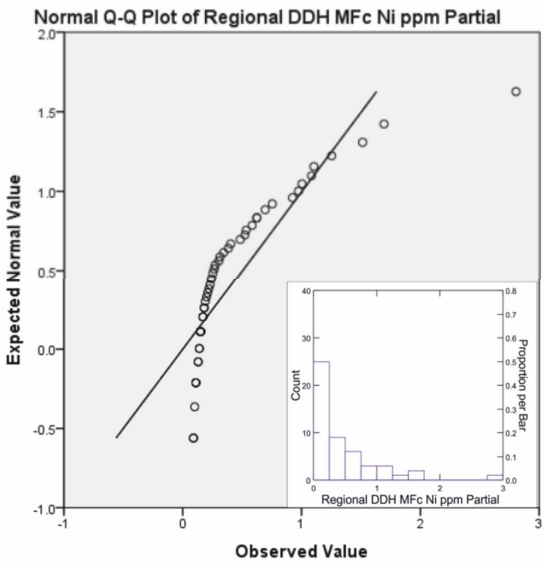
Normal Q-Q Plot of Regional DDH MFc Ni ppm Partial
Expected Normal Value
Observed Value
Regional DDH MFc Ni ppm Partial
Count
Proportion per Bar

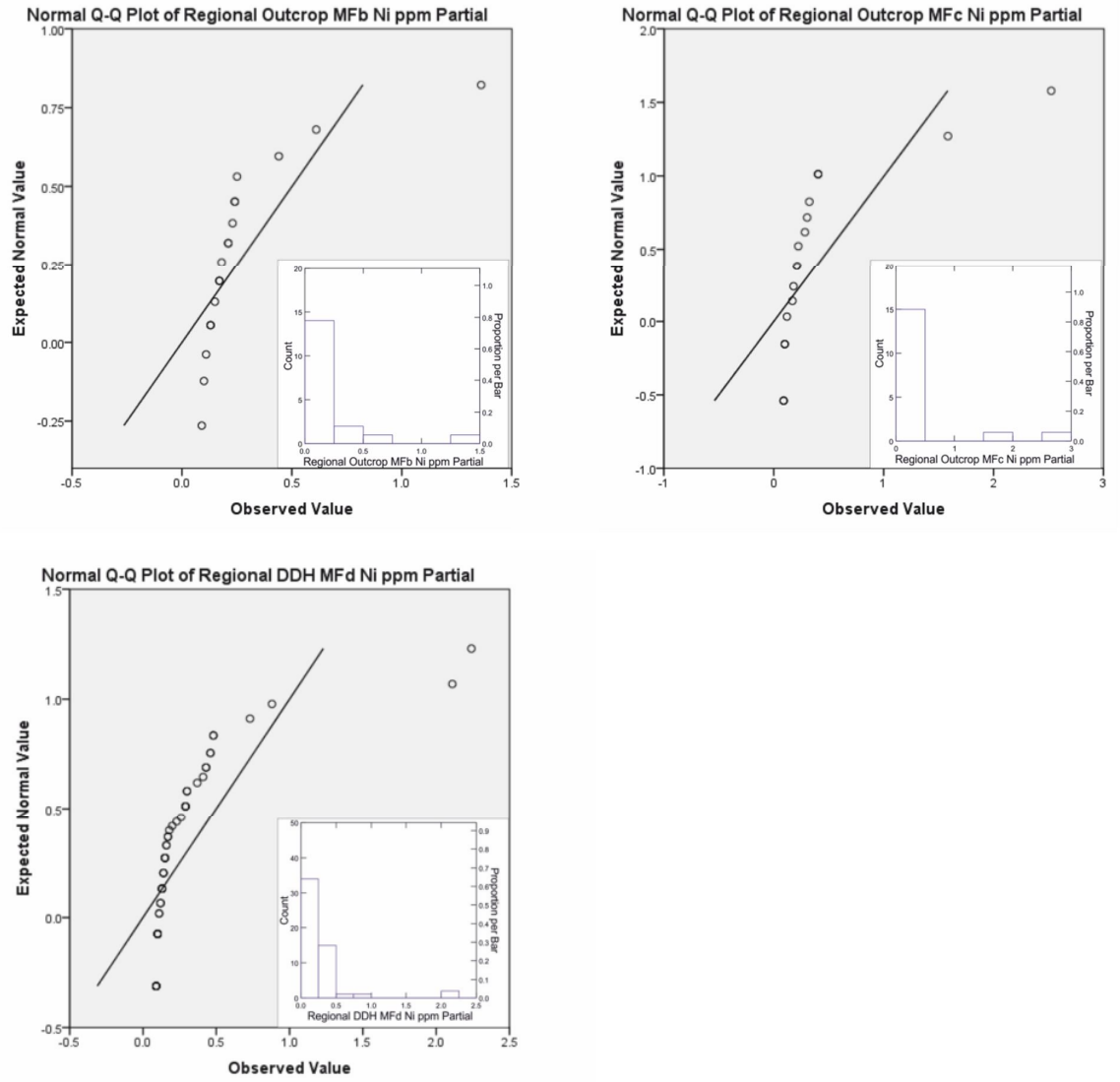

Figure 15: Q-Q and histogram (insets) plots of partial leach nickel values from regional outcrop, regional DDH and sandstones overlying the Phoenix deposit.

Vanadium

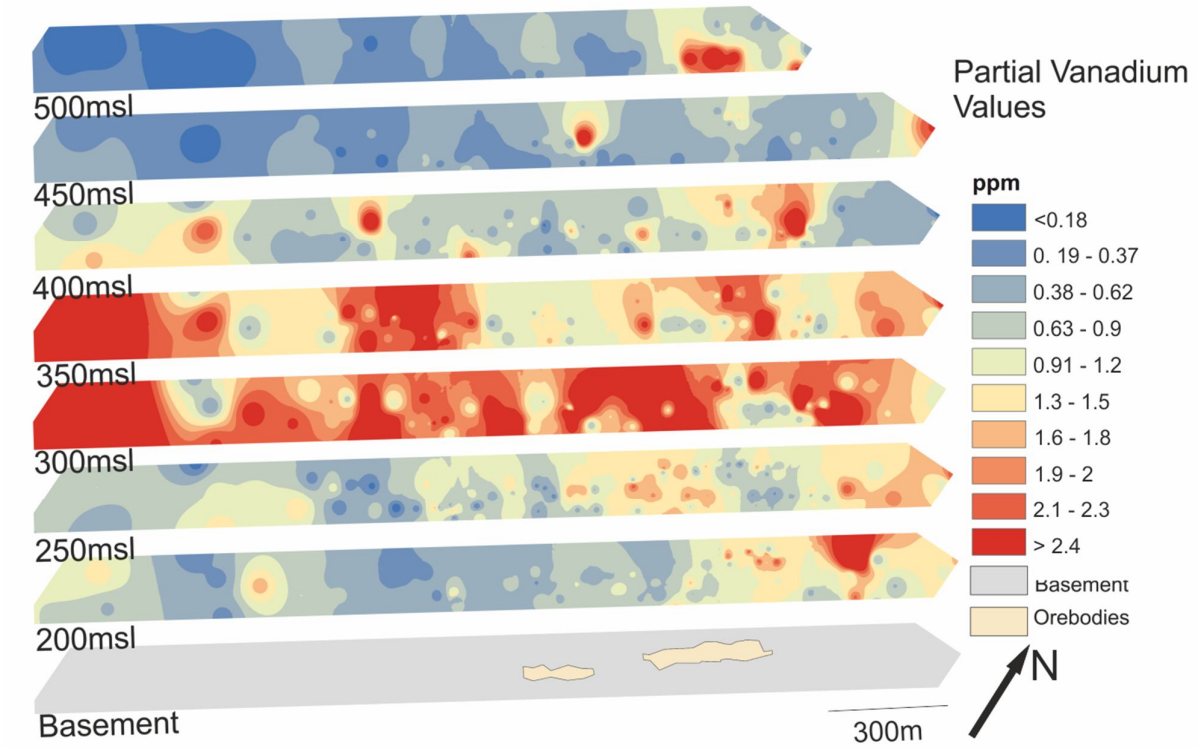

Figure 16: Partial leach vanadium values from sandstone overlying the Phoenix deposit. Detection Limit of 0.01ppm V.

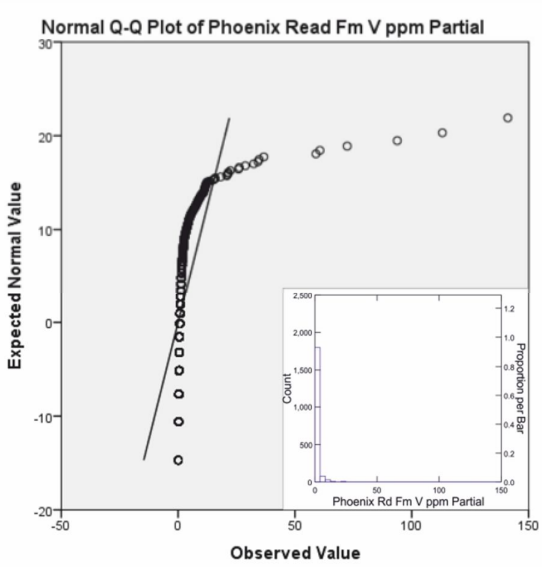
Normal Q-Q Plot of Phoenix Read Fm V ppm Partial
Expected Normal Value
Observed Value
Count
Proportion per Bar
Phoenix Rd Fm V ppm Partial

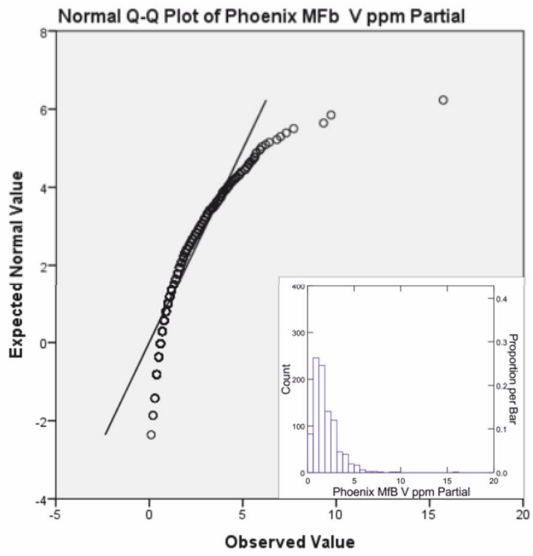
Normal Q-Q Plot of Phoenix MFb V ppm Partial
Expected Normal Value
Observed Value
Count
Proportion per Bar
Phoenix MfB V ppm Partial

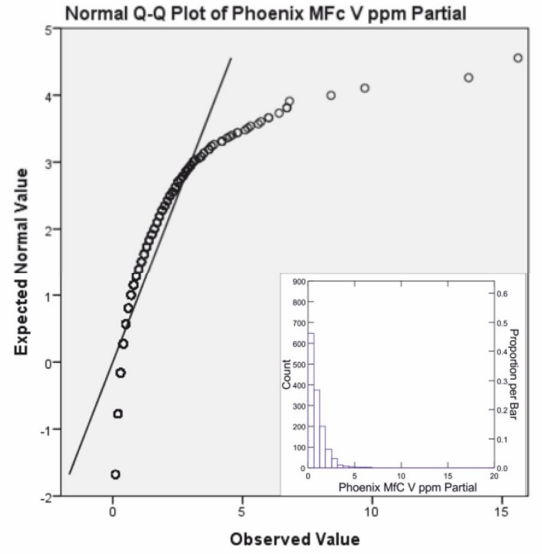
Normal Q-Q Plot of Phoenix MFc V ppm Partial
Expected Normal Value
Observed Value
Count
Proportion per Bar
Phoenix MfC V ppm Partial

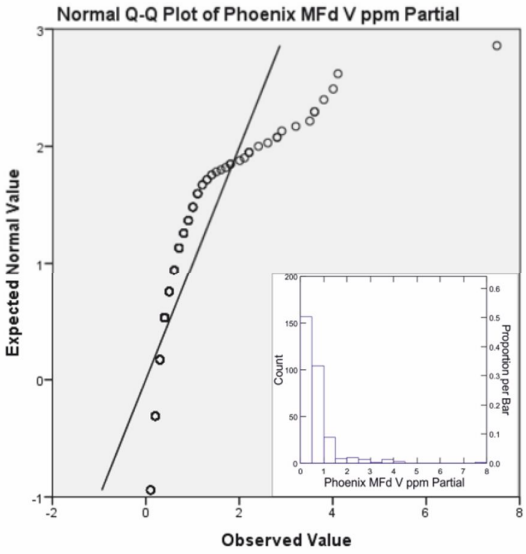
Normal Q-Q Plot of Phoenix MFd V ppm Partial
Expected Normal Value
Observed Value
Count
Proportion per Bar
Phoenix MFd V ppm Partial

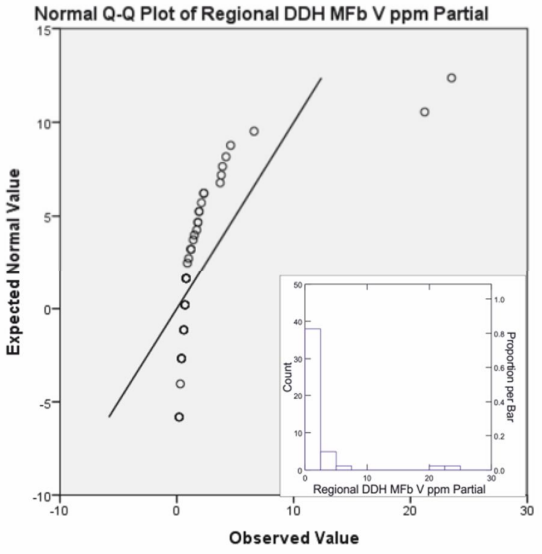
Normal Q-Q Plot of Regional DDH MFb V ppm Partial
Expected Normal Value
Observed Value
Count
Proportion per Bar
Regional DDH MFb V ppm Partial

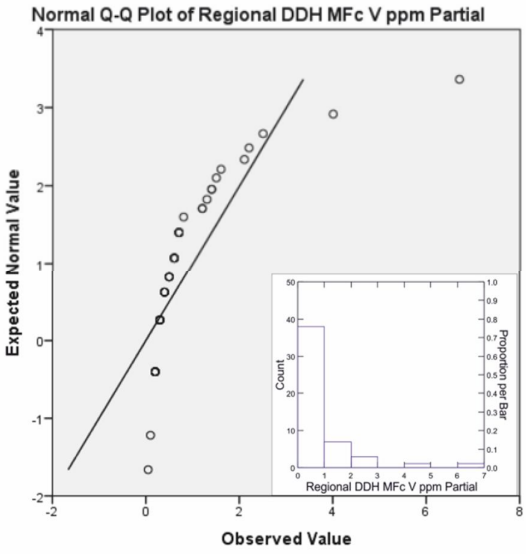
Normal Q-Q Plot of Regional DDH MFc V ppm Partial
Expected Normal Value
Observed Value
Count
Proportion per Bar
Regional DDH MFc V ppm Partial

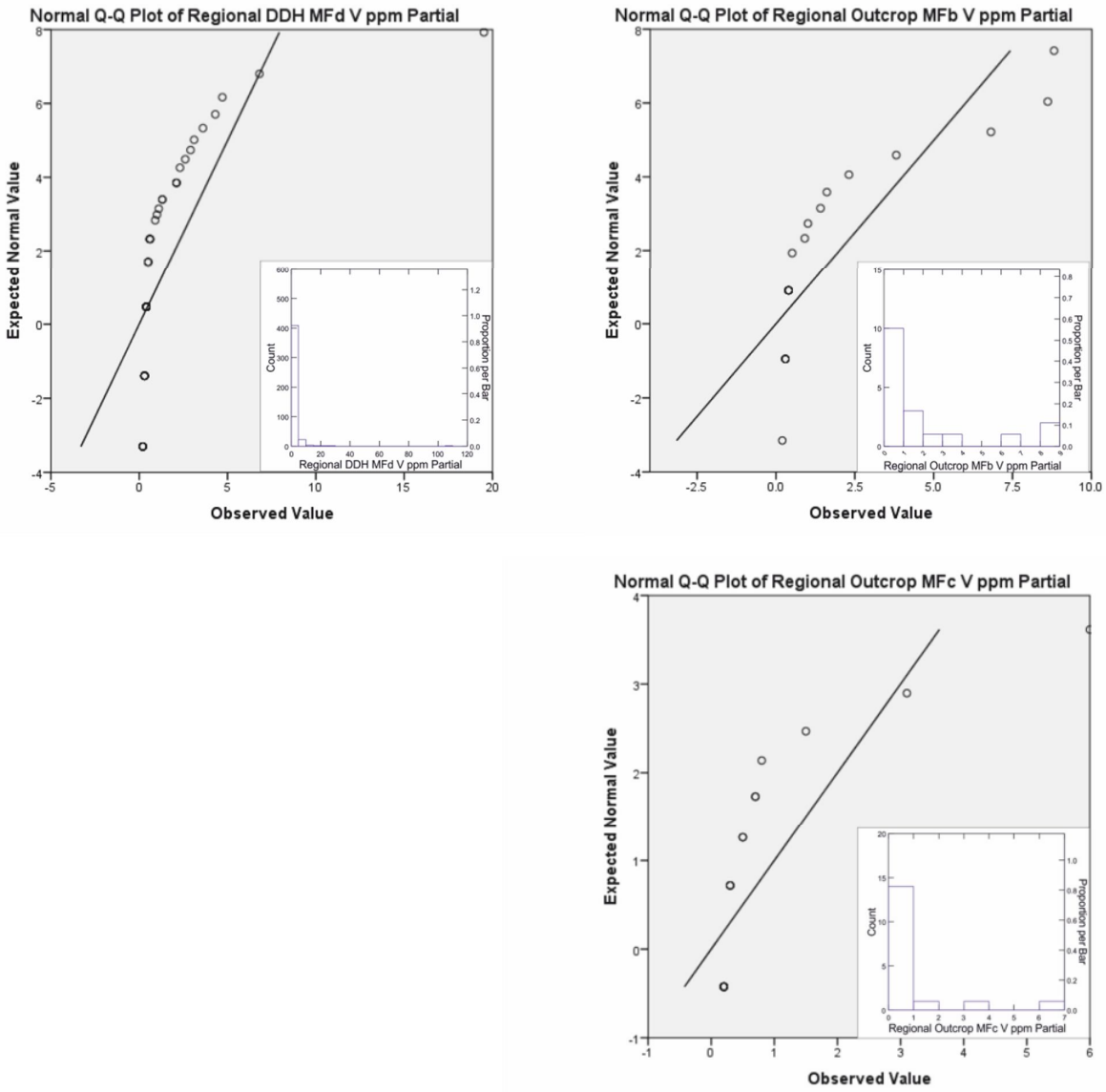

Figure 17: Q-Q and histogram (insets) plots of vanadium values from regional outcrop, regional DDH and sandstones overlying the Phoenix deposit.

Lead

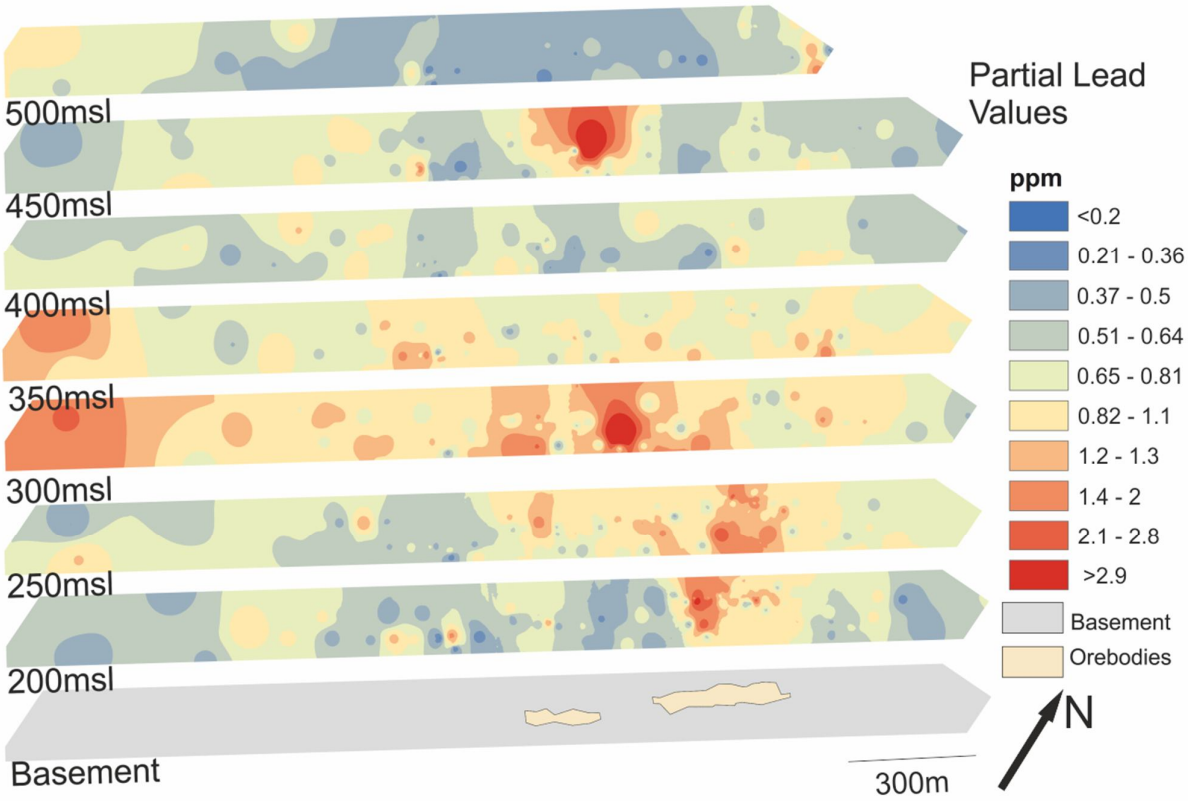

Figure 18: Partial leach lead values from sandstone overlying the Phoenix deposit. Detection Limit of 0.02ppm Pb.

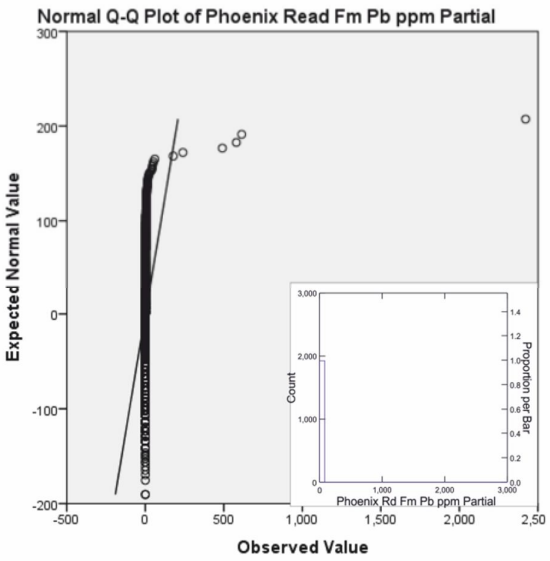
Normal Q-Q Plot of Phoenix Read Fm Pb ppm Partial
Expected Normal Value
Observed Value
Count
Proportion per Bar
Phoenix Rd Fm Pb ppm Partial

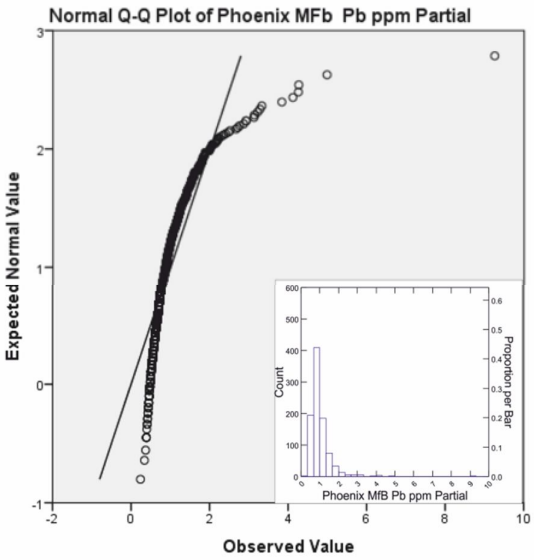
Normal Q-Q Plot of Phoenix MFb Pb ppm Partial
Expected Normal Value
Observed Value
Count
Proportion per Bar
Phoenix MfB Pb ppm Partial

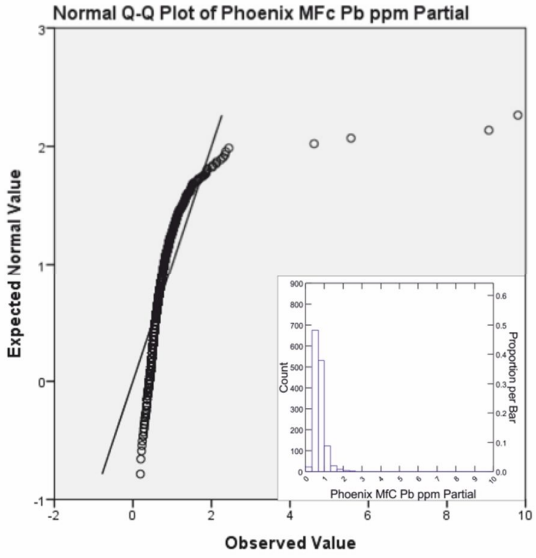
Normal Q-Q Plot of Phoenix MFc Pb ppm Partial
Expected Normal Value
Observed Value
Count
Proportion per Bar
Phoenix MfC Pb ppm Partial

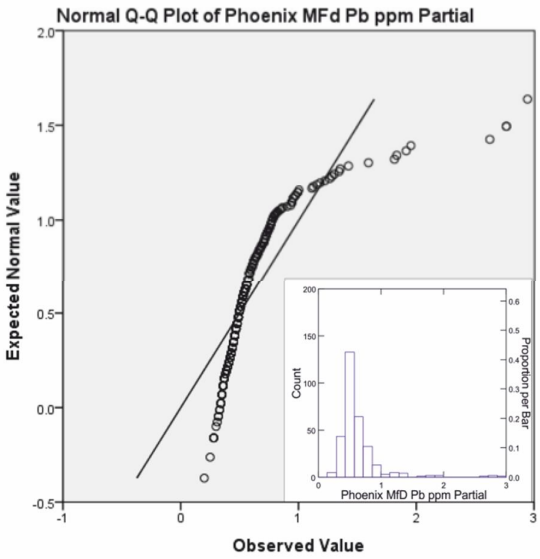
Normal Q-Q Plot of Phoenix MFd Pb ppm Partial
Expected Normal Value
Observed Value
Count
Proportion per Bar
Phoenix MfD Pb ppm Partial

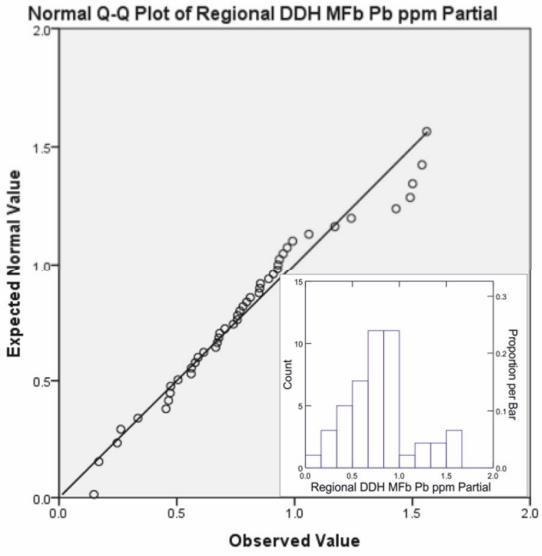
Normal Q-Q Plot of Regional DDH MFb Pb ppm Partial
Expected Normal Value
Observed Value
Count
Proportion per Bar
Regional DDH MFb Pb ppm Partial

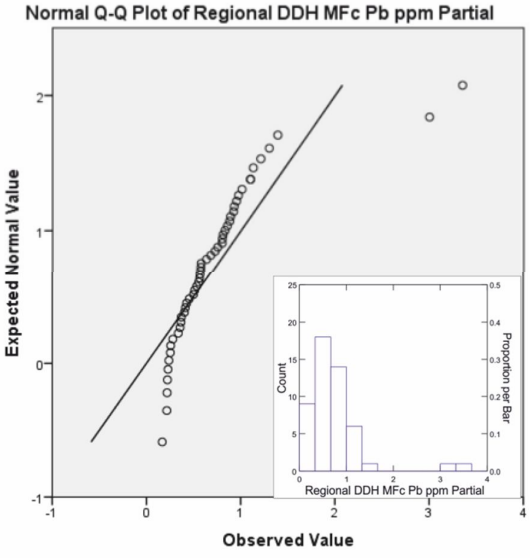
Normal Q-Q Plot of Regional DDH MFc Pb ppm Partial
Expected Normal Value
Observed Value
Count
Proportion per Bar
Regional DDH MFc Pb ppm Partial

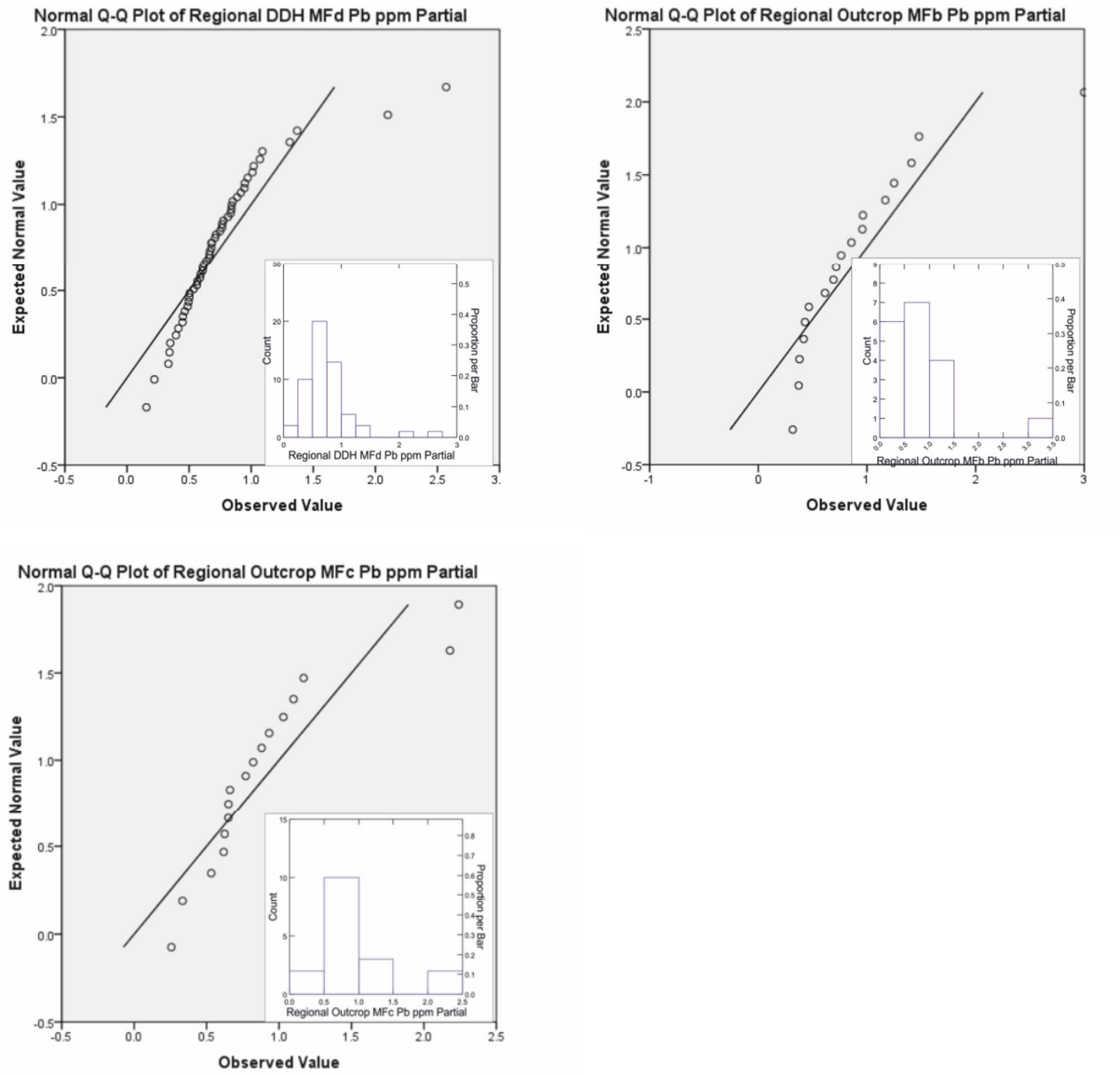

Figure 19: Q-Q and histogram (insets) plots of partial leach lead values from regional outcrop, regional DDH and sandstones overlying the Phoenix deposit.

Magnesium

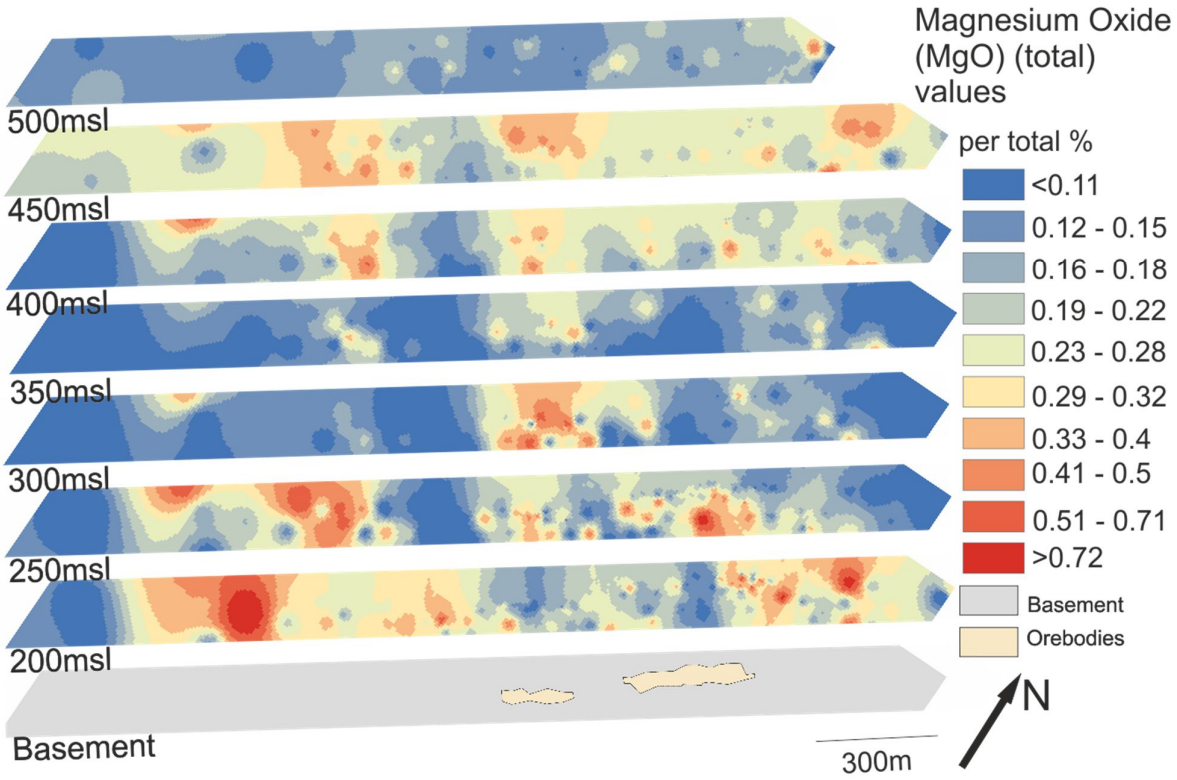

Figure 20: Total digestion magnesium oxide values from sandstone overlying the Phoenix deposit. Detection limit of 0.001% MgO.

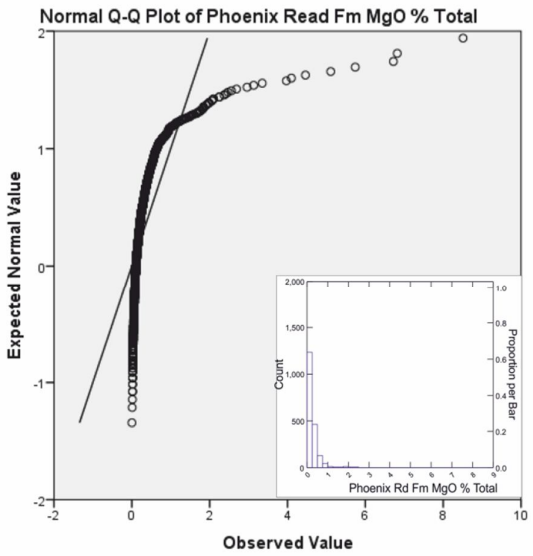
Normal Q-Q Plot of Phoenix Read Fm MgO % Total
Expected Normal Value
Observed Value
Count
Proportion per Bar
Phoenix Rd Fm MgO % Total

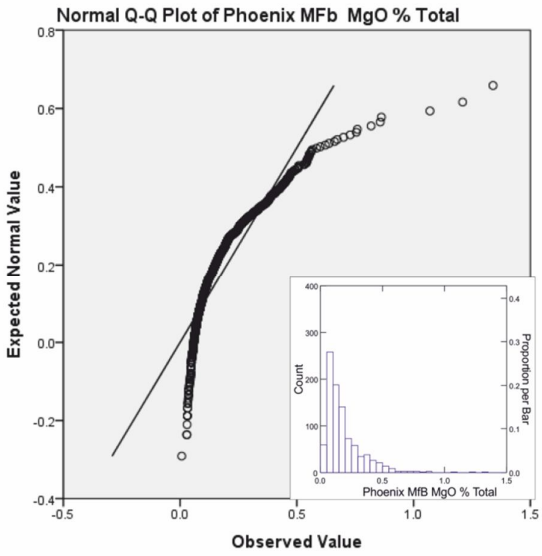
Normal Q-Q Plot of Phoenix MFb MgO % Total
Expected Normal Value
Observed Value
Count
Proportion per Bar
Phoenix MfB MgO % Total

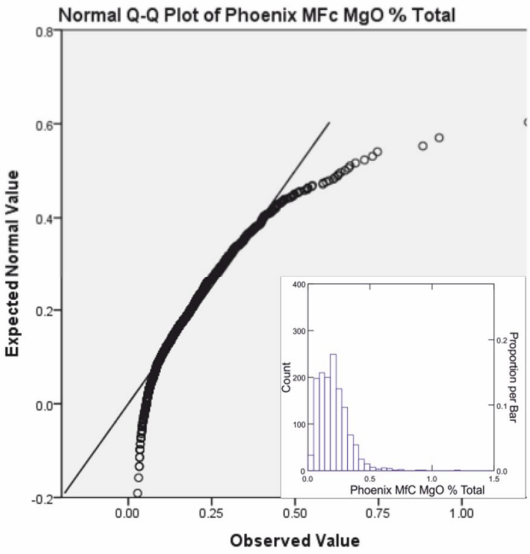
Normal Q-Q Plot of Phoenix MFc MgO % Total
Expected Normal Value
Observed Value
Count
Proportion per Bar
Phoenix MfC MgO % Total

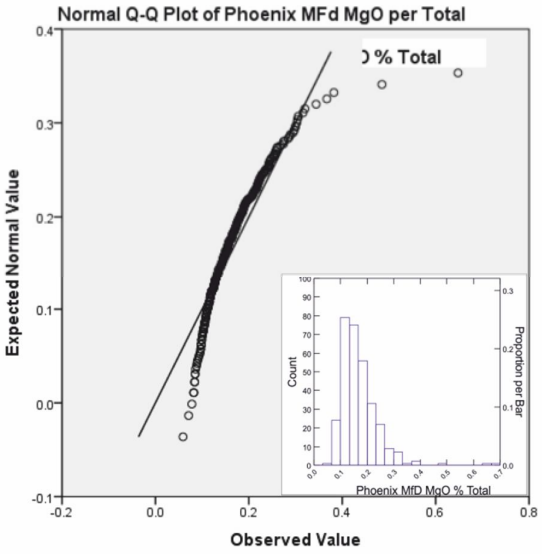
Normal Q-Q Plot of Phoenix MFd MgO per Total
Expected Normal Value
Observed Value
Count
Proportion per Bar
Phoenix MfD MgO % Total

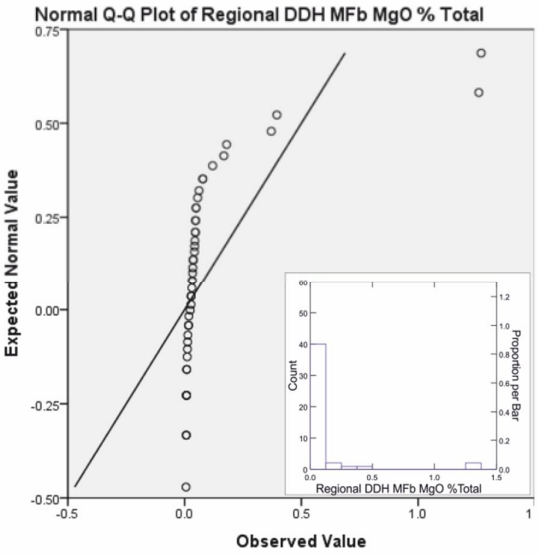
Normal Q-Q Plot of Regional DDH MFb MgO % Total
Expected Normal Value
Observed Value
Count
Proportion per Bar
Regional DDH MFb MgO %Total

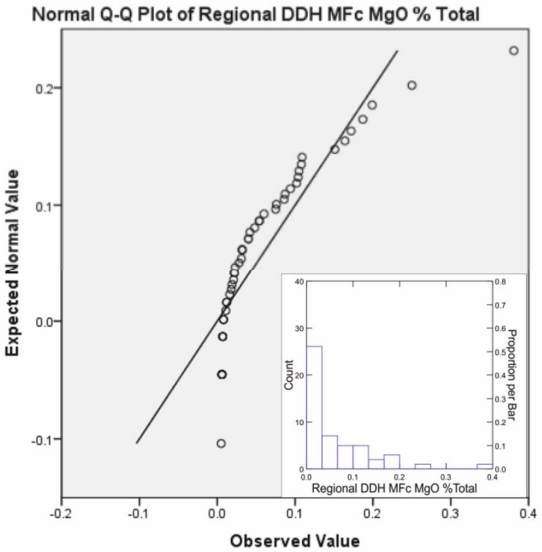
Normal Q-Q Plot of Regional DDH MFc MgO % Total
Expected Normal Value
Observed Value
Count
Proportion per Bar
Regional DDH MFc MgO %Total

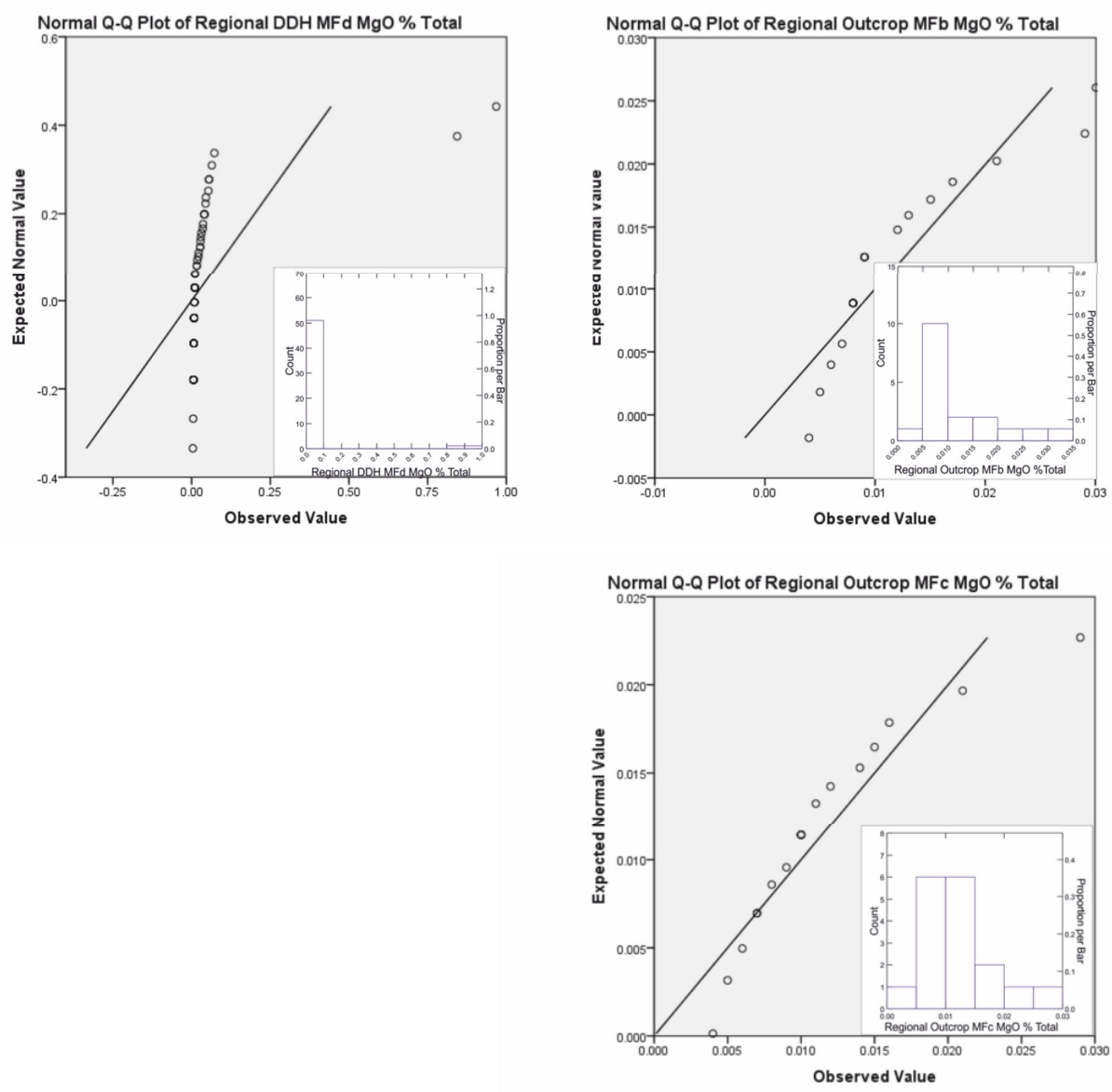

Figure 21: Q-Q and histogram (insets) plots of total digestion MgO values from regional outcrop, regional DDH and sandstones overlying the Phoenix deposit.

Lithium

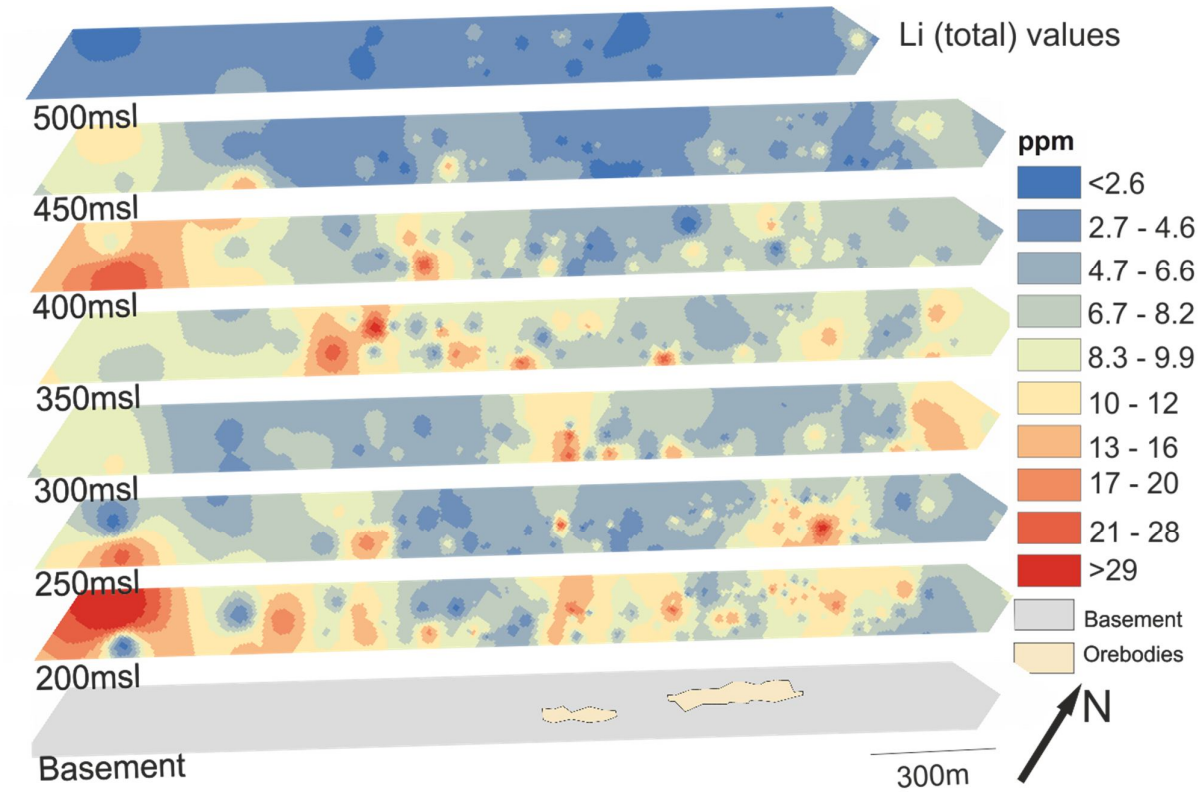

Figure 22: Total lithium values from sandstone overlying the Phoenix deposit. Detection limit of 1 ppm Li.

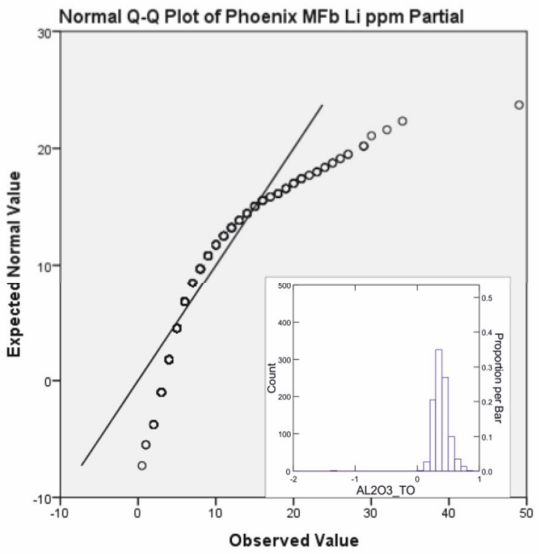
Normal Q-Q Plot of Phoenix MFb Li ppm Partial
Expected Normal Value
Observed Value
Count
Proportion per Bar
AL2O3_TO

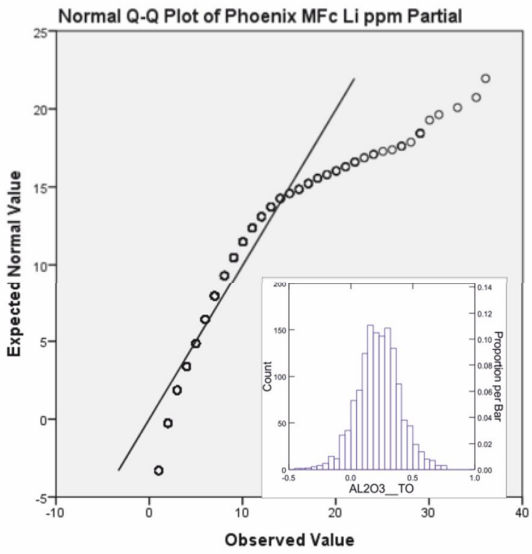
Normal Q-Q Plot of Phoenix MFc Li ppm Partial
Expected Normal Value
Observed Value
Count
Proportion per Bar
AL2O3__TO

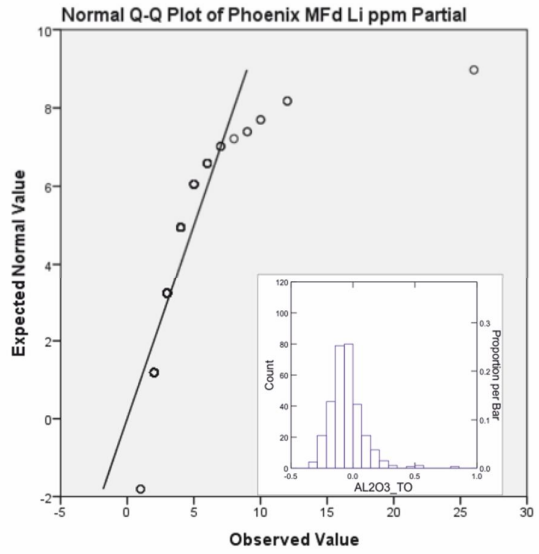
Normal Q-Q Plot of Phoenix MFd Li ppm Partial
Expected Normal Value
Observed Value
Count
Proportion per Bar
AL2O3_TO

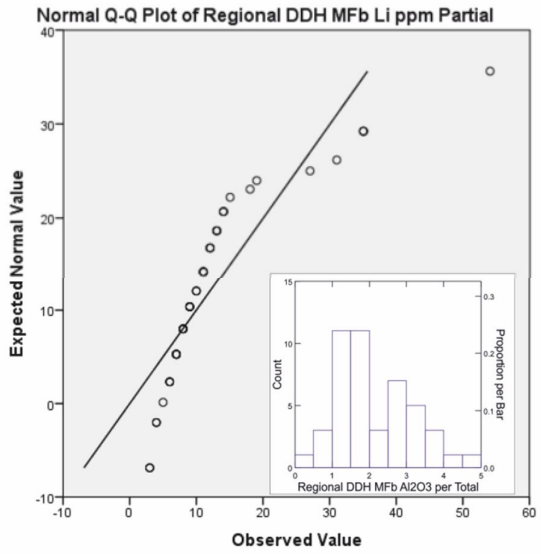
Normal Q-Q Plot of Regional DDH MFb Li ppm Partial
Expected Normal Value
Observed Value
Count
Proportion per Bar
Regional DDH MFb Al2O3 per Total

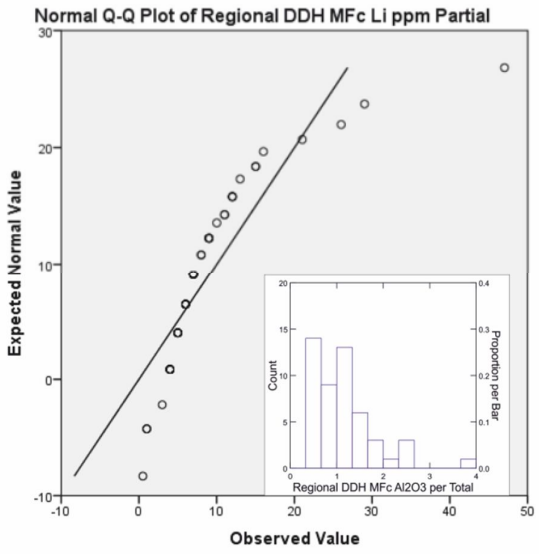
Normal Q-Q Plot of Regional DDH MFc Li ppm Partial
Expected Normal Value
Observed Value
Count
Proportion per Bar
Regional DDH MFc Al2O3 per Total

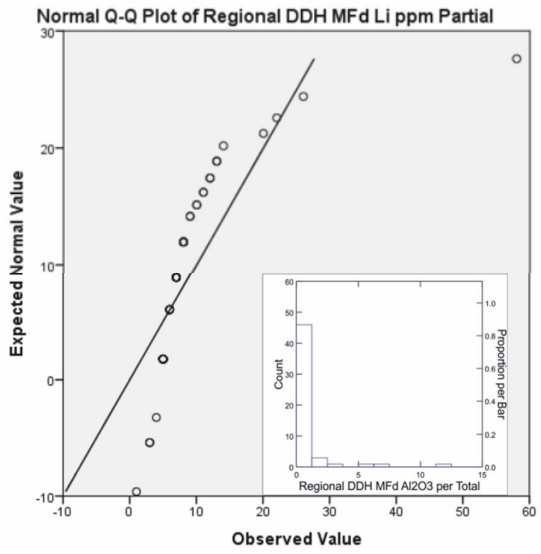
Normal Q-Q Plot of Regional DDH MFd Li ppm Partial
Expected Normal Value
Observed Value
Count
Proportion per Bar
Regional DDH MFd Al2O3 per Total

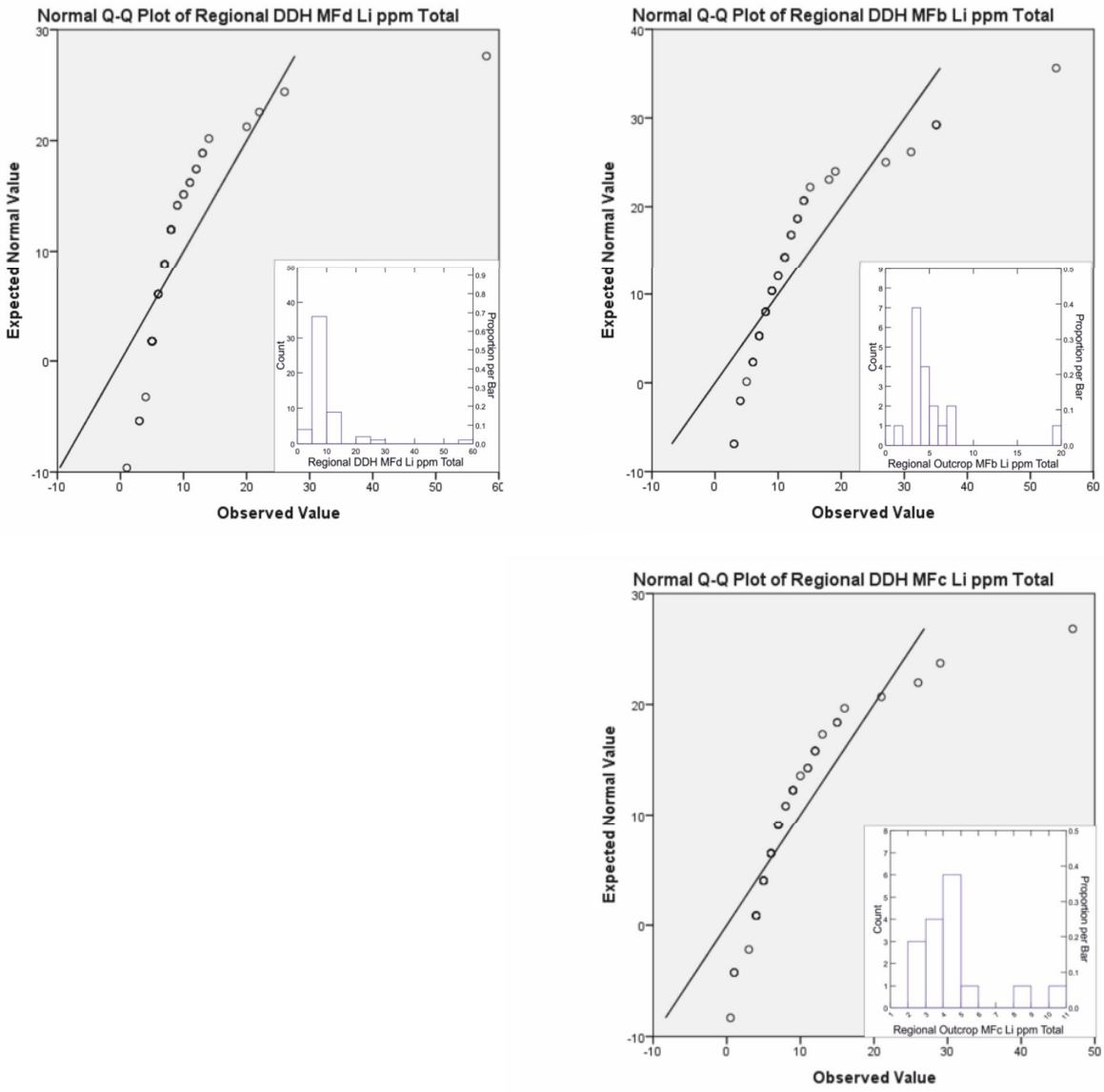

Figure 23: Q-Q and histogram (insets) plots of total digestion lithium values from regional outcrop, regional DDH and sandstones overlying the Phoenix deposit.

Boron

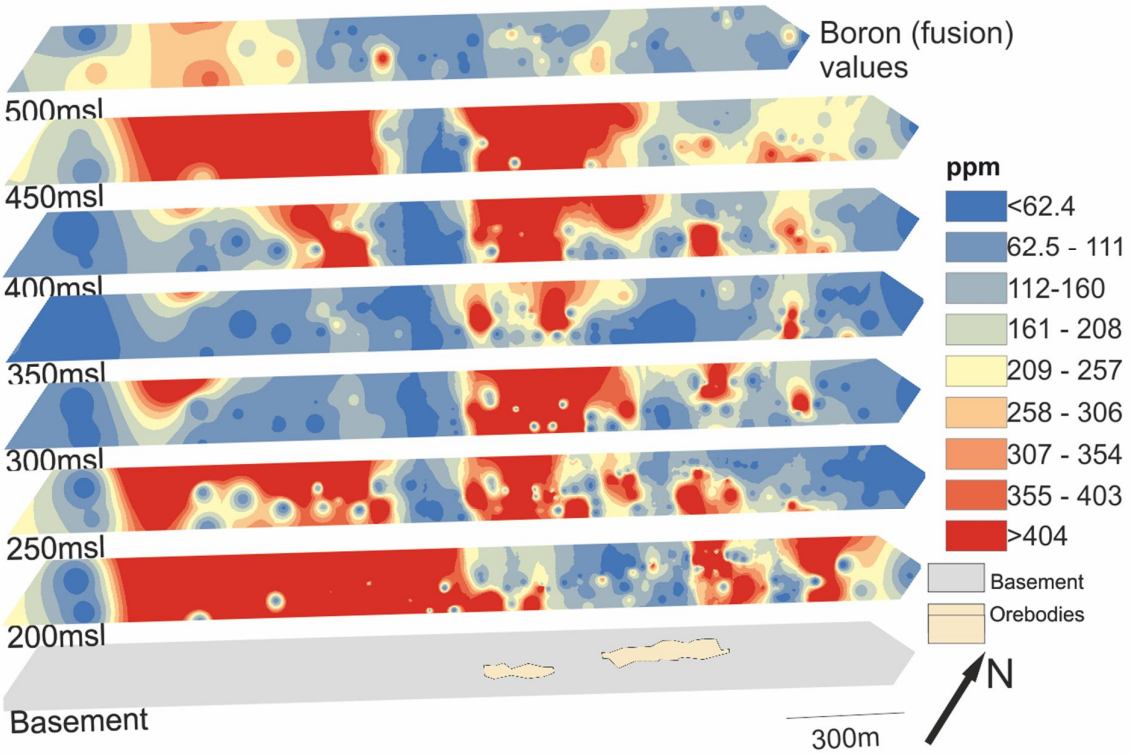

Figure 24: Total fusion values of boron from sandstone overlying the Phoenix deposit. Detection limit of 2 ppm B.

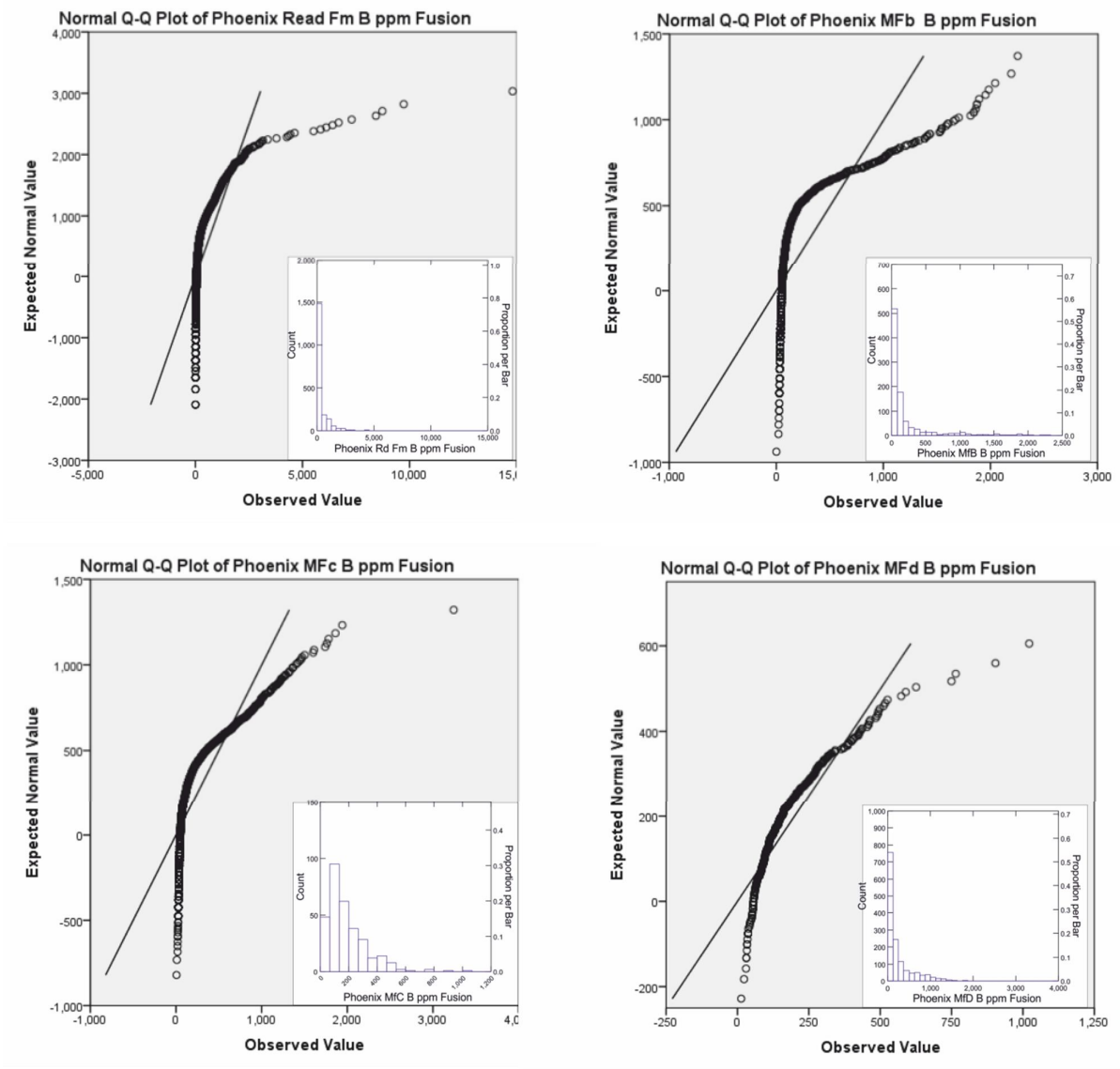

Figure 25: Q-Q and histogram (insets) plots of fusion boron values from sandstones overlying the Phoenix deposit. B data from the regional surveys is absent.

Aluminium

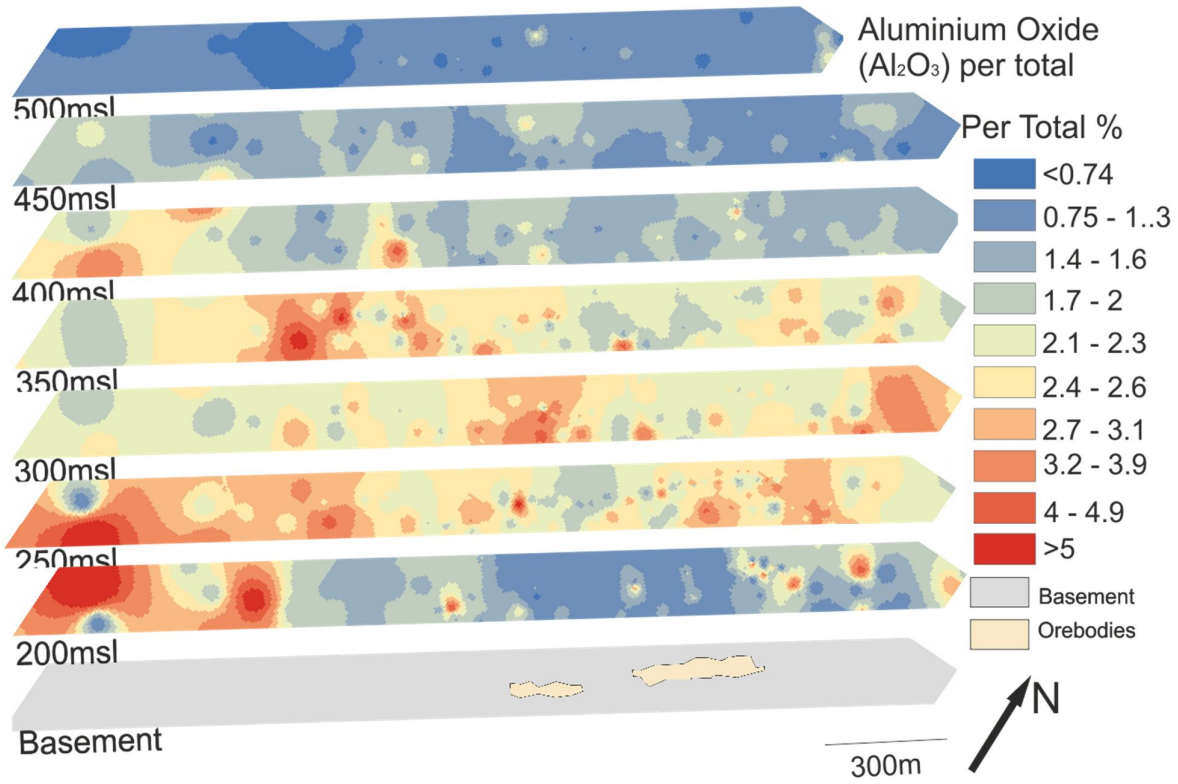

Figure 26: Total digestion aluminium oxide values from sandstone overlying the Phoenix deposit. Detection limit of 0.01% Al_2O_3.

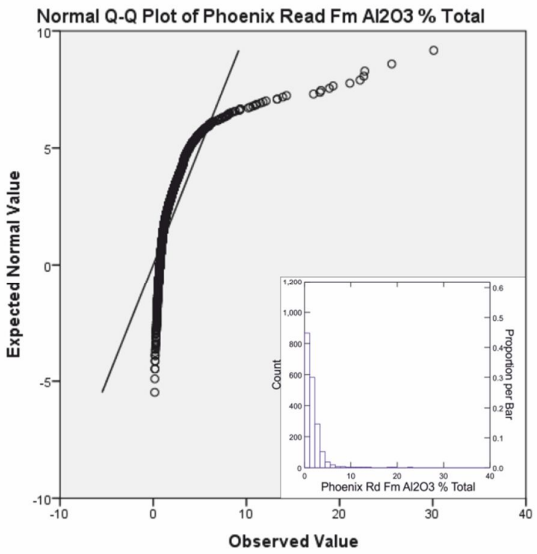
Normal Q-Q Plot of Phoenix Read Fm Al2O3 % Total
Expected Normal Value
Observed Value
Count
Proportion per Bar
Phoenix Rd Fm Al2O3 % Total

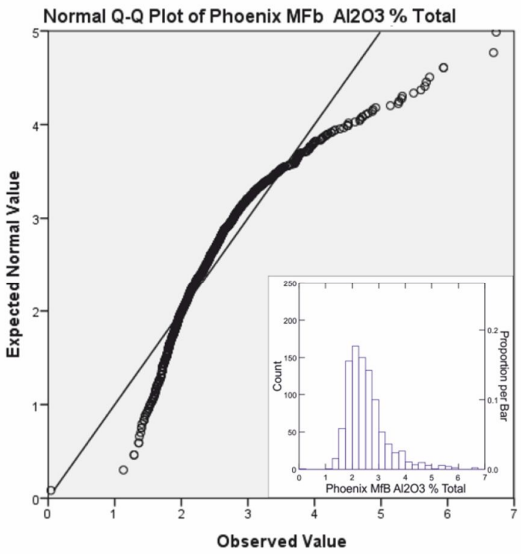
Normal Q-Q Plot of Phoenix MFb Al2O3 % Total
Expected Normal Value
Observed Value
Count
Proportion per Bar
Phoenix MfB Al2O3 % Total

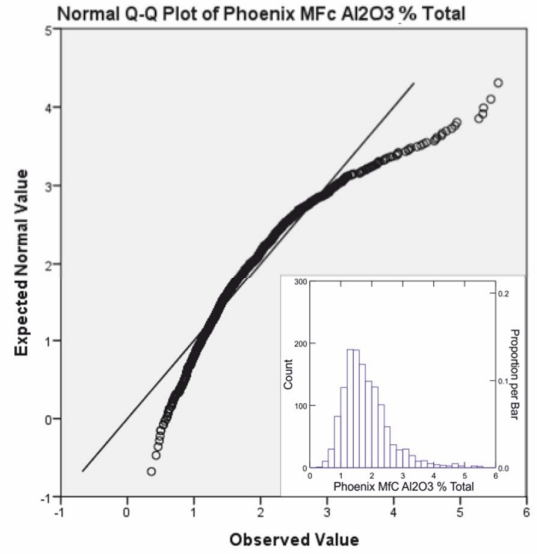
Normal Q-Q Plot of Phoenix MFc Al2O3 % Total
Expected Normal Value
Observed Value
Count
Proportion per Bar
Phoenix MfC Al2O3 % Total

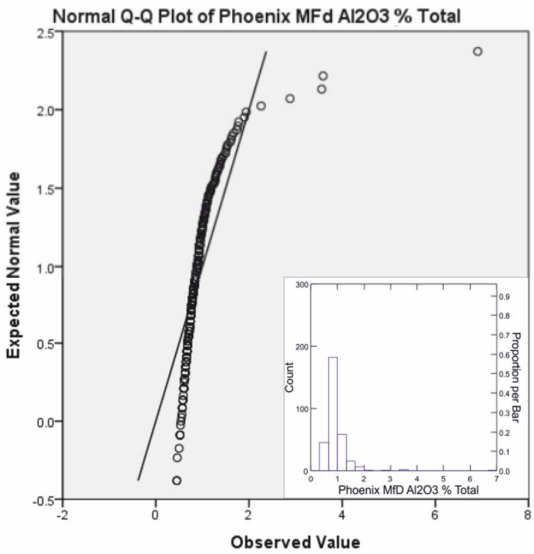
Normal Q-Q Plot of Phoenix MFd Al2O3 % Total
Expected Normal Value
Observed Value
Count
Proportion per Bar
Phoenix MfD Al2O3 % Total

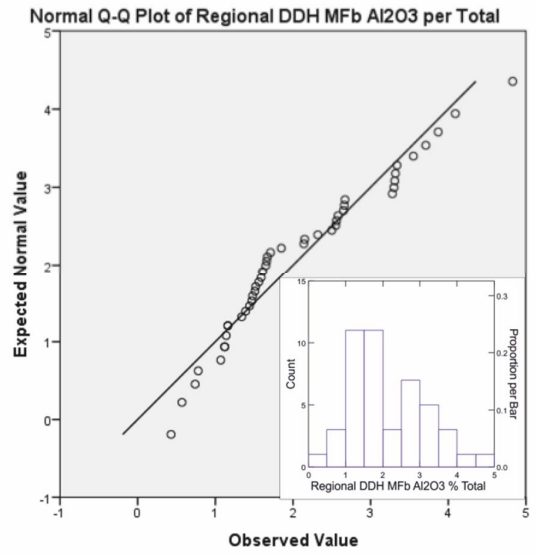
Normal Q-Q Plot of Regional DDH MFb Al2O3 per Total
Expected Normal Value
Observed Value
Count
Proportion per Bar
Regional DDH MFb Al2O3 % Total

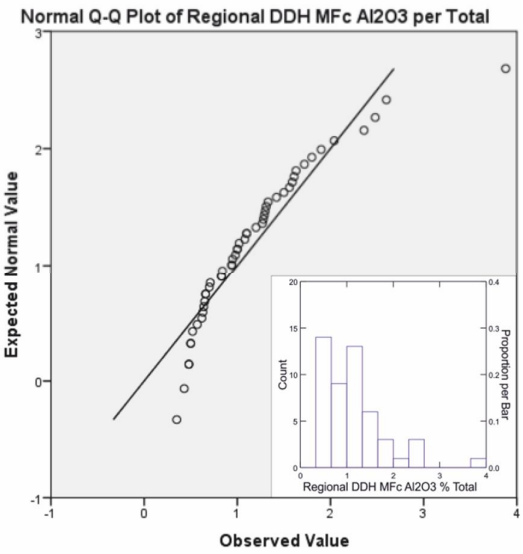
Normal Q-Q Plot of Regional DDH MFc Al2O3 per Total
Expected Normal Value
Observed Value
Count
Proportion per Bar
Regional DDH MFc Al2O3 % Total

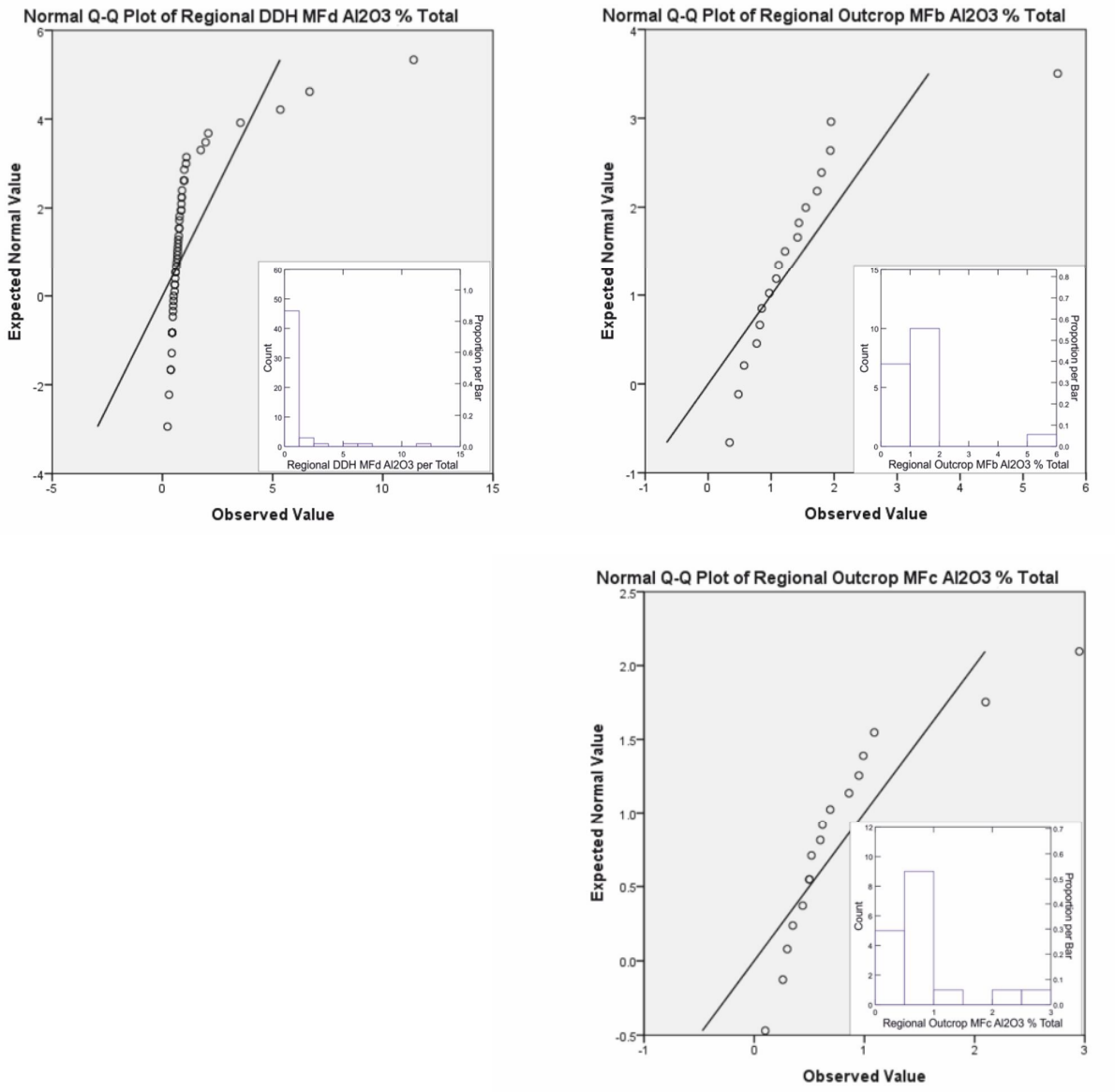

Figure 27: Q-Q and histogram (insets) plots of total digestion aluminium oxide values from regional outcrop, regional DDH and sandstones overlying the Phoenix deposit.

Yttrium

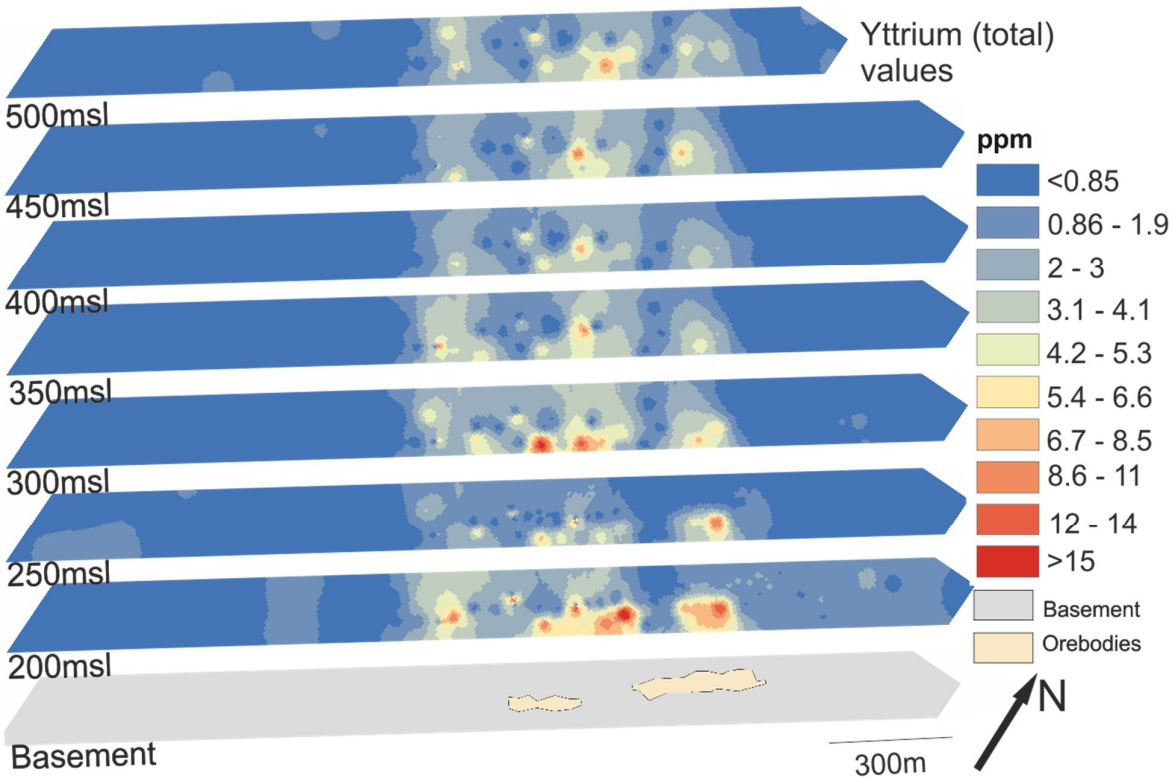

Figure 28: Total digestion yttrium values from sandstone overlying the Phoenix deposit. Detection limit of 0.1 ppm Y.

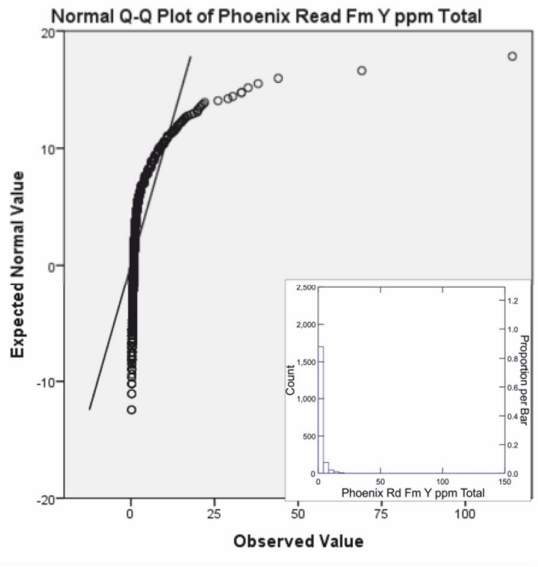
Normal Q-Q Plot of Phoenix Read Fm Y ppm Total
Expected Normal Value
Observed Value
Count
Proportion per Bar
Phoenix Rd Fm Y ppm Total

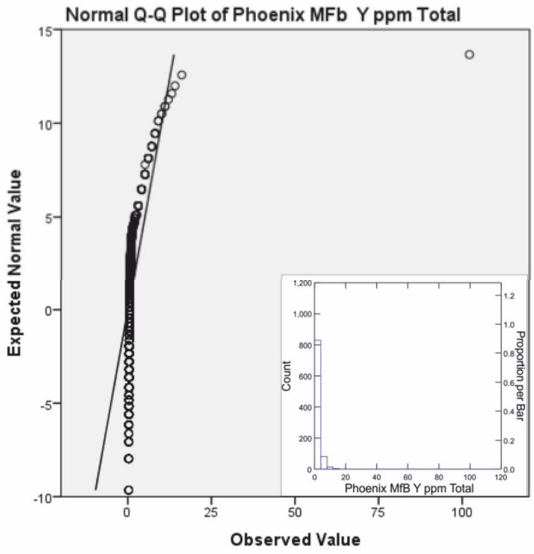
Normal Q-Q Plot of Phoenix MFb Y ppm Total
Expected Normal Value
Observed Value
Count
Proportion per Bar
Phoenix MfB Y ppm Total

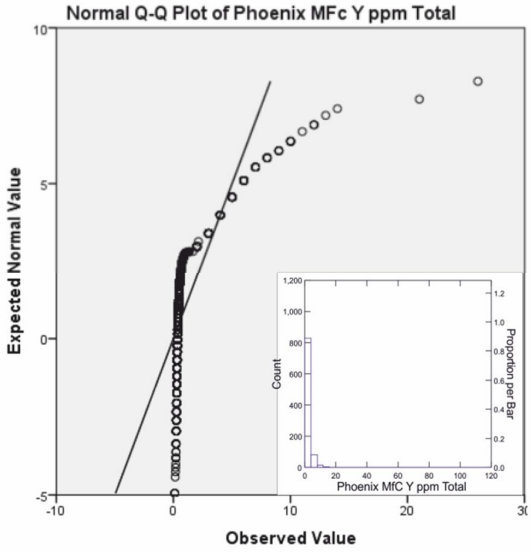
Normal Q-Q Plot of Phoenix MFc Y ppm Total
Expected Normal Value
Observed Value
Count
Proportion per Bar
Phoenix MfC Y ppm Total

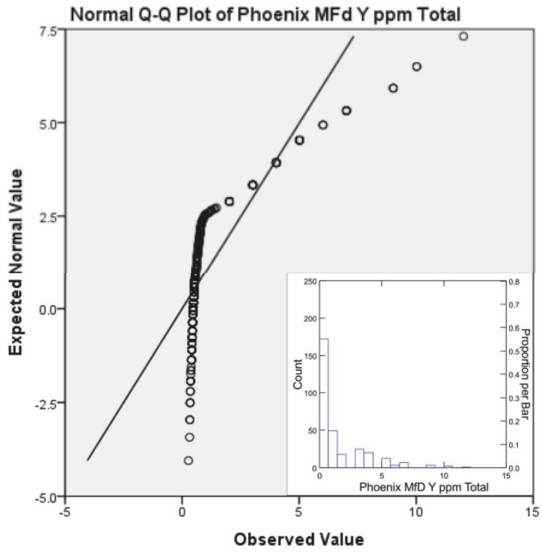
Normal Q-Q Plot of Phoenix MFd Y ppm Total
Expected Normal Value
Observed Value
Count
Proportion per Bar
Phoenix MfD Y ppm Total

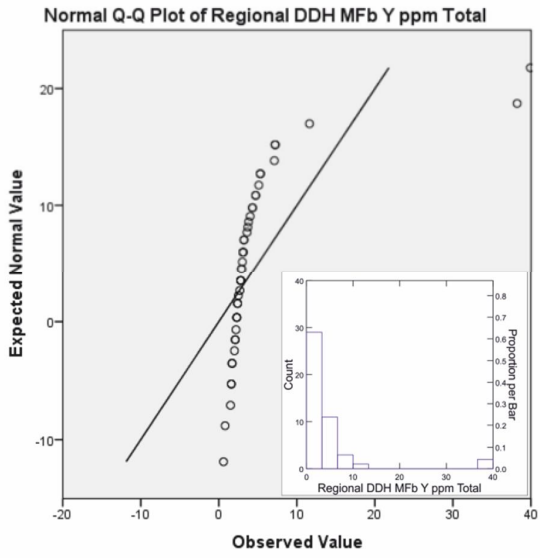
Normal Q-Q Plot of Regional DDH MFb Y ppm Total
Expected Normal Value
Observed Value
Count
Proportion per Bar
Regional DDH MFb Y ppm Total

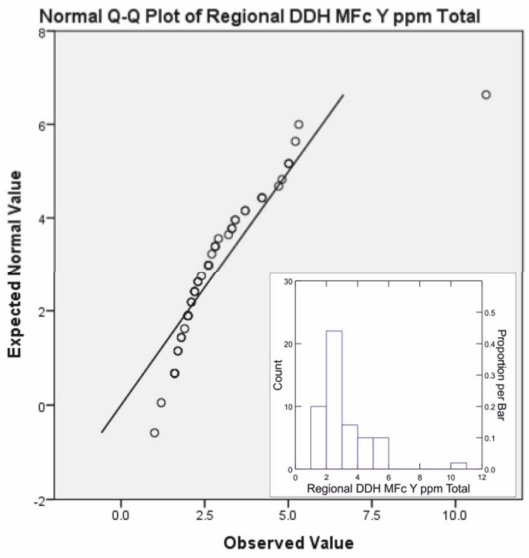
Normal Q-Q Plot of Regional DDH MFc Y ppm Total
Expected Normal Value
Observed Value
Count
Proportion per Bar
Regional DDH MFc Y ppm Total

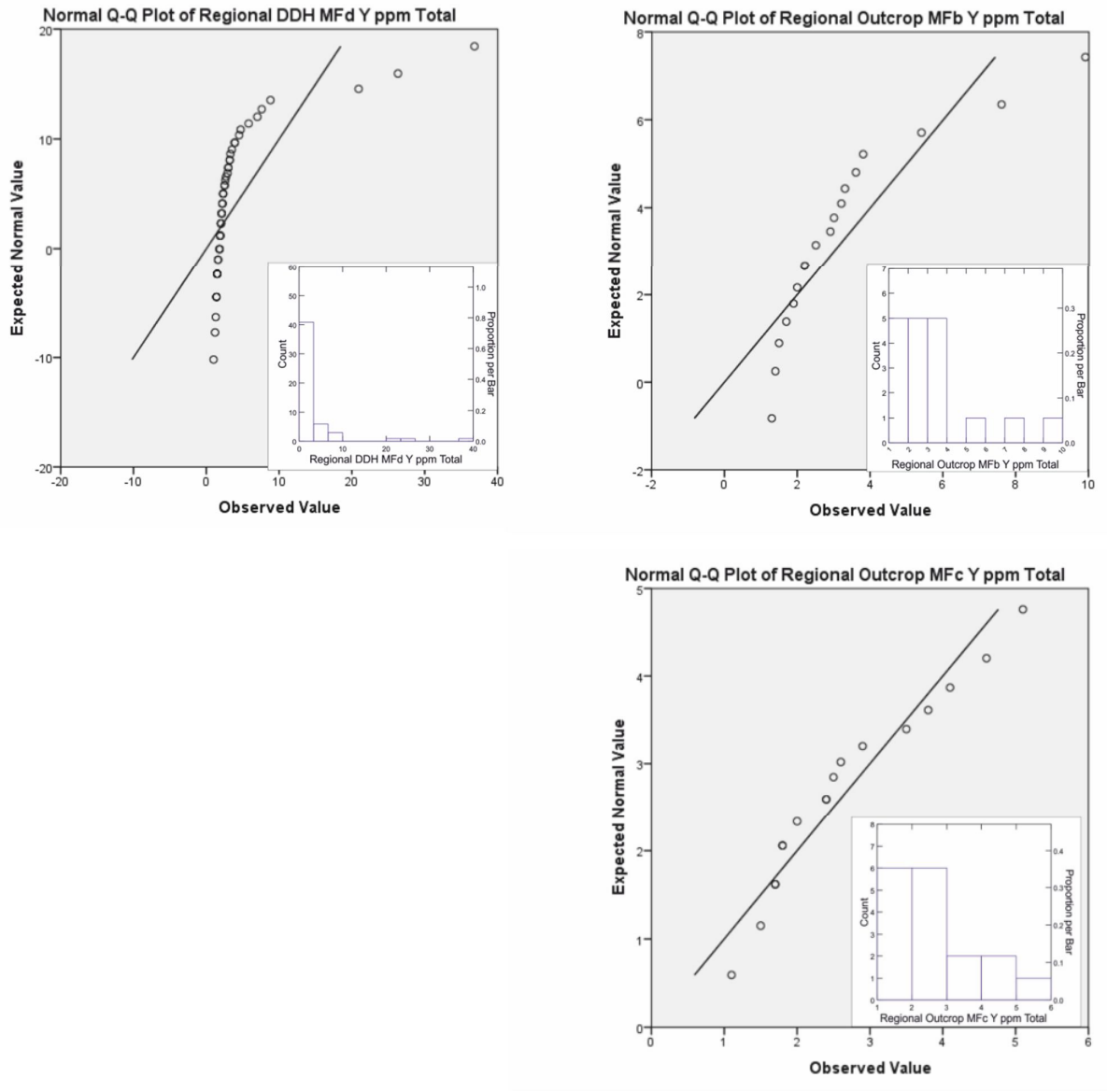

Figure 29: Q-Q and histogram (insets) plots of total digestion yttrium from regional outcrop, regional DDH and sandstones overlying the Phoenix deposit. Statistical analysis includes values at detection limit.

Potassium

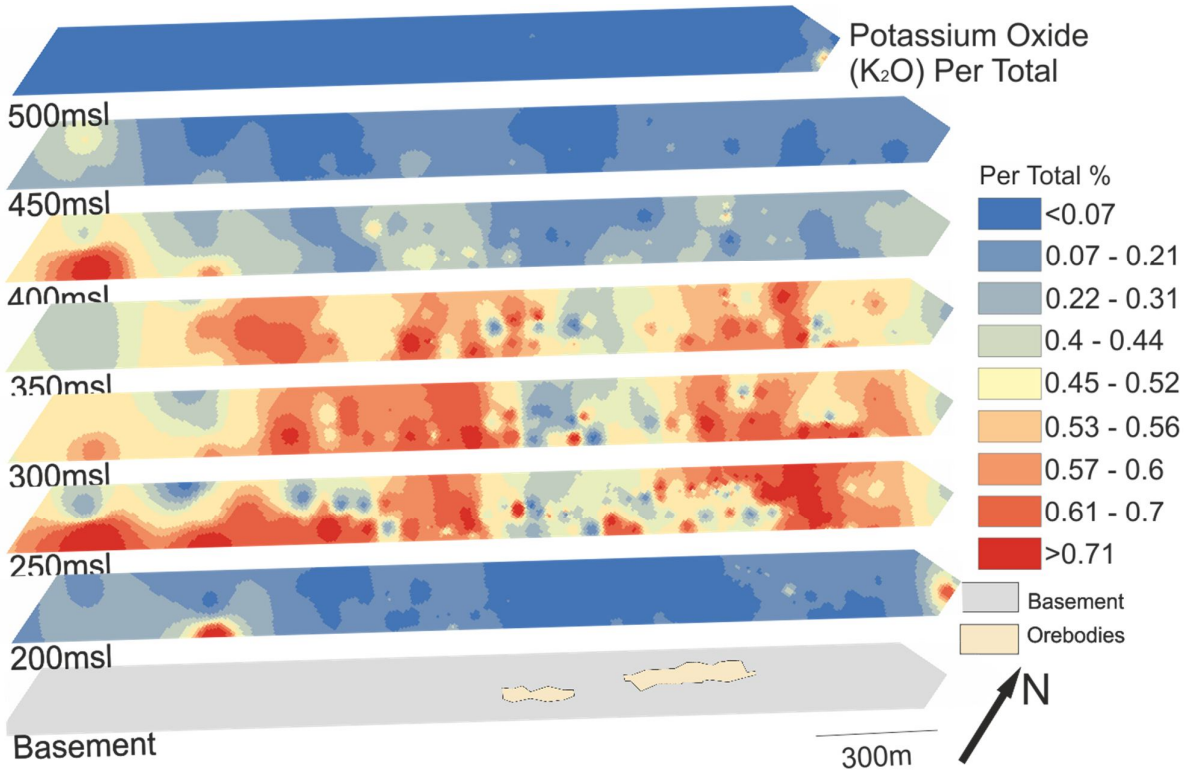

Figure 30: Total digestion potassium oxide values from sandstone overlying the Phoenix deposit.

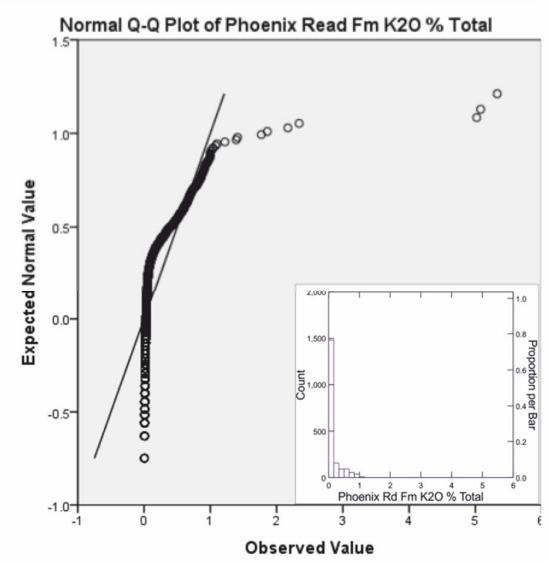
Normal Q-Q Plot of Phoenix Read Fm K2O % Total
Expected Normal Value
Observed Value
Count
Proportion per Bar
Phoenix Rd Fm K2O % Total

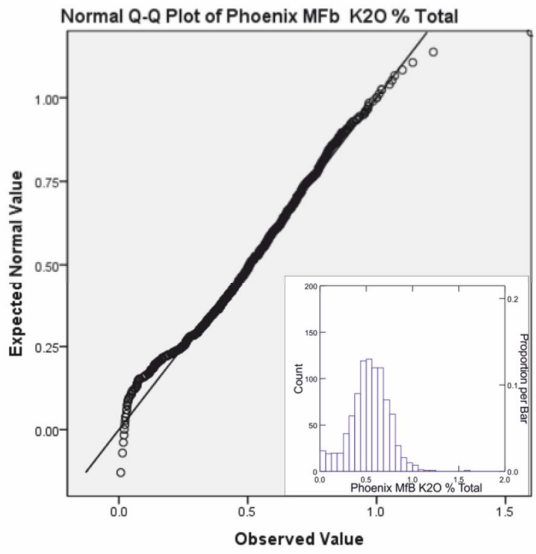
Normal Q-Q Plot of Phoenix MFb K2O % Total
Expected Normal Value
Observed Value
Count
Proportion per Bar
Phoenix MfB K2O % Total

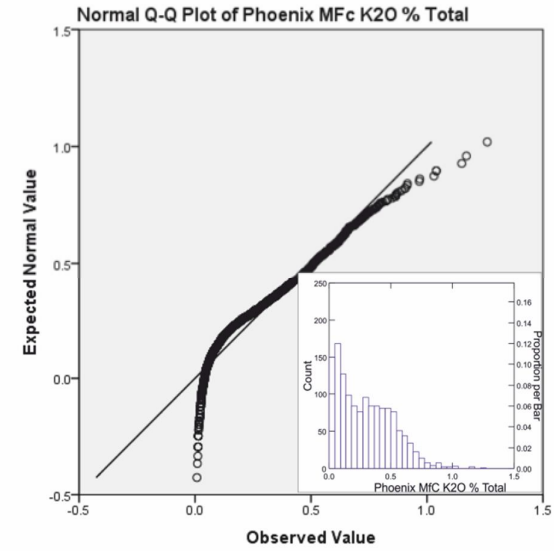
Normal Q-Q Plot of Phoenix MFc K2O % Total
Expected Normal Value
Observed Value
Count
Proportion per Bar
Phoenix MfC K2O % Total

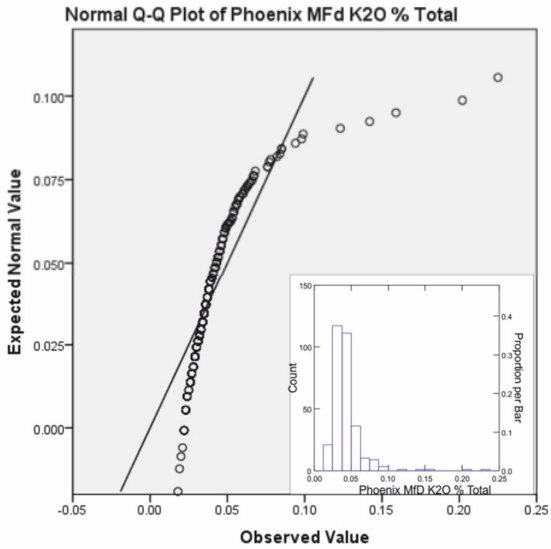
Normal Q-Q Plot of Phoenix MFd K2O % Total
Expected Normal Value
Observed Value
Count
Proportion per Bar
Phoenix MfD K2O % Total

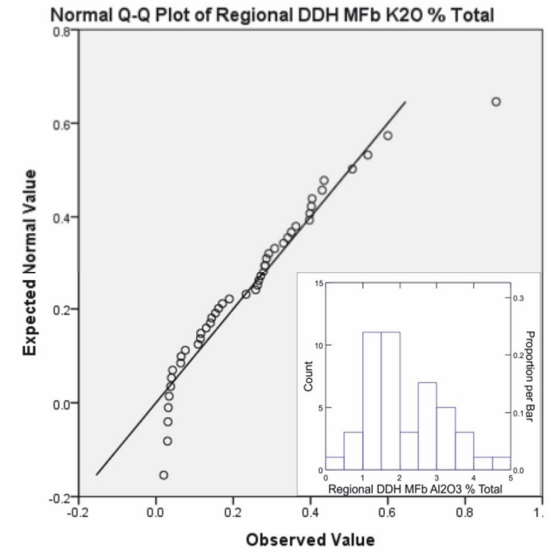
Normal Q-Q Plot of Regional DDH MFb K2O % Total
Expected Normal Value
Observed Value
Count
Proportion per Bar
Regional DDH MFb Al2O3 % Total

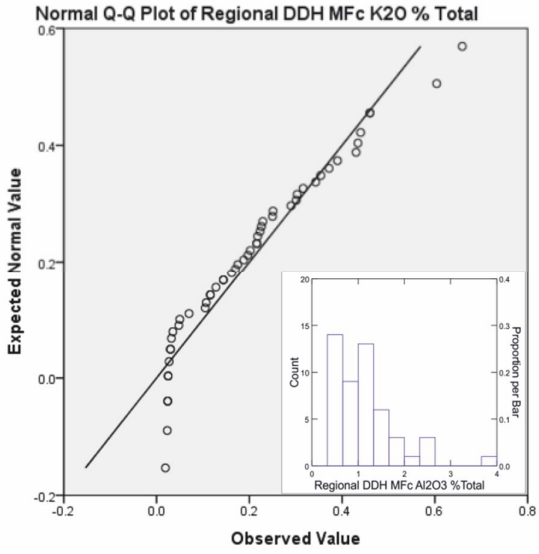
Normal Q-Q Plot of Regional DDH MFc K2O % Total
Expected Normal Value
Observed Value
Count
Proportion per Bar
Regional DDH MFc Al2O3 %Total

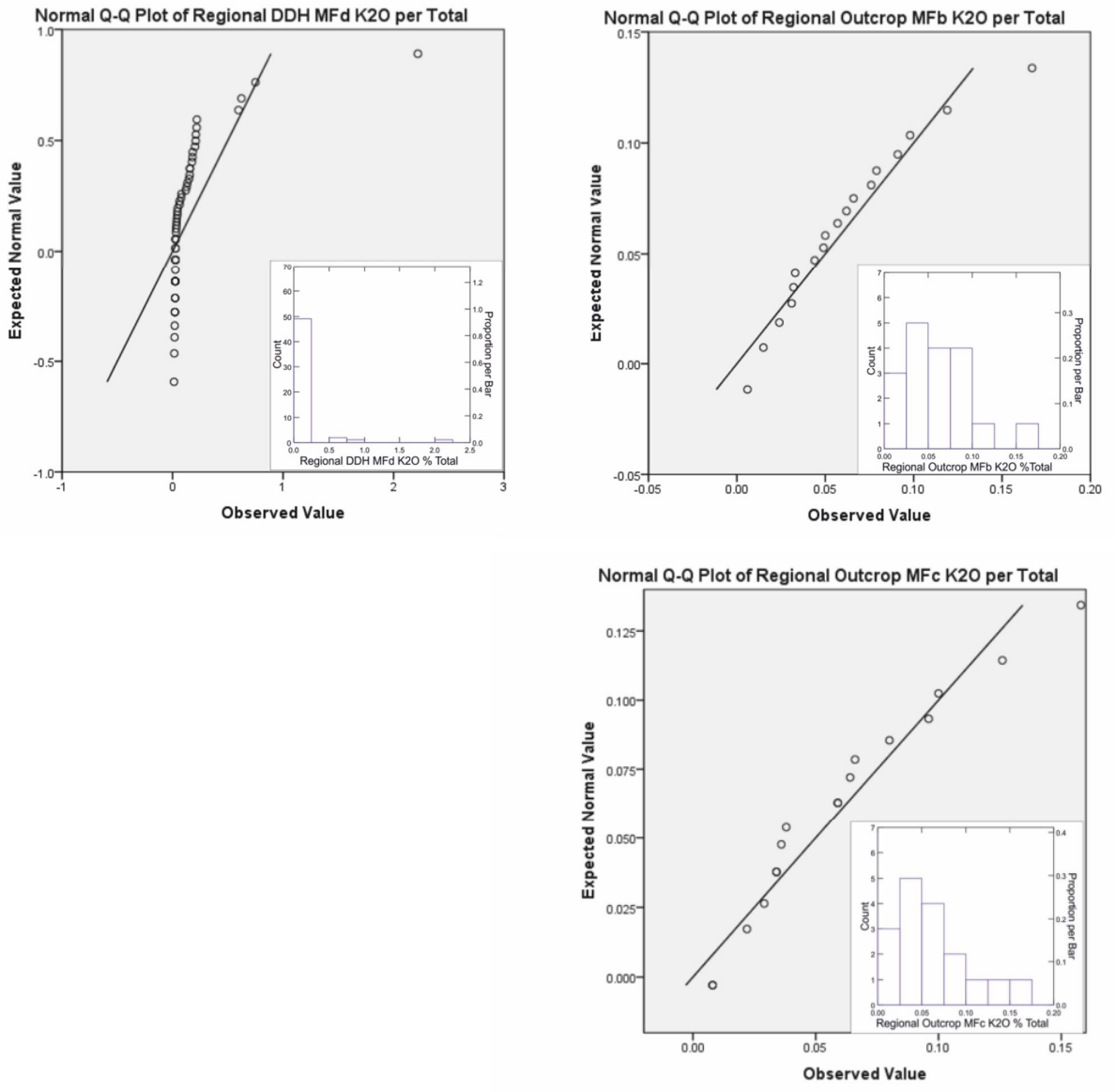

Figure 31: Q-Q and histogram (insets) plots of total digestion potassium oxide values from regional outcrop, regional DDH and sandstones overlying the Phoenix.

Cerium

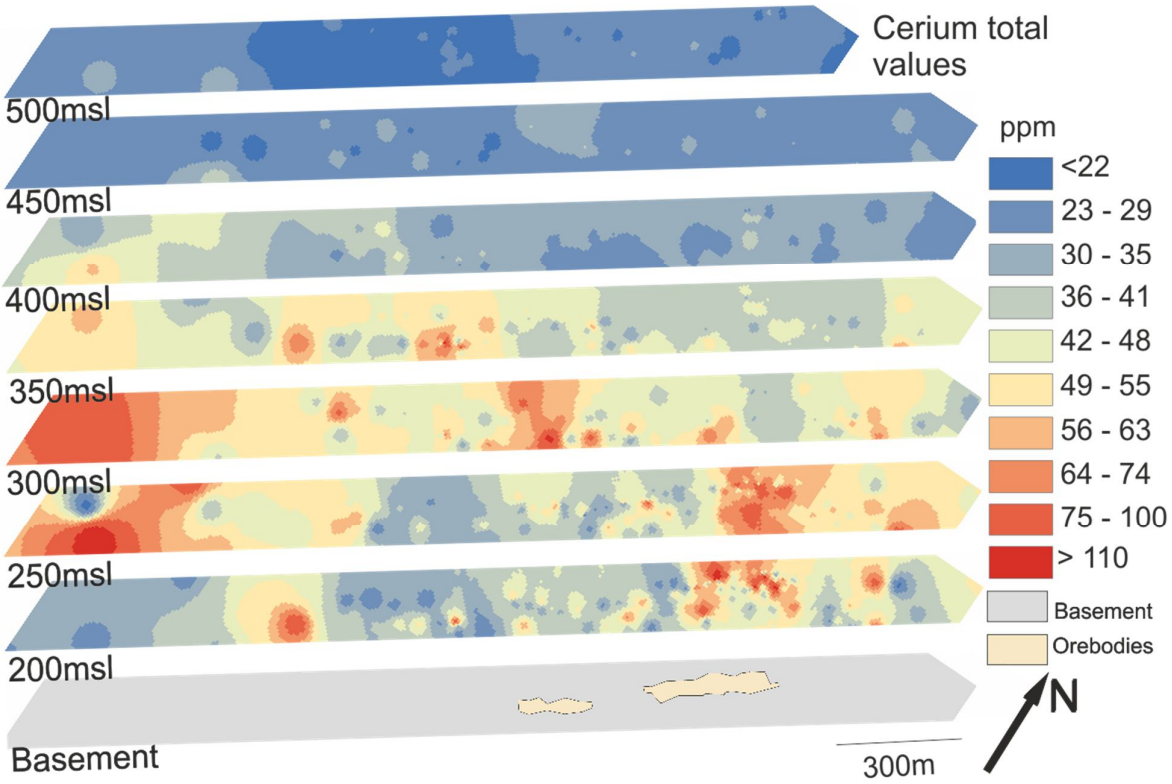

Figure 32: Total digestion cerium values from sandstone overlying the Phoenix deposit. Detection limit of 0.1ppm Ce.

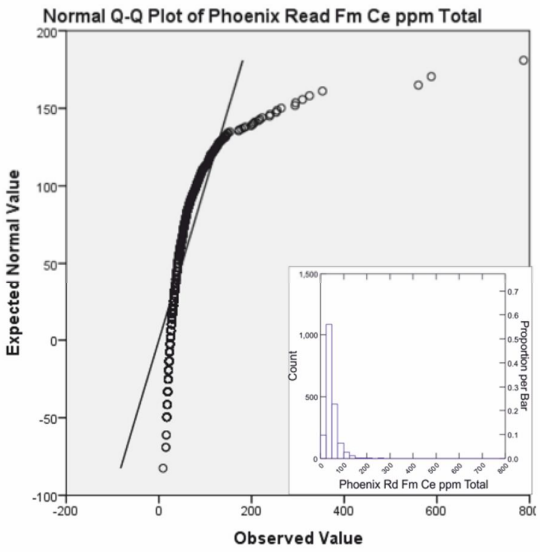
Normal Q-Q Plot of Phoenix Read Fm Ce ppm Total
Expected Normal Value
Observed Value
Phoenix Rd Fm Ce ppm Total
Count
Proportion per Bar

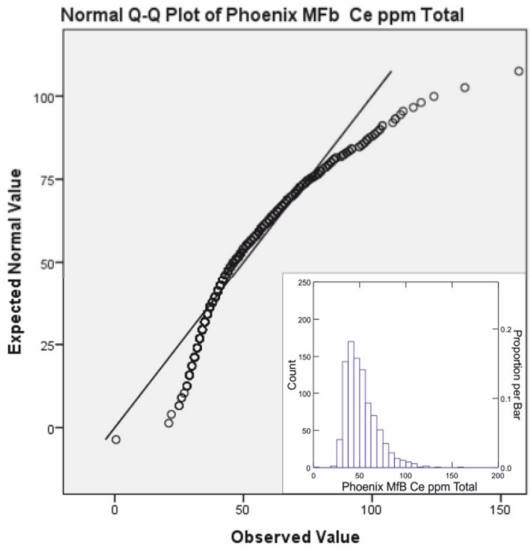
Normal Q-Q Plot of Phoenix MFb Ce ppm Total
Expected Normal Value
Observed Value
Phoenix MfB Ce ppm Total
Count
Proportion per Bar

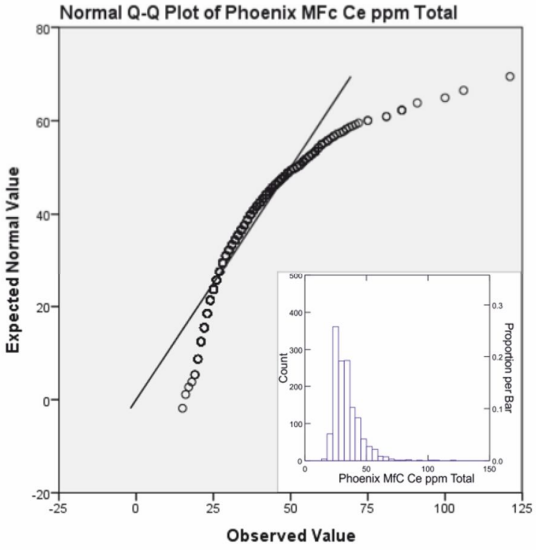
Normal Q-Q Plot of Phoenix MFc Ce ppm Total
Expected Normal Value
Observed Value
Phoenix MfC Ce ppm Total
Count
Proportion per Bar

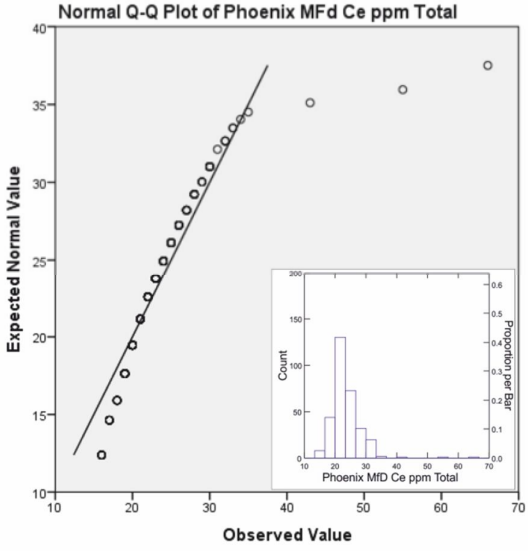
Normal Q-Q Plot of Phoenix MFd Ce ppm Total
Expected Normal Value
Observed Value
Phoenix MfD Ce ppm Total
Count
Proportion per Bar

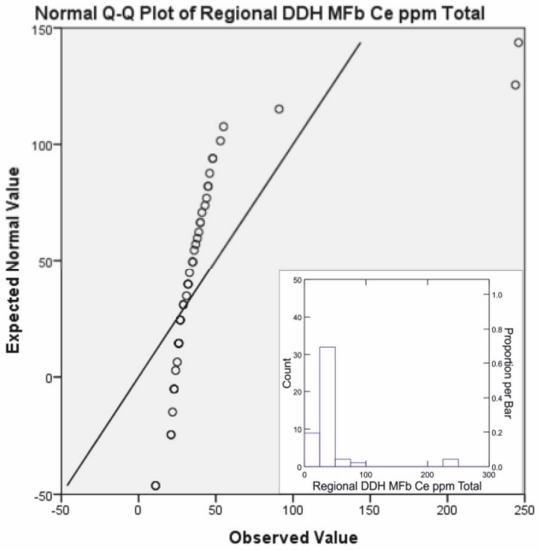
Normal Q-Q Plot of Regional DDH MFb Ce ppm Total
Expected Normal Value
Observed Value
Regional DDH MFb Ce ppm Total
Count
Proportion per Bar

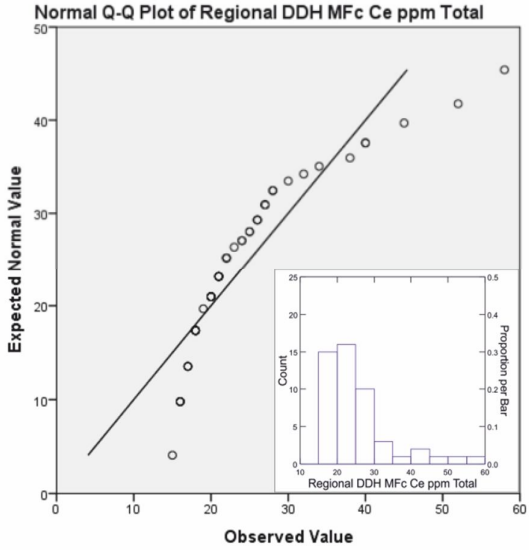
Normal Q-Q Plot of Regional DDH MFc Ce ppm Total
Expected Normal Value
Observed Value
Regional DDH MFc Ce ppm Total
Count
Proportion per Bar

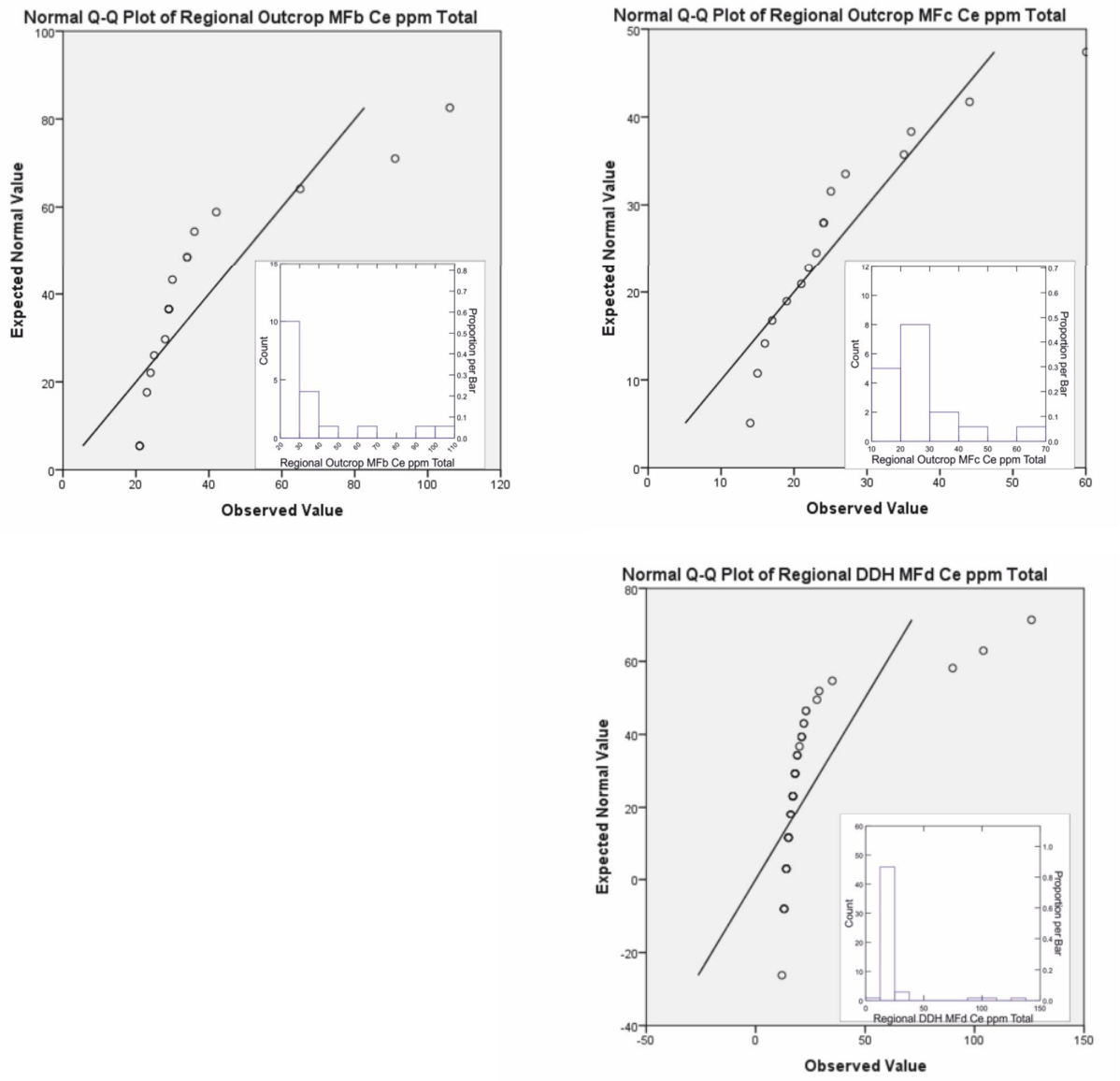

Figure 33: Q-Q and histogram (insets) plots of total digestion cerium values from regional outcrop, regional DDH and sandstones overlying the Phoenix deposit.

Tungsten

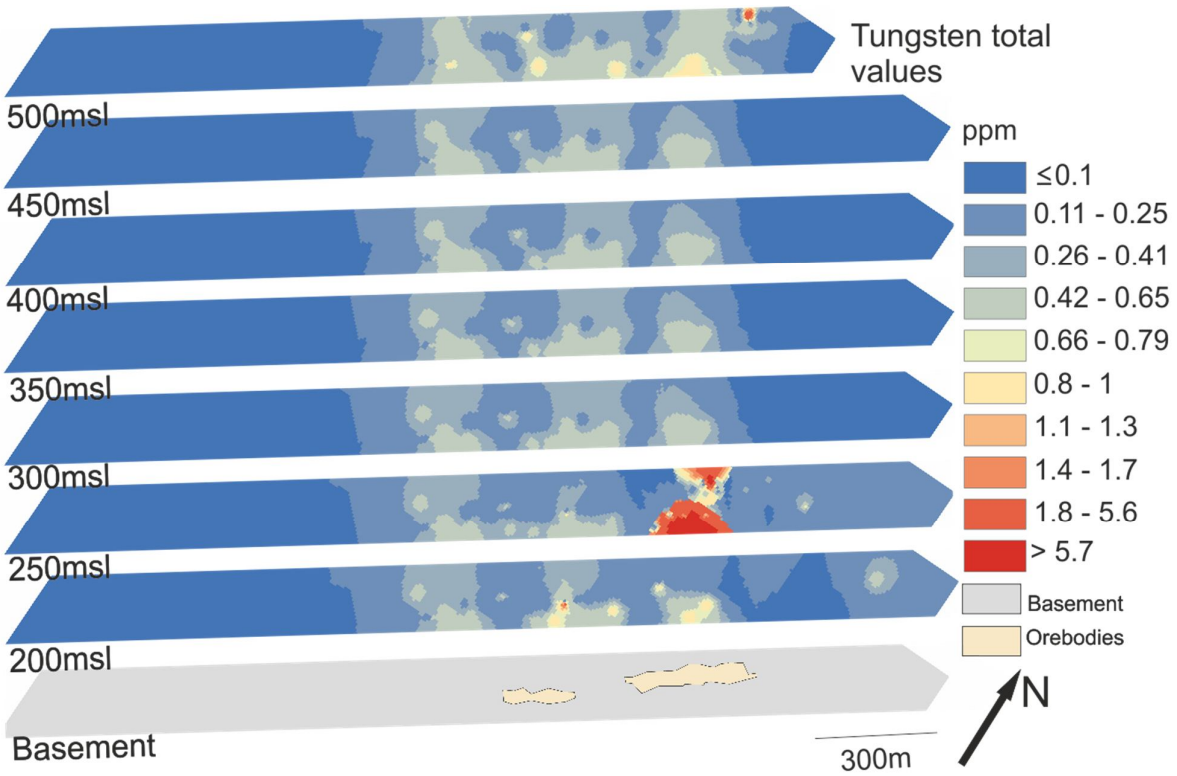

Figure 34: Total digestions tungsten values from sandstone overlying the Phoenix deposit. Detection limit of 0.1ppm W. Median values include values at detection limit. MFb median: 0.1ppm W, σ: 1.82 ppm, MFc median: 0.1ppm W, σ: 0.26 ppm, MFd median: 0.1ppm W, σ: 0.47 ppm.

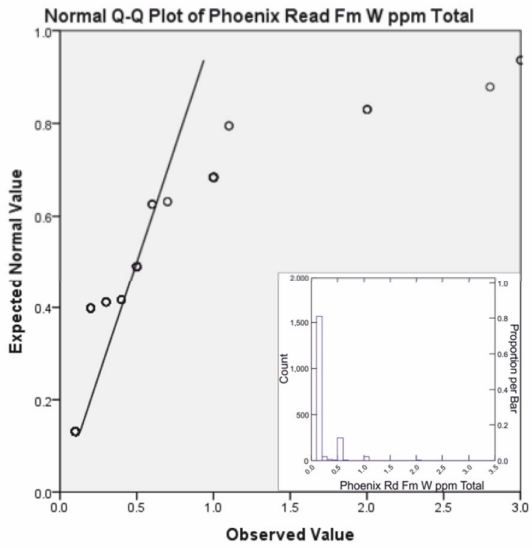
Normal Q-Q Plot of Phoenix Read Fm W ppm Total
Expected Normal Value
Observed Value
Count
Proportion per Bar
Phoenix Rd Fm W ppm Total

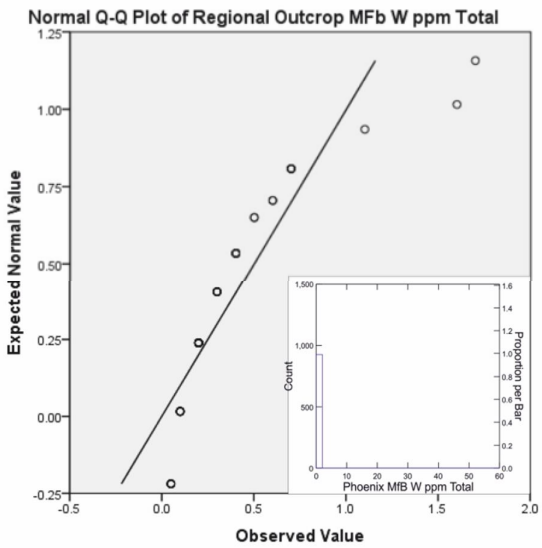
Normal Q-Q Plot of Regional Outcrop MFb W ppm Total
Expected Normal Value
Observed Value
Count
Proportion per Bar
Phoenix MfB W ppm Total

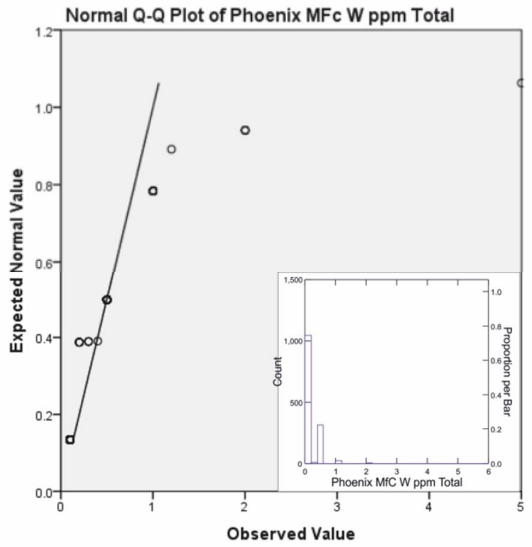
Normal Q-Q Plot of Phoenix MFc W ppm Total
Expected Normal Value
Observed Value
Count
Proportion per Bar
Phoenix MfC W ppm Total

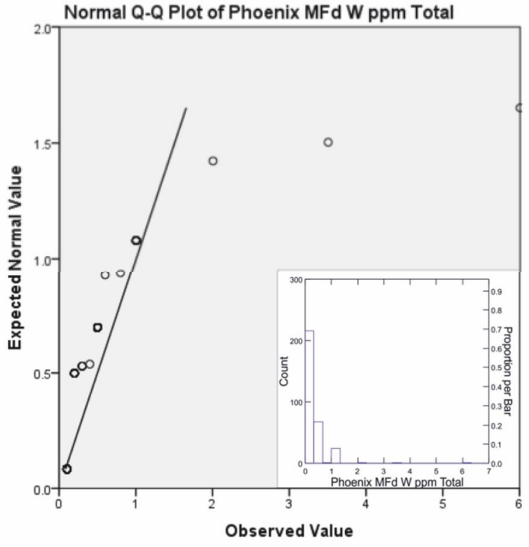
Normal Q-Q Plot of Phoenix MFd W ppm Total
Expected Normal Value
Observed Value
Count
Proportion per Bar
Phoenix MFd W ppm Total

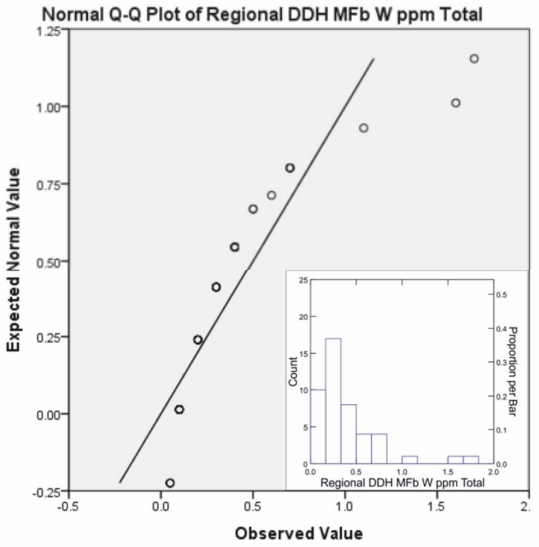
Normal Q-Q Plot of Regional DDH MFb W ppm Total
Expected Normal Value
Observed Value
Count
Proportion per Bar
Regional DDH MFb W ppm Total

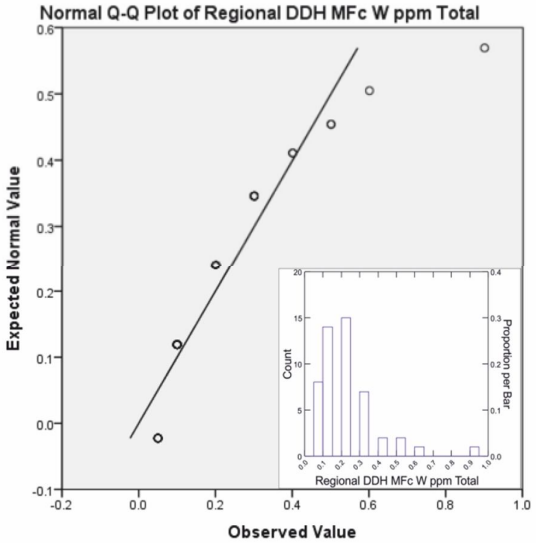
Normal Q-Q Plot of Regional DDH MFc W ppm Total
Expected Normal Value
Observed Value
Count
Proportion per Bar
Regional DDH MFc W ppm Total

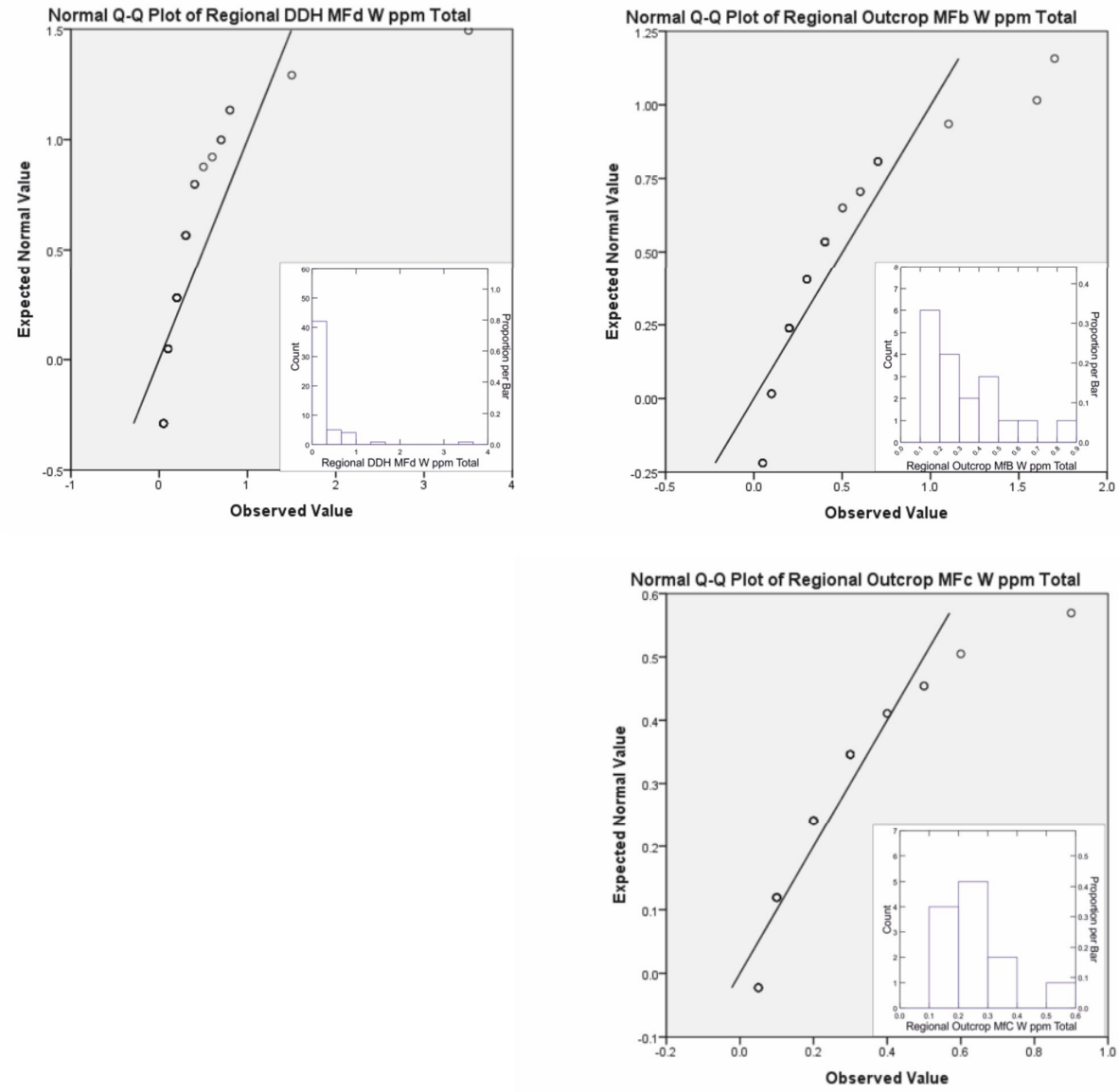

Figure 35: Q-Q and histogram (insets) plots of total digestion tungsten values from regional outcrop, regional DDH and sandstones overlying the Phoenix deposit.

Analysis

Although partial leach uranium values are elevated up to 125m from the deposit, significant areas of elevated values do not extend above 250 msl (Fig. 5). When compared to the MFc regional DDH data (Fig. 6), the Phoenix MFc dataset has a comparable median value, and excluding one 16 ppm U highly elevated value, a smaller range. However, the Phoenix MFc data has a higher population mean (0.34ppm U) and a larger spread in the data than both regional outcrop and DDH data. This is attributed to the single highly elevated value noted above which has skewed the statistics within the MFc.

Partial leach arsenic data yield elevated values in the 250, 300 and 350 msl slices overlying the ore zones, some of which in the 250 msl slice are greatly different, and considerably higher with respect to the regional datasets. While overlying the ore zones, partial leach values in the 200 msl slice are considerably lower than those present at higher msl. Although a cluster of elevated arsenic values is present at the southern extent of the drilling area, it does not contain values that are considerably larger than regional data for any of the Manitou Falls members overlying the Phoenix deposit.

The partial leach cobalt values (Fig. 8) dataset contains numerous elevated values in the sandstones. In particular, elevated values occur: 1) above the northern end of the 'A' ore zone, which has values up to 3 ppm Co at 300msl; and 2) at 400 msl in a multipoint cluster of values (up to 15.2 ppm Co). In comparison to regional data (Fig. 9), the Phoenix cobalt dataset contains elevated values within all the sandstone members, but the highly elevated values overlying ore zone A are concentrated in the MFb member. The Phoenix MFb data has a median of 0.18 ppm and mean of 0.3 ppm Co, while regional outcrop MFb data are significantly lower with a median of 0.02 ppm and a mean of 0.03 ppm Co. The difference between the values of σ for both is also significant, 0.304 and 0.1ppm, respectively.

Partial leach copper concentrations exhibit similar distributions as the partial leach uranium data, with localized, elevated values over the ore zones in the 200 and 250 msl slices (Fig. 10). In relation to regional DDH and outcrop data, partial leach copper values overlying the Phoenix deposit are elevated in all members of the sandstone column, particularly in the MFb member (Fig. 11).

Partial leach molybdenum values (Fig. 12) are weakly elevated in the 200 msl and 250 msl slices overlying the ore zones. Within these slices, there are also numerous single point values above the ore zones that are elevated relative to the regional datasets (Fig. 13 – box whisker plot). At 450msl a single highly elevated point exists, although with no apparent spatial correlation to the ore zones or the major shear structures.

Partial leach nickel values are elevated in the 200 msl slice, with the majority of the slice yielding elevated values with respect to the regional MFb datasets (Fig. 14). These elevated values also extend up to the 300 msl slice directly overlying ore zone A (Fig. 15). The one data point which falls within the MFb contains only 0.48 ppm Ni, while the rest of the MFb over Phoenix contains a mean of 1.78ppm, in contrast to the slice mean of 3.6 ppm. While regional MFb data has a mean of 0.145ppm, regional data for the RD is not available. Overall, nickel concentrations are considerably higher than the regional values over the Phoenix deposit in the MFb and MFc

members, with median and mean values 7.7 times and 9.8 times greater than the regional MFb data, respectively, and a median value 10 times greater than the regional MFc data.

Vanadium concentrations determined by total digestion display a different behaviour than the aforementioned elements. Although there is a small area of elevated values to the north of the ore zones, directly above the ore zones there is no substantial elevation in values (Fig. 16). At 300 msl, values are consistently higher throughout the slice, extending through the sedimentary package into three areas of elevated values at 400 msl.

Partial leach lead concentrations are highly variable in the sandstone units immediately above the ore zones. A 'chimney' of elevated values appears to rise from the ore zones discontinuously to 350 msl, then extend laterally (Fig. 18). While elevated relative to the adjacent slices, the lead concentrations in the chimney are comparable to the regional MFc and MFb datasets. Greatly elevated lead values are present above the 'B' zone at 450 msl, although closer to the surface, at 500 msl, the mean value is lower than the regional mean values for the MFd (Card et al., 2011).

Elevated total digestion magnesium values (Fig. 20) appear to form broad 'chimneys' to the north and south of the ore zones that are considerably higher when compared to the regional datasets. Between 300 and 350 msl, elevated, values do occur over the B ore zone and appear to link with elevated data points in the 400 and 450 msl slices.

Total digestion lithium concentrations are slightly elevated above the orebodies (Fig. 22) and include many multipoint areas of elevated values. This distribution is similar to cobalt, with elevated values to the southwest of the ore zones and elevated values throughout the MFb and MFc members. To the north of the 'A' ore zone, there is a cluster of multipoint, elevated values extending up from the basement to the 250 msl slice. In comparison to the regional data, lithium is elevated in the MFb and MFc members over the Phoenix deposit, but lower in the MFd.

Boron fusion data displays clear 'chimneys' composed of elevated values rising from the vicinity of the ore zones and which extend above the 450 msl slice. The most notable area of greatly elevated values are directly above the northern terminus of the 'B' ore zone and the southern terminus of 'A' ore zone, with two smaller minor multipoint areas of elevated valuesrising from the north of the 'A' ore zone. At 200 msl, boron values are lower (relative to the rest of the slice) directly above the ore zones.

The distribution of total digestion aluminium oxide values (Fig. 25) form features similar to lithium and cobalt concentrations, with a southwesterly trend of elevated values comprised of single point elevated values extending through the MFb, MFc and MFd members. Also, the

aluminium oxide concentrations mirror the behaviour of MgO and B, with a zone of lower values directly overlying the ore zones in the 200 and 400 msl slices. In comparison to regional values, Al_2O_3 is consistently elevated overlying the Phoenix deposit, particularly within the MFc member where it has a much higher median value when compared to regional data (1.68 versus 0.68 wt.% Al_2O_3, respectively) and mean (1.819 wt.% versus 0.9 wt.% Al_2O_3).

Total digestion yttrium values (Fig. 27) exhibit three, multipoint vertical areas of elevated values that extend from directly above the ore zones through the sandstone in large 'chimneys' to the near surface. It should be noted that the values which form the vertical features in Y are considerably higher than the detection limit, indicating these features are not a relic of the differing detection limits within the two differing analyses. Values throughout the rest of the slices are low (typically below 1ppm Y). Despite these chimneys, the mean Y values above the Phoenix deposit are lower than the regional DDH and outcrop mean values (Fig.28); with the Phoenix Y total from the MFb having a mean of 1.46ppm, and the regional outcrop data and DDH data having means of 3.96ppm and 4.95ppm respectively. In the MFc the low values of the data surrounding Phoenix are more apparent; with the mean from Phoenix (1.38ppm) lower than all values from the regional DDH and outcrop data.

Potassium oxide concentrations, determined by total digestion (Fig. 29), display highly elevated values in the 250, 300 and 350 msl slices. Overall the high values of potassium oxide in the sandstones analysed as part of this study match the observed (via Short Wave Infrared spectrometry; SWIR) distribution of illite in the sandstones and as such, could be treated as a proxy for illite. A vertical column of lower values (relative to the Phoenix dataset) overlies the ore zones, extending from the basement to the 400 msl slice. Overall, when compared to the regional data (Fig. 30) potassium oxide concentrations overlying the Phoenix deposit are elevated, with median values in the MFc double that of regional data and a much greater variance, with σ of 0.218 for MFc Phoenix data, versus σ of 0.039 for the MFc regional data.

Cerium total digestion values (Fig. 31) exhibit elevated values overlying the northern part of the 'A' ore zone and which extend to the 250msl slice. Elevated values sporadically continue up to 400msl to the south of the ore zones in the 300 and 350 msl slices. When compared to regional data (Fig. 32) cerium concentrations are elevated, with population mean and median values all greater than the regional data.

Tungsten total digestion data displays a pattern similar to yttrium, with well-defined vertical columns extending from the lowest slice to the near surface, these columns are at values close to detection limit, and thus their level of spatial and statistical robustness is questionable. In the MFb,

there are many highly elevated values with up to 52 ppm W. While there are insufficient data in the Phoenix dataset for formal statistical comparisons of the Phoenix deposit with the regional datasets, generally the sandstones overlying the Phoenix deposit contain considerably lower tungsten concentrations then the regional data, an observation which is also noted with Y (Fig. 23).

Discussion

The Phoenix deposit is associated with a basement shear zone (the WS Shear) that has dip of 55° to the southeast in the basement and splays into a number of small faults in the overlying sandstones (Arseneau and Revering, 2010). The basement fault may have been a major fluid pathway and the fault splays in the sandstones may have focused fluid movement pre-, syn- and post-ore formation (Arseneau and Revering, 2010; this study). Drilling at the Phoenix deposit was centred on the ore zones, with the majority of inclined DDH angled towards the northeast. Consequently there are few DDH and geochemical data which intersect the WS Shear.

Since there are no major lithological differences between different sandstone members (Yeo et al., 2007), distribution of the elevated values in the geochemistry should not reflect lithological changes between the Manitou Falls members. For certain elements, this lack of stratigraphic control is supported by the presence of elevated values within the geochemistry that extend across member transitions (e.g., partial leach U values in the 300msl slice occur in both the MFb and the MFc members; Table 1). However the distribution of some elements does appear to reflect boundaries between sandstone members. For instance, highly elevated concentrations of aluminium (values containing greater than 4 wt% Al_2O_3), terminate at 350 msl, which is the transition between the MFc and MFb members. In this study, XRD, SWIR and thin section analysis has indicated abundant interstitial clays in samples with elevated Al_2O_3 contents. The sandstones overlying the Phoenix deposit contain considerably higher Al_2O_3 values within the MFb (median 0.12wt% mean: 0.15 wt.% Al_2O_3; Fig 26A) and MFc (median: 0.14 wt.% and mean: 0.22 wt.% Al_2O_3; Fig. 26B) than the regional datasets.

The sample containing highly elevated lead at 450 msl, over 250m above the ore zones, is also elevated in uranium (partial), zinc (partial), vanadium (partial) and copper (partial), elements which have elevated concentrations within the ore zones (Arseneau and Revering, 2010). The sample of highly elevated 27ppm As (partial) in the MFd sandstone is also elevated in also cobalt (partial), nickel (partial), lead (partial), bismuth (partial), vanadium (partial) and REEs. The present study indicates that bulk rock geochemistry and interpolations of laterally continuous, subsurface datasets can indicate the potential pathways of elements associated with mineralization. This study does have limitations, in that the behaviour of elements and potential structures away from the

drilling area (including the shallow projection of the shear) are unknown, and that elevated values and trends observed in this study may be part of a regional alteration trend which has no relationship to the Phoenix deposit. For example, elevated values of boron may be part of the regional trend of tourmaline alteration and elevated values of K_2O may be derived from a regional illite trend (Earle and Sopuck, 1989). Low values of elements associated with alteration, such as B, MgO, Al and K, directly above the deposits are interpreted to reflect intense silicification in the sandstones.

The mean yttrium concentrations in sandstones overlying the Phoenix deposit are, although forming a definite feature considerably lower than regional DDH and regional outcrop data. MgO, locally associated with the intense chlorite (and to a lesser extend tourmaline) alteration around the Phoenix deposit, yields elevated values in relation to regional data. Al_2O_3 contents are also elevated when compared to regional data, reflecting the widespread presence of clay alteration. Compared to the regional DDH and outcrop data, there are significant elevations in the majority of elements in the MFb and MFc sandstones overlying the Phoenix deposit. However, a number of elements have lower than regional averages in the MFd (i.e., As, Ni, Pb, Li and K). This may record property-scale leaching during formation of the deposit in these elements and that any subsequent enrichment in these elements derived from Phoenix deposit has not reached the MFd unit. Cu, Co, Ce, MgO and Al_2O_3 are enriched across the whole dataset relative to regional DDH and outcrop data.

Implications for Exploration

Geospatial analysis sandstone lithogeochemical data from sandstones overlying the Phoenix deposit indicates that a number of elements do form geochemically elevated features which not only reflect the alteration mineralogy (Mg and B) but also remobilization of 'pathfinder' elements as reported from unconformity-related uranium deposits (W, LREE, Co, Cu and Pb; Jefferson et al., 2007). However, very high concentrations of certain elements (e.g. Ni and As) do not necessarily directly overlie the ore zones, possibly indicated a structural control not captured in the present study. Furthermore, some elements exhibit well-defined features directly above mineralization, but with values below the regional DDH and outcrop mean values, possibly indicating localized depletion then remobilization. Overall, the preliminary results of this study indicate that certain elements can play a guiding role in the exploration of unconformity-related uranium deposits.

Acknowledgements

This study was made possible through funding from Natural Resources of Canada, Targeted Geoscience Initiative Four (TGI-4) program via a grant to KH and a RAP bursary to JD. Denison Mines Corporation graciously provided logistic support to access the property, access to the geochemical database and is thanked for permission to publish the results.

References

Annesley, I.R., Madore, C. and Portella, P., 2005. Geology and thermotectonic evolution of the western margin of the Trans-Hudson Orogen: Evidence from the eastern sub-Athabasca basement, Saskatchewan; Canadian Journal of Earth Sciences, v. 42, p. 573-597.

Arseneau, G. and Revering, C., 2010. Technical Report on the Phoenix Deposit (Zones A & B) – Wheeler River Project, Eastern Athabasca Basin, Northern Saskatchewan, Canada; NI 43-101 technical report prepared for Denison Mines Corp., SRK Consulting.

Bartier, P.M. and Kelley, C.P., 1996. Multivariate interpolation to incorporate thematic surface data using inverse distance weighting (IDW); Computers and Geosciences, v.22, p. 795-799

Bosman, S.A. and Korness, J., 2007. Building Athabasca stratigraphy; revising, redefining, and repositioning; in Summary of Investigations 2007, Volume 2, Saskatchewan Geological Survey, Saskatchewan Ministry of Energy and Resources, Misc. RE. 2007-4.2, CD-ROM, Paper A-8, 29p.

Bosman S.A. and Card, C. D., 2012. Geochemical Analyses of Athabasca Group Drillholes in Saskatchewan (NTS 64L, 74F to 74K, and 74N to 74P) – Supplementary to Data File Reports 24, 29, and 30; Saskatchewan Geological Survey Data File Series DF31: http://www.er.gov.sk.ca/DF31

Card, C.D., Bosman, S.A., Slimmon, W.L., Zmetana, D.J. and Delaney, G.D., 2011. Geochemical Analyses of Athabasca Group Outcrops in Saskatchewan (NTS 64L, 74F to 74K, and 74N to 74P); Saskatchewan Geological Survey Data File Series DF30: http://www.er.gov.sk.ca/DF30

Earle, S. and Sopuck, V.J., 1989. Regional lithogeochemistry of the eastern part of the Athabasca Basin uranium province, Saskatchewan, Canada; in Uranium Resources and Geology of North America; IAEA-TECDOC-500, p.264-296.

Grunsky, E.C., 2010. The interpretation of geochemical survey data; Geochemistry: Exploration, Environment, Analysis v. 10, p. 27–74.

Jefferson, C.W., Thomas, D.J., Gandhi, S.S., Ramaekers, P., Delaney, G., Brisbin, D., Cutts, C., Portella, P. and Olson, R.A., 2007. Unconformity-associated uranium deposits of the Athabasca basin, Saskatchewan and Alberta; in EXTECH IV: Geology and Uranium EXploration TECHnology of the Proterozoic Athabasca Basin, Saskatchewan and Alberta, (eds.) C.W. Jefferson and G. Delaney; Geological Survey of Canada Bulletin 588, p. 23-67.

Kane, V., Begovich, C., Butz, T. and Myers, D.E., 1982. Interpretation of regional geochemistry; Computers and Geoscience v.8, p. 117-136

Kerr, W.C., 2010. The Discovery of the Phoenix Deposit: a New High-Grade, Athabasca Basin Unconformity-Type Uranium Deposit, Saskatchewan, Canada; Society of Economic Geologists, Special Publication 15, p. 703-728.

Ramaekers, P., Jefferson, C.W., Yeo, G.M., Collier, B., Long, D.G.F., Drever, G., McHardy, S., Jiricka, D., Cutts, C., Wheatley, K., Catuneanu, O., Bernier, S., Kupsch, B. and Post, R.T., 2007. Revised geological map and stratigraphy of the Athabasca Group, Saskatchewan and Alberta; in EXTECH IV: Geology and Uranium EXploration TECHnology of the Proterozoic Athabasca Basin, Saskatchewan and Alberta, (eds.) C.W. Jefferson and G. Delaney; Geological Survey of Canada Bulletin 588, p. 155-191.

Roscoe, W.E. 2012. Technical report on a mineral Resource estimate update for the Phoenix uranium deposits, Wheeler river project, Eastern Athabasca basin, Northern Saskatchewan, Canada; NI 43-101 Report prepared for Denison Mines Corp.

Yeo, G.M., Jefferson, C.W. and Ramaekers, P., 2007. Comparison of lower Athabasca Group stratigraphy among depositional systems, Saskatchewan and Alberta, in EXTECH IV: Geology and Uranium EXploration TECHnology of the Proterozoic Athabasca Basin, Saskatchewan and Alberta, (eds.) C.W. Jefferson and G. Delaney; Geological Survey of Canada Bulletin 588, p.465-488.

Zhang, C., Fay, D., McGrath, D., Grennan, E. and Carton, O.T., 2008. Statistical analyses of geochemical variables in soils of Ireland; Geoderma v.146, p. 378–390.

Appendix 2 Sample Locations

2.1	Whole Drillcore Sample Locations	177
2.2	Thin section and SEM sample locations	184

Appendix 2.1: Drill core Sample Locations

A total of 299 samples were collected from 28 drill cores located directly above, below, around and up to 1.8 km from the Phoenix Deposit A and B zones, including 97 basement samples and 202 sandstone samples. Basement samples were hydrothermally altered metasedimentary rocks, pegmatite and quartzite, while the sandstone samples collected were variably altered, silicified and fractured, no samples were collected from the ore zone due to restrictions on taking radioactive material off site.

Samples have been collected over two periods; the majority of basement samples and some sandstone samples (JD1A-JD4A, DPX1-DPX88 and the WS Shear and WS Shear Extension samples) were collected in early September 2011, while the second, sandstone dominated samples (DPX100+) were collected August 2012. Where necessary, samples were split into subsamples based on their composition, texture and features:

Sample Number (DPX)	**Drill core Collar Number**	**Depth Down Core**	**Latitude**	**Longitude**	**Inclination of Drillhole**	**Lithology (sandstone or basement)**
JD1A	***WR-267***	498.52	477137.1	6374123.947	-80	Basement
JD2A	***WR-273***	492.53	477274.4	6374221.78	-80	Basement
JD5A	***WR-281***	464.7	477216.8	6374280.633	-90	Basement
DPX001	***WR-408***	457.25	Drillcore location unknown		-90	Basement
DPX002	***WR-408***	456.3	Drillcore location unknown		-90	Basement
DPX003	***WR-408***	455.15	Drillcore location unknown		-90	Basement
DPX004	***WR-383***	454.2	477278.5	6374284.557	-90	Basement
DPX005	***WR-383***	453.25	477278.5	6374284.557	-90	Basement
DPX006	***WR-376***	452.3	477270.9	6374290.41	-90	Basement
DPX007	***WR-376***	451.75	477270.9	6374290.41	-90	Basement
DPX008	***WR-376***	451.24	477270.9	6374290.41	-90	Basement
DPX009	***WR-376***	450.28	477270.9	6374290.41	-90	Basement
DPX010	***WR-376***	449.2	477270.9	6374290.41	-90	Basement
DPX011	***WR-376***	448.48	477270.9	6374290.41	-90	Basement
DPX012	***WR-376***	447.37	477270.9	6374290.41	-90	Basement
DPX013	***WR-376***	447.27	477270.9	6374290.41	-90	Basement
DPX014	***WR-376***	446.75	477270.9	6374290.41	-90	Basement
DPX015	***WR-376***	446.55	477270.9	6374290.41	-90	Basement
DPX016	***WR-332***	445.7	477246.9	6374329.761	-90	Basement
DPX017	***WR-332***	444.8	477246.9	6374329.761	-90	Basement
DPX018	***WR-332***	443.8	477246.9	6374329.761	-90	Basement
DPX019	***WR-332***	442.8	477246.9	6374329.761	-90	Basement
DPX020	***WR-332***	442.5	477246.9	6374329.761	-90	Basement
DPX021	***WR-332***	441.52	477246.9	6374329.761	-90	Basement
DPX022	***WR-332***	440.5	477246.9	6374329.761	-90	Basement
DPX023	***WR-332***	439.7	477246.9	6374329.761	-90	Basement
DPX024	***WR-332***	436.41	477246.9	6374329.761	-90	Basement
DPX026A	***WR-300***	434.6	477252.5	6374320.921	-90	Basement
DPX026B	***WR-300***	434.37	477252.5	6374320.921	-90	Basement
DPX027	***WR-300***	432.4	477252.5	6374320.921	-90	Basement
DPX030	***WR-282***	428.62	477230.3	6374267.377	-90	Basement
DPX031	***WR-282***	428.6	477230.3	6374267.377	-90	Basement
DPX032	***WR-282***	428.51	477230.3	6374267.377	-90	Basement
DPX033	***WR-282***	428.51	477230.3	6374267.377	-90	Basement

DPX034	***WR-282***	428	477230.3	6374267.377	-90	Basement
DPX035	***WR-282***	427.26	477230.3	6374267.377	-90	Basement
DPX036	***WR-282***	426.67	477230.3	6374267.377	-90	Basement
DPX037	***WR-282***	424.5	477230.3	6374267.377	-90	Basement
DPX038	***WR-282***	424	477230.3	6374267.377	-90	Basement
DPX039	***WR-282***	421.3	477230.3	6374267.377	-90	Basement
DPX040	***WR-282***	421.14	477230.3	6374267.377	-90	Basement
DPX041	***WR-282***	420.87	477230.3	6374267.377	-90	Basement
DPX042	***WR-282***	420.6	477230.3	6374267.377	-90	Basement
DPX043	***WR-282***	418.4	477230.3	6374267.377	-90	Basement
DPX044	***WR-282***	418.35	477230.3	6374267.377	-90	Basement
DPX045	***WR-282***	416.6	477230.3	6374267.377	-90	Basement
DPX046	***WR-282***	416.06	477230.3	6374267.377	-90	Basement
DPX047	***WR-282***	415.77	477230.3	6374267.377	-90	Basement
DPX048	***WR-282***	415.6	477230.3	6374267.377	-90	Basement
DPX049	***WR-282***	415.25	477230.3	6374267.377	-90	Basement
DPX050	***WR-282***	415	477230.3	6374267.377	-90	Basement
DPX051	***WR-282***	414.98	477230.3	6374267.377	-90	Basement
DPX052	***WR-282***	414.82	477230.3	6374267.377	-90	Basement
DPX053	***WR-349***	414.77	477239.5	6374276.126	-90	Basement
DPX054	***WR-349***	413.47	477239.5	6374276.126	-90	Basement
DPX055a	***WR-349***	412.16	477239.5	6374276.126	-90	Basement
DPX55b	***WR-349***	411.9	477239.5	6374276.126	-90	Basement
DPX056	***WR-349***	410.26	477239.5	6374276.126	-90	Basement
DPX057	***WR-349***	407.82	477239.5	6374276.126	-90	Basement
DPX058	***WR-349***	407.71	477239.5	6374276.126	-90	Basement
DPX059	***WR-358***	407.46	476411	6373597.99	-80	Basement
DPX060	***WR-358***	403.6	476411	6373597.99	-80	Basement
DPX061	***WR-358***	403.2	476411	6373597.99	-80	Basement
DPX062	***WR-358***	403.1	476411	6373597.99	-80	Basement
DPX063	***WR-358***	403.1	476411	6373597.99	-80	Basement
DPX064	***WR-358***	402.89	476411	6373597.99	-80	Basement
DPX065	***WR-256***	402.5	476895.6	6373957.076	-80	Basement
DPX066	***WR-263***	401.28	476724.2	6373776.442	-80	Basement
DPX067	***WR-408***	400.77	Drillcore location unknown			Basement
DPX068	***WR-329***	400.77	477210.4	6374287.242	-90	Basement
DPX069	***WR-329***	400.05	477210.4	6374287.242	-90	Basement
DPX070	***WR-329***	399.17	477210.4	6374287.242	-90	Sandstone
DPX070	***WR-329***	382.9	477210.4	6374287.242	-90	Sandstone
DPX071	***WR-329***	373	477210.4	6374287.242	-90	Sandstone
DPX072	***WR-329***	371.46	477210.4	6374287.242	-90	Sandstone
DPX073	***WR-329***	367.3	477210.4	6374287.242	-90	Sandstone
DPX074	***WR-329***	360.7	477210.4	6374287.242	-90	Sandstone
DPX075	***WR-301***	358.58	477186.5	6374281.308	-90	Sandstone
DPX076	***WR-301***	358.58	477186.5	6374281.308	-90	Sandstone
DPX077	***WR-301***	344.05	477186.5	6374281.308	-90	Sandstone
DPX078	***WR-315***	321.4	477078	6374186.808	-90	Sandstone
DPX079	***WR-256***	303.45	476895.6	6373957.076	-80	Sandstone
DPX080	***WR-293***	301.4	476833.1	6373965.354	-90	Sandstone

DPX081	***WR-293***	300.9	476833.1	6373965.354	-90	Sandstone
DPX082	***WR-293***	288.06	476833.1	6373965.354	-90	Sandstone
DPX083	***WR-293***	418.4	476833.1	6373965.354	-90	Basement
DPX084	***WR-358***	371	476411	6373597.99	-80	Sandstone
DPX085	***WR-387***	253	Drillcore location unknown			Sandstone
DPX086	***WR-257***	250.5	476597	6373808	-90	Sandstone
DPX100	***WR-347***	409.5	476939.8	6374023.04	-90	Basement
DPX101	***WR-347***	413.6	476939.8	6374023.04	-90	Basement
DPX102	***WR-367***	487.4	473721.3	6372425.61	-80	Basement
DPX103	***WR-367***	425.7	473721.3	6372425.61	-80	Basement
DPX104	***WR-317***	430	476193.2	6373381.6	-80	Basement
DPX105	***WR-317***	407.4	476193.2	6373381.6	-80	Basement
DPX106	***WR-325***	544.3	477378.3	6374267.599	-75	Basement
DPX107	***WR-325***	546.2	477378.3	6374267.599	-75	Basement
DPX108	***WR-366***	372	477290.3	6374315.498	-90	Sandstone
DPX109	***WR-366***	427.6	477290.3	6374315.498	-90	Basement
DPX110	***WR-371***	550.7	477644.2	6375374.839	-76	Basement
DPX111	***WR-371***	555.2	477644.2	6375374.839	-76	Basement
DPX112	***WR-374***	374.8	476402.6	6373668.494	-90	Sandstone
DPX113	***WR-380***	352.3	475931.6	6373230.64	-80	Sandstone
DPX114	***WR-367***	535.73	473721.3	6372425.61	-80	Basement
DPX115	***WR-337***	421.8	477272.6	6374342.769	-90	Basement
DPX116	***WR-320***	502.6	477623.3	6374313.857	-80	Basement
DPX117	***WR-320***	488.9	477623.3	6374313.857	-80	Basement
DPX118	***WR-320***	487	477623.3	6374313.857	-80	Basement
DPX119	***WR-285***	423.6	477424.9	6374348.685	-90	Basement
DPX120	***WR-285***	428.2	477424.9	6374348.685	-90	Basement
DPX121	***WR-285***	433.4	477424.9	6374348.685	-90	Basement
DPX122	***WR-285***	436.3	477424.9	6374348.685	-90	Basement
DPX123	***WR-296***	501.7	477424.9	6374348.685	-90	Basement
DPX124	***WR-296***	455	477429.8	6374343.566	-90	Basement
DPX125	***WR-294***	411.6	476855.4	6373972.1	-90	Basement
DPX127	***WR-380***	88.1	475931.6	6373230.64	-80	Sandstone
DPX128	***WR-380***	146.5	475931.6	6373230.64	-80	Sandstone
DPX129	***WR-380***	187.7	475931.6	6373230.64	-80	Sandstone
DPX130	***WR-380***	190.8	475931.6	6373230.64	-80	Sandstone
DPX131	***WR-380***	216.4	475931.6	6373230.64	-80	Sandstone
DPX132	***WR-380***	202.8	475931.6	6373230.64	-80	Sandstone
DPX133	***WR-380***	270	475931.6	6373230.64	-80	Sandstone
DPX134	***WR-380***	308.3	475931.6	6373230.64	-80	Sandstone
DPX135	***WR-380***	313.8	475931.6	6373230.64	-80	Sandstone
DPX136	***WR-380***	320.2	475931.6	6373230.64	-80	Sandstone
DPX137	***WR-380***	282.2	475931.6	6373230.64	-80	Sandstone
DPX138	***WR-380***	268.8	475931.6	6373230.64	-80	Sandstone
DPX139	***WR-380***	270.7	475931.6	6373230.64	-80	Sandstone
DPX140	***WR-380***	220.8	475931.6	6373230.64	-80	Sandstone
DPX141	***WR-380***	70.2	475931.6	6373230.64	-80	Sandstone
DPX142	***WR-380***	28.2	475931.6	6373230.64	-80	Sandstone
DPX143	***WR-380***	34.7	475931.6	6373230.64	-80	Sandstone

DPX144	***WR-380***	62.7	475931.6	6373230.64	-80	Sandstone
DPX145	***WR-380***	326.8	475931.6	6373230.64	-80	Sandstone
DPX146	***WR-284***	100.3	477424.9	6374348.685	-90	Sandstone
DPX147	***WR-284***	94.5	477424.9	6374348.685	-90	Sandstone
DPX148	***WR-277***	278.7	477386.6	6374321.92	-82	Sandstone
DPX149	***WR-277***	282	477386.6	6374321.92	-82	Sandstone
DPX150	***WR-277***	240	477386.6	6374321.92	-82	Sandstone
DPX151	***WR-277***	203.3	477386.6	6374321.92	-82	Sandstone
DPX152	***WR-277***	186.5	477386.6	6374321.92	-82	Sandstone
DPX153	***WR-277***	18.1	477386.6	6374321.92	-82	Sandstone
DPX154	***WR-277***	168.7	477386.6	6374321.92	-82	Sandstone
DPX155	***WR-277***	29.9	477386.6	6374321.92	-82	Sandstone
DPX156	***WR-277***	139.1	477386.6	6374321.92	-82	Sandstone
DPX157	***WR-277***	58.9	477386.6	6374321.92	-82	Sandstone
DPX158	***WR-277***	50.4	477386.6	6374321.92	-82	Sandstone
DPX159	***WR-277***	84.9	477386.6	6374321.92	-82	Sandstone
DPX160	***WR-277***	90.7	477386.6	6374321.92	-82	Sandstone
DPX161	***WR-277***	111.7	477386.6	6374321.92	-82	Sandstone
DPX162	***WR-277***	114.3	477386.6	6374321.92	-82	Sandstone
DPX163	***WR-277***	123	477386.6	6374321.92	-82	Sandstone
DPX167	***WR-277***	46.3	477386.6	6374321.92	-82	Sandstone
DPX168	***WR-277***	104.1	477386.6	6374321.92	-82	Sandstone
DPX169	***WR-277***	174.4	477386.6	6374321.92	-82	Sandstone
DPX170	***WR-277***	187.1	477386.6	6374321.92	-82	Sandstone
DPX171	***WR-379***	403.7	477326.8	6374340.48	-90	Basement
DPX172	***WR-379***	403.1	477326.8	6374340.48	-90	Basement
DPX173	***WR-378***	303.2	475867.4	6373289.918	-80	Sandstone
DPX174	***WR-378***	297.1	475867.4	6373289.918	-80	Sandstone
DPX175	***WR-286***	25.7	477196.9	6374268.244	-90	Sandstone
DPX176	***WR-286***	28.1	477196.9	6374268.244	-90	Sandstone
DPX177	***WR-286***	31.1	477196.9	6374268.244	-90	Sandstone
DPX178	***WR-286***	43.4	477196.9	6374268.244	-90	Sandstone
DPX179	***WR-286***	9	477196.9	6374268.244	-90	Sandstone
DPX180	***WR-286***	46.8	477196.9	6374268.244	-90	Sandstone
DPX181	***WR-286***	57	477196.9	6374268.244	-90	Sandstone
DPX182	***WR-286***	59	477196.9	6374268.244	-90	Sandstone
DPX183	***WR-286***	67.8	477196.9	6374268.244	-90	Sandstone
DPX184	***WR-286***	84.2	477196.9	6374268.244	-90	Sandstone
DPX185	***WR-286***	84.2	477196.9	6374268.244	-90	Sandstone
DPX186	***WR-286***	90.8	477196.9	6374268.244	-90	Sandstone
DPX187	***WR-286***	108.1	477196.9	6374268.244	-90	Sandstone
DPX188	***WR-286***	118.2	477196.9	6374268.244	-90	Sandstone
DPX189	***WR-286***	125.5	477196.9	6374268.244	-90	Sandstone
DPX190	***WR-286***	119.2	477196.9	6374268.244	-90	Sandstone
DPX191	***WR-286***	144.6	477196.9	6374268.244	-90	Sandstone
DPX192	***WR-286***	146.5	477196.9	6374268.244	-90	Sandstone
DPX193	***WR-286***	156.6	477196.9	6374268.244	-90	Sandstone
DPX194	***WR-286***	188.5	477196.9	6374268.244	-90	Sandstone
DPX195	***WR-286***	192.9	477196.9	6374268.244	-90	Sandstone

DPX196	***WR-286***	185.3	477196.9	6374268.244	-90	Sandstone
DPX197	***WR-286***	211.4	477196.9	6374268.244	-90	Sandstone
DPX198	***WR-286***	22.6	477196.9	6374268.244	-90	Sandstone
DPX199			477196.9	6374268.244	-90	Sandstone
DPX200	***WR-286***	283.3	477196.9	6374268.244	-90	Sandstone
DPX201	***WR-286***	283.5	477196.9	6374268.244	-90	Sandstone
DPX202	***WR-321***	13.7	477039	6374106.044	-90	Sandstone
DPX203	***WR-321***	30.5	477039	6374106.044	-90	Sandstone
DPX204	***WR-321***	31	477039	6374106.044	-90	Sandstone
DPX205	***WR-321***	40.9	477039	6374106.044	-90	Sandstone
DPX206	***WR-321***	71.1	477039	6374106.044	-90	Sandstone
DPX207	***WR-321***	75.2	477039	6374106.044	-90	Sandstone
DPX208	***WR-321***	80.7	477039	6374106.044	-90	Sandstone
DPX209	***WR-321***	94.2	477039	6374106.044	-90	Sandstone
DPX210	***WR-321***	99.6	477039	6374106.044	-90	Sandstone
DPX211	***WR-321***	110.6	477039	6374106.044	-90	Sandstone
DPX212	***WR-321***	127.4	477039	6374106.044	-90	Sandstone
DPX213	***WR-321***	133.7	477039	6374106.044	-90	Sandstone
DPX214	***WR-321***	133.7	477039	6374106.044	-90	Sandstone
DPX215	***WR-321***	134.4	477039	6374106.044	-90	Sandstone
DPX216	***WR-321***	138	477039	6374106.044	-90	Sandstone
DPX217	***WR-321***	144.3	477039	6374106.044	-90	Sandstone
DPX218	***WR-321***	153.3	477039	6374106.044	-90	Sandstone
DPX219	***WR-321***	161.9	477039	6374106.044	-90	Sandstone
DPX220	***WR-321***	170.15	477039	6374106.044	-90	Sandstone
DPX221	***WR-321***	170.3	477039	6374106.044	-90	Sandstone
DPX222	***WR-321***	216.8	477039	6374106.044	-90	Sandstone
DPX223	***WR-321***	227	477039	6374106.044	-90	Sandstone
DPX224	***WR-321***	231.3	477039	6374106.044	-90	Sandstone
DPX225	***WR-321***	234.7	477039	6374106.044	-90	Sandstone
DPX226	***WR-321***	259.8	477039	6374106.044	-90	Sandstone
DPX227	***WR-321***	339	477039	6374106.044	-90	Sandstone
DPX228	***WR-321***	215.3	477039	6374106.044	-90	Sandstone
DPX229	***WR-321***	281.4	477039	6374106.044	-90	Sandstone
DPX230	***WR-321***	183.6	477039	6374106.044	-90	Sandstone
DPX231	***WR-321***	274.7	477039	6374106.044	-90	Sandstone
DPX232	***WR-321***	292.9	477039	6374106.044	-90	Sandstone
DPX233	***WR-321***	293.4	477039	6374106.044	-90	Sandstone
DPX234	***WR-321***	302.2	477039	6374106.044	-90	Sandstone
DPX235	***WR-321***	307.1	477039	6374106.044	-90	Sandstone
DPX236	***WR-321***	327.1	477039	6374106.044	-90	Sandstone
DPX237	***WR-321***	326.6	477039	6374106.044	-90	Sandstone
DPX238	***WR-321***	312.8	477039	6374106.044	-90	Sandstone
DPX239	***WR-321***	361	477039	6374106.044	-90	Sandstone
DPX240	***WR-321***	365.9	477039	6374106.044	-90	Sandstone
DPX241	***WR-321***	364.9	477039	6374106.044	-90	Sandstone
DPX242	***WR-321***	379	477039	6374106.044	-90	Sandstone
DPX243	***WR-321***	373.7	477039	6374106.044	-90	Sandstone
DPX244	***WR-321***	380.4	477039	6374106.044	-90	Sandstone

DPX245	***WR-321***	74.2	477039	6374106.044	-90	Sandstone
DPX246	***WR-321***	80.9	477039	6374106.044	-90	Sandstone
DPX247	***WR-190***	103.5	477197.7	6374018.818	-80	Sandstone
DPX250	***WR-350***	433.4	476789.9	6373918.644	-90	Basement
DPX251	***WR-286***	410.3	477196.9	6374268.244	-90	Basement
DPX252	***WR-286***	411	477196.9	6374268.244	-90	Basement
DPX253	***WR-358***	366.2	476411	6373597.99	-80	Sandstone
DPX254	***WR-341a***	390	476991.4	6374071.139	-90	Sandstone
DPX255	***WR-341a***	403.8	476991.4	6374071.139	-90	Basement
DPX256	***WR-373***	397.5	477326.8	6374340.48	-90	Sandstone
DPX257	***WR-291***	29.2	476860.5	6373963.85	-90	Sandstone
DPX258	***WR-291***	29.8	476860.5	6373963.85	-90	Sandstone
DPX259	***WR-291***	36.8	476860.5	6373963.85	-90	Sandstone
DPX260	***WR-291***	56	476860.5	6373963.85	-90	Sandstone
DPX261	***WR-291***	56.1	476860.5	6373963.85	-90	Sandstone
DPX262	***WR-291***	63	476860.5	6373963.85	-90	Sandstone
DPX263	***WR-291***	66.4	476860.5	6373963.85	-90	Sandstone
DPX264	***WR-291***	85.4	476860.5	6373963.85	-90	Sandstone
DPX265	***WR-291***	88.7	476860.5	6373963.85	-90	Sandstone
DPX266	***WR-291***	86	476860.5	6373963.85	-90	Sandstone
DPX267	***WR-291***	86.7	476860.5	6373963.85	-90	Sandstone
DPX268	***WR-291***	113.3	476860.5	6373963.85	-90	Sandstone
DPX269	***WR-291***	134.1	476860.5	6373963.85	-90	Sandstone
DPX270	***WR-291***	139.4	476860.5	6373963.85	-90	Sandstone
DPX271	***WR-291***	146.5	476860.5	6373963.85	-90	Sandstone
DPX272	***WR-291***	146.9	476860.5	6373963.85	-90	Sandstone
DPX273	***WR-291***	188.3	476860.5	6373963.85	-90	Sandstone
DPX274	***WR-291***	219	476860.5	6373963.85	-90	Sandstone
DPX275	***WR-291***	223.5	476860.5	6373963.85	-90	Sandstone
DPX276	***WR-291***	228	476860.5	6373963.85	-90	Sandstone
DPX277	***WR-291***	236	476860.5	6373963.85	-90	Sandstone
DPX278	***WR-291a***	324.5	476860.5	6373963.85	-90	Sandstone
DPX279	***WR-291a***	641.5	476860.5	6373963.85	-90	Basement
DPX280	***WR-353***	23.55	476710.9	6373854.44	-90	Sandstone
DPX281	***WR-353***	33.6	476710.9	6373854.44	-90	Sandstone
DPX282	***WR-353***	44	476710.9	6373854.44	-90	Sandstone
DPX283	***WR-353***	61.7	476710.9	6373854.44	-90	Sandstone
DPX284	***WR-353***	96.9	476710.9	6373854.44	-90	Sandstone
DPX285	***WR-353***	106.3	476710.9	6373854.44	-90	Sandstone
DPX286	***WR-353***	131.5	476710.9	6373854.44	-90	Sandstone
DPX287	***WR-353***	188.8	476710.9	6373854.44	-90	Sandstone
DPX288	***WR-353***	204.1	476710.9	6373854.44	-90	Sandstone
DPX289	***WR-353***	204.1	476710.9	6373854.44	-90	Sandstone
DPX290	***WR-353***	262	476710.9	6373854.44	-90	Sandstone
DPX291	***WR-353***	277.4	476710.9	6373854.44	-90	Sandstone
DPX292	***WR-353***	325.3	476710.9	6373854.44	-90	Sandstone
DPX293	***WR-353***	326.3	476710.9	6373854.44	-90	Sandstone
DPX294	***WR-353***	358.4	476710.9	6373854.44	-90	Sandstone
DPX295	***WR-359***	312.5	476327.7	6373537.877	-80	Sandstone

DPX296	***WR-296***	313.5	477210.4	6374287.242	-90	Sandstone
WS Shear Samples						
WR281-C	**WR-281**	417.4	477216.8	6374280.633	-90	Basement
WR281-C	**WR-281**	412.7	477216.8	6374280.633	-90	Basement
WR281-A	**WR-281**	410.8	477216.8	6374280.633	-90	Basement
WR282-A	**WR-282**	398.9	477230.3	6374267.377	-90	Basement
WR352-B	**WR-352**	323.8	477174.2	6374272.596	-90	Sandstone
WR404-MFA	**WR-404**	323.3	477116	6374228.763	-90	Sandstone
WR409-B	**WR-409**	319.9	477146.5	6374241.755	-90	Sandstone
WR301-B	**WR-301**	319	477186.5	6374281.308	-90	Sandstone
WR409-A	**WR-409**	317.7	477146.5	6374241.755	-90	Sandstone
WR352-A	**WR-352**	316.2	477174.2	6374272.596	-90	Sandstone
WR315-B	**WR-315**	316	477078	6374186.808	-90	Sandstone
WR301-A	**WR-301**	315	477186.5	6374281.308	-90	Sandstone
WR315-A	**WR-315**	312.8	477078	6374186.808	-90	Sandstone
WR293-B	**WR-293**	251	476833.1	6373965.354	-90	Sandstone
WR293-A	**WR-293**	244.9	476833.1	6373965.354	-90	Sandstone
WR256-B	**WR-256**	224.1	476895.6	6373957.076	-80	Sandstone
WR256-A	**WR-256**	190.7	476895.6	6373957.076	-80	Sandstone

Location of Sampled DDH Drillcore Collars used in this Study.

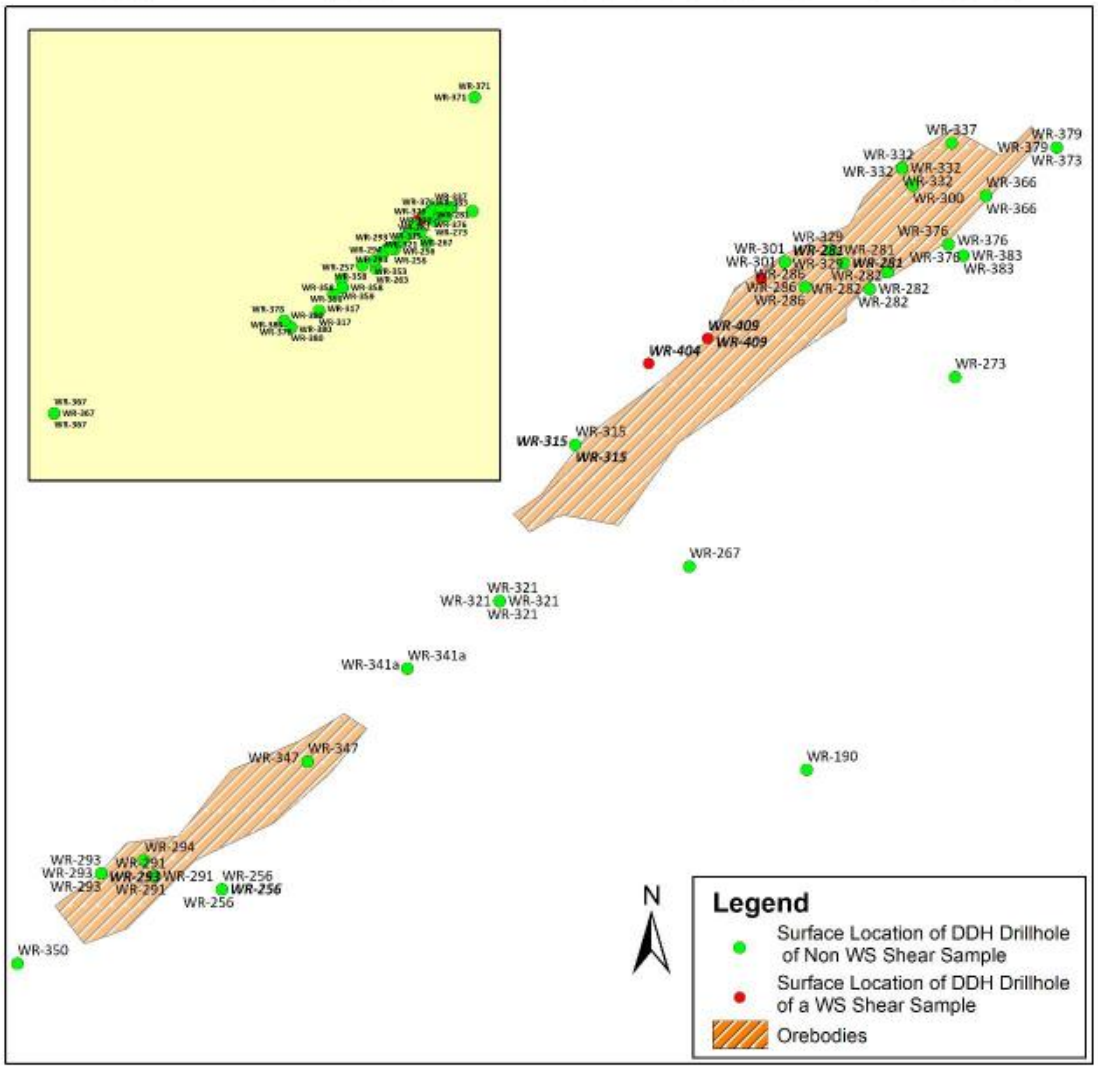

Appendix 2.2: Location of thin section and electron microprobe samples analysed as part of this study.

The locations of samples used for thin section analyses are presented below.

Sample (DPX)	Location	HOLE NUMBER	azimuth decimal	dip decimal
WS Shear Samples				
256-a	190.7	WR-256	312	-80
256-b	224.1	WR-256	312	-80
281-b	*412.7*	*WR-281*	*0*	*-90*
281c	*417.4*	*WR-281*	*0*	*-90*
293-a	244.9	WR-293	0	-90
293-b	251	WR-293	0	-90
301a	315	WR-301	0	-90
315a	312.8	WR-315	0	-90
404	323.3	WR-404	0	-90
409a	317.7	WR-409	0	-90
Non Shear Samples				
DPX005	*453.25*	*WR-383*	*0*	*-90*
DPX011	*448.48*	*WR-376*	*0*	*-90*
DPX012	*447.37*	*WR-376*	*0*	*-90*
DPX013	*447.27*	*WR-376*	*0*	*-90*
DPX015	*446.55*	*WR-376*	*0*	*-90*
DPX018	*443.8*	*WR-332*	*0*	*-90*
DPX019	*442.8*	*WR-332*	*0*	*-90*
DPX021	*441.52*	*WR-332*	*0*	*-90*
DPX022	*440.5*	*WR-332*	*0*	*-90*
DPX023	*439.7*	*WR-332*	*0*	*-90*
DPX024	*436.41*	*WR-332*	*0*	*-90*
DPX027	*432.4*	*WR-302*	*0*	*-90*
DPX035	*427.26*	*WR-282*	*0*	*-90*

Sample (DPX)	Location	HOLE NUMBER	azimuth decimal	dip decimal
DPX050	*415*	*WR-282*	*0*	*-90*
DPX051	*414.98*	*WR-282*	*0*	*-90*
DPX056	*410.26*	*WR-349*	*0*	*-90*
DPX060	*403.6*	*WR-358*	*312*	*-80*
DPX061	*403.2*	*WR-358*	*312*	*-80*
DPX062	*403.1*	*WR-358*	*312*	*-80*
DPX063	*403.1*	*WR-358*	*312*	*-80*
DPX067	*400.77*	*WR-408*	*0*	*-90*
DPX070	*399.17*	*WR-329*	*0*	*-90*
DPX081	*300.9*	*WR-293*	*0*	*-90*
DPX085	253	WR-358	312	-80
DPX086	250.5	WR-257	312	-90
DPX100	409.5	WR-347	0	-90
DPX103	425.7	WR-367	312	-80
DPX105	407.4	WR-105	312	-80
DPX107	546.2	WR-107	42	-75
DPX124	455	WR-296	0	-90
DPX133	270	WR-380	312	-80
DPX136	320.2	WR-380	312	-80
DPX137	282.2	WR-380	312	-80
DPX138	268.8	WR-380	312	-80
DPX149	282	WR-277	312	-82
DPX162	114.3	WR-277	312	-82
DPX170	187.1	WR-277	312	-82
DPX171	403.7	WR-379	0	-90
DPX176	28.1	WR-287	0	-90
DPX196	185.3	WR-307	0	-90
DPX209	94.2	WR-321	0	-90

The locations of samples used for electron microprobe analysis are presented below:

Sample (DPX)	Location	HOLE NUMBER	Sample (DPX)	Location	HOLE NUMBER
WS Shear Samples			**Non Shear Samples**		
256-a	**190.7**	**WR-256**	**DPX042**	**420.6**	**WR-282**
281-a	**410.8**	**WR -281**	***DPX062***	***403.1***	***WR-358***
281-b	***412.7***	***WR-281***	**DPX070**	***399.17***	***WR-329***
282B	***399.9***	***WR282***	**DPX124**	**455**	**WR-296**
409a	**317.7**	**WR-409**			

Appendix 3 Electron Microprobe Results

3.1	Tourmaline raw EMPA Data	186
3.2	Chlorite raw EMPA Data	189
3.3	Illite raw EMPA Data	192

Appendix 3.1; Tourmaline raw EMPA data

Tur 1 chemical compostition

Raw EMPA Data

Samples Used for Analysis	SiO2	TiO2	Al2O3	FeO	MnO	ZnO	MgO	CaO	Na2O	K2O	Cl	BaO	F	SrO	Calc Total	Comments
292 dpx281b_1.1_7	37.03	0.869	31.798	5.193	0.011	0.023	7.735	0.871	1.948	0.044	0	0	0.56	0.044	86.13	
279 dpx281b_1_7	35.27	1.214	32.892	5.36	0.024	0	7.458	1.705	1.539	0.09	0	0.038	0.447	0.019	86.05	
283 dpx281b_1_11	34.12	1.211	32.412	5.542	0.012	0	7.342	1.927	1.488	0.092	0.001	0.017	0.397	0.039	84.6	
319 dpx281b_3.1_1	35.13	0.915	32.591	5.31	0.036	0.027	7.597	2.232	1.483	0.093	0	0	0.542	0.034	85.99	
312 dpx281b_2_18	34.52	1.295	32.057	5.309	0	0	7.654	2.1	1.408	0.104	0.004	0.041	0.466	0.013	84.97	
303 dpx281b_2_9	34.63	1.372	32.246	5.597	0.012	0.032	7.463	2.167	1.401	0.101	0	0	0.39	0.087	85.5	
282 dpx281b_1_10	34.4	1.374	31.928	5.54	0.024	0.041	7.668	2.135	1.381	0.083	0	0	0.426	0.011	85.01	
313 dpx281b_2_19	34.88	1.077	32.739	5.396	0.005	0	7.359	1.91	1.502	0.107	0	0.015	0.398	0	85.38	rim of zoned grains
321 dpx281b_3.1_3	35.63	0.921	32.115	5.162	0.019	0.03	7.765	1.827	1.562	0.071	0.002	0.02	0.604	0	85.73	

Average of Results

Average Results	SiO2	TiO2	Al2O3	FeO	MnO	ZnO	MgO	CaO	Na2O	K2O	Cl	BaO	F	SrO	Calc Total			
Average Chemistry	35.07	1.1386667	32.3087	5.3788	0.016	0.017	7.56	1.875	1.524	0.087	8E-04	0.015	0.47	0.027	85.48444444			
Stoichiometry																		
Numbers of ions in formula based on 31 (O,H,F,Cl)	Si	Ti	Cr	V	Al	Fe3+	Fe2+	Mg	Mn	Zn	Li*	Ca	Na	K	B	F		H
Average Chemistry	5.79	0.14	0	0	6.29	0	0.741	1.86	0.002	0.002	0	0.33	0.49	0.018	3	0.2450		3.75

Balancing	CatSum		Si excess	X+B+Si excess			Li*		T+Z+Y	Ideal T+Z+Y								
	18.449		0.000		3.395			-0.550		15.055		15.055						
	Normalised Y+T+Z (15)																	
	Si	Ti	Al	Fe3+	Fe2+	Mg	Mn	Zn										
	5.85	0.143	6.36		0.75	1.88	0.002	0.002										

Site	X Site				Y Site						Z Site	B Site	T Site		V Site	W Site		
Element	□	Ca	K	Na	Mg	Fe2+	Al	Fe3+	Ti	Mn	Al		Si	Al	O	O	OH	F
Value	0.18	0.33		0.49	1.88	0.752	0.22	0	0.14	0.002	6		5.86	0.14	18.00	0.75		0.25

Final Average Chemistry	(XX0.18Ca0.33Na0.49)(Mg1.88Fe2+0.75Al0.22Ti0.14)Al6(Si5.86Al0.14O18)(BO3)3OH3(F0.25O0.75)

Tur 2 (sample WR281B; basement shear) chemical compostition

Raw EMPA Data

Samples Used for Analysis	**SiO2**	**TiO2**	**Al2O3**	**FeO**	**MnO**	**ZnO**	**MgO**	**CaO**	**Na2O**	**K2O**	**Cl**	**BaO**	**F**	**SrO**	**Calc Total**	**Comments**
297 dpx281b_2_3	36.65	0.02	36.13	0.43	0.01	0.00	7.91	0.04	0.46	0.01	0.01	0.00	0.00	0.05	81.72	
298 dpx281b_2_4	35.84	0.78	31.60	3.23	0.00	0.02	7.67	1.23	0.98	0.06	0.01	0.01	0.24	0.00	81.67	

Average of Results

Average Results	SiO2	TiO2	Al2O3	FeO	MnO	ZnO	MgO	CaO	Na2O	K2O	Cl	BaO	F	SrO	Calc Total	
Average Chemistry	36.25	0.40	33.86	1.83	0.01	0.01	7.79	0.64	0.72	0.04	0.01	0.01	0.12	0.02	81.70	

Stoichiometry

Numbers of ions in formula based on 31 (O,H,F,Cl)	Si	Ti	Cr	V	Al	Fe3+	Fe2+	Mg	Mn	Zn	Li*	Ca	Na	K	B	F		H
Average Chemistry	6.00	0.06	0.00	0.00	6.64	0.00	0.31	1.93	0.00	0.00	0.00	0.00	0.30	0.01	3.00	0.13		3.87

Balancing	Catsum	Si excess	X+B+Si excess	Li*	T+Z+Y	Ideal T+Z+Y
	18.26	0.00	3.33	0.06	14.95	14.94

Normalised Y+T+Z (15)

Si	Ti	Al	Fe3+	Fe2+	Mg	Mn	Zn
6.03	0.06	6.66		0.31	1.94	0.01	0.001

Site	X Site				Y Site						Z Site	B Site	T Site		V Site	W Site		
Element	XX	Ca	K	Na	Mg	Fe2+	Al	Fe3+	Ti	Mn	Al	(BO3)3OH3	Si	Al	O	O	OH	F
Value	0.64	0.00		0.23	1.93	0.31	0.70	0.00	0.06	0.00	6.00		6.00	0.00	18.00	0.88	-	0.13

Final Average Chemistry	(XX0.64Na0.23)(Mg1.93Al0.7Fe2+0.31)Al6(Si6O18)(BO3)3OH3(F0.13O0.88)

Tur 2 (sandstone) chemical compostition

Raw EMPA Data

Samples Used for Analysis	SiO2	TiO2	Al2O3	FeO	MnO	ZnO	MgO	CaO	Na2O	K2O	Cl	BaO	F	SrO	Calc Tot	Comments
107 dpx81.1.11	36.831	0.007	37.001	1.063	0	0	7.581	0.092	0.704	0.011	0.004	0.087	0.125	0	83.51	
108 dpx81.1.12	35.454	0.002	37.522	0.847	0	0.01	7.284	0.159	0.649	0.013	0.014	0	0.024	0	81.98	
140 dpx81.3.11	33.936	0.012	38.249	0.825	0.001	0.011	7.061	0.212	0.617	0.017	0.022	0.044	0.068	0	81.08	
110 dpx81.1.14	36.784	0.002	37.574	0.769	0	0.017	7.526	0.101	0.588	0.012	0.011	0	0.068	0	83.45	
111 dpx81.1.15	36.223	0.133	35.908	0.756	0.006	0.011	7.664	0.084	0.588	0.011	0.014	0.044	0.126	0	81.57	
142 dpx81.3.13	35.011	0.011	38.432	0.682	0.005	0	7.154	0.167	0.585	0.004	0.009	0.025	0.005	0	82.09	
109 dpx81.1.13	35.198	0.002	38.275	0.77	0	0	7.419	0.193	0.565	0.006	0.008	0.05	0.14	0	82.63	
132 dpx81.3.3	34.281	0	38.744	0.719	0	0.018	7.141	0.179	0.56	0	0.012	0.019	0	0	81.67	
134 dpx81.3.5	34.017	0	38.451	0.721	0.004	0.007	7.071	0.183	0.511	0.002	0.012	0.038	0.087	0	81.1	
114 dpx81.1.18	33.672	0.049	38.658	0.651	0	0.008	7.271	0.229	0.487	0.005	0.012	0.013	0.082	0	81.14	

Average of Results

Average Results	SiO2	TiO2	Al2O3	FeO	MnO	ZnO	MgO	CaO	Na2O	K2O	Cl	BaO	F	SrO	Calc Total
Average Chemistry	35.141	0.022	37.881	0.780	0.002	0.008	7.317	0.160	0.585	0.008	0.012	0.032	0.073	0.000	82.022

Stoichiometry

Numbers of ions in formula based on 31 (O,H,F,Cl)	Si	Ti	Cr	V	Al	Fe3+	Fe2+	Mg	Mn	Zn	Li*	Ca	Na	K	B	F		H
Average Chemistry	5.72	0.002	0	0	7.36	0.107		1.77	0	0.001	0	0	1.85	0.001	3	0.0000		3.95

Balancing	Catsum	Si excess	X+B+Si excess	Li*	T+Z+Y	Ideal T+Z+Y
	18.200	0.000	3.210	0.003	14.970	14.972

Normalised Y+T+Z (15)

Si	Ti	Al	Fe3+	Fe2+	Mg	Mn	Zn
5.72	0.02	7.38		0.31	1.94	0.01	0.001

Site	X Site				Y Site						Z Site	B Site	T Site		V Site	W Site		
Element	XX	Ca	K	Na	Mg	Fe2+	Al	Fe3+	Ti	Mn	Al	(BO3)3OH	Si	Al	O	O	OH	F
Value	0.78	0.03	0.00	0.19	1.79		1.08	0.11	0.00		6.00		5.72	0.28	18.00	0.96	0	0.04

Final Average Chemistry: (□0.78Na0.19)(Mg1.79Fe2+0.11Al1.07)(Al6)(BO3)3(Si5.72Al0.28)O18(OH3.96F0.04)

Appendix 3.2; Chlorite raw EMPA Data and Sample Chemistry																
C1 Chlorite																
		Raw EMPA Data														
Sample Name	Formulea	SiO2	TiO2	Al2O3	FeO	MnO	ZnO	MgO	CaO	Na2O	K2O	Cl	BaO	F	SrO	Total
281 dpx281b_1_9	(Mg2.6Fe1.38Al1.53)Si2.7Al1.3)O10(OH7.92F0.08)	27.906	0.06	23.652	16.253	0.19	0.07	17.139	0.085	0	0.047	0.024	0.007	0.241	0	85.67
288 dpx281b_1.1_3	(Mg2.87Fe1.45Al1.32)Si2.68Al1.32)O10(OH7.95F0.05)	27.731	0.032	21.973	16.987	0.246	0.021	18.875	0.045	0.007	0	0.01	0	0.157	0	86.08
280 dpx281b_1_8	(Mg2.72Fe1.73Al1.22)Si2.58Al1.42)O10(OH7.9F0.1)	26.666	0.061	21.704	20.002	0.257	0.031	17.678	0.026	0.004	0.011	0.007	0.002	0.317	0	86.77
276 dpx281b_1_4	(Mg2.81Fe1.55Al1.27)Si2.64Al1.36)O10(OH7.92F0.08)	26.83	0.102	21.404	17.782	0.214	0.014	18.085	0.091	0.005	0.024	0.019	0.012	0.229	0.014	84.82
274 dpx281b_1_2	(Mg2.83Fe1.55Al1.27)Si2.63Al1.37)O10(OH7.91F0.09)	26.603	0.074	21.324	17.694	0.234	0	18.085	0.044	0	0.021	0.026	0	0.26	0	84.36
244 dpx124_3_7	(Mg3.08Fe1.46Al1.25)Si2.53Al1.47)O10(OH7.94F0.06)	26.064	0.035	22.608	17.046	0.016	0.072	20.215	0.005	0	0	0.021	0	0.171	0	86.25
225 dpx124_2_4	(Mg2.28Fe2.12Al1.23)Si2.61Al1.39)O10(OH7.99F0.01)	26.75	0.06	21.07	24.13	0.25	0.00	14.54	0.02	0.00	0.03	0.01	0.02	0.04	0.03	86.94
212 dpx124_1_6	(Mg2.28Fe2.18Al1.19)Si2.59Al1.41)O10(OH7.97F0.03)	26.667	0.023	20.947	24.817	0.251	0.026	14.553	0.059	0.017	0.028	0	0	0.089	0	87.48
210 dpx124_1_4	(Mg2.26Fe2.13Al1.17)Si2.59Al1.41)O10(OH7.96F0.04)	26.58	0.64	20.93	24.34	0.24	0.04	14.43	0.03	0.007	0.02	0.001	0.01	0.11	0.03	87.39
250 dpx124_3_13	(Mg0.01Fe0.04Al1.44)Si0.55Al3.45)O10(OH7.98F0.02)	25.186	3.176	20.824	23.753	0.263	0.033	14.406	0.023	0.004	0.002	0.004	0	0.062	0.043	87.78
208 dpx124_1_2	(Mg2.28Fe2.14Al1.2)Si2.64Al1.36)O10(OH7.97F0.03)	27.19	0.04	20.686	24.41	0.228	0.05	14.579	0.05	0.005	0.06	0.015	0.00	0.09	0.00	87.4
211 dpx124_1_5	(Mg2.28Fe2.15Al1.19)Si2.63Al1.37)O10(OH7.98F0.02)	26.982	0.027	20.597	24.476	0.212	0	14.54	0.046	0.007	0.028	0.012	0	0.067	0.045	87.04
Average	(Mg2.55Fe1.82Al1.24)Si2.61Al1.39)O10(OH7.95F0.05)	26.76	0.36	21.48	20.97	0.22	0.03	16.43	0.04	0.00	0.02	0.01	0.00	0.15	0.01	86.50
STD dev		0.679	0.864	0.862	3.456	0.064	0.024	2.043	0.025	0.005	0.017	0.009	0.005	0.087	0.017	1.044
Max		27.906	3.176	23.652	24.817	0.263	0.072	20.215	0.091	0.017	0.056	0.026	0.017	0.317	0.045	87.78
Min		25.186	0.023	20.597	16.253	0.016	0	14.406	0.005	0	0	0	0	0.037	0	84.36
n =		12	12	12	12	12	12	12	12	12	12	12	12	12	12	12

C2 Chlorite																
		Raw EMPA Data														
Sample Name	Formulea	SiO2	TiO2	Al2O3	FeO	MnO	ZnO	MgO	CaO	Na2O	K2O	Cl	BaO	F	SrO	Total
176 wr282b_3_2	(Mg2.41Fe0.05Al3.72)(Si3.75Al0.25)O20(OH)16	36.12	0.029	32.362	0.61	0.018	0.006	15.536	0.05	0.023	0.197	0.035	0	0.119	0.026	85.13
177 wr282b_3_3	(Mg2.25Fe0.83Al3.27)(Si3.52Al0.48)O20(OH)16	33.532	0	29.442	9.236	0.026	0.041	14	0.084	0.007	0.13	0.021	0.015	0.09	0	86.62
178 wr282b_3_4	(Mg2.29Fe0.07Al3.78)(Si3.75Al0.25)O20(OH)16	35.503	0	32.138	0.82	0	0.019	14.482	0.094	0.045	0.187	0.079	0.015	0.119	0	83.5
180 wr282b_3_6	(Mg2.39Fe0.5Al3.38)(Si3.65Al0.35)O20(OH)16	33.737	0	28.68	5.47	0.019	0.036	14.505	0.072	0.023	0.402	0.047	0.005	0.123	0	83.12
181 wr282b_3_7	(Mg2.01Fe0.74Al3.38)(Si3.67Al0.33)O20(OH)16	35.28	0.009	29.369	8.206	0.018	0.023	12.59	0.045	0.004	1.107	0.021	0	0.204	0	86.88
183 wr282b_3_9	(Mg2.4Fe0.05Al3.73)(Si3.73Al0.27)O20(OH)16	35.945	0	32.502	0.609	0.01	0	15.433	0.063	0.013	0.177	0.039	0	0.161	0.054	85.01
184 wr282b_3_10	(Mg2.45Fe0.9Al3.12)(Si3.44Al0.56)O20(OH)16	31.28	0.00	27.59	9.54	0.02	0.01	14.52	0.07	0.00	0.09	0.04	0.03	0.06	0.00	83.26
185 wr282b_3_11	(Mg2.28Fe0.09Al3.79)(Si3.69Al0.31)O20(OH)16	35.092	0.006	32.812	1.045	0	0.011	14.478	0.098	0.008	0.188	0.042	0.014	0.156	0.009	83.96
188 wr282b_3_14	(Mg2.11Fe0.86Al3.27)(Si3.6Al0.4)O20(OH)16	34.16	0.01	28.63	9.40	0.01	0.04	13.04	0.03	0.009	0.86	0.03	0.03	0.14	0.00	86.38
Average	(Mg2.29Fe0.45Al3.5)(Si3.65Al0.35)O20(OH)16	34.5159	0.0056	30.3921	4.99311	0.0137	0.0207	14.2866	0.0676	0.0147	0.3714	0.039	0.0117	0.1309	0.0099	84.873
STD dev		1.44121	0.01	1.91634	3.95	0.0091	0.01	0.91679	0.02	0.013	0.34	0.0164	0.01	0.0387	0.02	1.4075
Max		36.12	0.029	32.812	9.54	0.026	0.041	15.536	0.098	0.045	1.107	0.079	0.031	0.204	0.054	86.88
Min		31.28	0.00	27.59	0.61	0.00	0.00	12.59	0.03	0.00	0.09	0.02	0.00	0.06	0.00	83.12
n =		9	9	9	9	9	9	9	9	9	9	9	9	9	9	9

C3 Chlorite																
		Raw EMPA Data														
Sample Name	Formulea	SiO2	TiO2	Al2O3	FeO	MnO	ZnO	MgO	CaO	Na2O	K2O	Cl	BaO	F	SrO	Total
42.3.3	(Mg1.92Fe0.07Al3.95)(Si3.81Al0.19)O20(OH)16	38.755	0.023	35.389	0.812	0	0.011	12.983	0.062	0.014	0.933	0.013	0.035	0.302	0.052	89.254
281a3-7	(Mg1.28Fe0.06Al4.32)(Si4.02Al-0.02)O20(OH)16	37.856	0.015	34.125	0.651	0.028	0.016	8.005	0.102	0.577	0.114	0.036	0.019	0.155	0	81.626
108 dpx62_5_27	(Mg2Fe0.13Al3.89)(Si3.78Al0.22)O20(OH)16	37.107	0.02	33.935	1.502	0.012	0	13.046	0.047	0.022	0.841	0.006	0	0.06	0.01	86.61
42.1.7	(Mg1.74Fe0.06Al3.99)(Si3.92Al0.08)O20(OH)16	38.224	0.022	33.242	0.745	0	0.023	11.24	0.087	0.015	1.737	0.004	0	0.22	0.028	85.493
42.1.3	(Mg2.09Fe0.06Al3.89)(Si3.74Al0.26)O20(OH)16	35.45	0.014	33.082	0.697	0.009	0.031	13.158	0.056	0.012	0.775	0.013	0.023	0.185	0	83.424
42.2.4	(Mg1.4Fe0.05Al4.2)(Si3.93Al0.07)O20(OH)16	36.203	0.004	32.988	0.559	0.021	0	8.585	0.383	0.032	1.827	0.009	0	0.104	0	80.669
42.1.4	(Mg2.06Fe0.07Al3.87)(Si3.81Al0.19)O20(OH)16	36.49	0.02	32.73	0.77	0.01	0.00	13.15	0.05	0.01	0.90	0.01	0.00	0.18	0.01	84.24
281a-1-3	(Mg2.25Fe0.13Al3.71)(Si3.84Al0.16)O20(OH)16	37.37	0.022	31.716	1.522	0.016	0.023	14.582	0.188	0.018	0.279	0.068	0	0.17	0.015	85.902
42.2.3	(Mg1.72Fe0.08Al3.97)(Si3.82Al0.18)O20(OH)16	34.75	0.01	31.66	0.82	0.00	0.00	10.33	0.15	0.017	1.99	0.01	0.00	0.34	0.00	79.93
281a-1-1	(Mg2.21Fe0.04Al3.8)(Si3.87Al0.13)O20(OH)16	36.659	0	31.387	0.494	0	0	13.955	0.121	0.038	0.423	0.069	0	0.098	0.009	83.196
281a3-6	(Mg2.09Fe0.11Al3.76)(Si3.96Al0.04)O20(OH)16	38.34	0.00	30.88	1.21	0.00	0.04	13.45	0.07	0.067	1.09	0.07	0.06	0.07	0.00	85.29
281a-1-8	(Mg2.09Fe0.18Al3.71)(Si3.91Al0.09)O20(OH)16	37.416	0.008	30.46	1.986	0	0	13.281	0.103	0.02	1.003	0.056	0	0.198	0.098	84.533
255 dpx124_3_18	(Mg2.54Fe0.47Al3.39)(Si3.55Al0.45)O20(OH)16	33.52	0.01	30.26	5.18	0.00	0.01	15.82	0.08	0.002	0.11	0.033	0.00	0.00	0.00	85.03
240 dpx124_3_3	(Mg2.47Fe0.16Al3.47)(Si3.94Al0.06)O20(OH)16	38.564	0	29.1	1.899	0.016	0.04	16.05	0.095	0.014	0.745	0.073	0	0.205	0	86.8
259 dpx124_3_22	(Mg2.57Fe0.69Al3.2)(Si3.5Al0.5)O20(OH)16	32.63	0.01	28.58	7.51	0.00	0.02	15.71	0.10	0.001	0.05	0.053	0.00	0.05	0.03	84.74
256 dpx124_3_19	(Mg2.81Fe0.45Al3.2)(Si3.6Al0.4)O20(OH)16	34.184	0.002	28.558	5.078	0.003	0	17.619	0.092	0	0.073	0.047	0	0.075	0	85.73
239 dpx124_3_2	(Mg2.96Fe0.7Al2.98)(Si3.34Al0.66)O20(OH)16	31.09	0.01	28.07	7.58	0.01	0.03	18.04	0.06	0.013	0.06	0.048	0.01	0.15	0.00	85.16
261 dpx124_3_24	(Mg2.8Fe0.65Al3.07)(Si3.48Al0.52)O20(OH)16	32.318	0.002	27.711	7.033	0.018	0.04	17.039	0.108	0.004	0.05	0.044	0	0.138	0.006	84.51
257 dpx124_3_20	(Mg2.9Fe0.65Al3.01)(Si3.49Al0.51)O20(OH)16	32.59	0.00	27.28	7.11	0.01	0.04	17.79	0.10	0.017	0.06	0.046	0.02	0.09	0.03	85.16
258 dpx124_3_21	(Mg2.91Fe0.66Al3.01)(Si3.48Al0.52)O20(OH)16	32.477	0.013	27.277	7.205	0.015	0.008	17.801	0.081	0.011	0.034	0.044	0	0.03	0	85
281a-1-7	(Mg2.54Fe0.22Al3.31)(Si4.2Al-0.2)O20(OH)16	43.31	0.01	26.93	2.64	0.00	0.05	17.39	0.13	0.072	0.40	0.065	0.08	0.19	0.02	91.19
Average	(Mg2.25Fe0.27Al3.61)(Si3.77Al0.23)O20(OH)16	35.966	0.010	30.731	3.000	0.008	0.018	14.239	0.108	0.047	0.643	0.039	0.011	0.143	0.015	84.927
STD dev		2.860	0.008	2.521	2.707	0.008	0.016	2.919	0.070	0.120	0.611	0.024	0.021	0.083	0.023	2.455
Max		43.314	0.023	35.389	7.575	0.028	0.045	18.035	0.383	0.577	1.993	0.073	0.078	0.337	0.098	91.186
Min		31.09	0.00	26.93	0.49	0.00	0.00	8.01	0.05	0.00	0.03	0.00	0.00	0.00	0.00	79.93
n =		21	21	21	21	21	21	21	21	21	21	21	21	21	21	21

Appendix 3.3 Illite raw EMPA Data and Sample Chemistry

Basement hosted M1 Illite																
		Raw EMPA Data														
Sample Name	Formulea	SiO2	TiO2	Al2O3	FeO	MnO	ZnO	MgO	CaO	Na2O	K2O	Cl	BaO	F	SrO	Calc Total
9 dpx62_1_1	K0.9Mg0.34Fe2+0.34Al0.67(Si3.42Al0.58O10)(OH1.99F0.01)	46.513	0.008	33.175	1.191	0	0	1.036	0	0.089	9.649	0.011	0	0.295	0.024	91.99
10 dpx62_1_2	K0.91Mg0.13Fe2+0.07Al0.67(Si3.49Al0.51O10)(OH1.99F0.01)	48.052	0	34.133	1.082	0	0	1.181	0	0.052	9.83	0.014	0.007	0.266	0	94.62
31 dpx62_2_7	K0.89Mg0.2Fe2+0.17Al0.63(Si3.46Al0.54O10)(OH1.98F0.02)	46.434	0.393	32.059	2.776	0	0.001	1.836	0	0.082	9.347	0.06	0.033	0.388	0.025	93.43
32 dpx62_2_8	K0.91Mg0.24Fe2+0.23Al0.59(Si3.42Al0.58O10)(OH1.99F0.01)	45.774	0.979	31.223	3.7	0.015	0	2.145	0	0.105	9.534	0.1	0.017	0.136	0.014	93.74
37 dpx62_3_	K0.84Mg0.15Fe2+0.06Al0.65(Si3.53Al0.47O10)(OH1.98F0.02)	49.253	0.016	33.885	1.062	0	0	1.441	0	0.044	9.174	0.007	0	0.3	0	95.18
38 dpx62_3_2	K0.84Mg0.17Fe2+0.13Al0.59(Si3.52Al0.48O10)(OH1.98F0.02)	48.1	1.047	31.93	2.086	0.015	0.018	1.542	0	0.083	9.023	0.069	0.017	0.315	0	94.24
40 dpx62_3_4	K0.88Mg0.14Fe2+0.12Al0.65(Si3.53Al0.47O10)(OH1.98F0.02)	48.975	0.204	33.027	2.024	0.036	0	1.262	0	0.111	9.552	0.042	0	0.309	0	95.54
41 dpx62_3_5	K0.88Mg0.16Fe2+0.14Al0.64(Si3.54Al0.46O10)(OH1.98F0.02)	48.31	0.349	32.043	2.251	0	0.011	1.462	0	0.074	9.434	0.042	0.044	0.357	0	94.38
42 dpx62_3_6	K0.52Mg0.71Fe2+0.1Al0.65(Si3.28Al0.72O10)(OH1.98F0.02)	44.486	0.078	33.411	1.63	0.001	0	6.497	0	0.07	5.554	0.017	0	0.386	0	92.13
44 dpx62_3_8	K0.82Mg0.25Fe2+0.1Al0.65(Si3.45Al0.55O10)(OH1.98F0.02)	47.273	0.096	33.385	1.666	0.012	0.008	2.283	0	0.066	8.804	0.018	0.027	0.38	0	94.02
48 dpx62_3_12	K0.82Mg0.22Fe2+0.07Al0.66(Si3.48Al0.52O10)(OH1.98F0.02)	48.274	0.02	33.984	1.167	0.003	0	2.014	0	0.05	8.885	0.004	0	0.304	0	94.71
49 dpx62_3_13	K0.76Mg0.14Fe2+0.06Al0.64(Si3.55Al0.45O10)(OH1.97F0.03)	49.926	0	33.991	1.04	0.004	0.085	1.352	0	0.563	8.387	0.008	0.053	0.488	0.033	95.93
76 dpx62_4_16	K0.66Mg0.56Fe2+0.08Al0.66(Si3.37Al0.63O10)(OH1.99F0.01)	43.777	0.02	31.371	1.241	0	0.058	4.893	0	0.047	6.721	0.04	0.013	0.169	0	88.35
77 dpx62_4_17	K0.84Mg0.23Fe2+0.08Al0.66(Si3.44Al0.56O10)(OH1.99F0.01)	47.146	0.006	34.023	1.249	0.031	0	2.15	0	0.057	8.999	0.002	0	0.24	0	93.9
79 dpx62_4_19	K0.9Mg0.1Fe2+0.07Al0.66(Si3.51Al0.49O10)(OH1.97F0.03)	48.299	0.029	33.764	1.177	0	0.034	0.909	0	0.117	9.749	0.01	0.019	0.486	0	94.59
80 dpx62_4_20	K0.79Mg0.29Fe2+0.08Al0.66(Si3.35Al0.65O10)(OH1.99F0.01)	45.68	0.024	34.846	1.285	0.028	0.031	2.651	0	0.076	8.472	0.001	0	0.146	0	93.24
91 dpx62_5_10	K0.91Mg0.12Fe2+0.07Al0.66(Si3.44Al0.56O10)(OH1.99F0.01)	46.922	0.022	34.441	1.182	0.027	0	1.103	0	0.073	9.697	0.007	0	0.202	0.035	93.71
136 dpx62_8_8	K0.7Mg0.47Fe2+0.05Al0.66(Si3.29Al0.71O10)(OH2)	44.322	0.017	34.719	0.807	0.005	0.061	4.238	0	0.024	7.382	0.009	0	0.034	0	91.62
144 dpx62_8_16	K0.7Mg0.43Fe2+0.06Al0.66(Si3.29Al0.71O10)(OH1.99F0.01)	43.986	0.002	34.534	0.915	0	0	3.853	0	0.03	7.334	0.009	0	0.17	0.031	90.86
214 dpx124_1_8	K0.94Mg0.18Fe2+0.12Al0.65(Si3.54Al0.46O10)(OH1.99F0.01)	48.281	0.027	31.816	1.959	0.04	0.024	1.685	0	0.102	10.04	0.004	0.244	0.162	0.033	94.42
230 dpx124_2_9	K0.61Mg0.77Fe2+0.64Al0.65(Si3.2Al0.8O10)(OH1.99F0.01)	40.838	0.054	27.782	9.77	0.114	0	6.621	0	0.029	6.088	0.002	0.081	0.117	0	91.5
237 dpx124_2_16	K0.89Mg0.17Fe2+0.1Al0.66(Si3.57Al0.43O10)(OH1.99F0.01)	48.803	0.028	32.062	1.576	0.005	0.017	1.567	0	0.084	9.522	0.001	0.251	0.113	0.034	94.06
251 dpx124_3_14	K0.95Mg0.2Fe2+0.11Al0.66(Si3.55Al0.45O10)(OH1.99F0.01)	48.248	0.004	31.656	1.743	0.023	0	1.818	0	0.093	10.136	0.005	0.127	0.216	0	94.07
252 dpx124_3_15	K0.83Mg0.18Fe2+0.06Al0.65(Si3.63Al0.37O10)(OH1.99F0.01)	50.736	0.014	32.117	1.042	0.036	0.009	1.646	0	0.117	9.136	0.01	0.22	0.108	0	95.19
262 dpx124_4_1	K0.97Mg0.25Fe2+0.13Al0.66(Si3.49Al0.51O10)(OH1.99F0.01)	46.948	0.007	31.484	2.097	0	0	2.254	0	0.111	10.193	0.011	0.163	0.166	0	93.43
264 dpx124_4_3	K0.97Mg0.2Fe2+0.12Al0.66(Si3.53Al0.47O10)(OH1.99F0.01)	47.472	0.021	31.455	1.931	0.029	0.002	1.83	0	0.109	10.192	0	0.177	0.122	0.025	93.36
265 dpx124_4_4	K0.91Mg0.1Fe2+0.07Al0.66(Si3.6Al0.4O10)(OH1.99F0.01)	49.543	0.018	32.435	1.156	0.01	0	0.933	0	0.095	9.857	0.002	0.058	0.109	0.037	94.25
281a-1-6	K0.83Mg0.17Fe2+0.05Al0.66(Si3.71Al0.29O10)(OH1.99F0.01)	50.238	0.013	30.099	0.838	0.009	0	1.499	0	0.266	8.778	0.042	0.149	0.139	0	92.002
281a-1-9	K0.85Mg0.2Fe2+0.05Al0.65(Si3.69Al0.31O10)(OH1.99F0.01)	50.086	0	30.003	0.881	0.009	0.028	1.842	0	0.247	9.057	0.075	0.065	0.134	0.014	92.368
281a2-10	K0.9Mg0.2Fe2+0.06Al0.66(Si3.68Al0.32O10)(OH1.99F0.01)	49.195	0	29.653	0.964	0	0.006	1.798	0	0.229	9.422	0.13	0.353	0.227	0	91.852
281a2-6	K0.88Mg0.27Fe2+0.07Al0.66(Si3.68Al0.32O10)(OH1.99F0.01)	49.67	0.006	29.473	1.117	0	0	2.404	0	0.175	9.284	0.053	0.095	0.139	0	92.345
281a2-7	K0.9Mg0.2Fe2+0.05Al0.65(Si3.69Al0.31O10)(OH2)	49.868	0	29.793	0.853	0.021	0	1.829	0	0.124	9.487	0.019	0.079	0.06	0.048	92.152
281a2-8	K0.76Mg0.33Fe2+0.06Al0.65(Si3.7Al0.3O10)(OH2)	50.482	0	29.427	1.009	0	0	3.002	0	0.297	8.159	0.081	0	0.069	0.003	92.482
281a2-9	K0.87Mg0.2Fe2+0.05Al0.66(Si3.7Al0.3O10)(OH2)	50.25	0.018	30.014	0.857	0.021	0.061	1.795	0	0.189	9.249	0.022	0.265	0.06	0.016	92.787
281a3-1	K0.83Mg0.2Fe2+0.06Al0.66(Si3.67Al0.33O10)(OH1.99F0.01)	49.76	0.008	30.469	1.018	0.018	0.067	1.806	0	0.205	8.822	0.122	0.165	0.143	0.007	92.522
281a3-10	K0.86Mg0.22Fe2+0.06Al0.65(Si3.67Al0.33O10)(OH1.99F0.01)	47.501	0	28.792	0.923	0.02	0.042	1.879	0	0.317	8.729	0.137	0	0.203	0	88.427
281a3-3	K0.85Mg0.2Fe2+0.05Al0.65(Si3.65Al0.35O10)(OH1.99F0.01)	46.259	0.009	28.725	0.76	0	0.055	1.672	0	0.315	8.478	0.107	0	0.188	0.03	86.495
Average	K0.85Mg0.22Fe2+0.09Al1.66(Si3.54Al0.46O10)(OH1.99F0.01)	47.721	0.096	31.924	1.622	0.014	0.017	2.209	0	0.133	8.923	0.035	0.074	0.212	0.011	92.970
STD dev		2.17	0.23	1.89	1.47	0.02	0.02	1.32	0.00	0.11	1.06	0.04	0.09	0.11	0.01	1.95
Max		50.736	1.047	34.846	9.770	0.114	0.085	6.621	0	0.563	10.193	0.137	0.353	0.488	0.048	95.930
Min		40.838	0.000	27.782	0.760	0.000	0.000	0.909	0	0.024	5.554	0.000	0.000	0.034	0.000	86.495
n =		37	37	37	37	37	37	37	37	37	37	37	37	37	37	37

Sandstone hosted M1 Illite																
		Raw EMPA Data														
Sample Name	Formulea	SiO2	TiO2	Al2O3	FeO	MnO	ZnO	MgO	CaO	Na2O	K2O	Cl	BaO	F	SrO	Calc Total
101 256a_2_2	K0.82Mg0.36Fe2+0.07Al0.66(Si3.44Al0.56O10)(OH1.99F0.01)	44.859	0	31.621	1.031	0.009	0.014	3.184	0	0.061	8.389	0.051	0	0.131	0.045	89.4
102 256a_2_3	K0.63Mg0.66Fe2+0.07Al0.67(Si3.19Al0.81O10)(OH1.99F0.01)	38.422	0.015	31.129	1.071	0	0.003	5.298	0	0.039	5.942	0.122	0.021	0.218	0	82.28
103 256a_2_4	K0.26Mg0.94Fe2+0.09Al0.64(Si3.1Al0.9O10)(OH1.99F0.01)	37.687	0	31.768	1.295	0.008	0.015	7.696	0.017	0.348	2.496	0.041	0.021	0.145	0	81.54
125 256a_4_7	K0.61Mg0.42Fe2+0.08Al0.65(Si3.33Al0.67O10)(OH2)	44.078	0	33.858	1.238	0.002	0.021	3.751	0	0.394	6.301	0.016	0	0.075	0.036	89.77
126 256a_4_8	K0.85Mg0.23Fe2+0.05Al0.65(Si3.47Al0.53O10)(OH1.99F0.01)	48.083	0.002	33.923	0.905	0.003	0	2.152	0	0.076	9.239	0.007	0.015	0.229	0	94.63
127 256a_4_9	K0.35Mg0.94Fe2+0.07Al0.67(Si3.1Al0.9O10)(OH1.99F0.01)	38.564	0	32.575	1.045	0.001	0.056	7.816	0	0.037	3.454	0.018	0.024	0.122	0	83.71
131 256a_5_2	K0.78Mg0.31Fe2+0.07Al0.65(Si3.37Al0.63O10)(OH1.99F0.01)	42.935	0	32.233	1.134	0.03	0	2.685	0	0.238	7.755	0.01	0.009	0.106	0	87.14
49 dpx195-1.6	K0.94Mg0.08Fe2+0.05Al0.66(Si3.52Al0.48O10)(OH1.99F0.01)	44.387	0	31.102	0.828	0.001	0.001	0.674	0	0.029	9.289	0.009	0.076	0.201	0	86.6
52 dpx195-1.9	K0.82Mg0.24Fe2+0.08Al0.67(Si3.49Al0.51O10)(OH2)	43.788	0.004	30.482	1.177	0.013	0	2.04	0	0.029	8.087	0.013	0.032	0.082	0	85.75
409b-4-2	K0.48Mg0.69Fe2+0.05Al0.66(Si3.3Al0.7O10)(OH1.99F0.01)	41.971	0	31.707	0.755	0	0.03	5.891	0	0.015	4.823	0.016	0	0.27	0	85.36
113 256a_3_4	K0.94Mg0.14Fe2+0.05Al0.66(Si3.56Al0.44O10)(OH2)	45.838	0.013	30.733	0.722	0.017	0	1.194	0	0.03	9.511	0.013	0	0.041	0	88.11
161 dpx76.2.8	K0.74Mg0.27Fe2+0.04Al0.66(Si3.45Al0.55O10)(OH1.99F0.01)	44.752	0	32.355	0.632	0.011	0.004	2.376	0	0.128	7.549	0.021	0.032	0.275	0	88.14
162 dpx76.2.9	K0.86Mg0.18Fe2+0.04Al0.67(Si3.47Al0.53O10)(OH1.99F0.01)	45.844	0.007	32.916	0.598	0	0	1.6	0	0.063	8.924	0.017	0	0.231	0	90.2
167 dpx76.2.14	K0.82Mg0.17Fe2+0.04Al0.67(Si3.5Al0.5O10)(OH1.99F0.01)	46.862	0.005	33.231	0.591	0.013	0	1.517	0	0.068	8.563	0.031	0.025	0.216	0	91.12
169 dpx76.2.16	K0.89Mg0.2Fe2+0.04Al0.66(Si3.48Al0.52O10)(OH1.99F0.01)	45.909	0.011	32.394	0.69	0	0	1.732	0	0.052	9.175	0.022	0	0.216	0	90.2
70.2.1.4	K0.88Mg0.1Fe2+0.06Al0.66(Si3.6Al0.4O10)(OH1.98F0.02)	45.724	0.01	30.119	0.924	0	0	0.892	0	0.049	8.752	0.021	0	0.327	0.009	86.684
70.2.1.5	K0.9Mg0.09Fe2+0.06Al0.67(Si3.57Al0.43O10)(OH1.99F0.01)	45.131	0.01	30.465	0.875	0.02	0	0.804	0	0.038	8.903	0.017	0.022	0.248	0.011	86.436
70.2.1.11	K0.91Mg0.1Fe2+0.06Al0.67(Si3.59Al0.41O10)(OH1.98F0.02)	44.149	0	29.361	0.816	0	0	0.82	0	0.041	8.735	0.03	0.099	0.322	0.066	84.296
Average	K0.75Mg0.34Fe2+0.06Al0.66(Si3.42Al0.58O10)(OH1.99F0.01)	43.832	0.004	31.776	0.907	0.007	0.008	2.896	9E-04	0.096	7.549	0.026	0.021	0.192	0.009	87.29811
STD dev		2.85	0.01	1.24	0.22	0.01	0.01	2.23	0.00	0.11	2.04	0.03	0.03	0.08	0.02	3.21
Max		48.08	0.02	33.92	1.30	0.03	0.06	7.82	0.02	0.39	9.51	0.12	0.10	0.33	0.07	94.63
Min		37.69	0.00	29.36	0.59	0.00	0.00	0.67	0.00	0.02	2.50	0.01	0.00	0.04	0.00	81.54
n =		18	18	18	18	18	18	18	18	18	18	18	18	18	18	18

Appendix 4 Short Wave Infrared Spectroscopy (SWIR) Analysis

4.1	Short Wave Infrared Spectra of samples collected	195
4.2	Samples identified through The Spectral Geologist Software	327

Appendix 4.1; Short Wave Infrared Spectra of samples collected from the Phoenix Deposit.

Table of Contents

Rationale for Appendix 2

SWIR Analytical conditions 2

Results: SWIR Samples Analysed via Terraspec 4 4

General Samples 4

Spectra from WR380 57

Spectra from WR277 65

Spectra from WR286 76

Samples from WR291 109

Samples from WR353 121

SWIR Spectra from the WS Shear Structure 129

Rationale for Appendix

This document exists to illustrate the spectra analysed as part of this study.

SWIR Analytical conditions

Short Wave Infrared (SWIR) was carried out on all samples at the University of Ottawa using a PANalytical (formerly ASD, Inc., Boulder, CO) FieldSpec Pro® TerraSpec 4 Standard-Res Mineral Analyser,. Samples DPX1 – DPX89 and shear samples (WR256A to WR404) were analysed in one session, and samples DPX100-DPX341 were analysed in a separate session. Clean reference plates (SpectralonTM panel) were used every ten samples to minimise sample deviation, and analysis on the whole rock samples was carried out on the clean, dry, broken or band-sawn core or core fragments. Analysis on clay fractions was carried out on powders spread on plastic sample trays, but always thick enough to ensure no reflectance of the container. Care was taken to avoid contamination of samples by detritus on the LightSource, and it was cleaned after each sample and wiped down every 10 samples with de-ionised water.

Data was acquired using Indico® Pro acquisition software and spliced using ASD ViewSpec™ Pro for post-processing. Terraspec is considered comparable to 'Portable Infrared Mineral Analyser' (PIMA) which has been used prior to samples from the Wheeler River Property (amongst elsewhere in the Athabasca Basin), however PIMA does not detect before 900nm, while Terraspec detects Near Infrared (NIR) and Visible Near Infrared (VNIR), both methods are comparable between 900nm and 2500nm. Conditions and instrument were kept the same for both analyses, as suggested by Zhang et al., 2003.

Technical Specifications of the Terraspec 4 utilised in this study

Wavelength Range	350-2500 nm
Resolution	3 nm @ 700 nm and 10 nm @ 1400/2100 nm
Scanning time	100 milliseconds per analysis
Signal-to-noise ratio	VNIR: 9,000:1 @ 700 nm SWIR 1: 9,000:1 @ 1400 nm SWIR 2: 4,000:1 @ 2100 nm
Photometric noise	VNIR: 48 μAU @ 700 nm SWIR 1: 48 μAU @ 1400 nm SWIR 2: 110 μAU @ 2100 nm
Stray light	VNIR: 5000:1 (0.02%) NIR: 10,000:1 (0.01%)
Wavelength reproducibility	0.1 nm
Wavelength accuracy	0.5 nm
Channels	2151
VNIR detector	(350-1000 nm) 512 element silicon array
SWIR 1 & 2 detectors	(1001-1800 nm) & (1801-2500 nm) Graded Index InGaAs Photodiode, TE Cooled

Results: SWIR Samples Analysed via Terraspec 4

General Samples

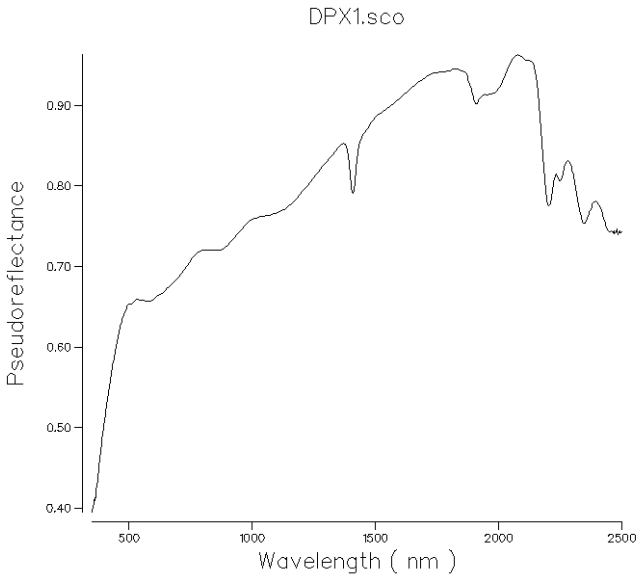

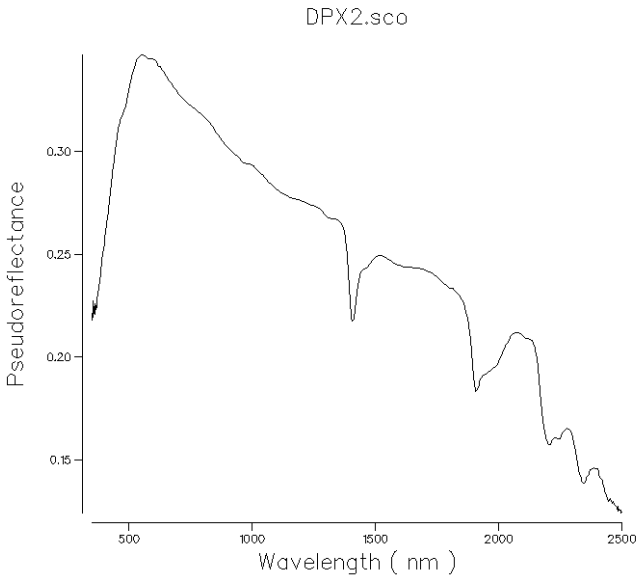

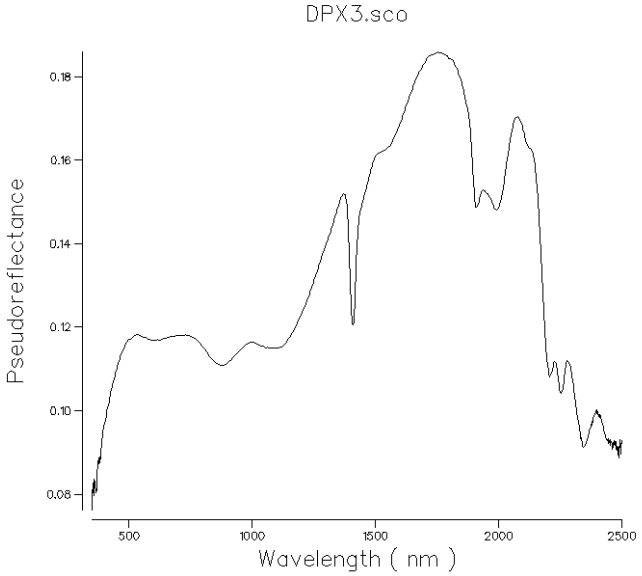
DPX3.sco
Pseudoreflectance
0.18
0.16
0.14
0.12
0.10
0.08
500
1000
1500
2000
2500
Wavelength (nm)

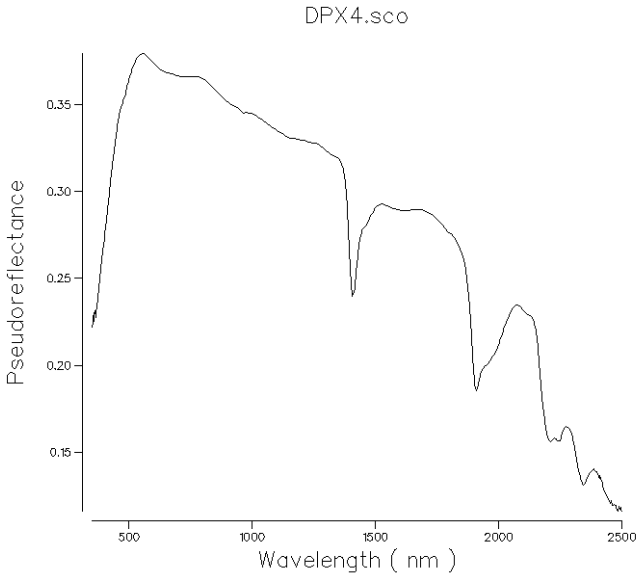
DPX4.sco
Pseudoreflectance
0.35
0.30
0.25
0.20
0.15
500
1000
1500
2000
2500
Wavelength (nm)

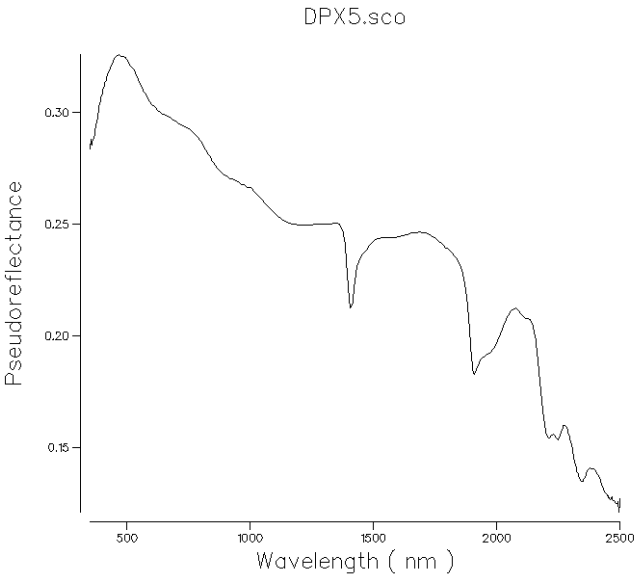
DPX5.sco
Pseudoreflectance
0.30
0.25
0.20
0.15
500
1000
1500
2000
2500
Wavelength (nm)

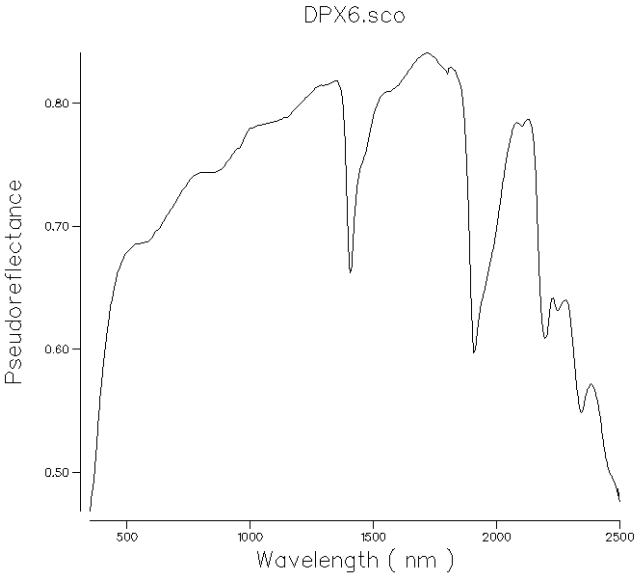
DPX6.sco
Pseudoreflectance
0.80
0.70
0.60
0.50
500
1000
1500
2000
2500
Wavelength (nm)

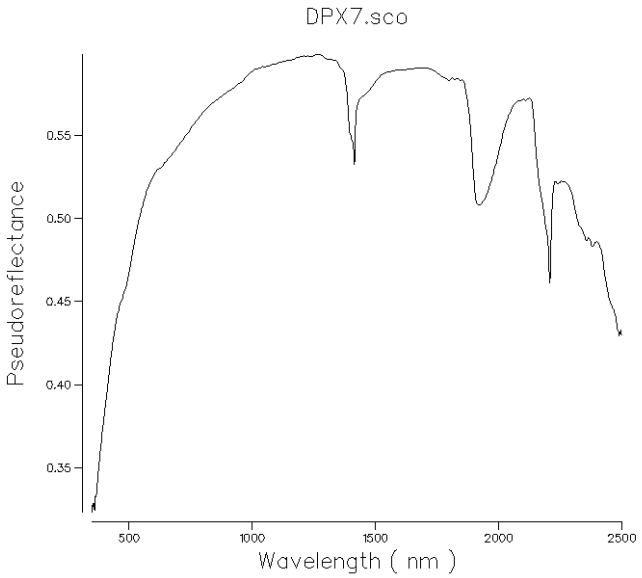
DPX7.sco
Pseudoreflectance
0.55
0.50
0.45
0.40
0.35
500
1000
1500
2000
2500
Wavelength (nm)

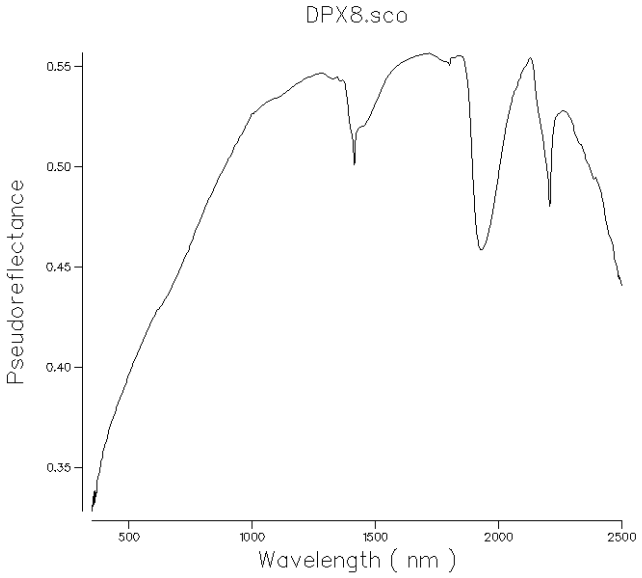
DPX8.sco
Pseudoreflectance
0.55
0.50
0.45
0.40
0.35
500
1000
1500
2000
2500
Wavelength (nm)

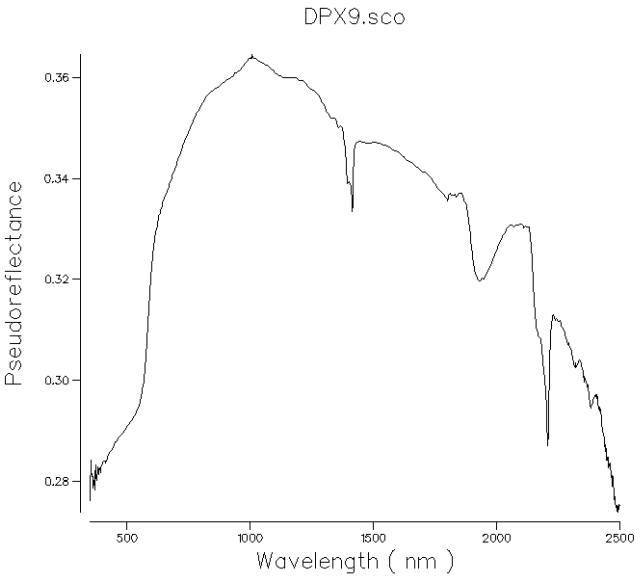
DPX9.sco
Pseudoreflectance
0.36
0.34
0.32
0.30
0.28
500
1000
1500
2000
2500
Wavelength (nm)

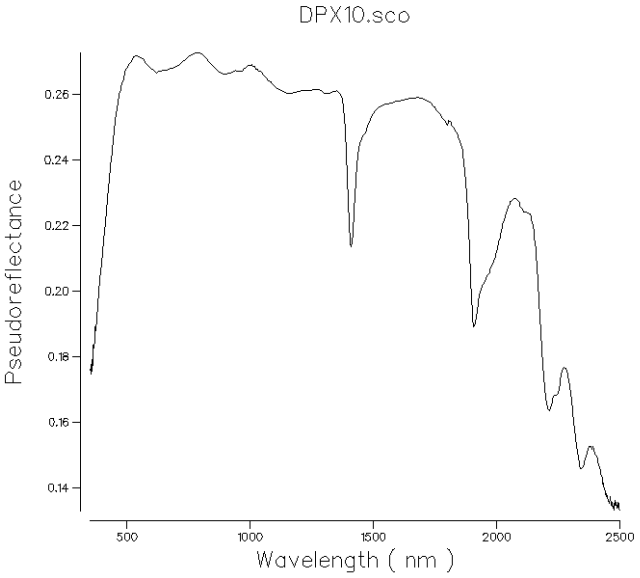
DPX10.sco
Pseudoreflectance
0.26
0.24
0.22
0.20
0.18
0.16
0.14
500
1000
1500
2000
2500
Wavelength (nm)

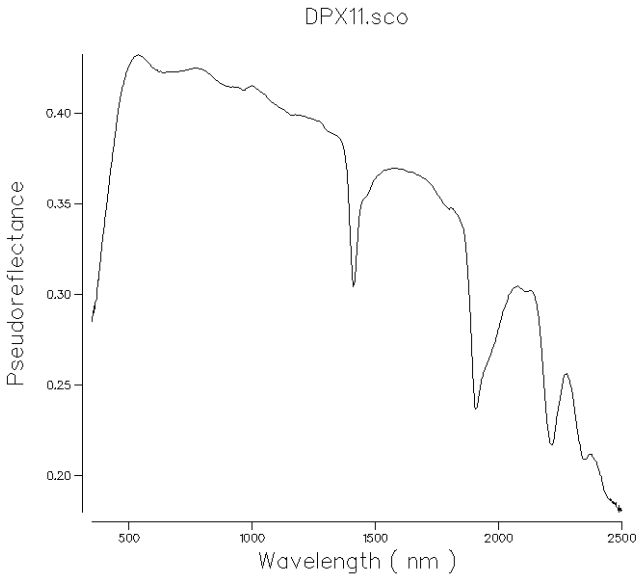
DPX11.sco
Pseudoreflectance
0.40
0.35
0.30
0.25
0.20
500
1000
1500
2000
2500
Wavelength (nm)

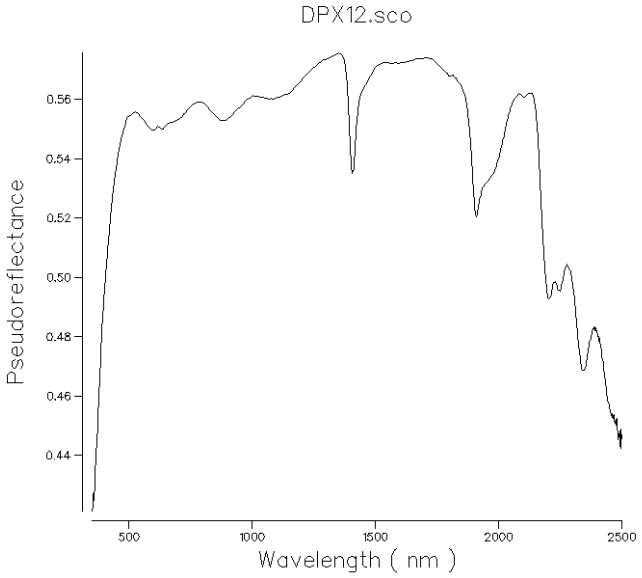
DPX12.sco
Pseudoreflectance
0.56
0.54
0.52
0.50
0.48
0.46
0.44
500
1000
1500
2000
2500
Wavelength (nm)

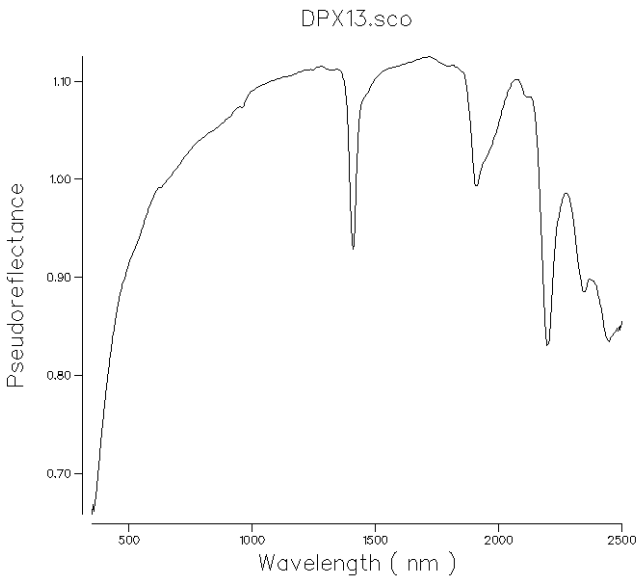
DPX13.sco
Pseudoreflectance
1.10
1.00
0.90
0.80
0.70
500
1000
1500
2000
2500
Wavelength (nm)

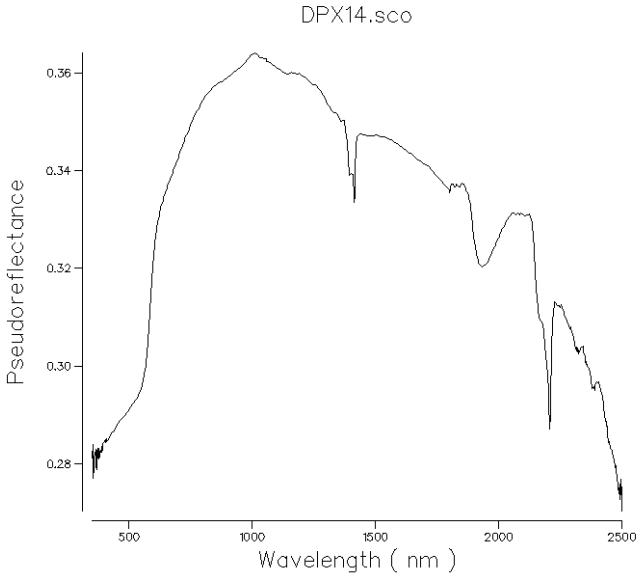
DPX14.sco
Pseudoreflectance
0.36
0.34
0.32
0.30
0.28
500
1000
1500
2000
2500
Wavelength (nm)

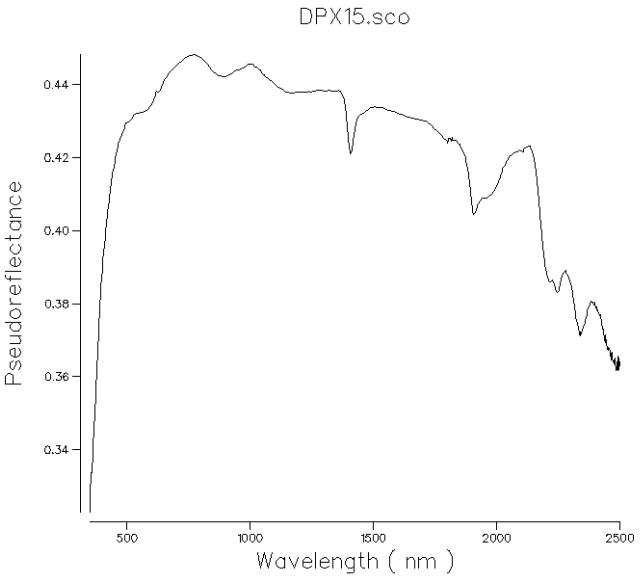
DPX15.sco
Pseudoreflectance
0.44
0.42
0.40
0.38
0.36
0.34
500
1000
1500
2000
2500
Wavelength (nm)

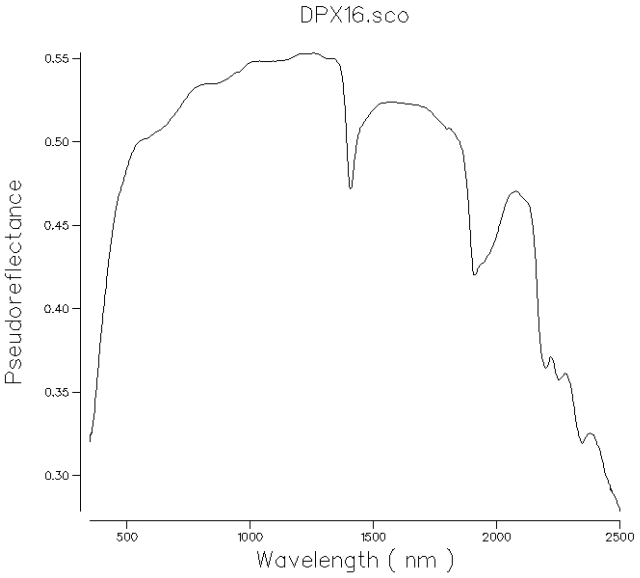
DPX16.sco
Pseudoreflectance
0.55
0.50
0.45
0.40
0.35
0.30
500
1000
1500
2000
2500
Wavelength (nm)

DPX17 was missed from the SWIR Analysis.

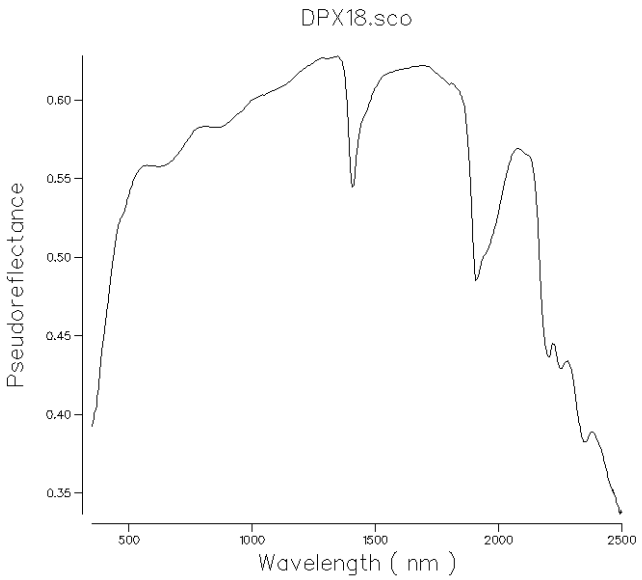

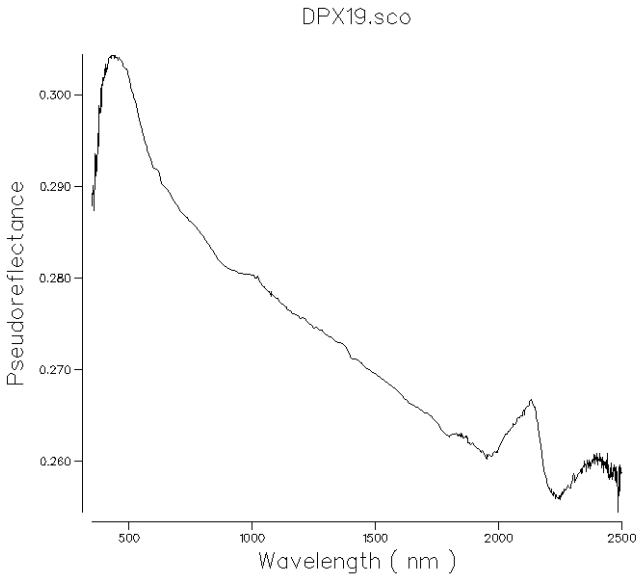
DPX19.sco
Pseudoreflectance
0.300
0.290
0.280
0.270
0.260
500
1000
1500
2000
2500
Wavelength (nm)

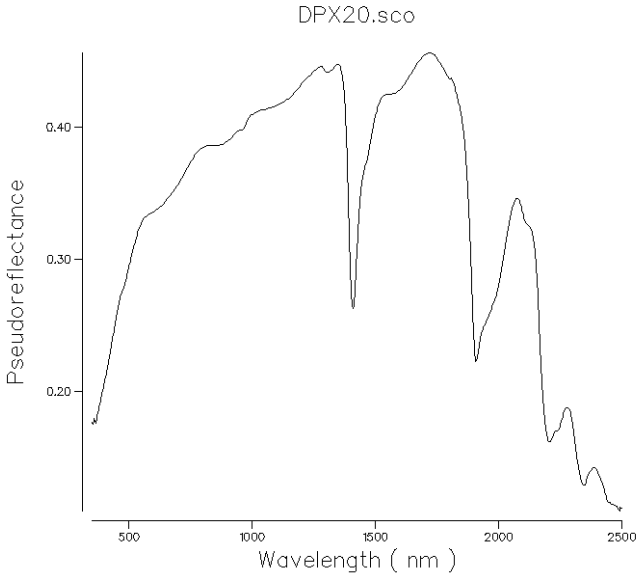
DPX20.sco
Pseudoreflectance
0.40
0.30
0.20
500
1000
1500
2000
2500
Wavelength (nm)

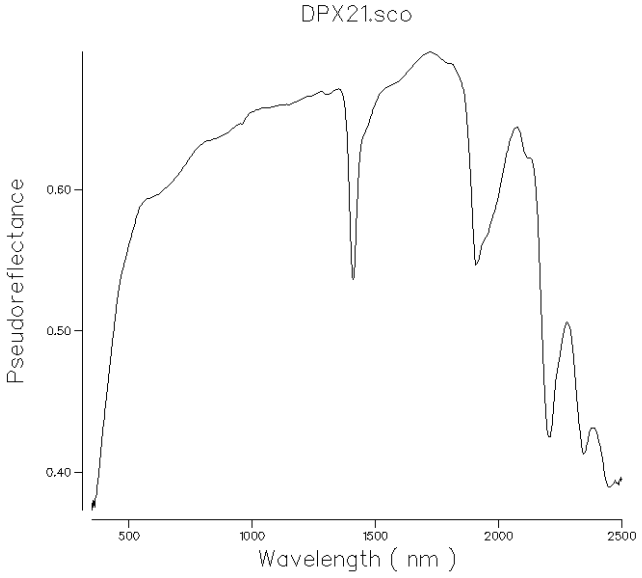
DPX21.sco
Pseudoreflectance
0.60
0.50
0.40
500
1000
1500
2000
2500
Wavelength (nm)

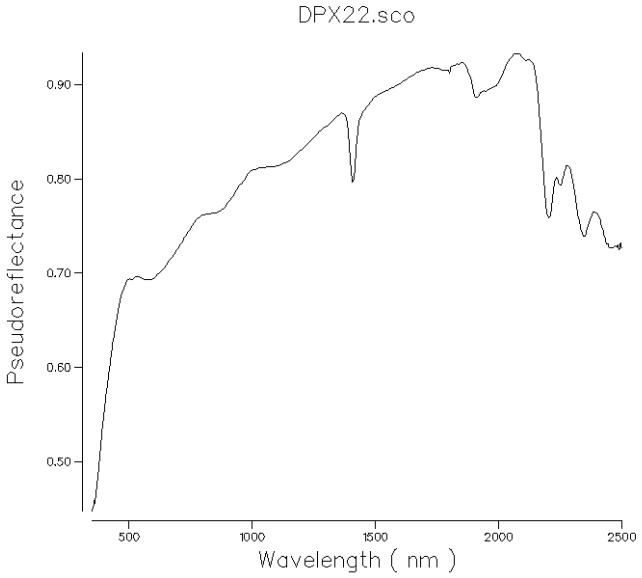
DPX22.sco
Pseudoreflectance
0.90
0.80
0.70
0.60
0.50
500
1000
1500
2000
2500
Wavelength (nm)

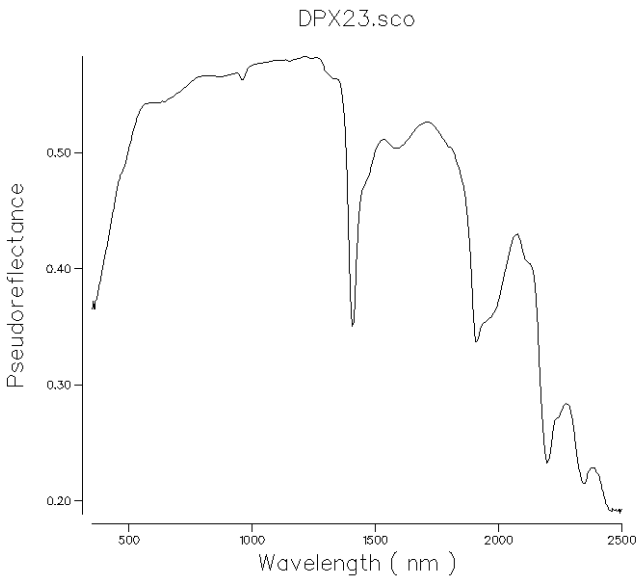
DPX23.sco
Pseudoreflectance
0.50
0.40
0.30
0.20
500
1000
1500
2000
2500
Wavelength (nm)

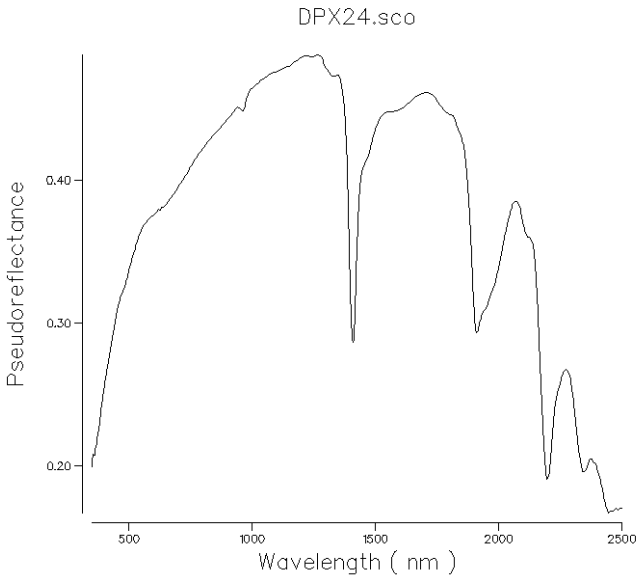
DPX24.sco
Pseudoreflectance
0.40
0.30
0.20
500
1000
1500
2000
2500
Wavelength (nm)

DPX25 was missed from the SWIR Analysis

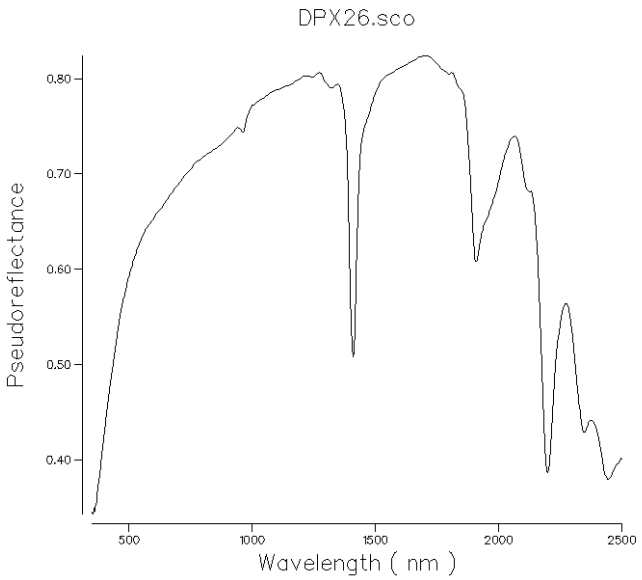

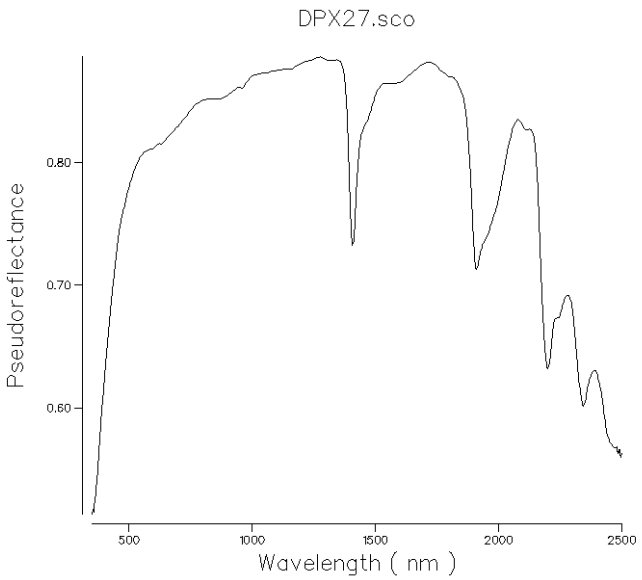

DPX 28 and 29 were missed from the SWIR Analyses

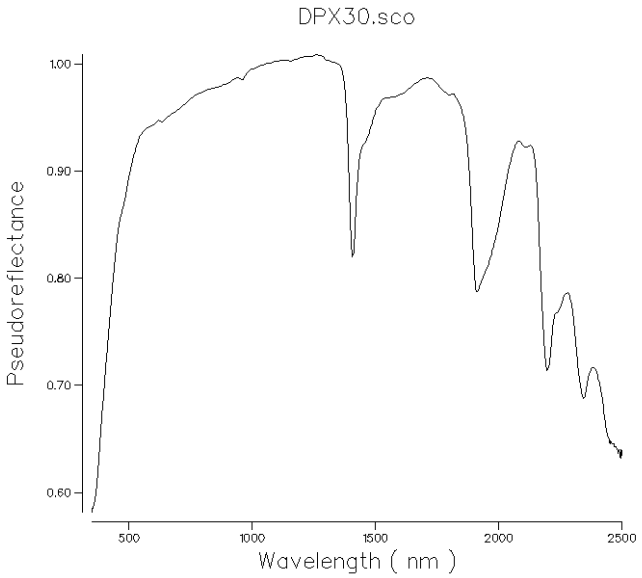
DPX30.sco
Pseudoreflectance
1.00
0.90
0.80
0.70
0.60
500
1000
1500
2000
2500
Wavelength (nm)

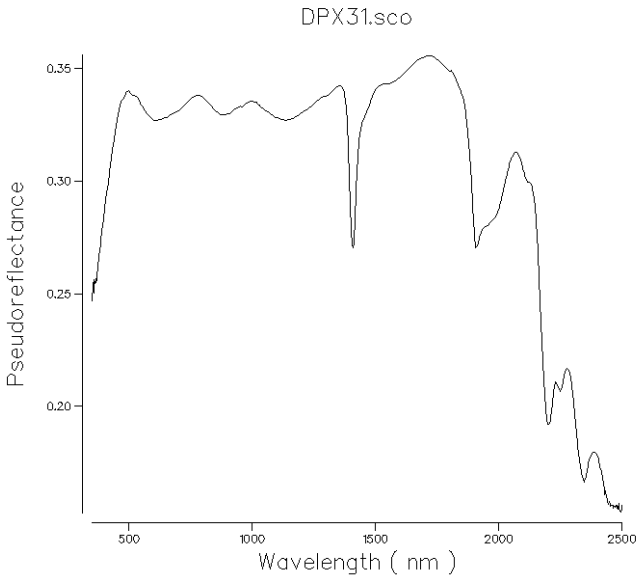
DPX31.sco
Pseudoreflectance
0.35
0.30
0.25
0.20
500
1000
1500
2000
2500
Wavelength (nm)

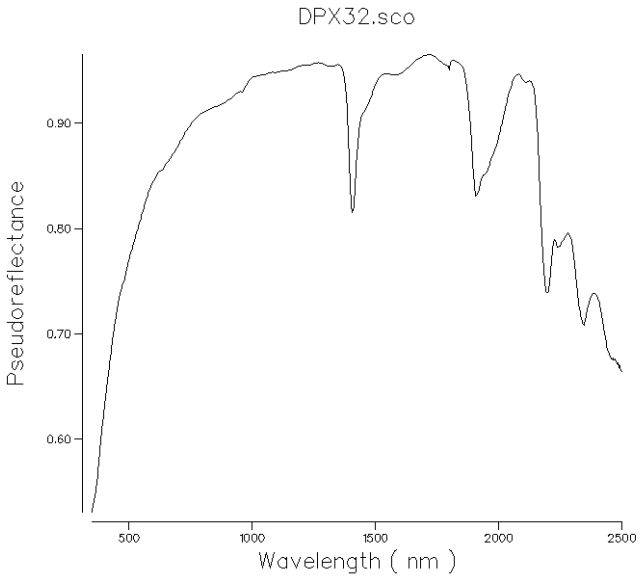
DPX32.sco
Pseudoreflectance
0.90
0.80
0.70
0.60
500
1000
1500
2000
2500
Wavelength (nm)

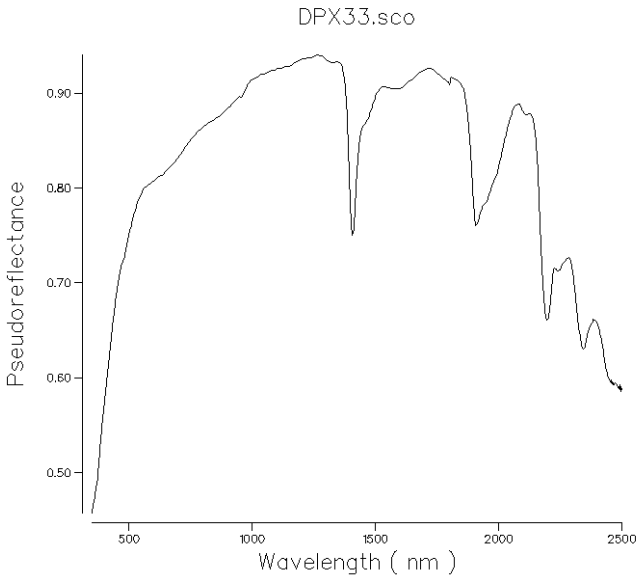
DPX33.sco
Pseudoreflectance
0.90
0.80
0.70
0.60
0.50
500
1000
1500
2000
2500
Wavelength (nm)

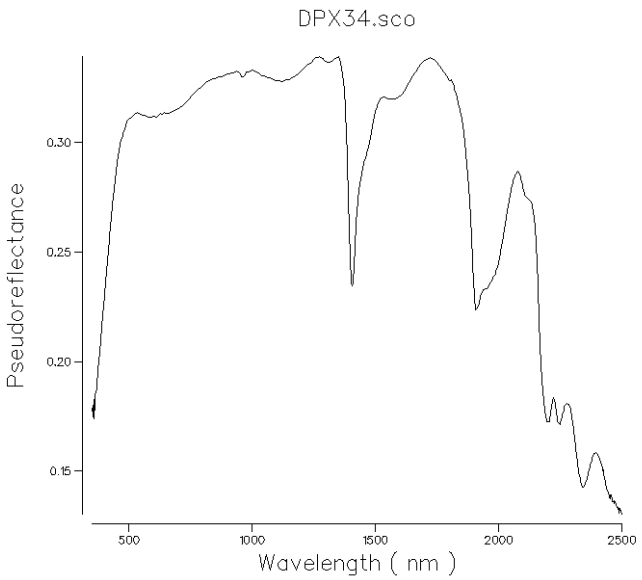
DPX34.sco
Pseudoreflectance
0.30
0.25
0.20
0.15
500
1000
1500
2000
2500
Wavelength (nm)

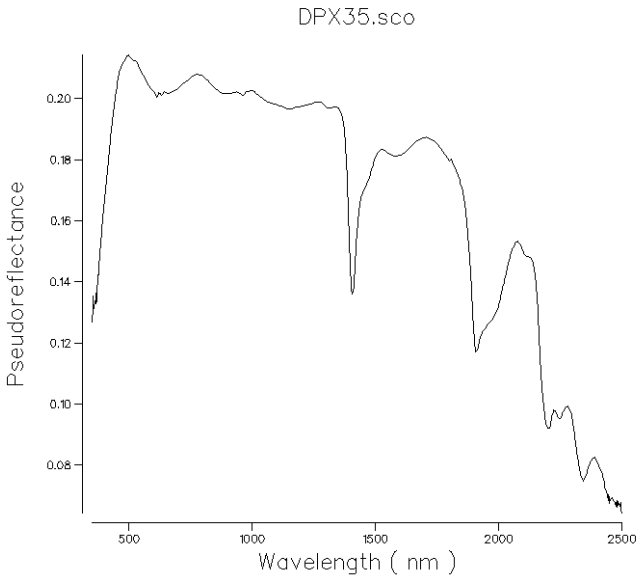
DPX35.sco
Pseudoreflectance
0.20
0.18
0.16
0.14
0.12
0.10
0.08
500
1000
1500
2000
2500
Wavelength (nm)

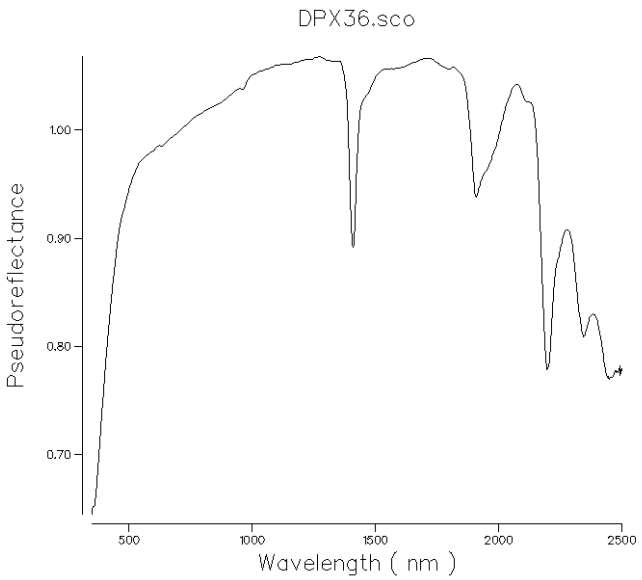

DPX37 was missed from the SWIR Analysis

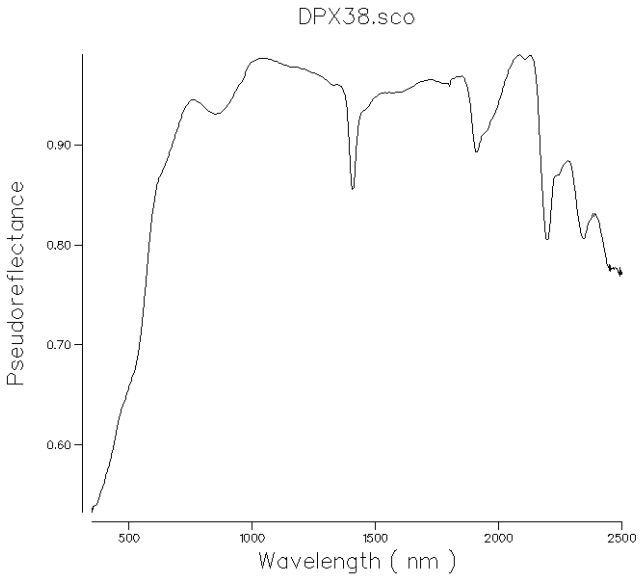
DPX38.sco
Pseudoreflectance
0.90
0.80
0.70
0.60
500
1000
1500
2000
2500
Wavelength (nm)

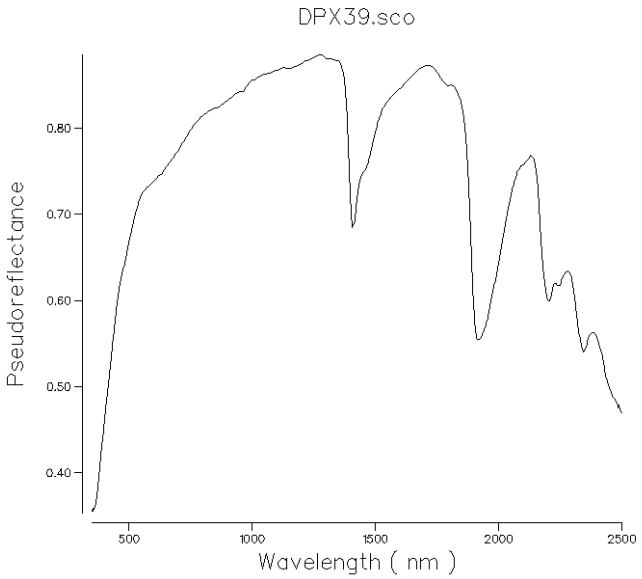
DPX39.sco
Pseudoreflectance
0.80
0.70
0.60
0.50
0.40
500
1000
1500
2000
2500
Wavelength (nm)

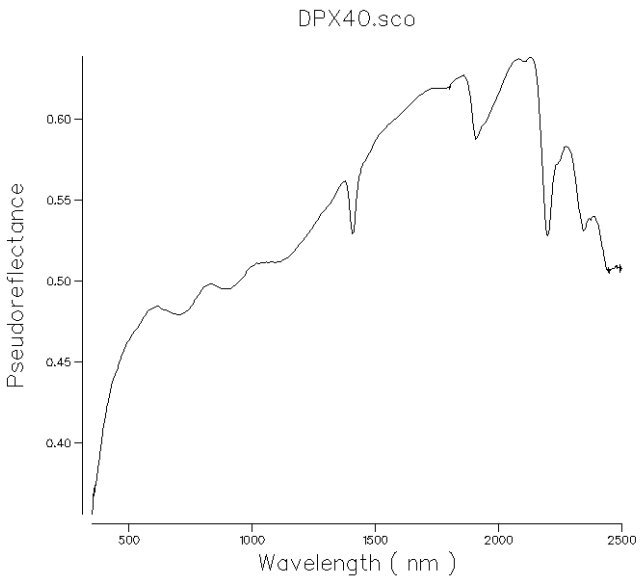

DPX41,42 and 43 were missed from the SWIR Analysis

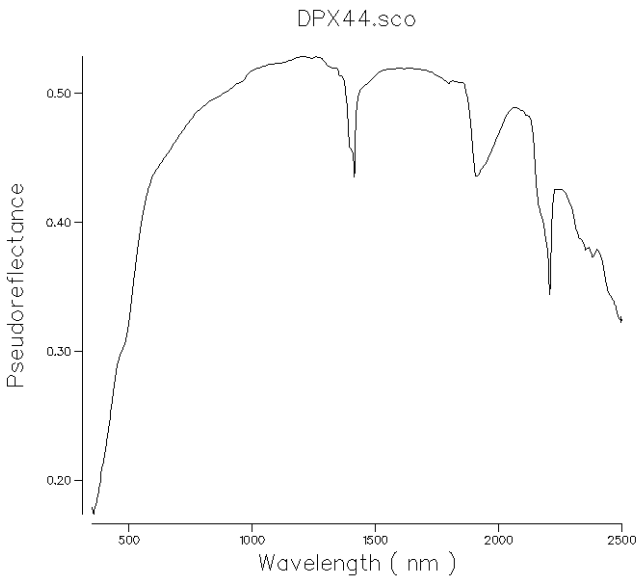

DPX45 was missed from the SWIR Analysis

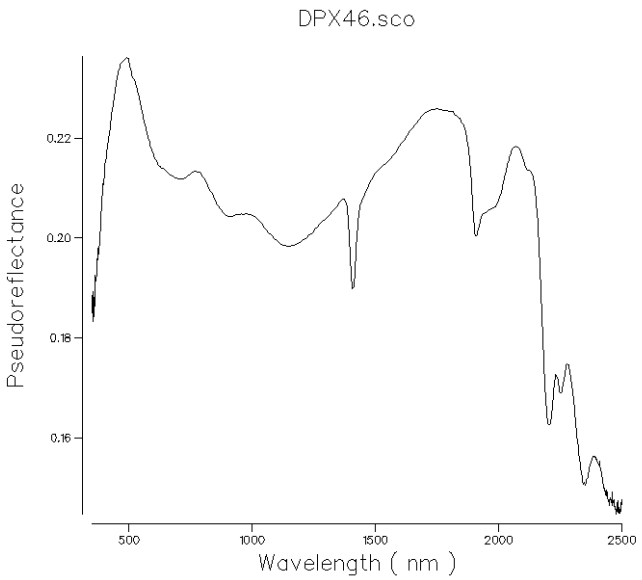
DPX46.sco
Pseudoreflectance
0.22
0.20
0.18
0.16
500
1000
1500
2000
2500
Wavelength (nm)

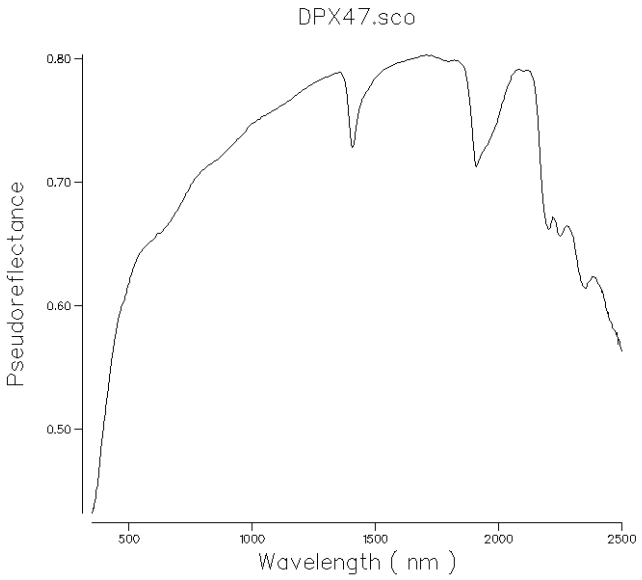
DPX47.sco
Pseudoreflectance
0.80
0.70
0.60
0.50
500
1000
1500
2000
2500
Wavelength (nm)

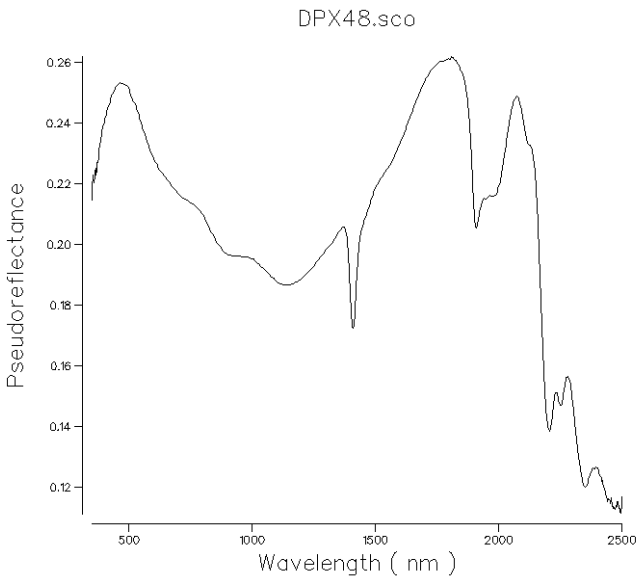
DPX48.sco
Pseudoreflectance
0.26
0.24
0.22
0.20
0.18
0.16
0.14
0.12
500
1000
1500
2000
2500
Wavelength (nm)

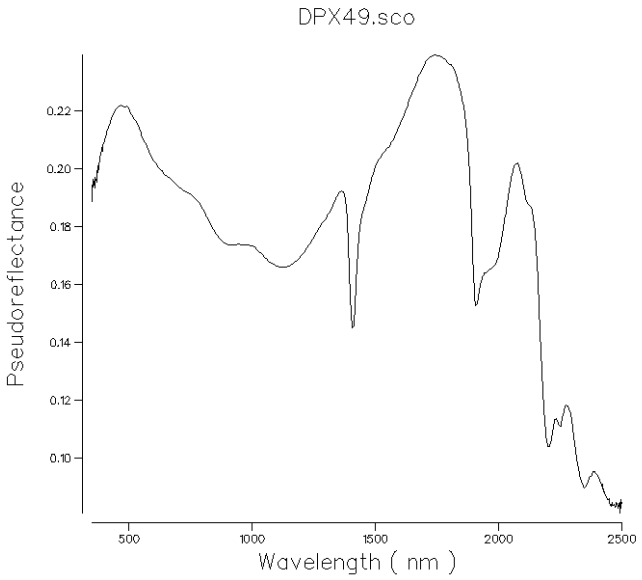
DPX49.sco
Pseudoreflectance
0.22
0.20
0.18
0.16
0.14
0.12
0.10
500
1000
1500
2000
2500
Wavelength (nm)

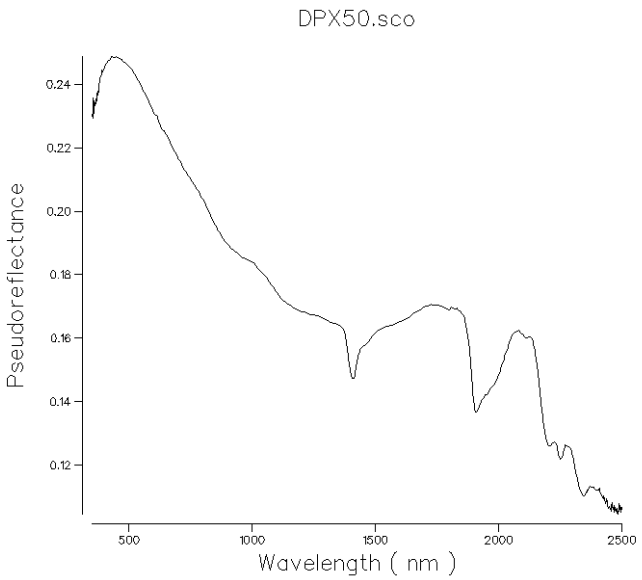
DPX50.sco
Pseudoreflectance
0.24
0.22
0.20
0.18
0.16
0.14
0.12
500
1000
1500
2000
2500
Wavelength (nm)

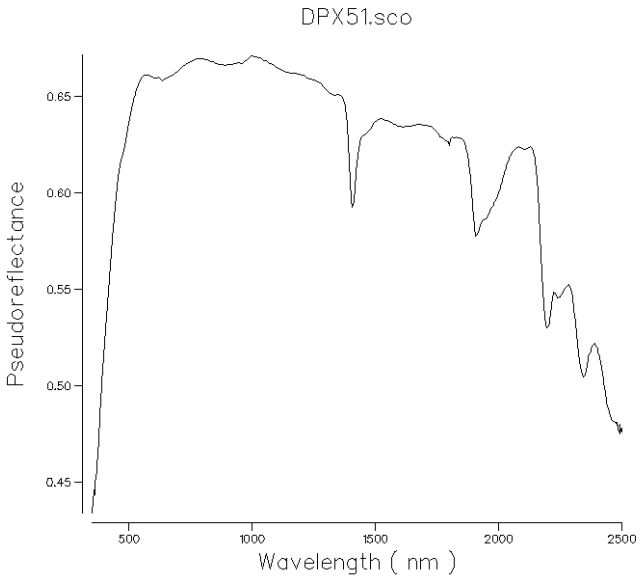
DPX51.sco
Pseudoreflectance
0.65
0.60
0.55
0.50
0.45
500
1000
1500
2000
2500
Wavelength (nm)

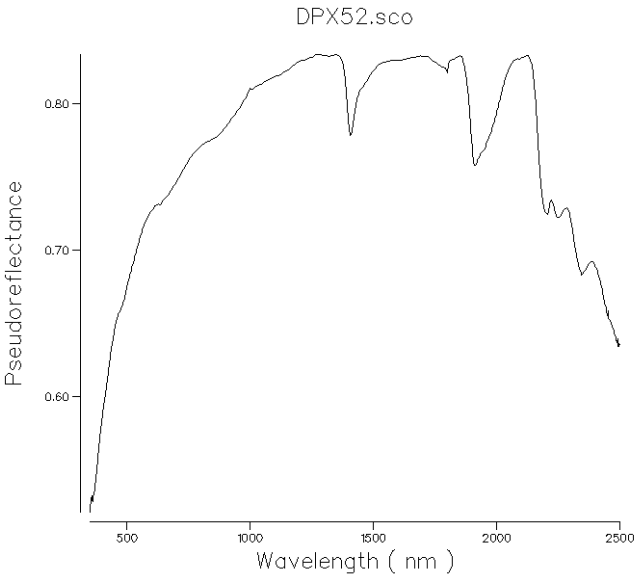
DPX52.sco
Pseudoreflectance
0.80
0.70
0.60
500
1000
1500
2000
2500
Wavelength (nm)

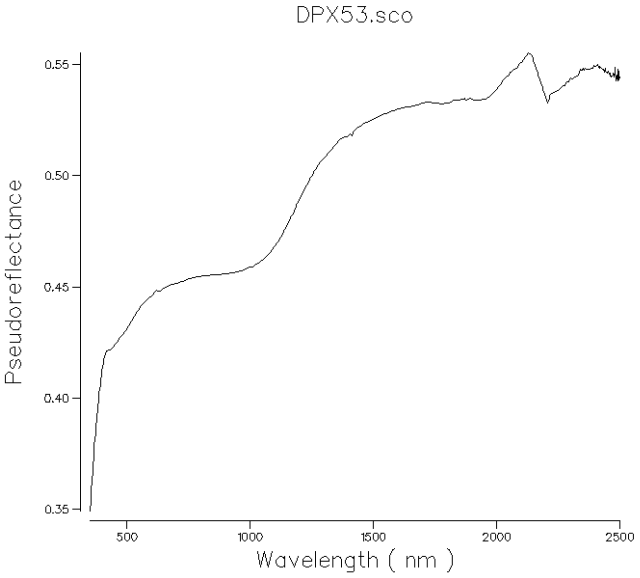
DPX53.sco
Pseudoreflectance
0.55
0.50
0.45
0.40
0.35
500
1000
1500
2000
2500
Wavelength (nm)

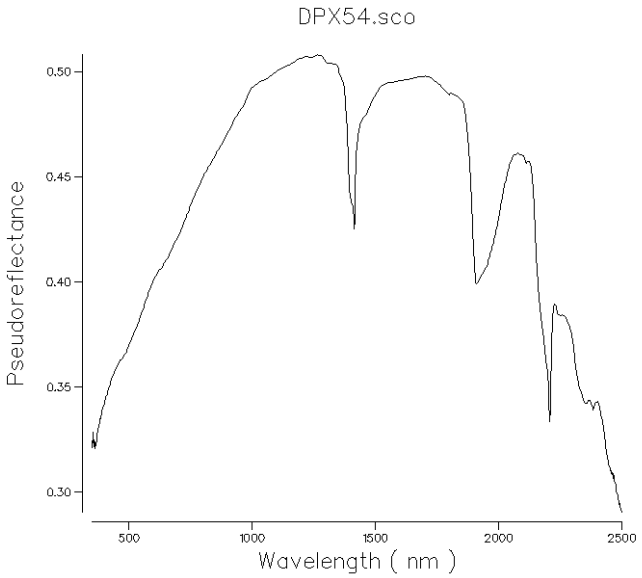
DPX54.sco
Pseudoreflectance
0.50
0.45
0.40
0.35
0.30
500
1000
1500
2000
2500
Wavelength (nm)

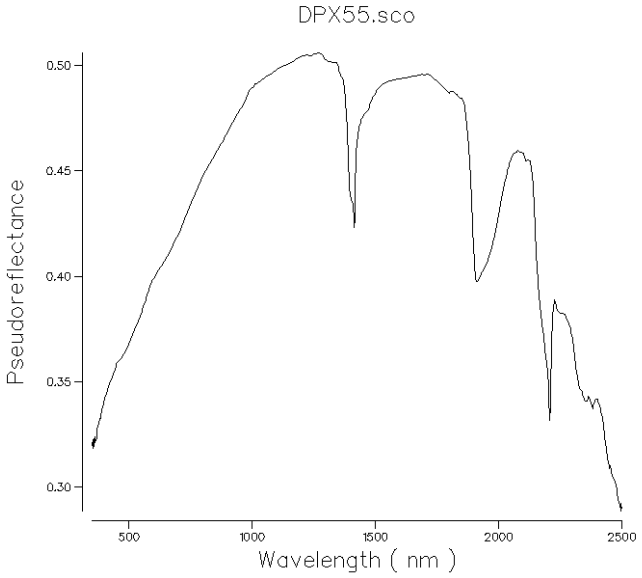
DPX55.sco
Pseudoreflectance
0.50
0.45
0.40
0.35
0.30
500
1000
1500
2000
2500
Wavelength (nm)

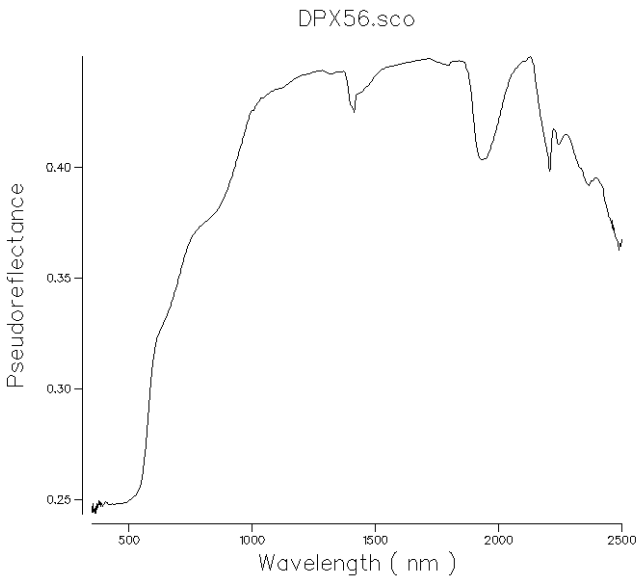

DPX 57 and 58 were missed from the SWIR Analysis

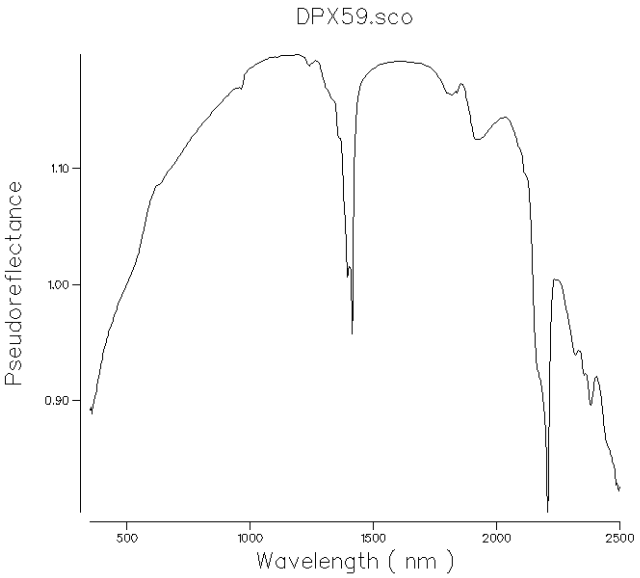
DPX59.sco
Pseudoreflectance
1.10
1.00
0.90
500
1000
1500
2000
2500
Wavelength (nm)

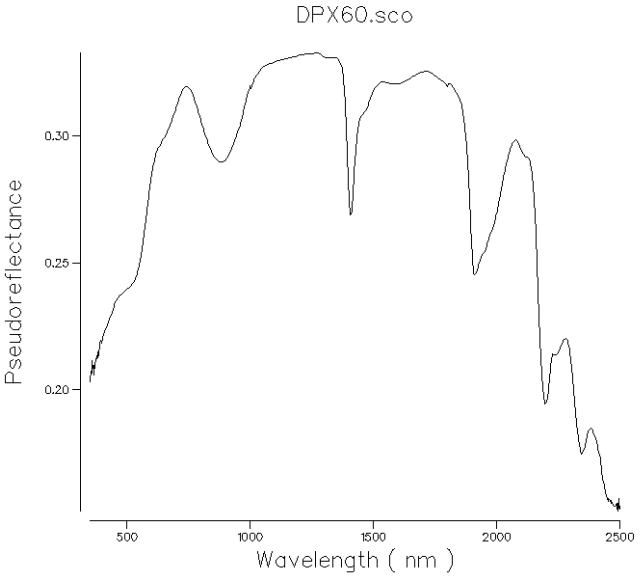
DPX60.sco
Pseudoreflectance
0.30
0.25
0.20
500
1000
1500
2000
2500
Wavelength (nm)

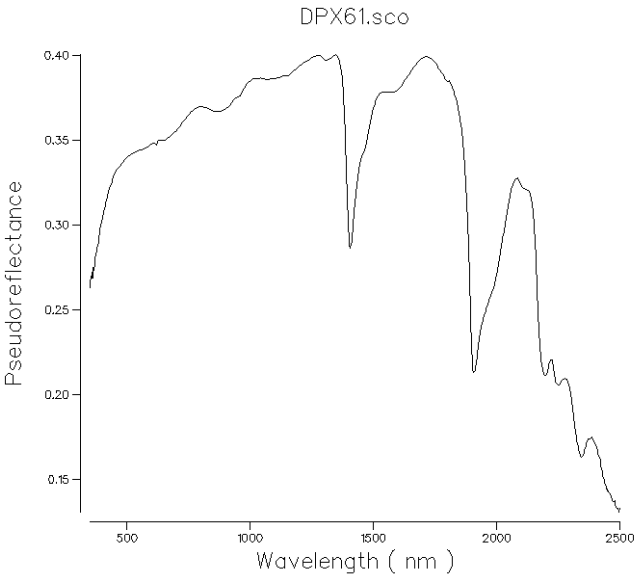
DPX61.sco
Pseudoreflectance
0.40
0.35
0.30
0.25
0.20
0.15
500
1000
1500
2000
2500
Wavelength (nm)

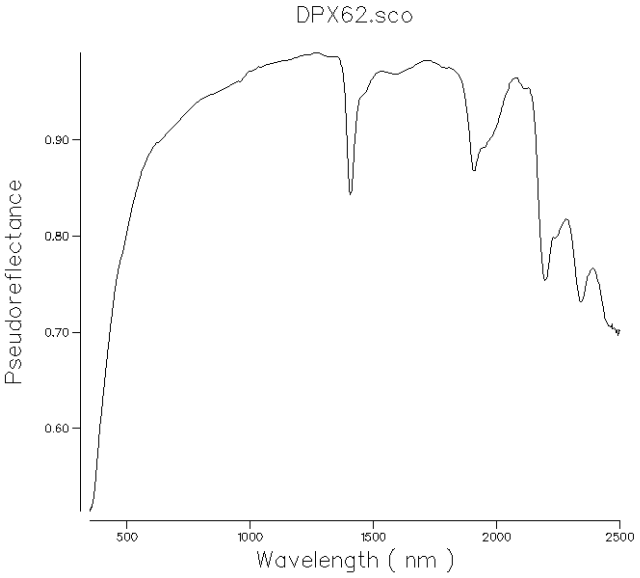
DPX62.sco
Pseudoreflectance
0.90
0.80
0.70
0.60
500
1000
1500
2000
2500
Wavelength (nm)

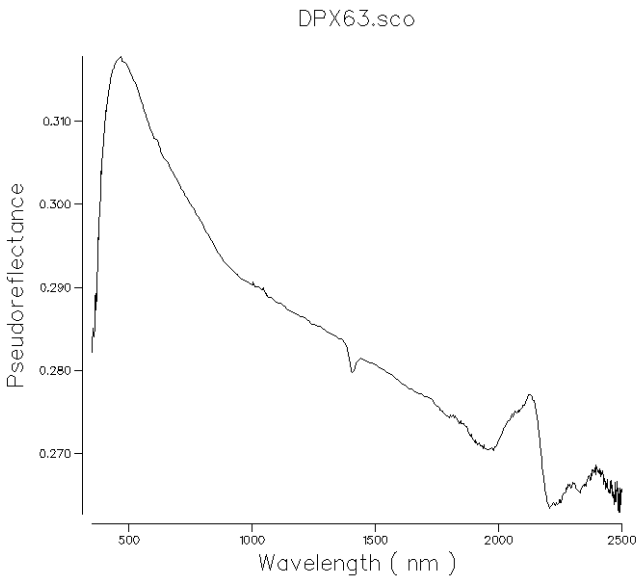
DPX63.sco
Pseudoreflectance
0.310
0.300
0.290
0.280
0.270
500
1000
1500
2000
2500
Wavelength (nm)

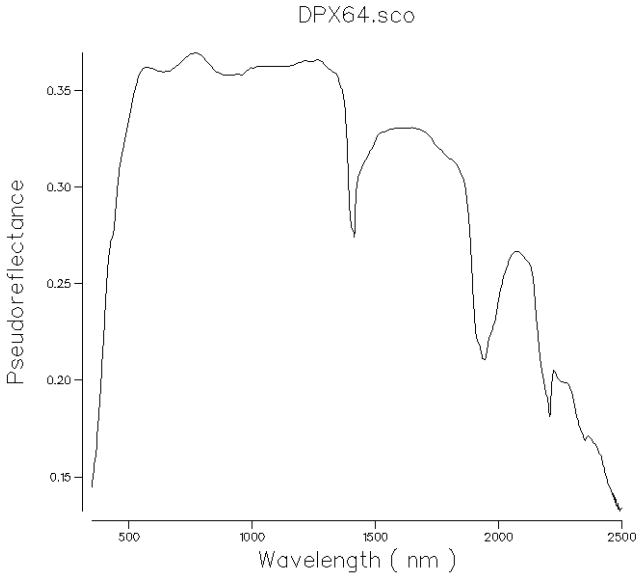
DPX64.sco
Pseudoreflectance
0.35
0.30
0.25
0.20
0.15
500
1000
1500
2000
2500
Wavelength (nm)

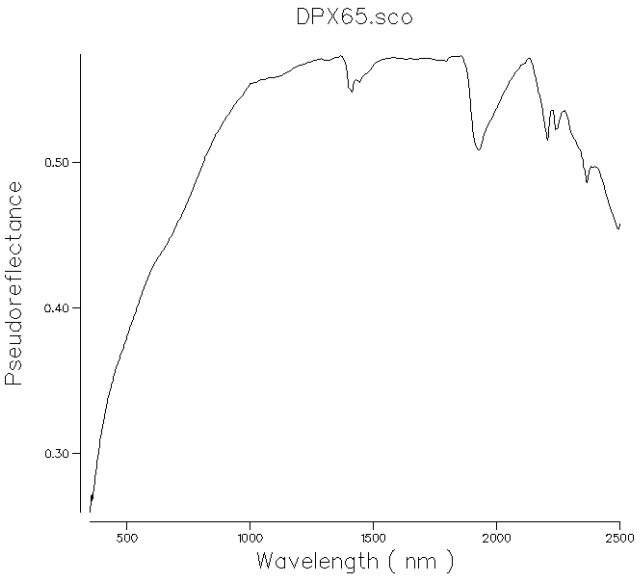
DPX65.sco
Pseudoreflectance
0.50
0.40
0.30
500
1000
1500
2000
2500
Wavelength (nm)

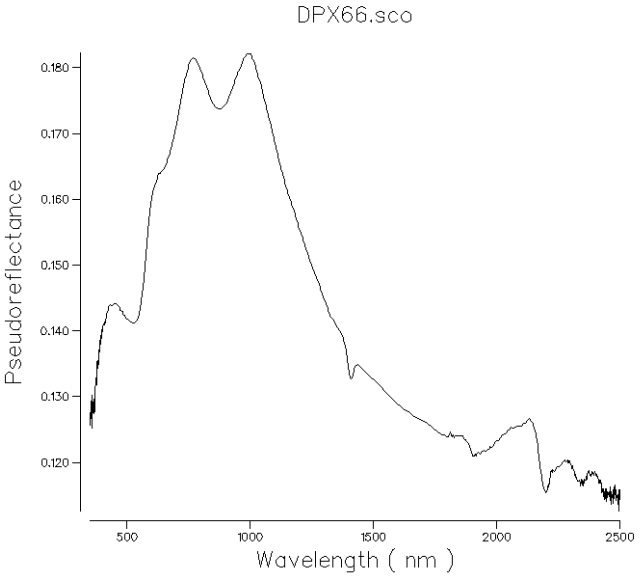
DPX66.sco
Pseudoreflectance
0.180
0.170
0.160
0.150
0.140
0.130
0.120
500
1000
1500
2000
2500
Wavelength (nm)

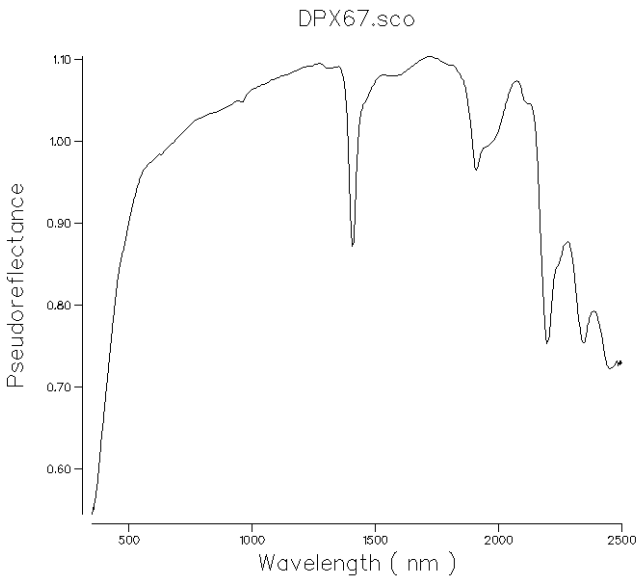
DPX67.sco
Pseudoreflectance
1.10
1.00
0.90
0.80
0.70
0.60
500
1000
1500
2000
2500
Wavelength (nm)

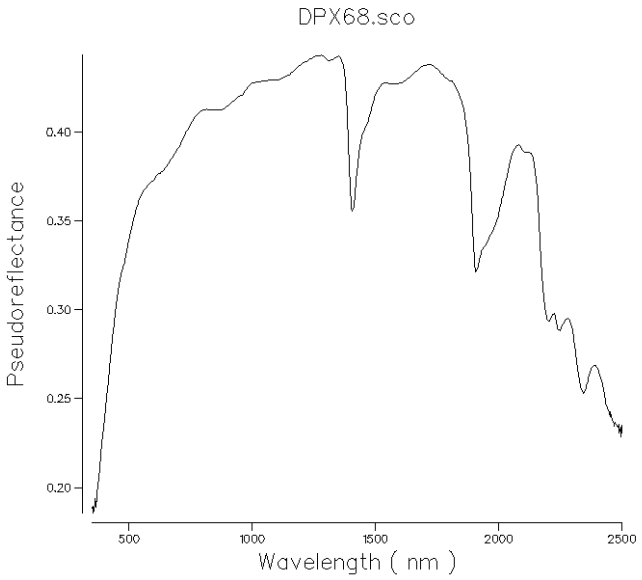
DPX68.sco
Pseudoreflectance
0.40
0.35
0.30
0.25
0.20
500
1000
1500
2000
2500
Wavelength (nm)

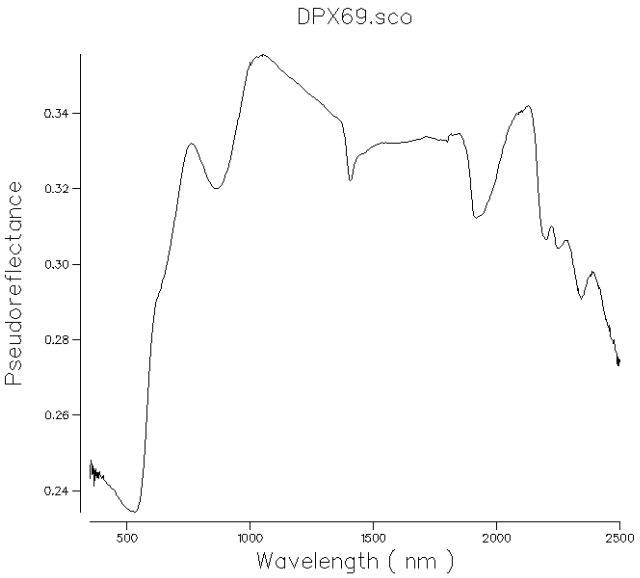
DPX69.sco
Pseudoreflectance
0.34
0.32
0.30
0.28
0.26
0.24
500
1000
1500
2000
2500
Wavelength (nm)

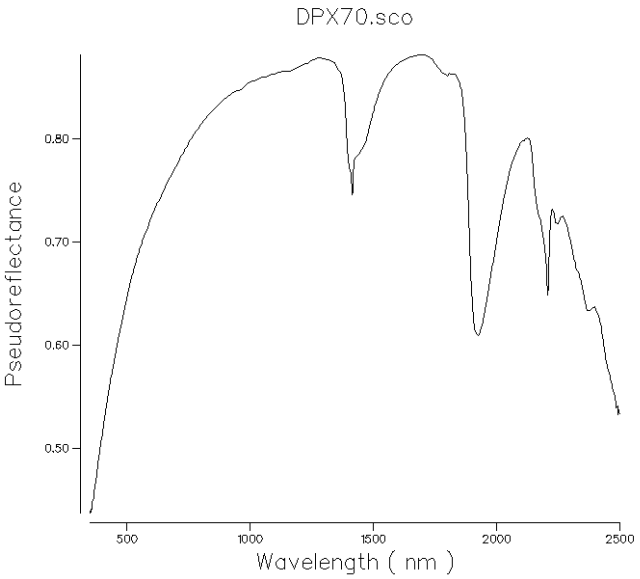
DPX70.sco
Pseudoreflectance
0.80
0.70
0.60
0.50
500
1000
1500
2000
2500
Wavelength (nm)

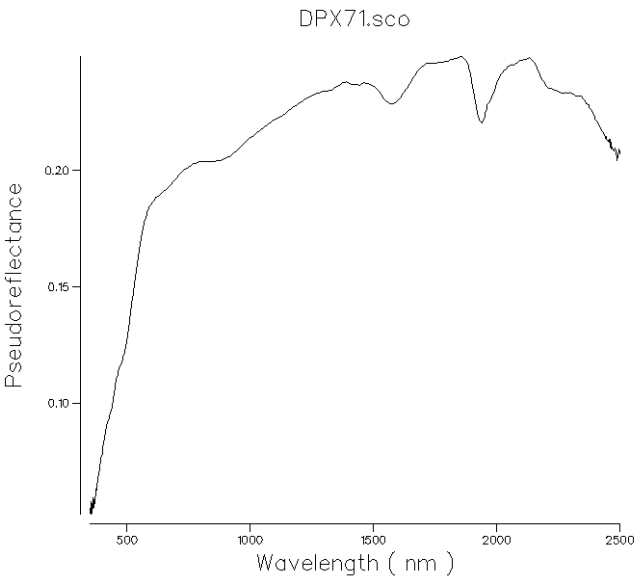
DPX71.sco
Pseudoreflectance
0.20
0.15
0.10
500
1000
1500
2000
2500
Wavelength (nm)

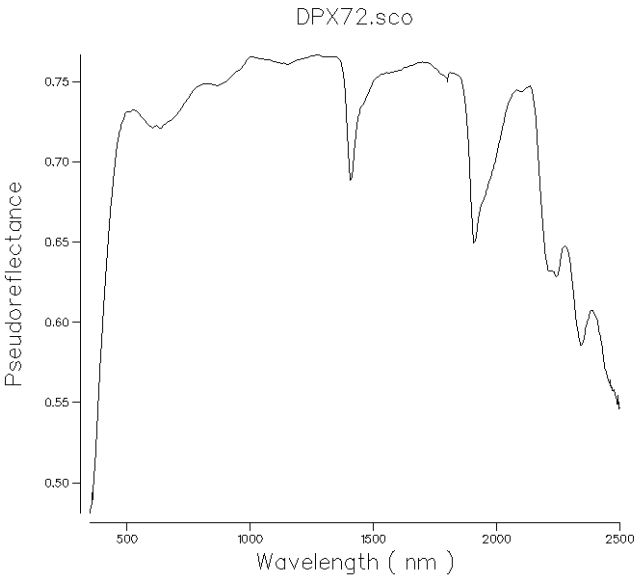
DPX72.sco
Pseudoreflectance
0.75
0.70
0.65
0.60
0.55
0.50
500
1000
1500
2000
2500
Wavelength (nm)

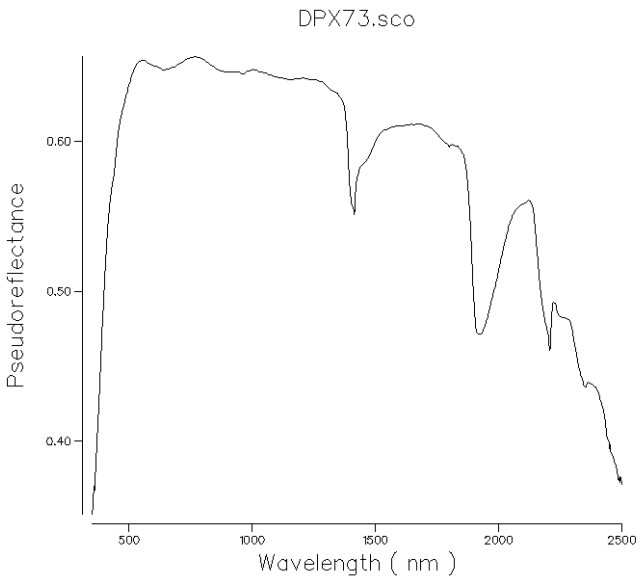

DPX 74 was missed from the SWIR analysis

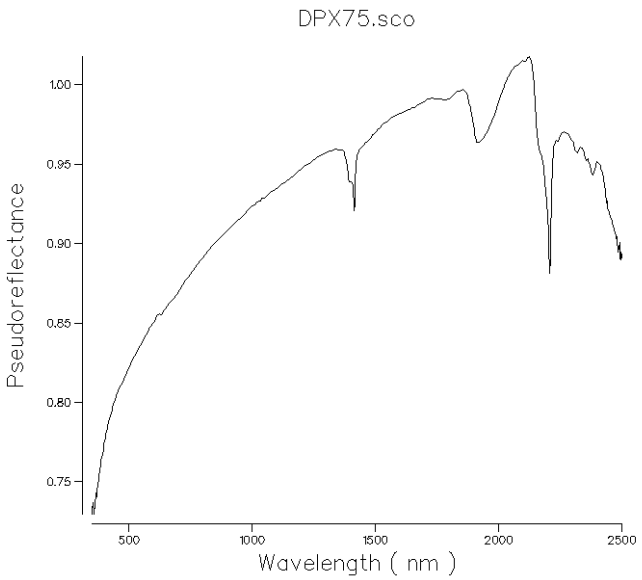
DPX75.sco
Pseudoreflectance
1.00
0.95
0.90
0.85
0.80
0.75
500
1000
1500
2000
2500
Wavelength (nm)

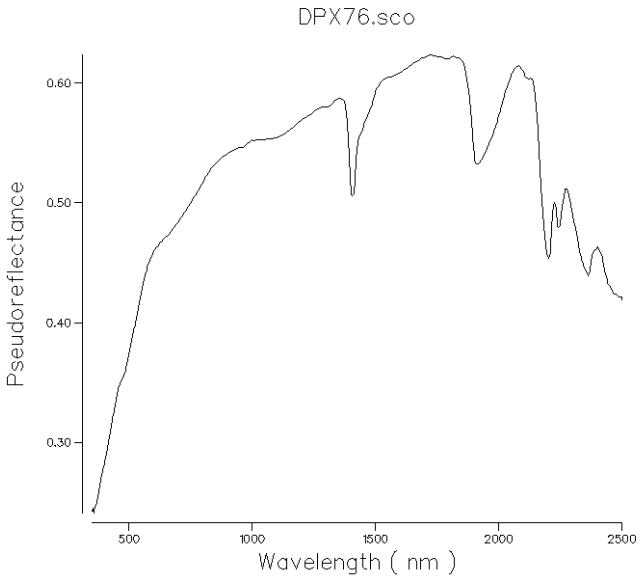
DPX76.sco
Pseudoreflectance
0.60
0.50
0.40
0.30
500
1000
1500
2000
2500
Wavelength (nm)

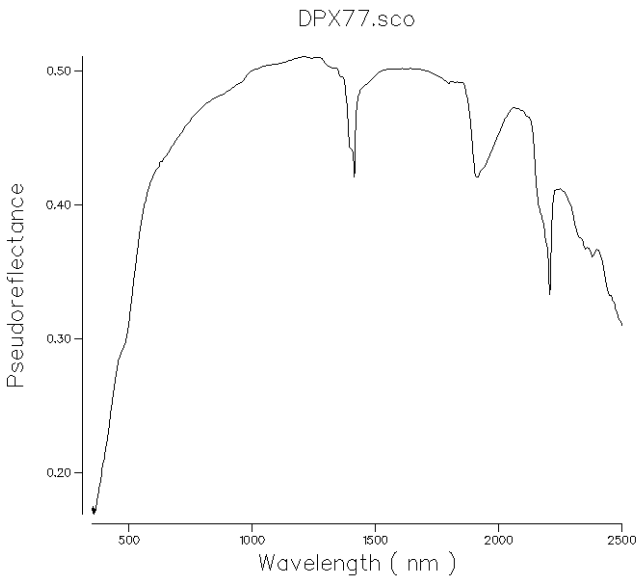
DPX77.sco
Pseudoreflectance
0.50
0.40
0.30
0.20
500
1000
1500
2000
2500
Wavelength (nm)

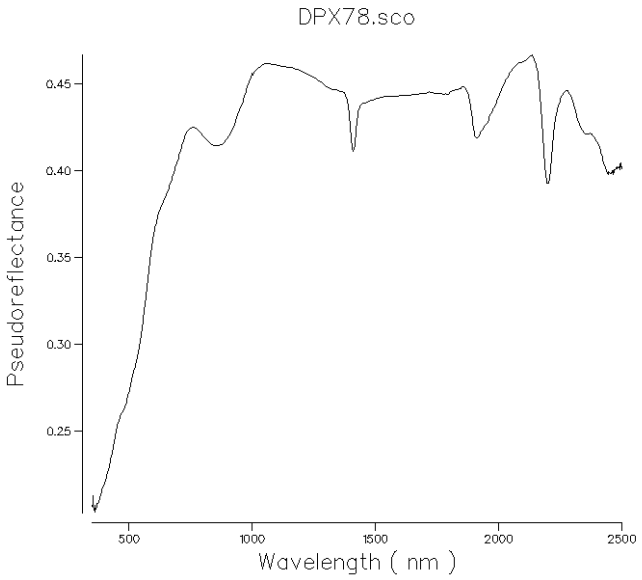
DPX78.sco
Pseudoreflectance
0.45
0.40
0.35
0.30
0.25
500
1000
1500
2000
2500
Wavelength (nm)

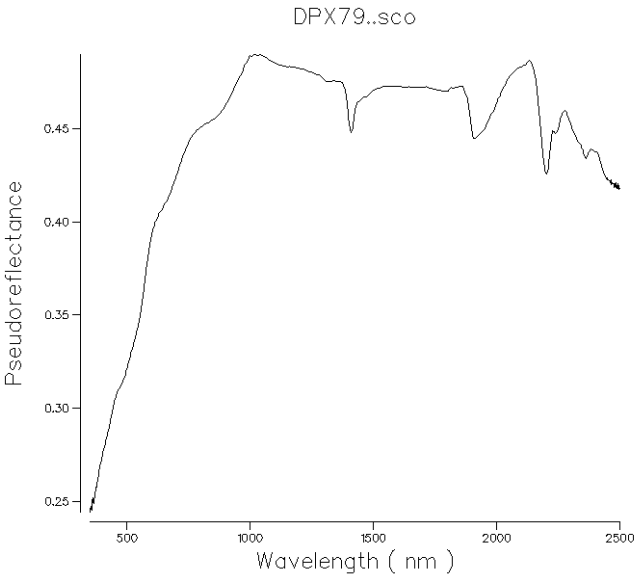
DPX79..sco
Pseudoreflectance
0.45
0.40
0.35
0.30
0.25
500
1000
1500
2000
2500
Wavelength (nm)

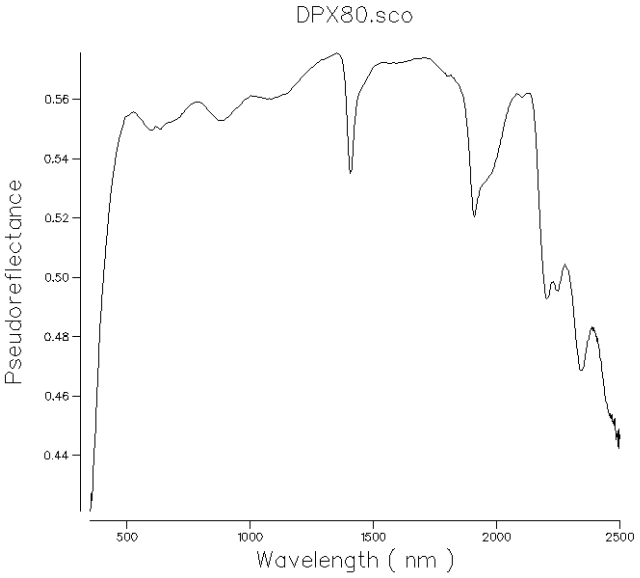
DPX80.sco
Pseudoreflectance
0.56
0.54
0.52
0.50
0.48
0.46
0.44
500
1000
1500
2000
2500
Wavelength (nm)

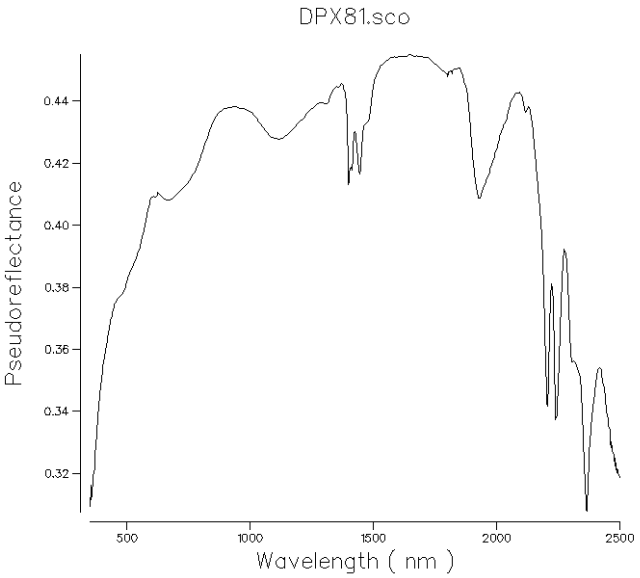

No samples were collected between DPX82 and DPX100, as DPX 100 was collected in summer 2011.

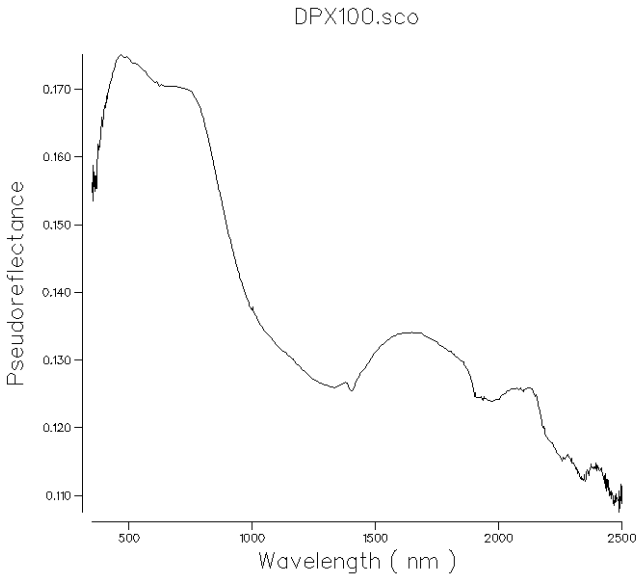
DPX100.sco
Pseudoreflectance
0.170
0.160
0.150
0.140
0.130
0.120
0.110
500
1000
1500
2000
2500
Wavelength (nm)

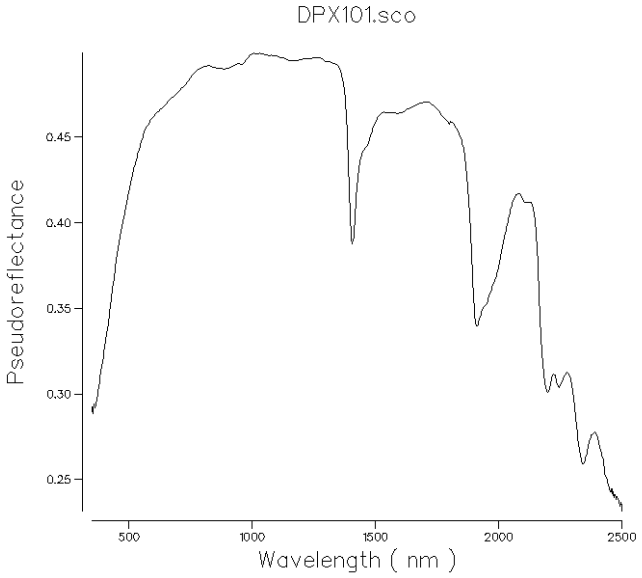
DPX101.sco
Pseudoreflectance
0.45
0.40
0.35
0.30
0.25
500
1000
1500
2000
2500
Wavelength (nm)

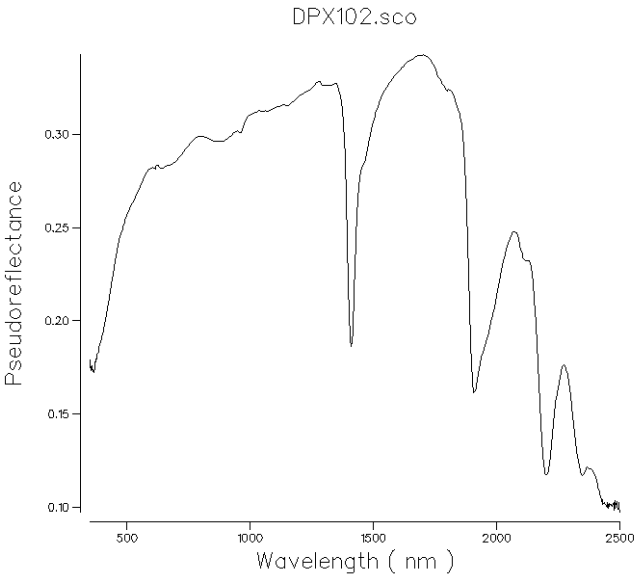
DPX102.sco
Pseudoreflectance
0.30
0.25
0.20
0.15
0.10
500
1000
1500
2000
2500
Wavelength (nm)

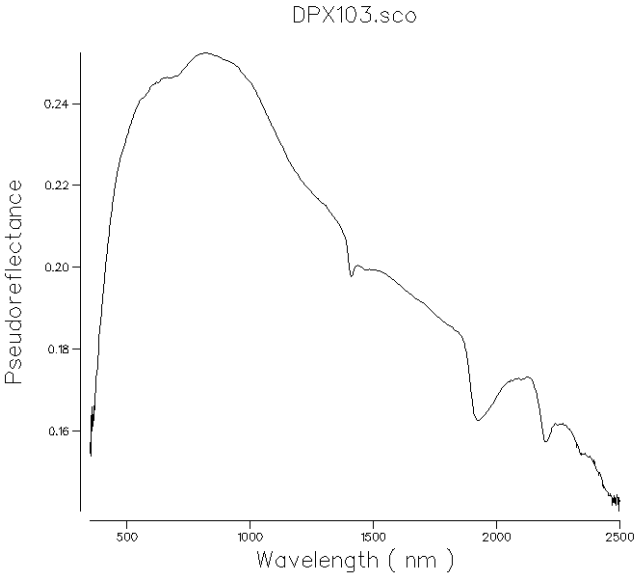
DPX103.sco
Pseudoreflectance
0.24
0.22
0.20
0.18
0.16
500
1000
1500
2000
2500
Wavelength (nm)

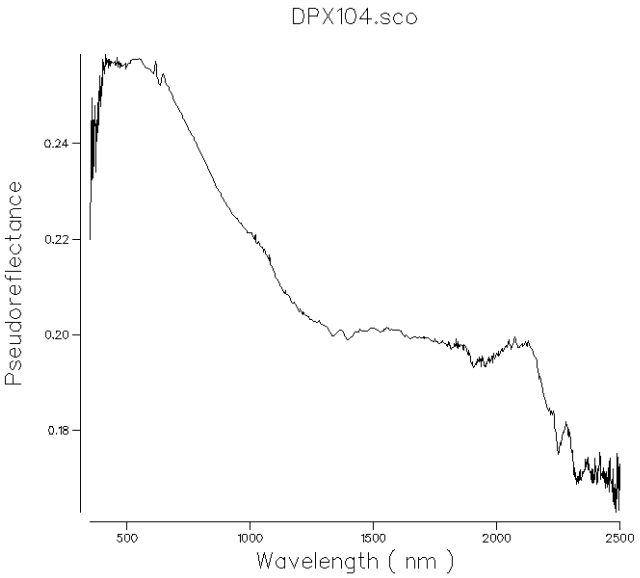
DPX104.sco
Pseudoreflectance
0.24
0.22
0.20
0.18
500
1000
1500
2000
2500
Wavelength (nm)

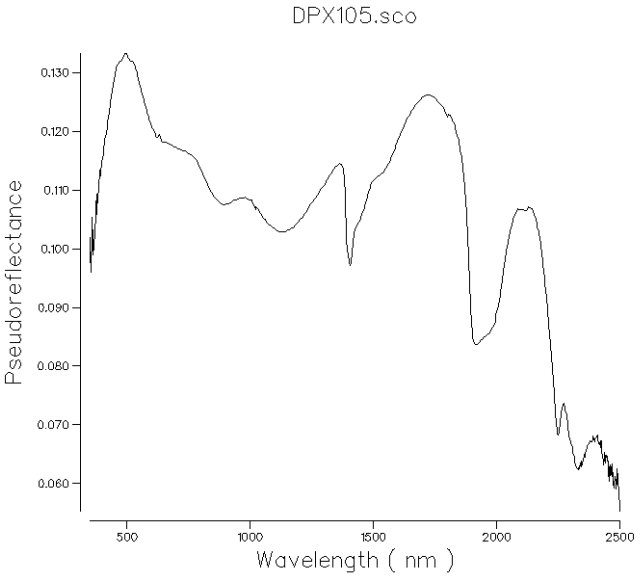
DPX105.sco
Pseudoreflectance
0.130
0.120
0.110
0.100
0.090
0.080
0.070
0.060
500
1000
1500
2000
2500
Wavelength (nm)

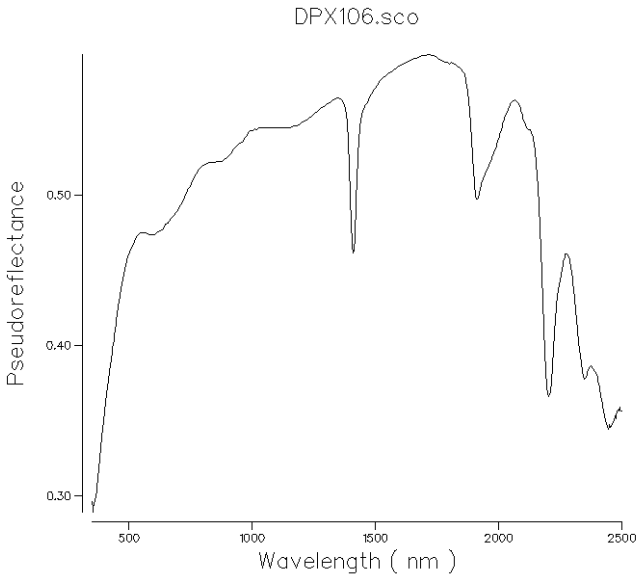
DPX106.sco
Pseudoreflectance
0.50
0.40
0.30
500
1000
1500
2000
2500
Wavelength (nm)

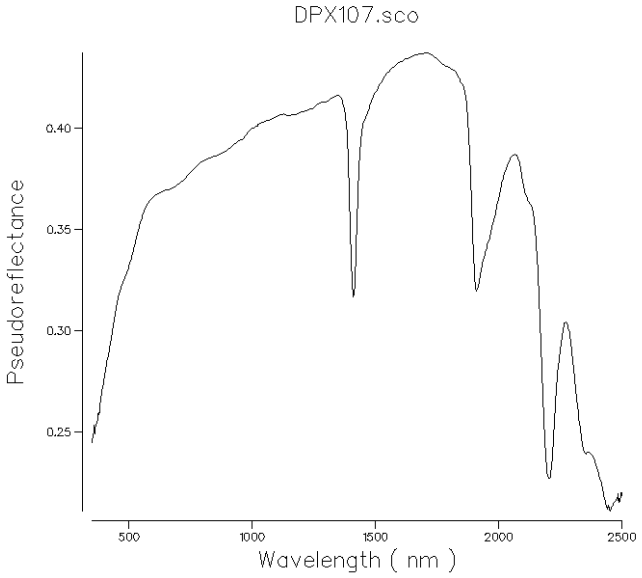
DPX107.sco
Pseudoreflectance
0.40
0.35
0.30
0.25
500
1000
1500
2000
2500
Wavelength (nm)

DPX108 was missed from the SWIR Analysis

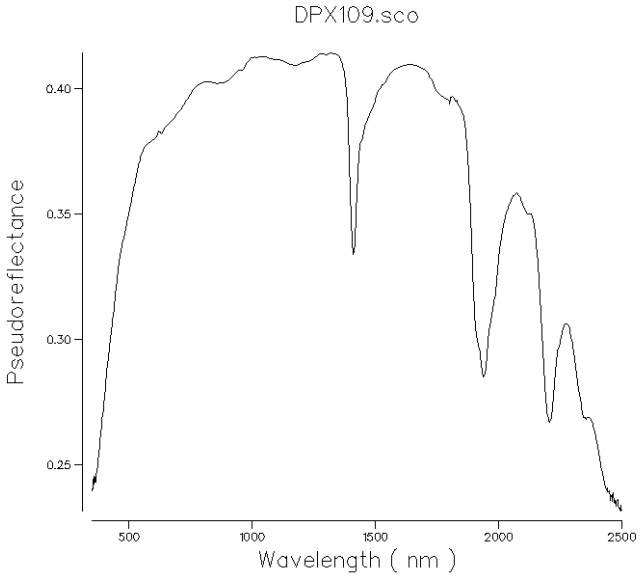

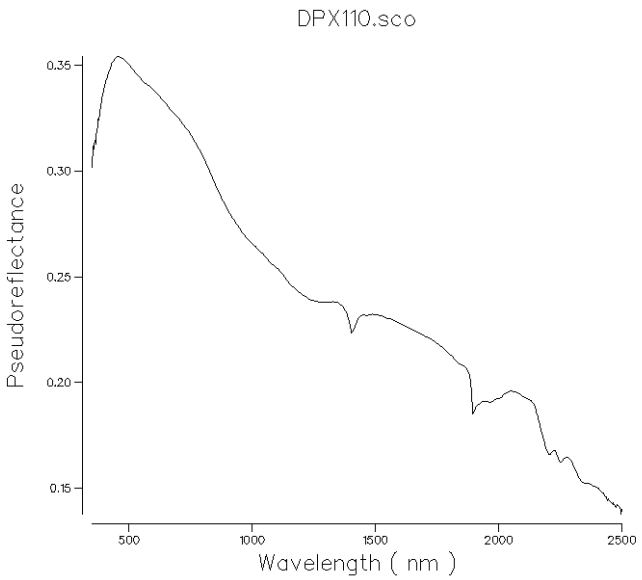
DPX110.sco
Pseudoreflectance
0.35
0.30
0.25
0.20
0.15
500
1000
1500
2000
2500
Wavelength (nm)

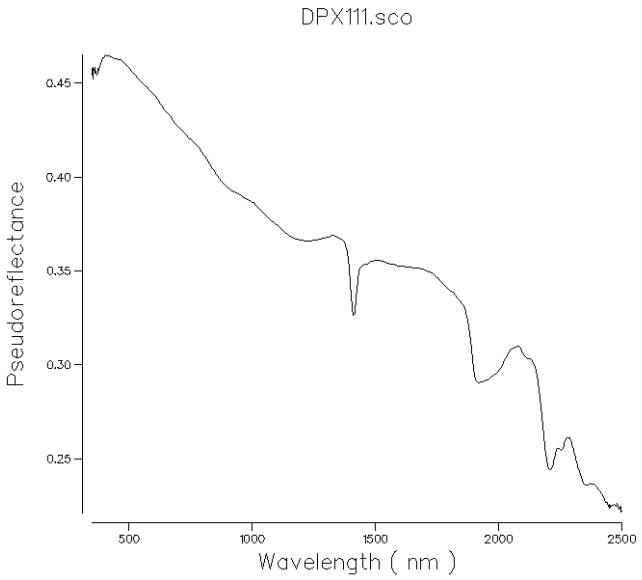
DPX111.sco
Pseudoreflectance
0.45
0.40
0.35
0.30
0.25
500
1000
1500
2000
2500
Wavelength (nm)

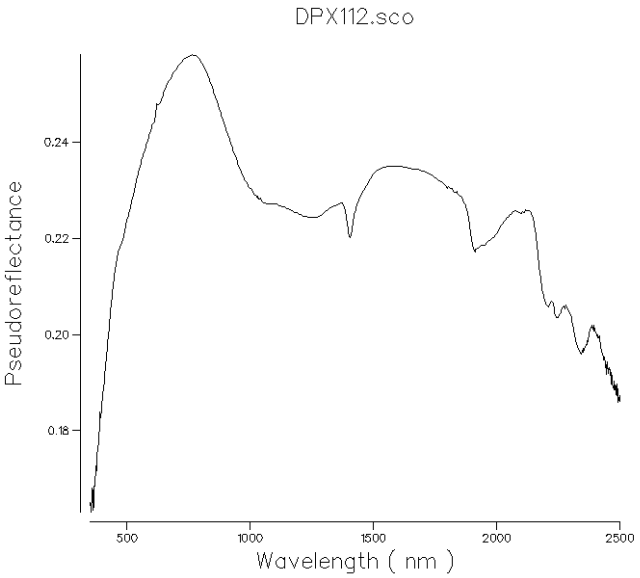
DPX112.sco
Pseudoreflectance
0.24
0.22
0.20
0.18
500
1000
1500
2000
2500
Wavelength (nm)

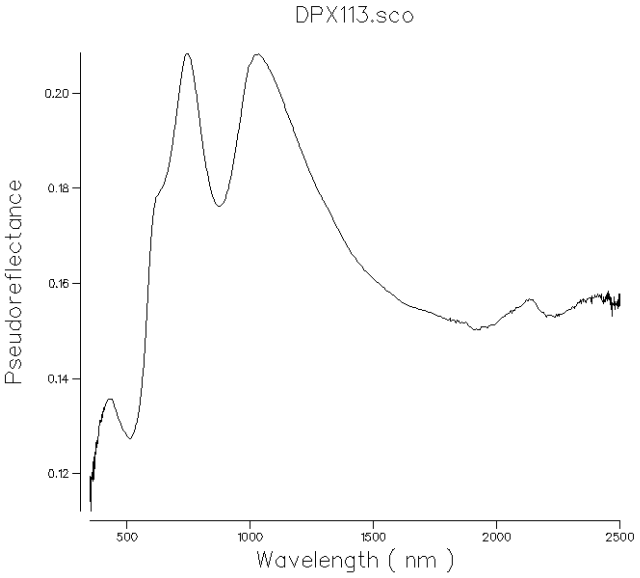
DPX113.sco
Pseudoreflectance
0.20
0.18
0.16
0.14
0.12
500
1000
1500
2000
2500
Wavelength (nm)

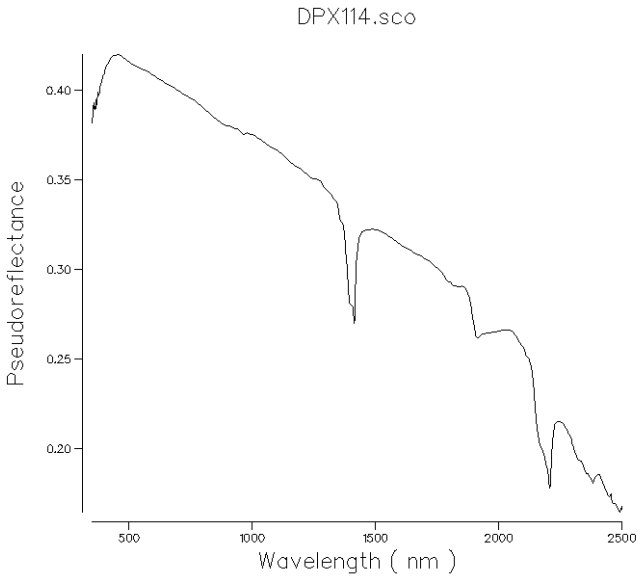
DPX114.sco
Pseudoreflectance
0.40
0.35
0.30
0.25
0.20
500
1000
1500
2000
2500
Wavelength (nm)

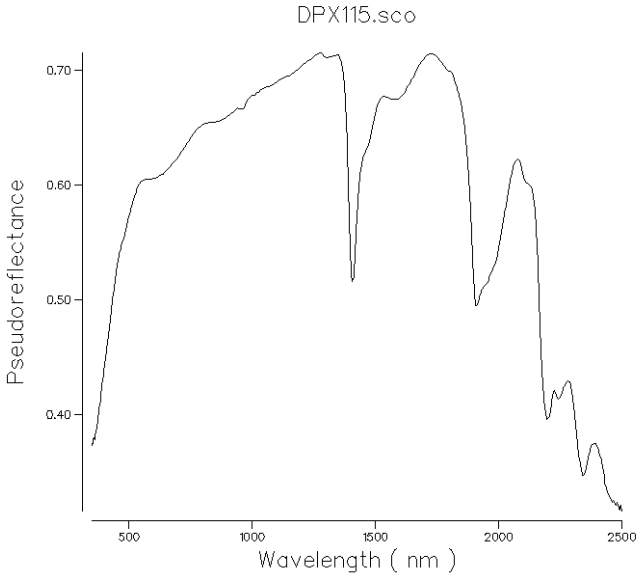
DPX115.sco
Pseudoreflectance
0.70
0.60
0.50
0.40
500
1000
1500
2000
2500
Wavelength (nm)

DPX116 was missed from SWIR Analysis

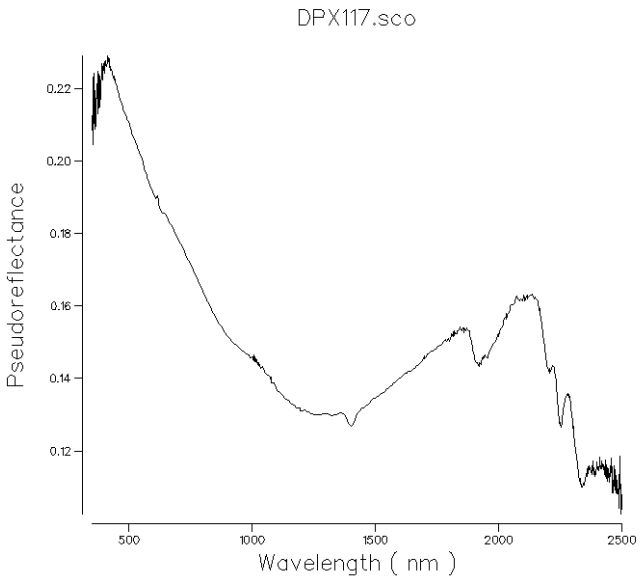

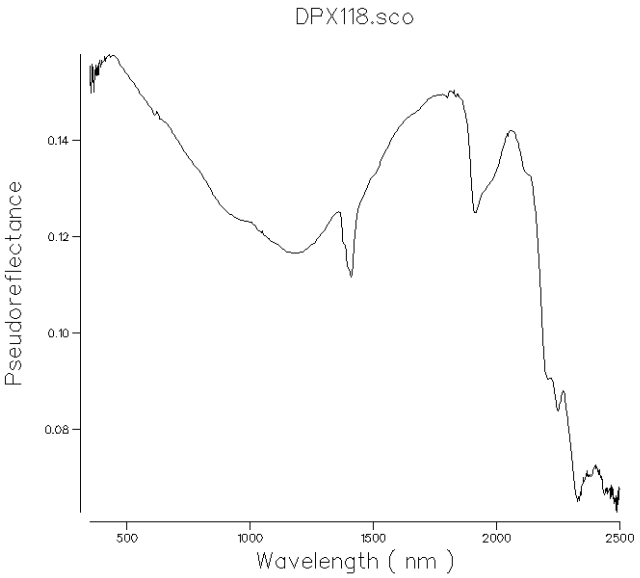
DPX118.sco
Pseudoreflectance
0.14
0.12
0.10
0.08
500
1000
1500
2000
2500
Wavelength (nm)

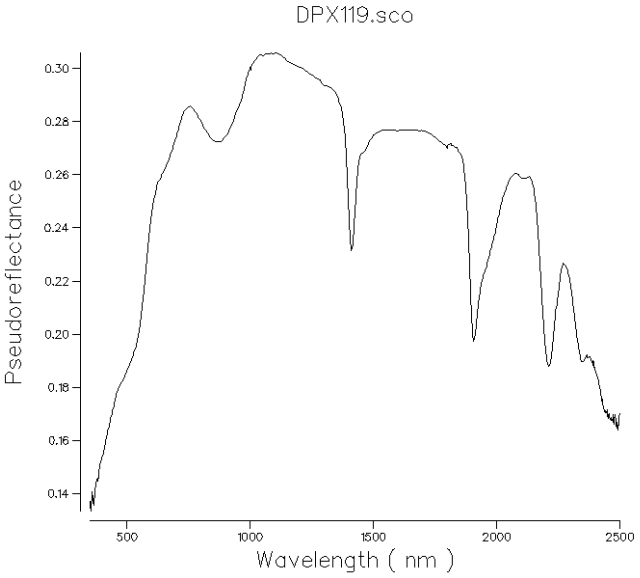
DPX119.sco
Pseudoreflectance
0.30
0.28
0.26
0.24
0.22
0.20
0.18
0.16
0.14
500
1000
1500
2000
2500
Wavelength (nm)

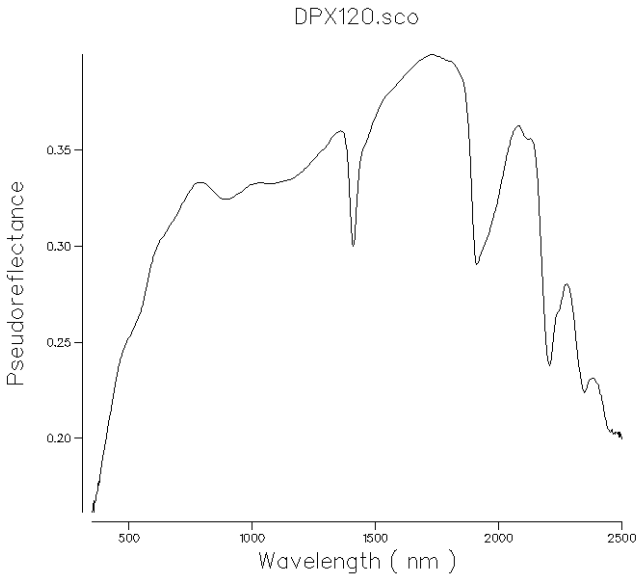
DPX120.sco
Pseudoreflectance
0.35
0.30
0.25
0.20
500
1000
1500
2000
2500
Wavelength (nm)

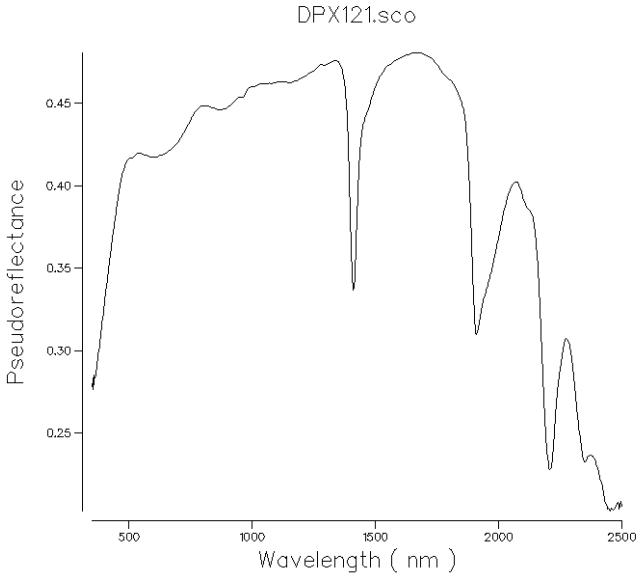
DPX121.sco
Pseudoreflectance
0.45
0.40
0.35
0.30
0.25
500
1000
1500
2000
2500
Wavelength (nm)

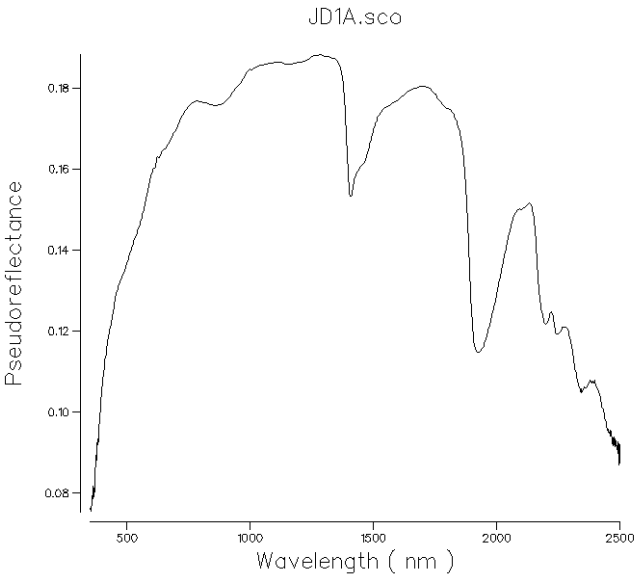
JD1A.sco
Pseudoreflectance
0.18
0.16
0.14
0.12
0.10
0.08
500
1000
1500
2000
2500
Wavelength (nm)

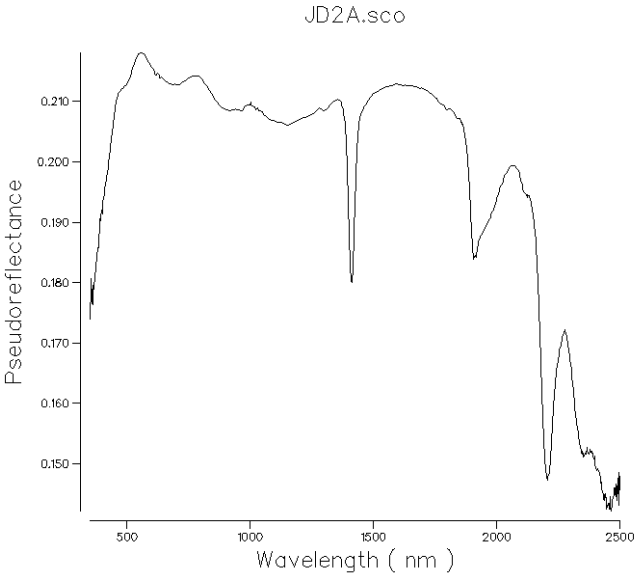
JD2A.sco
Pseudoreflectance
0.210
0.200
0.190
0.180
0.170
0.160
0.150
500
1000
1500
2000
2500
Wavelength (nm)

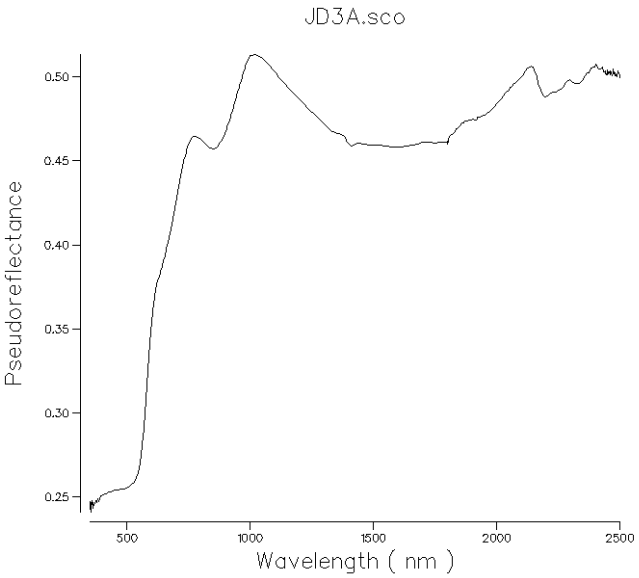
JD3A.sco
Pseudoreflectance
0.50
0.45
0.40
0.35
0.30
0.25
500
1000
1500
2000
2500
Wavelength (nm)

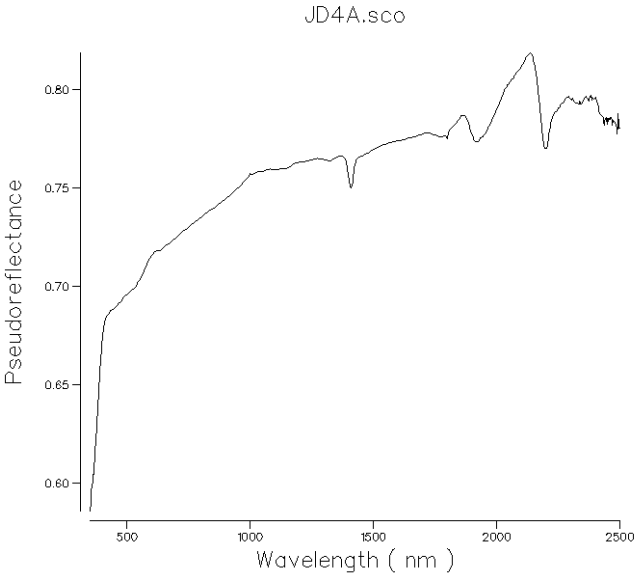
JD4A.sco
Pseudoreflectance
0.80
0.75
0.70
0.65
0.60
500
1000
1500
2000
2500
Wavelength (nm)

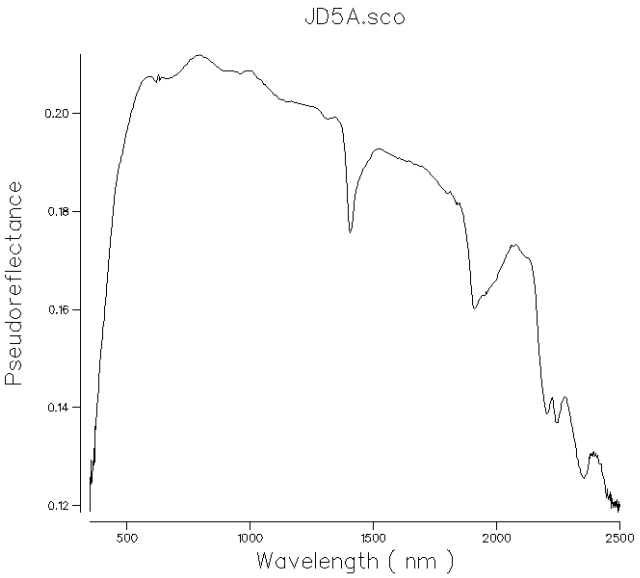
JD5A.sco
Pseudoreflectance
0.20
0.18
0.16
0.14
0.12
500
1000
1500
2000
2500
Wavelength (nm)

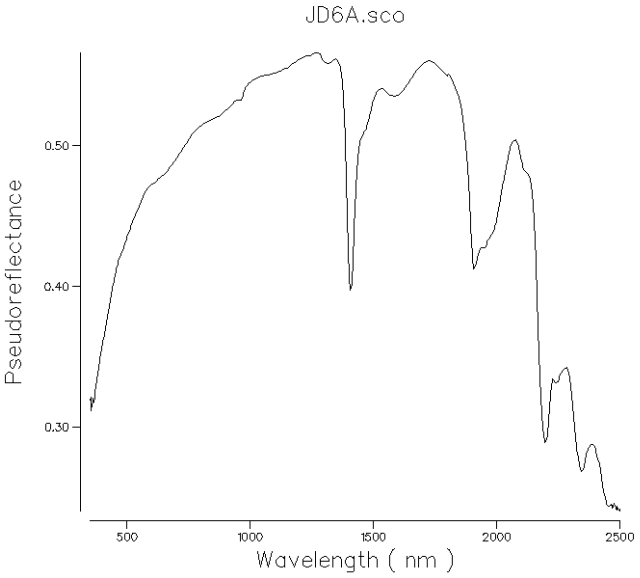
JD6A.sco
Pseudoreflectance
0.50
0.40
0.30
500
1000
1500
2000
2500
Wavelength (nm)

Spectra from WR380

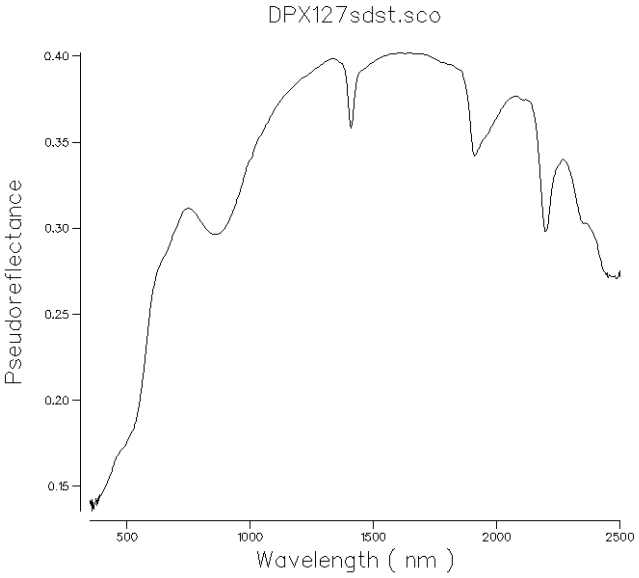

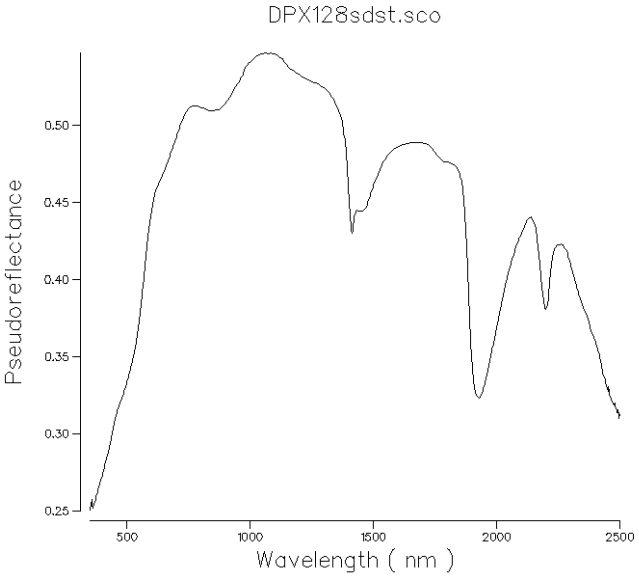

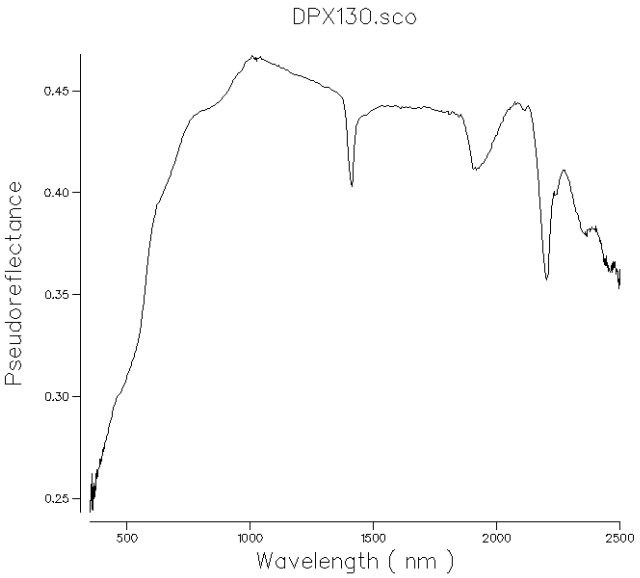
DPX130.sco
Pseudoreflectance
0.45
0.40
0.35
0.30
0.25
500
1000
1500
2000
2500
Wavelength (nm)

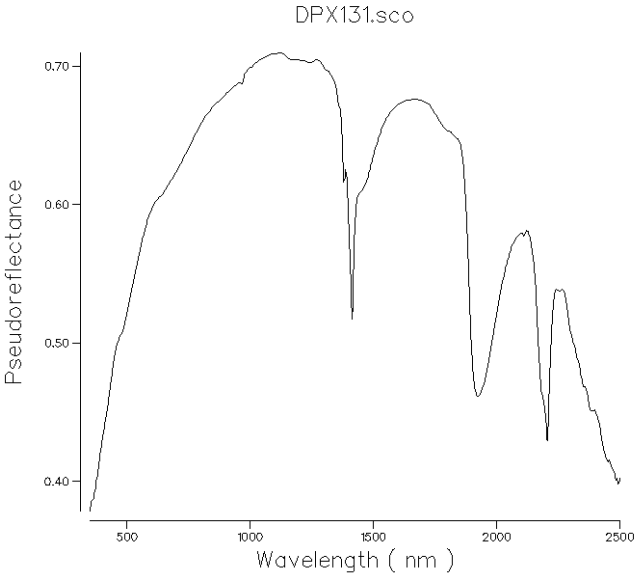
DPX131.sco
Pseudoreflectance
0.70
0.60
0.50
0.40
500
1000
1500
2000
2500
Wavelength (nm)

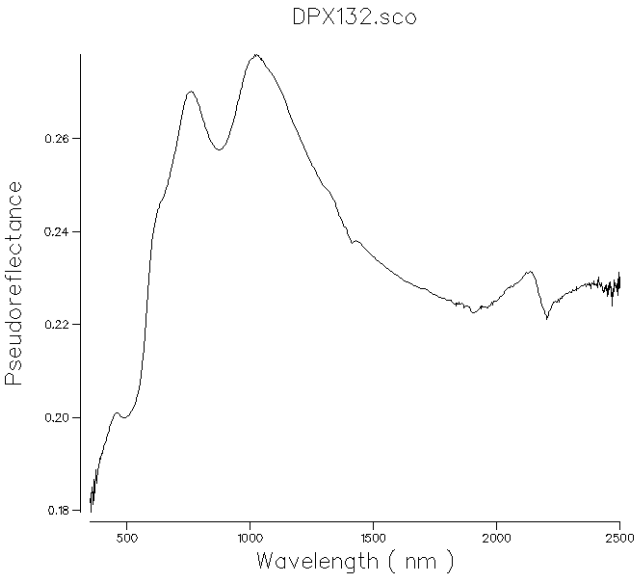
DPX132.sco
Pseudoreflectance
0.26
0.24
0.22
0.20
0.18
500
1000
1500
2000
2500
Wavelength (nm)

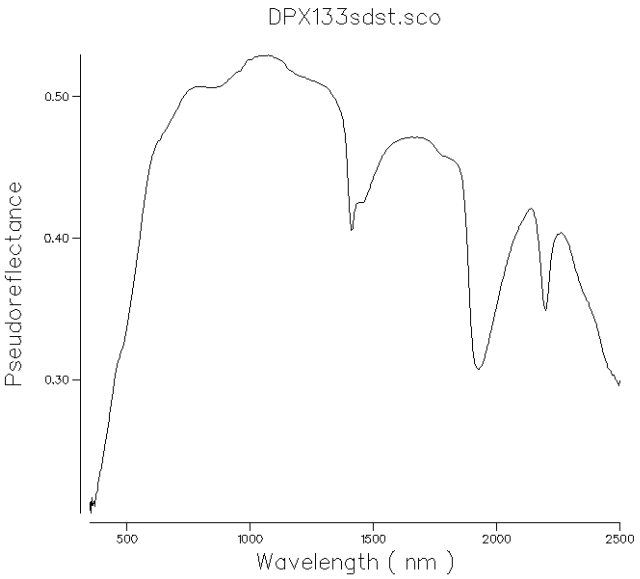
DPX133sdst.sco
Pseudoreflectance
0.50
0.40
0.30
500
1000
1500
2000
2500
Wavelength (nm)

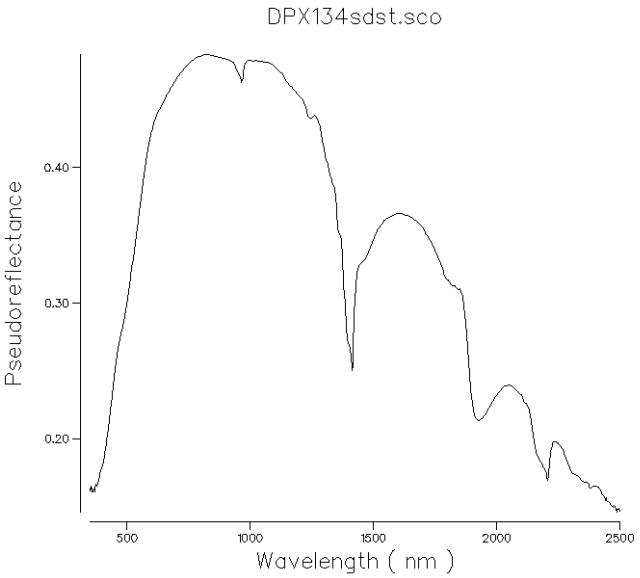
DPX134sdst.sco
Pseudoreflectance
0.40
0.30
0.20
500
1000
1500
2000
2500
Wavelength (nm)

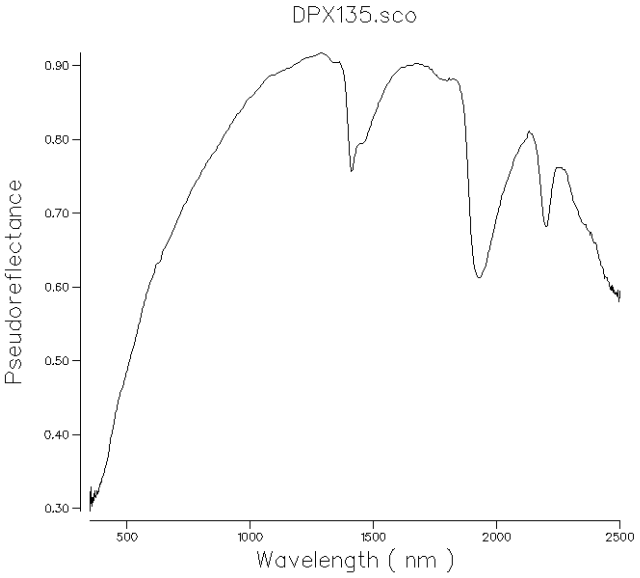
DPX135.sco
Pseudoreflectance
0.90
0.80
0.70
0.60
0.50
0.40
0.30
500
1000
1500
2000
2500
Wavelength (nm)

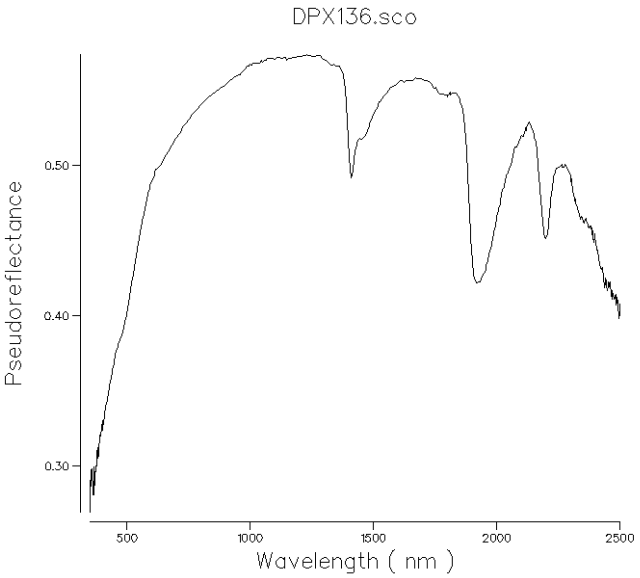
DPX136.sco
Pseudoreflectance
0.50
0.40
0.30
500
1000
1500
2000
2500
Wavelength (nm)

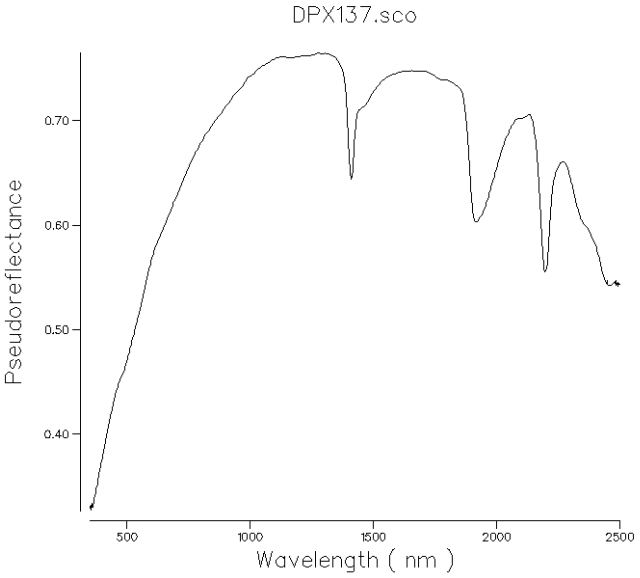
DPX137.sco
Pseudoreflectance
0.70
0.60
0.50
0.40
500
1000
1500
2000
2500
Wavelength (nm)

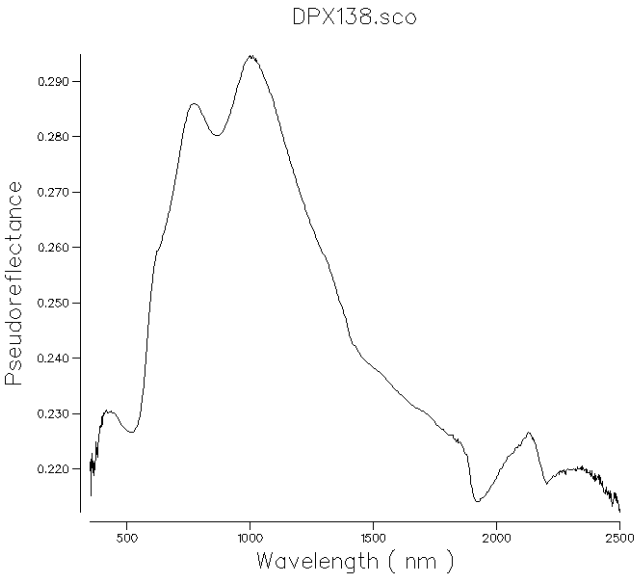
DPX138.sco
Pseudoreflectance
0.290
0.280
0.270
0.260
0.250
0.240
0.230
0.220
500
1000
1500
2000
2500
Wavelength (nm)

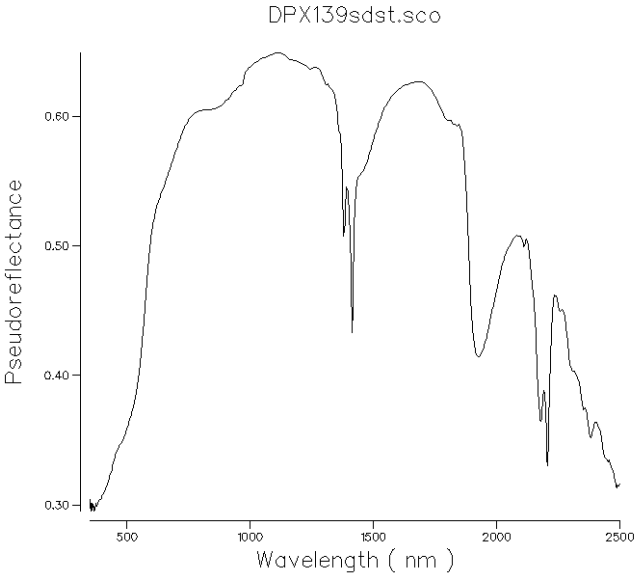
DPX139sdst.sco
Pseudoreflectance
0.60
0.50
0.40
0.30
500
1000
1500
2000
2500
Wavelength (nm)

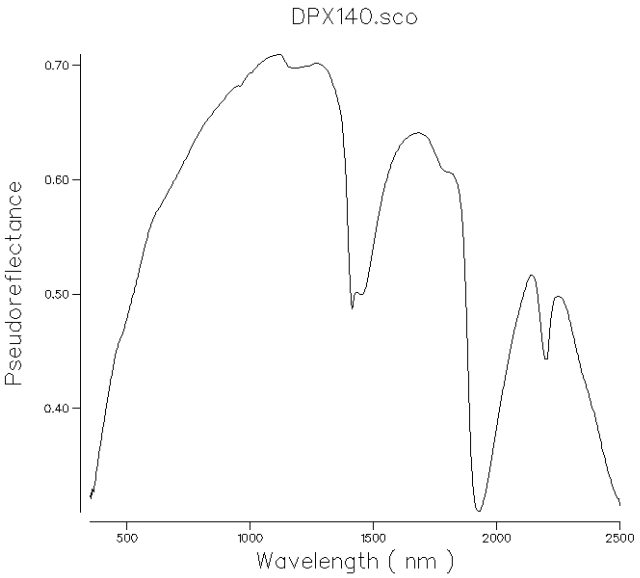
DPX140.sco
Pseudoreflectance
0.70
0.60
0.50
0.40
500
1000
1500
2000
2500
Wavelength (nm)

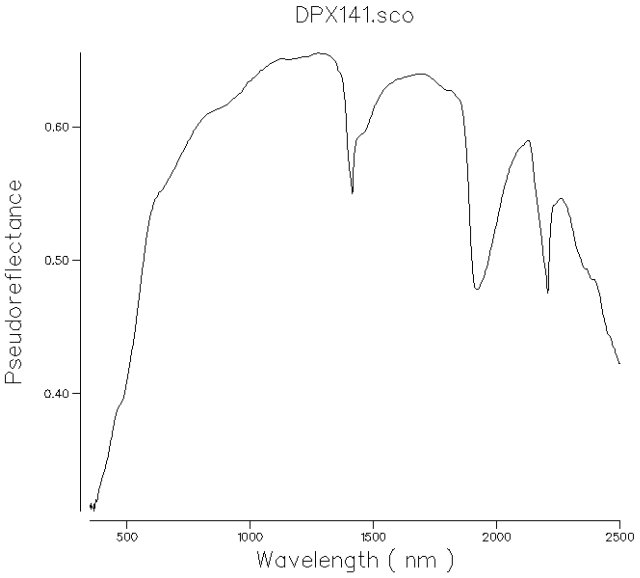
DPX141.sco
Pseudoreflectance
0.60
0.50
0.40
500
1000
1500
2000
2500
Wavelength (nm)

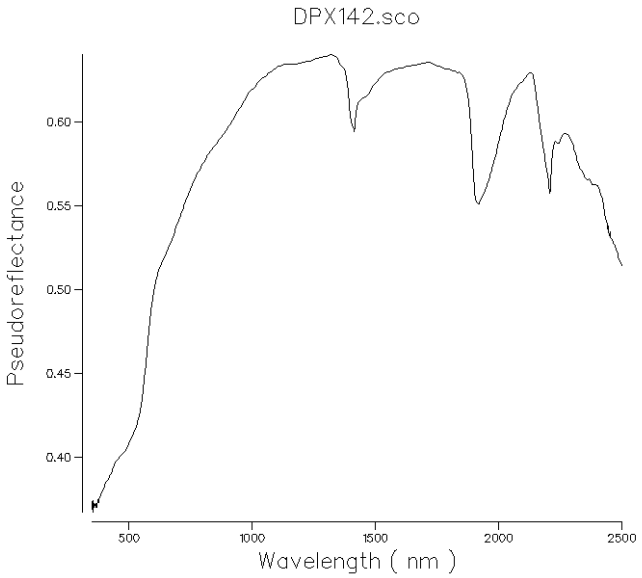
DPX142.sco
Pseudoreflectance
0.60
0.55
0.50
0.45
0.40
500
1000
1500
2000
2500
Wavelength (nm)

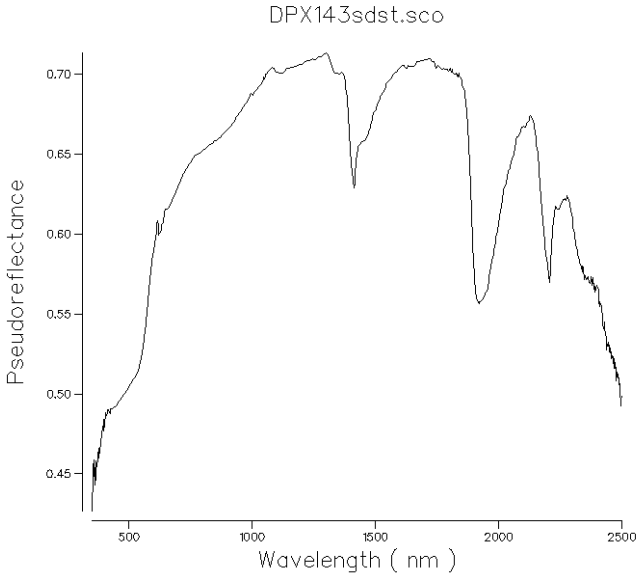
DPX143sdst.sco
Pseudoreflectance
0.70
0.65
0.60
0.55
0.50
0.45
500
1000
1500
2000
2500
Wavelength (nm)

Spectra from WR277

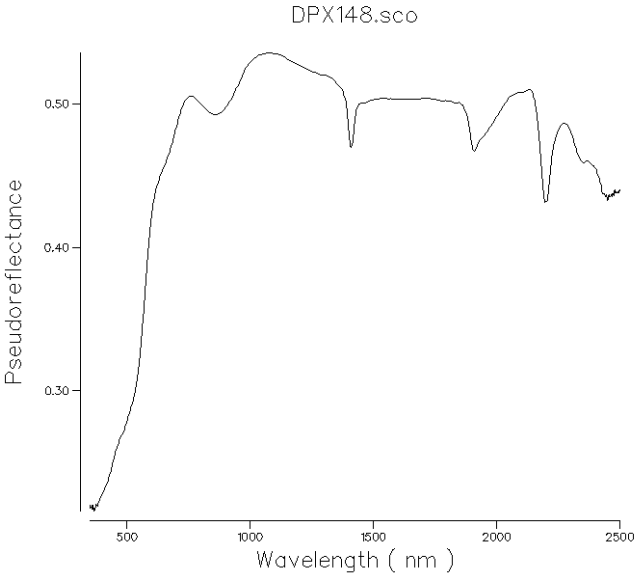

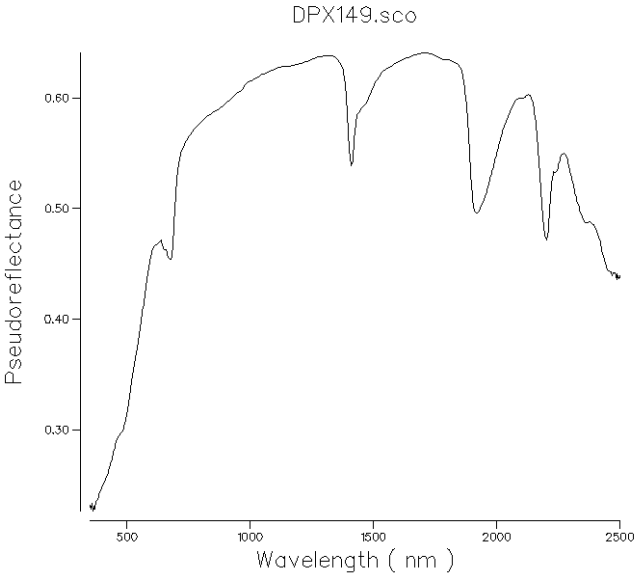

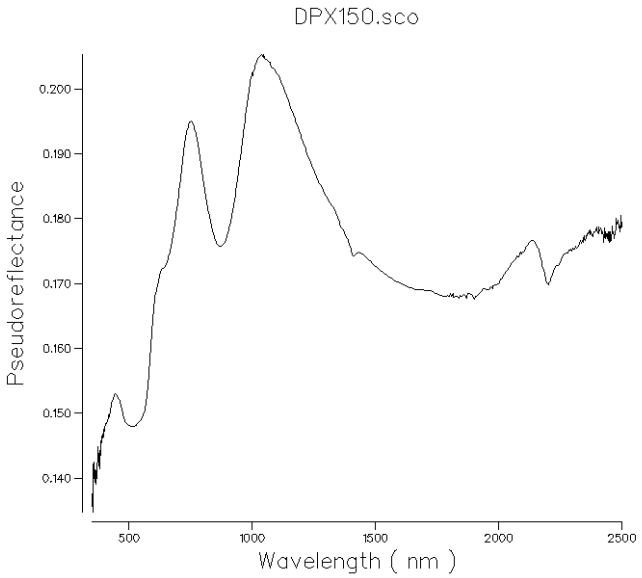
DPX150.sco
Pseudoreflectance
0.200
0.190
0.180
0.170
0.160
0.150
0.140
500
1000
1500
2000
2500
Wavelength (nm)

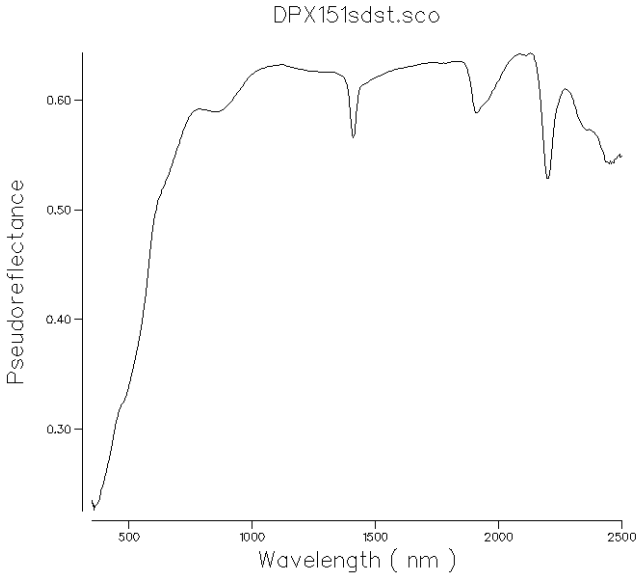
DPX151sdst.sco
Pseudoreflectance
0.60
0.50
0.40
0.30
500
1000
1500
2000
2500
Wavelength (nm)

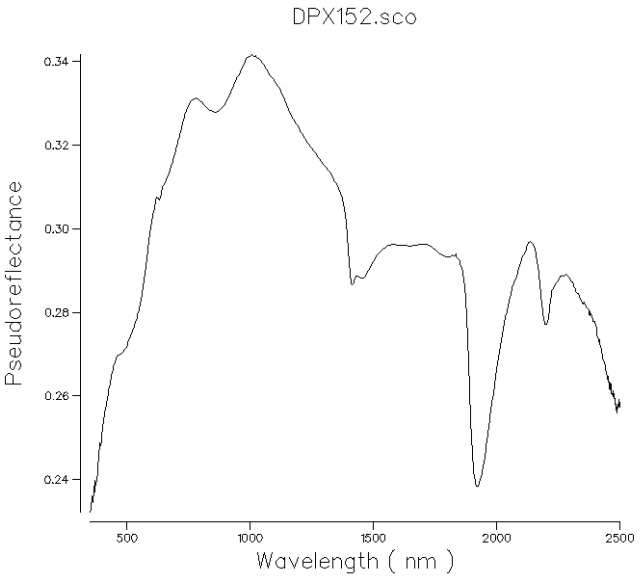
DPX152.sco
Pseudoreflectance
0.34
0.32
0.30
0.28
0.26
0.24
500
1000
1500
2000
2500
Wavelength (nm)

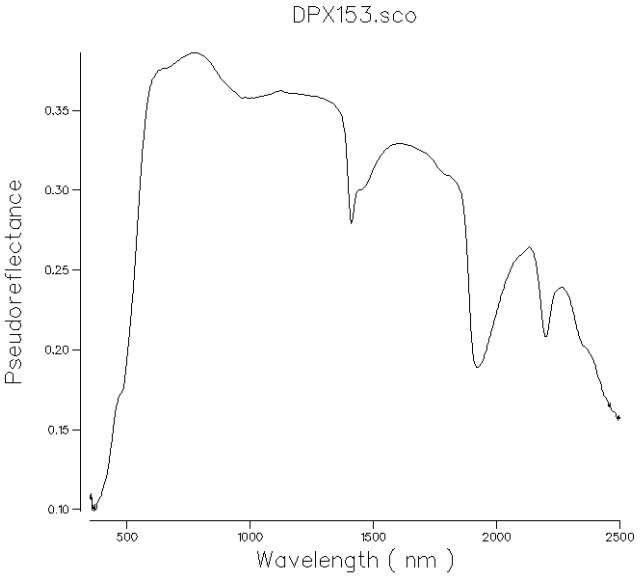
DPX153.sco
Pseudoreflectance
0.35
0.30
0.25
0.20
0.15
0.10
500
1000
1500
2000
2500
Wavelength (nm)

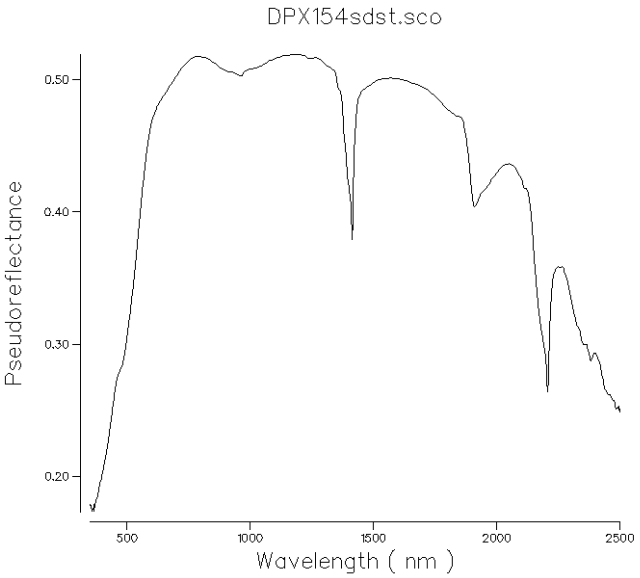
DPX154sdst.sco
Pseudoreflectance
0.50
0.40
0.30
0.20
500
1000
1500
2000
2500
Wavelength (nm)

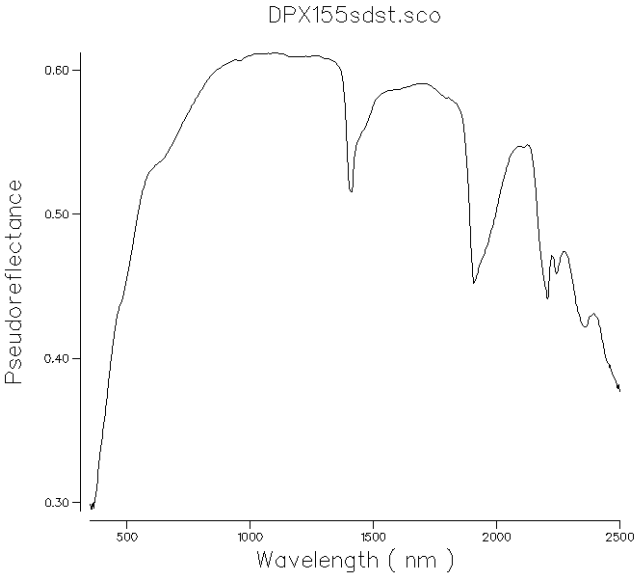
DPX155sdst.sco
Pseudoreflectance
0.60
0.50
0.40
0.30
500
1000
1500
2000
2500
Wavelength (nm)

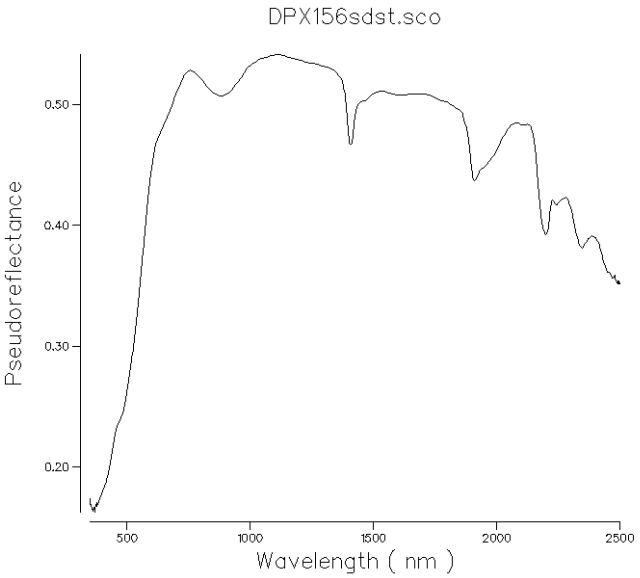
DPX156sdst.sco
Pseudoreflectance
0.50
0.40
0.30
0.20
500
1000
1500
2000
2500
Wavelength (nm)

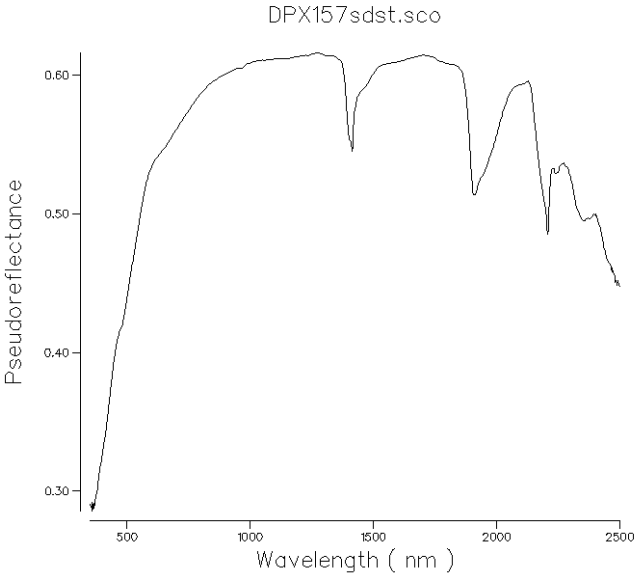
DPX157sdst.sco
Pseudoreflectance
0.60
0.50
0.40
0.30
500
1000
1500
2000
2500
Wavelength (nm)

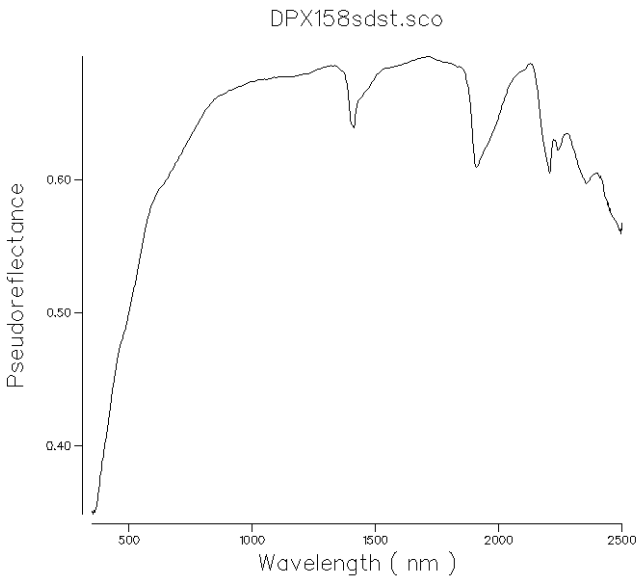
DPX158sdst.sco
Pseudoreflectance
0.60
0.50
0.40
500
1000
1500
2000
2500
Wavelength (nm)

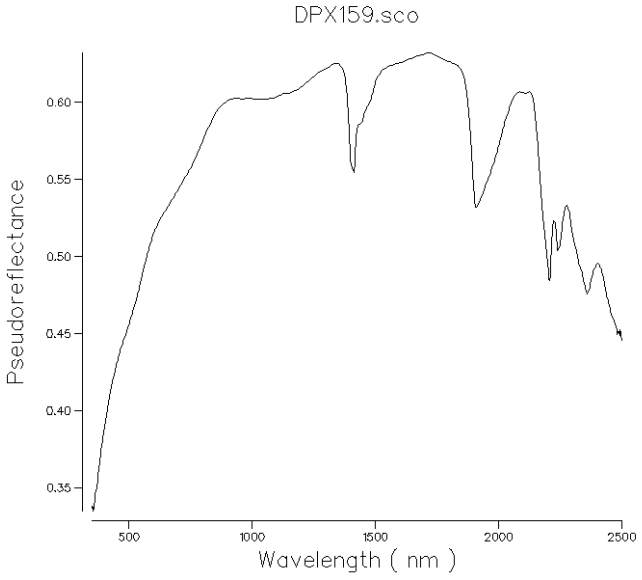
DPX159.sco
Pseudoreflectance
0.60
0.55
0.50
0.45
0.40
0.35
500
1000
1500
2000
2500
Wavelength (nm)

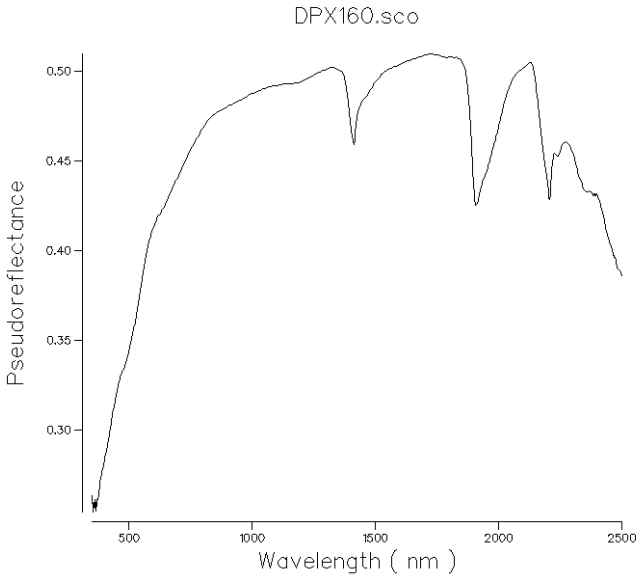
DPX160.sco
Pseudoreflectance
0.50
0.45
0.40
0.35
0.30
500
1000
1500
2000
2500
Wavelength (nm)

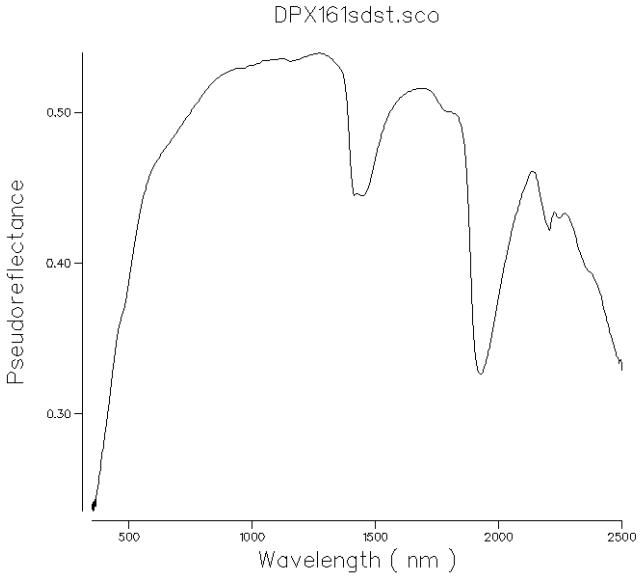
DPX161sdst.sco
Pseudoreflectance
0.50
0.40
0.30
500
1000
1500
2000
2500
Wavelength (nm)

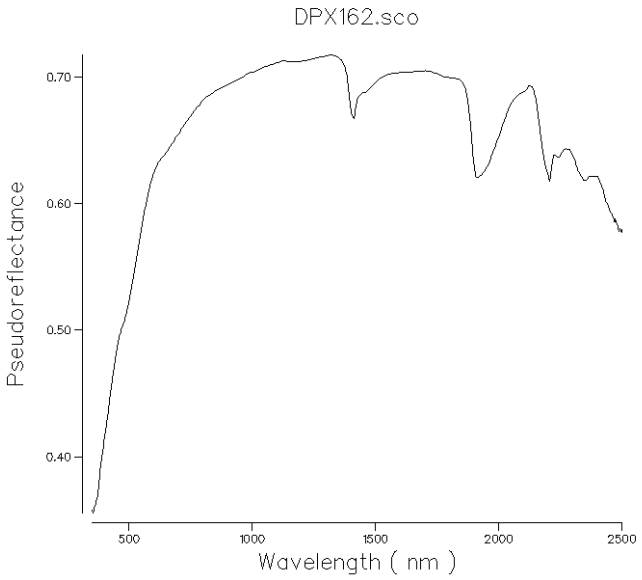
DPX162.sco
Pseudoreflectance
0.70
0.60
0.50
0.40
500
1000
1500
2000
2500
Wavelength (nm)

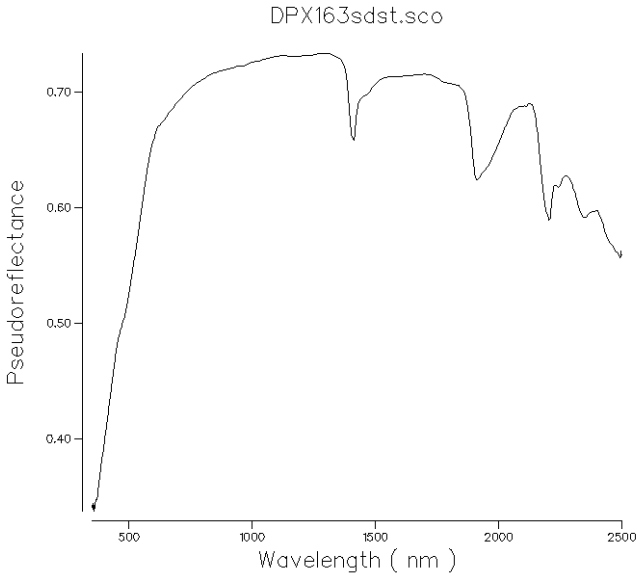
DPX163sdst.sco
Pseudoreflectance
0.70
0.60
0.50
0.40
500
1000
1500
2000
2500
Wavelength (nm)

DPX164 was not analysed via SWIR

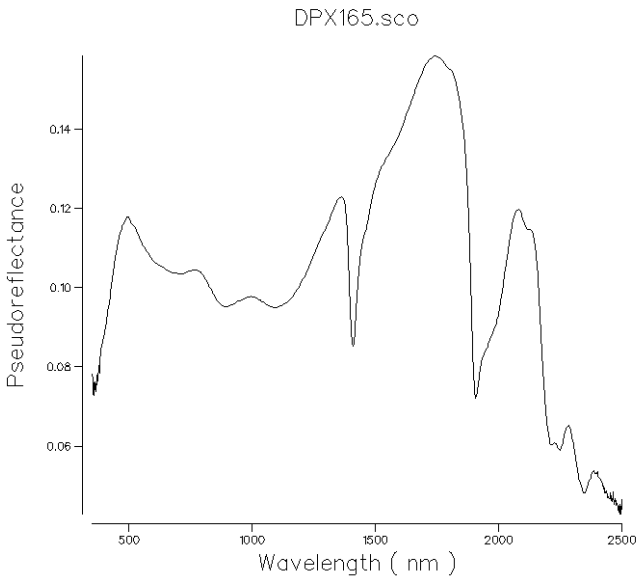

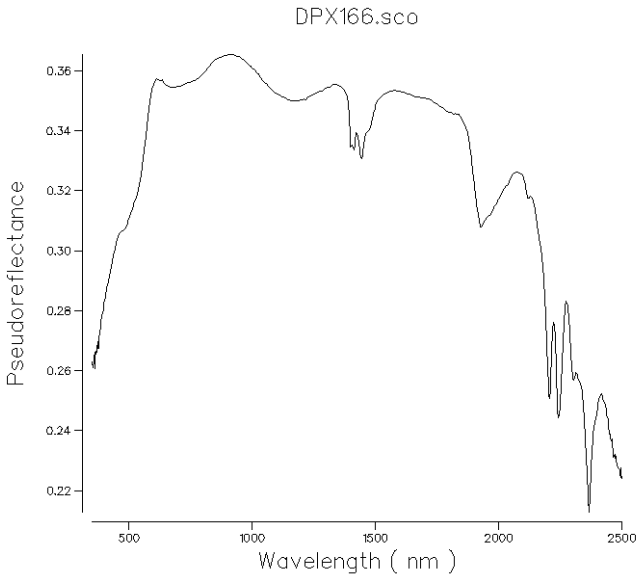
DPX166.sco
Pseudoreflectance
0.36
0.34
0.32
0.30
0.28
0.26
0.24
0.22
500
1000
1500
2000
2500
Wavelength (nm)

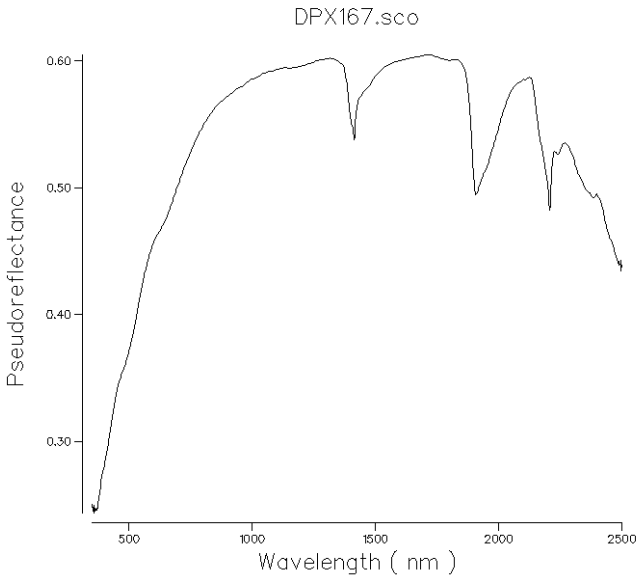
DPX167.sco
Pseudoreflectance
0.60
0.50
0.40
0.30
500
1000
1500
2000
2500
Wavelength (nm)

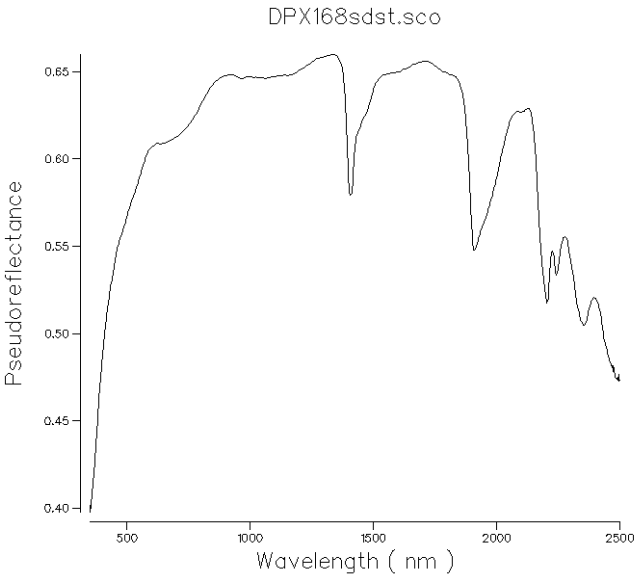
DPX168sdst.sco
Pseudoreflectance
0.65
0.60
0.55
0.50
0.45
0.40
500
1000
1500
2000
2500
Wavelength (nm)

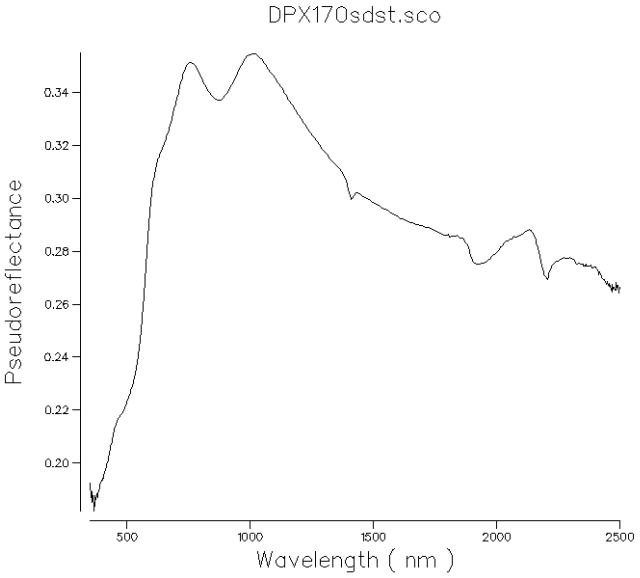
DPX170sdst.sco
Pseudoreflectance
0.34
0.32
0.30
0.28
0.26
0.24
0.22
0.20
500
1000
1500
2000
2500
Wavelength (nm)

Spectra from WR286

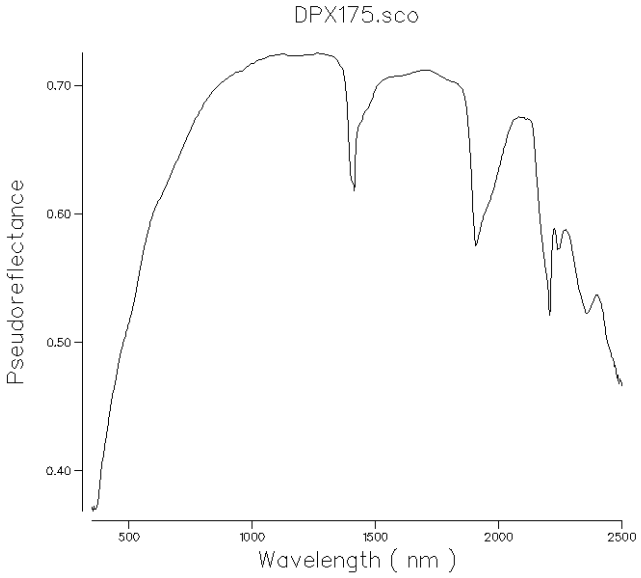

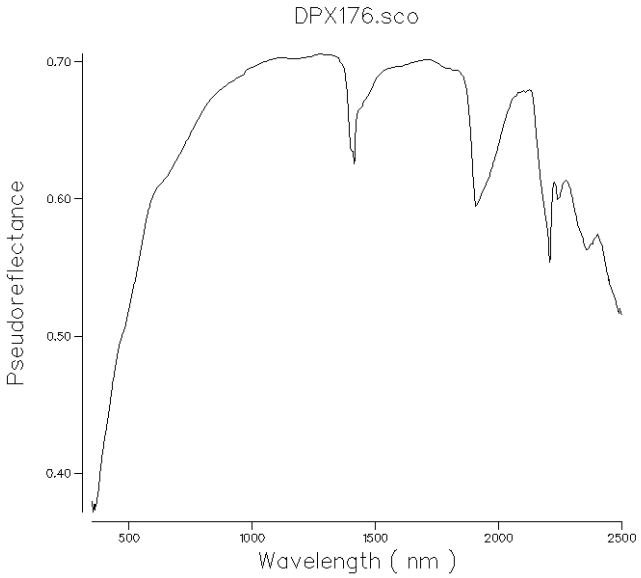

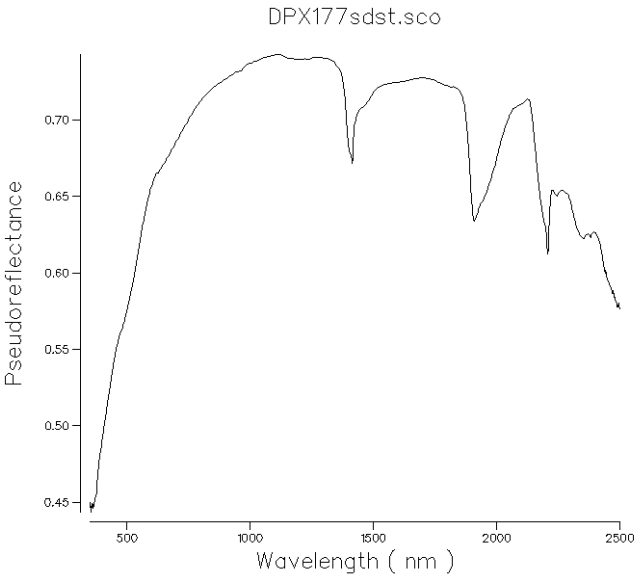
DPX177sdst.sco
Pseudoreflectance
0.70
0.65
0.60
0.55
0.50
0.45
500
1000
1500
2000
2500
Wavelength (nm)

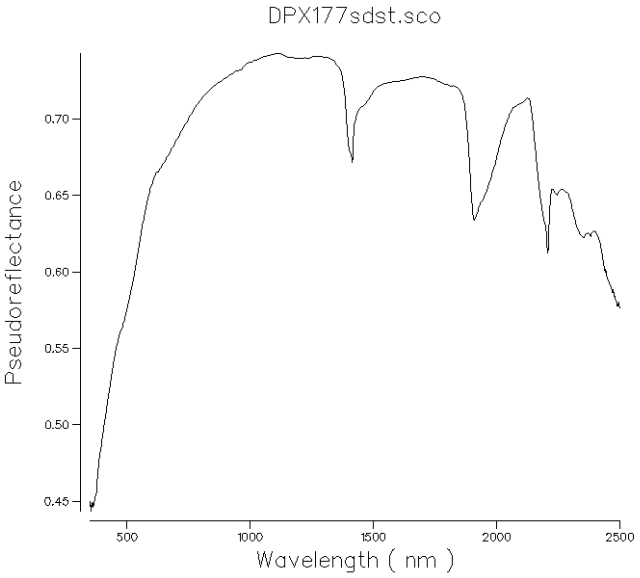
DPX177sdst.sco
Pseudoreflectance
0.70
0.65
0.60
0.55
0.50
0.45
500
1000
1500
2000
2500
Wavelength (nm)

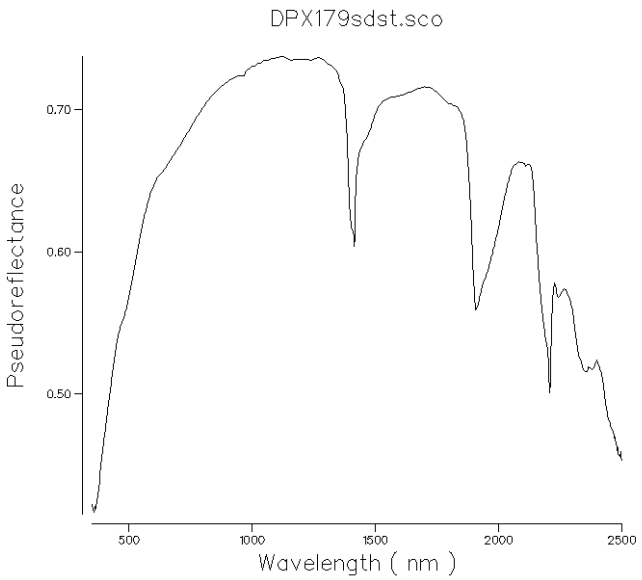
DPX179sdst.sco
Pseudoreflectance
0.70
0.60
0.50
500
1000
1500
2000
2500
Wavelength (nm)

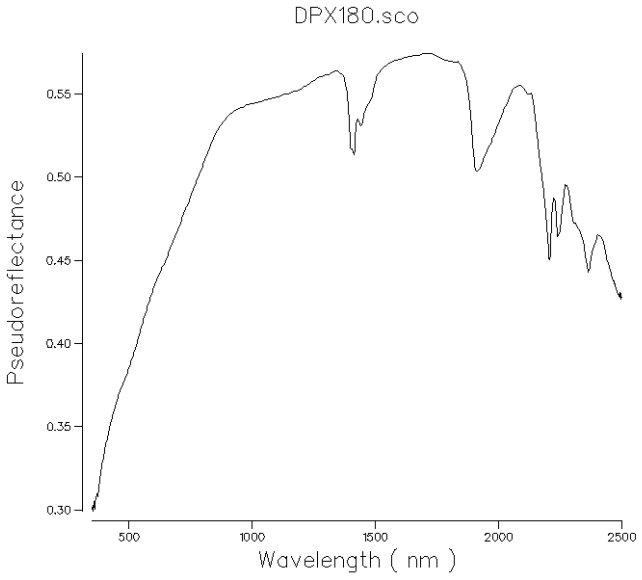
DPX180.sco
Pseudoreflectance
0.55
0.50
0.45
0.40
0.35
0.30
500
1000
1500
2000
2500
Wavelength (nm)

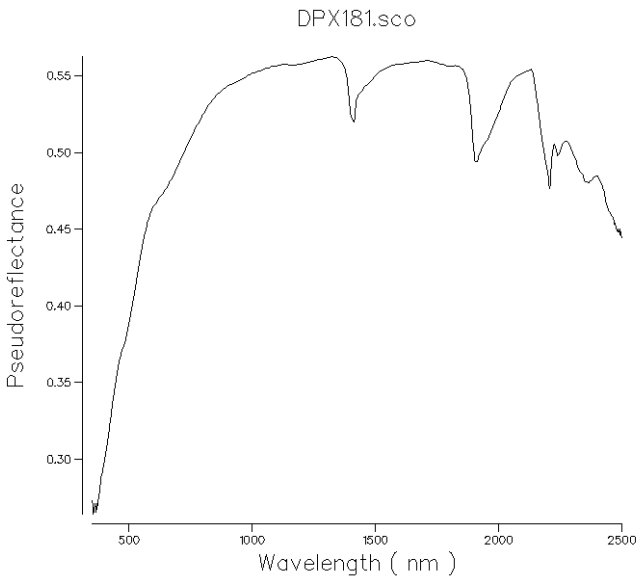
DPX181.sco
Pseudoreflectance
0.55
0.50
0.45
0.40
0.35
0.30
500
1000
1500
2000
2500
Wavelength (nm)

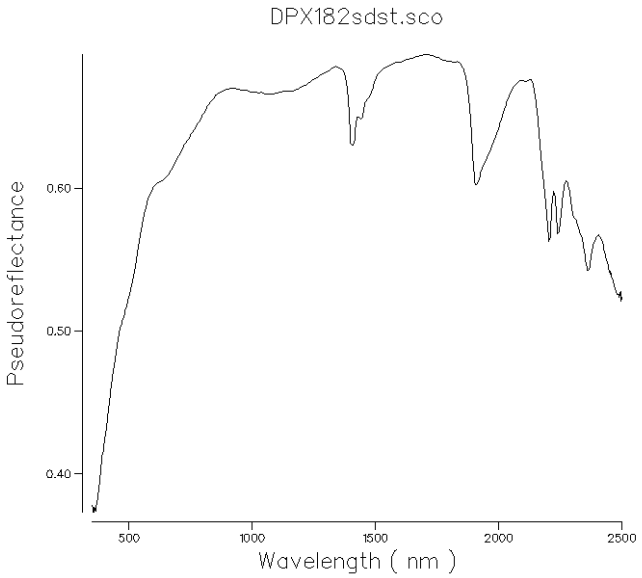
DPX182sdst.sco
Pseudoreflectance
0.60
0.50
0.40
500
1000
1500
2000
2500
Wavelength (nm)

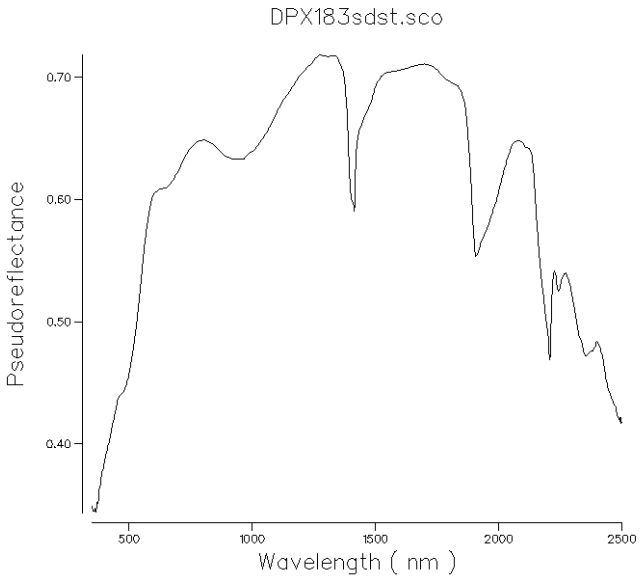
DPX183sdst.sco
Pseudoreflectance
0.70
0.60
0.50
0.40
500
1000
1500
2000
2500
Wavelength (nm)

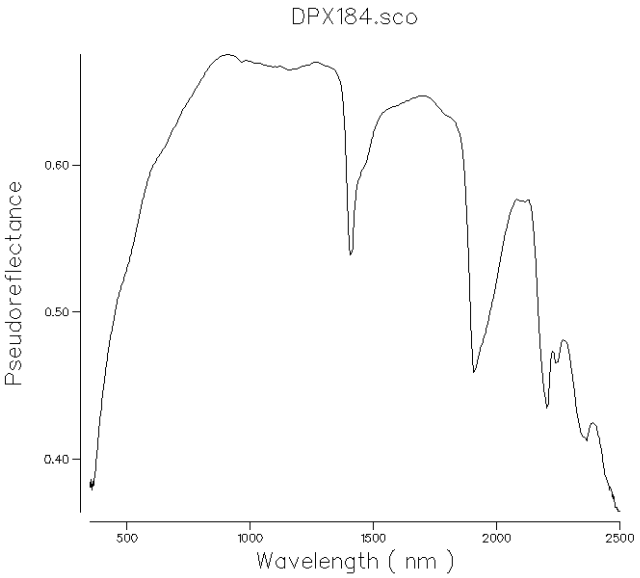
DPX184.sco
Pseudoreflectance
0.60
0.50
0.40
500
1000
1500
2000
2500
Wavelength (nm)

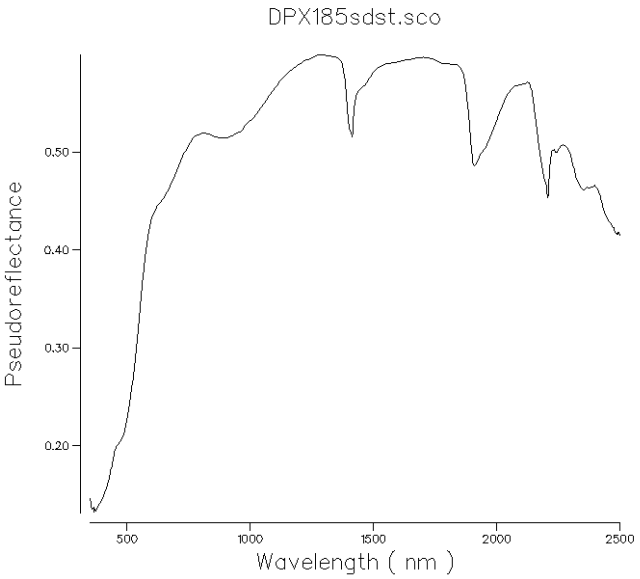
DPX185sdst.sco
Pseudoreflectance
0.50
0.40
0.30
0.20
500
1000
1500
2000
2500
Wavelength (nm)

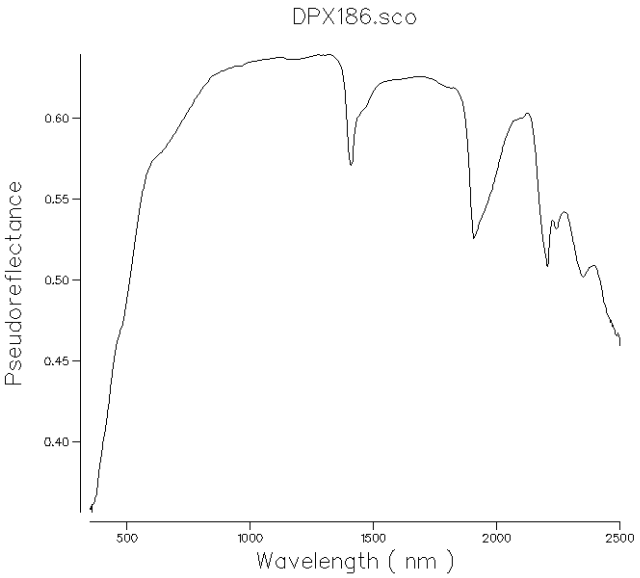
DPX186.sco
Pseudoreflectance
0.60
0.55
0.50
0.45
0.40
500
1000
1500
2000
2500
Wavelength (nm)

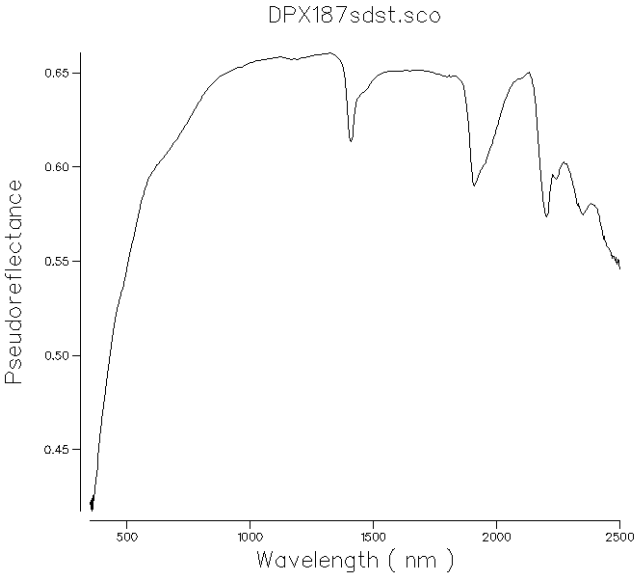
DPX187sdst.sco
Pseudoreflectance
0.65
0.60
0.55
0.50
0.45
500
1000
1500
2000
2500
Wavelength (nm)

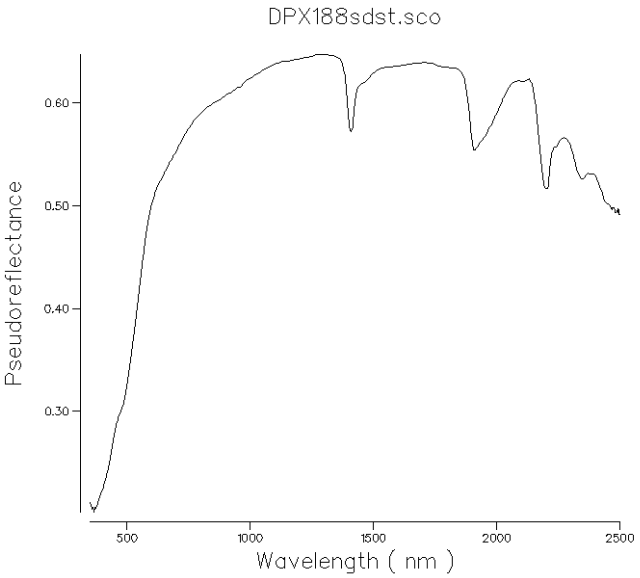
DPX188sdst.sco
Pseudoreflectance
0.60
0.50
0.40
0.30
500
1000
1500
2000
2500
Wavelength (nm)

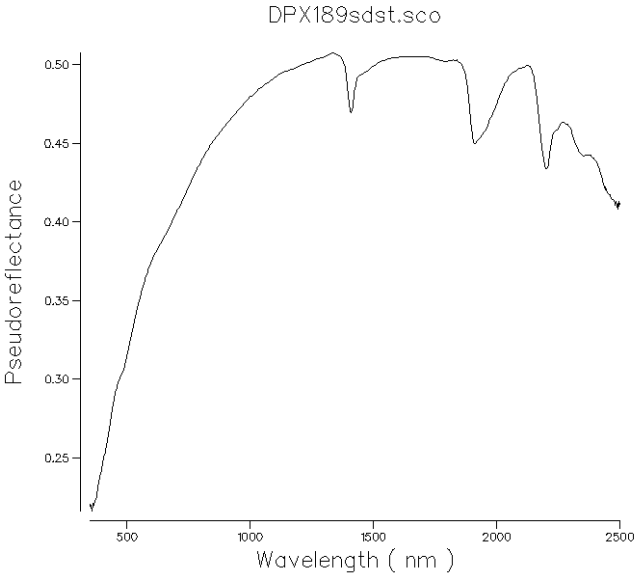
DPX189sdst.sco
Pseudoreflectance
0.50
0.45
0.40
0.35
0.30
0.25
500
1000
1500
2000
2500
Wavelength (nm)

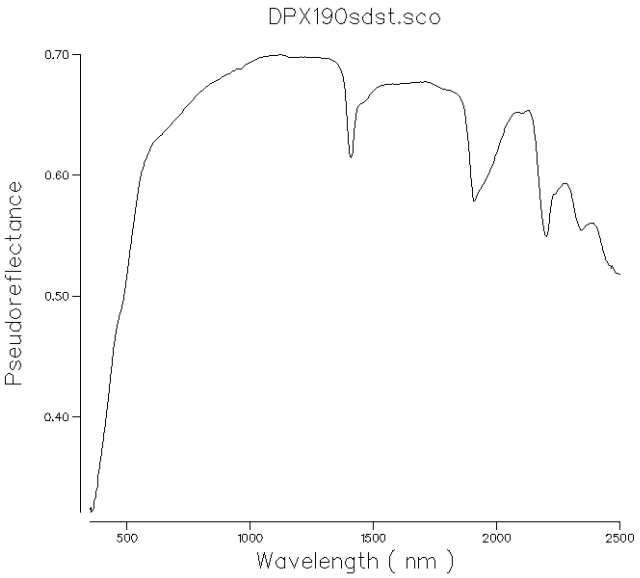
DPX190sdst.sco
Pseudoreflectance
0.70
0.60
0.50
0.40
500
1000
1500
2000
2500
Wavelength (nm)

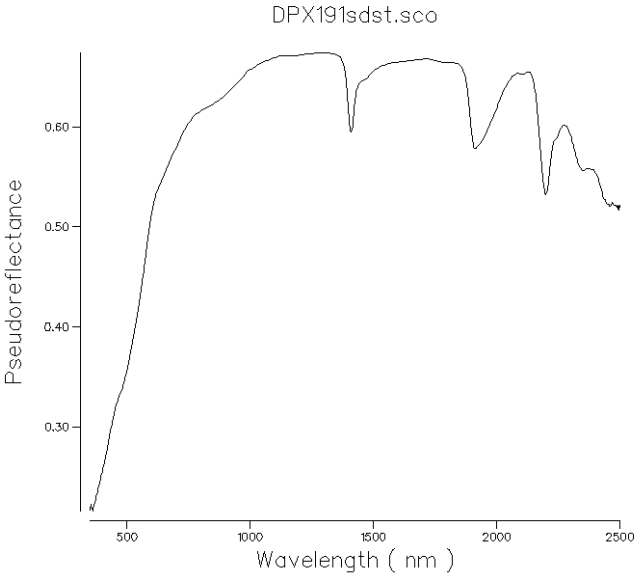
DPX191sdst.sco
Pseudoreflectance
0.60
0.50
0.40
0.30
500
1000
1500
2000
2500
Wavelength (nm)

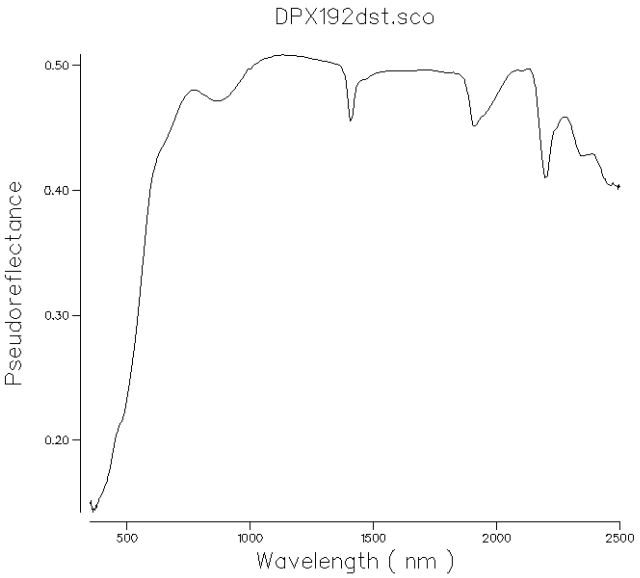
DPX192dst.sco
Pseudoreflectance
0.50
0.40
0.30
0.20
500
1000
1500
2000
2500
Wavelength (nm)

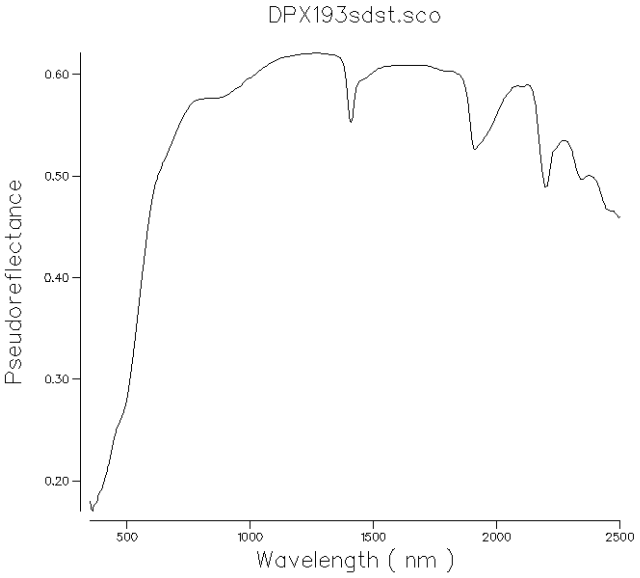
DPX193sdst.sco
Pseudoreflectance
0.60
0.50
0.40
0.30
0.20
500
1000
1500
2000
2500
Wavelength (nm)

File DPX194 was corrupted. No analysis is presented

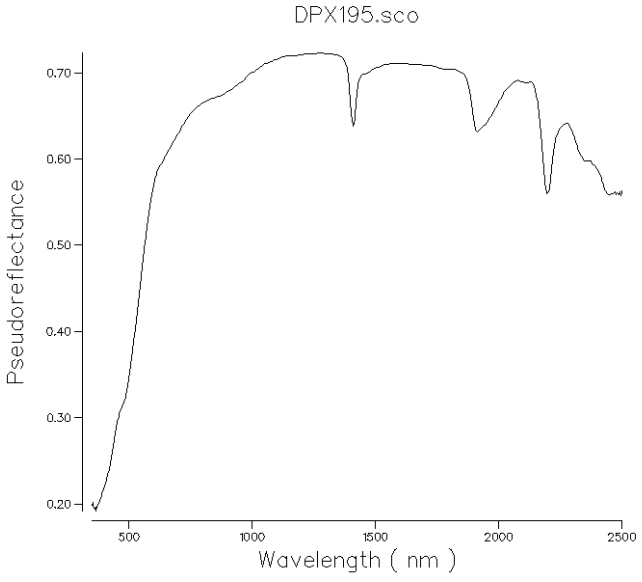

Sample DPX196 was not analysed via SWIR

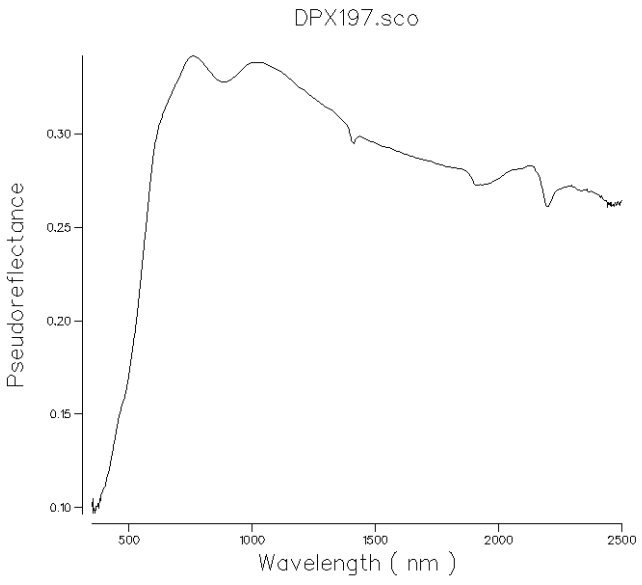

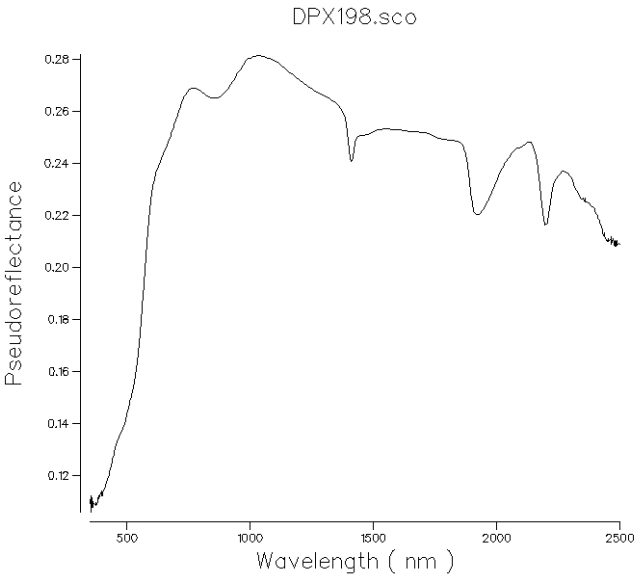
DPX198.sco
Pseudoreflectance
0.28
0.26
0.24
0.22
0.20
0.18
0.16
0.14
0.12
500
1000
1500
2000
2500
Wavelength (nm)

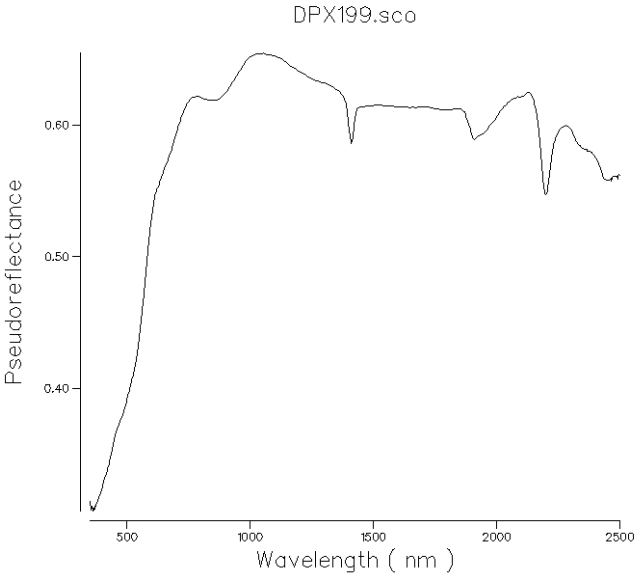
DPX199.sco
Pseudoreflectance
0.60
0.50
0.40
500
1000
1500
2000
2500
Wavelength (nm)

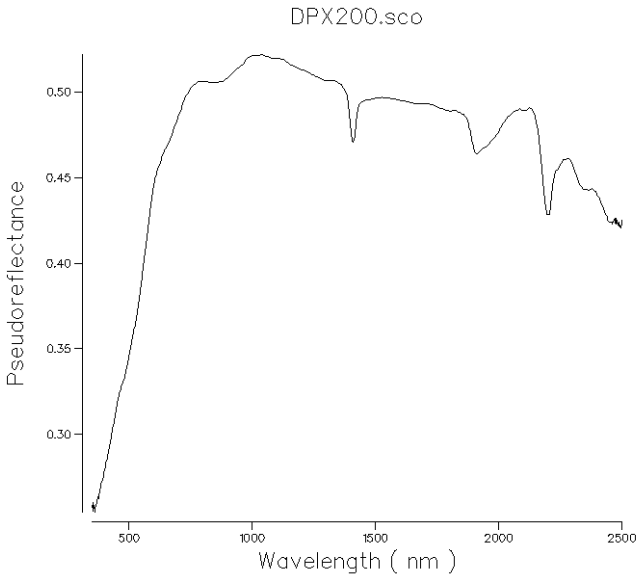
DPX200.sco
Pseudoreflectance
0.50
0.45
0.40
0.35
0.30
500
1000
1500
2000
2500
Wavelength (nm)

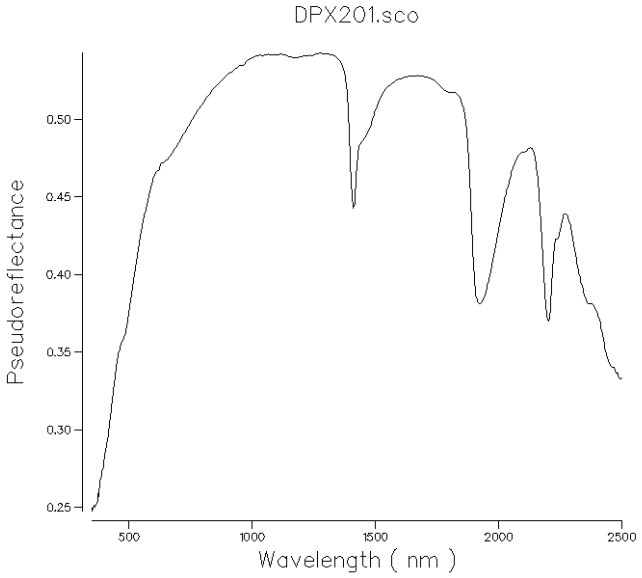
DPX201.sco
Pseudoreflectance
0.50
0.45
0.40
0.35
0.30
0.25
500
1000
1500
2000
2500
Wavelength (nm)

Samples from WR321

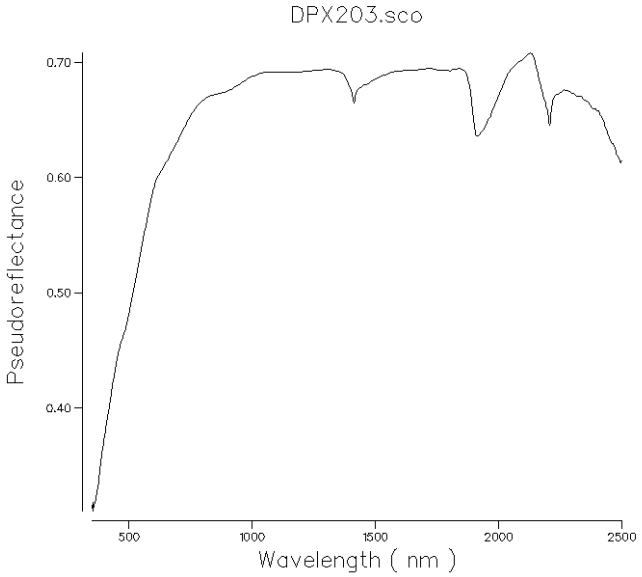

DPX204 was not analysed via SWIR

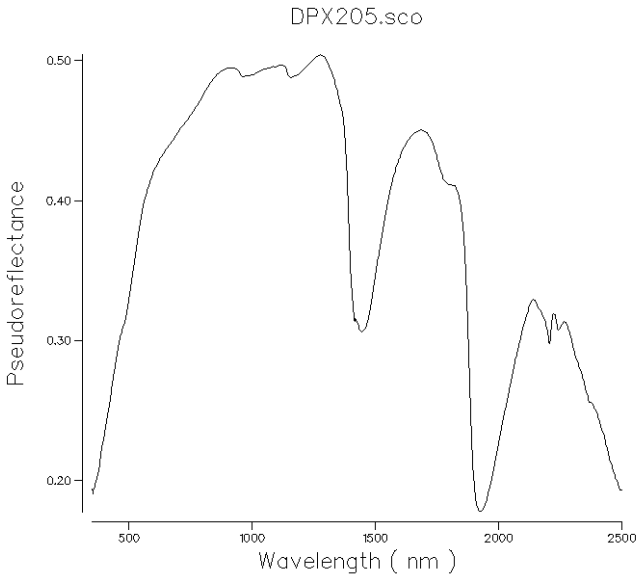
DPX205.sco
Pseudoreflectance
0.50
0.40
0.30
0.20
500
1000
1500
2000
2500
Wavelength (nm)

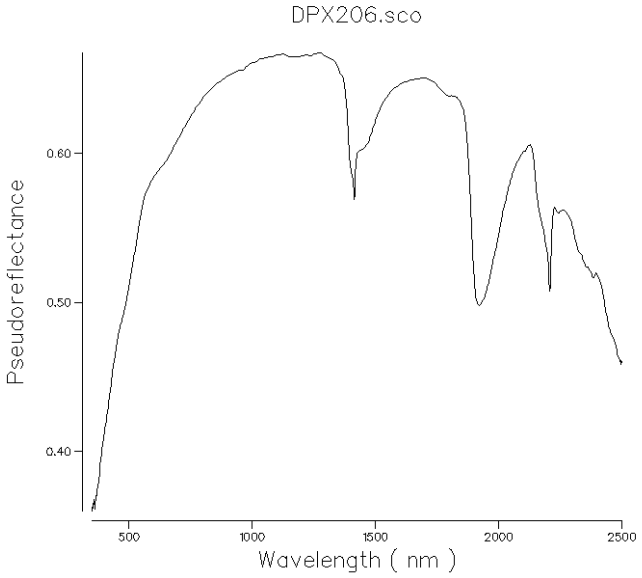
DPX206.sco
Pseudoreflectance
0.60
0.50
0.40
500
1000
1500
2000
2500
Wavelength (nm)

DPX207 and DPX208 were not analysed via SWIR

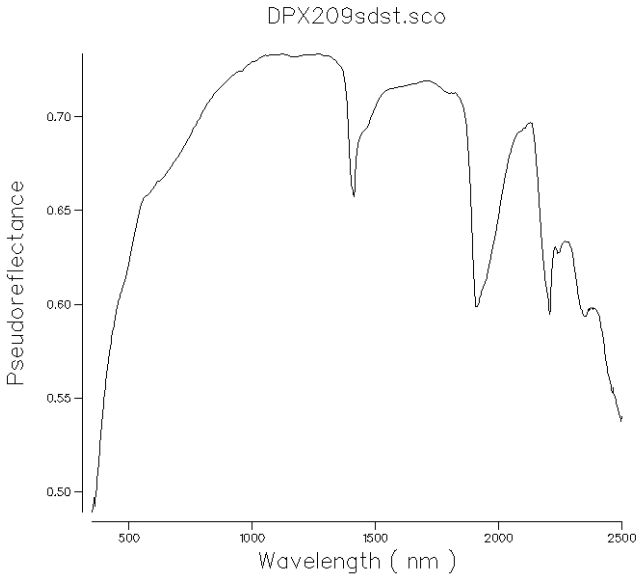

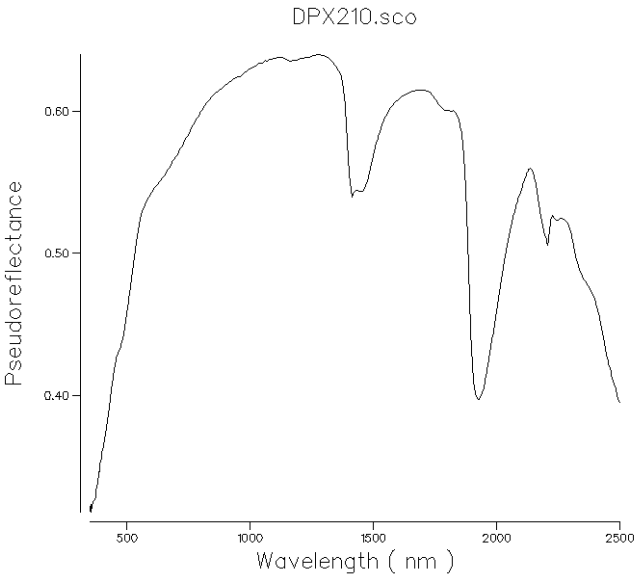
DPX210.sco
Pseudoreflectance
0.60
0.50
0.40
500
1000
1500
2000
2500
Wavelength (nm)

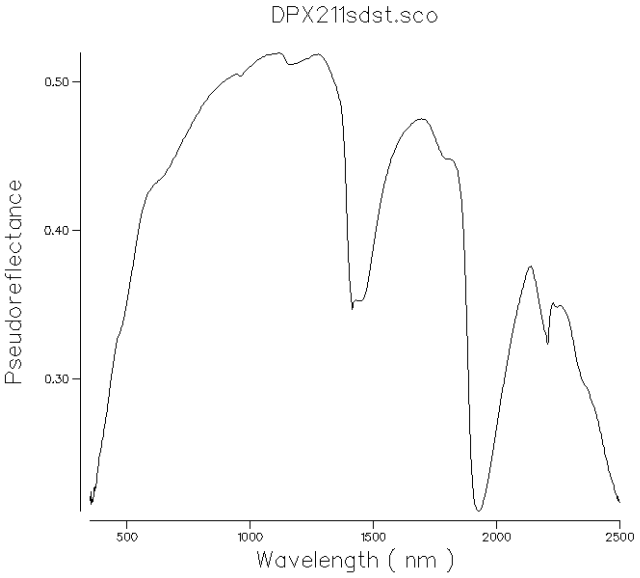
DPX211sdst.sco
Pseudoreflectance
0.50
0.40
0.30
500
1000
1500
2000
2500
Wavelength (nm)

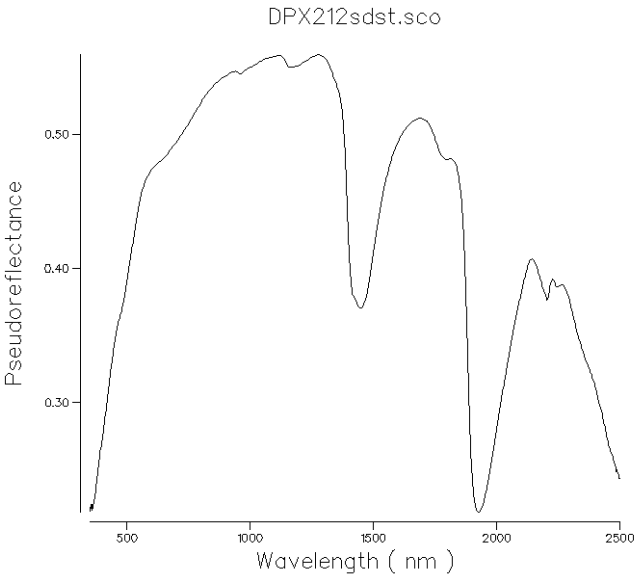
DPX212sdst.sco
Pseudoreflectance
0.50
0.40
0.30
500
1000
1500
2000
2500
Wavelength (nm)

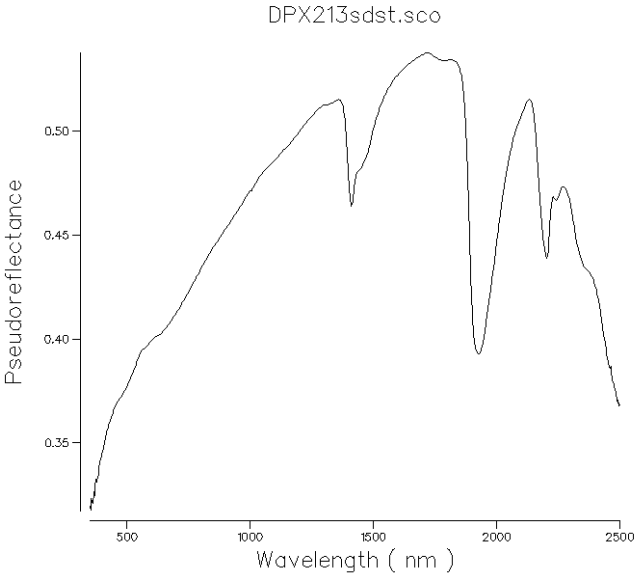
DPX213sdst.sco
Pseudoreflectance
0.50
0.45
0.40
0.35
500
1000
1500
2000
2500
Wavelength (nm)

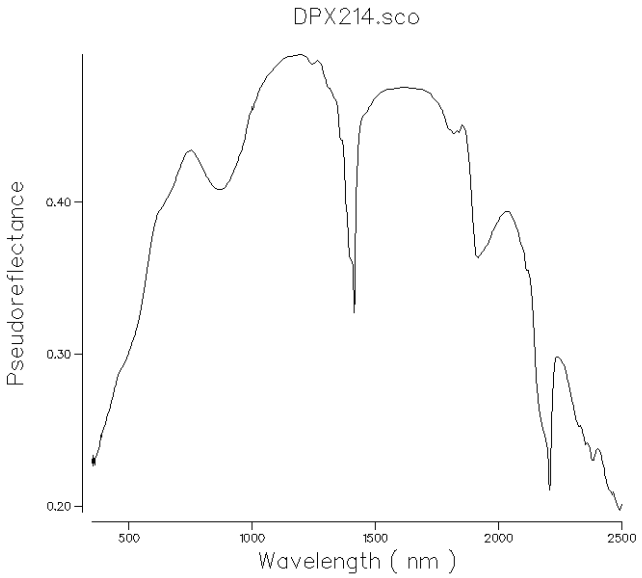
DPX214.sco
Pseudoreflectance
0.40
0.30
0.20
500
1000
1500
2000
2500
Wavelength (nm)

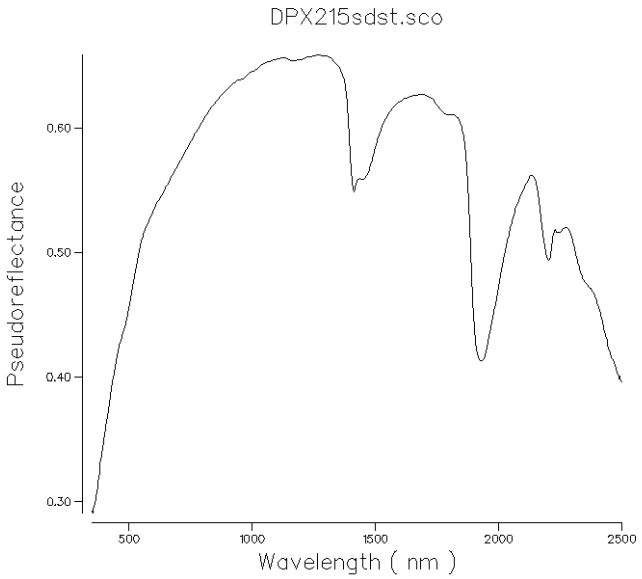
DPX215sdst.sco
Pseudoreflectance
0.60
0.50
0.40
0.30
500
1000
1500
2000
2500
Wavelength (nm)

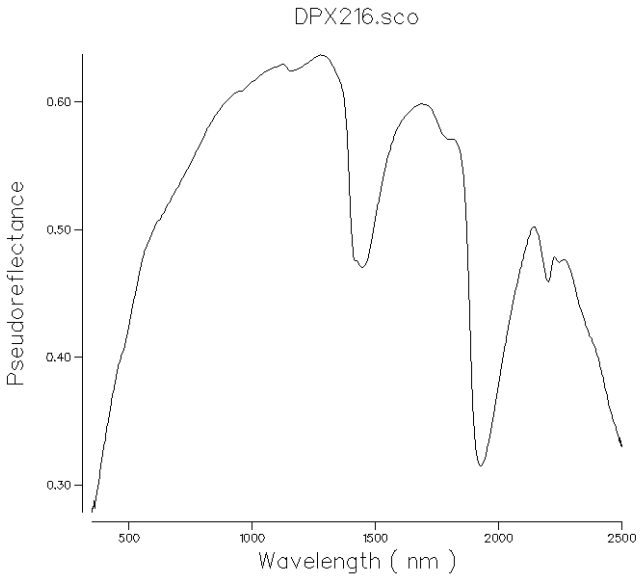
DPX216.sco
Pseudoreflectance
0.60
0.50
0.40
0.30
500
1000
1500
2000
2500
Wavelength (nm)

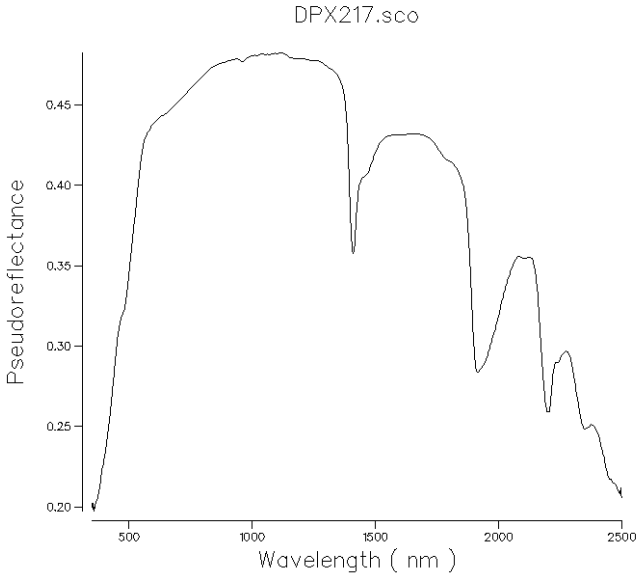
DPX217.sco
Pseudoreflectance
0.45
0.40
0.35
0.30
0.25
0.20
500
1000
1500
2000
2500
Wavelength (nm)

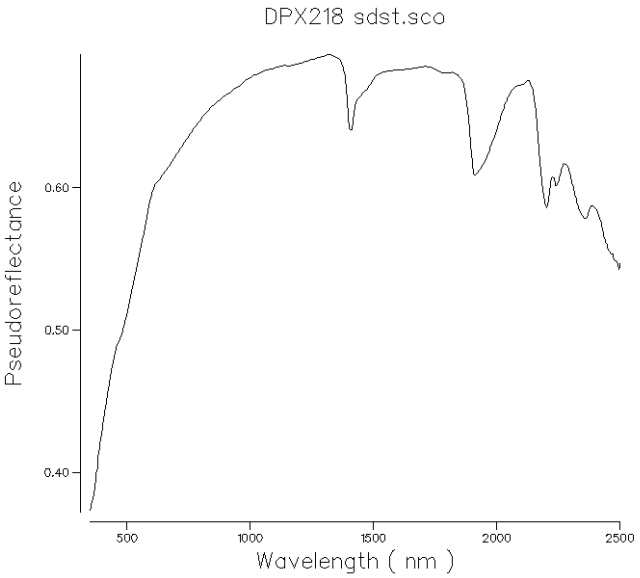
DPX218 sdst.sco
Pseudoreflectance
0.60
0.50
0.40
500
1000
1500
2000
2500
Wavelength (nm)

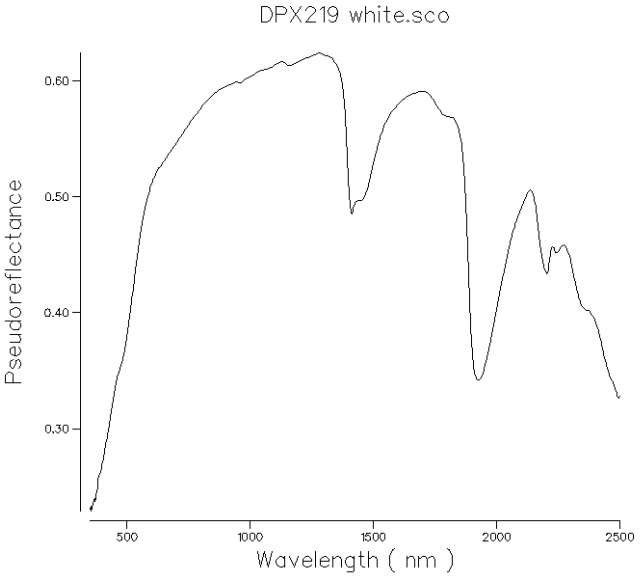
DPX219 white.sco
Pseudoreflectance
0.60
0.50
0.40
0.30
500
1000
1500
2000
2500
Wavelength (nm)

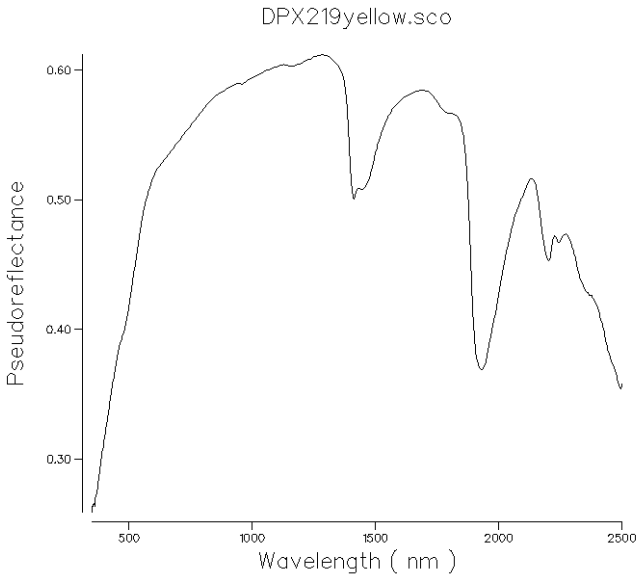
DPX219yellow.sco
Pseudoreflectance
0.60
0.50
0.40
0.30
500
1000
1500
2000
2500
Wavelength (nm)

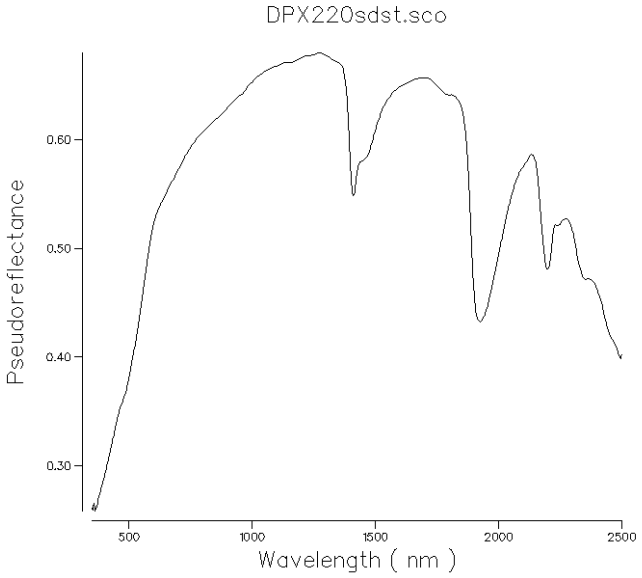
DPX220sdst.sco
Pseudoreflectance
0.60
0.50
0.40
0.30
500
1000
1500
2000
2500
Wavelength (nm)

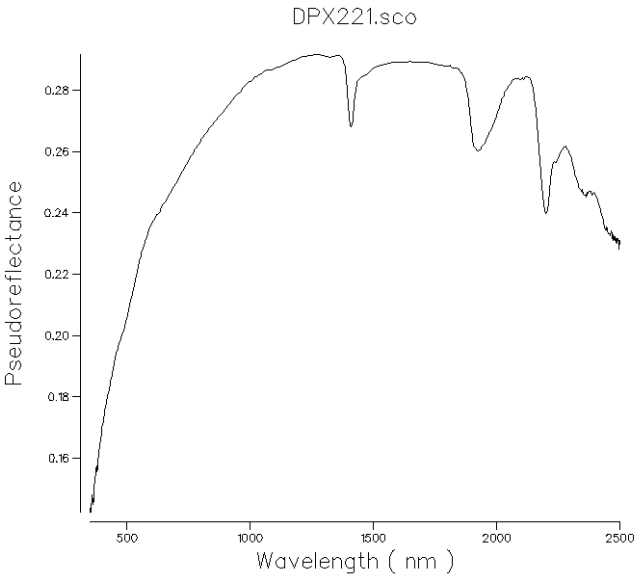
DPX221.sco
Pseudoreflectance
0.28
0.26
0.24
0.22
0.20
0.18
0.16
500
1000
1500
2000
2500
Wavelength (nm)

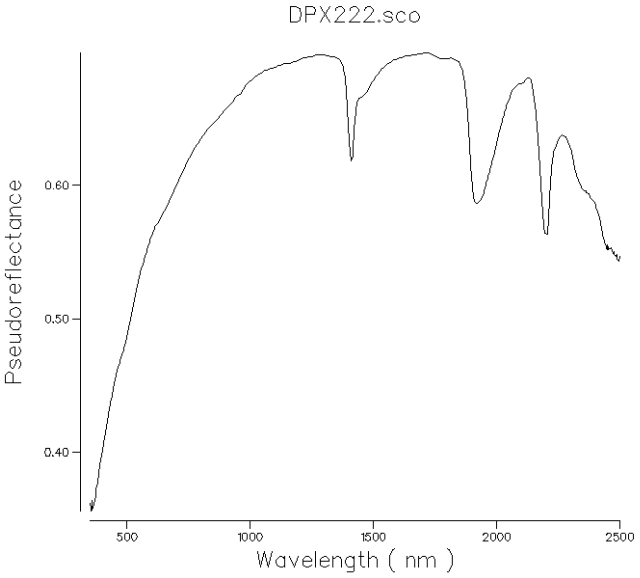
DPX222.sco
Pseudoreflectance
0.60
0.50
0.40
500
1000
1500
2000
2500
Wavelength (nm)

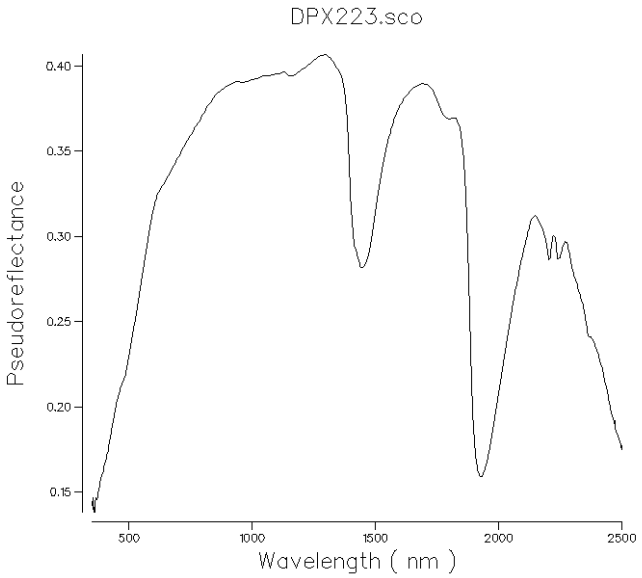
DPX223.sco
Pseudoreflectance
0.40
0.35
0.30
0.25
0.20
0.15
500
1000
1500
2000
2500
Wavelength (nm)

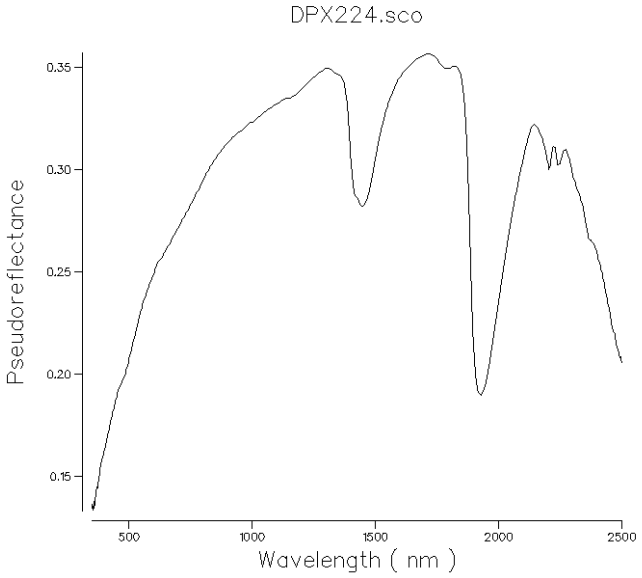
DPX224.sco
Pseudoreflectance
0.35
0.30
0.25
0.20
0.15
500
1000
1500
2000
2500
Wavelength (nm)

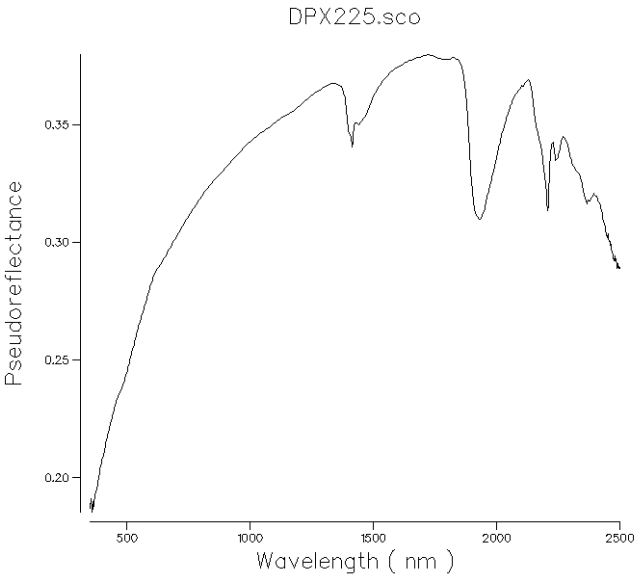
DPX225.sco
Pseudoreflectance
0.35
0.30
0.25
0.20
500
1000
1500
2000
2500
Wavelength (nm)

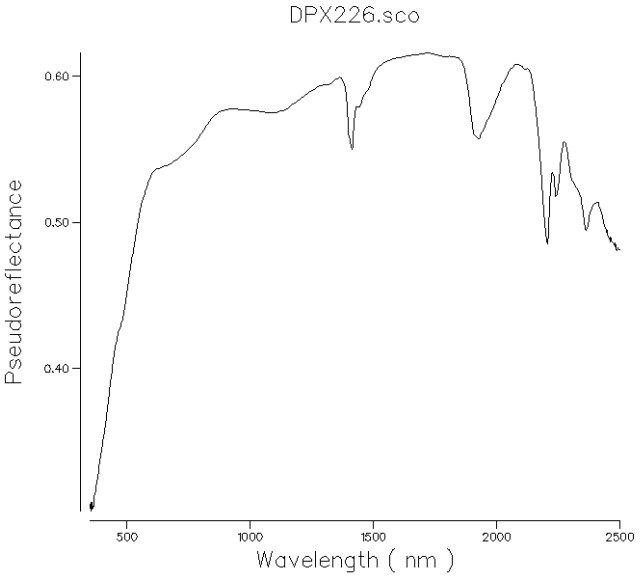
DPX226.sco
Pseudoreflectance
0.60
0.50
0.40
500
1000
1500
2000
2500
Wavelength (nm)

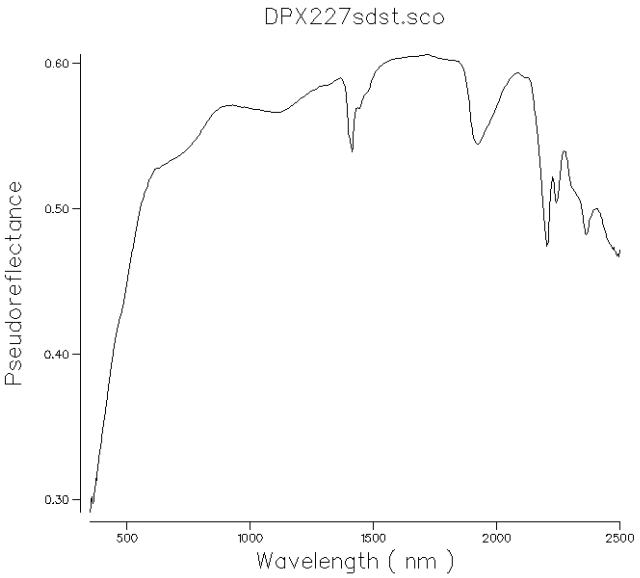
DPX227sdst.sco
Pseudoreflectance
0.60
0.50
0.40
0.30
500
1000
1500
2000
2500
Wavelength (nm)

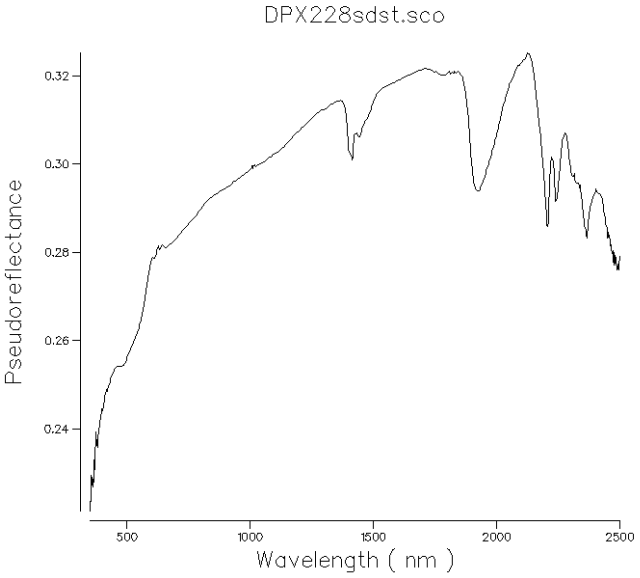
DPX228sdst.sco
Pseudoreflectance
0.32
0.30
0.28
0.26
0.24
500
1000
1500
2000
2500
Wavelength (nm)

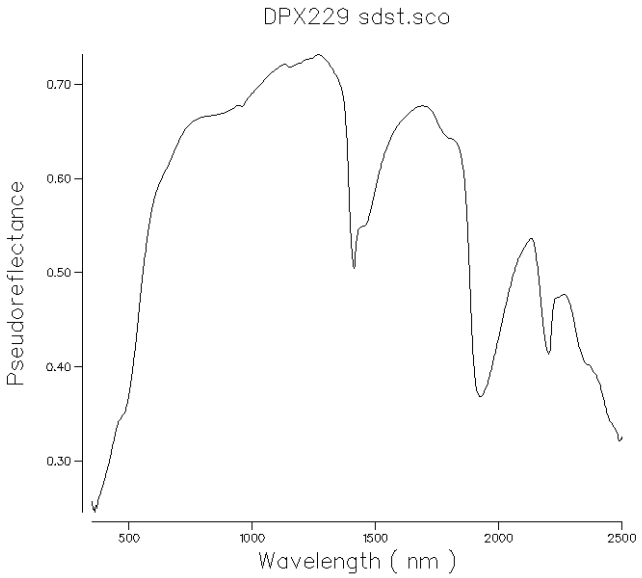

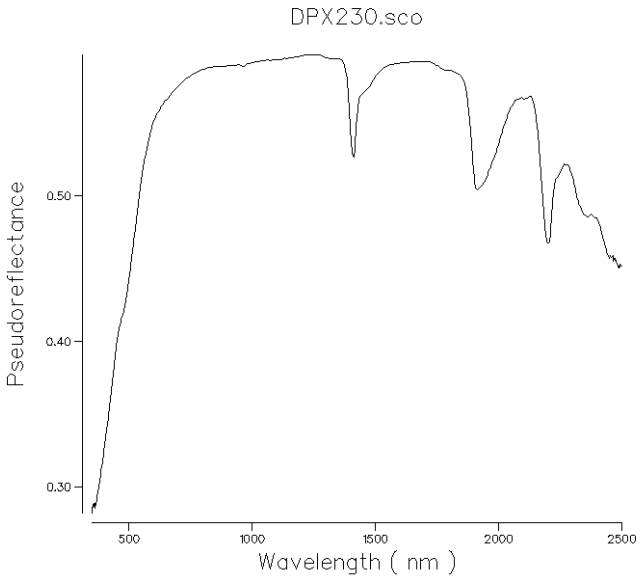

DPX231 was not analysed via SWIR

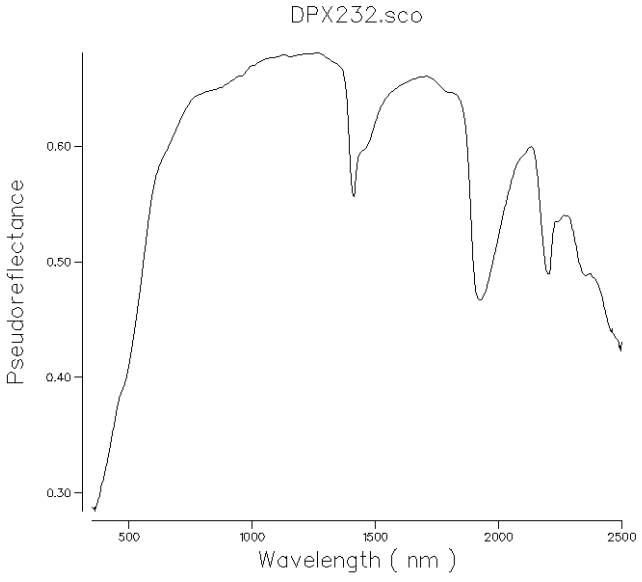

DPX233 and DPX234 were not analysed via SWIR

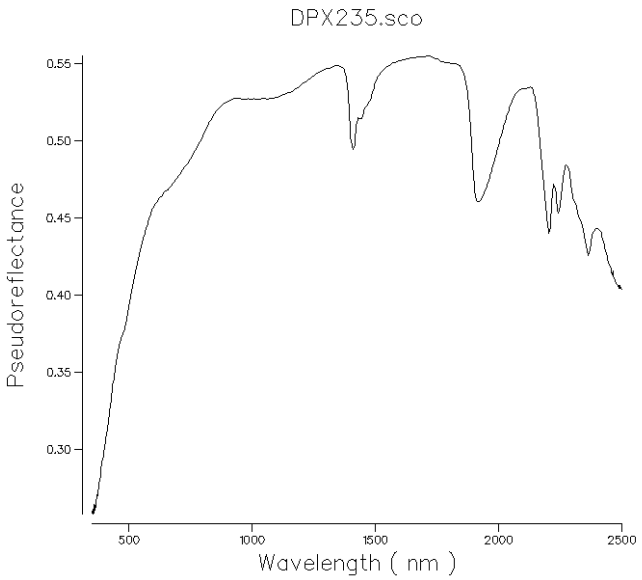

DPX236 was not analysed via SWIR

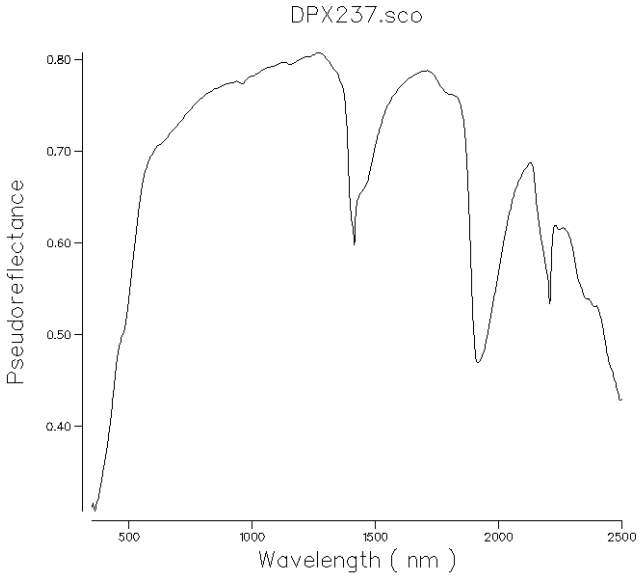
DPX237.sco
Pseudoreflectance
0.80
0.70
0.60
0.50
0.40
500
1000
1500
2000
2500
Wavelength (nm)

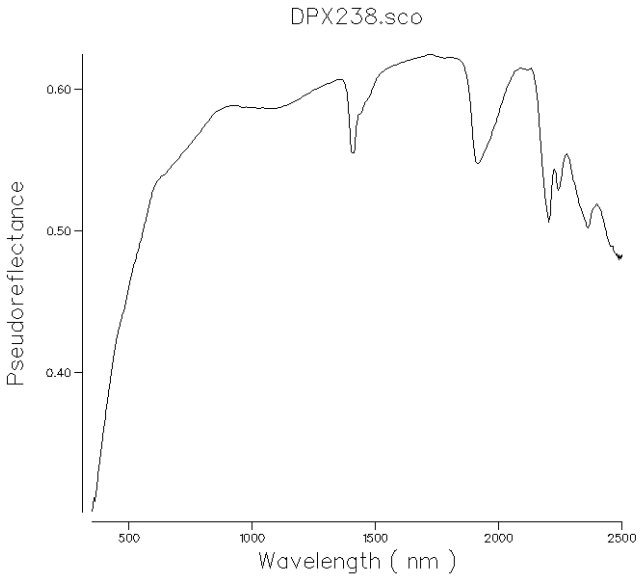
DPX238.sco
Pseudoreflectance
0.60
0.50
0.40
500
1000
1500
2000
2500
Wavelength (nm)

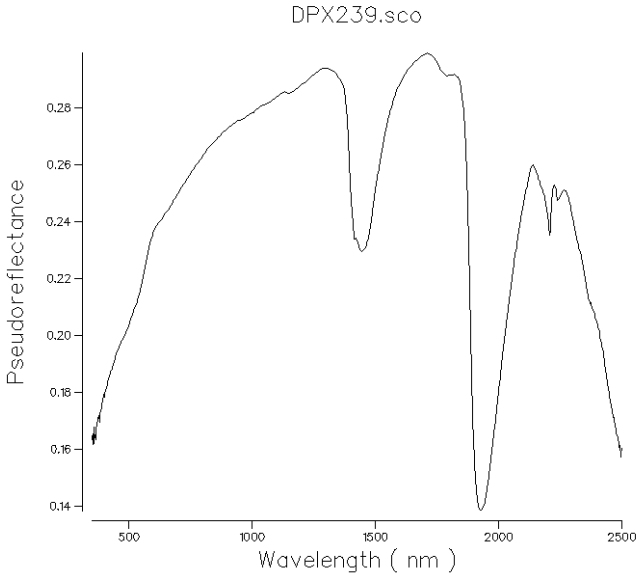
DPX239.sco
Pseudoreflectance
0.28
0.26
0.24
0.22
0.20
0.18
0.16
0.14
500
1000
1500
2000
2500
Wavelength (nm)

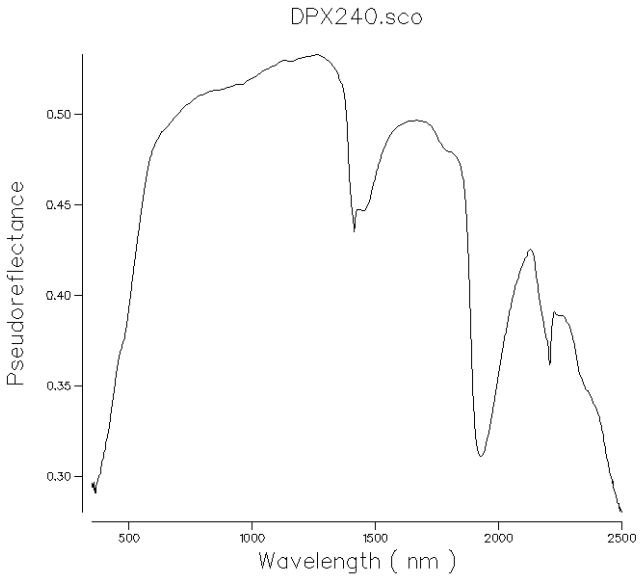
DPX240.sco
Pseudoreflectance
0.50
0.45
0.40
0.35
0.30
500
1000
1500
2000
2500
Wavelength (nm)

Samples from WR291

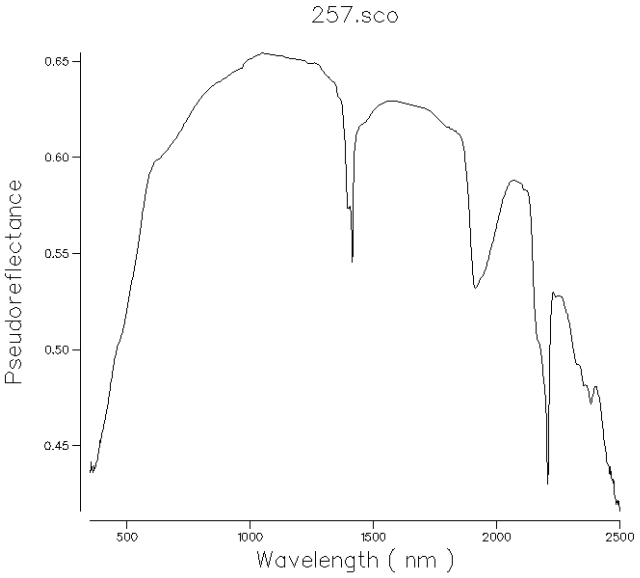

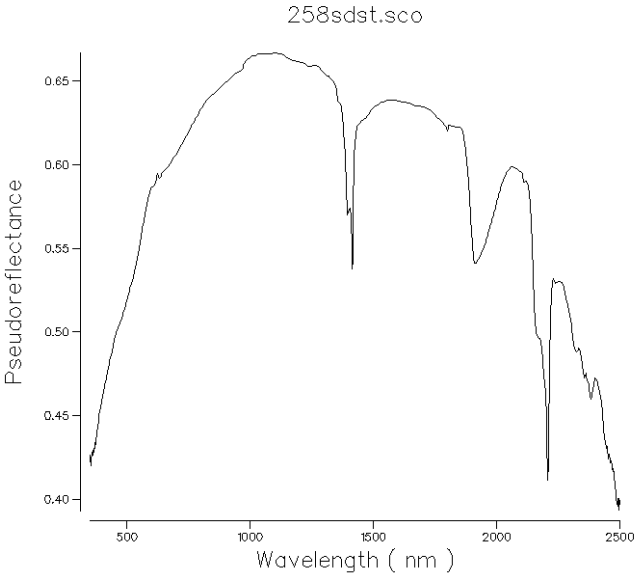

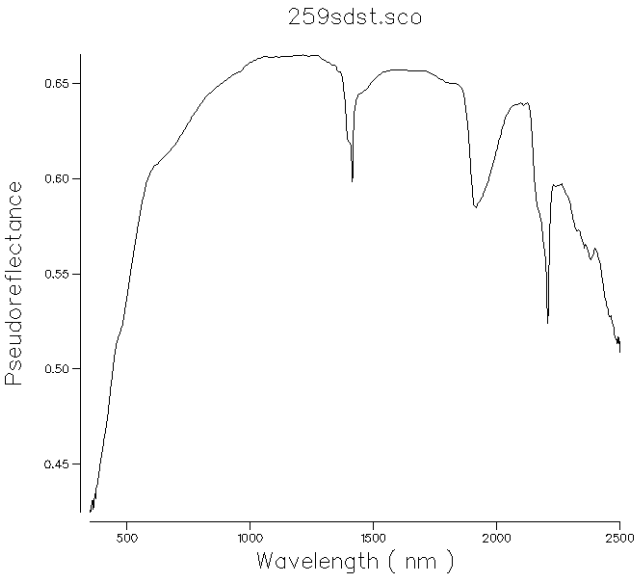
259sdst.sco
Pseudoreflectance
0.65
0.60
0.55
0.50
0.45
500
1000
1500
2000
2500
Wavelength (nm)

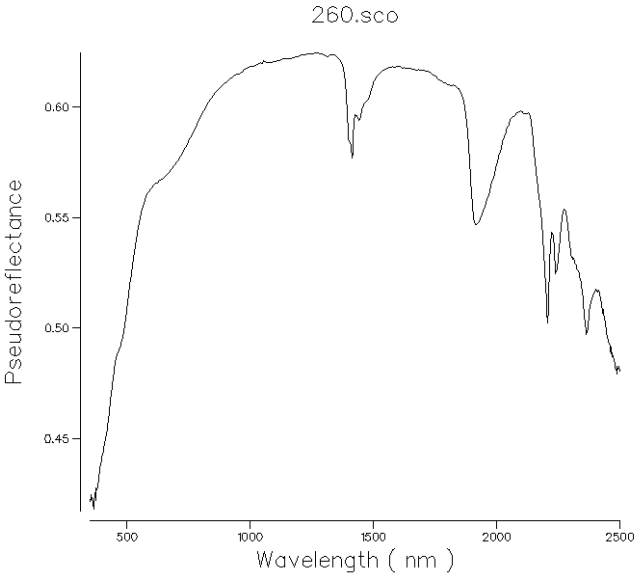
260.sco
Pseudoreflectance
0.60
0.55
0.50
0.45
500
1000
1500
2000
2500
Wavelength (nm)

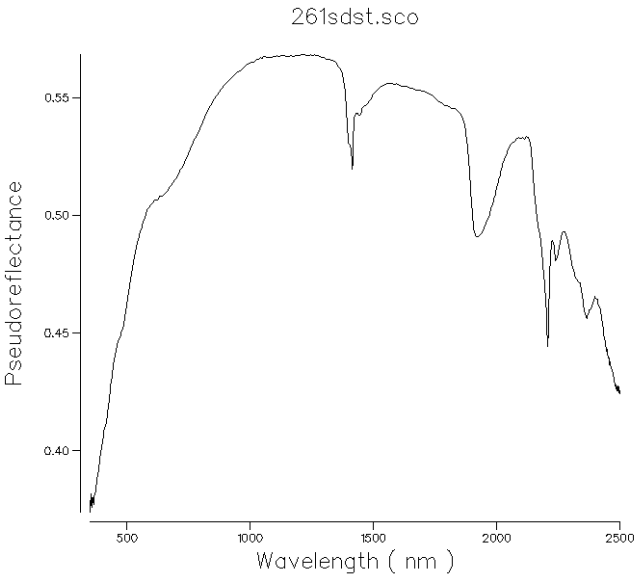
261sdst.sco
Pseudoreflectance
0.55
0.50
0.45
0.40
500
1000
1500
2000
2500
Wavelength (nm)

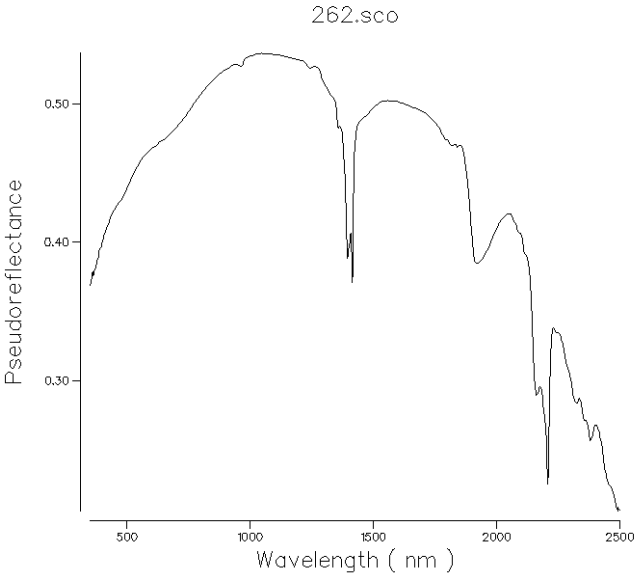
262.sco
Pseudoreflectance
0.50
0.40
0.30
500
1000
1500
2000
2500
Wavelength (nm)

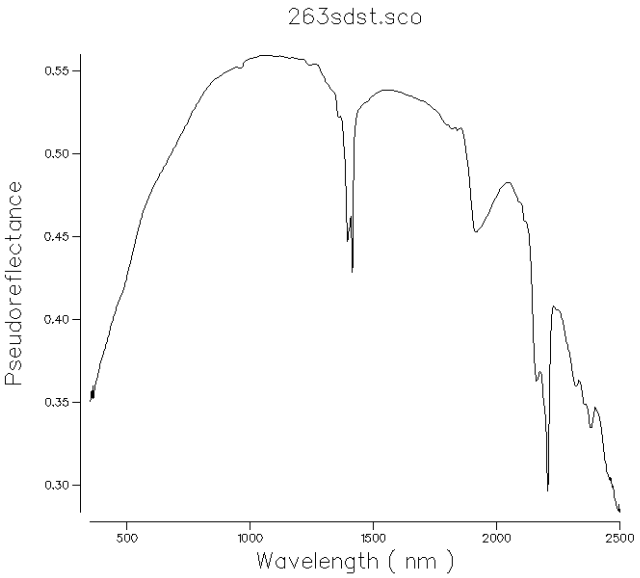
263sdst.sco
Pseudoreflectance
0.55
0.50
0.45
0.40
0.35
0.30
500
1000
1500
2000
2500
Wavelength (nm)

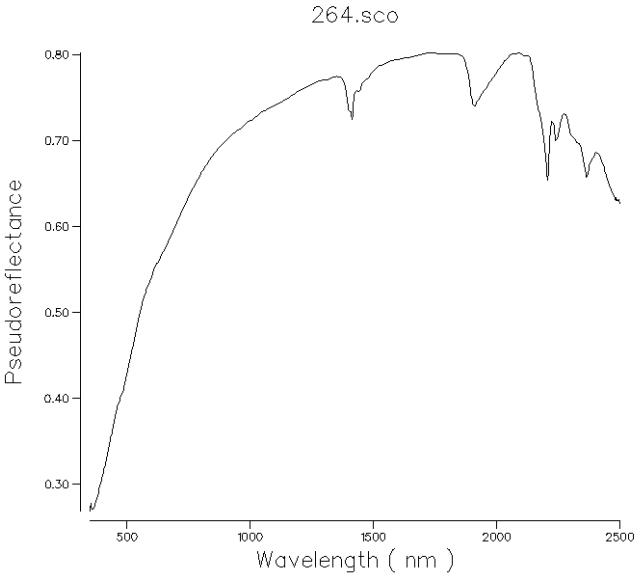
264.sco
Pseudoreflectance
0.80
0.70
0.60
0.50
0.40
0.30
500
1000
1500
2000
2500
Wavelength (nm)

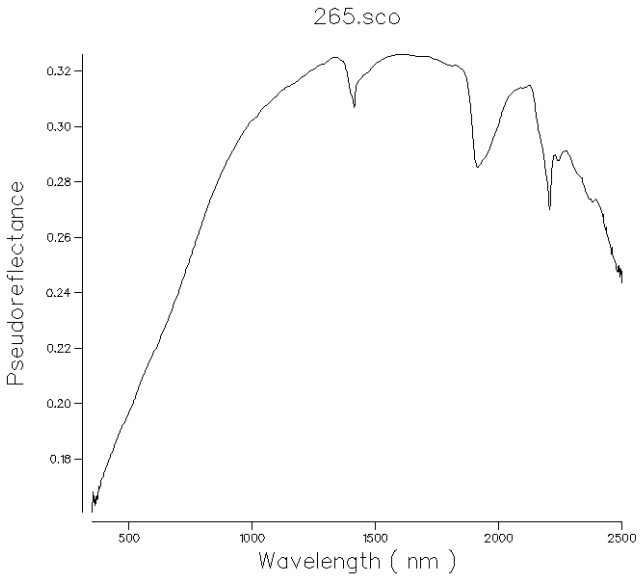
265.sco
Pseudoreflectance
0.32
0.30
0.28
0.26
0.24
0.22
0.20
0.18
500
1000
1500
2000
2500
Wavelength (nm)

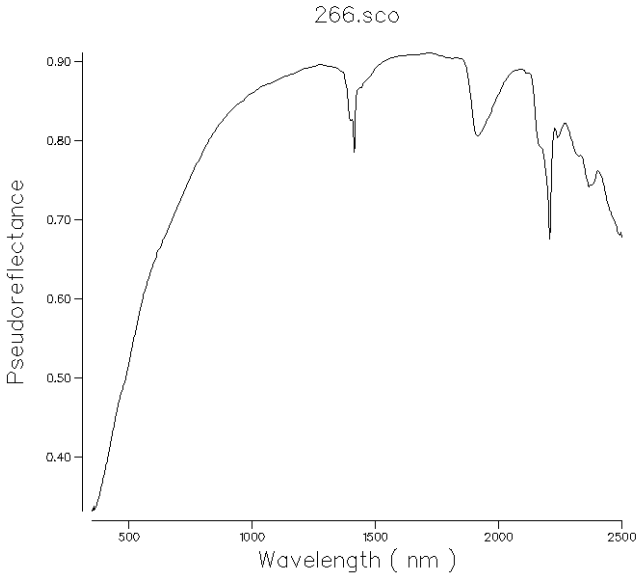
266.sco
Pseudoreflectance
0.90
0.80
0.70
0.60
0.50
0.40
500
1000
1500
2000
2500
Wavelength (nm)

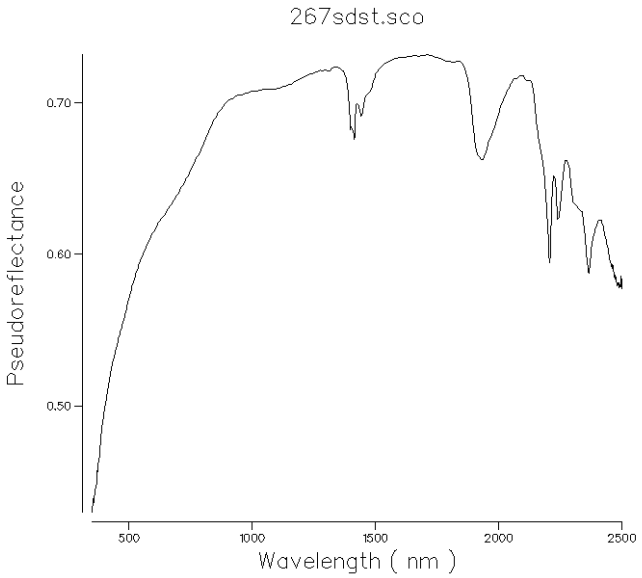

DPX268 was not analysed via SWIR

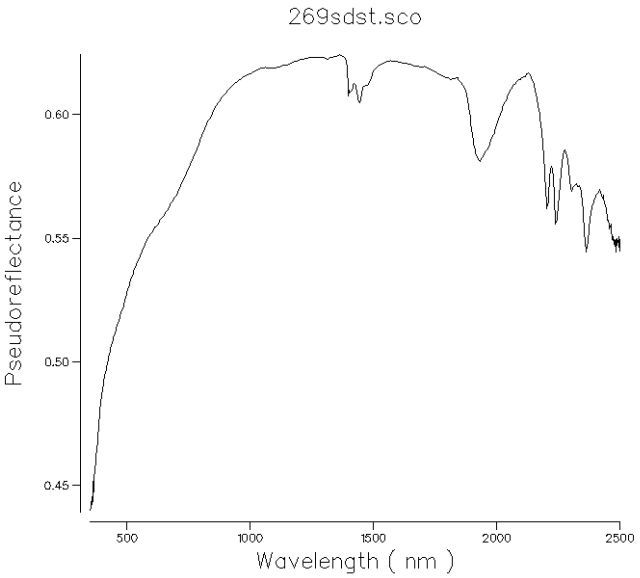
269sdst.sco
Pseudoreflectance
0.60
0.55
0.50
0.45
500
1000
1500
2000
2500
Wavelength (nm)

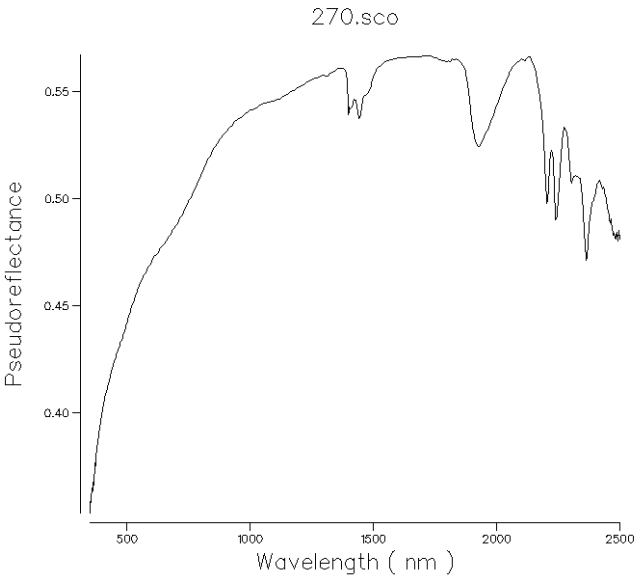
270.sco
Pseudoreflectance
0.55
0.50
0.45
0.40
500
1000
1500
2000
2500
Wavelength (nm)

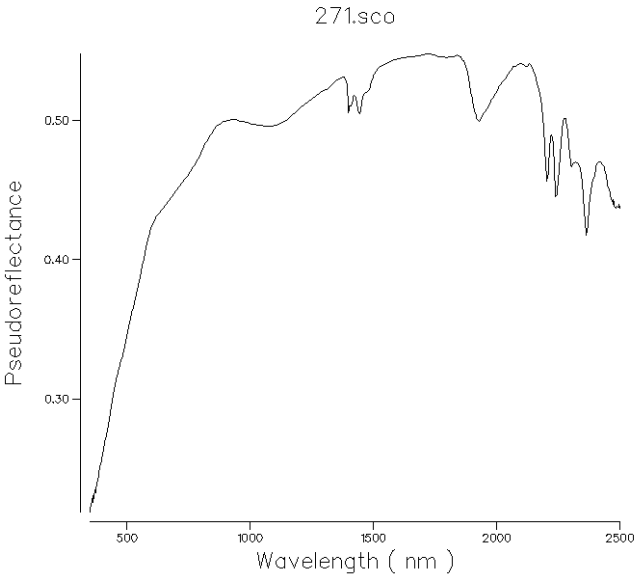
271.sco
Pseudoreflectance
0.50
0.40
0.30
500
1000
1500
2000
2500
Wavelength (nm)

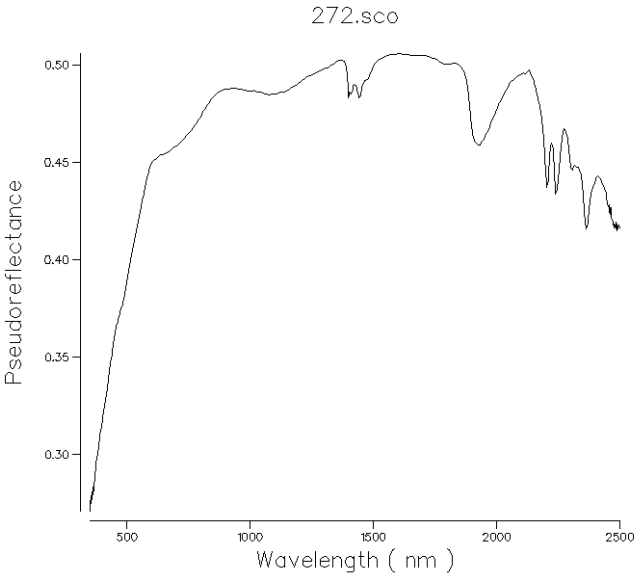
272.sco
Pseudoreflectance
0.50
0.45
0.40
0.35
0.30
500
1000
1500
2000
2500
Wavelength (nm)

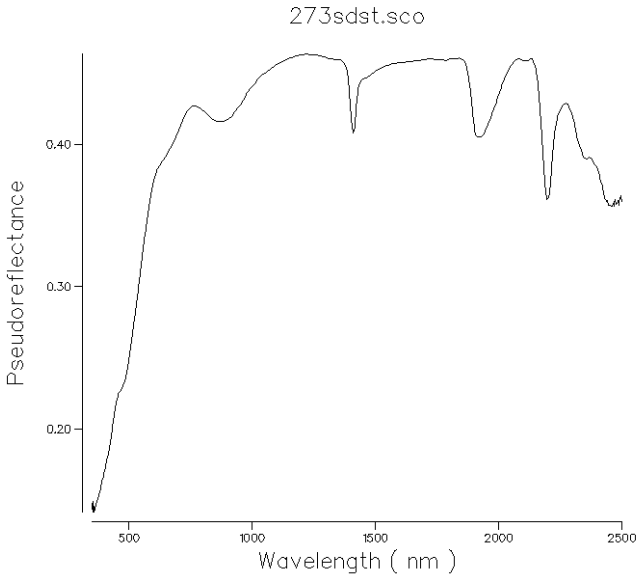
273sdst.sco
Pseudoreflectance
0.40
0.30
0.20
500
1000
1500
2000
2500
Wavelength (nm)

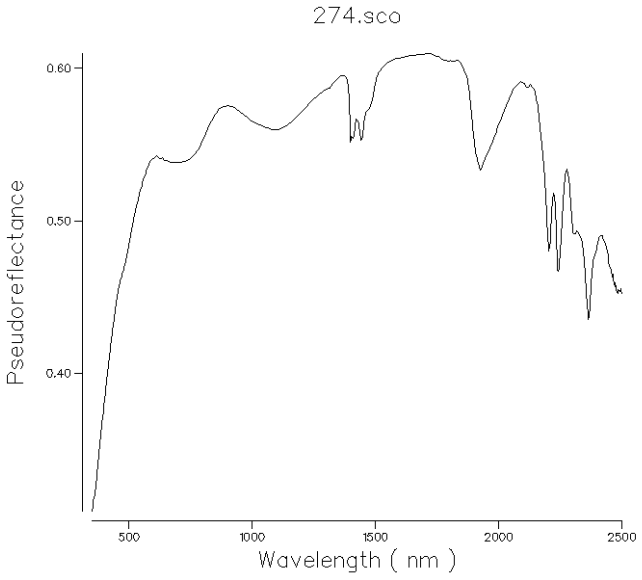
274.sco
Pseudoreflectance
0.60
0.50
0.40
500
1000
1500
2000
2500
Wavelength (nm)

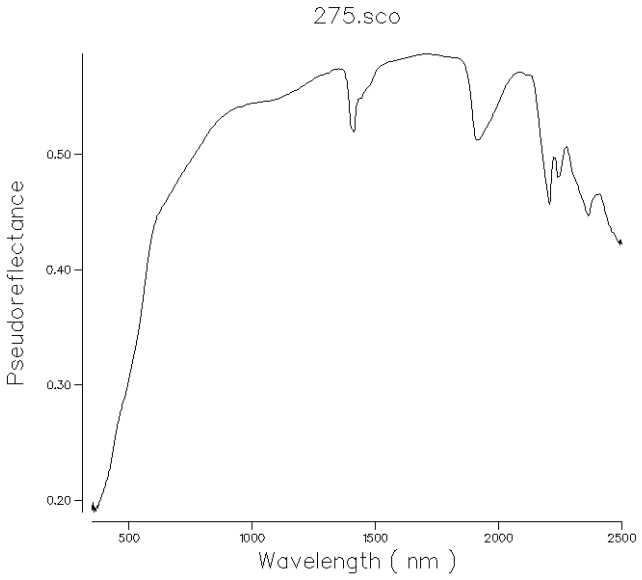
275.sco
Pseudoreflectance
0.50
0.40
0.30
0.20
500
1000
1500
2000
2500
Wavelength (nm)

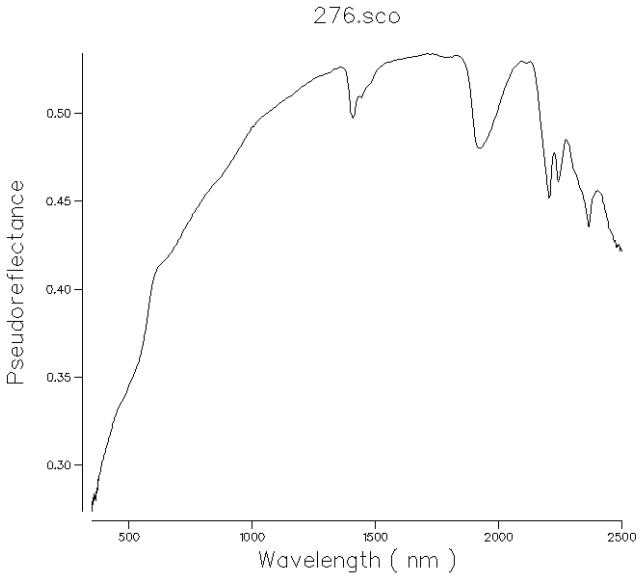
276.sco
Pseudoreflectance
0.50
0.45
0.40
0.35
0.30
500
1000
1500
2000
2500
Wavelength (nm)

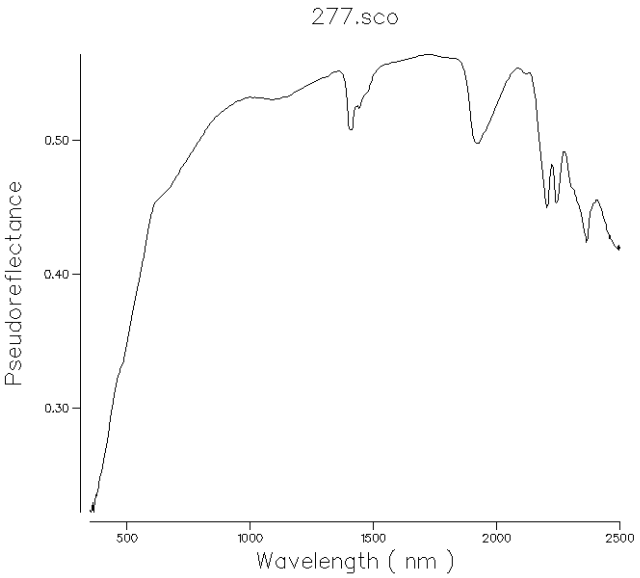
277.sco
Pseudoreflectance
0.50
0.40
0.30
500
1000
1500
2000
2500
Wavelength (nm)

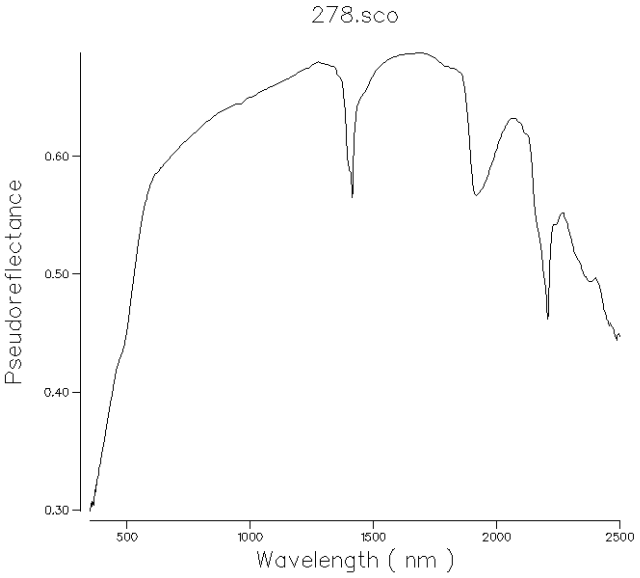
278.sco
Pseudoreflectance
0.60
0.50
0.40
0.30
500
1000
1500
2000
2500
Wavelength (nm)

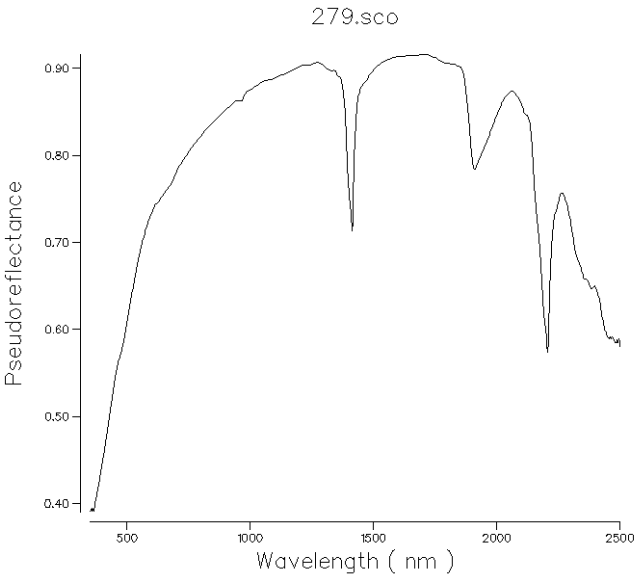
279.sco
Pseudoreflectance
0.90
0.80
0.70
0.60
0.50
0.40
500
1000
1500
2000
2500
Wavelength (nm)

Samples from WR353

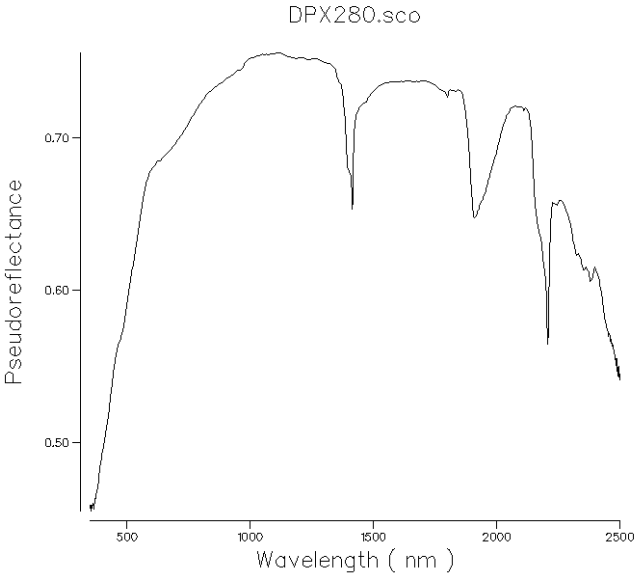

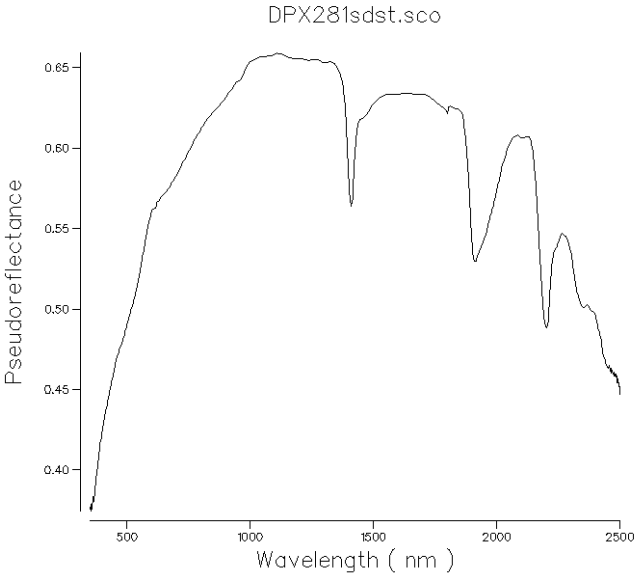

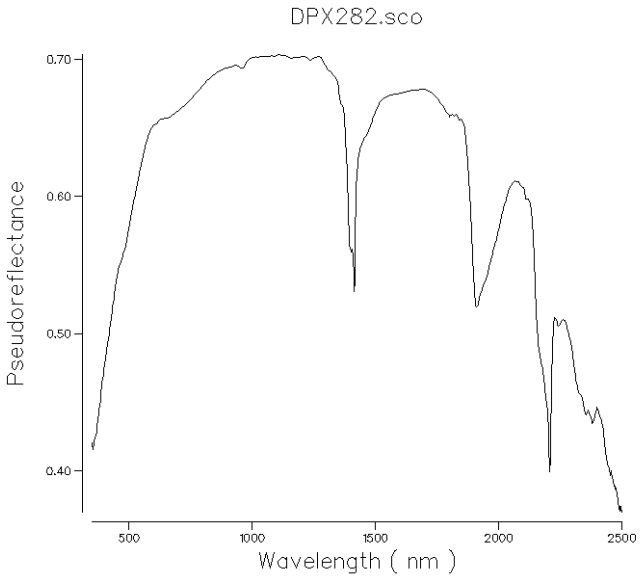
DPX282.sco
Pseudoreflectance
0.70
0.60
0.50
0.40
500
1000
1500
2000
2500
Wavelength (nm)

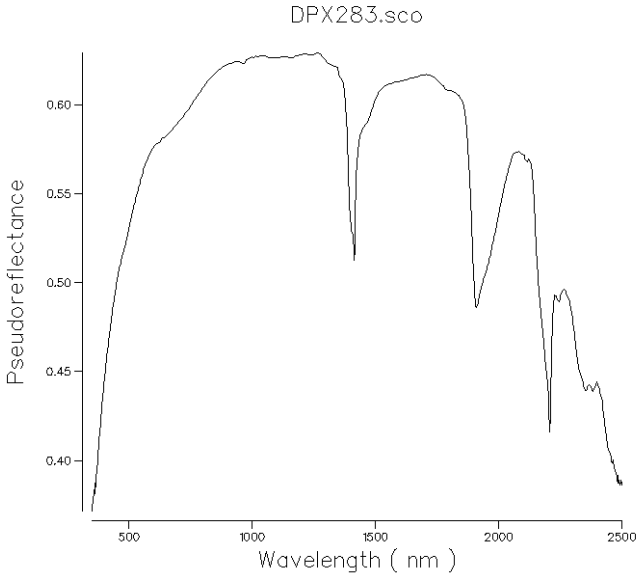
DPX283.sco
Pseudoreflectance
0.60
0.55
0.50
0.45
0.40
500
1000
1500
2000
2500
Wavelength (nm)

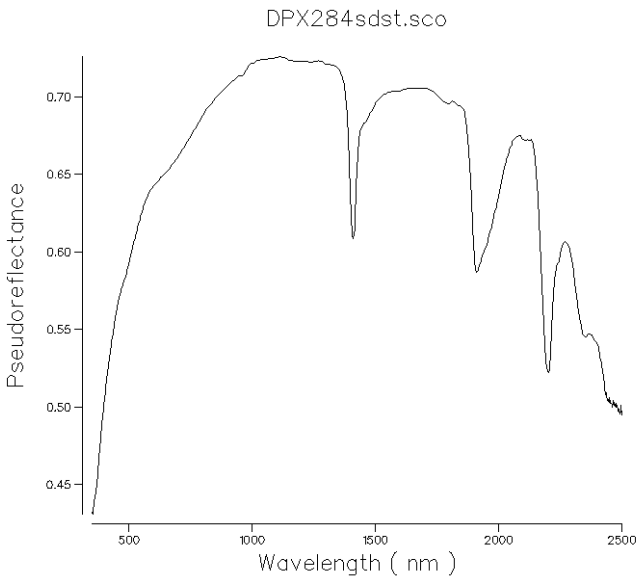

Sample DPX285 was not samples via SWIR

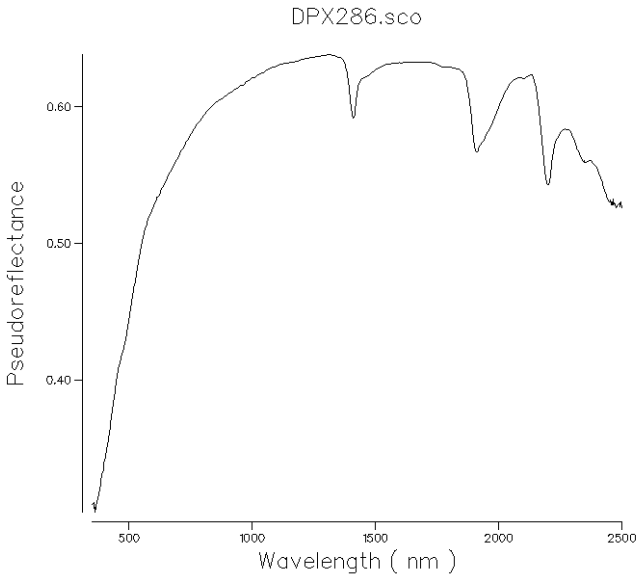
DPX286.sco
Pseudoreflectance
0.60
0.50
0.40
500
1000
1500
2000
2500
Wavelength (nm)

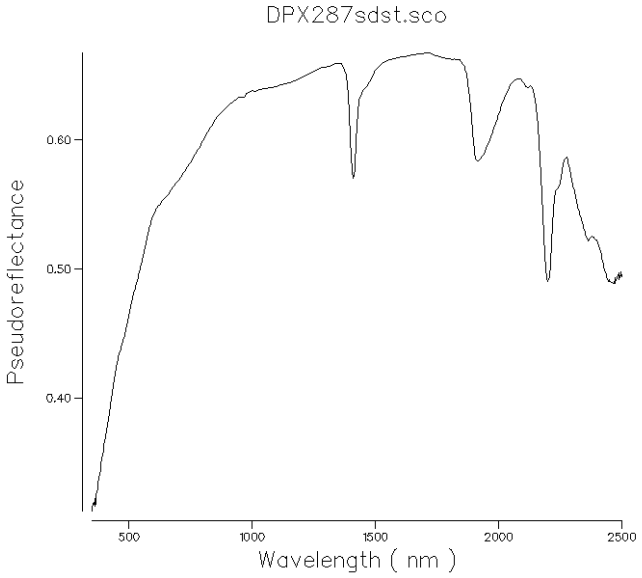
DPX287sdst.sco
Pseudoreflectance
0.60
0.50
0.40
500
1000
1500
2000
2500
Wavelength (nm)

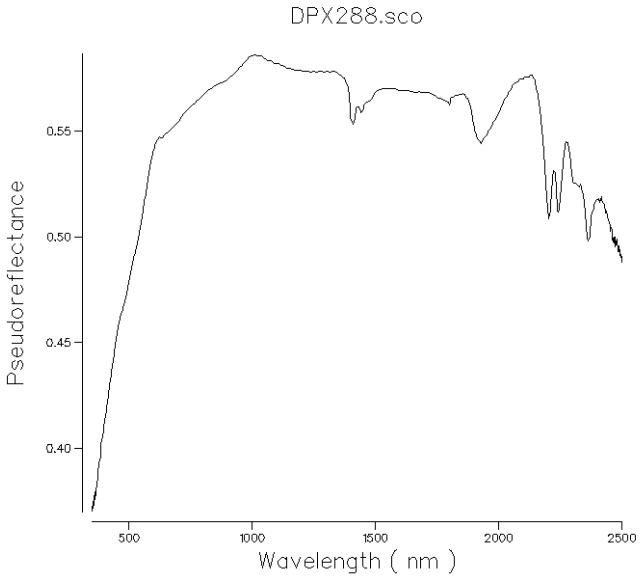

Sample DPX289 was not analysed via SWIR

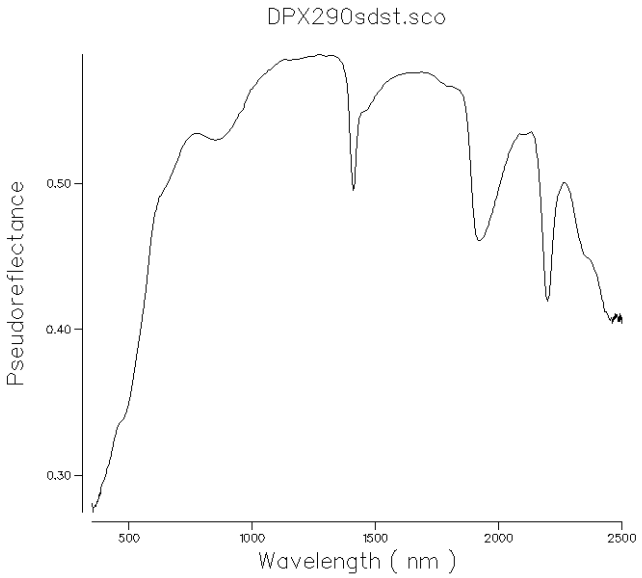
DPX290sdst.sco
Pseudoreflectance
0.50
0.40
0.30
500
1000
1500
2000
2500
Wavelength (nm)

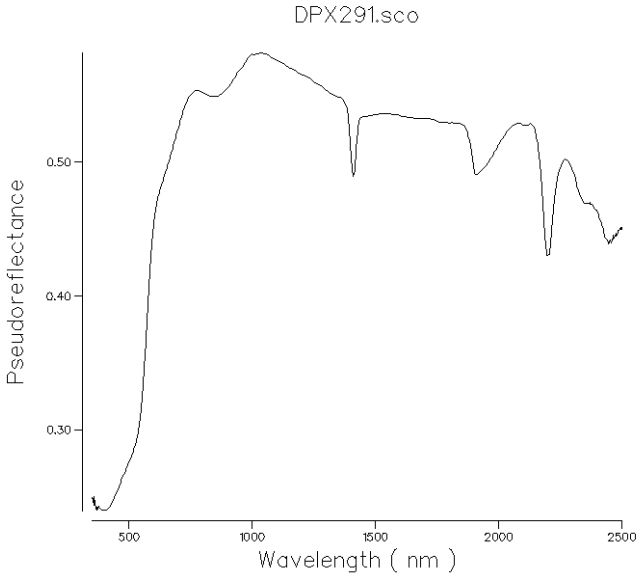
DPX291.sco
Pseudoreflectance
0.50
0.40
0.30
500
1000
1500
2000
2500
Wavelength (nm)

Sample DPX292 was not analysed via SWIAr

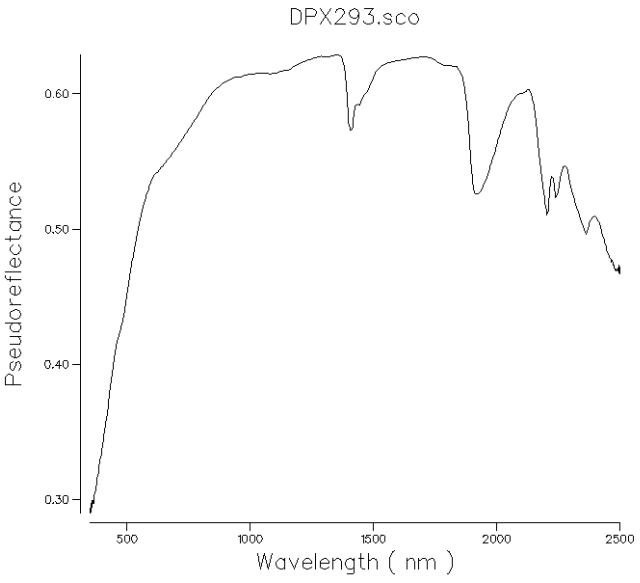

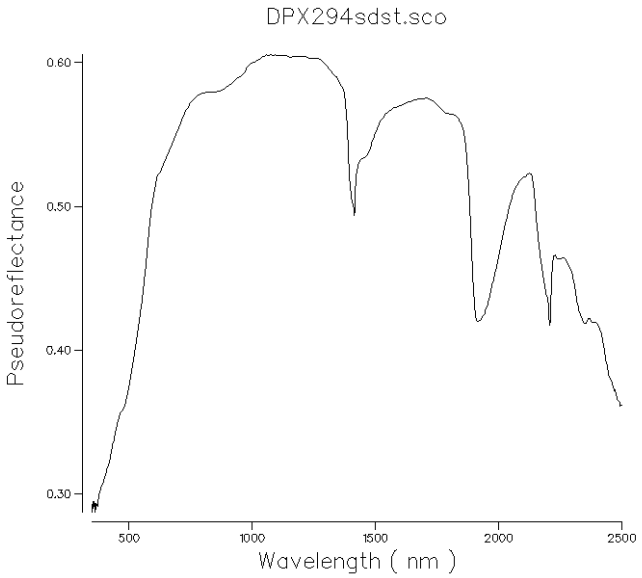
DPX294sdst.sco
Pseudoreflectance
0.60
0.50
0.40
0.30
500
1000
1500
2000
2500
Wavelength (nm)

SWIR Spectra from the WS Shear Structure

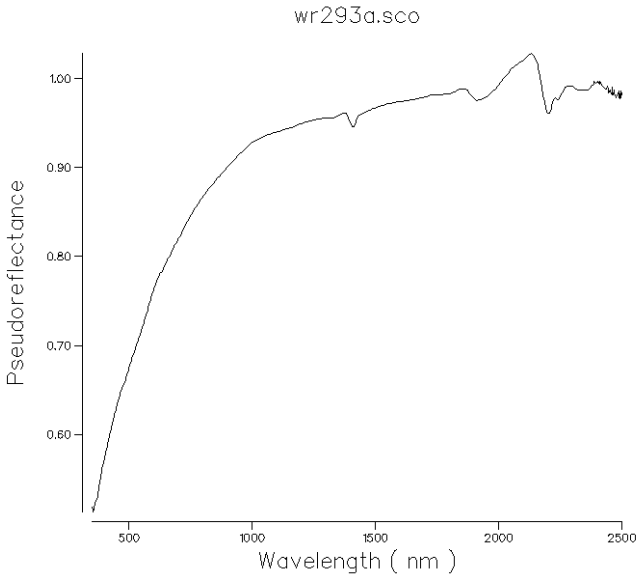

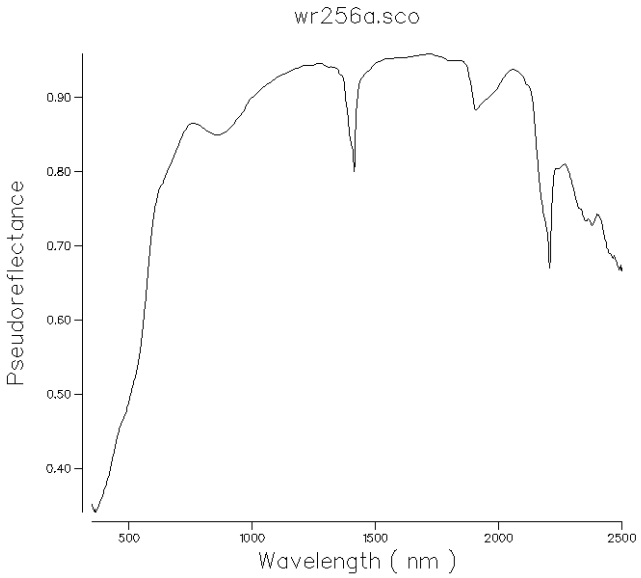

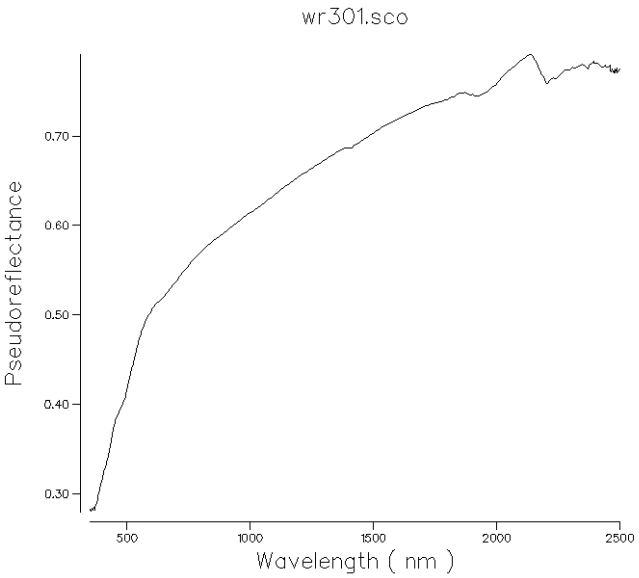
wr301.sco
Pseudoreflectance
0.70
0.60
0.50
0.40
0.30
500
1000
1500
2000
2500
Wavelength (nm)

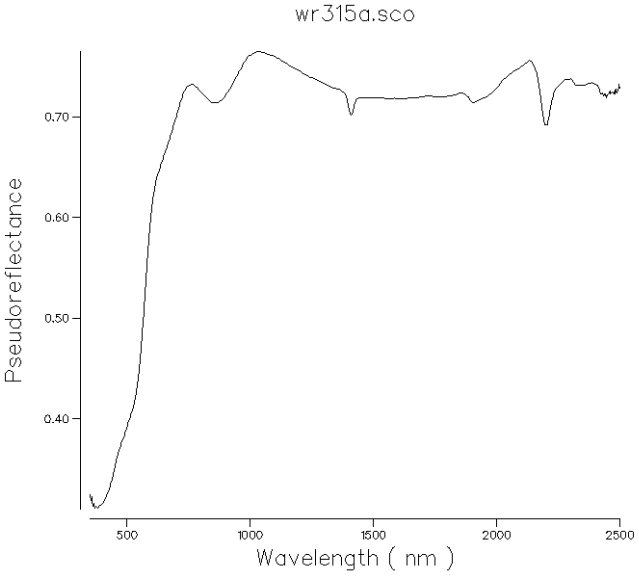
wr315a.sco
Pseudoreflectance
0.70
0.60
0.50
0.40
500
1000
1500
2000
2500
Wavelength (nm)

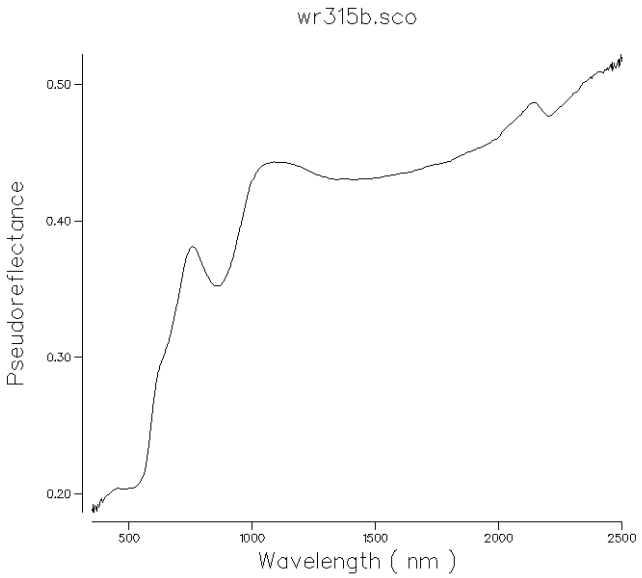
wr315b.sco
Pseudoreflectance
0.50
0.40
0.30
0.20
500
1000
1500
2000
2500
Wavelength (nm)

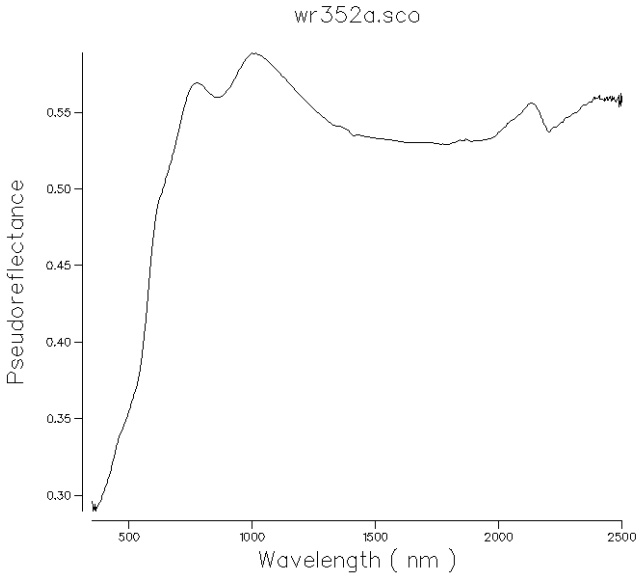
wr352a.sco
Pseudoreflectance
0.55
0.50
0.45
0.40
0.35
0.30
500
1000
1500
2000
2500
Wavelength (nm)

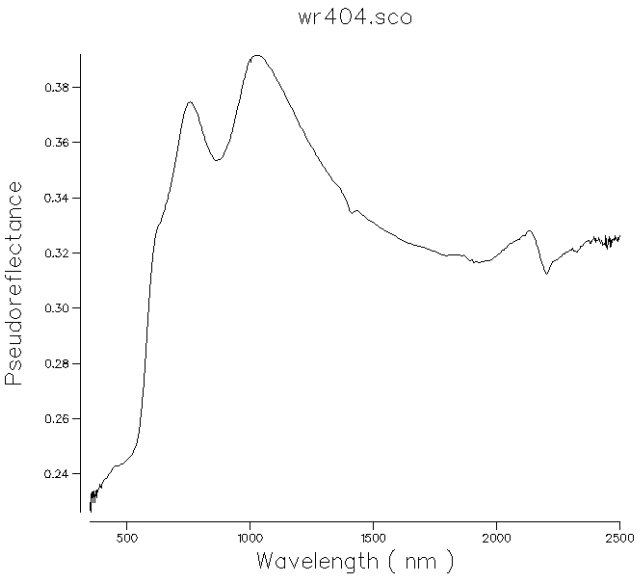
wr404.sco
Pseudoreflectance
0.38
0.36
0.34
0.32
0.30
0.28
0.26
0.24
500
1000
1500
2000
2500
Wavelength (nm)

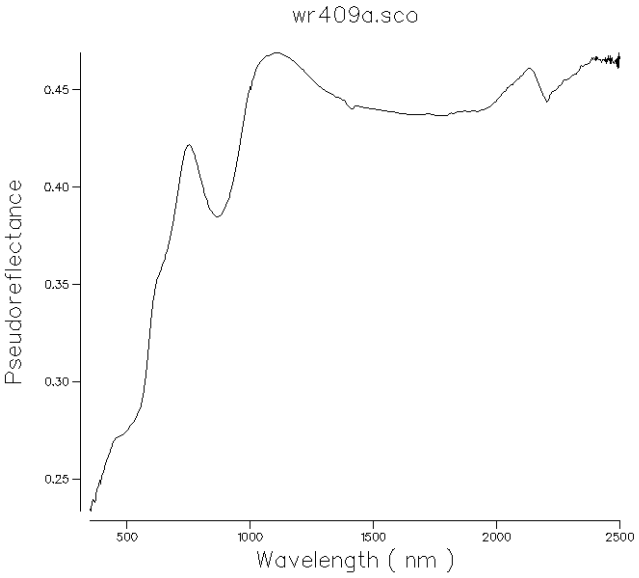
wr409a.sco
Pseudoreflectance
0.45
0.40
0.35
0.30
0.25
500
1000
1500
2000
2500
Wavelength (nm)

Appendix 4.2: Samples from the Phoenix Deposit identified through The Spectral Geologist Software

As part of this study access was granted to 'The Spectral Geologist' trial edition software (https://research.csiro.au/thespectralgeologist/) for which the majority of samples were analysed with to provide backup and secondary automated results.

Sample	Primary Mineral Identified	Primary Mineral Abundance	Secondary Mineral Identified	Secondary Mineral Abundance	Error
DPX101gfpl	Paragonitic Illite	1	NULL	NULL	353.87
DPX101gfpl	Paragonitic Illite	Ill		1	NULL
DPX102gfpl	Montmorillonite	0.527	Paragonitic Illite	0.473	77.952
DPX102vein	Muscovitic Illite	0.747	Montmorillonite	0.253	66.64
DPX103	Muscovite	1	NULL	NULL	145.67
DPX106	Muscovitic Illite	1	NULL	NULL	52.844
DPX107_blk_mineral_band	Muscovite	1	NULL	NULL	457.33
DPX107_wholerock	Muscovitic Illite	1	NULL	NULL	87.7
DPX109rock	Muscovite	1	NULL	NULL	198.79
DPX111	Muscovitic Illite	1	NULL	NULL	65.592
DPX117qtz	Muscovite	1	NULL	NULL	156.75
DPX121	Muscovitic Illite	0.723	Montmorillonite	0.277	58.99
DPX122	Muscovitic Illite	1	NULL	NULL	86.75
DPX123	Muscovitic Illite	1	NULL	NULL	69.419
DPX126	Muscovitic Illite	1	NULL	NULL	79.306
DPX13	Paragonitic Illite	0.603	Montmorillonite	0.397	68.898
DPX133_brnveins	Muscovite	1	NULL	NULL	161.43
DPX136_desic&vein	Muscovite	1	NULL	NULL	162.31
DPX136desic	Muscovite	1	NULL	NULL	162.31
DPX136sdst	Muscovite	1	NULL	NULL	205.33
DPX137desic	Muscovite	1	NULL	NULL	173.7
DPX137sdst	Muscovite	1	NULL	NULL	108.51
DPX143_vein	Muscovite	1	NULL	NULL	237.27
DPX148	Muscovitic Illite	1	NULL	NULL	63.638
DPX149	Muscovite	1	NULL	NULL	106.18
DPX150	Muscovite	1	NULL	NULL	506.63
DPX151	Muscovitic Illite	1	NULL	NULL	64.704
DPX152	Muscovite	0.708	DryVegetation	0.292	211.75
DPX153	Muscovite	1	NULL	NULL	90.548
DPX158	Montmorillonite	0.527	Paragonitic Illite	0.473	290.7
DPX158_limonite	Montmorillonite	0.624	Paragonitic Illite	0.376	214.54
DPX159	Paragonitic Illite	0.502	Kaolinite PX	0.498	454.91
DPX16	Paragonitic Illite	1	NULL	NULL	288.95
DPX160	Muscovitic Illite	0.573	Kaolinite PX	0.427	232.87
DPX163	Paragonitic Illite	0.564	Montmorillonite	0.436	184.64
DPX163_vein	Paragonitic Illite	0.587	Montmorillonite	0.413	187.72
DPX169	Muscovitic Illite	1	NULL	NULL	92.363
DPX170desic	Muscovite	1	NULL	NULL	149.2

DPX170sdst	Muscovite	1	NULL	NULL	233.16
DPX175	Kaolinite PX	0.613	Paragonitic Illite	0.387	290.78
DPX176	Kaolinite WX	0.597	Muscovitic Illite	0.403	163.54
DPX177	Kaolinite PX	0.599	Paragonitic Illite	0.401	277.94
DPX178	Kaolinite WX	0.59	Muscovitic Illite	0.41	142.98
DPX179	Kaolinite WX	0.66	Paragonitic Illite	0.34	142.35
DPX180	FeTourmaline	0.6	Kaolinite PX	0.4	250.2
DPX181	Kaolinite PX	0.562	Paragonitic Illite	0.438	334.51
DPX182	FeTourmaline	0.651	Kaolinite PX	0.349	281.92
DPX183	Kaolinite WX	0.635	Paragonitic Illite	0.365	157.5
DPX184	Paragonitic Illite	0.502	Montmorillonite	0.498	186.15
DPX185	Kaolinite PX	0.521	Paragonitic Illite	0.479	202.55
DPX186	Montmorillonite	0.505	Paragonitic Illite	0.495	203.7
DPX187	Paragonitic Illite	0.564	Montmorillonite	0.436	168.32
DPX188	Paragonitic Illite	0.595	Montmorillonite	0.405	118.57
DPX189	Muscovitic Illite	1	NULL	NULL	158.77
DPX190	Paragonitic Illite	0.563	Montmorillonite	0.437	124.01
DPX191	Muscovitic Illite	1	NULL	NULL	106.44
DPX192	Muscovitic Illite	1	NULL	NULL	119.5
DPX193	Paragonitic Illite	0.604	Montmorillonite	0.396	121.58
DPX194	Muscovite	1	NULL	NULL	370.24
DPX195	Muscovite	1	NULL	NULL	101.98
DPX196	Muscovite	1	NULL	NULL	96.23
DPX198	Muscovite	1	NULL	NULL	115.96
DPX199	Muscovitic Illite	1	NULL	NULL	71.423
DPX200	Muscovitic Illite	1	NULL	NULL	122.43
DPX201	Muscovite	1	NULL	NULL	101.52
DPX18	Paragonitic Illite	0.526	Montmorillonite	0.474	327.66
DPX186	Montmorillonite	0.505	Paragonitic Illite	0.495	203.7
DPX187	Paragonitic Illite	0.564	Montmorillonite	0.436	168.32
DPX187_vein	Paragonitic Illite	0.576	Montmorillonite	0.424	183.38
DPX188	Paragonitic Illite	0.595	Montmorillonite	0.405	118.57
DPX188_vein	Paragonitic Illite	0.559	Montmorillonite	0.441	118.94
DPX189	Muscovitic Illite	1	NULL	NULL	158.77
DPX190	Paragonitic Illite	0.563	Montmorillonite	0.437	124.01
DPX191	Muscovitic Illite	1	NULL	NULL	106.44
DPX192	Muscovitic Illite	1	NULL	NULL	119.5
DPX193	Paragonitic Illite	0.604	Montmorillonite	0.396	121.58
DPX193_vein	Montmorillonite	Mont		1	NULL
DPX194	Muscovite	1	NULL	NULL	370.24
DPX195	Muscovite	1	NULL	NULL	101.98
DPX195_vein	Muscovitic Illite	Ill		1	NULL
DPX198	Muscovite	1	NULL	NULL	115.96
DPX199	Muscovitic Illite	1	NULL	NULL	71.423
DPX200	Muscovitic Illite	1	NULL	NULL	122.43
DPX201	Muscovite	1	NULL	NULL	101.52
DPX215_vein	Muscovite	1	NULL	NULL	258.87
DPX229_infill	Paragonite	0.666	Montmorillonite	0.334	144.96
DPX257	Kaolinite WX	1	NULL	NULL	105.09
DPX258	Kaolinite WX	1	NULL	NULL	96.426
DPX259	Kaolinite WX	1	NULL	NULL	120.21
DPX260	FeTourmaline	0.618	Kaolinite PX	0.382	203.62

DPX261	Kaolinite WX	0.597	FeTourmaline	0.403	133.08
DPX262	Kaolinite WX	1	NULL	NULL	84.337
DPX263	Kaolinite WX	1	NULL	NULL	83.172
DPX264	FeTourmaline	0.565	Kaolinite WX	0.435	114.29
DPX265	Kaolinite PX	1	NULL	NULL	299.07
DPX266	Kaolinite WX	1	NULL	NULL	130.04
DPX267	FeTourmaline	0.609	Kaolinite WX	0.391	182.98
DPX269	FeTourmaline	1	NULL	NULL	236.49
DPX270	FeTourmaline	1	NULL	NULL	260.91
DPX271	FeTourmaline	1	NULL	NULL	201.76
DPX272	FeTourmaline	1	NULL	NULL	250.37
DPX273	Muscovite	1	NULL	NULL	97.105
DPX274	FeTourmaline	1	NULL	NULL	188.32
DPX275	FeTourmaline	0.573	Paragonite	0.427	208.51
DPX276	FeTourmaline	0.669	Paragonite	0.331	197.17
DPX277	FeTourmaline	0.671	Paragonite	0.329	195.42
DPX278	Kaolinite WX	0.677	Muscovite	0.323	56.457
DPX279	Muscovitic Illite	0.551	Kaolinite WX	0.449	32.873
DPX203	Kaolinite PX	1	NULL	NULL	380.03
DPX205	NULL	NULL	NULL	NULL	NULL
DPX206	Kaolinite WX	0.765	Paragonite	0.235	131.74
DPX209	Paragonitic Illite	0.521	Kaolinite PX	0.479	277.47
DPX210	Paragonite	0.581	Kaolinite PX	0.419	555.92
DPX211	Montmorillonite	0.513	Paragonite	0.487	222.76
DPX212	Palygorskite	0.587	Paragonite	0.413	244.51
DPX213	Paragonite	1	NULL	NULL	419.13
DPX214	Kaolinite WX	0.636	Dickite	0.364	98.972
DPX215	Muscovite	1	NULL	NULL	236.55
DPX216	Paragonite	0.502	Palygorskite	0.498	162.99
DPX217	Paragonitic Illite	0.602	Montmorillonite	0.398	134.73
DPX218	Paragonite	0.824	Tourmaline	0.176	392.37
DPX219	Paragonite	0.582	Montmorillonite	0.418	227.52
DPX220	Paragonite	0.666	Montmorillonite	0.334	144.54
DPX221	Muscovite	1	NULL	NULL	144.6
DPX222	Muscovite	1	NULL	NULL	106.37
DPX223	NULL	NULL	NULL	NULL	NULL
DPX224	NULL	NULL	NULL	NULL	NULL
DPX224i	FeTourmaline	1	NULL	NULL	181.45
DPX225	Kaolinite WX	0.556	FeTourmaline	0.444	147.2
DPX226	Muscovite	0.519	FeTourmaline	0.481	138.8
DPX227	Muscovite	0.51	FeTourmaline	0.49	142.37
DPX228	FeTourmaline	0.689	Kaolinite PX	0.311	208.77
DPX229	Paragonite	0.687	Kaolinite PX	0.313	136.82
DPX230	Paragonitic Illite	0.621	Montmorillonite	0.379	105.48
DPX232	Paragonite	0.7	Kaolinite PX	0.3	194.04

DPX235	FeTourmaline	0.611	Paragonite	0.389	201.62
DPX237	Kaolinite WX	0.663	Paragonite	0.337	171.84
DPX238	Paragonite	0.811	Tourmaline	0.189	406.6
DPX239	NULL	NULL	NULL	NULL	NULL
DPX240	Kaolinite WX	0.606	Paragonite	0.394	234.88
DPX280	Kaolinite WX	1	NULL	NULL	119.53
DPX281	Paragonitic Illite	0.594	Montmorillonite	0.406	101.91
DPX282	Kaolinite WX	0.817	Paragonitic Illite	0.183	77.841
DPX283	Kaolinite WX	0.675	Paragonitic Illite	0.325	105.08
DPX284	Paragonitic Illite	0.598	Montmorillonite	0.402	88.981
DPX286	Paragonitic Illite	0.566	Montmorillonite	0.434	104.93
DPX287	Muscovite	1	NULL	NULL	103.86
DPX288	FeTourmaline	1	NULL	NULL	203.41
DPX290	Muscovite	1	NULL	NULL	83.984
DPX291	Muscovitic Illite	1	NULL	NULL	43.331
DPX293	Muscovite	0.557	FeMgChlorite	0.443	124.67
DPX294	Kaolinite WX	0.654	Paragonite	0.346	151.44
DPX24	Paragonitic Illite	0.616	Montmorillonite	0.384	93.99
DPX26a	Paragonitic Illite	0.586	Montmorillonite	0.414	68.812
DPX26B	Muscovitic Illite	1	NULL	NULL	70.388
DPX281	Paragonitic Illite	0.594	Montmorillonite	0.406	101.91
DPX281_vein	Paragonitic Illite	0.555	Montmorillonite	0.445	126.67
DPX284	Paragonitic Illite	0.598	Montmorillonite	0.402	88.981
DPX286	Paragonitic Illite	0.566	Montmorillonite	0.434	104.93
DPX287	Muscovite	1	NULL	NULL	103.86
DPX287_infill	Muscovite	1	NULL	NULL	106.85
DPX290	Muscovite	1	NULL	NULL	83.984
DPX291	Muscovitic Illite	1	NULL	NULL	43.331
DPX294mudstone	Paragonitic Illite	0.537	Montmorillonite	0.463	323.89
DPX32	Paragonitic Illite	0.644	Montmorillonite	0.356	218.14
DPX33	Paragonitic Illite	0.629	Montmorillonite	0.371	197.18
DPX341_vertfracture	Paragonite	Ill		1	NULL
DPX36	Muscovitic Illite	1	NULL	NULL	111.5
DPX38	Paragonitic Illite	0.672	Montmorillonite	0.328	227.85
DPX40	Muscovitic Illite	1	NULL	NULL	118.11
DPX47	Paragonitic Illite	1	NULL	NULL	455.45
DPX51	Paragonitic Illite	1	NULL	NULL	491.26
DPX52	Paragonitic Illite	1	NULL	NULL	741.89
DPX6	Paragonitic Illite	0.529	Montmorillonite	0.471	204.01
DPX61	Montmorillonite	0.535	Paragonitic Illite	0.465	358.52
DPX62	Paragonitic Illite	0.599	Montmorillonite	0.401	205.38
DPX66	Muscovite	1	NULL	NULL	210.97
DPX67	Paragonitic Illite	0.641	Montmorillonite	0.359	128.35
DPX79.	Muscovite	1	NULL	NULL	178.86
DPX87	Paragonite	1	NULL	NULL	415.17
JD2A	Muscovitic Illite	1	NULL	NULL	65.242
JD4A	Paragonite	Ill		1	NULL
JD6A	Paragonitic Illite	1	NULL	NULL	491.5

Appendix 5 X Ray Diffraction (XRD) Analysis

5.1	Whole Rock Powder Sample Diffractograms	332
5.2	Clay Concentrate Sample Diffractograms	358
5.3	Clay Fraction XRD Analysis of Clays from the Alteration Halo of the Phoenix Deposit.	380

Appendix 5.1 – Whole Rock XRD Samples

Sample Locations

Sample (DPX)	Drillhole Collar Number	Location	Lithology
DPX001	408	457	Basement
DPX004	383	454	Basement
DPX005	383	453	Basement
DPX006	376	452	Basement
DPX008	376	451	Basement
DPX014	376	446.75	Basement
DPX016	332	446	Basement
DPX021	332	442	Basement
DPX022	332	441	Basement
DPX023	332	440	Basement
DPX026	300	435	Basement
DPX030	282	429	Basement
DPX031	282	429	Basement
DPX033	282	429	Basement
DPX038	282	424	Basement
DPX039	282	421.3	Basement
DPX041	282	421	Basement
DPX043	282	418	Basement
DPX044	282	418	Basement
DPX046	282	416	Basement
DPX047	282	416	Basement
DPX048	282	416	Basement
DPX049	282	415	Basement
DPX052	282	415	Basement
DPX053	349	415	Basement
DPX054	349	413	Basement
DPX055	349	412	Basement
DPX060	358	404	Basement
DPX062	358	403	Basement
DPX064	358	403	Basement
DPX065a	256	403	Basement
DPX065b	256	403	Basement
DPX067	408|	401	Basement
DPX068	329	401	Basement
DPX069	329	400.05	Basement
DPX071	329	373	Basement
DPX072	329	414	Basement
DPX073	329	418	Basement

Sample (DPX)	Drillhole Collar Number	Location	Lithology
DPX074	329	428.5	Basement
DPX075	301	322.5	MfX
DPX077	301	344.05	MfX
DPX079	256	303.45	MfX
DPX080	293	301.4	MfX
DPX081	293	300.9	MfX
DPX082	293	288.06	MfX
DPX083	293	418.4	Basement
DPX084	358	371	MfX
DPX085	387	253	MfX
DPX086	257	250.5	MfX
DPX087	257	474	MfX
DPX089	278	424.5	MfX
DPX181V	286	57	MfX
DPX189	286	125.5	MfX
DPX194	286	188.5	MfX
DPX198	286	22.6	MfX
DPX199	286	257.9	MfX
DPX201	286	283.5	MfX
JD1A	267	498.52	Basement
JD2A	273	492.53	Basement
JD4A	273	436.41	Basement
WS Shear Samples			
256a	256	190.7	MfX
256b	256	224.1	MfX
281-a	281	410.8	Basement
281-b	281	412.7	Basement
281c	281	417.4	Basement
282-a	282	398.9	Basement
282-b	282	399.9	Basement
293-b	293	251	MfX
301-a	301	315	MfX
301-b	301	316	MfX
315-a	315	312.8	MfX
315-b	315	316	MfX
352a	352	316.2	MfX
404	404	323.3	MfX
409a	409	317.7	MfX

Methods

Samples were ground into a fine powder via hand pulverisation and a ball mill, with final fine grinding of samples prior to XRD analysis; All samples were analysed on a Philips PW 3020 X'Pert Diffractometer at the University of Ottawa's X-Ray Core Facility. Measurements were acquired at 45-kV accelerating voltage, 40-mA current, with exact measurement parameters varying per a sample.

DPX001

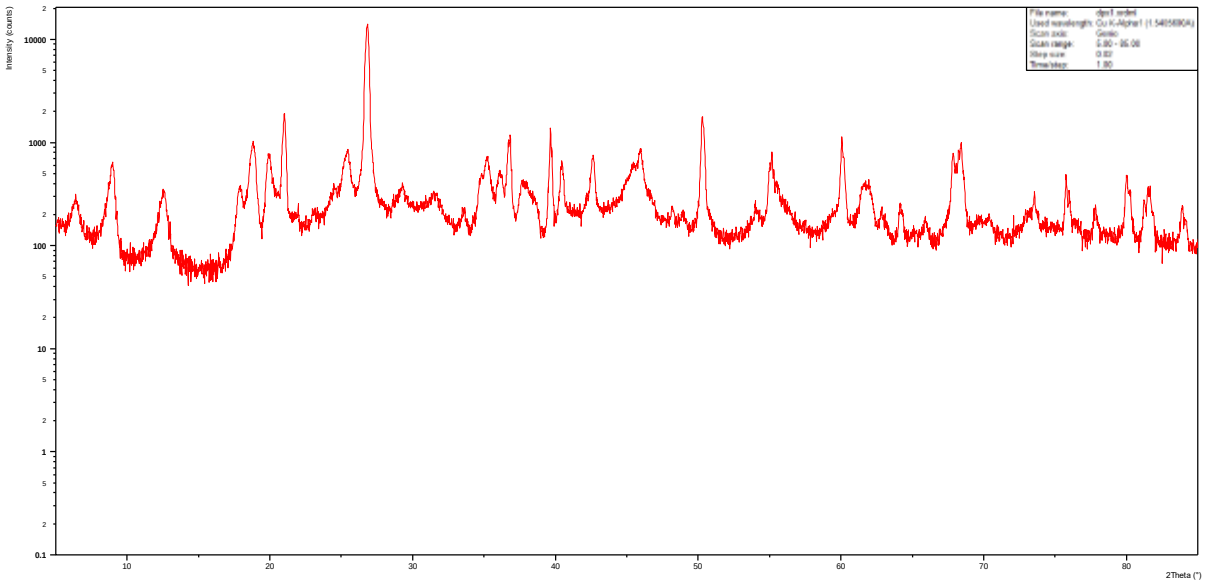

DPX004

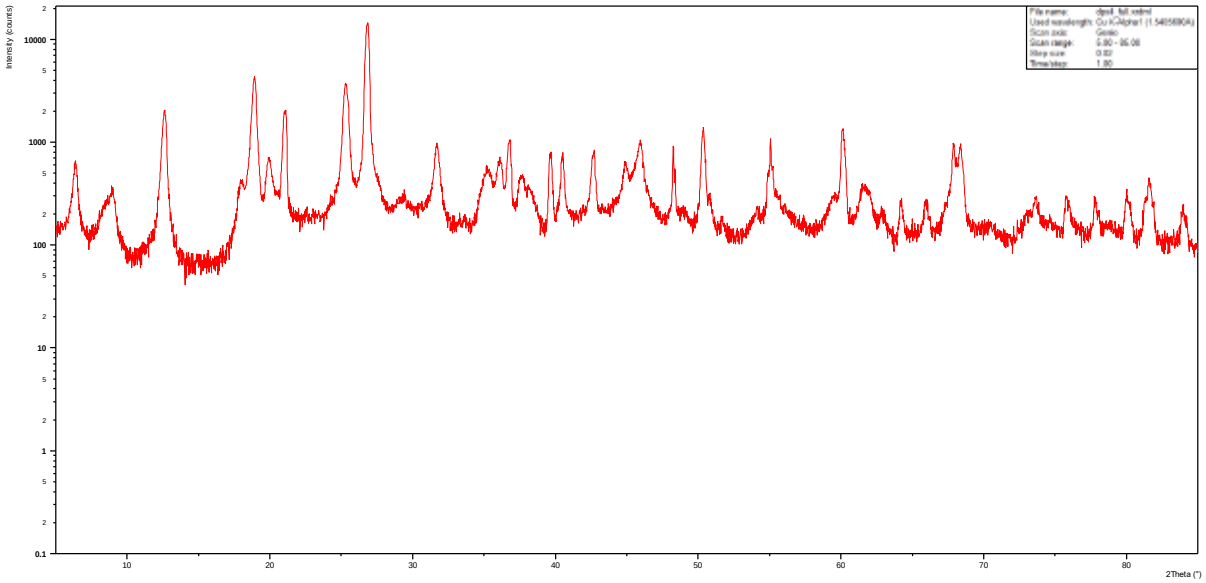

DPX005

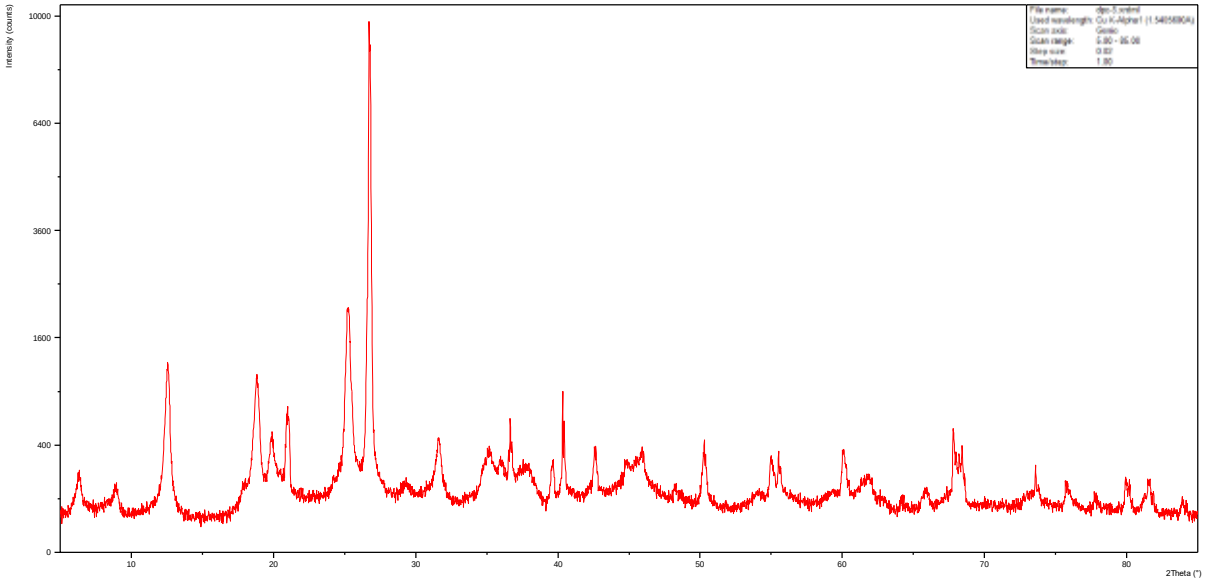

DPX006

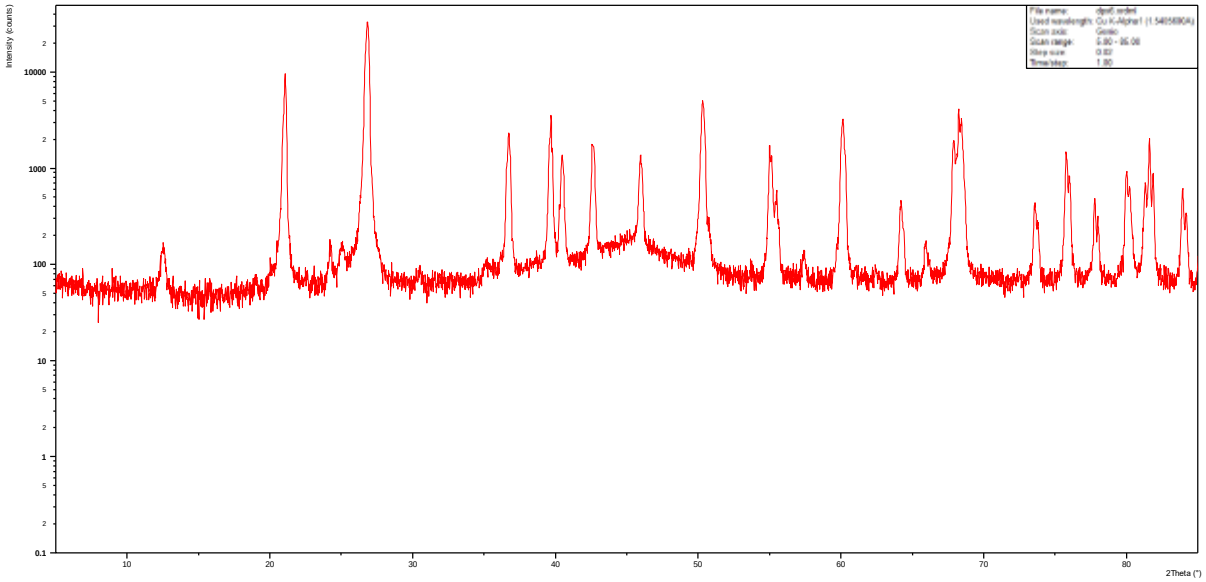

DPX008

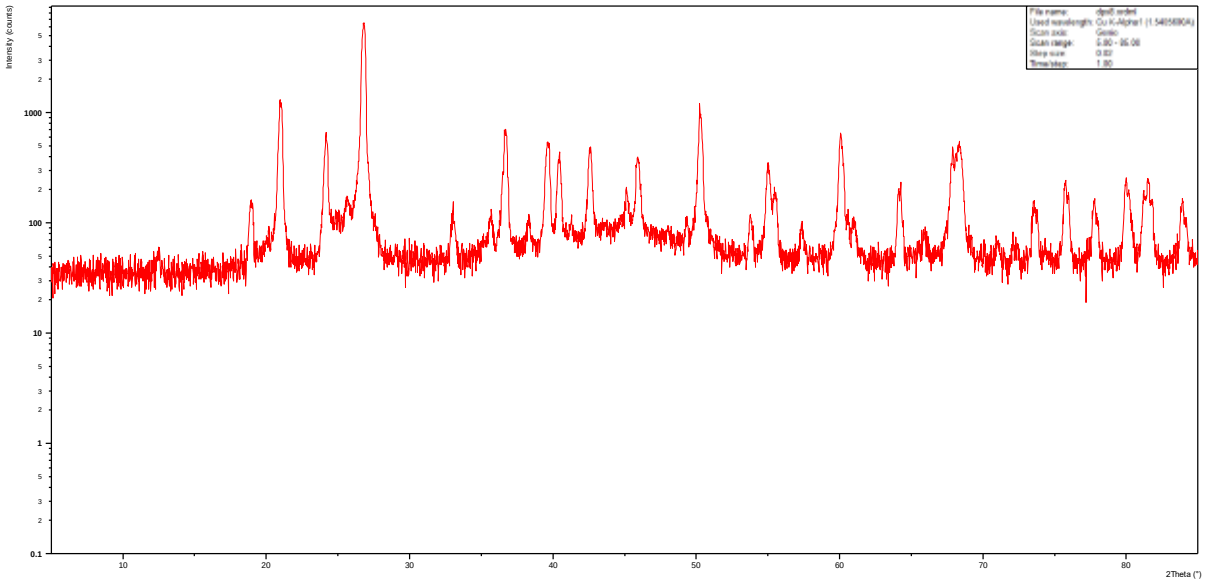

DPX014

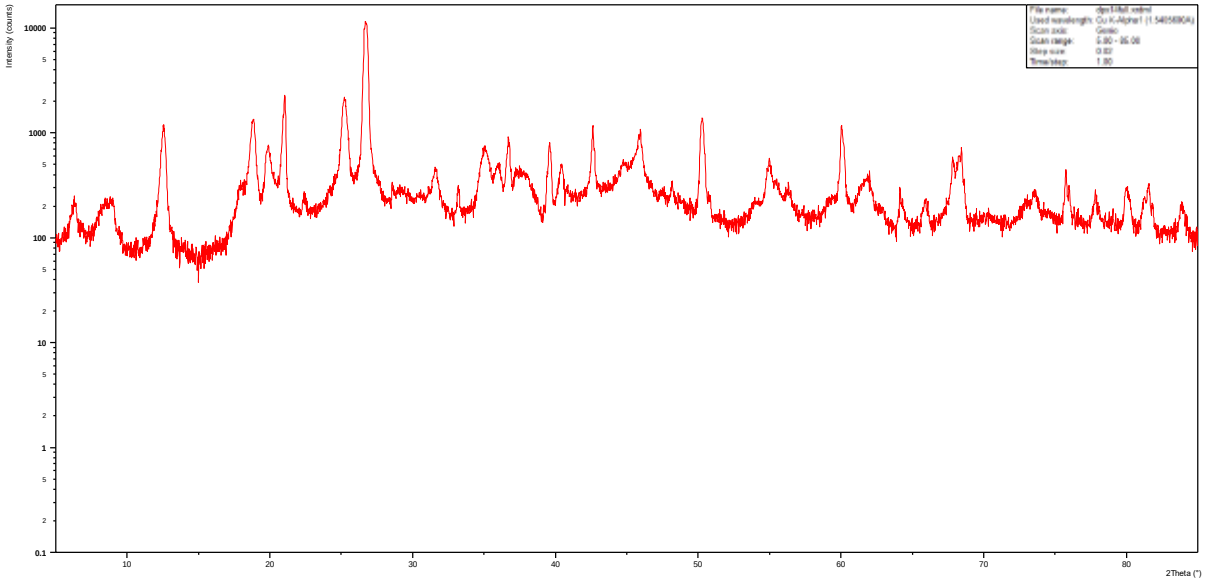

DPX016

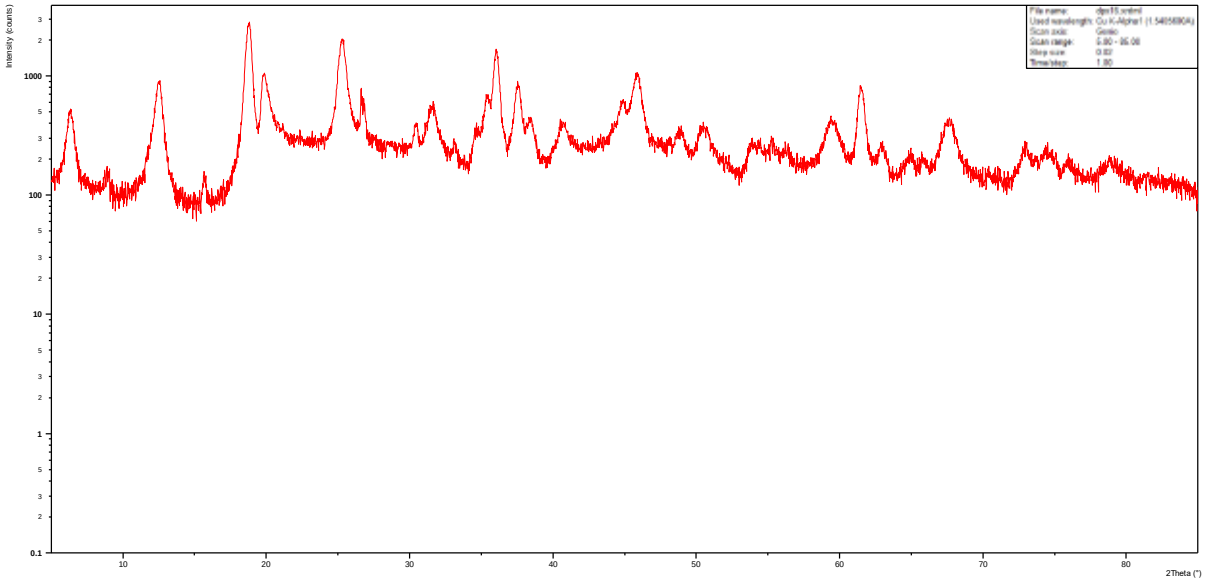

DPX021

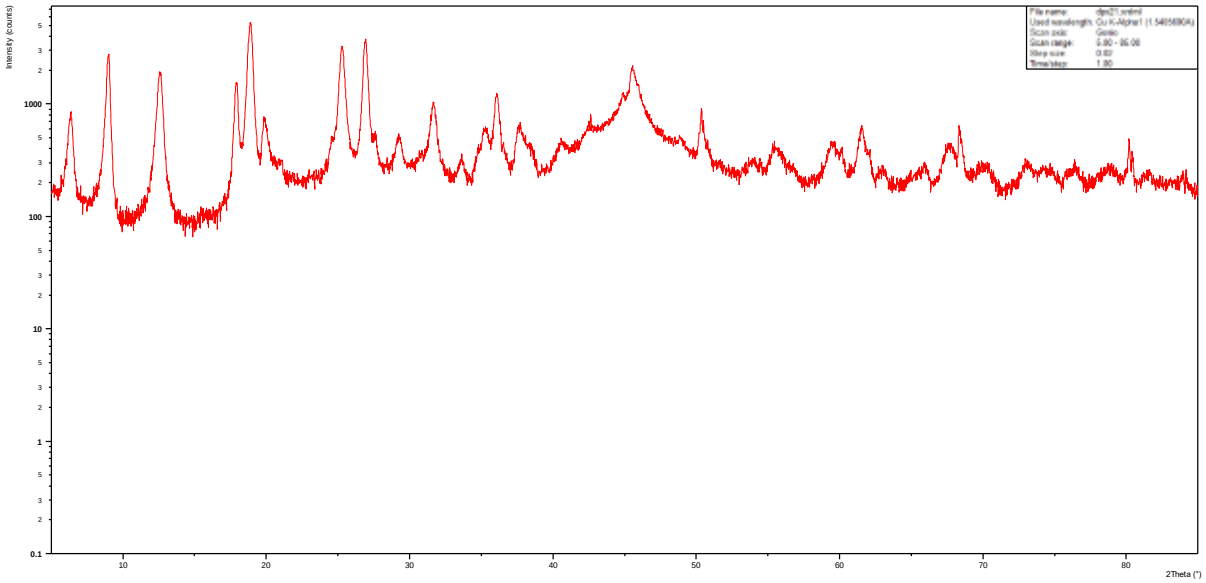

DPX022

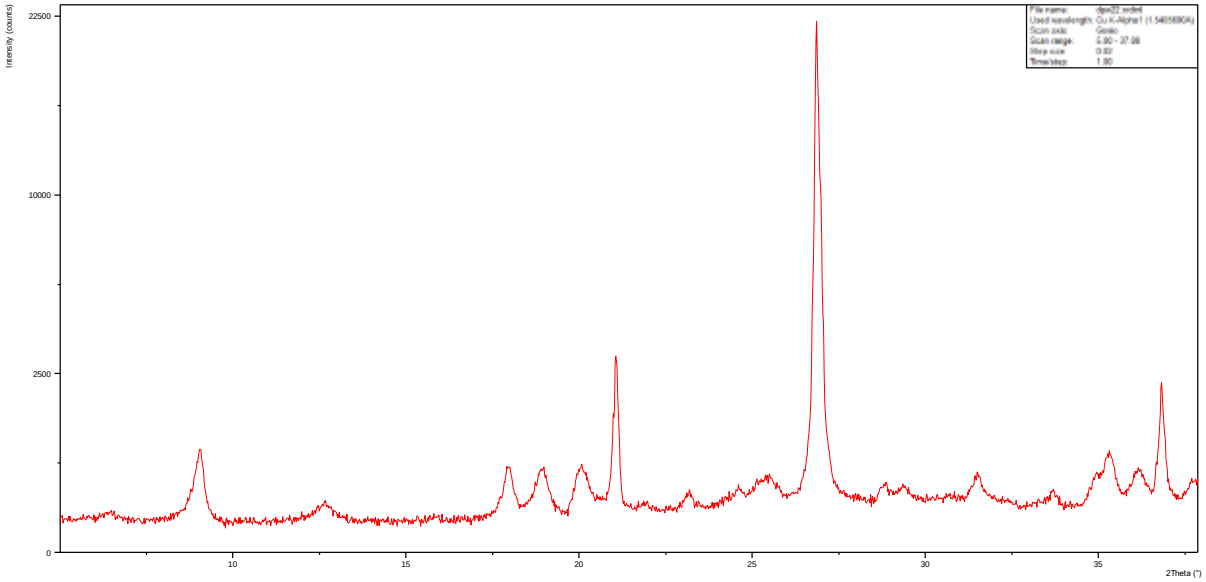

DPX023

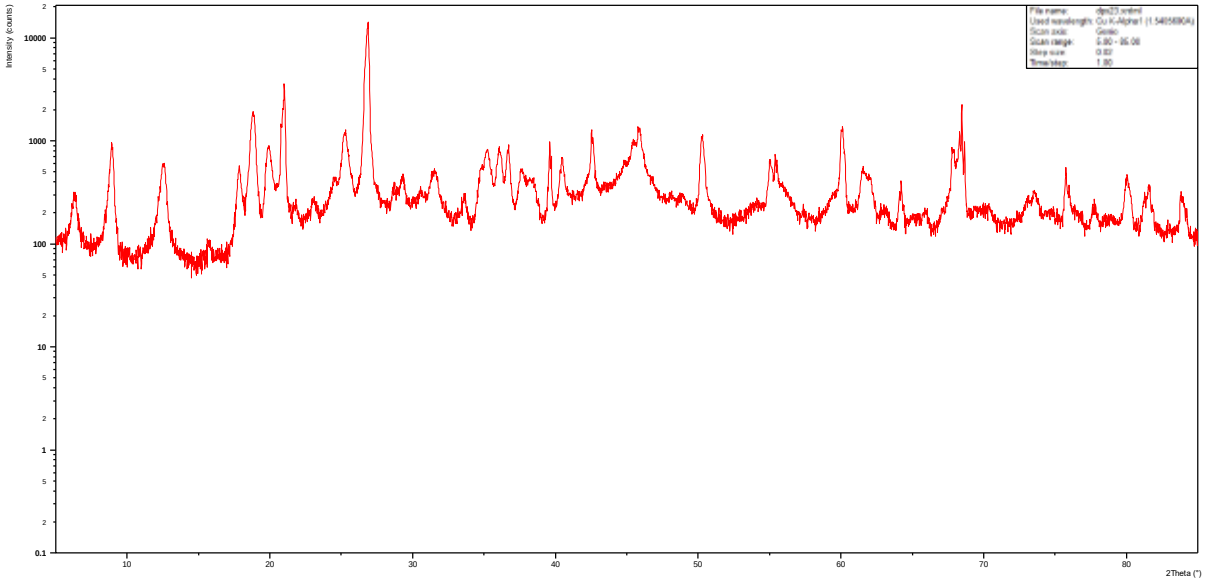

DPX026

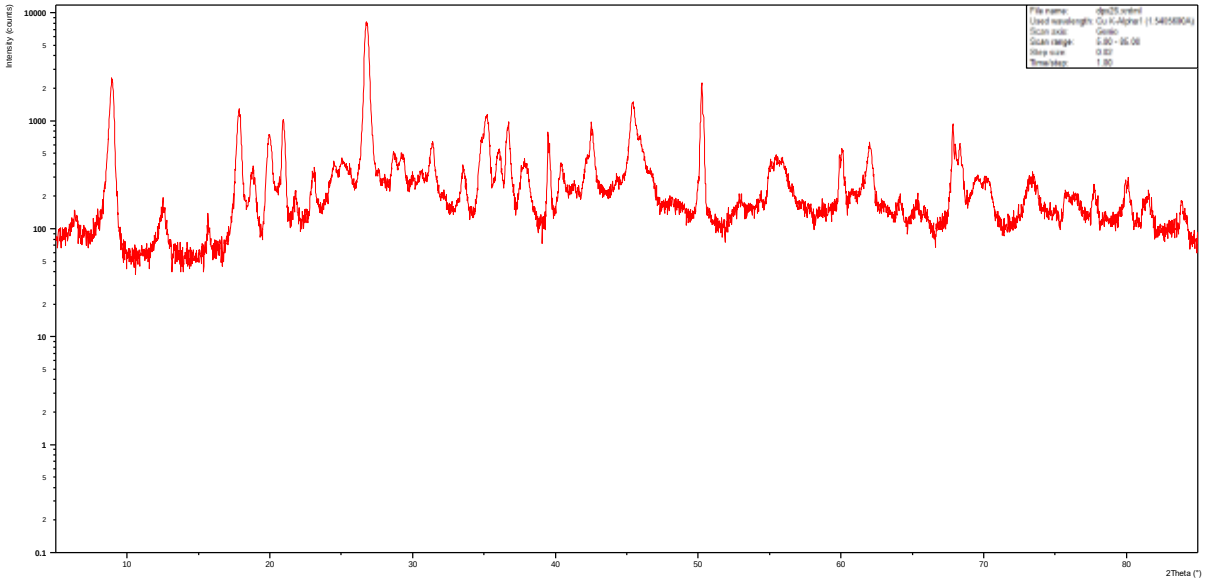

DPX030

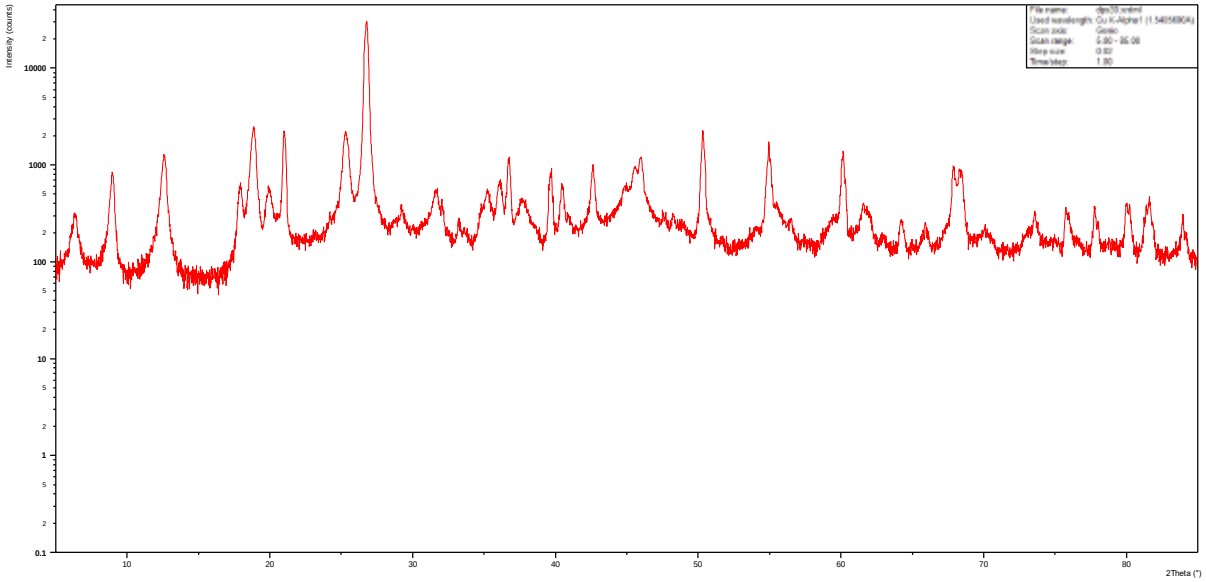

DPX031

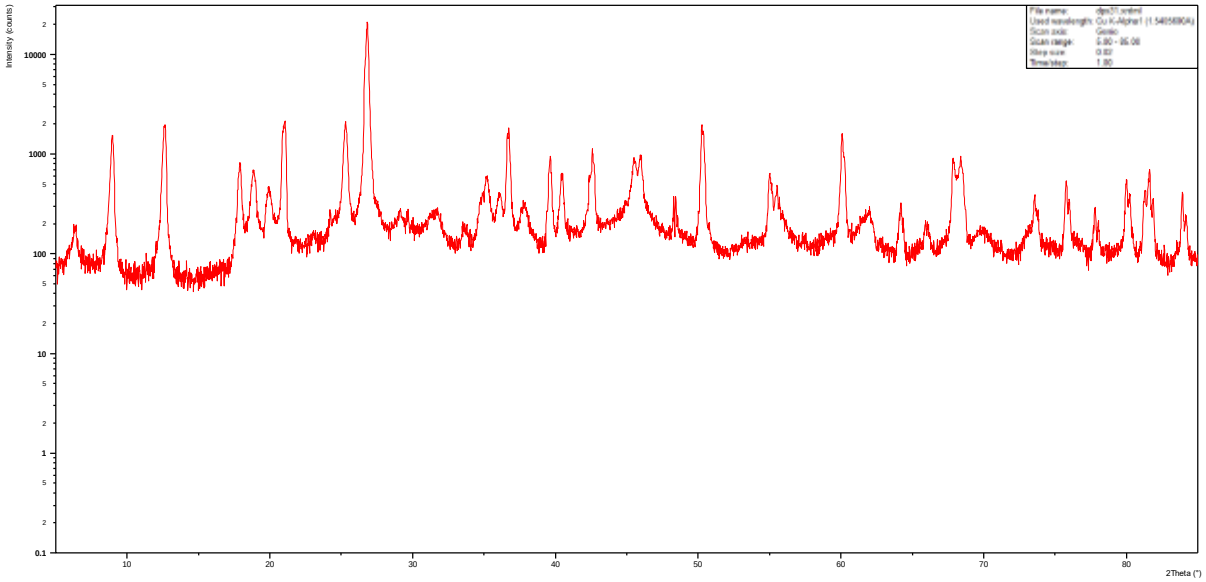

DPX033

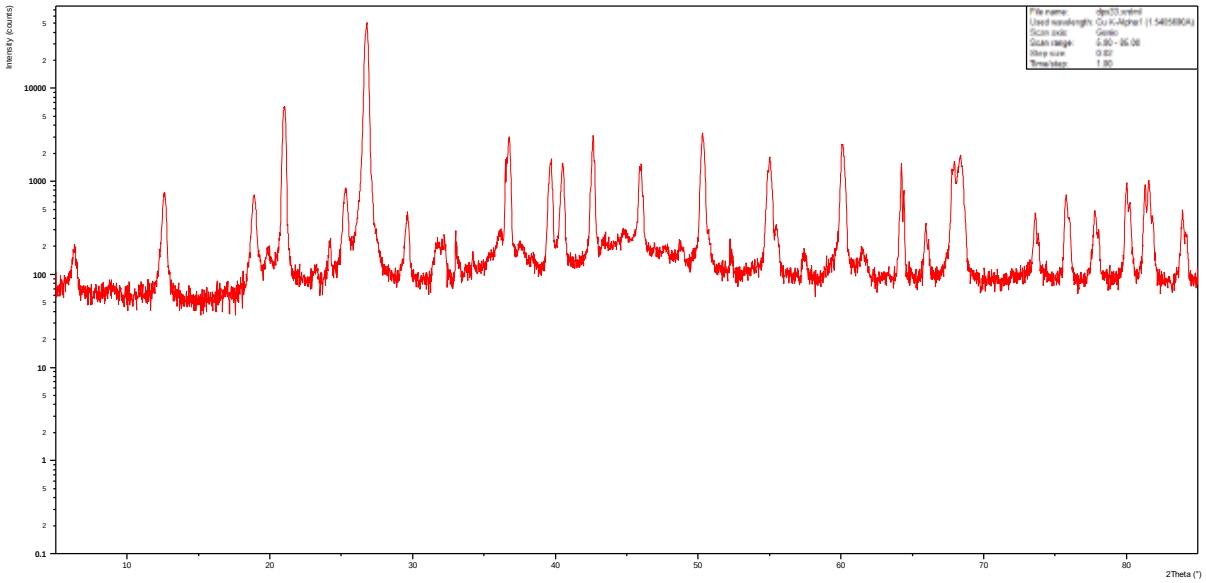

DPX038

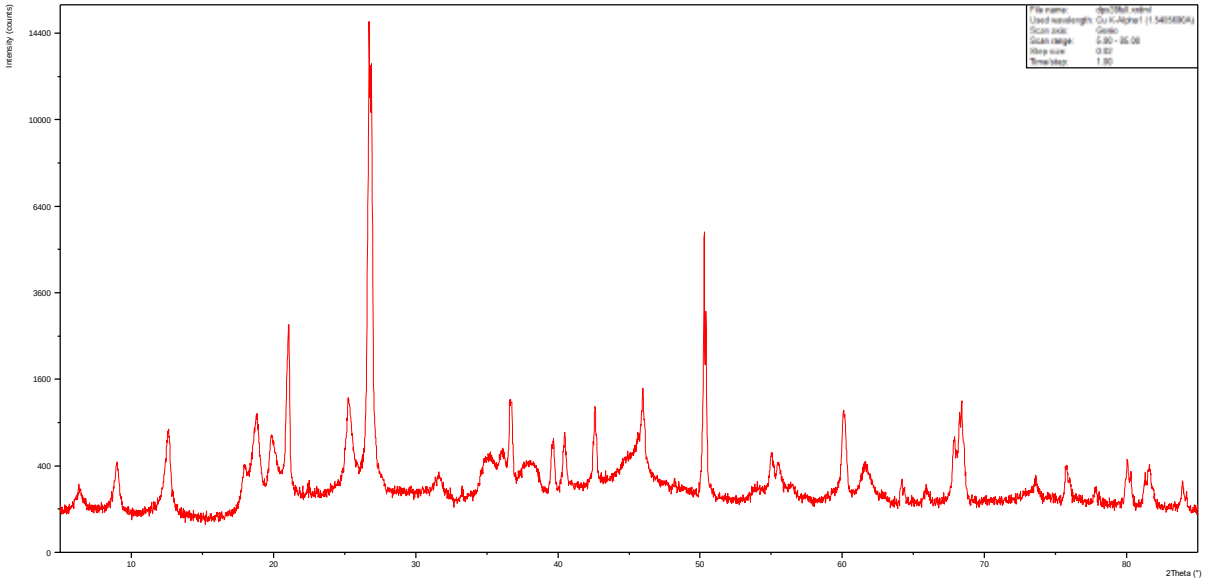

DPX039

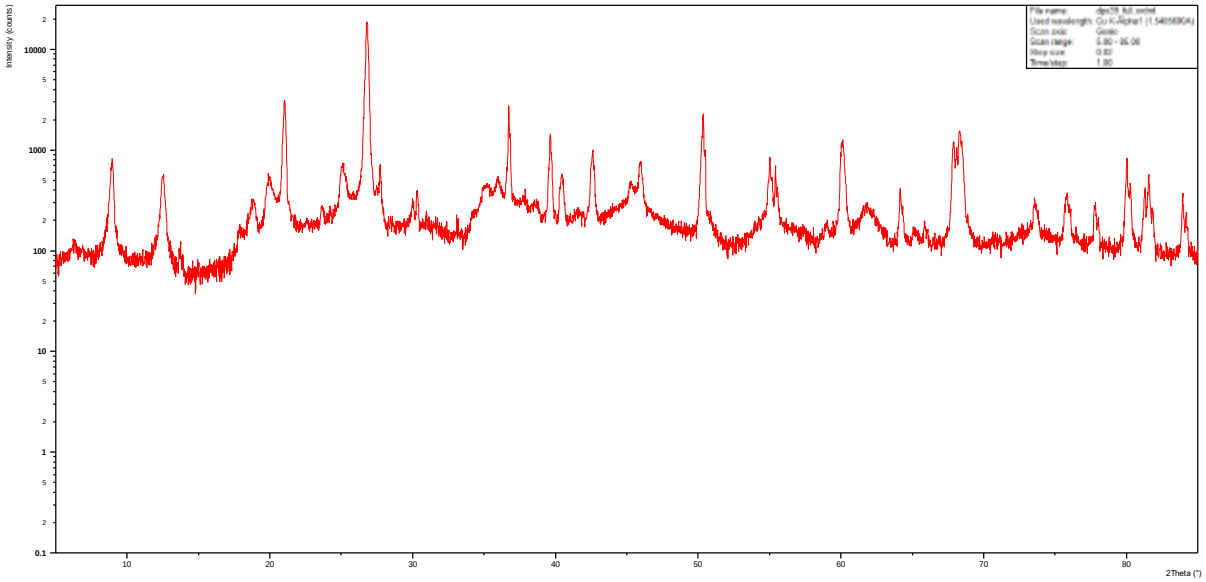

DPX041

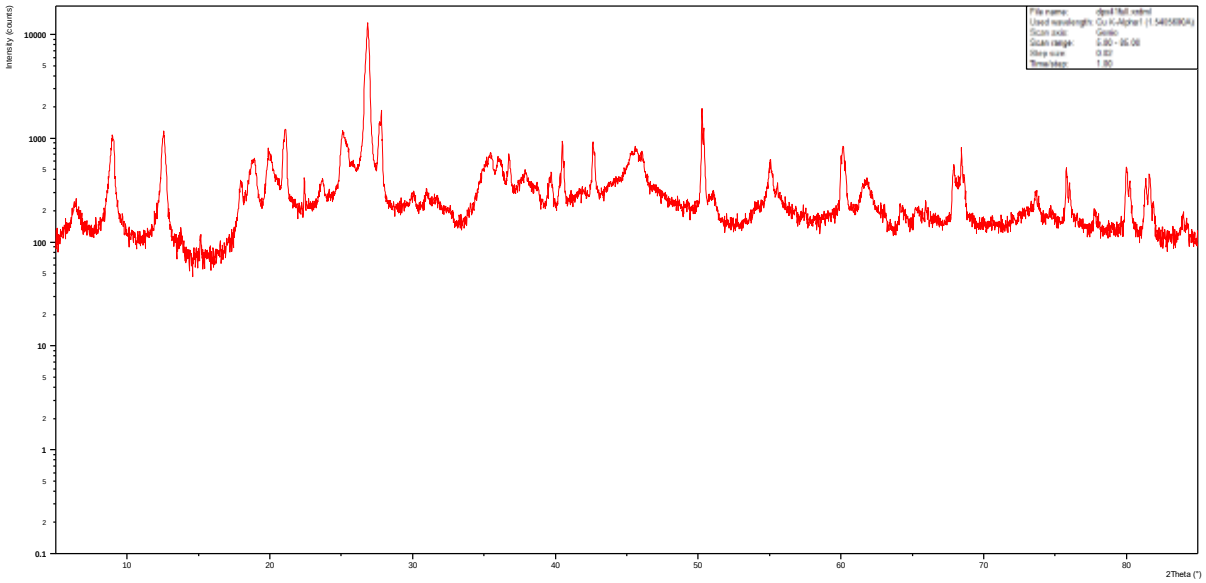

DPX043

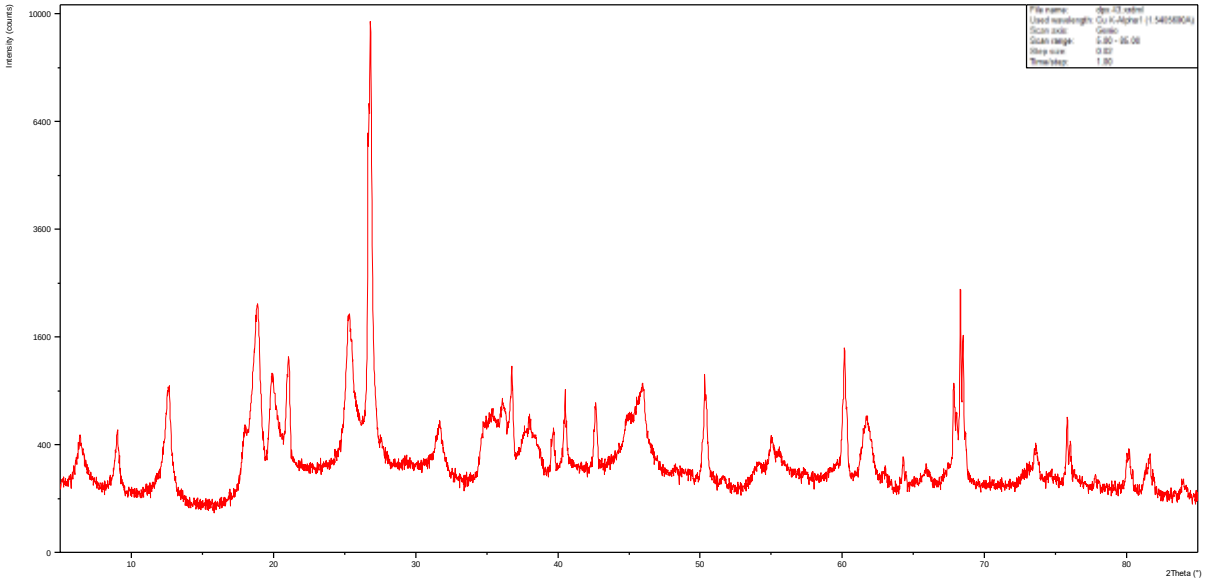

DPX044

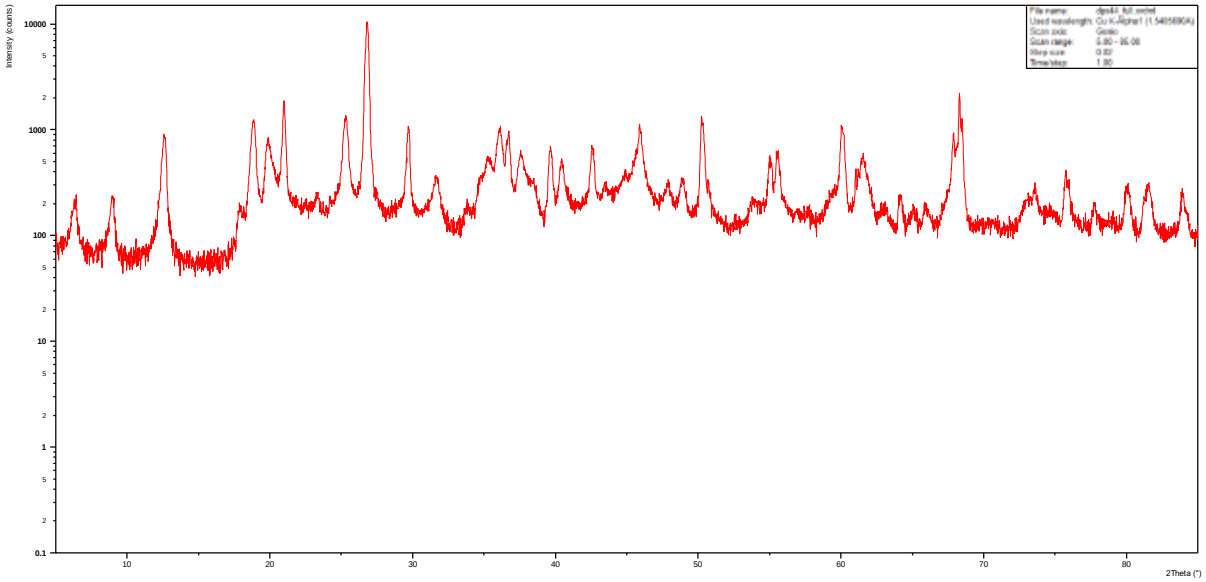

DPX046

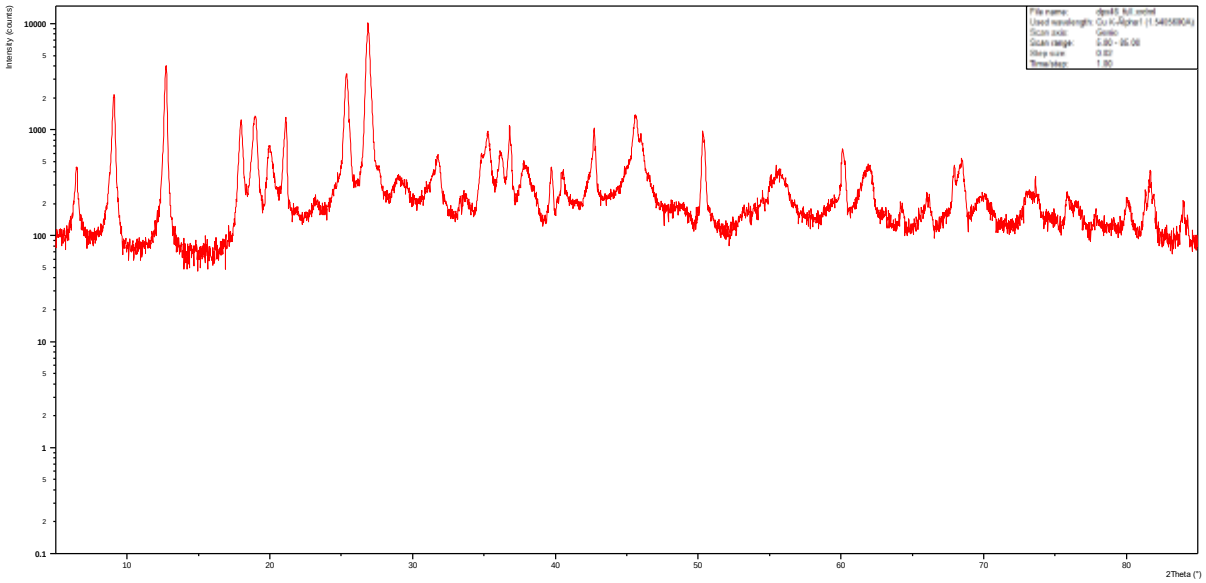

DPX047

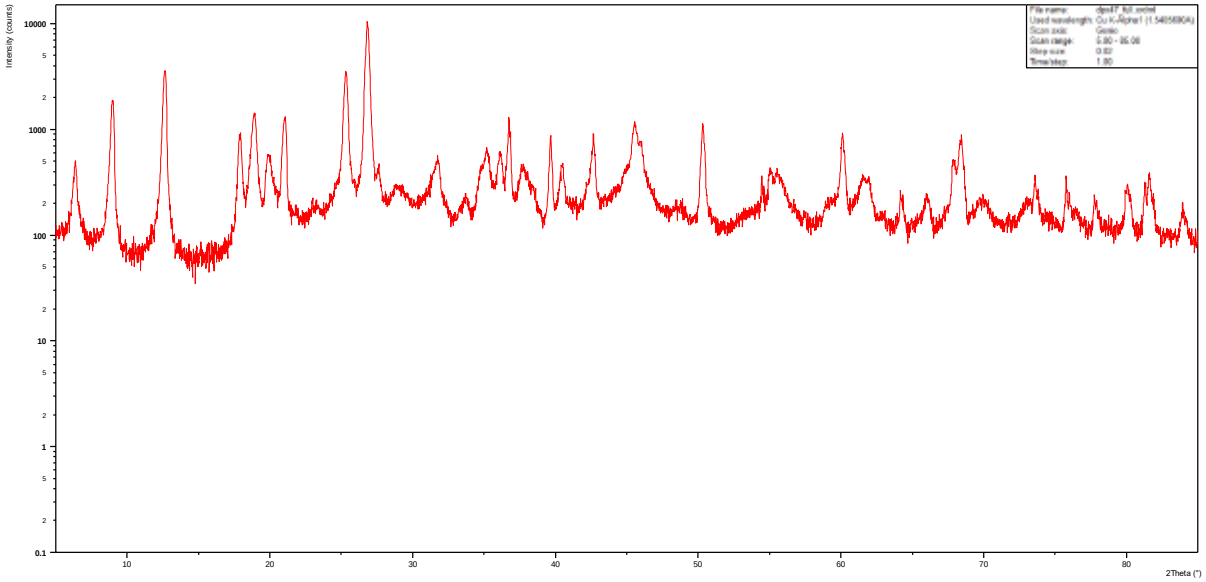

DPX048

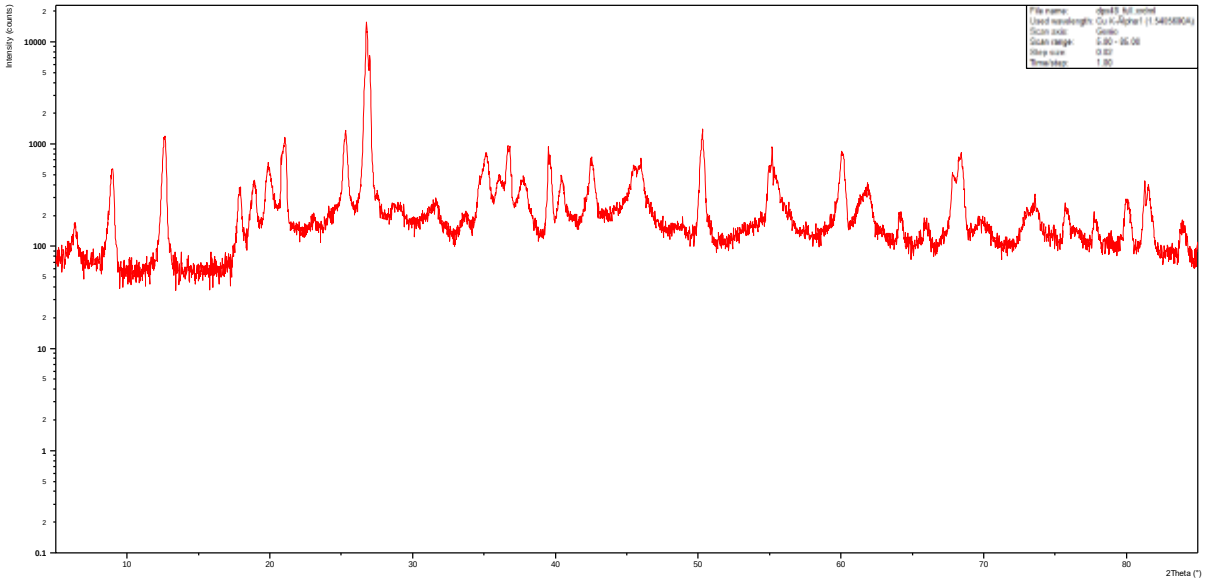

DPX049

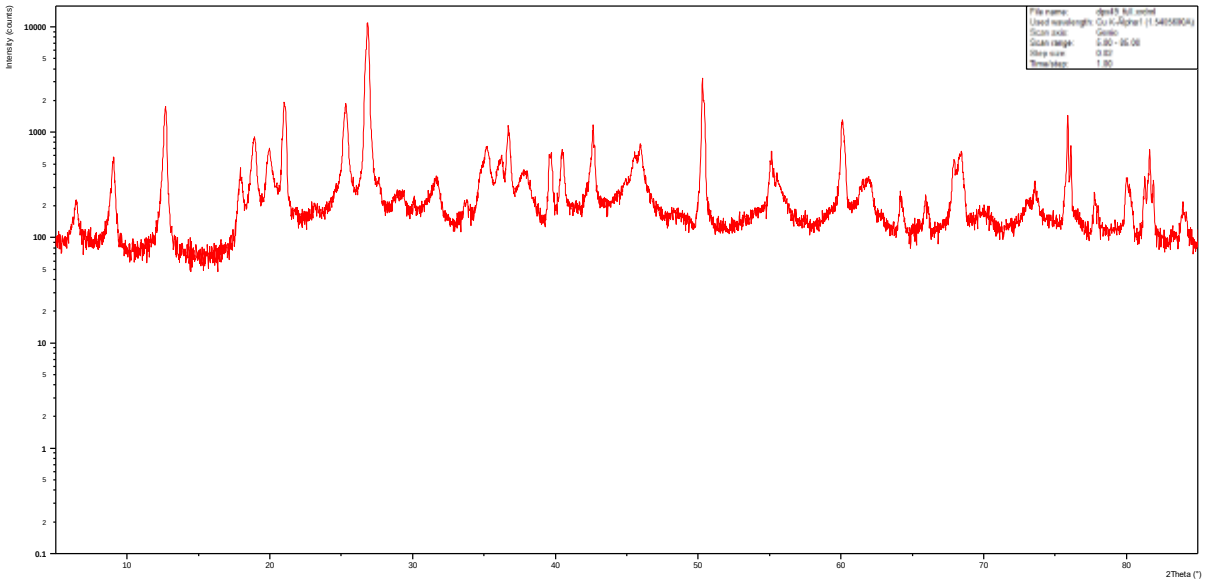

DPX052

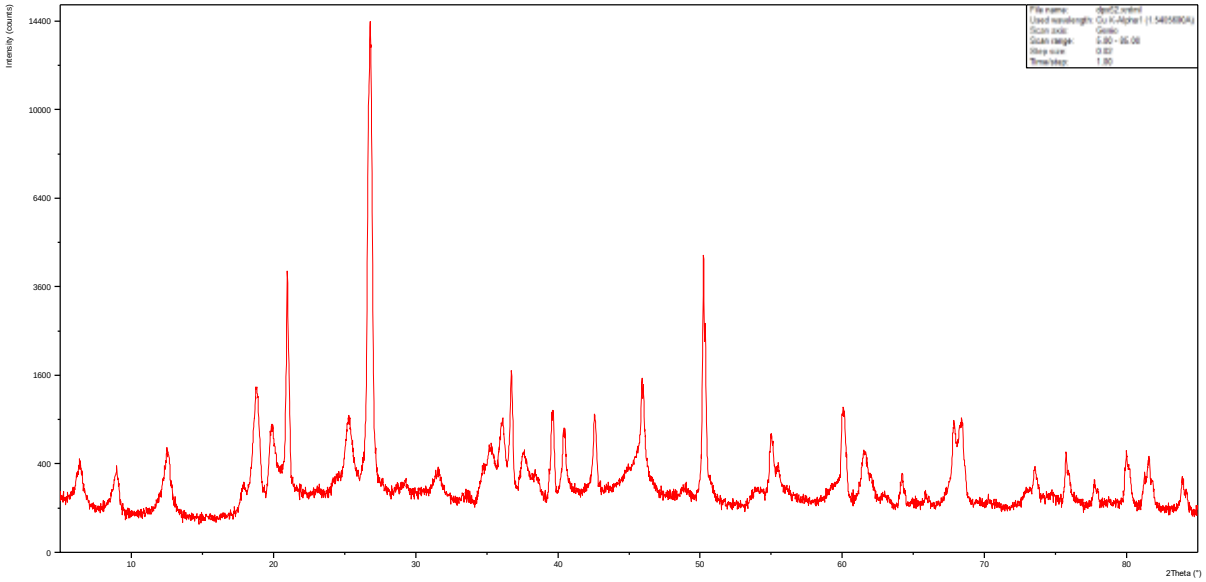

DPX053

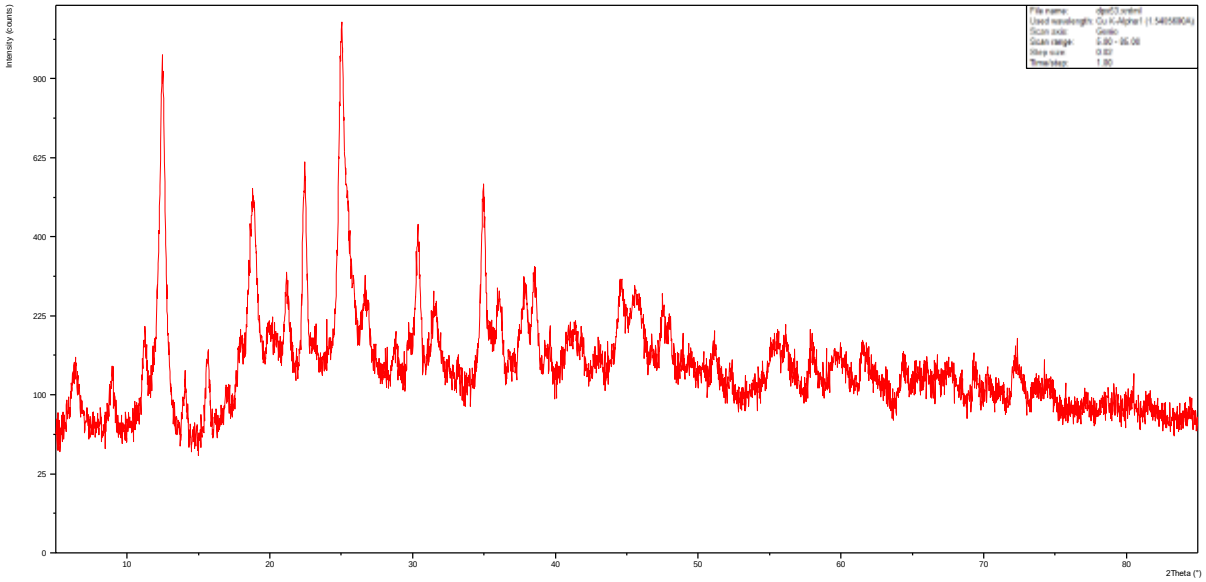

DPX054

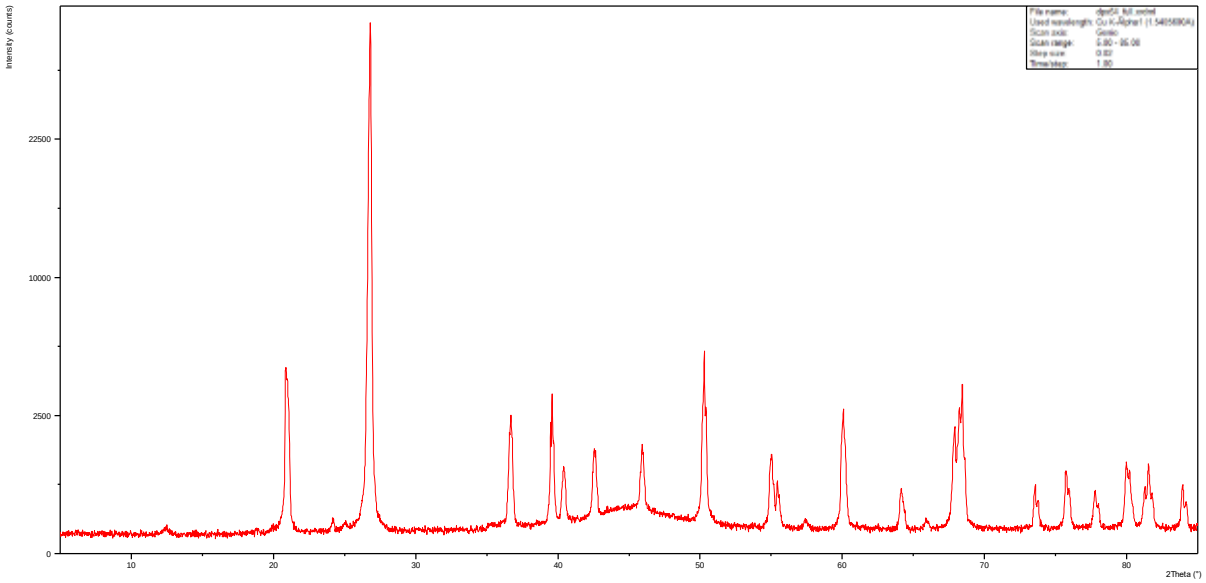

DPX055

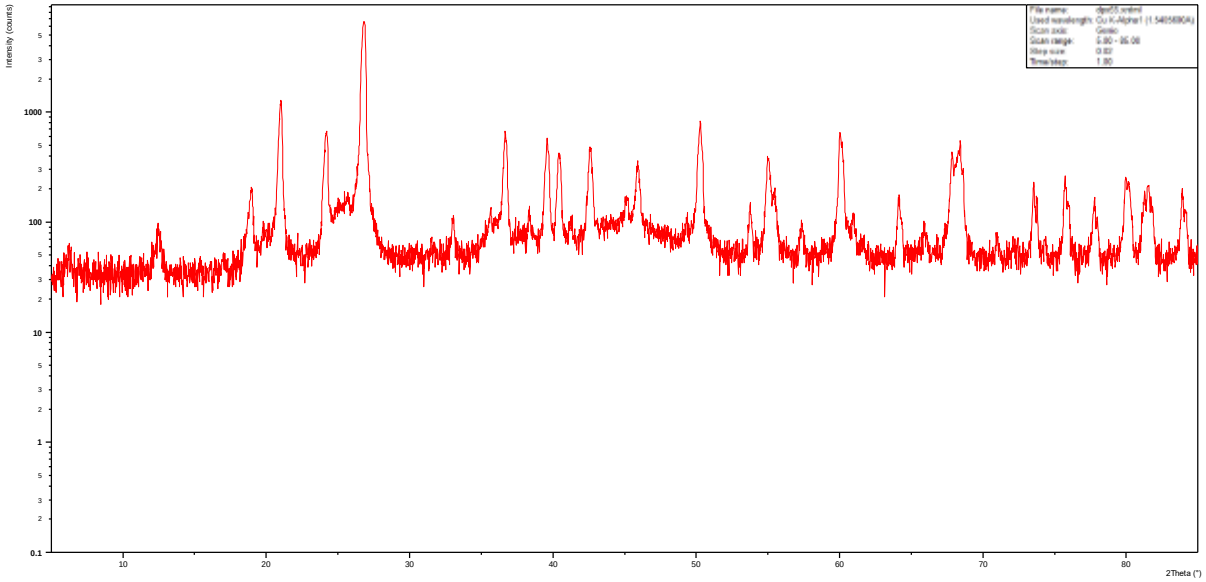

DPX060

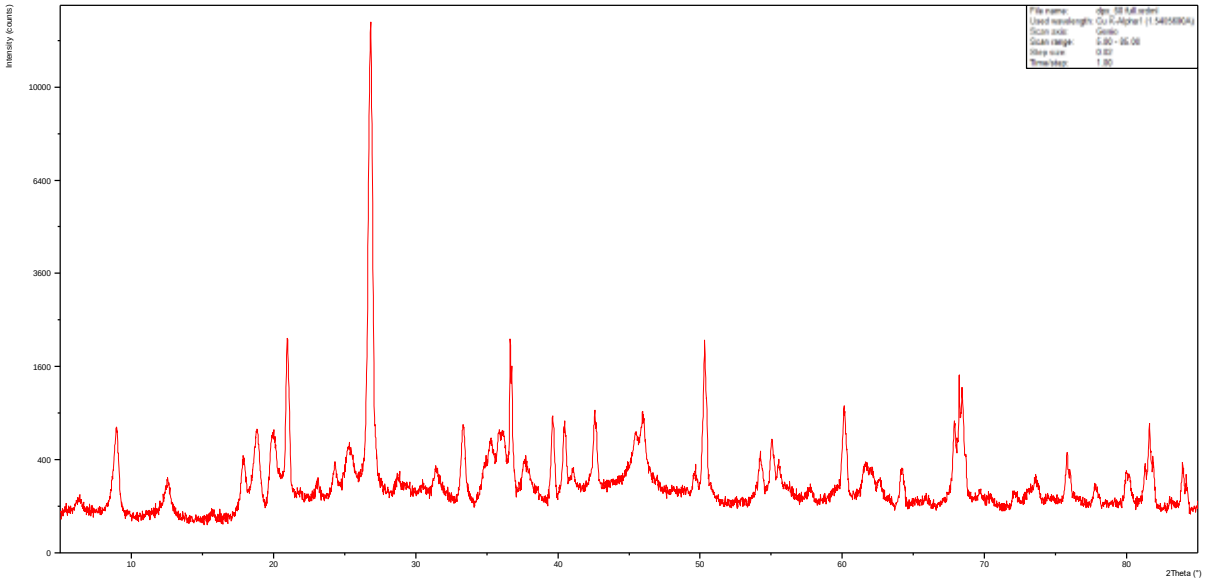

DPX062

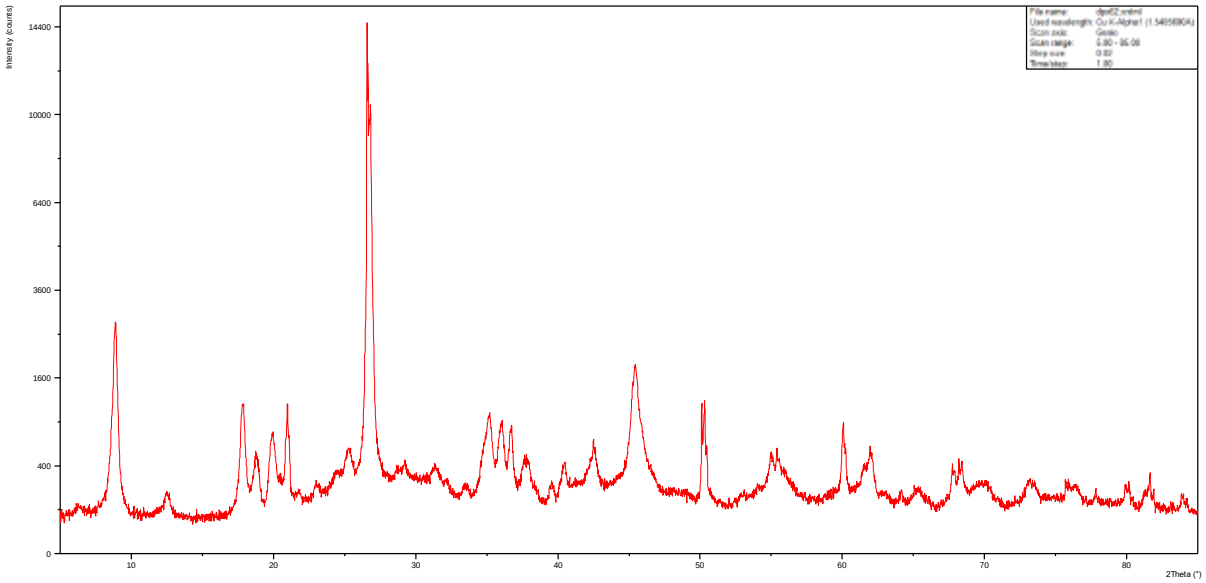

DPX064

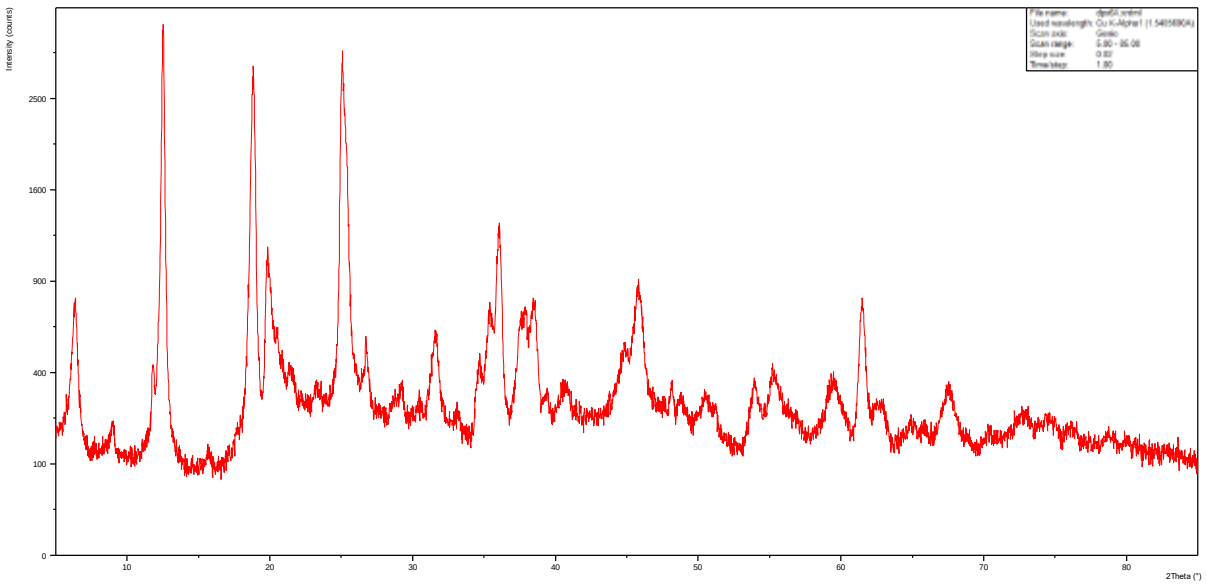

DPX065s (sandstone sample)

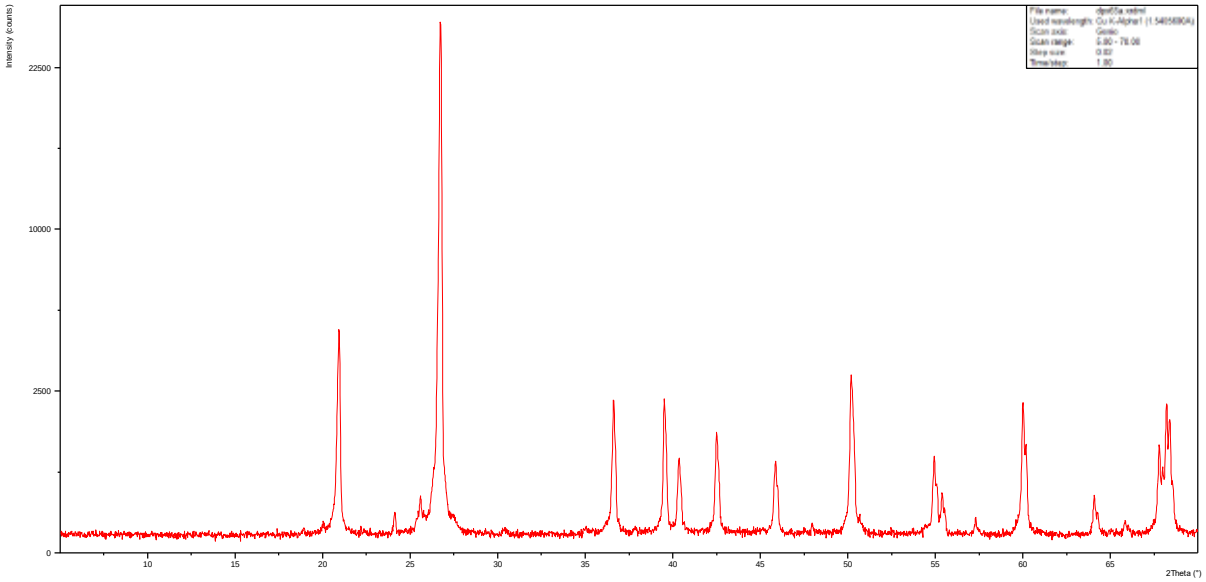

DPX65b (vein infill sample)

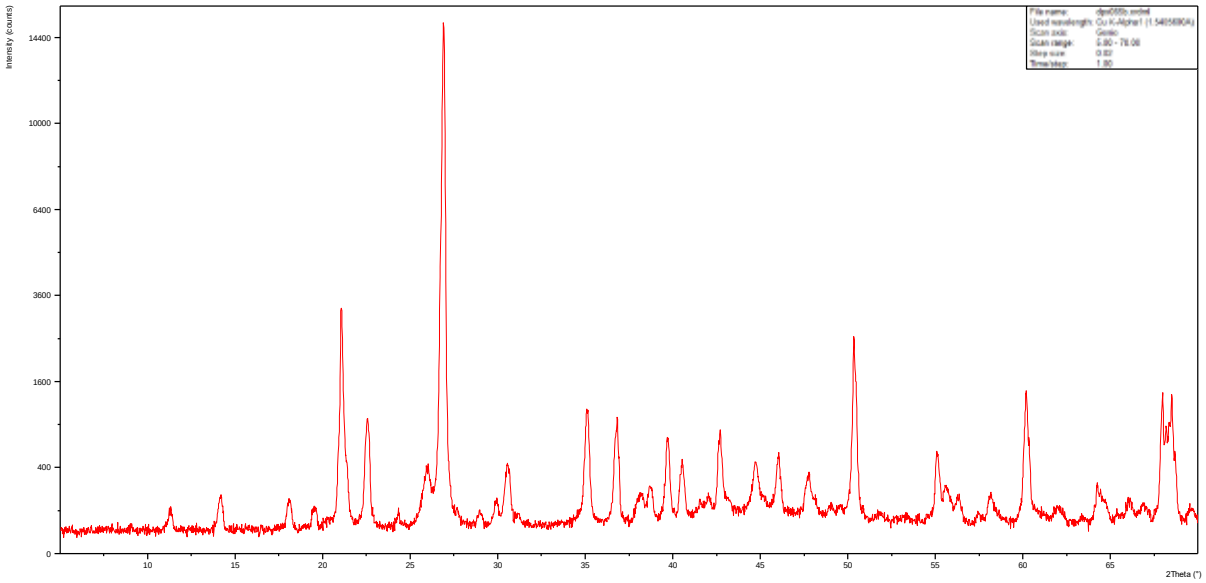

DPX067

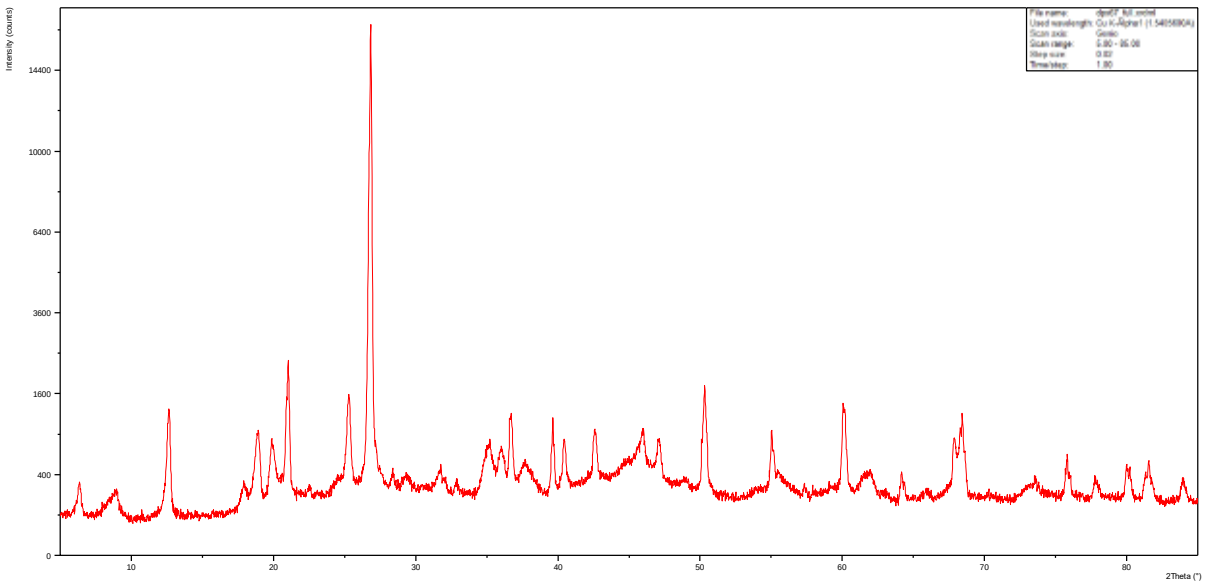

DPX068

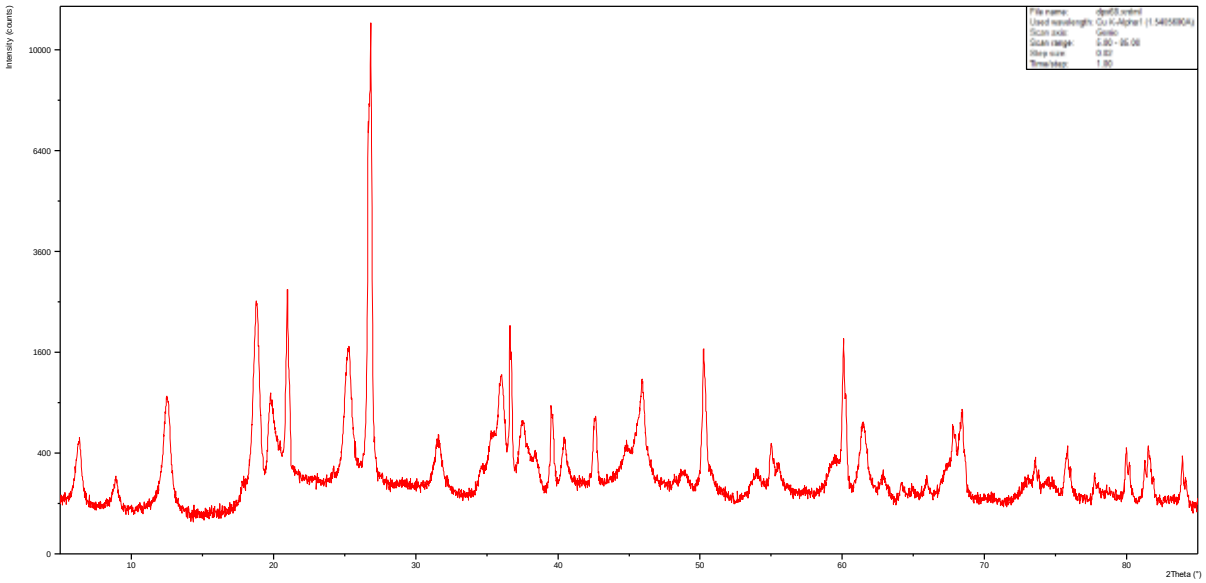

DPX069

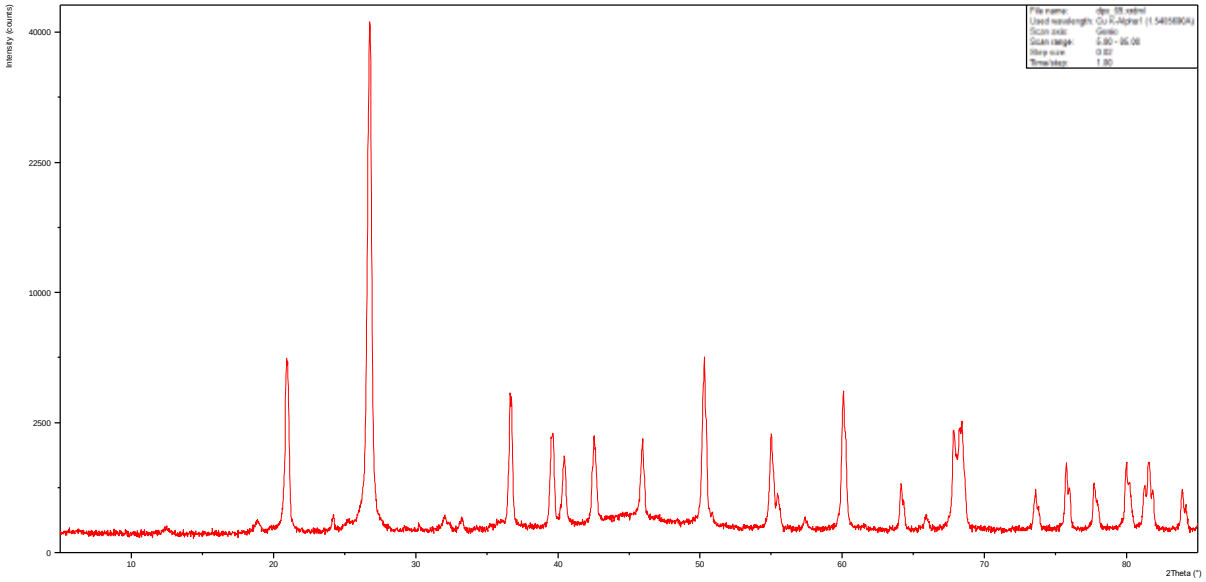

DPX071

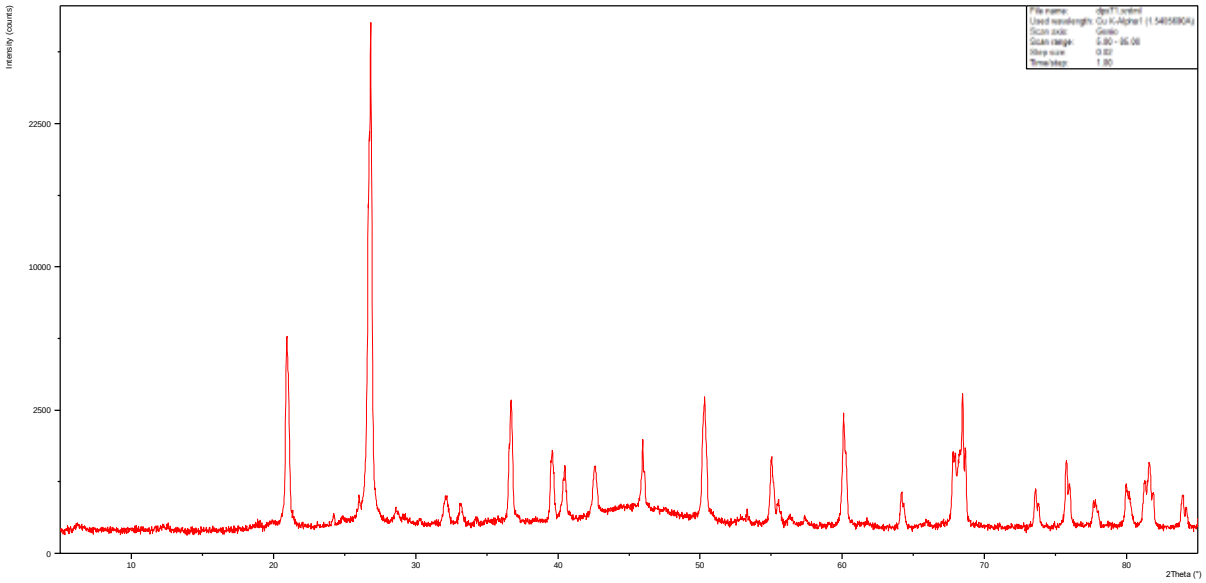

DPX072

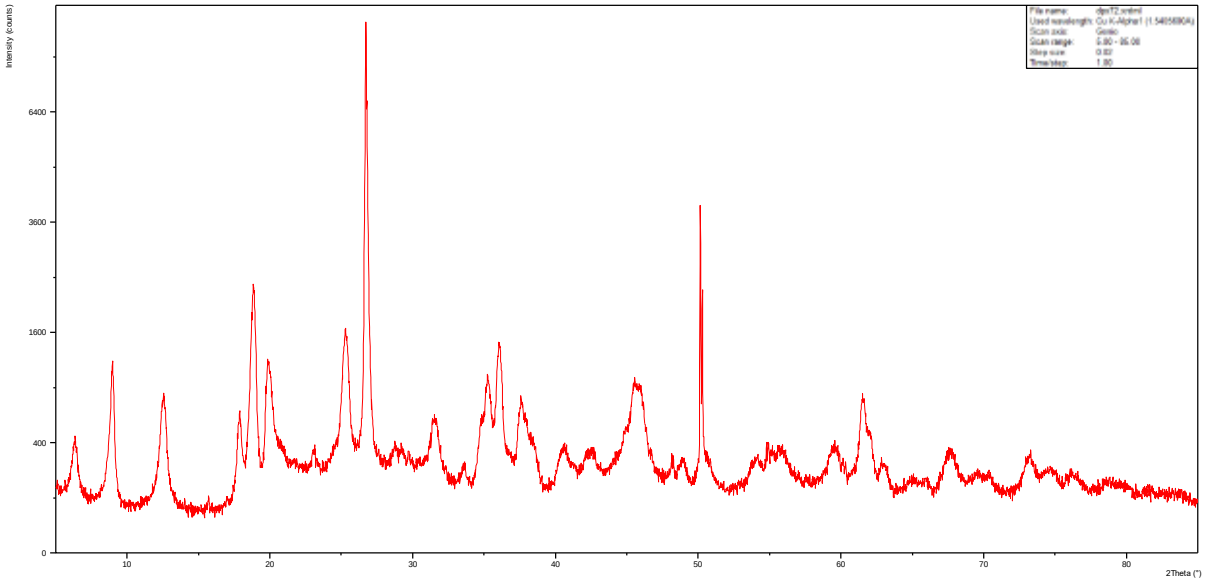

DPX073

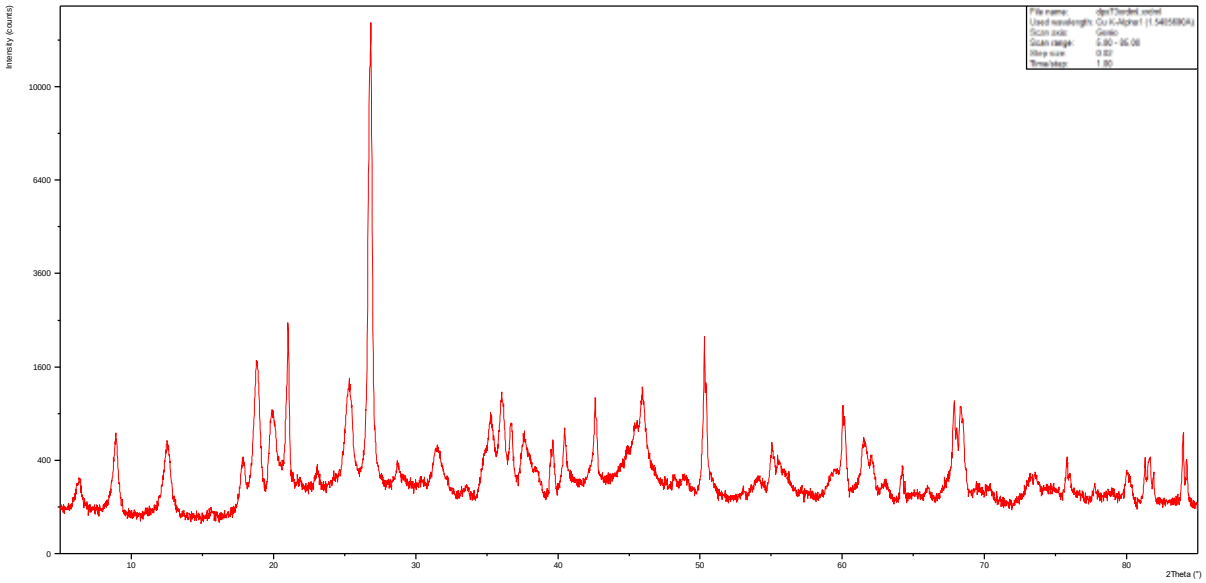

DPX074

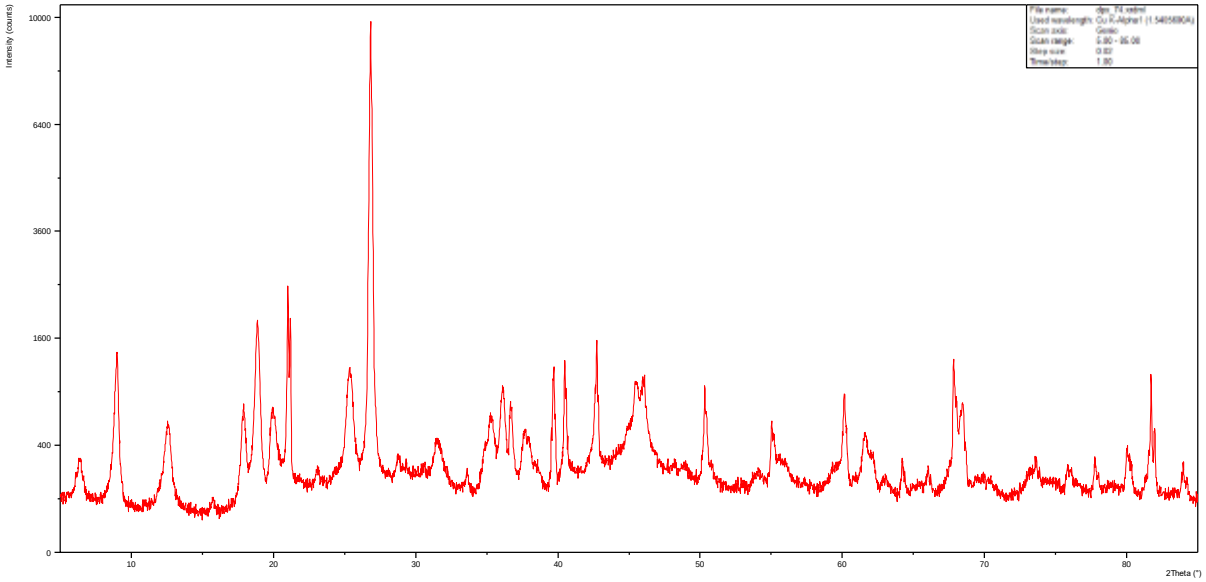

DPX075

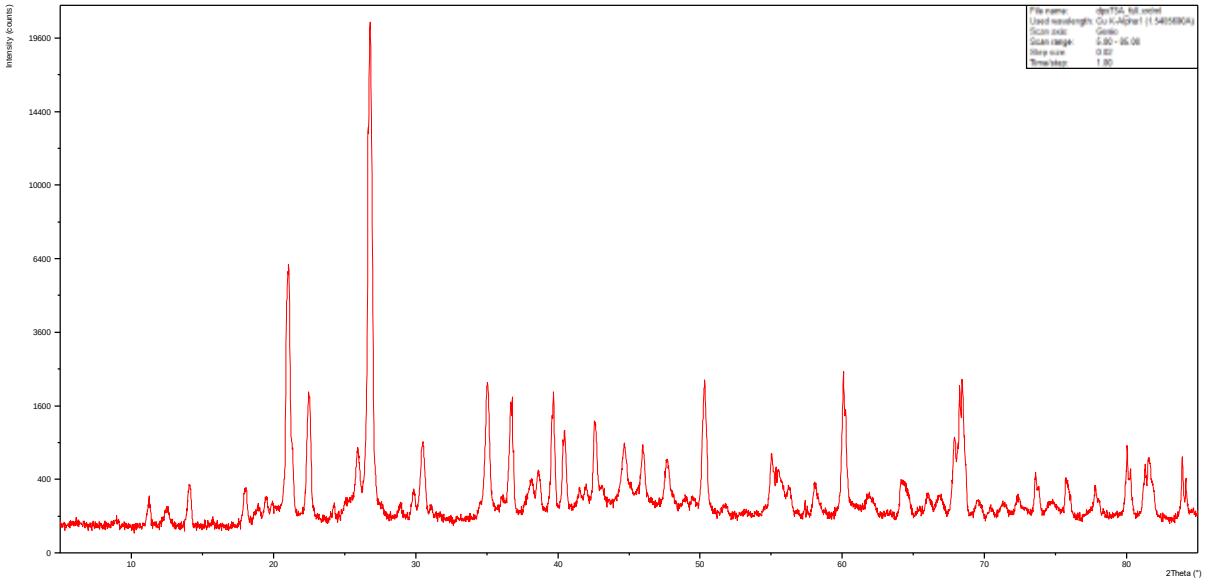

DPX077

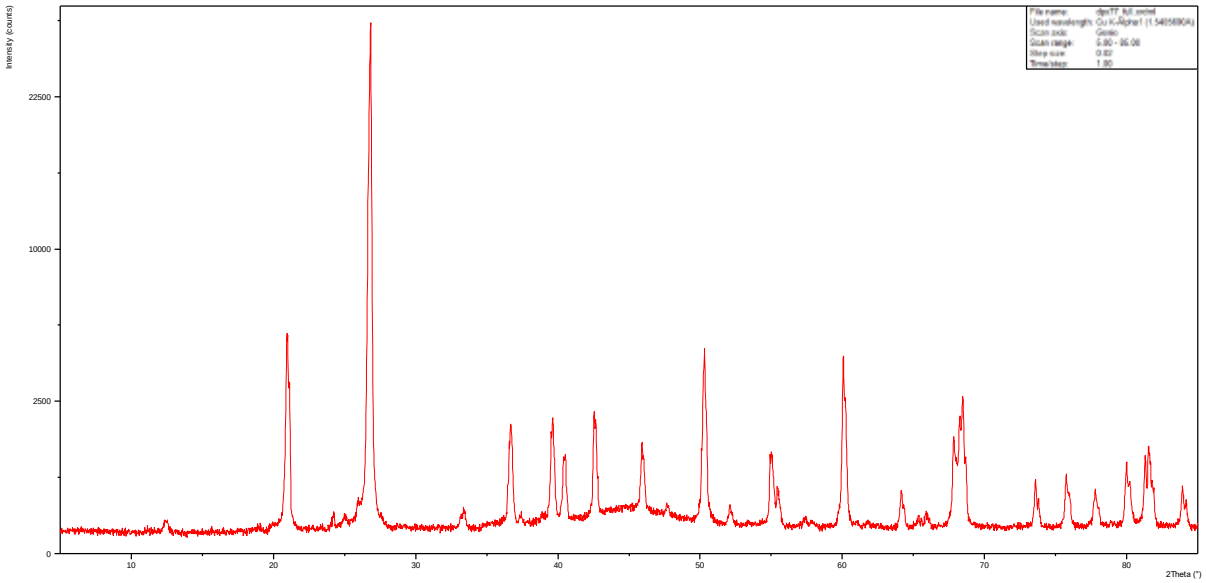

DPX079

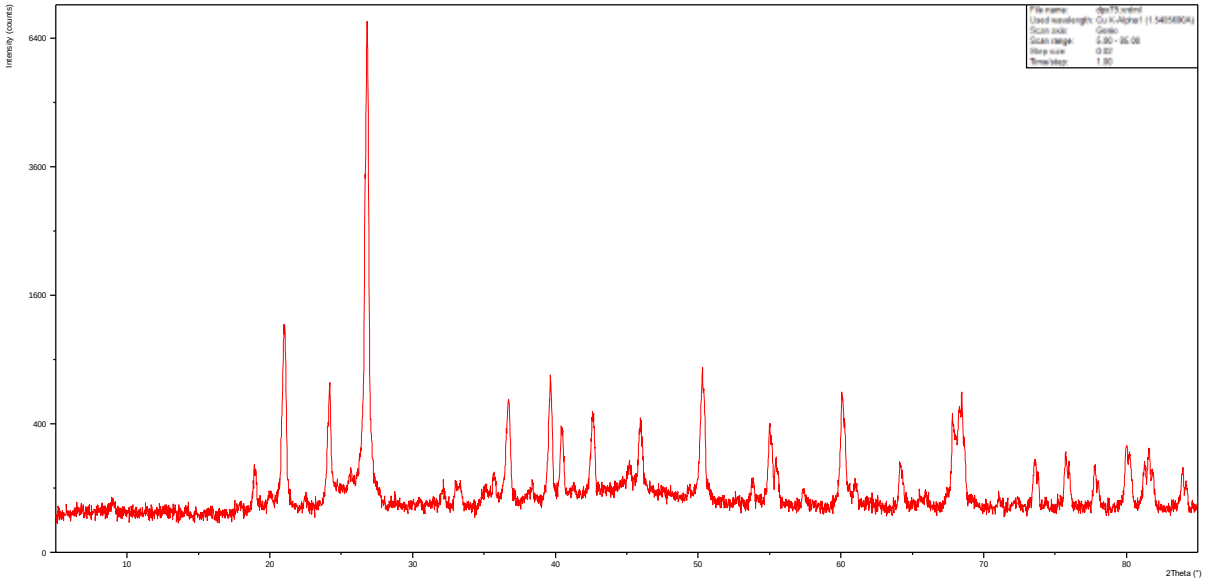

DPX080

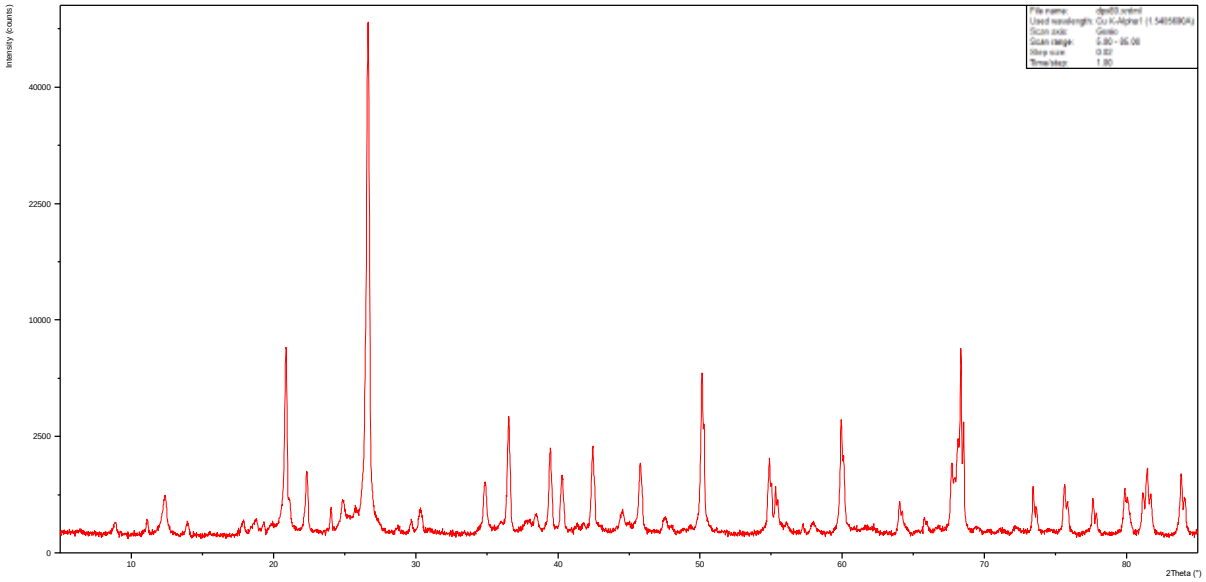

DPX081

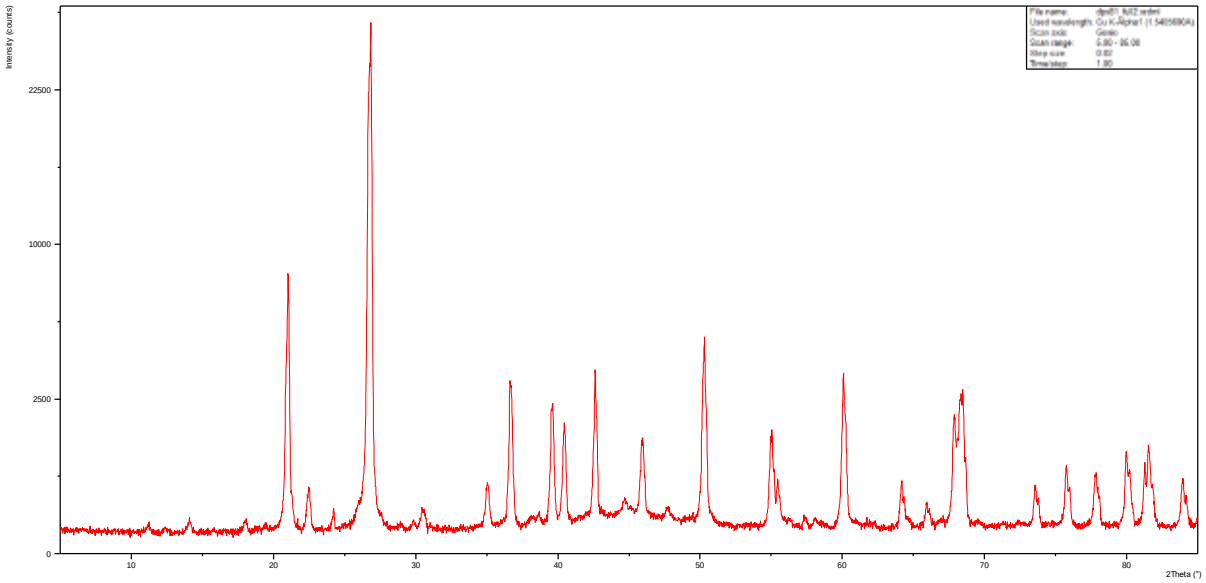

DPX082

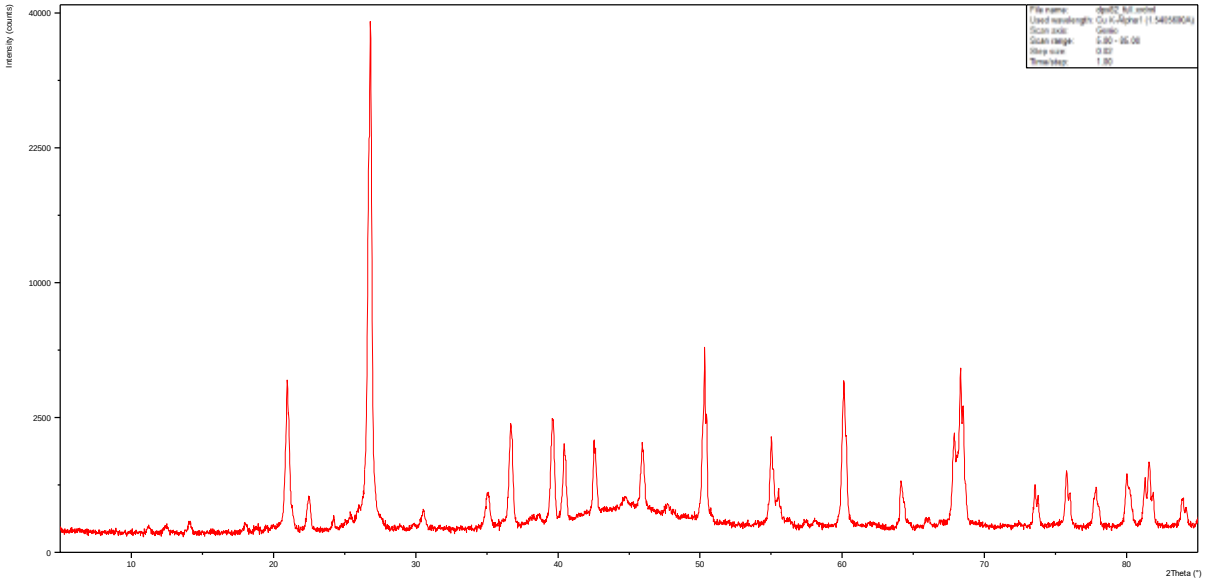

DPX083

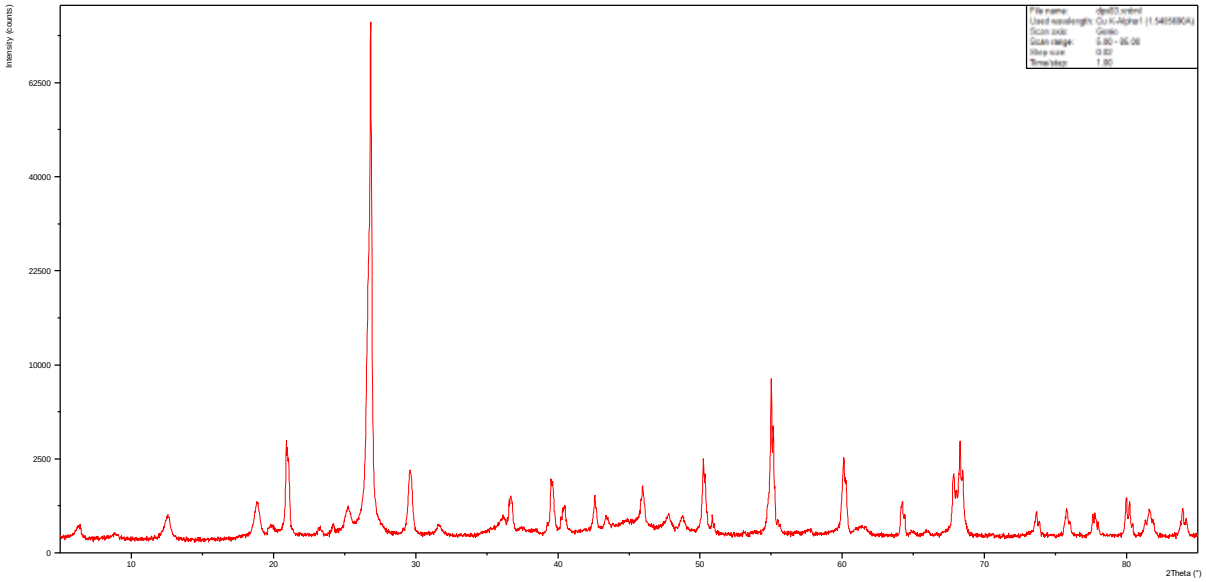

DPX084

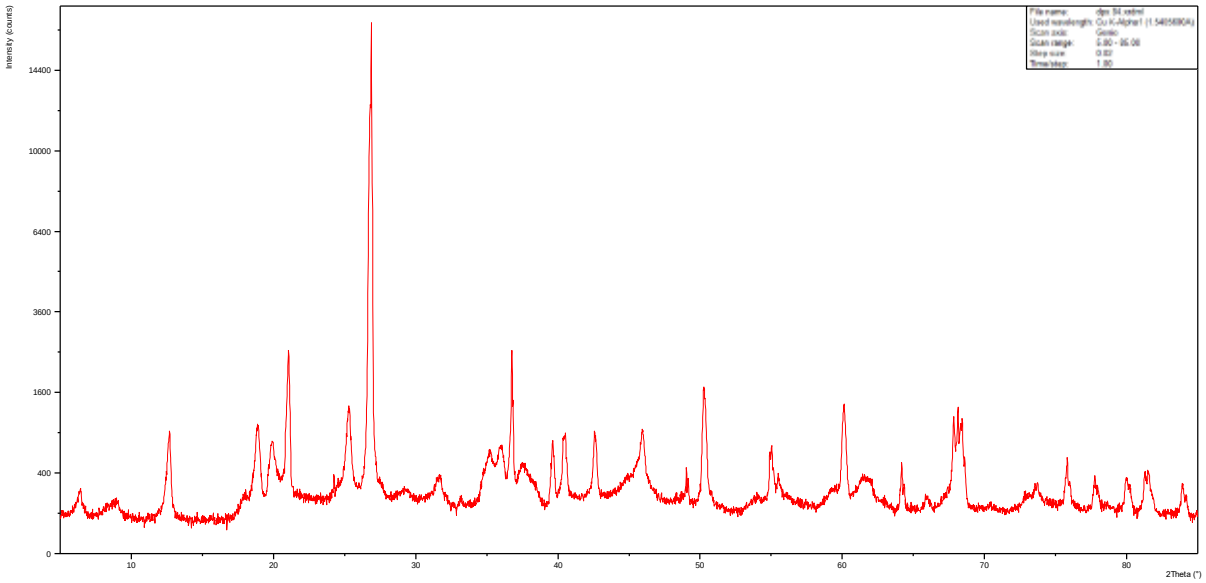

DPX085

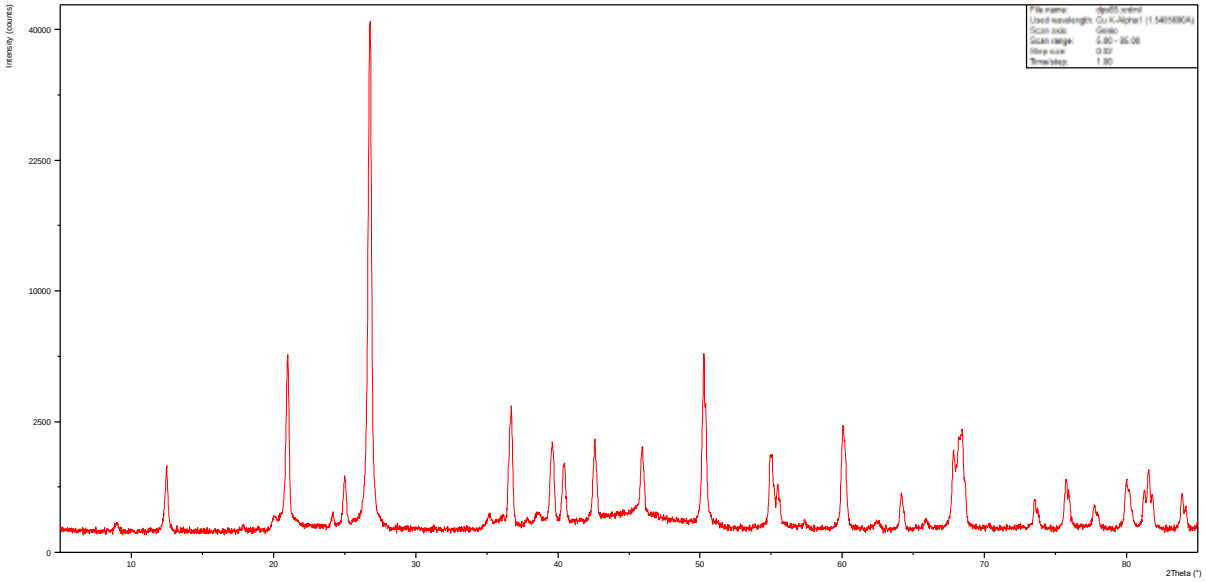

DPX086

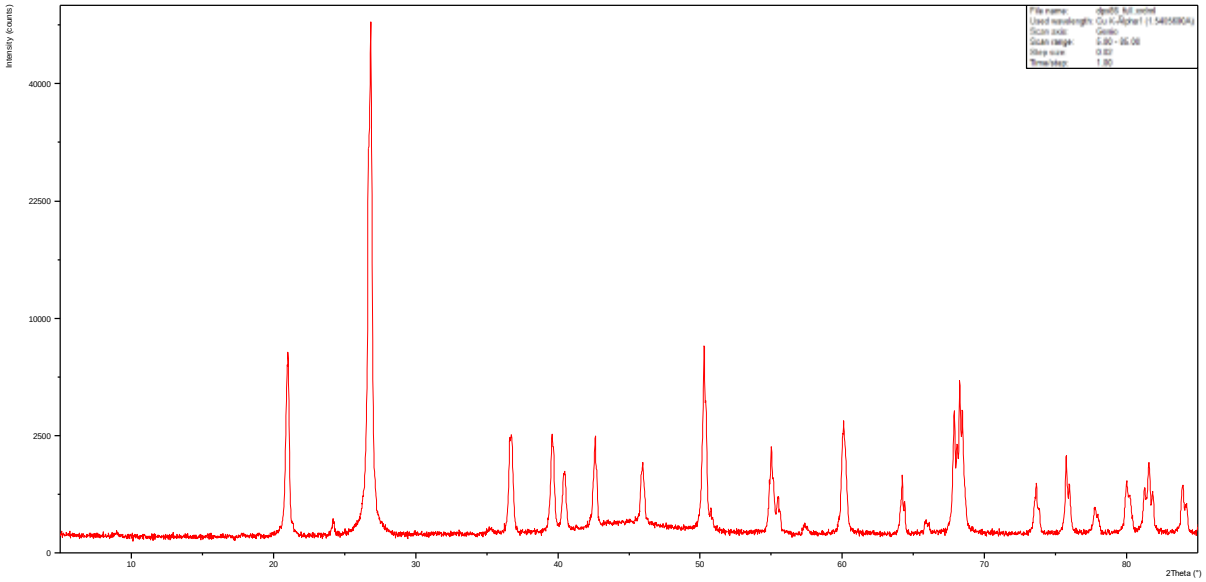

DPX087

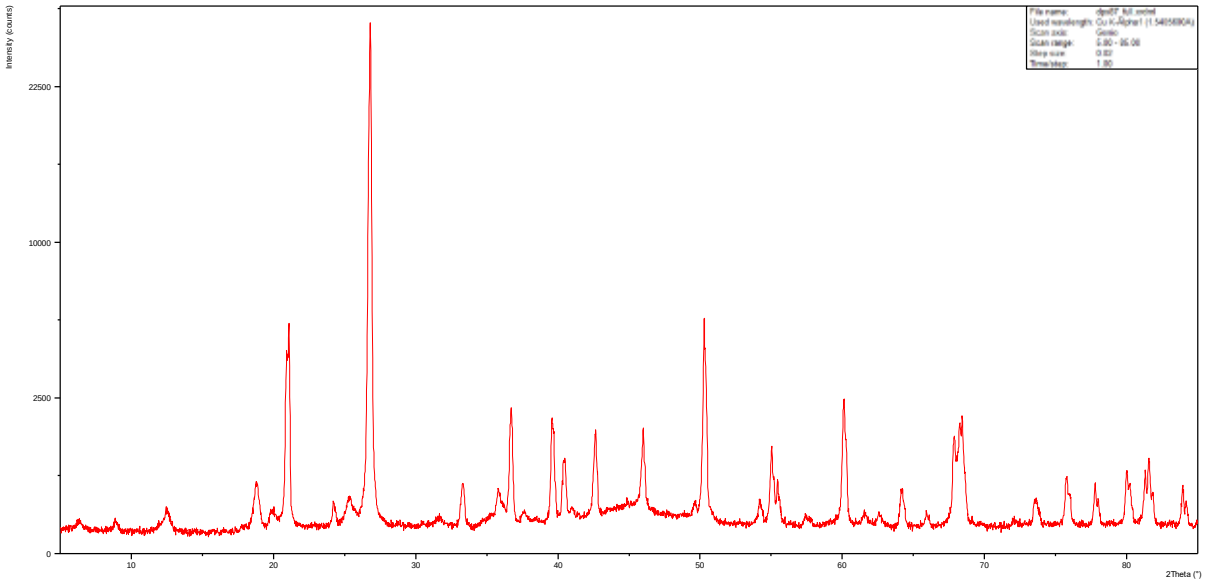

DPX089

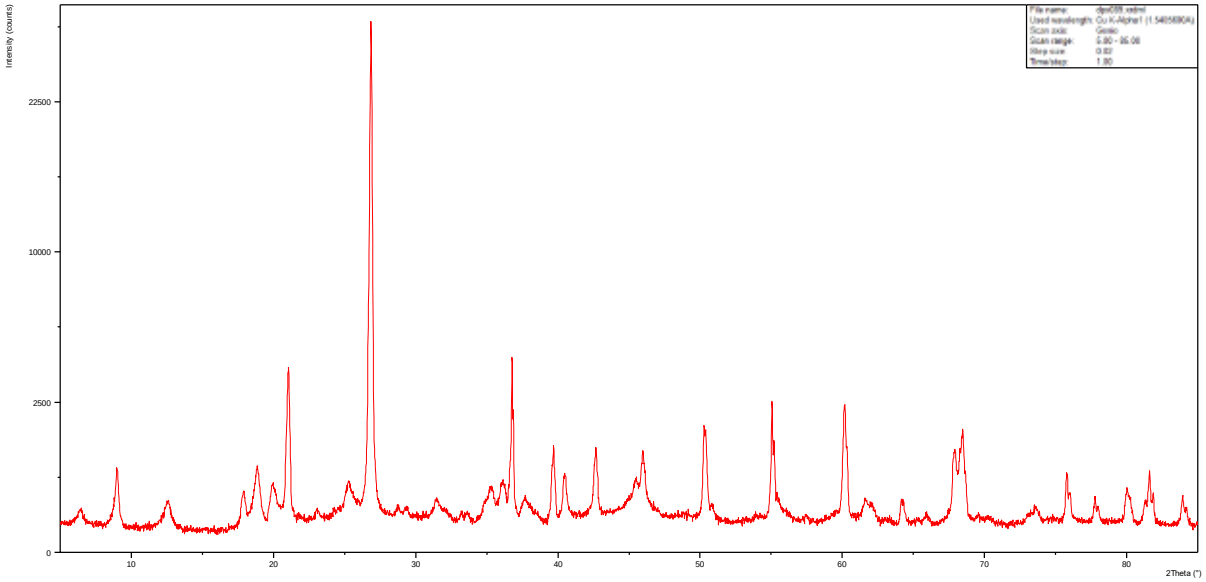

DPX181 vein

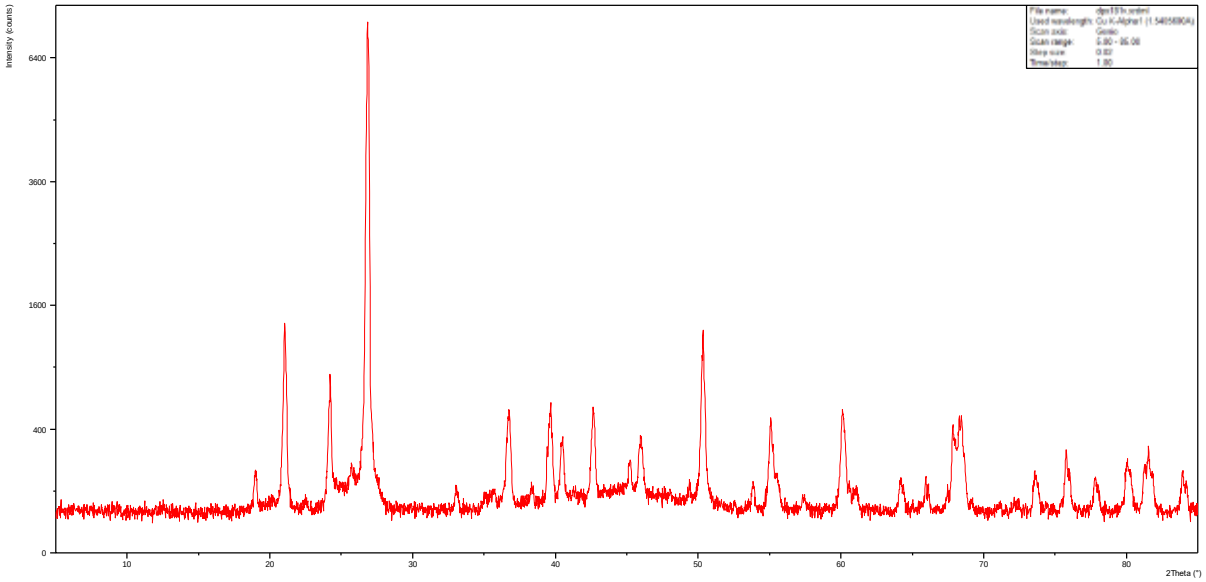

DPX189

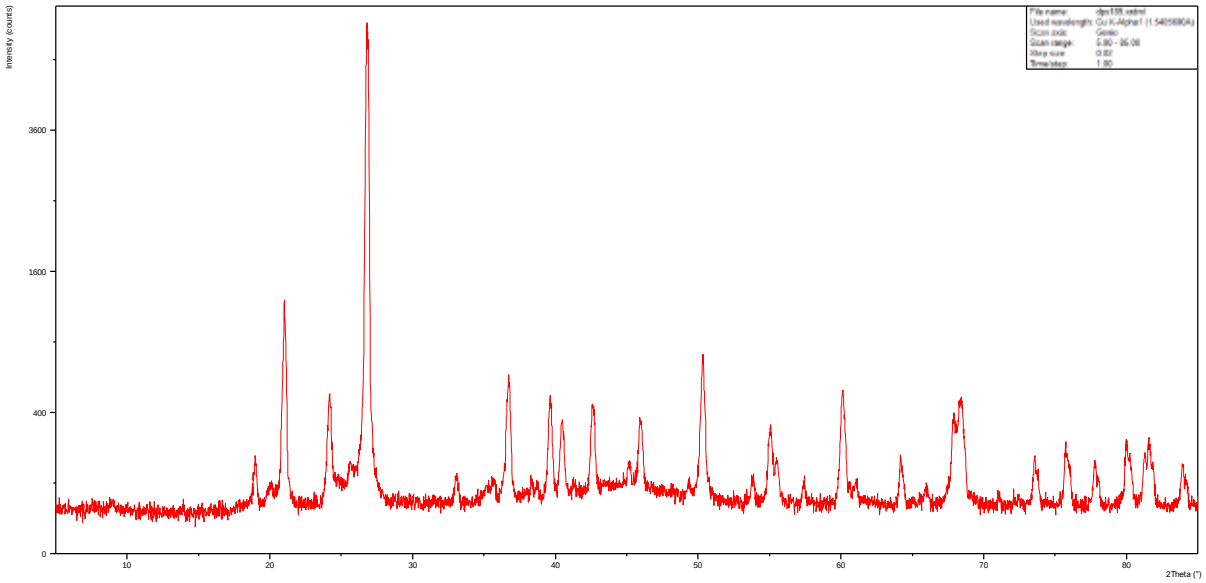

DPX194

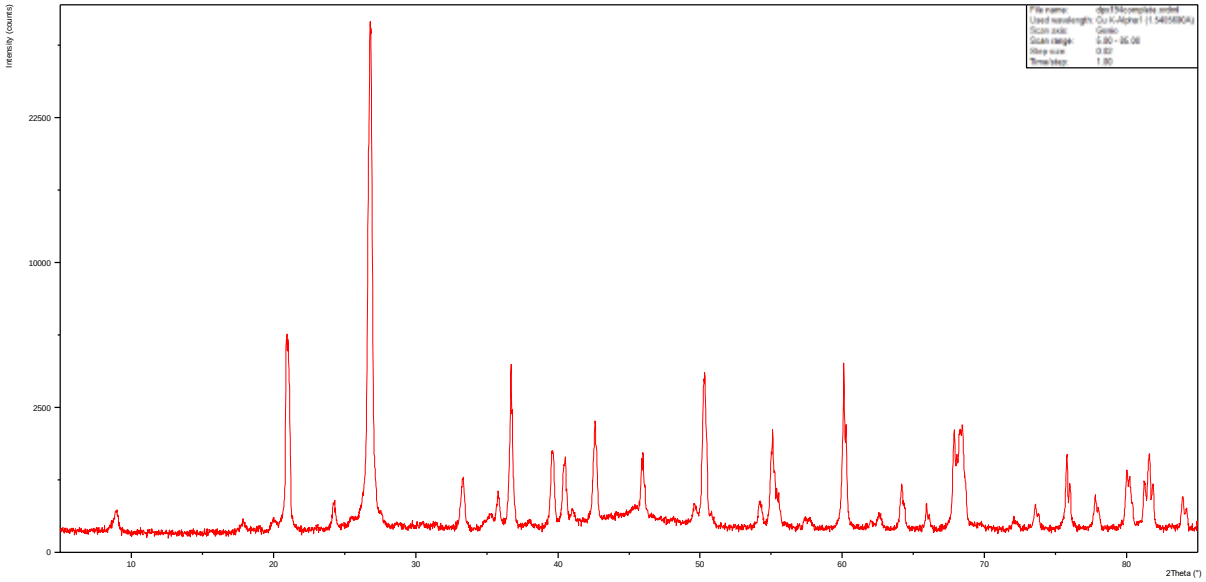

DPX198

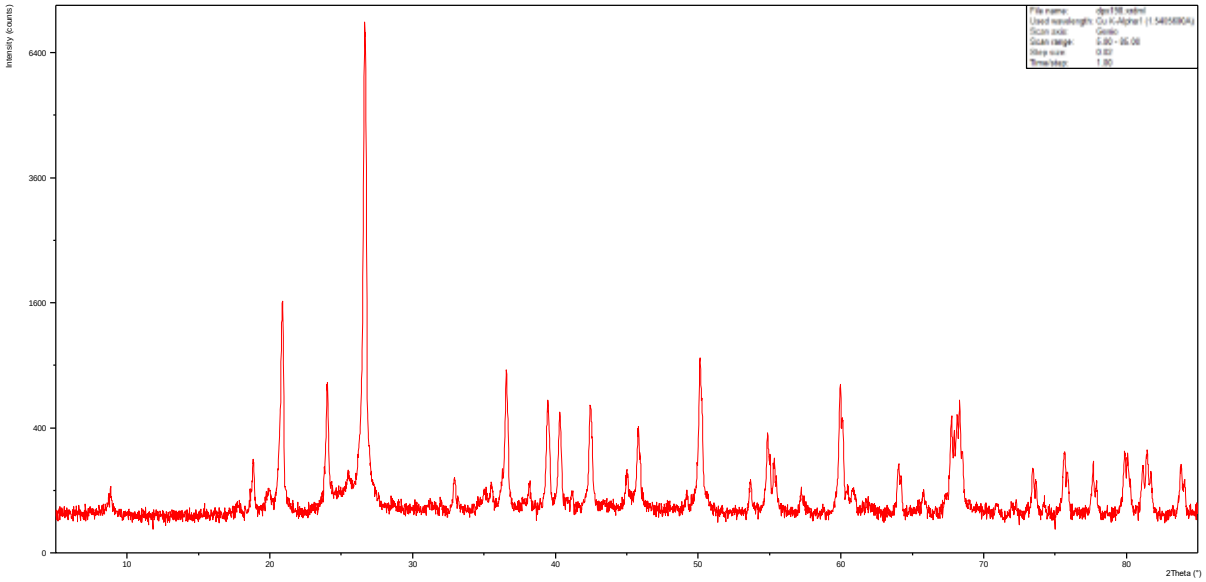

DPX199

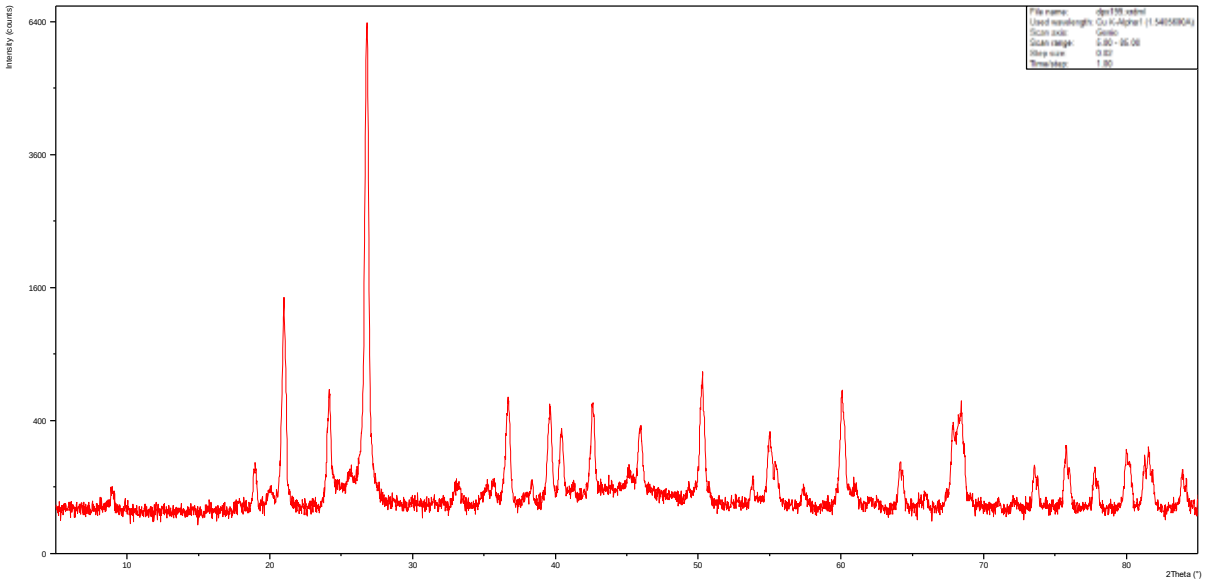

DPX201

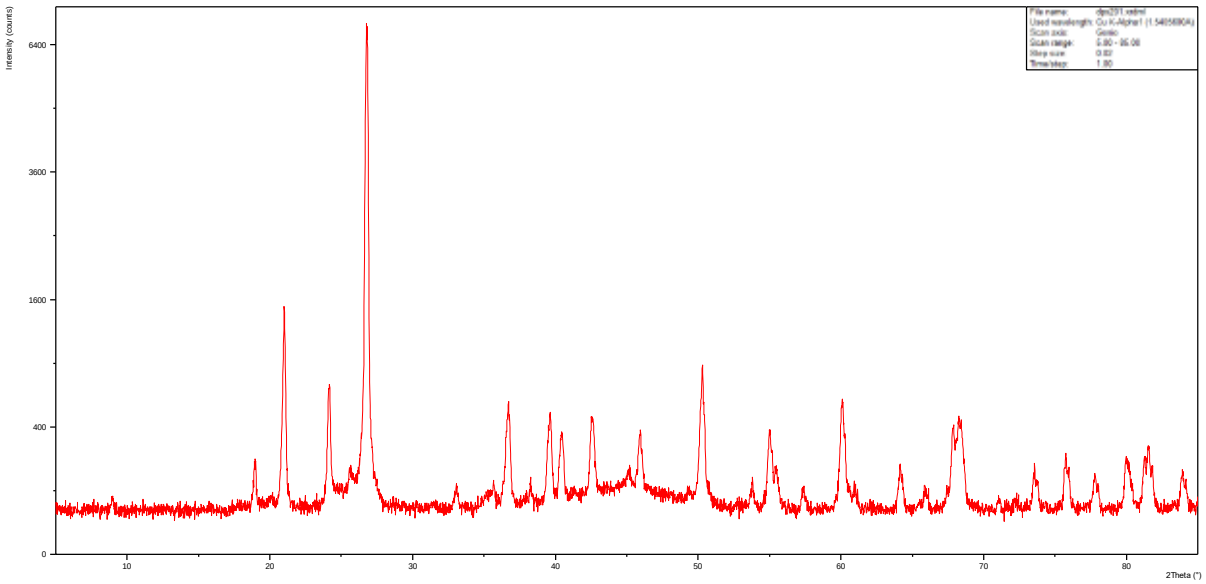

JD1A

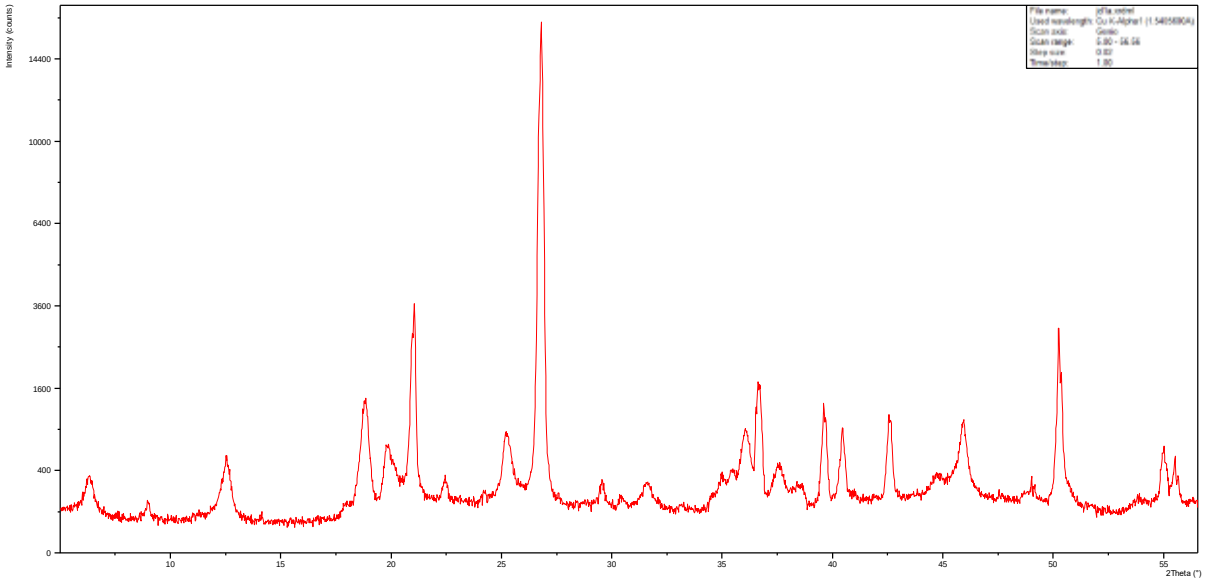

JD2A

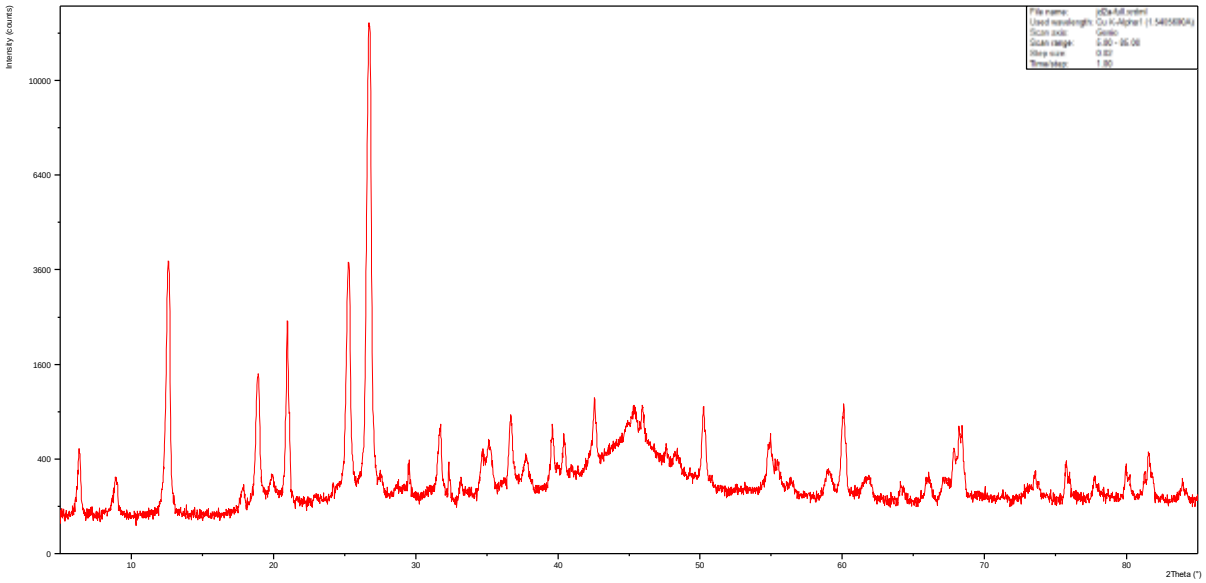

JD4A

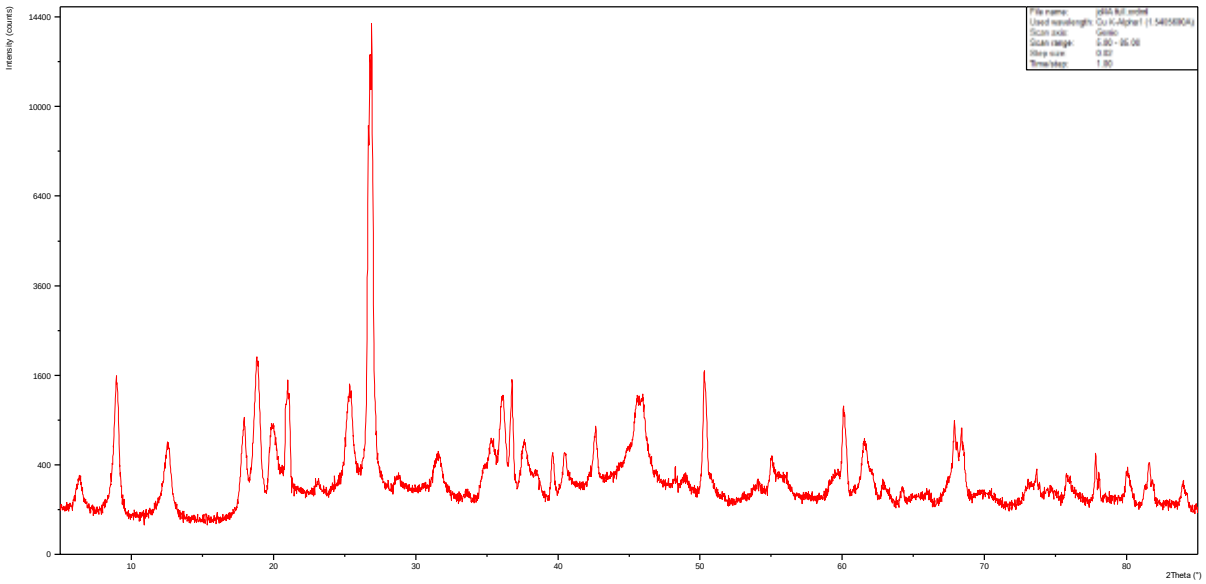

WS Shear Samples

WR256-a

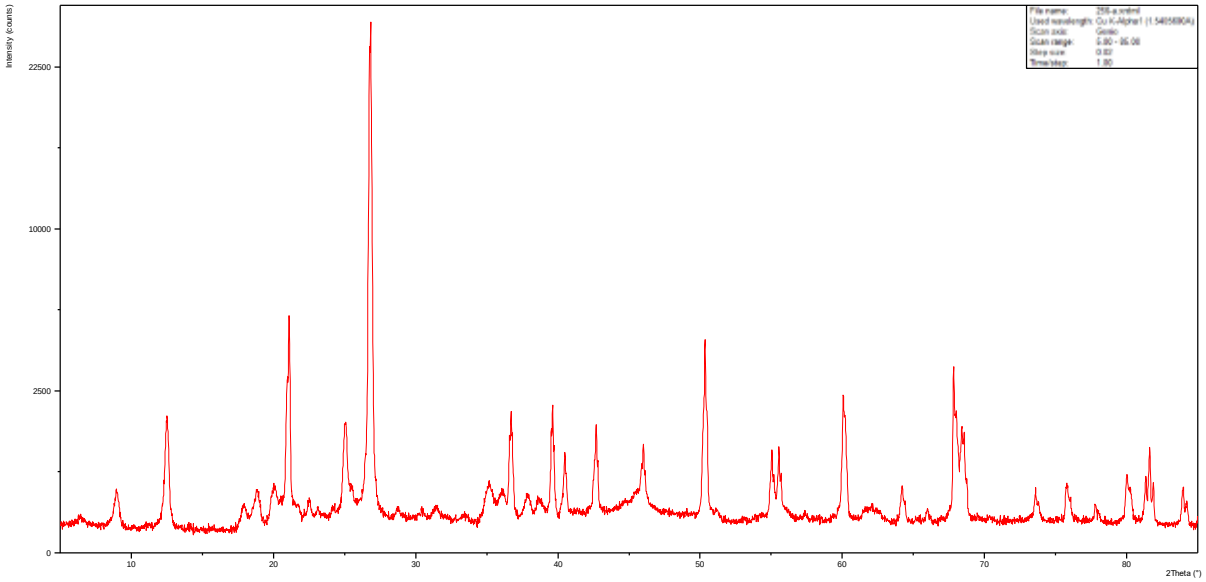

WR256-b

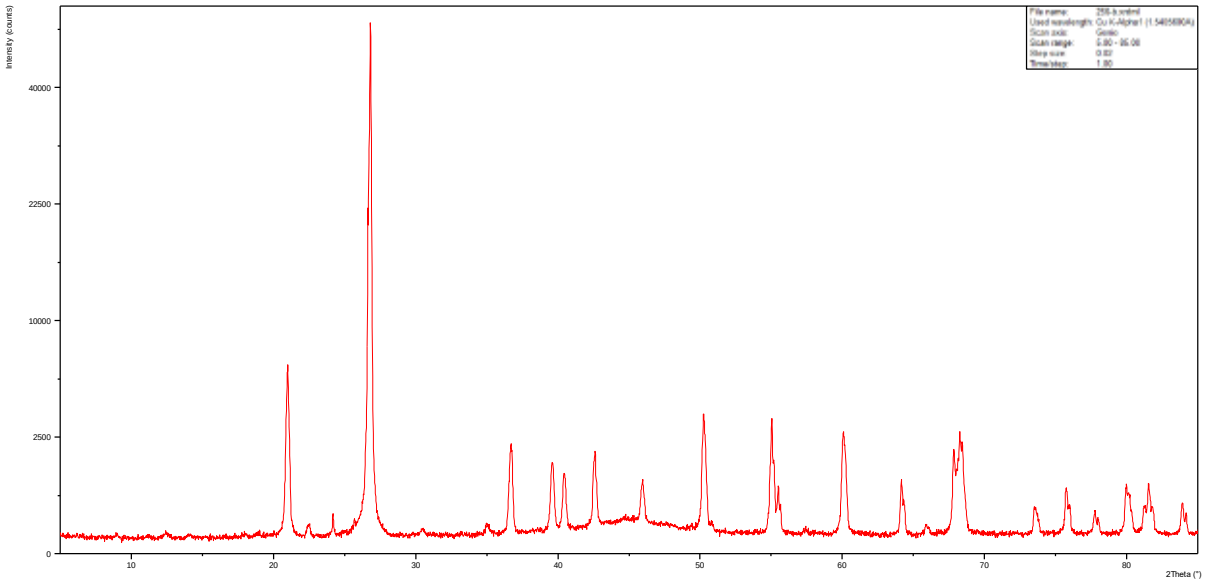

WR281-a

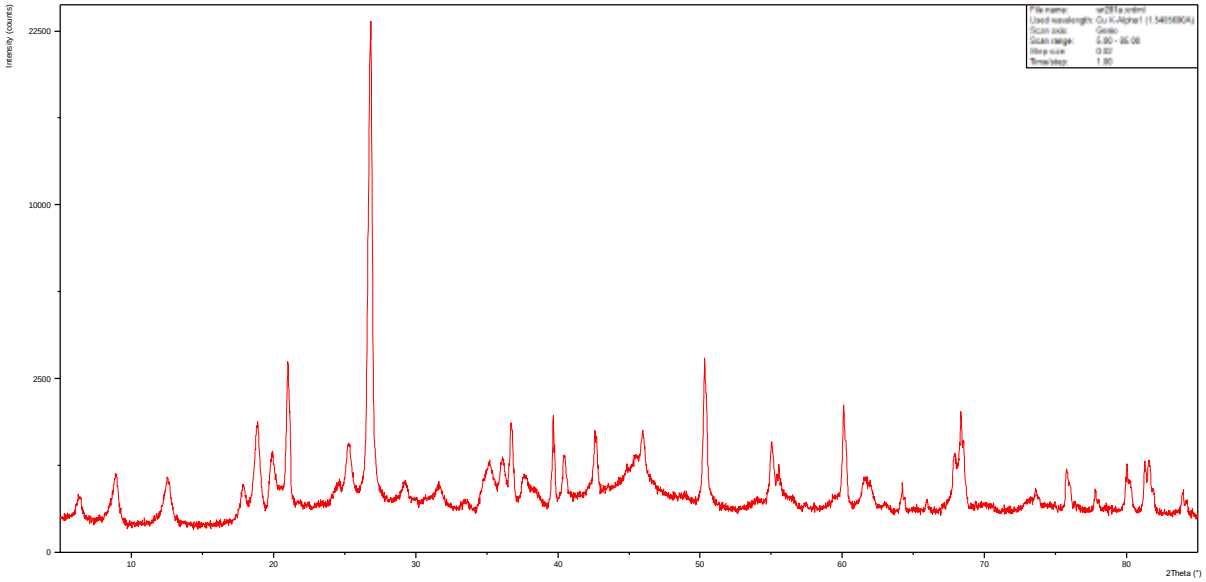

WR281-b

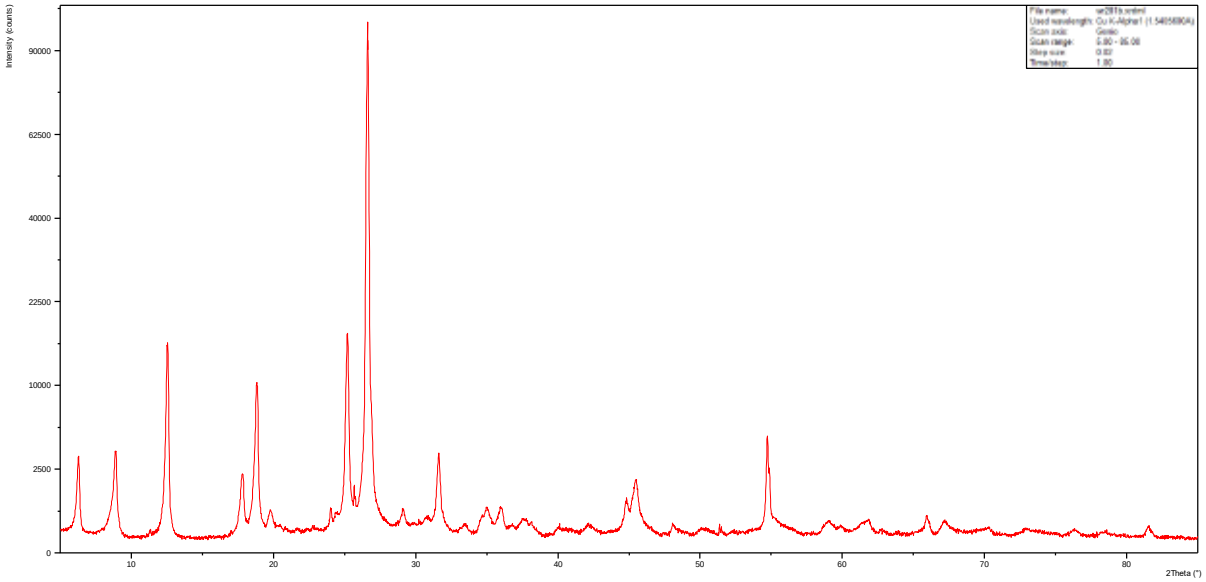

WR281c

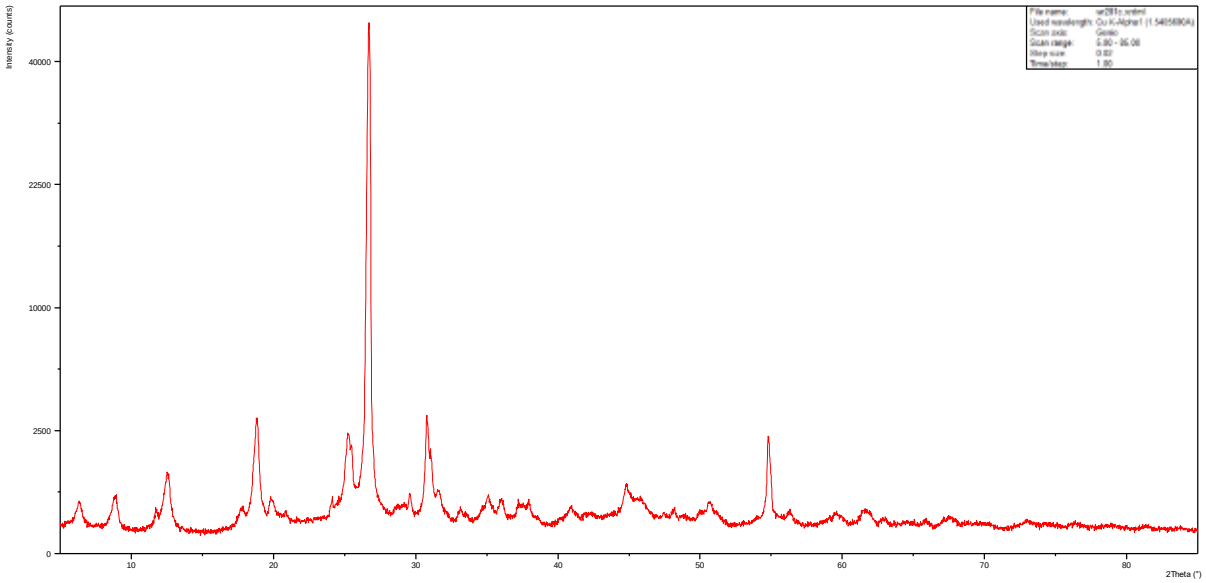

WR282-a

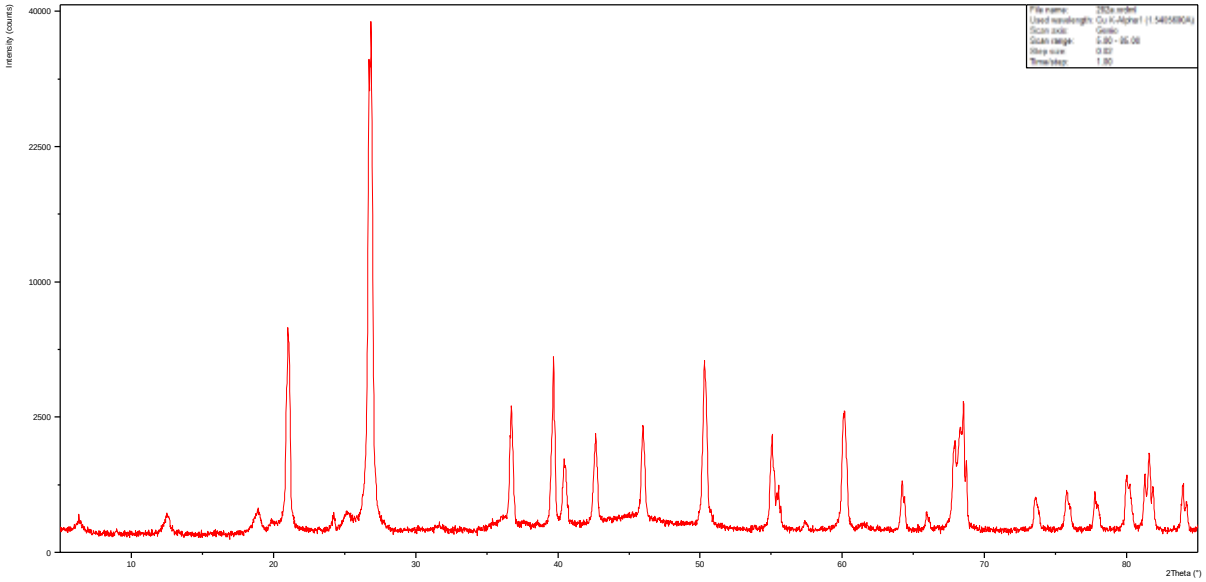

WR282-b

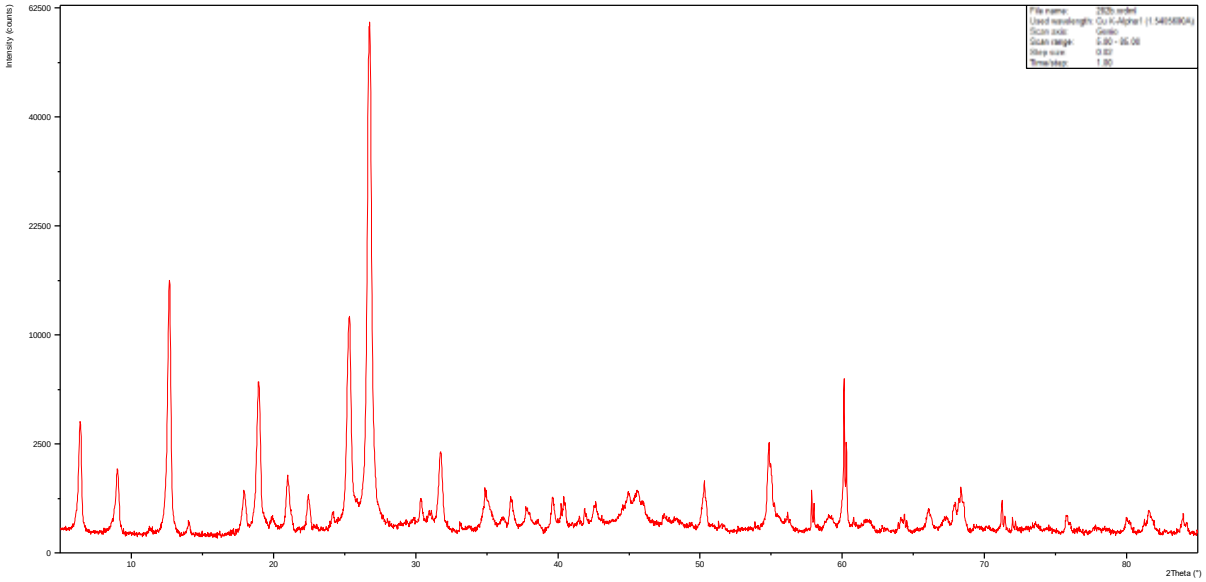

WR293-b

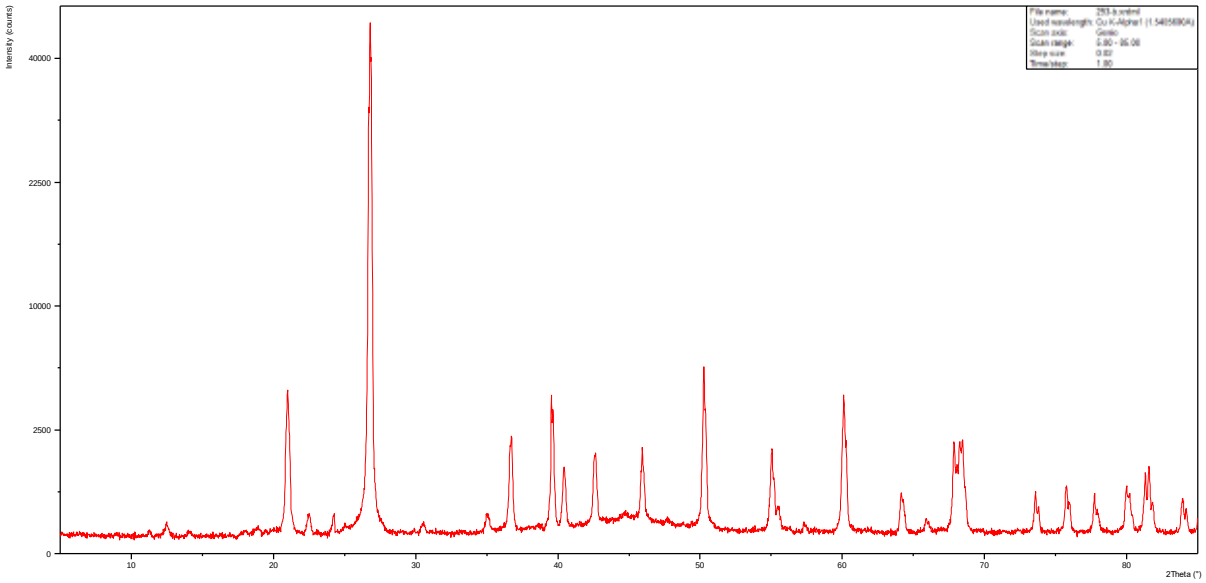

WR301-a

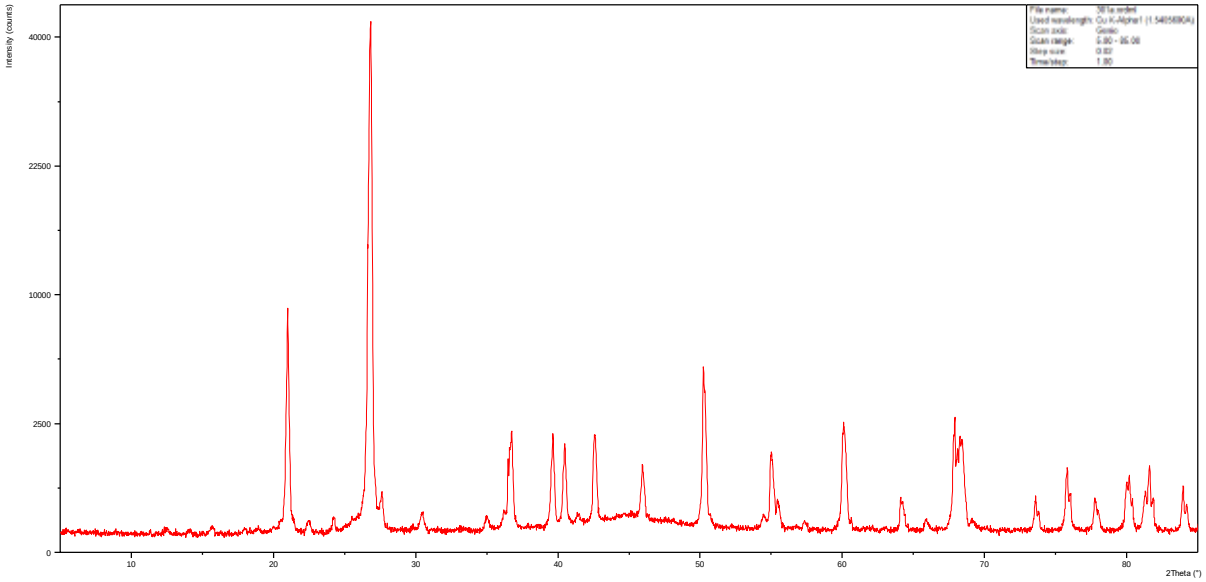

WR301-b

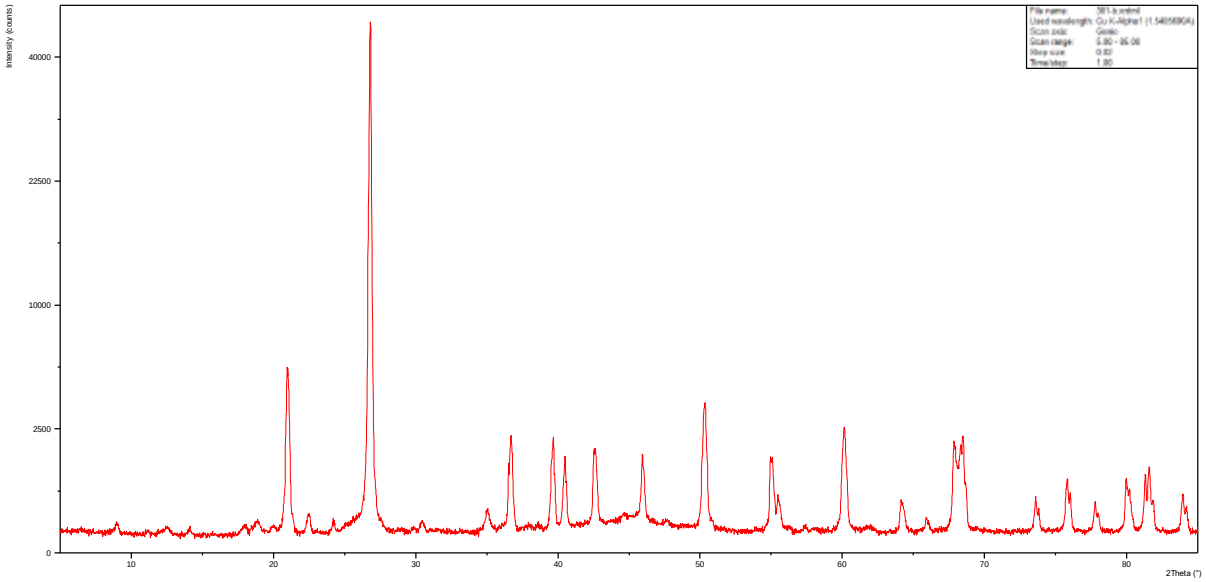

WR315-a

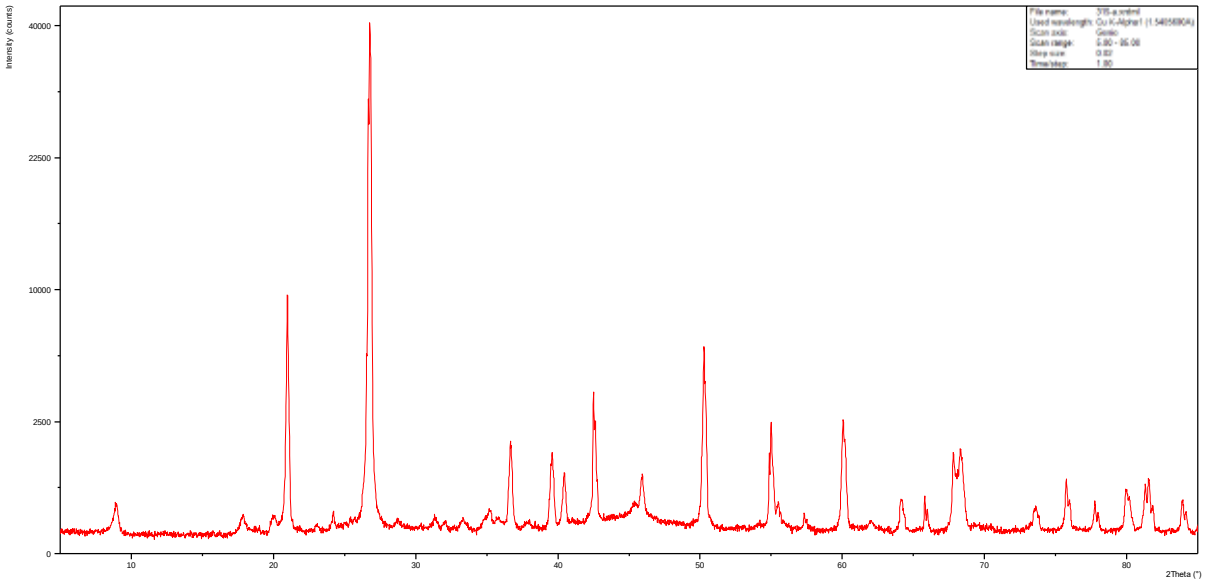

WR315-b

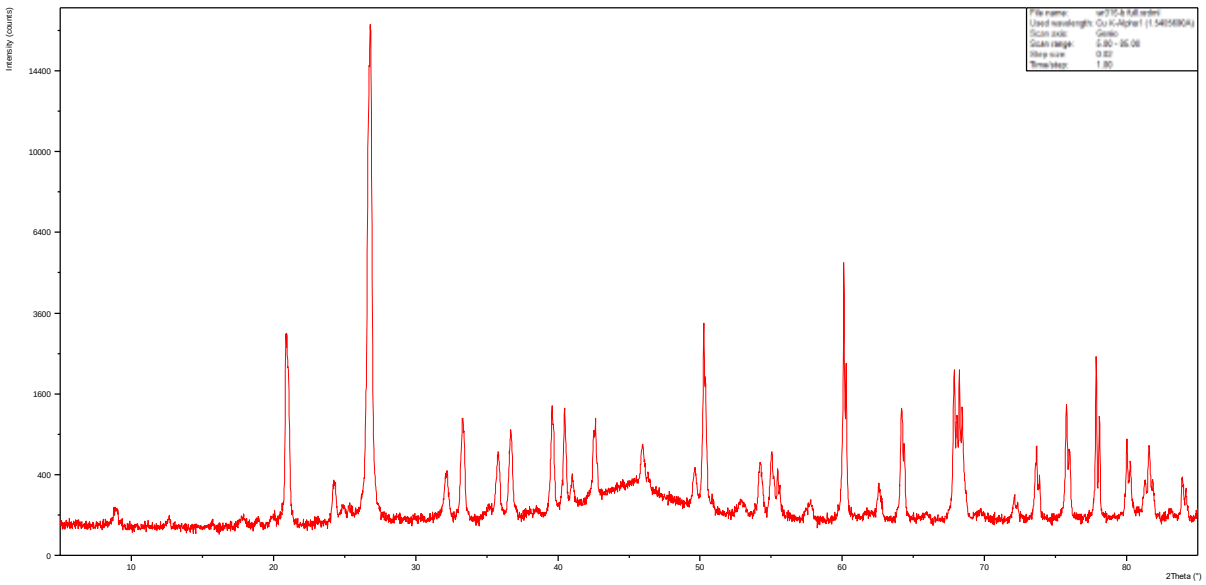

WR352-a

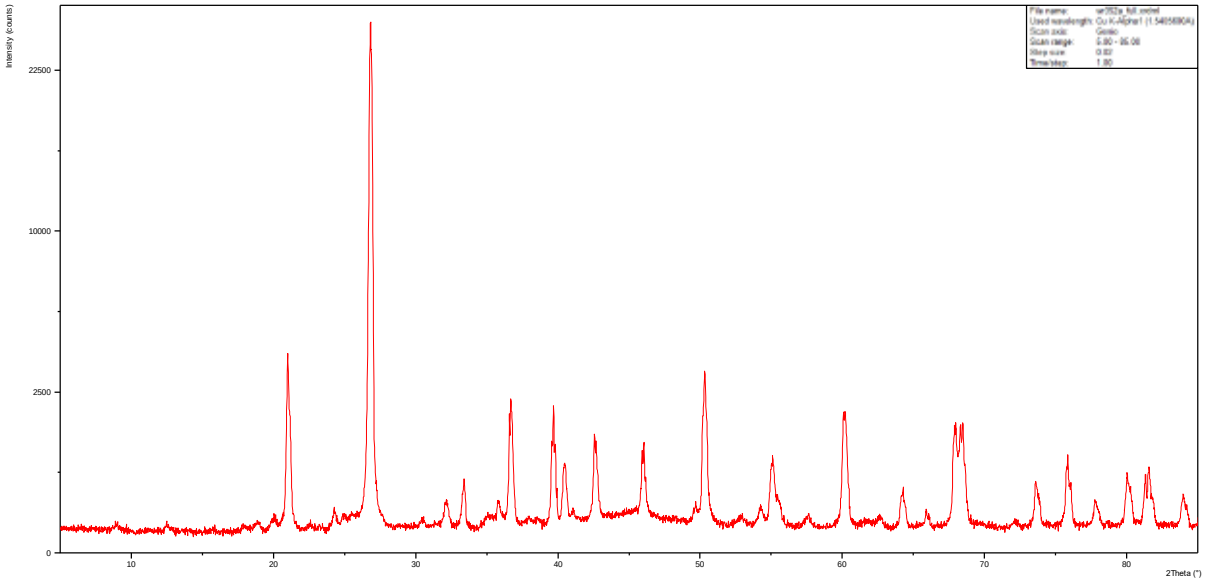

WR404

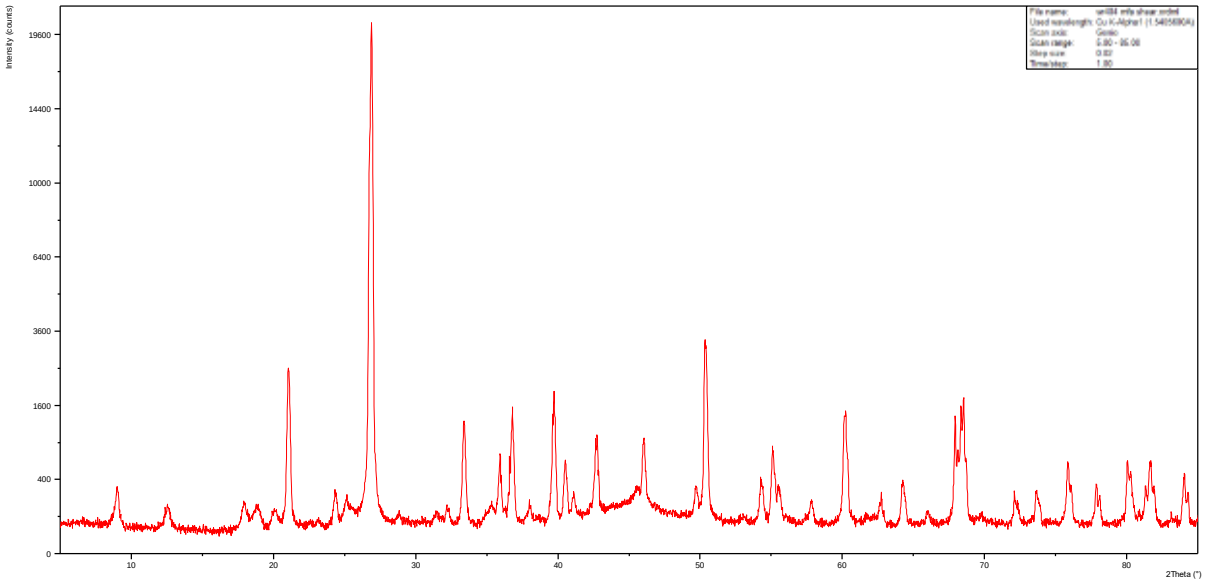

WR409-b

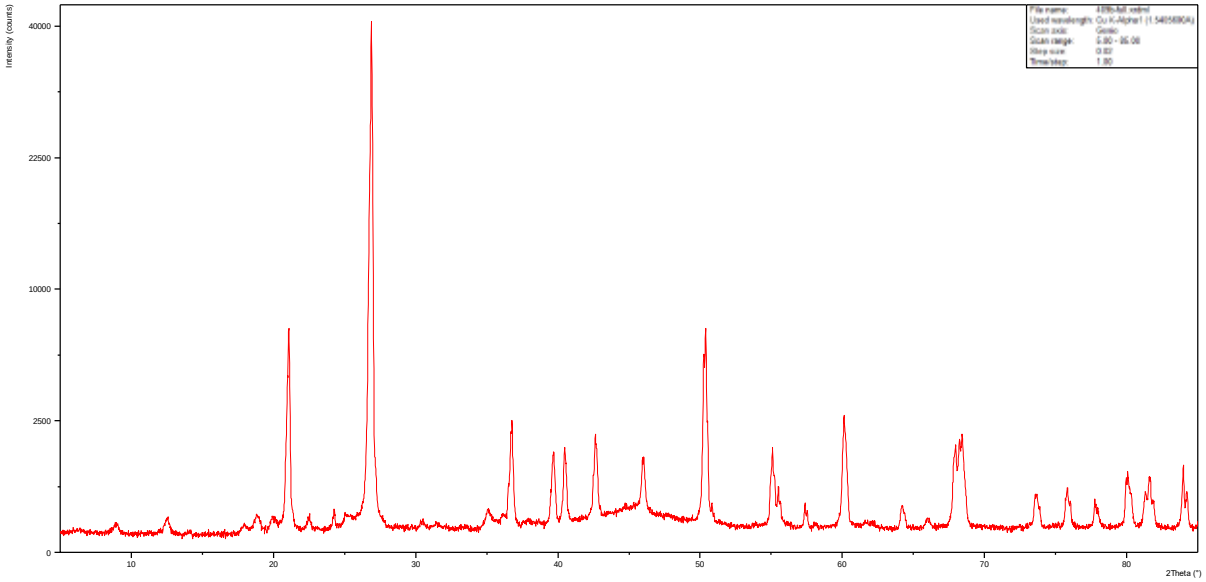

Appendix 5.2; Clay Fraction XRD Analysis of Samples from the Alteration Halo of the Phoenix Deposit.

Introduction

Smectite is a common clay mineral associated with alteration facies. As part of this study analysis has been undertaken using SWIR and XRD in which the presence of smectite invalidates results, and can lead to false information. This appendix serves to identify any samples which have smectite in them, to ensure that they are not used and to offer a further analysis into the mineralogy of clay fraction samples analysed as part of this study.

Methods

Separation of Clay Fractions

Clay fractions of samples were prepared by the Geological Survey of Canada, Booth Street, Ottawa, Ontario; This was achieved through separating the <2 micron fraction via ultrasound, shaking and centrifugation. Size fractions other than <2 microns (e.g. 2-16 micron) are obtained by varying the centrifuge speed and time. The total content of clay extracted is determined by removing a 20ml aliquot of the final clay suspension and evaporating to dryness.

Glycolation

Clays were solvated with ethylene glycol by exposing prepared samples to ethylene glycol within a sealed vessel at 75°C for a period of between 4-10 hours.

Dehydration

Samples were placed in an oven at 550°c for a period of 1 hour. After which they were stored in an airtight vessel containing silica gel pellets.

XRD Analysis of Samples

All samples were analysed on a Philips PW 3020 X'Pert Diffractometer at the University of Ottawa's X-Ray Core Facility. Measurements were acquired at 45-kV accelerating voltage, 40-mA current. Samples were analysed on polished glass slides and between 2° and 85° with a step size of 0.02° and a time/step of 0.5s

Samples Analysed

Non Shear Samples			Shear Samples		
Sample	Drillcore	Depth (m)	Sample	Drillcore	Depth (m)
DPX71	WR-329	373	WR256A	WR-256	190.7
DPX105	WR-317	407.4	WR256B	WR-256	224.1
DPX139	WR-380	270.7	WR293A	WR-293	244.9
DPX190	WR-286	119.2	WR293B	WR-293	251
DPX197	WR-286	211.4	WR301A	WR-301	315
DPX199	WR-286	257.9	WR315A	WR-315	312.8
DPX226	WR-321	259.8	WR315B	WR-315	316
DPX232	WR-321	292.9	WR352B	WR-352	316.2
DPX235	WR-321	307.1	WR404	WR-404	323.3
			WR409A	WR-409	317.7

Rationale of Samples Selected for Clay Fraction Analysis

The original plan behind clay fraction analysis of clays was to identifying the role of the WS Shear Structure in the alteration surrounding Phoenix; as such samples were selected to offer a comparison between those collected within the WS Shear Extension Structure and those collected in the sandstones away from the structure. A total of 9 samples were analysed from the WS Shear Extension structure and a total of 10 samples were analysed from drillcore located away from the WS Shear Extension.

Behaviour of peak after glycolation and drying at 550°C

Peak (Å)	presence on a dry sample	Behaviour on glycolation	Behaviour on heating 550°C
17	-	Smectite (001)	
14	Chlorite (001) or vermiculite		Vermiculite. if the peak collapses, chlorite otherwise
10	Illite (001)	If present indicates mica	
7.1	Kaolinite (001) and chlorite (002)	None	Kaolinite is the peak collapses.
5	Illite (002)	none	none
4.72	Chlorite (003)	none	none
4.26	Quartz	none	none
3.57	Kaolinite	none	Collapse
3.53	Chlorite (004)	none	Collapse
3.33	Illite (003) and quartz	none	none

Mineralogy Identified

Results

Non Shear Structure Samples

DPX71

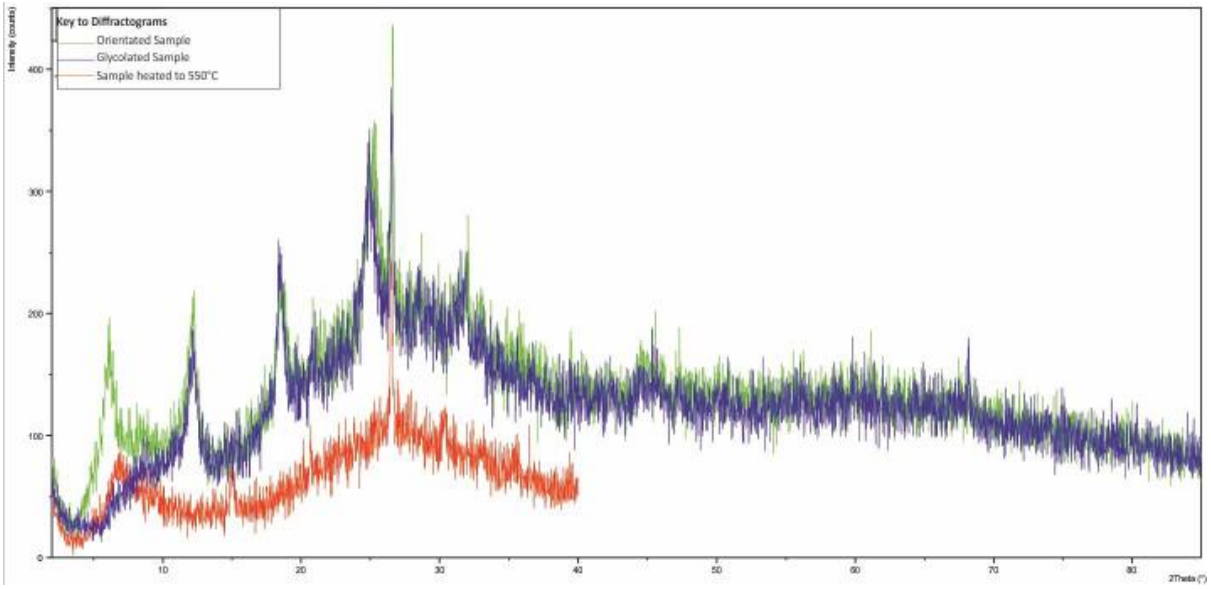

Peak observed in Orientated Sample? Å	Observed in Glycolated Sample? Å	Observed in Sample heated at 500°C Å	Applicable to which mineral? Å
Absent	14.57	Absent	
Absent	Absent	12.57	
7.4	Yes	Absent	Kaolinite [001]
Absent	Absent	5.8	
4.7	Yes	Absent	
3.56	Yes	Absent	Illite [003] / Chlorite
3.35	Yes	Yes, but only at 50% of the intensity of orientated samples	Kaolinite [002]
2.8	Yes	Absent	

DPX105

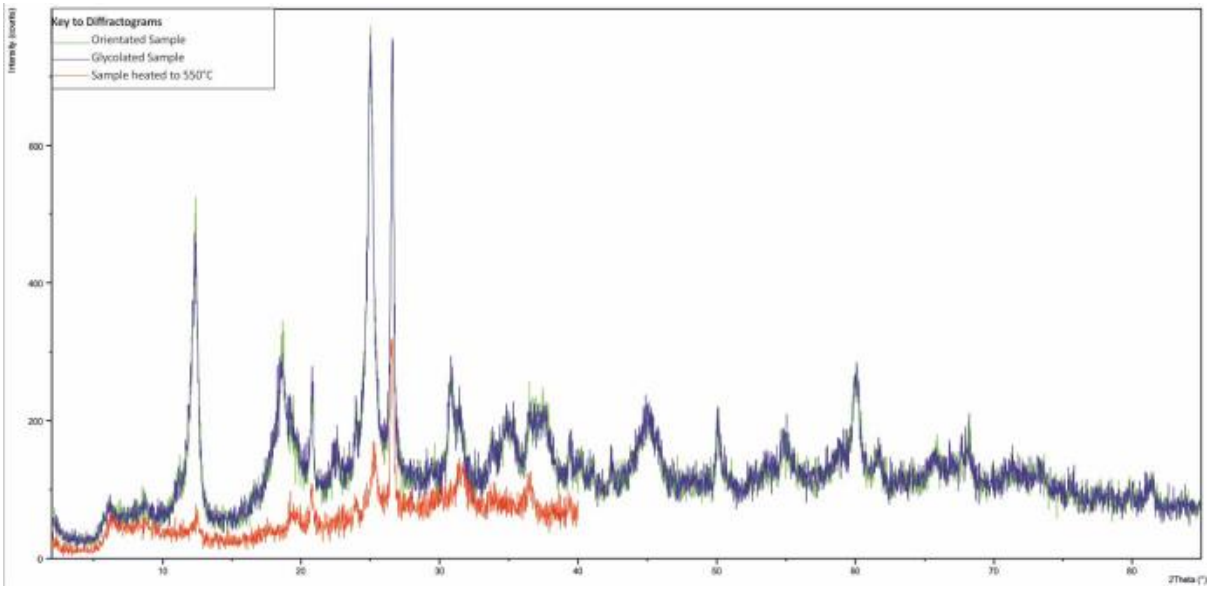

Peak observed in Orientated Sample? Å	Observed in Glycolated Sample? Å	Observed in Sample heated at 500°C Å	Applicable to which mineral? Å
14.2	Yes	Yes	Chlorite
10.1	Yes	No.	Illite [001]
7.1	Yes	Yes, but only as a minor peak (15% of orientated and glycolated sample)	Chlorite [002] / Illite - secondary
4.8	yes	no	Illite [002]?
4.25	Yes	Yes	Quartz
3.9	yes	no	
3.55	yes	Yes, but only at 22% of the intensity of the orientated and glycolated samples, also a shift from 3.55Å to 3.52Å	Illite [003] / Chlorite
3.47	yes	Yes, but only to 43% of the intensity of the orientated and glycolated samples.	Quartz?
2.9	yes	no	
2.84	yes	Yes, but only around 50% of the intensity of the orientated and glycolated samples.	
2.57 broad peak	Yes, same broad peak	absent.	
2.41 broad peak	Yes, same broad peak	absent	

DPX139

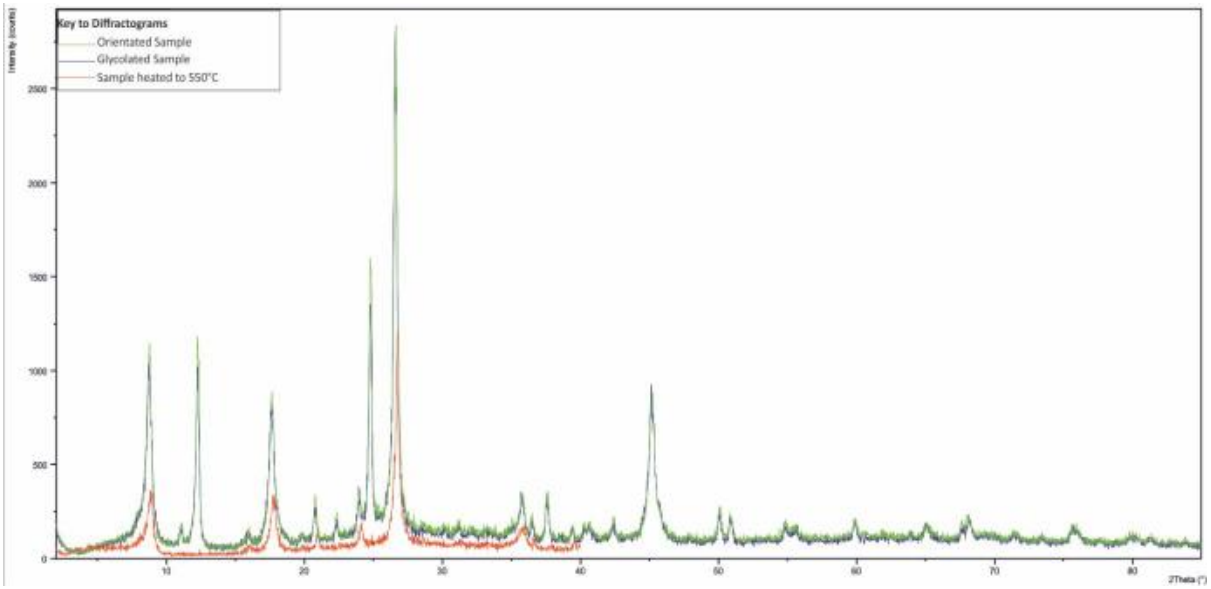

Peak observed in Orientated Sample? Å	Observed in Glycolated Sample? Å	Observed in Sample heated at 500°C Å	Applicable to which mineral? Å
10.1	Yes	Yes, but only as a minor peak (30% of orientated and glycolated sample)	Illite [001]
8	yes	no	Kaolinite
7.2	Yes	no	Kaolinite [001] – collapse of peak on heating / Illite - secondary
5.0	yes	Yes, but only around 50% of the intensity of the orientated and glycolated samples.	Illite [002]
4.2	yes	Yes, but only at 40% of the intensity of the orientated and glycolated samples	Quartz
3.98	yes	no	
3.7	yes	Yes, but only at 40% of the intensity of the orientated and glycolated samples	Kaolinite [002]?
3.35	yes	Yes, but only around 43% of the intensity of the orientated and glycolated samples.	Illite [003], Chlorite
2.5 broad peak	Yes, same broad peak	Yes, but only around 50% of the intensity of the orientated and glycolated samples	
2.41 broad peak	Yes, same broad peak	absent	
2.39	yes	absent	

DPX142

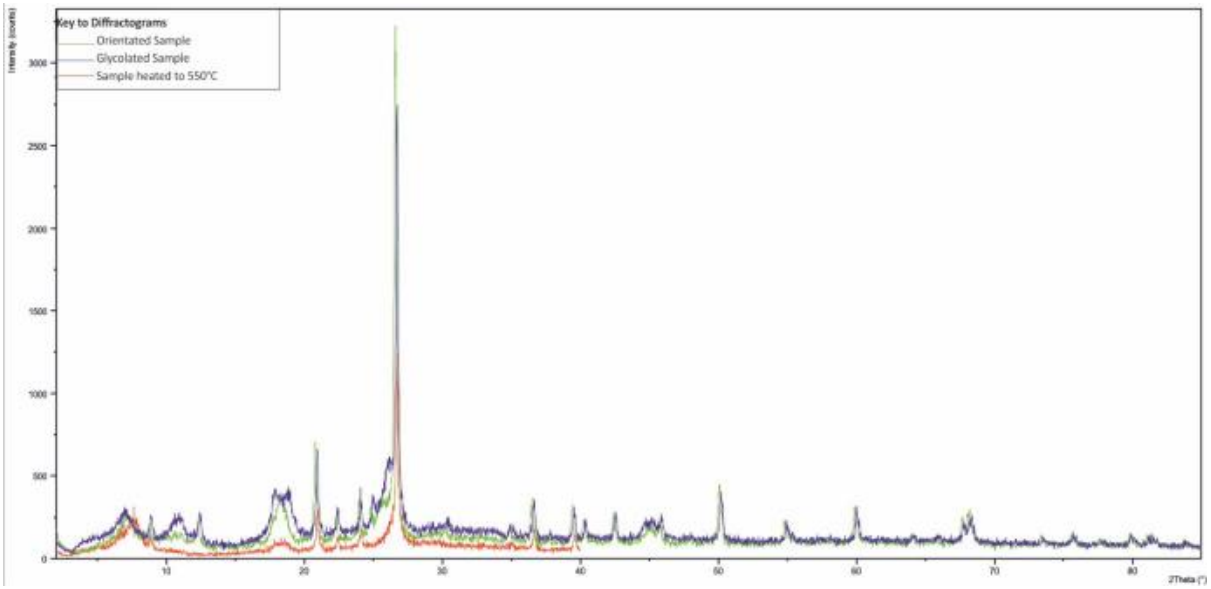

Peak observed in Orientated Sample? Å	Observed in Glycolated Sample? Å	Observed in Sample heated at 500°C Å	Applicable to which mineral? Å
12.7	Yes – but at 12.38Å	Yes – but at 11.59Å	
10	Yes	Yes, but only as a minor peak (50% of the oriented and glycolated samples).	Illite [001]
8	Yes – but at 100% greater intensity to the orientated sample	Absent.	Kaolinite
7.1	Yes – but at 33% greater intensity to the orientated sample	Absent	Kaolinite [001] – collapse of peak on heating / Illite - secondary
4.25	Yes	Yes, but only at 50% of the intensity of the orientated and glycolated samples	
3.9	yes	yes	
3.69	yes	Yes	
3.47	yes	Yes, but only to 43% of the intensity of the orientated and glycolated samples.	Kaolinite [002]
3.35	yes	Yes, but only around 43% of the intensity of the orientated and glycolated samples.	Illite [003] / Chlorite
2.5	yes	yes	
2.2	yes	yes	

DPX190

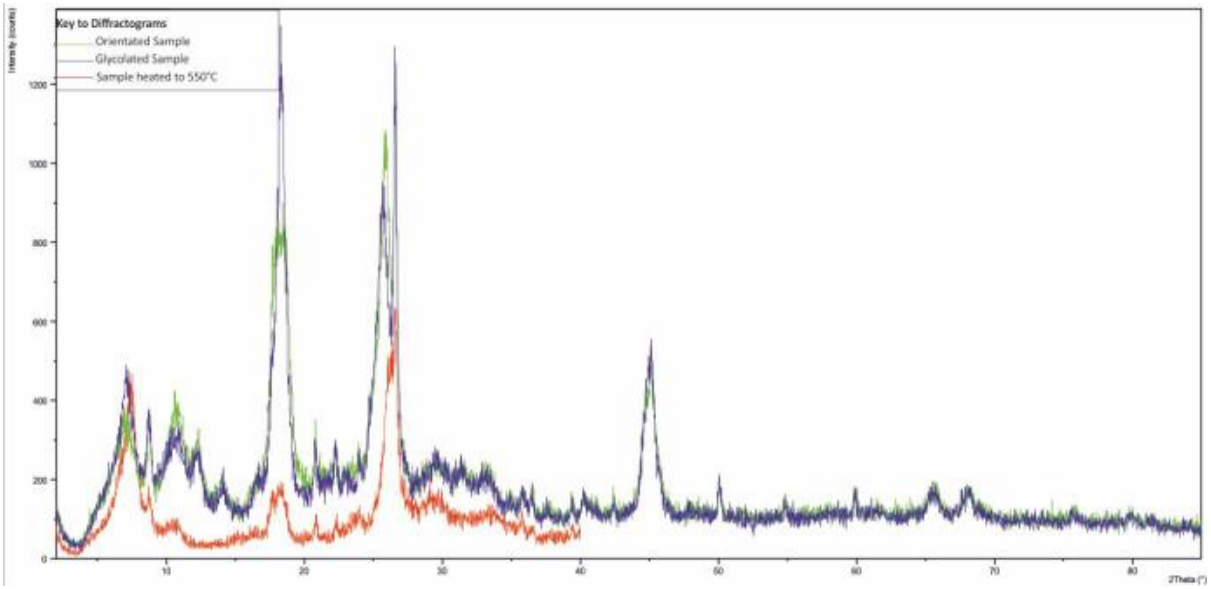

Peak observed in Orientated Sample? Å	Observed in Glycolated Sample? Å	Observed in Sample heated at 500°C Å	Applicable to which mineral? Å
12.39	Yes	Yes – but at 11.8Å	
10.1	Yes	Yes, but only as a minor peak (50% of the oriented and glycolated samples).	Illite [001]
8.2	Yes	Absent.	Kaolinite
7.24	Yes	Absent.	Kaolinite [001] – collapse of peak on heating
6.3	Yes	Absent	
4.8	Yes, but at 75% of the intensity of the orientated peak	Yes, but at15% of the intensity of the orientated peak	
4.26	yes	Yes, but only to 20% of the intensity of the orientated and glycolated samples.	
3.47	Yes, but has shifted to 3.44Å and increased by 15% relative to oriented sample	Possibly present, or in shoulder of 3.35Å peak	Kaolinite [002]
3.35	yes	Yes, but only around 40% of the intensity of the orientated and glycolated samples.	Illite [003] / Chlorite

DPX197

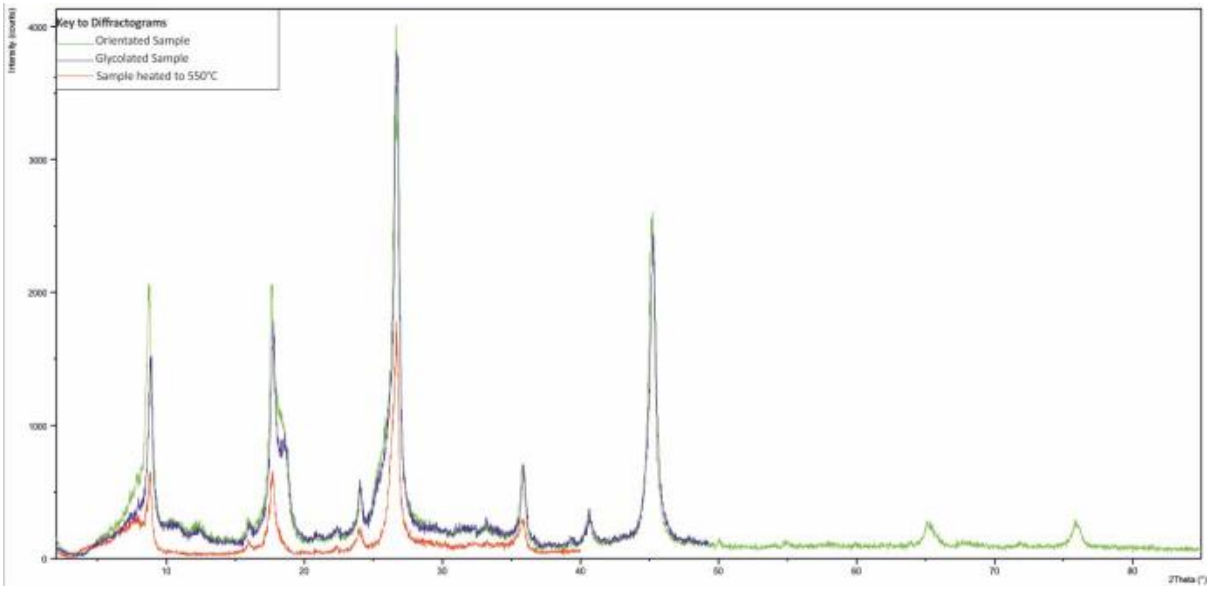

Peak observed in Orientated Sample? Å	Observed in Glycolated Sample? Å	Observed in Sample heated at 500°C Å	Applicable to which mineral? Å
10.1	Yes	Yes, but only as a minor peak (30% of the oriented and glycolated samples).	Illite [001]
4.8	Yes	Yes, but at 40% of the intensity of the orientated and glycolated samples	
5	Yes	Yes, but at 40% of the intensity of the orientated and glycolated samples	Illite [002]
4.8 shoulder of 5Å peak	Yes	Absent.	
3.7	Yes	Yes, but at 40% of the intensity of the orientated and glycolated samples	
3.34	Yes	Yes, but at 40% of the intensity of the orientated and glycolated samples	Illite [003] / Chlorite
2.5	yes	Yes, but only to 40% of the intensity of the orientated and glycolated samples.	

DPX199

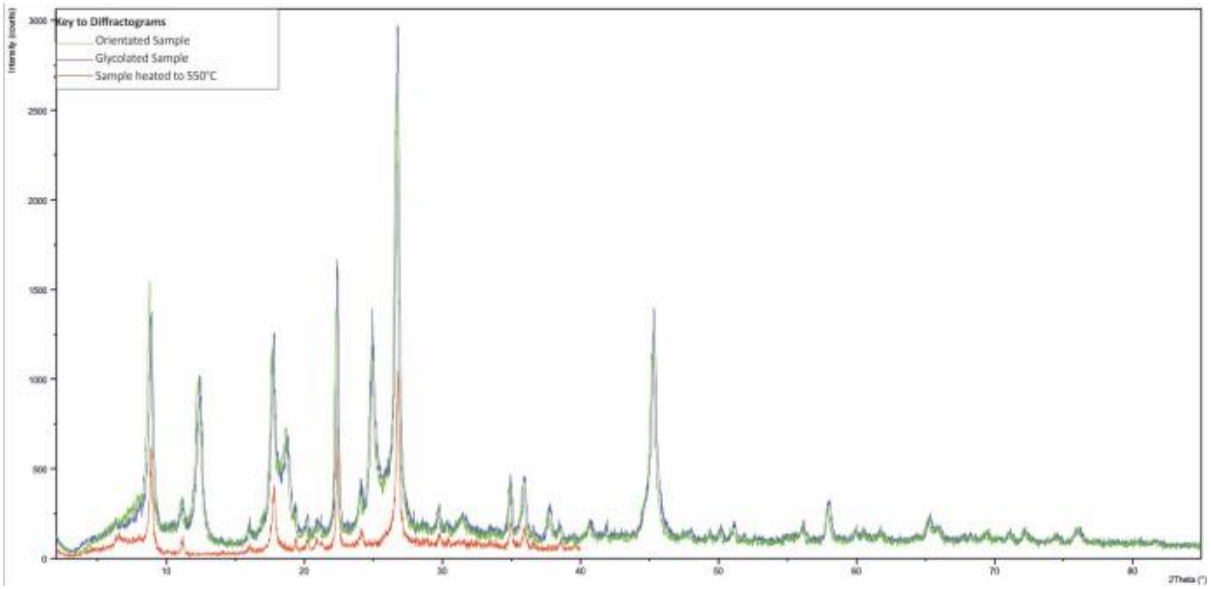

Peak observed in Orientated Sample? Å	Observed in Glycolated Sample? Å	Observed in Sample heated at 500°C Å	Applicable to which mineral? Å
8.7	Yes	Yes, but only as a minor peak (25% of the oriented and glycolated samples).	
5.58	Yes	Absent	
5.0	Yes – but at 20% greater intensity to the orientated sample	Yes, but only as a minor peak (20% of the oriented sample).	
4.25	Yes	Yes, but only at 30% of the intensity of the orientated and glycolated samples	
4.0	yes	absent	
3.69	yes	Yes, but only to 25% of the intensity of the orientated and glycolated samples.	
3.34	yes	Yes, but at 50% of the intensity of the orientated and glycolated samples	Illite [003]
2.5	yes	Yes, but only around 50% of the intensity of the orientated and glycolated samples.	

DPX226

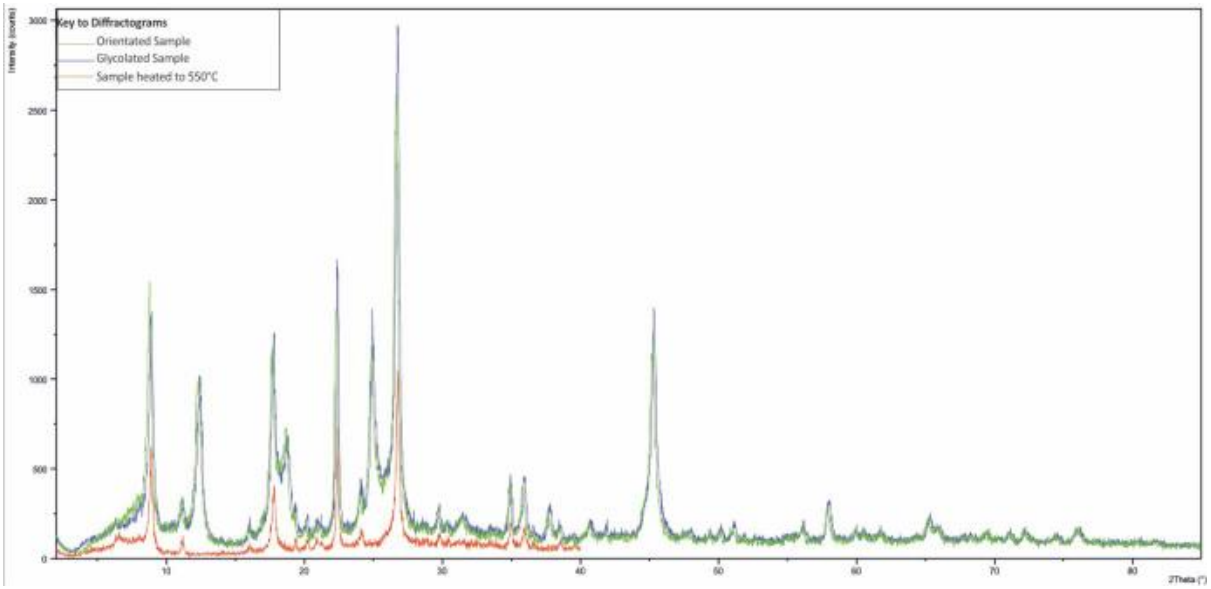

Peak observed in Orientated Sample? Å	Observed in Glycolated Sample? Å	Observed in Sample heated at 500°C Å	Applicable to which mineral? Å
No	No	Minor peak at 13.5Å	
9.9	Yes	Yes but only as a minor peak (35% of the oriented and glycolated samples).	Illite [001]
8.0	Yes	Yes, but only as a minor peak (20% of the oriented sample).	Kaolinite
7.12	Yes	Absent	Kaolinite [001] – collapse of peak on heating / Illite - secondary
5	Yes	Yes, but only at 30% of the intensity of the orientated and glycolated samples	Illite [002]
4.7	yes	absent	
4.6	yes	Yes, but only to 40% of the intensity of the orientated and glycolated samples.	
4.4	yes	Yes, but at 50% of the intensity of the orientated and glycolated samples	
4.0	Yes, at approximately 30% greater intensity of the orientated sample	Yes, but only around 30% of the intensity of the orientated sample.	
3.68	yes	Yes, but only around 30% of the intensity of the orientated sample.	
3.57	yes	Absent	Kaolinite [002]
3.32	yes	Yes, but only around 30% of the intensity of the orientated sample.	Illite [003]
3.0	yes	Yes, but only around 30% of the intensity of the orientated sample.	
2.56	yes	Yes, but only around 40% of the intensity of the orientated sample.	
2.5	yes	Yes, but only around 40% of the intensity of the orientated sample.	
2.37	yes	absent	

DPX232

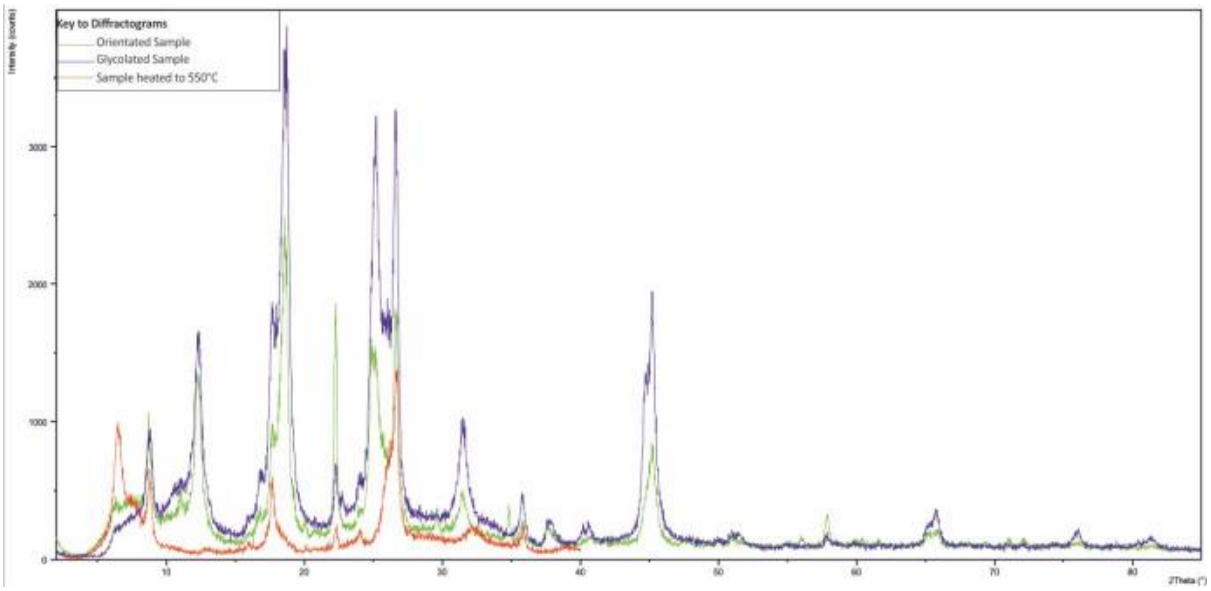

Peak observed in Orientated Sample? Å	Observed in Glycolated Sample? Å	Observed in Sample heated at 500°C Å	Applicable to which mineral? Å
No	No	Distinct peak at 13.5Å	
10.0	Yes	Yes but only as a minor peak (35% of the oriented and glycolated samples).	Illite [001]
8.0	Possibly, in an area of noise.	No	Kaolinite
7.18	Yes	Absent	Kaolinite [001] – collapse of peak on heating / Illite - secondary
5.2	yes	Absent	
5	Yes, at approximately 100% greater intensity of the orientated sample.	Yes, but only at 60% of the intensity of the orientated sample	Illite [002]
4.0	Yes, but at only 35% of the intensity of the ordinated sample	Yes, but at only 10% of the intensity of the ordinated sample	
4.6	yes	Yes, but only to 40% of the intensity of the orientated and glycolated samples.	
4.4	yes	Yes, but at 50% of the intensity of the orientated and glycolated samples	
4.0	Yes, at approximately 30% greater intensity of the orientated sample	Yes, but only around 30% of the intensity of the orientated sample.	
3.54	Yes, at approximately 40% greater intensity of the orientated sample	Absent	Kaolinite [002]
3.33	Yes, at approximately 40% greater intensity of the orientated sample	Yes, but only around 80% of the intensity of the orientated sample.	Illite [003]
2.8	Yes, but at only 35% of the intensity of the ordinated sample	Absent	
2.58	Absent	Absent	
2.5	Yes, at approximately 40% greater intensity of the orientated sample	Yes	

DPX235

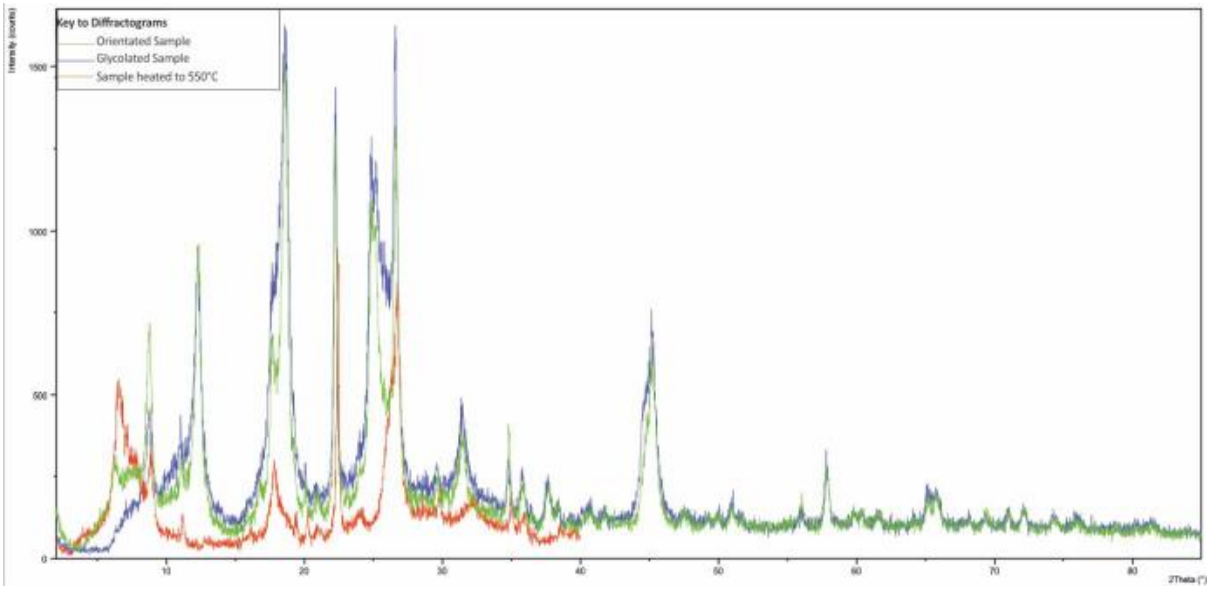

Peak observed in Orientated Sample? Å	Observed in Glycolated Sample? Å	Observed in Sample heated at 500°C Å	Applicable to which mineral? Å
14	No	No (Shoulder of peak at 13.5Å)	
No	No	Peak at 13.5Å	
10.00	Yes, but at 50% of the intensity of the orientated sample	Yes, but at 30% of the intensity of the orientated sample	Illite [001]
8.0	Yes	Yes, but only as a minor peak (20% of the oriented sample).	Kaolinite
7.12	Yes	Absent	Kaolinite [001] – collapse of peak on heating / Illite - secondary
5	Yes	Yes, but only at 30% of the intensity of the orientated and sample	Illite [002]
4.7	yes	absent	
4.6	yes	Yes, but only to 40% of the intensity of the orientated and glycolated samples.	
4.2	yes	Yes, but at 50% of the intensity of the orientated and glycolated samples	
3.9	yes	Yes, but only around 70% of the intensity of the orientated and glycolated samples.	
3.97	Yes	Yes, but only around 70% of the intensity of the orientated and glycolated samples .	
3.68	yes	Yes, but only around 30% of the intensity of the orientated sample.	
3.58	yes	Absent	Kaolinite [002]
3.35	yes	Yes, but only around 30% of the intensity of the orientated sample. Much wider peak (0.18Å)	Illite [003]
3.0	yes	Yes, but only around 30% of the intensity of the orientated sample.	
2.8	yes	Absent	
2.57	yes	Absent	
2.5	yes	Yes	
2.4	yes	Absent	

WR256A

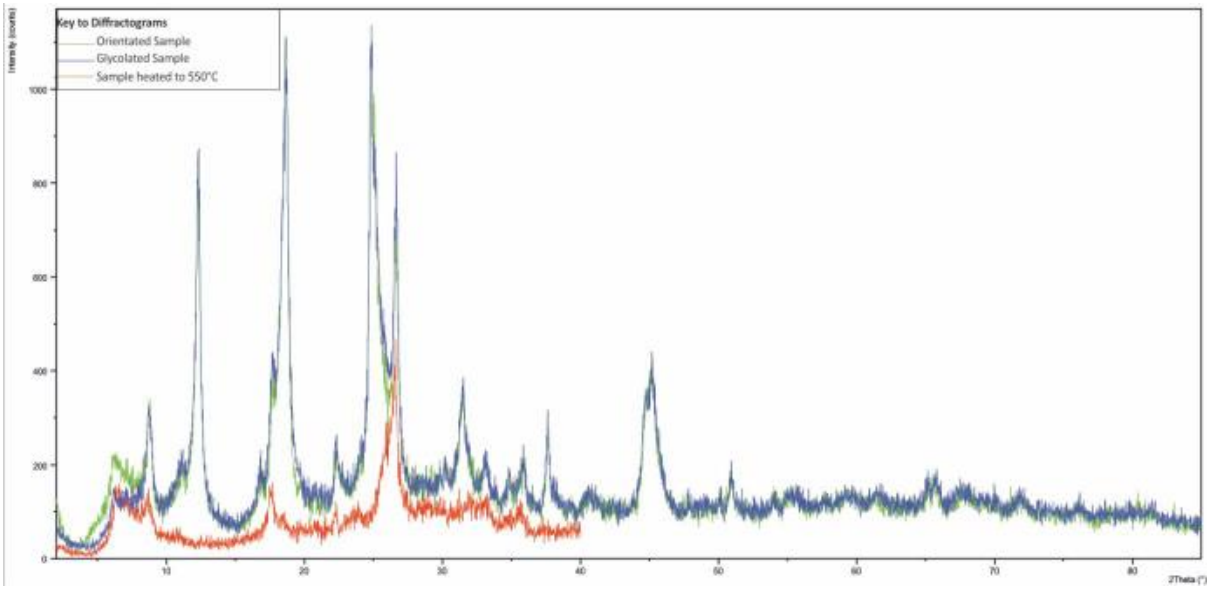

Peak observed in Orientated Sample? Å	Observed in Glycolated Sample? Å	Observed in Sample heated at 500°C Å	Applicable to which mineral? Å
13.8	Yes – but at 80% of the intensity of the orientated sample	Yes – but at 80% of the intensity of the orientated sample	
10.1	Yes	Absent	Illite [001]
8.0	Yes	Yes, but only as a minor peak (20% of the oriented sample).	Kaolinite
7.2	Yes	Absent	Kaolinite [001] – collapse of peak on heating / Illite - secondary
5.2	Yes	Absent	
5	yes	Yes, but only to 40% of the intensity of the orientated and glycolated samples.	Illite [002]
4.7	yes	Absent	
4.0	yes	Yes, but at 30% of the intensity of the orientated and glycolated samples	
3.6	yes	Absent	Kaolinite [002]
3.34	Yes	Yes, but only around 50% of the intensity of the orientated and glycolated samples .	Illite [003]
2.95	yes	Absent	
2.84	yes	Absent	
2.71	yes	Yes, but only around 30% of the intensity of the orientated sample. Much wider peak (0.18Å)	
2.57	yes	Absent	

WR256B

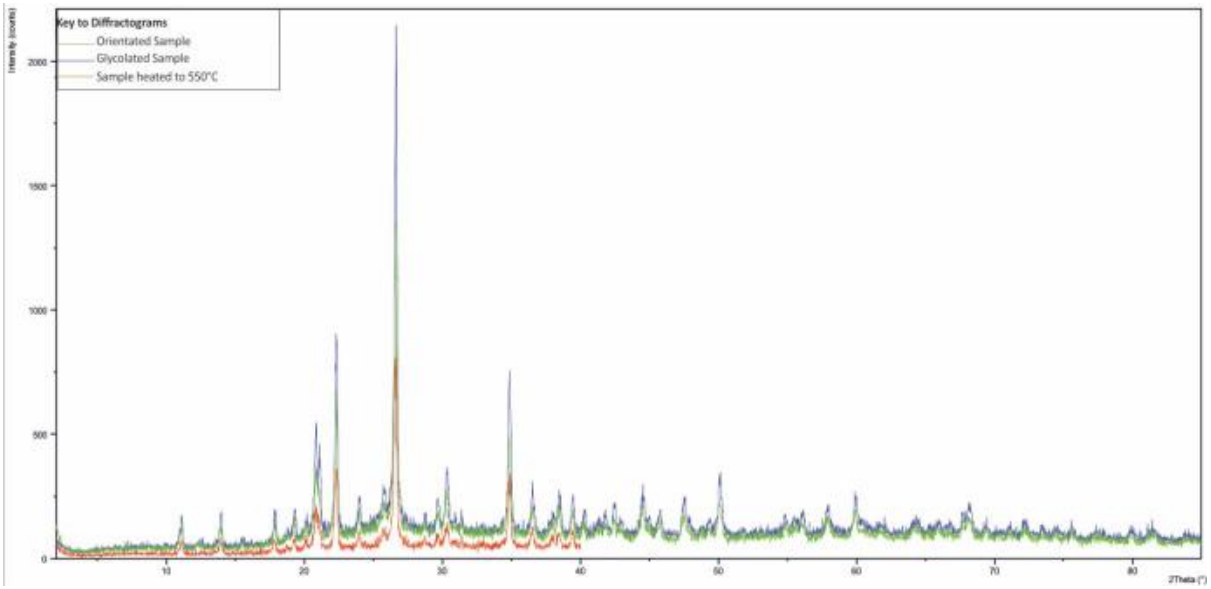

Peak observed in Orientated Sample? Å	Observed in Glycolated Sample? Å	Observed in Sample heated at 500°C Å	Applicable to which mineral? Å
No	14.0	Absent	
8.0	Yes, but at approximately 120% greater than the orientated sample	Yes, but only at 70% of the intensity of the orientated sample	Kaolinite
7.12	absent	Absent	Kaolinite [001] – collapse of peak on heating / Illite - secondary
6.3	Yes, but only at 70% of the intensity of the orientated sample	Yes, but only at 30% of the intensity of the orientated sample	
5	Yes, but at approximately 70% greater than the orientated sample	Yes, but only at 40% of the intensity of the orientated sample	Illite [002]
No	4.75	No	
4.6	Yes, but at approximately 120% greater than the orientated sample	Yes, but only at 70% of the intensity of the orientated sample	
4.4	Yes, but at approximately 70% greater than the orientated sample	Yes, but only at 40% of the intensity of the orientated sample	
4.26	No	These two peaks merge into one wide (0.4Å) peak at 4.26Å	
4.21	Yes, but at approximately 10% greater than the orientated sample		
3.9	yes	Absent	Kaolinite [002]?
3.35	yes	Yes, but only around 30% of the intensity of the orientated sample. Much wider peak (0.18Å)	Illite [003]
2.57	Yes, but at approximately 100% greater than the orientated sample	Yes, but only at 80% of the intensity of the orientated sample	
2.4	Absent	Yes, but only at 60% of the intensity of the orientated sample	
2.34	Yes, but at approximately 80% greater than the orientated sample	Yes, but only at 20% of the intensity of the orientated sample	

WR293A

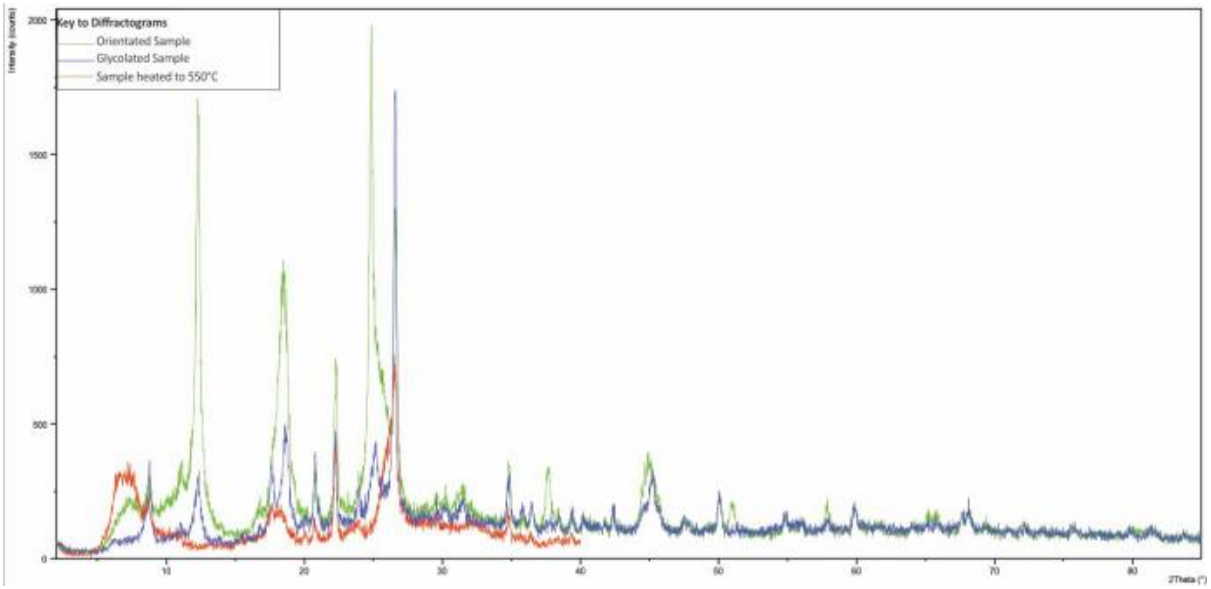

Peak observed in Orientated Sample? Å	Observed in Glycolated Sample? Å	Observed in Sample heated at 500°C Å	Applicable to which mineral? Å
14.36	No	No	Chlorite
No	No	Peak at 13.5Å	Unknown
10.00	Yes, but at 50% of the intensity of the orientated sample	Yes, but at 40% of the intensity of the orientated sample	Illite [001]
8.0	Yes	Possibly, low counts in sample resulting in noise.	Kaolinite
7.2	Yes	Absent	Kaolinite [001] – collapse of peak on heating / Illite - secondary
5	Yes, but only at 70% of the intensity of the orientated sample	Yes, but only at 30% of the intensity of the orientated sample	Illite [002]
4.7	Yes, but only at 70% of the intensity of the orientated sample	absent	
4.27	yes	Yes, but only to 40% of the intensity of the orientated and glycolated samples.	
4	yes	Yes, but at 50% of the intensity of the orientated and glycolated samples	
3.97	Yes	Yes, but only around 70% of the intensity of the orientated and glycolated samples .	
3.68	yes	Yes, but only around 30% of the intensity of the orientated sample.	
3.57	yes	Absent	Kaolinite [002]
3.35	yes	Yes, but only around 40% of the intensity of the orientated sample.	Illite [003]
2.57	yes	Yes, but only around 40% of the intensity of the orientated and glycolated sample.	
2.5	yes	Yes, but only around 40% of the intensity of the orientated and glycolated sample.	
2.4	yes	Yes, but only around 40% of the intensity of the orientated and glycolated sample.	

WR293B

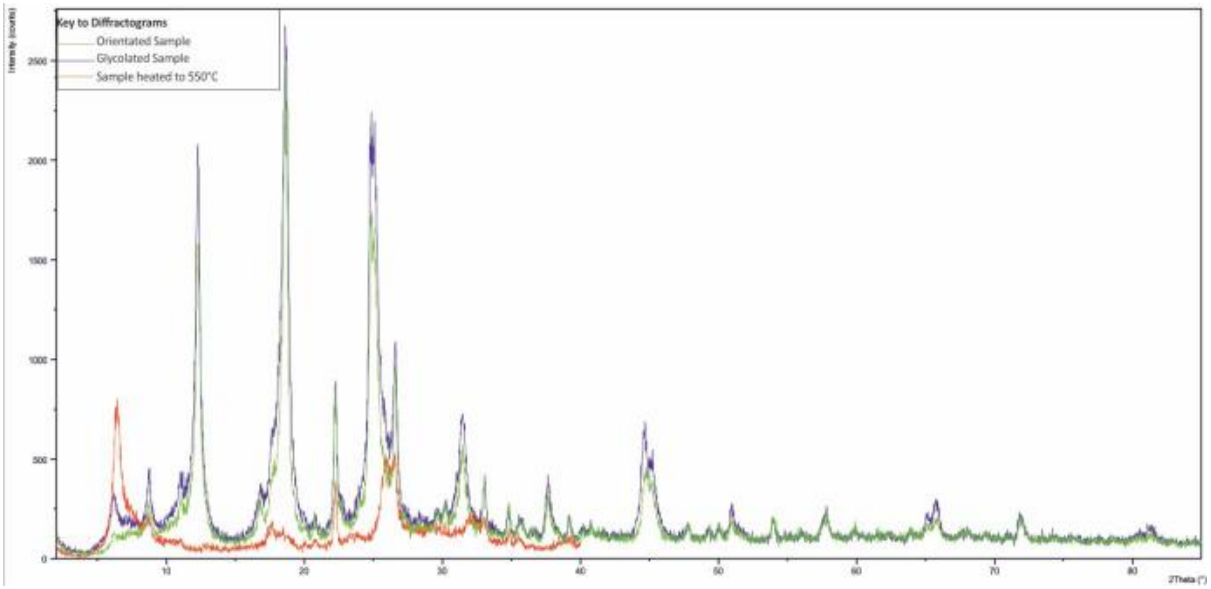

Peak observed in Orientated Sample? Å	Observed in Glycolated Sample? Å	Observed in Sample heated at 500°C Å	Applicable to which mineral? Å
No	14.36	Yes, but at 40% of the intensity of the glycolated sample , shift to 13.8Å	Chlorite?
10.00	Yes, but at 50% of the intensity of the orientated sample	absent	Illite [001]
8.0	Yes, but a noisy area of the Diffractograms	Possibly, low counts in sample resulting in noise.	Kaolinite
7.2	Yes, but at 30% of the intensity of the orientated sample	Absent	Kaolinite [001] – collapse of peak on heating / Illite - secondary
5.26	absent	absent.	
5	Yes, but only at 70% of the intensity of the orientated sample	Yes, but only at 30% of the intensity of the orientated sample	Illite [002]
4.7	Yes, but only at 12.5% of the intensity of the orientated sample	absent	
Obscured by 4.7 peak	4.6	absent	
4.4	absent	absent	
4.2	absent	absent	
4	Yes, but only at 50% of the intensity of the orientated sample	Yes, but only at 20% of the intensity of the orientated sample	
Wide peak from 3.6Å – 3.52Å	Wide peak from 3.6Å – 3.52Å, 600% the intensity of the orientated sample	absent	Kaolinite [002]
absent	Possibly present	Wide peak from 3.47Å – 3.36Å	
absent	3.35	absent	Illite [003]?
3.0	absent	absent	
2.9	yes	absent	
absent	2.84 wide peak	absent	
absent	2.7	absent	
2.57	yes	absent	
absent	2.38	absent	
2.34	absent	absent	

WR301A

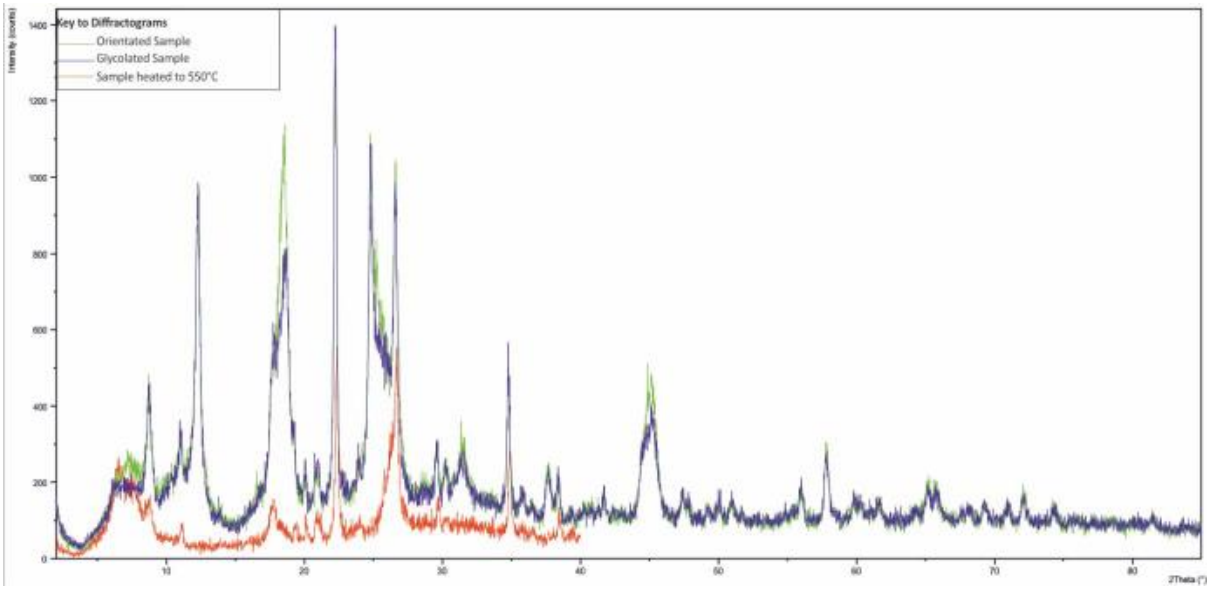

Peak observed in Orientated Sample? Å	Observed in Glycolated Sample? Å	Observed in Sample heated at 500°C Å	Applicable to which mineral? Å
No, but a general area of higher counts	No, but a general area of higher counts	Minor peak at 13.5Å	Chlorite?
10.00	Yes	Yes, but at 20% of the intensity of the orientated sample	Illite [001]
8.0	Yes	Yes, but only at 30% of the intensity of the orientated sample	Kaolinite
7.2	Yes	Absent	Kaolinite [001] – collapse of peak on heating / Illite - secondary
5	Yes	Yes, but only at 10% of the intensity of the orientated sample	Illite [002]
4.7 – wide peak, lots of noise	Yes, but only at 70% of the intensity of the orientated sample	absent	
4.27	yes	Yes, but only to 40% of the intensity of the orientated and glycolated samples.	
3.57 – slope to 3.39	Yes (as with orientated)	No	Kaolinite [002]
3.34	Yes	Yes, but only around 50% of the intensity of the orientated and glycolated samples .	Illite [003]
3.01	yes	Yes, but only around 30% of the intensity of the orientated sample.	
2.95	yes	Absent	
2.84 – broad peak	yes	Absent	
2.58	yes	Yes, but only around 40% of the intensity of the orientated and glycolated sample. Shift to 2.57	
2.38	yes	Absent	
2.34	yes	Yes, but only around 40% of the intensity of the orientated and glycolated sample.	

WR315A

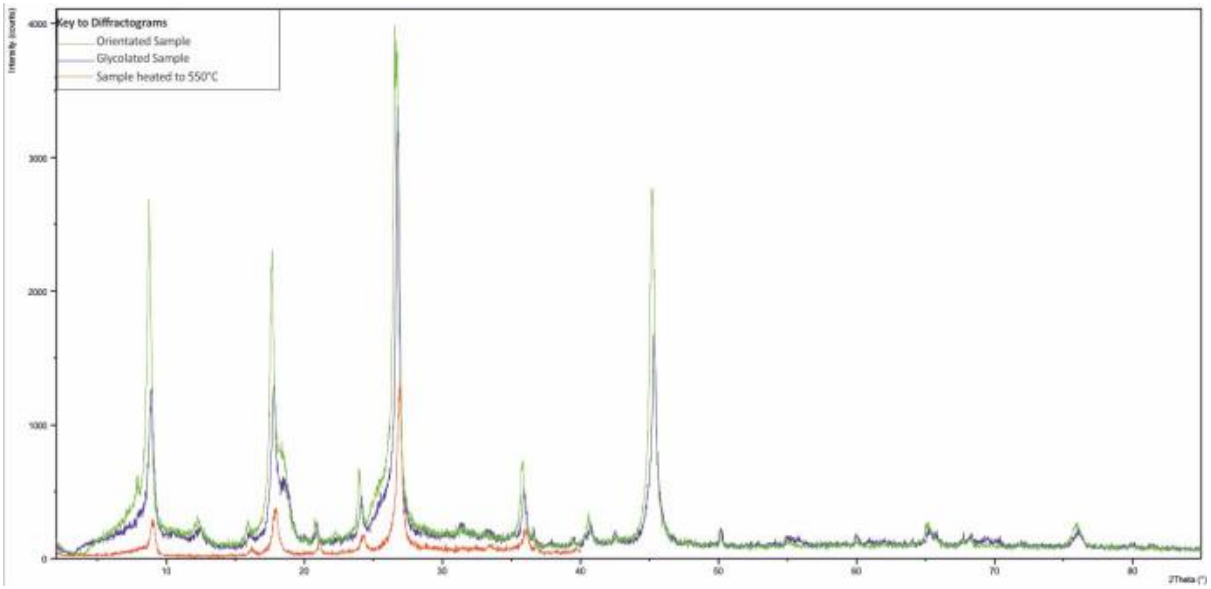

Peak observed in Orientated Sample? Å	Observed in Glycolated Sample? Å	Observed in Sample heated at 500°C Å	Applicable to which mineral? Å
10.17	Yes, but only at 40% of the intensity of the orientated sample	Yes, but at 30% of the intensity of the orientated sample	Illite [001]
7.0	Yes	Absent	Kaolinite [001] – collapse of peak on heating / Illite - secondary
5.5	Yes	Absent	
5.0	Yes, but only at 50% of the intensity of the orientated sample	Yes, but at 30% of the intensity of the orientated sample	Illite [002]
4.8	Yes, but only at 80% of the intensity of the orientated sample	Absent	
4.2	yes	Absent	
3.7	yes	Yes, but at 35% of the intensity of the orientated and glycolated samples	
3.44	Yes, but only at 80% of the intensity of the orientated sample	Yes, but at 40% of the intensity of the orientated sample.	Illite [003]?
2.5	yes	Yes, but only around 40% of the intensity of the orientated sample	

WR315B

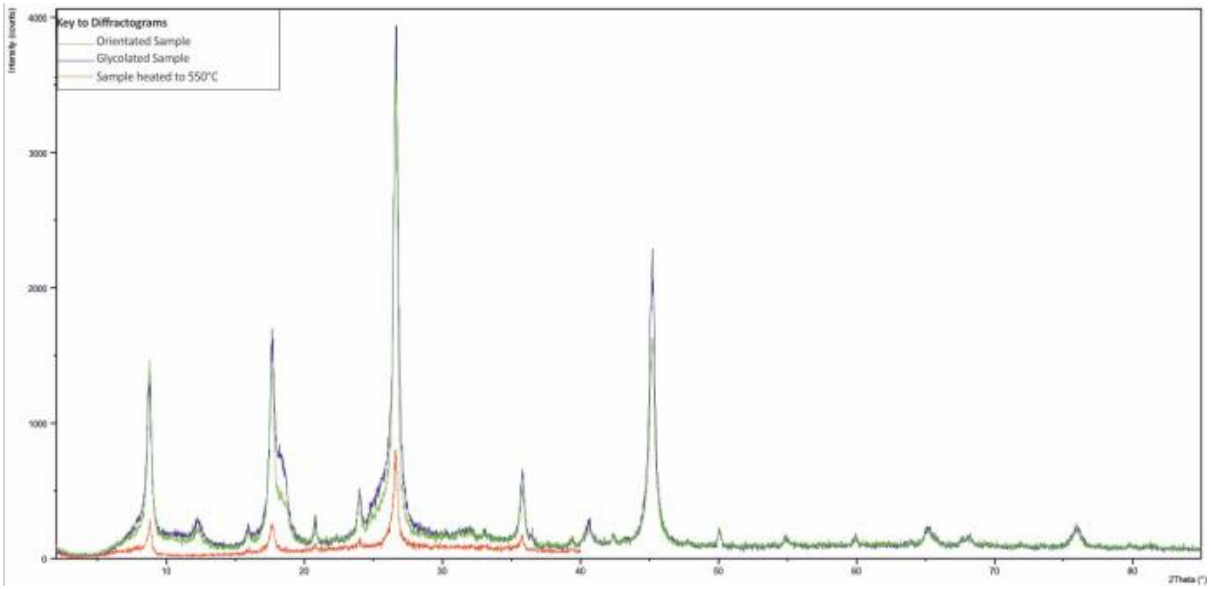

Peak observed in Orientated Sample? Å	Observed in Glycolated Sample? Å	Observed in Sample heated at 500°C Å	Applicable to which mineral? Å
10.00	Yes	Yes, but at 20% of the intensity of the orientated sample	Illite [001]
7.2	Yes	Absent	Kaolinite [001] – collapse of peak on heating / Illite - secondary
5.56	yes	Absent	
5	Yes	Yes, but only at 10% of the intensity of the orientated sample	Illite [002]
4.7 – wide peak, lots of noise	Yes, but only at 70% of the intensity of the orientated sample	absent	
4.27	yes	Yes, but only to 40% of the intensity of the orientated and glycolated samples.	
3.35	Yes	Yes, but only around 30% of the intensity of the orientated and glycolated samples .	Illite [003]
2.50	yes	Yes, but only around 25% of the intensity of the orientated and glycolated sample. Shift to 2.57	

WR352B

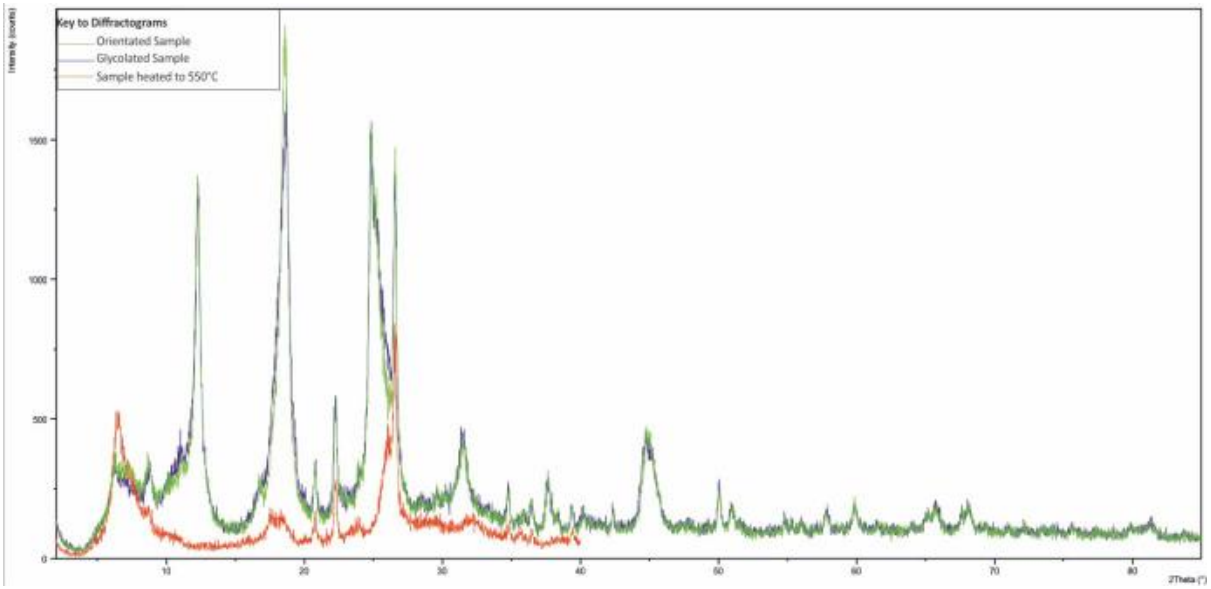

Peak observed in Orientated Sample? Å	Observed in Glycolated Sample? Å	Observed in Sample heated at 500°C Å	Applicable to which mineral? Å
No, but a general area of higher counts	No, but a general area of higher counts	Minor peak at 13.67Å	
10.00	Yes	Yes, but at 20% of the intensity of the orientated sample	Illite [001]
8.0	Yes	Yes, but only at 30% of the intensity of the orientated sample	Kaolinite
7.2	Yes	Absent	Kaolinite [001] – collapse of peak on heating / Illite - secondary
5	Yes	Yes, but only at 10% of the intensity of the orientated sample	Illite [002]
4.7 – wide peak, lots of noise	Yes, but only at 70% of the intensity of the orientated sample	absent	
4.27	yes	Yes, but only to 40% of the intensity of the orientated and glycolated samples.	
4.0	yes	Yes, but at 40% of the intensity of the orientated and glycolated samples	
3.7	Yes, very minor	Possibly, if present only at 20% of the intensity of the orientated and glycolated samples	
3.57 – slope to 3.39	Yes (as with orientated)	No	Kaolinite [002]
3.35	Yes	Yes, but only around 50% of the intensity of the orientated and glycolated samples .	Illite [003]
2.84 – broad peak	yes	Absent	
2.57	yes	Yes, but only around 40% of the intensity of the orientated and glycolated sample. Shift to 2.57	
2.46	yes	Absent	
2.38	yes	Absent	
2.28	yes	Absent	

WR404

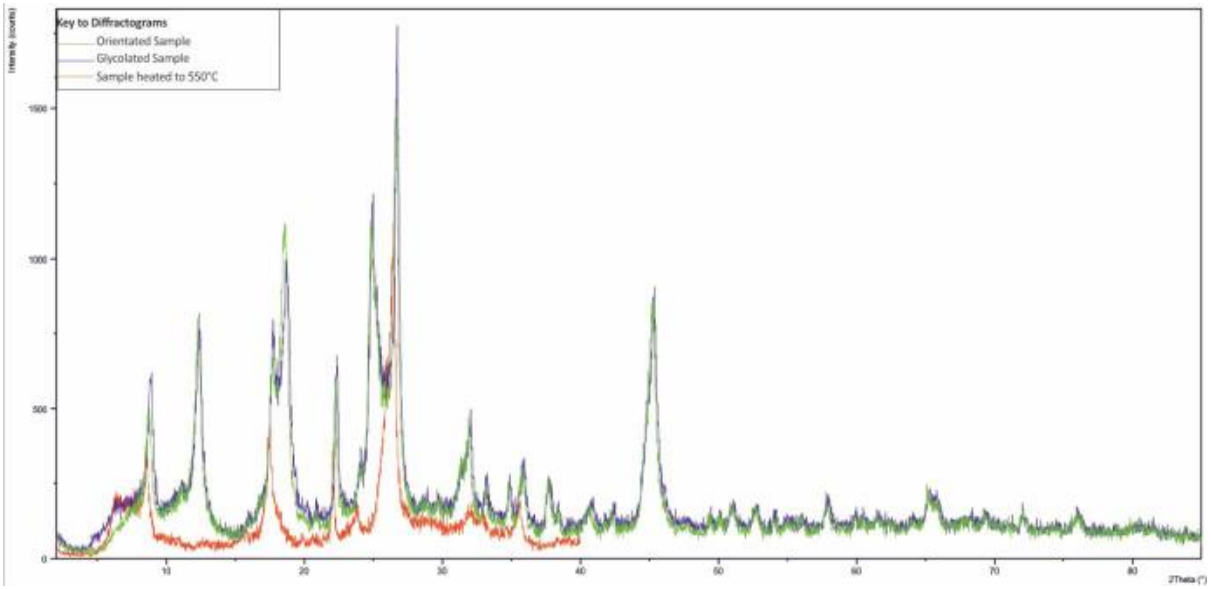

Peak observed in Orientated Sample? Å	Observed in Glycolated Sample? Å	Observed in Sample heated at 500°C Å	Applicable to which mineral? Å
No, but a general area of higher counts	No, but a general area of higher counts	Peak at 13.43Å	Unknown, possibly Chlorite.
10.00	Yes	Yes, but at 30% of the intensity of the orientated sample	Illite [001]
8.0	Yes	Yes, but only at 30% of the intensity of the orientated sample	Kaolinite
7.2 and an area of elevated counts between 9.4Å to 7.2Å	Yes	Absent	Kaolinite [001] – collapse of peak on heating / Illite - secondary
5.5	yes	Yes, but only at 30% of the intensity of the orientated sample	
5	Yes	Yes, but only at 10% of the intensity of the orientated sample	Illite [002]
4.0	yes	Yes, but at 40% of the intensity of the orientated and glycolated samples	
3.7	Yes, very minor	Possibly, if present only at 20% of the intensity of the orientated and glycolated samples	
3.57 – slope to 3.39	Yes (as with orientated)	No	Kaolinite [002]
3.35	Yes	Yes, but only around 40% of the intensity of the orientated and glycolated samples .	Illite [003]
2.84	yes	Absent	
2.5	yes	Yes, but only around 40% of the intensity of the orientated and glycolated sample. Shift to 2.57	
2.38	yes	Absent	

WR409A

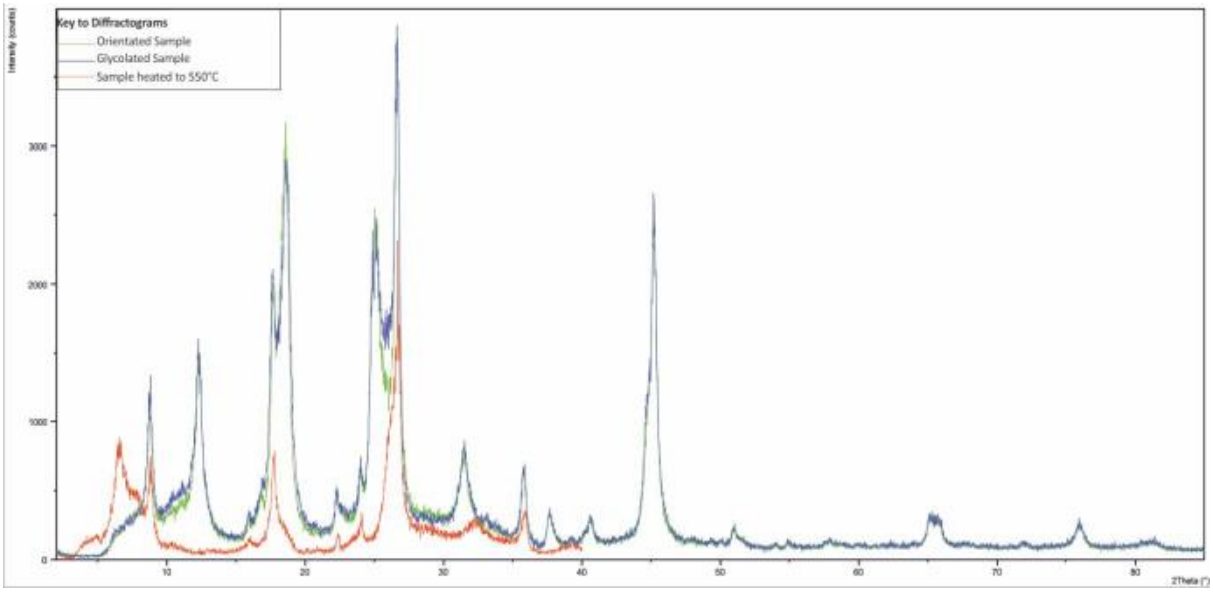

Peak observed in Orientated Sample? Å	Observed in Glycolated Sample? Å	Observed in Sample heated at 500°C Å	Applicable to which mineral? Å
No, but a part of the slope to 9Å	A wide, diffuse peak at 13.8Å to 11Å, also part of slope to 9Å	As with Glycolated sample	Unknown.
10.00	Yes, but at 70% of the intensity of the orientated sample	Yes, but at 30% of the intensity of the orientated sample	Illite [001]
8.0	Yes	Yes, but only at 30% of the intensity of the orientated sample	Kaolinite
7.2	Yes	Absent	Kaolinite [001] – collapse of peak on heating / Illite - secondary
5	Yes	Yes, but only at 40% of the intensity of the orientated sample, peak is at 5.07Å	Illite [002]
4.7	Yes, but only at 90% of the intensity of the orientated sample, peaks at 7.3Å	absent	
4.27	yes	Yes, but only to 40% of the intensity of the orientated and glycolated samples.	
4.0	yes	Yes, but at 40% of the intensity of the orientated and glycolated samples	
3.57 – slope to 3.39	Yes (as with orientated)	No	Kaolinite [002]
3.35	Yes	Yes, but only around 50% of the intensity of the orientated and glycolated samples. Broad peak from 3.55Å	Illite [003]
2.8	yes	Absent	
2.57	yes	Absent	
2.5	yes	Yes, but only around 40% of the intensity of the orientated and glycolated sample. Shift to 2.52	
2.46	yes	Absent	
2.38	yes	Absent	
2.28	yes	Absent	

Appendix 5.3 – Clay Concentrate XRD Samples

Sample Locations

Sample (DPX)	Lithology	Drillhole Collar Number	Location (mbrt)
DPX023	base	332	439.7
DPX030	MfX	282	428.62
DPX039	MfX	282	421.3
DPX042	MfX	282	420.6
DPX064	base	358	402.89
DPX069	base	329	400.05
DPX072	base	329	371.46
DPX074	base	329	360.7
DPX075	base	301	358.58
DPX076	base	301	358.58
DPX077	base	301	344.05
DPX079	base	256	303.45
DPX080	base	293	301.4
DPX085	base	387	253
DPX087	base	387	250.5
DPX131	MfX	380	216.4
DPX134	MfX	380	308.3
DPX136	MfX	380	320.2
DPX137	MfX	380	282.2
DPX138	MfX	380	268.8
DPX139	MfX	380	270.7
DPX141	MfX	380	70.2
DPX145	MfX	380	326.8
DPX147	MfX	284	94.5
DPX149	MfX	277	282
DPX150	MfX	277	240
DPX153	MfX	277	18.1
DPX161	MfX	277	111.7
DPX171	MfX	379	403.7
DPX201	MfX	286	283.5
DPX205	MfX	321	40.9
DPX208	MfX	321	80.7

Sample (DPX)	Lithology	Drillhole Collar Number	Location (mbrt)
DPX210	MfX	321	99.6
DPX221	MfX	321	170.3
DPX250	MfX	350	433.4
DPX256	MfX	373	397.5
DPX172	MfX	379	403.1
DPX175	MfX	286	25.7
DPX176	MfX	286	28.1
DPX177	MfX	286	31.1
DPX181	MfX	286	57
DPX189	MfX	286	125.5
DPX193	MfX	286	156.6
DPX194	MfX	286	188.5
DPX195	MfX	286	192.9
DPX198	MfX	286	22.6
DPX257	MfX	291	29.2
DPX265	MfX	291	88.7
DPX269	MfX	291	134.1
DPX280	MfX	353	23.55
WS Shear Samples			
WR256-a	MfX	256	190.7
WR256-b	MfX	256	224.1
WR282-a	base	282	398.9
WR293-a	MfX	293	244.9
WR293-b	MfX	293	251
WR301a	MfX	301	315
WR301-b	MfX	301	319
WR315a	MfX	315	312.8
WR352a	MfX	352	316.2
WR352b	MfX	352	323.8
WR404	MfX	404	323.3
WR409a	MfX	409	317.7

Methods

Clay concentrates were produced in-house at the University of Ottawa, seventy four clay concentrates have been used to identify illite polytypes in the coarser grained illites. They were produced by grinding at least 100 grams of dry samples to <64µm. Ground powder was placed into a 15ml centrifuge tube up to the 10ml level (around 15-20 grams of powder) to which water was added up to 15ml. Samples were then agitated for a period of 10 minutes, then subjected to whirlpool agitation for 5 minutes. After this time they were placed in a centrifuge and spun for 15 minutes at 2500rpm. Clays and fine particles were removed from the top of the centrifuge tubes, the processes repeated to enhance recovery and samples were dried at room temperature (~20°C). Samples typically formed a very fine-grained clay-rich powder. Quartz was intentionally retained in samples to act as calibration for the Diffractogram, recovery rates for clay within the sandstones ranged from 5% to up to 60%.

Clay concentrates were produced to circumvent the issue of low amounts of clay within the sandstones and the nature of X-Ray Diffraction (XRD) in the detection of minor phases (typically phases of <5 wt% cannot be detected), they were also used to provide coarse illite samples for illite polytype analysis along the clay fraction samples.

All samples were analysed on a Philips PW 3020 X'Pert Diffractometer at the University of Ottawa's X-Ray Core Facility. Measurements were acquired at 45-kV accelerating voltage, 40-mA current, with exact measurement parameters varying per a sample.

Results

The following diffractogram of samples analysed via XRD are presented; diffractograms are displayed on the y-axis as 'square root' and on the x-axis between 3° and 30° (29.1Å to 3Å).

DPX101

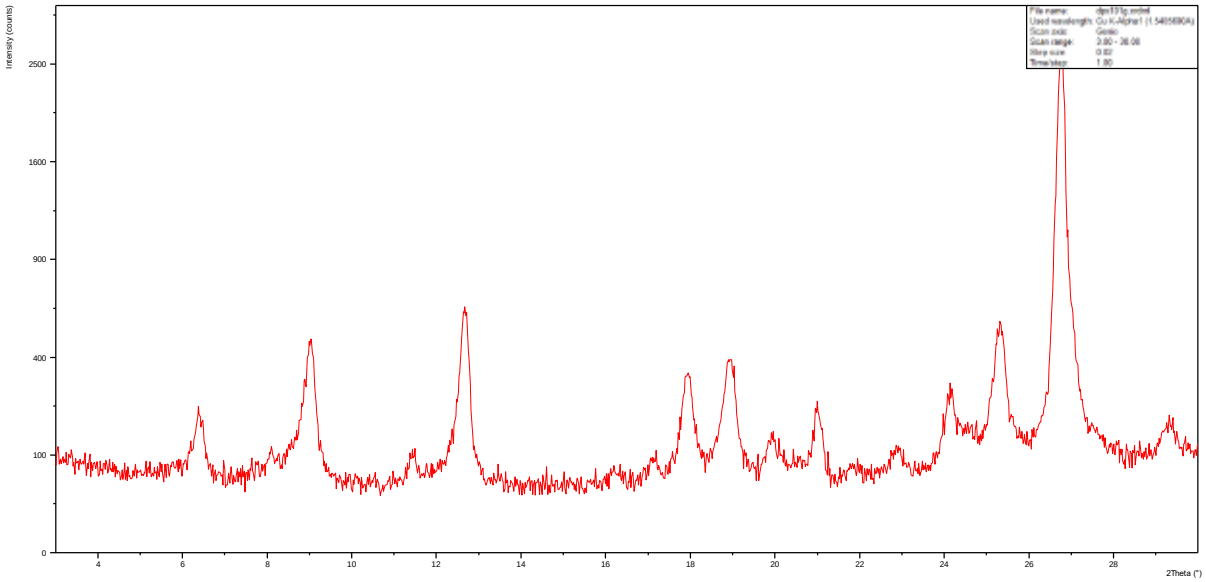

DPX105

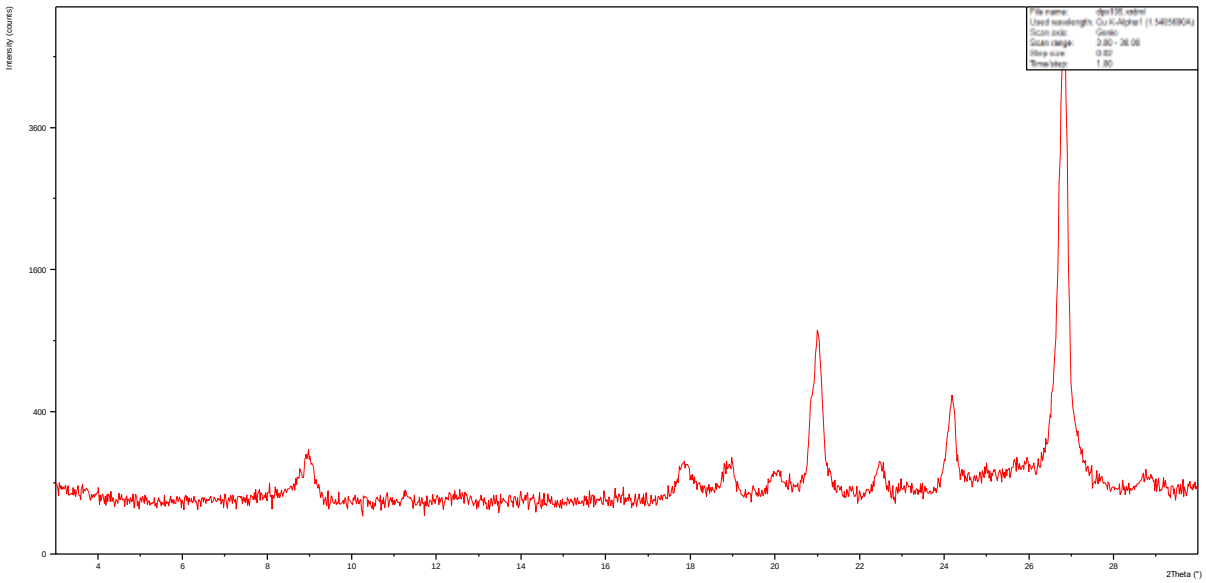

DPX131

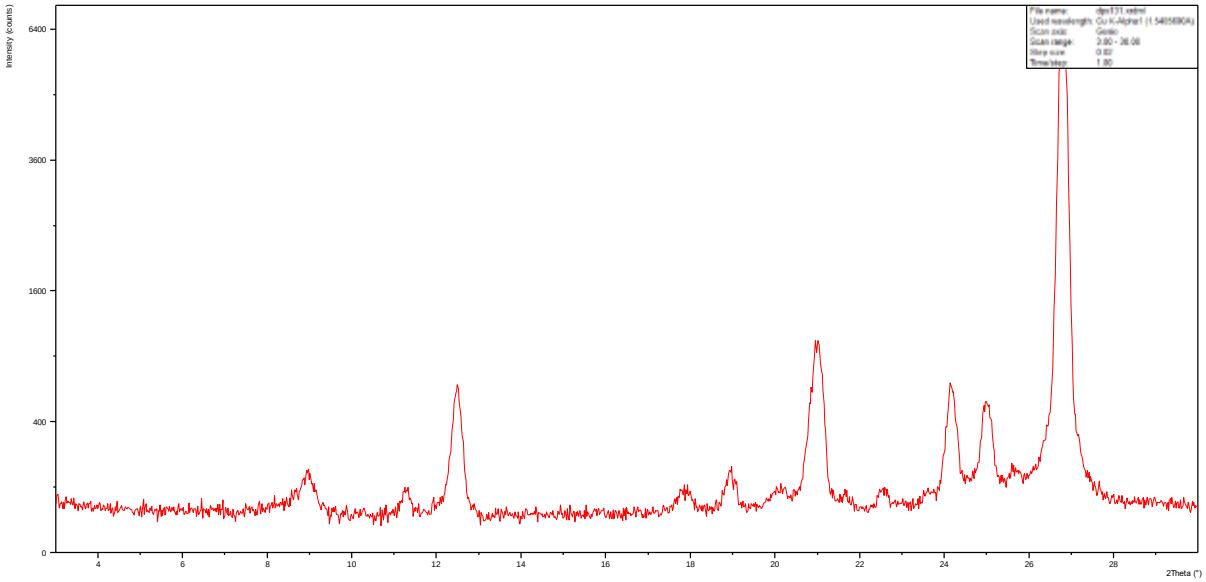

DPX134

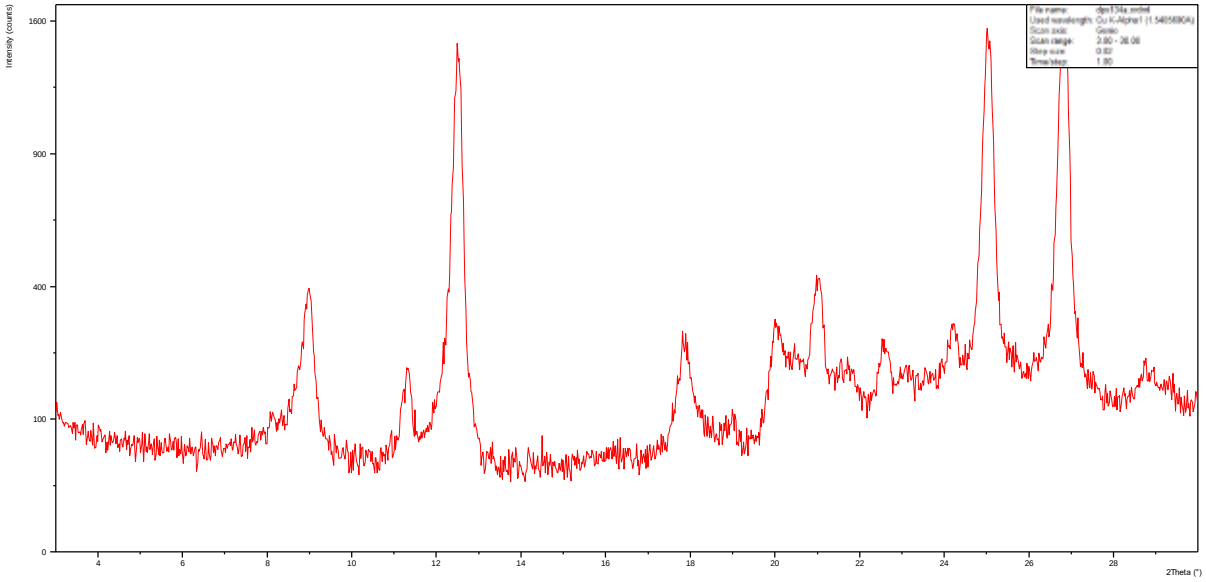

DPX137

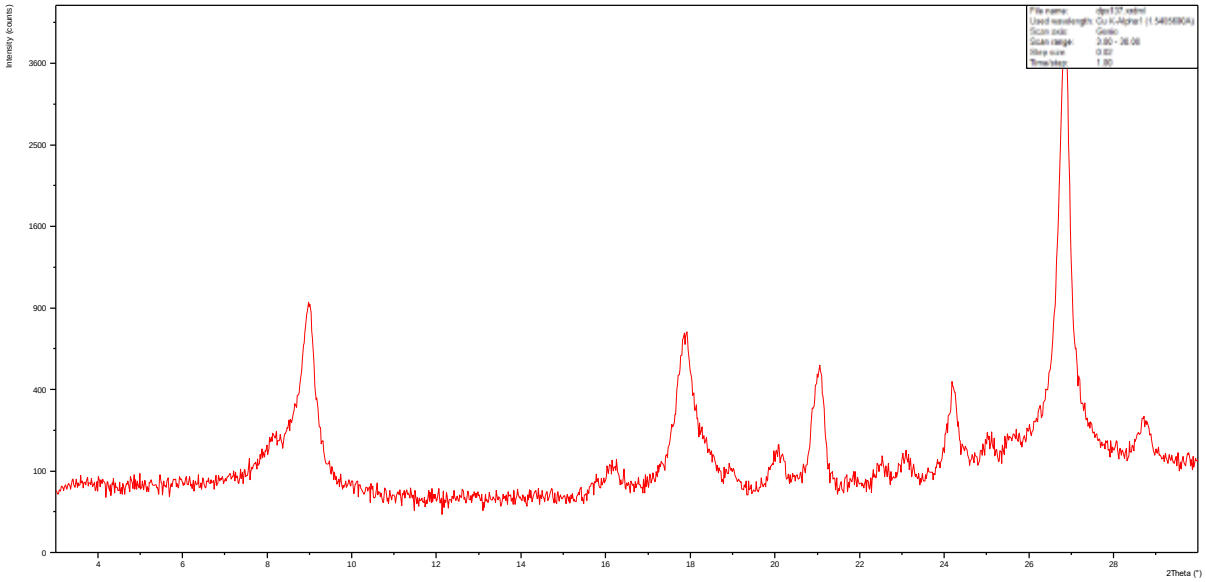

DPX138

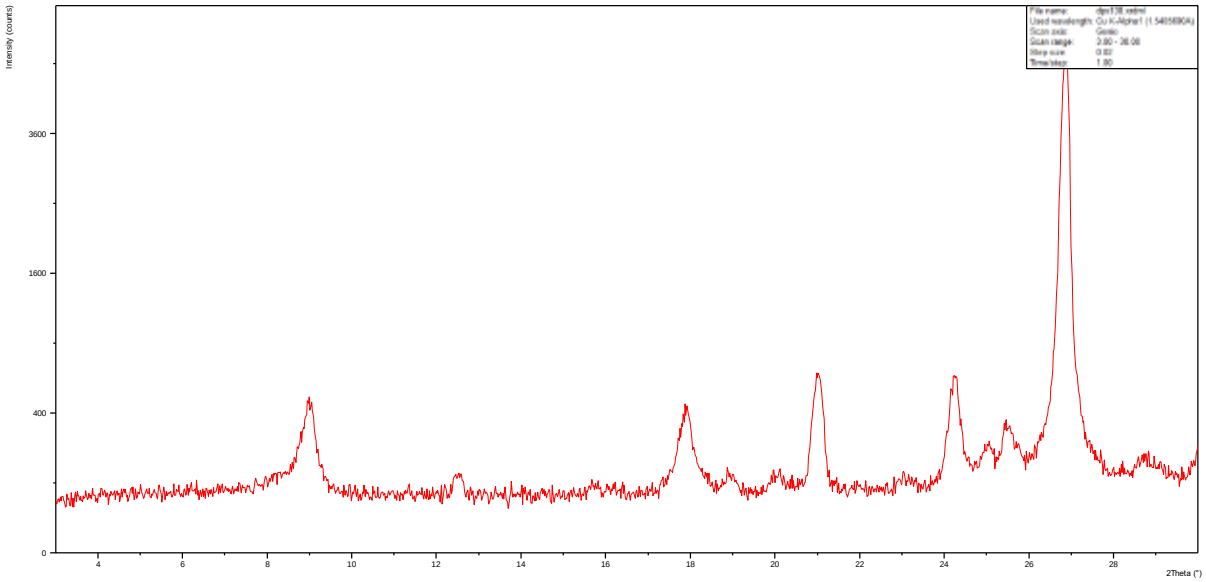

0DPX139

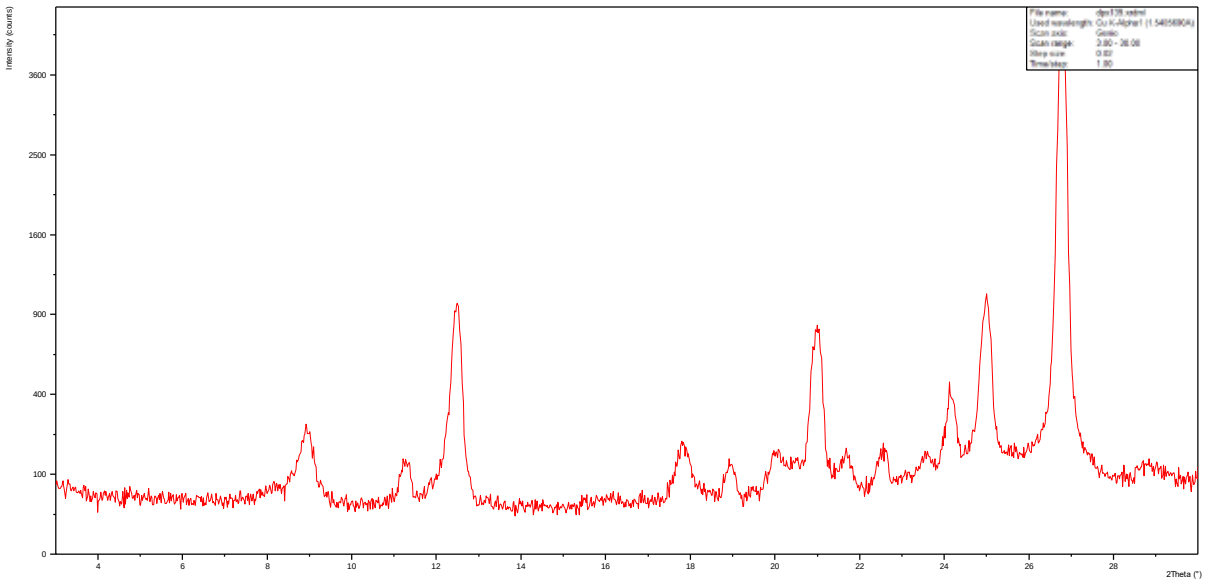

DPX141

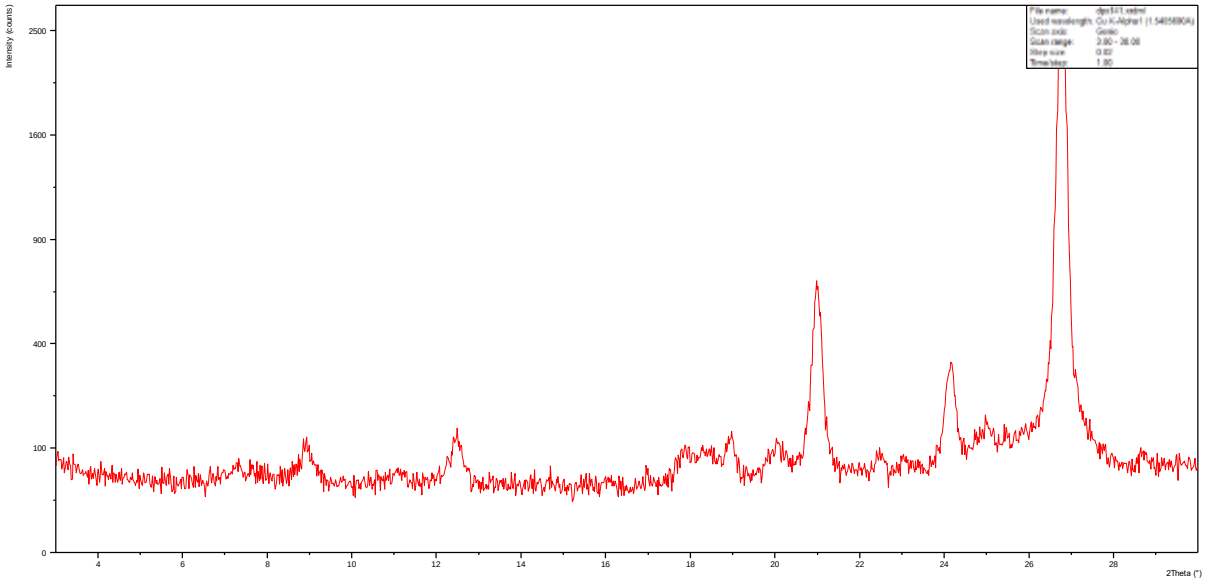

DPX145

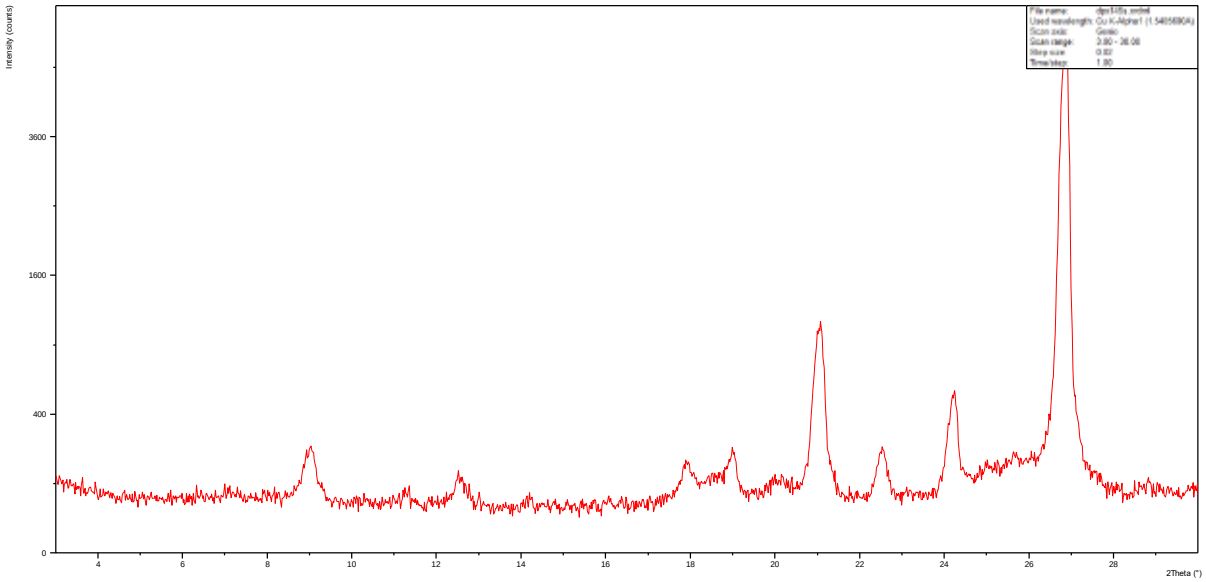

DPX 147

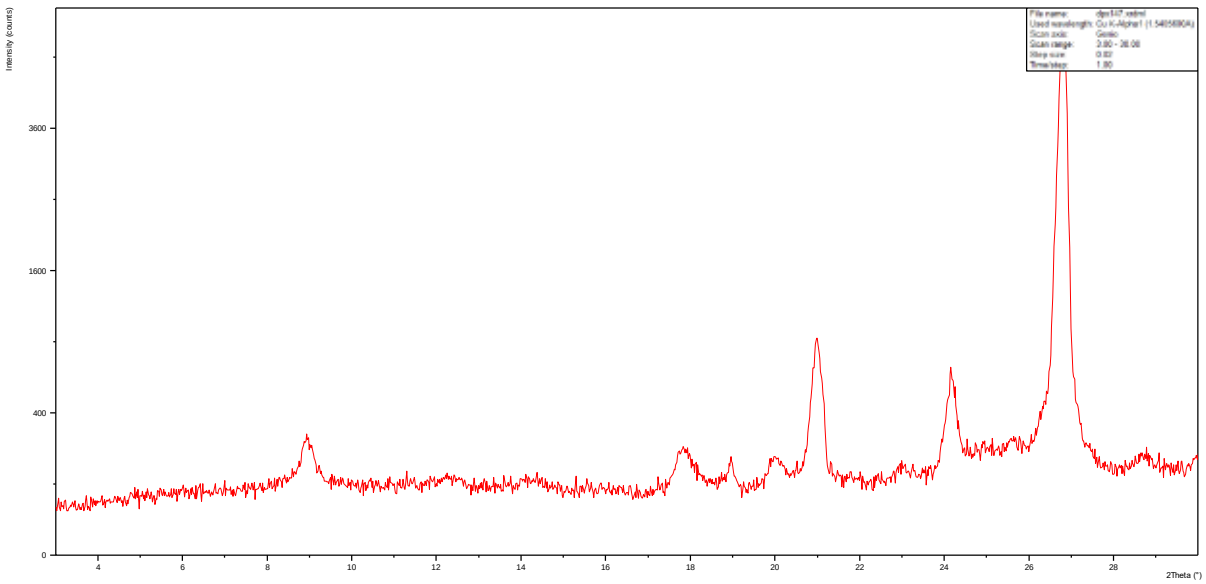

DPX149

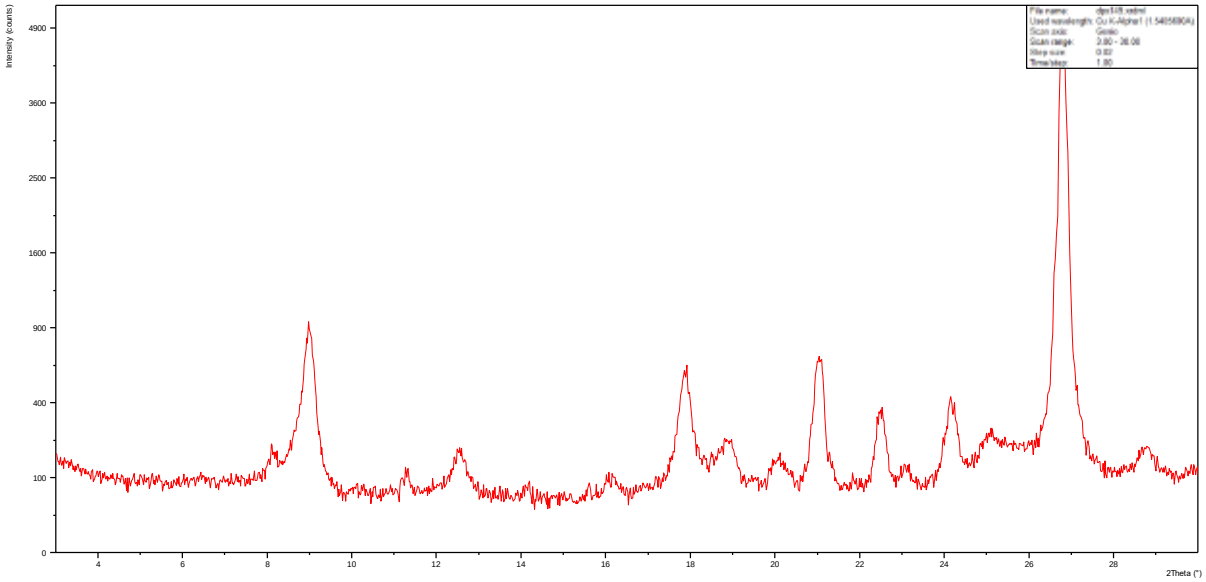

DPX150

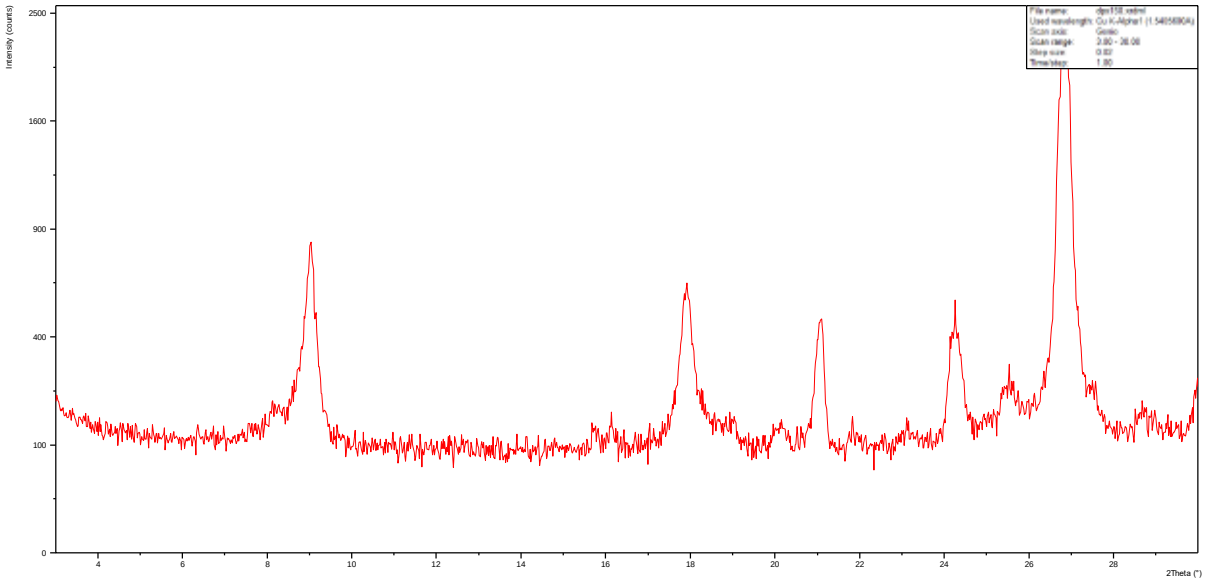

DPX153

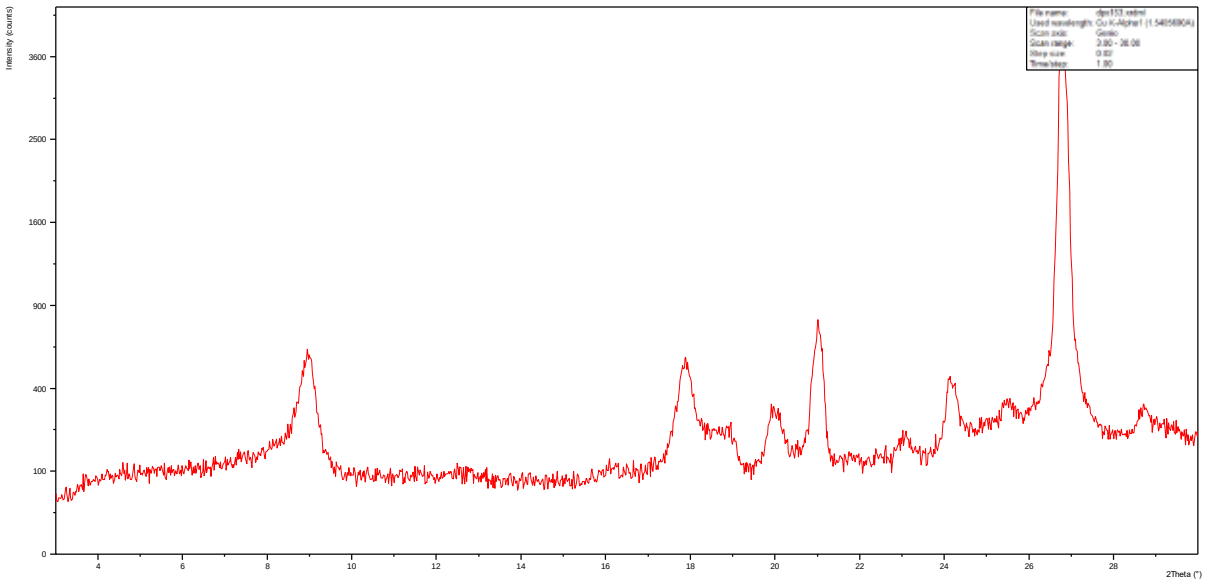

DPX155

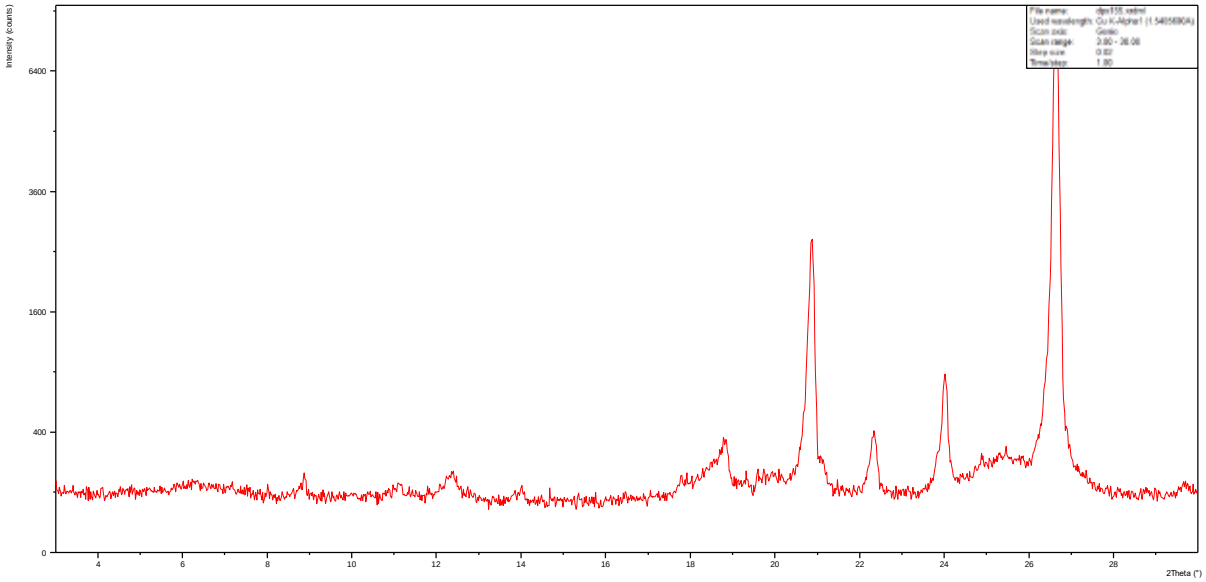

DPX161

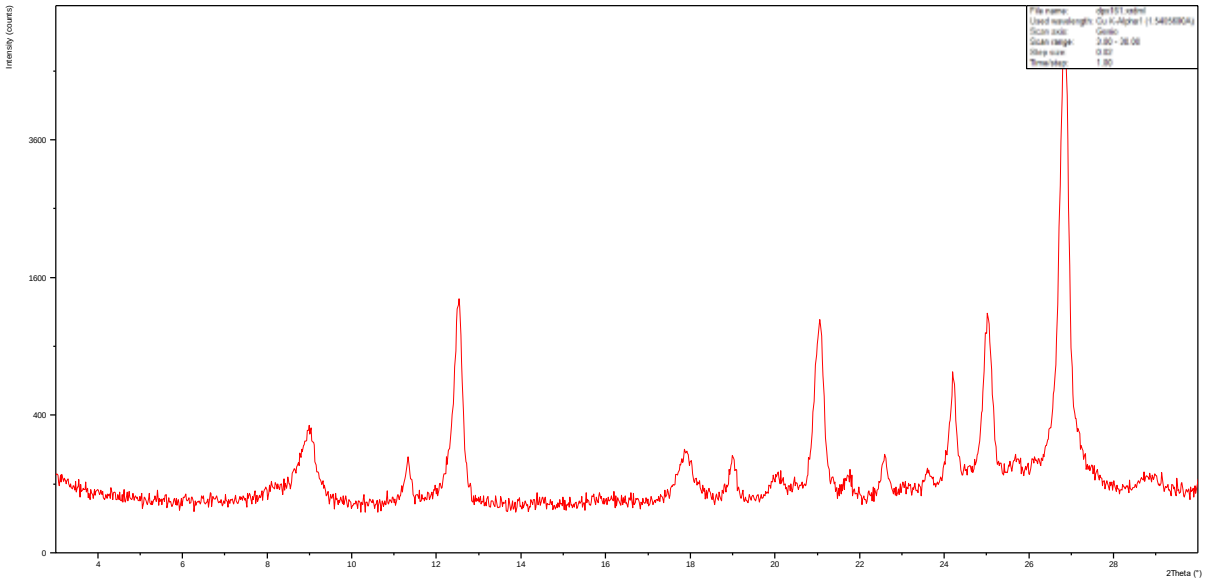

DPX162

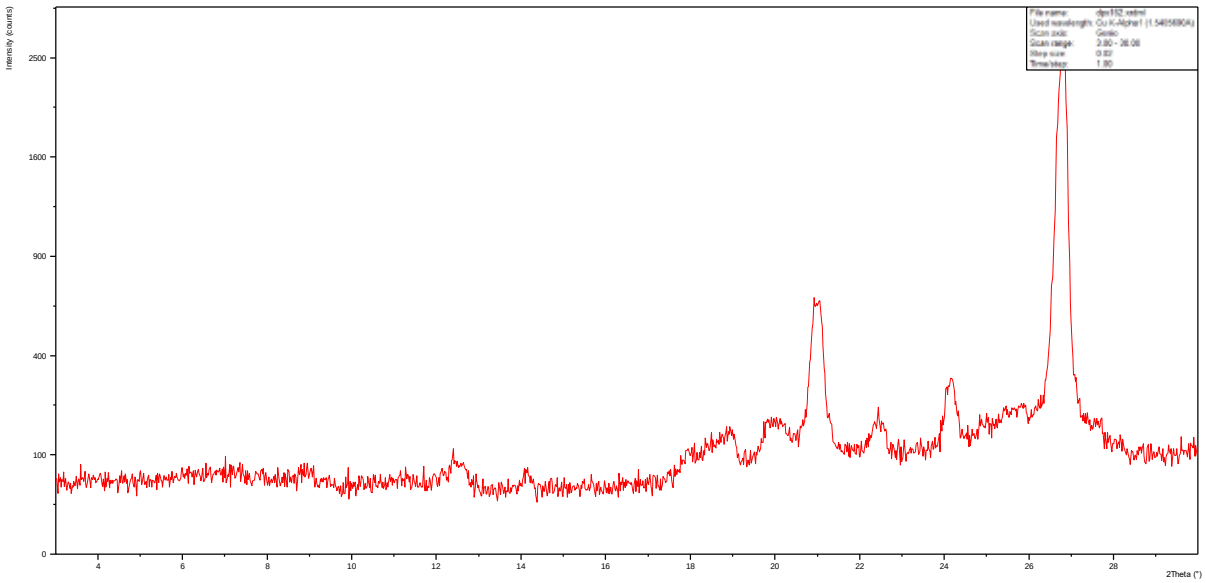

DPX165

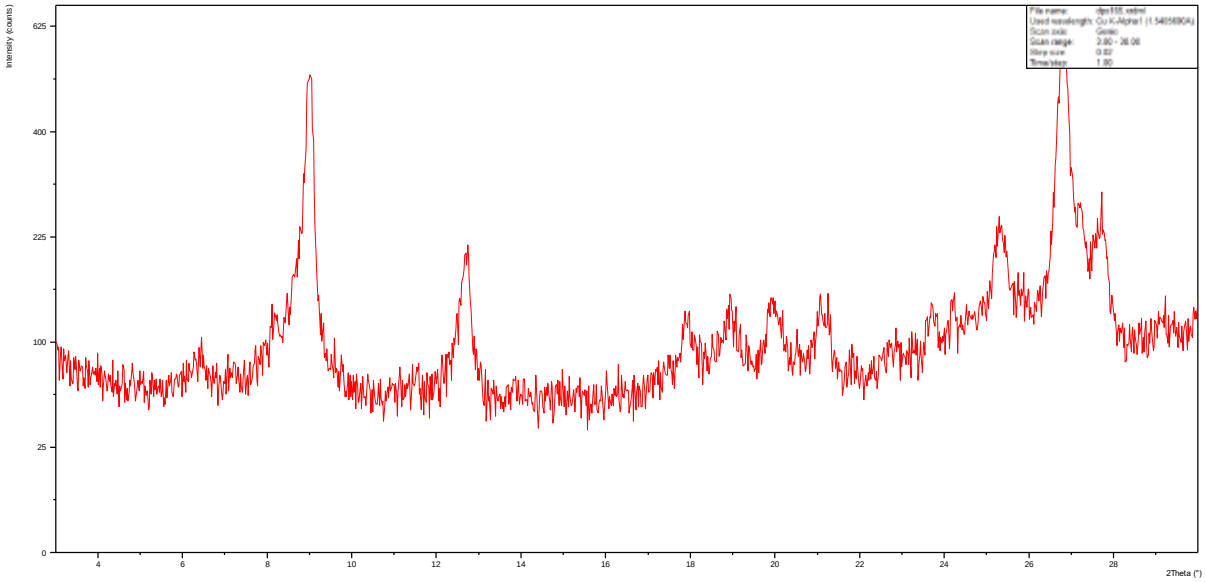

DPX166

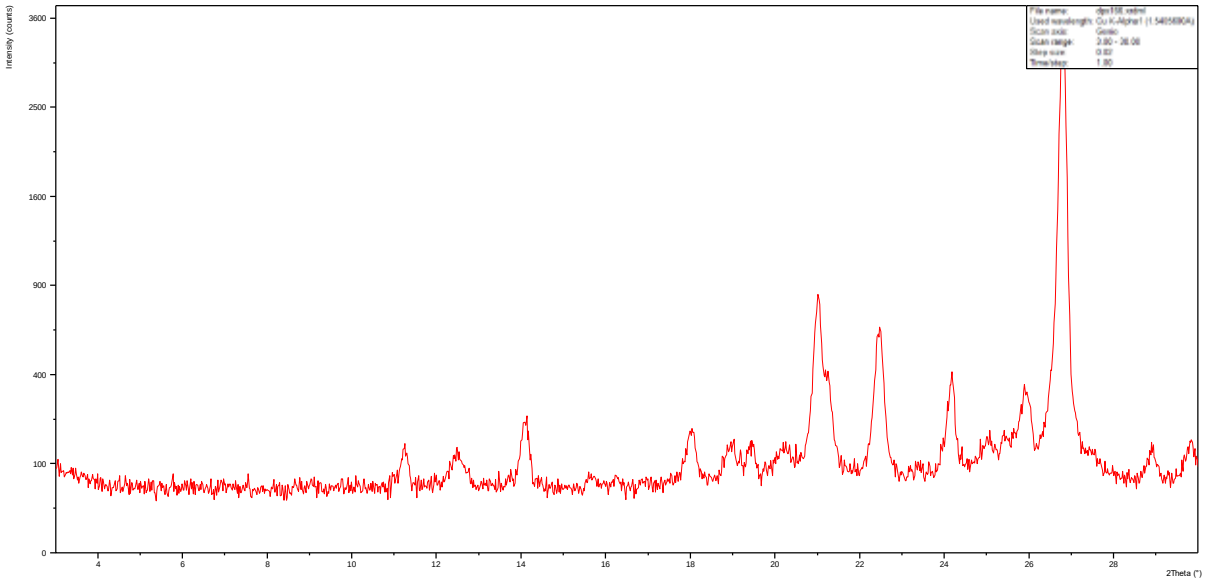

DPX172

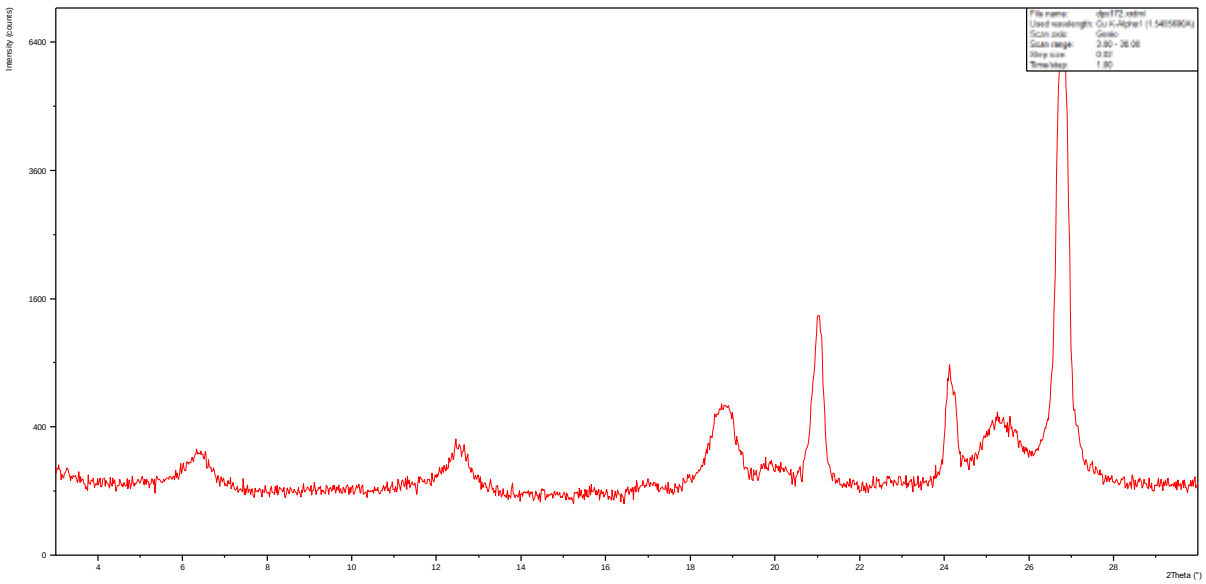

DPX175

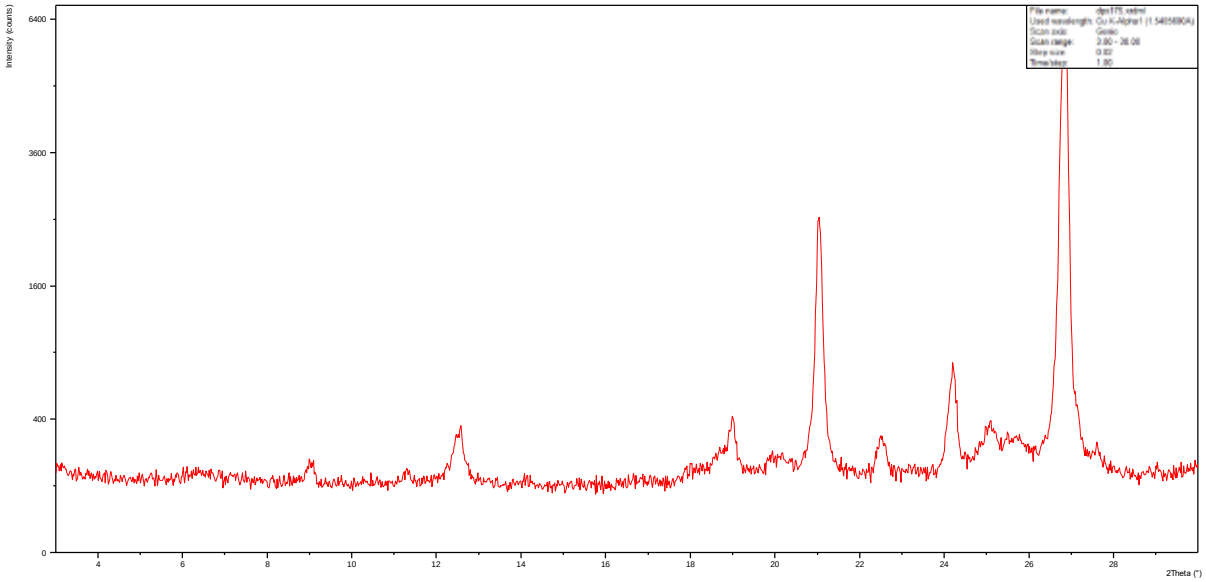

DPX176

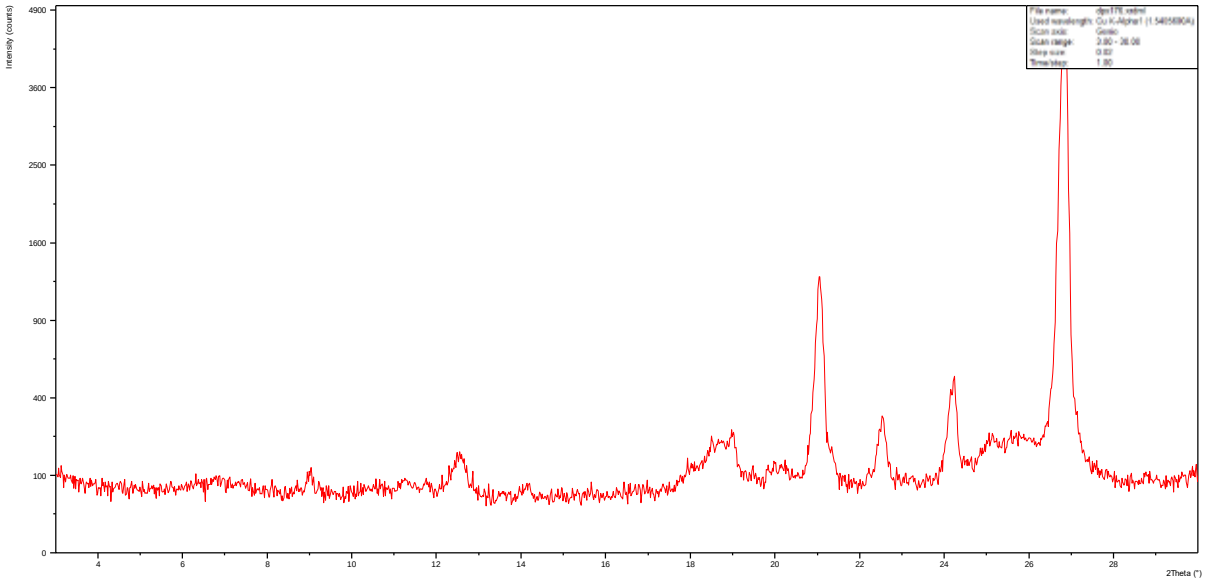

DPX177

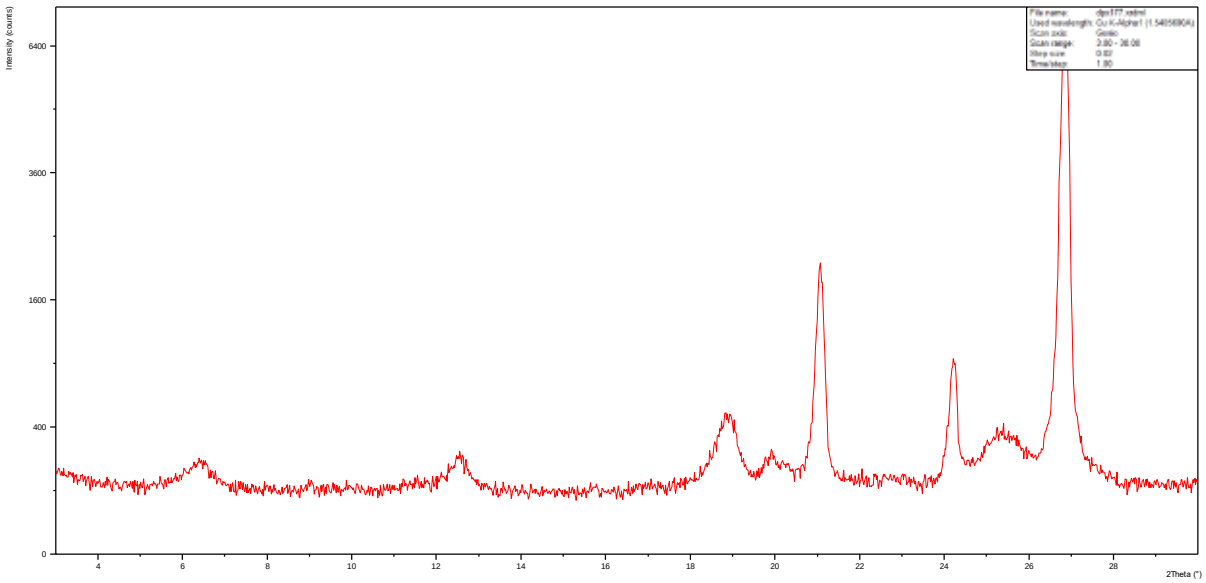

DPX178

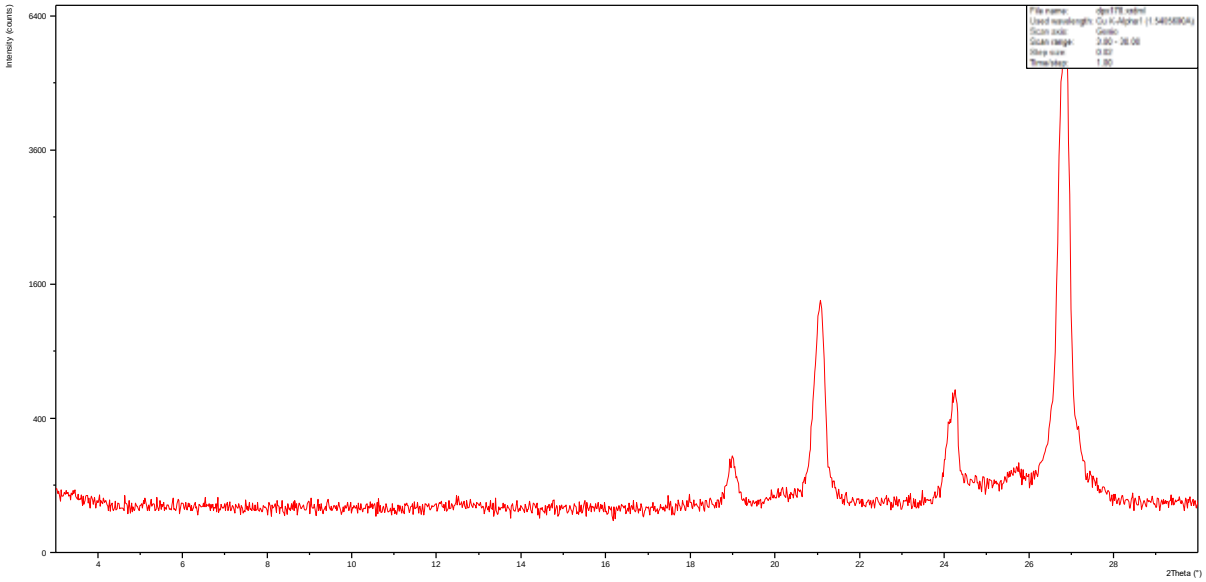

DPX179

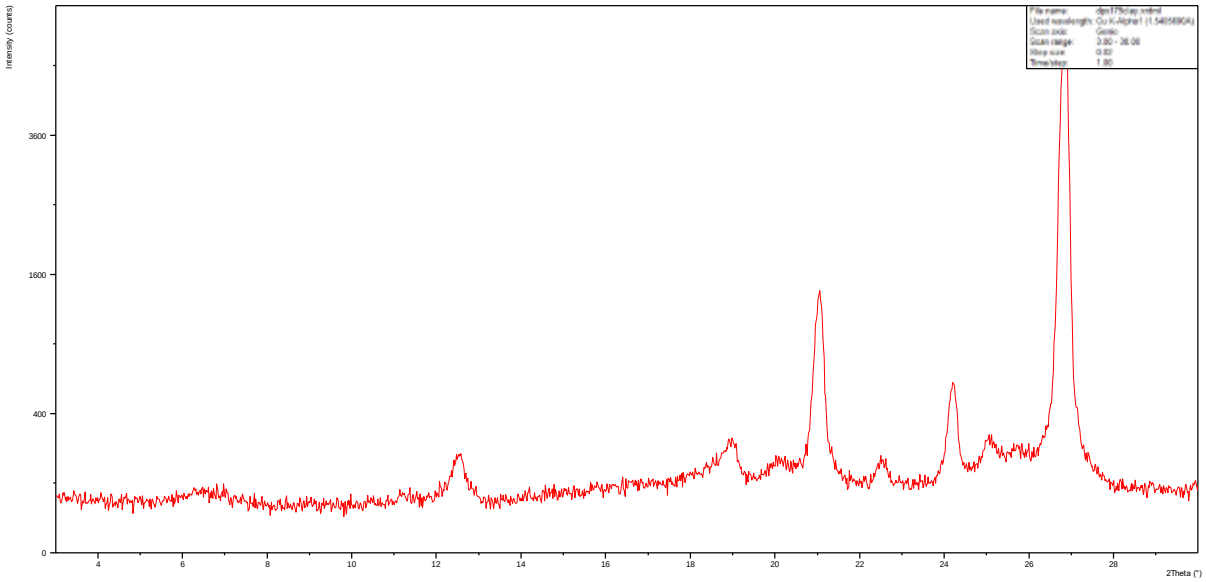

DPX181

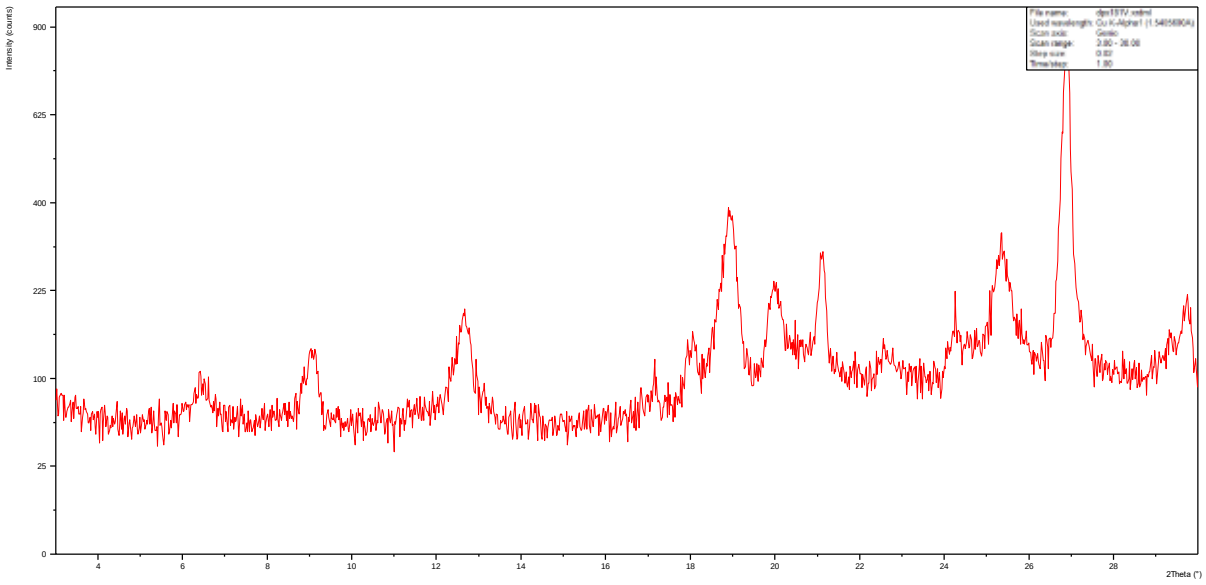

DPX189

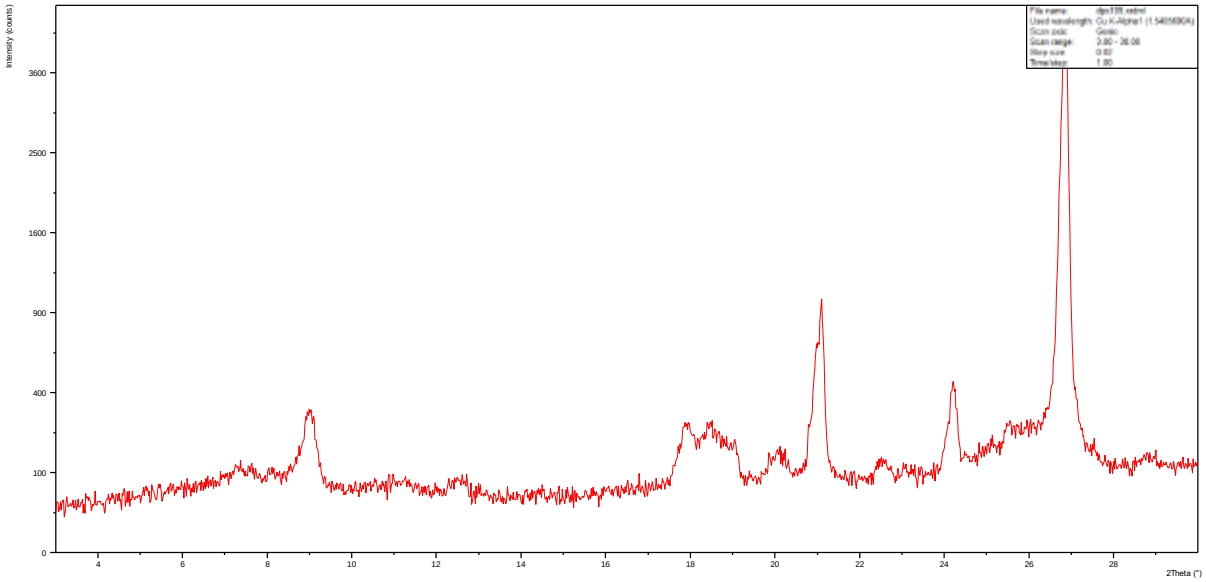

DPX193

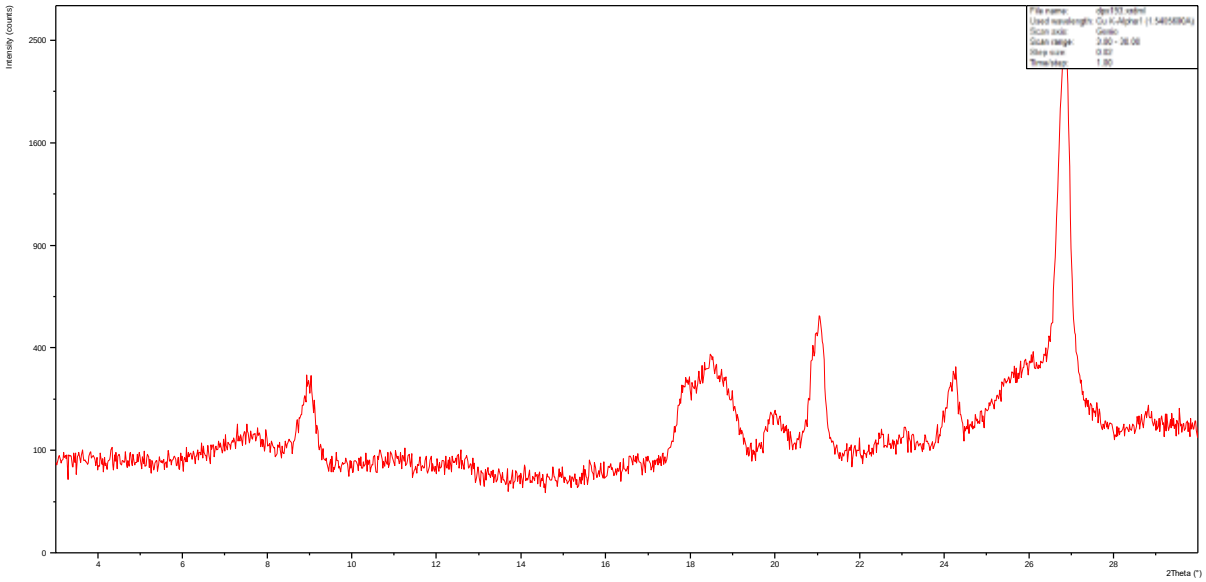

DPX194

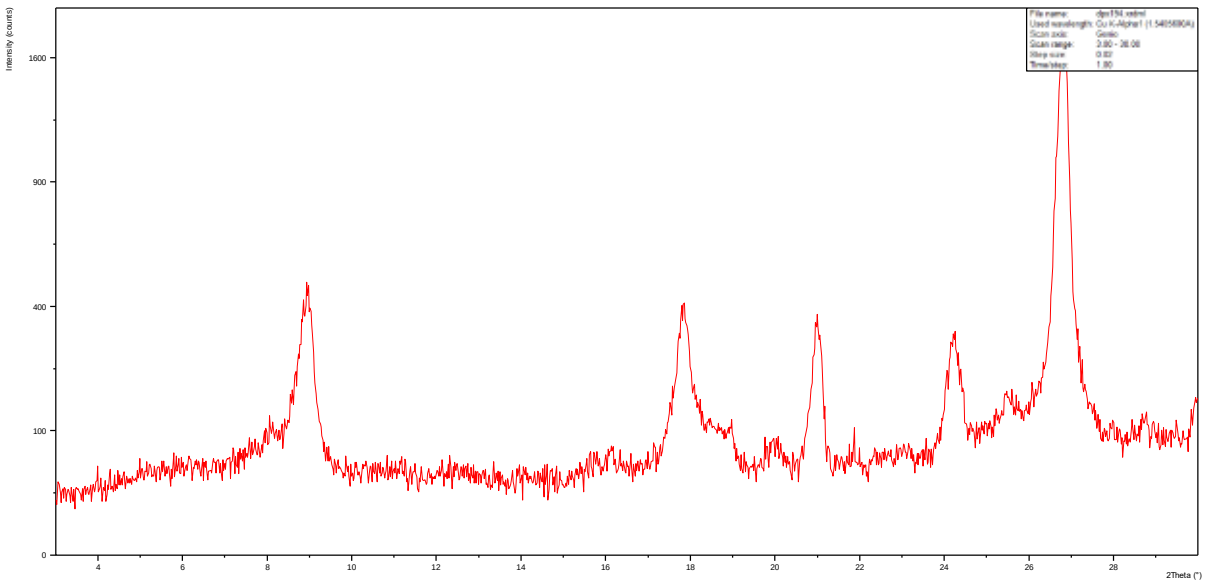

DPX195

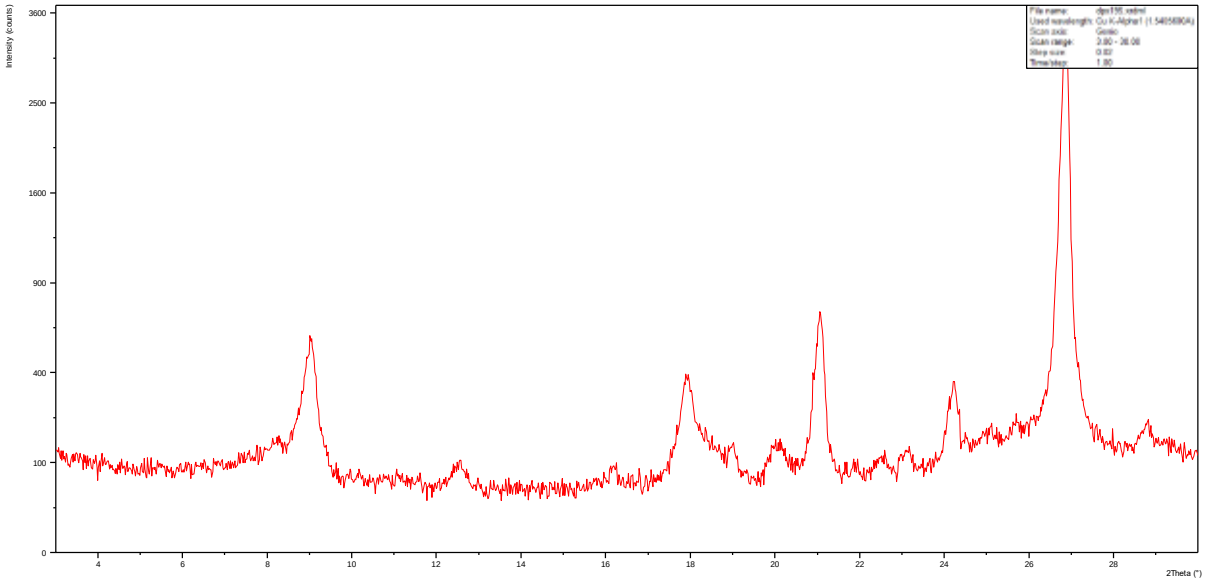

DPX198

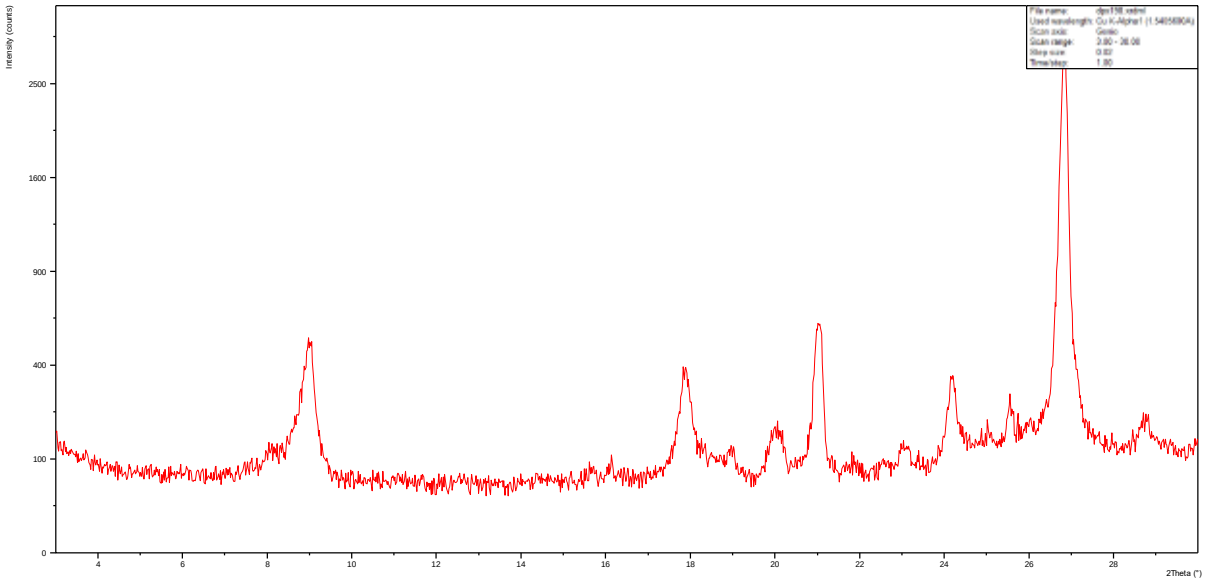

DPX201

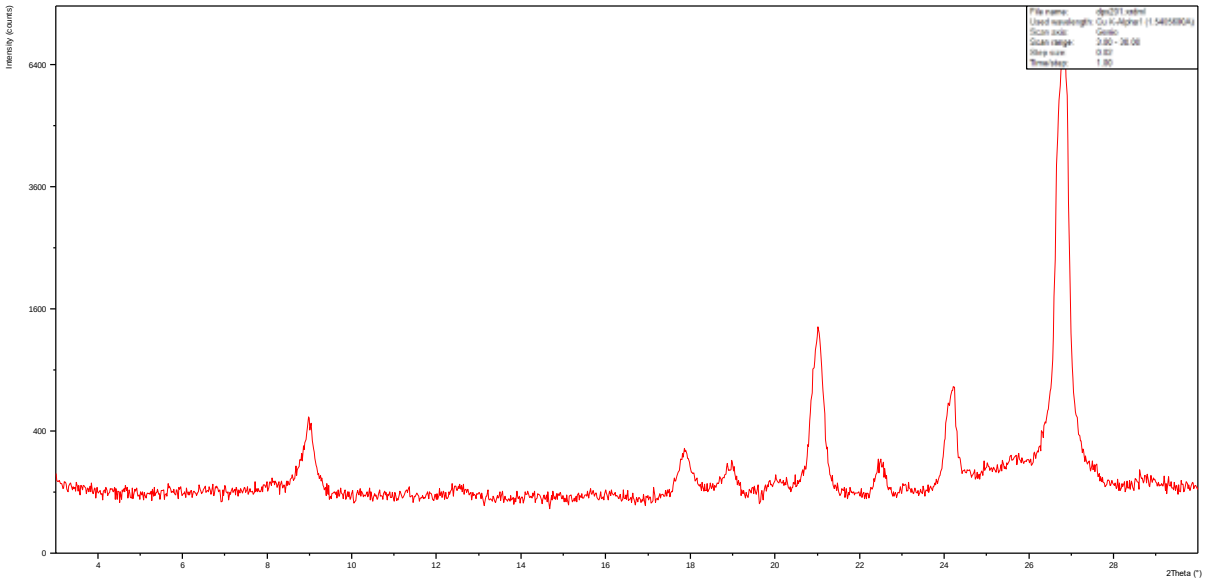

DPX205

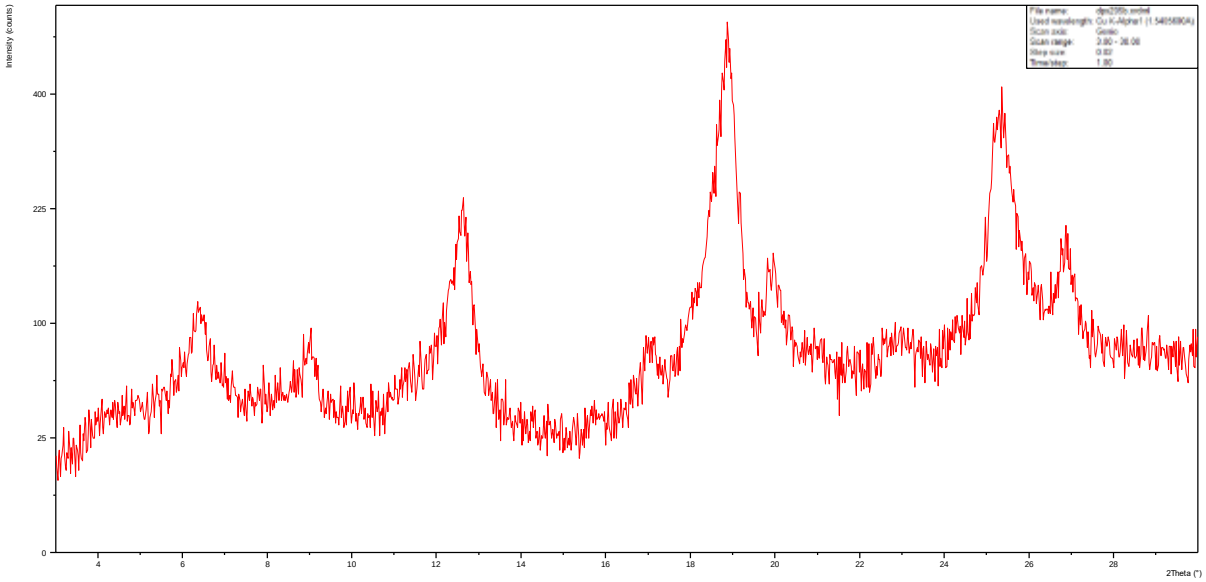

DPX208

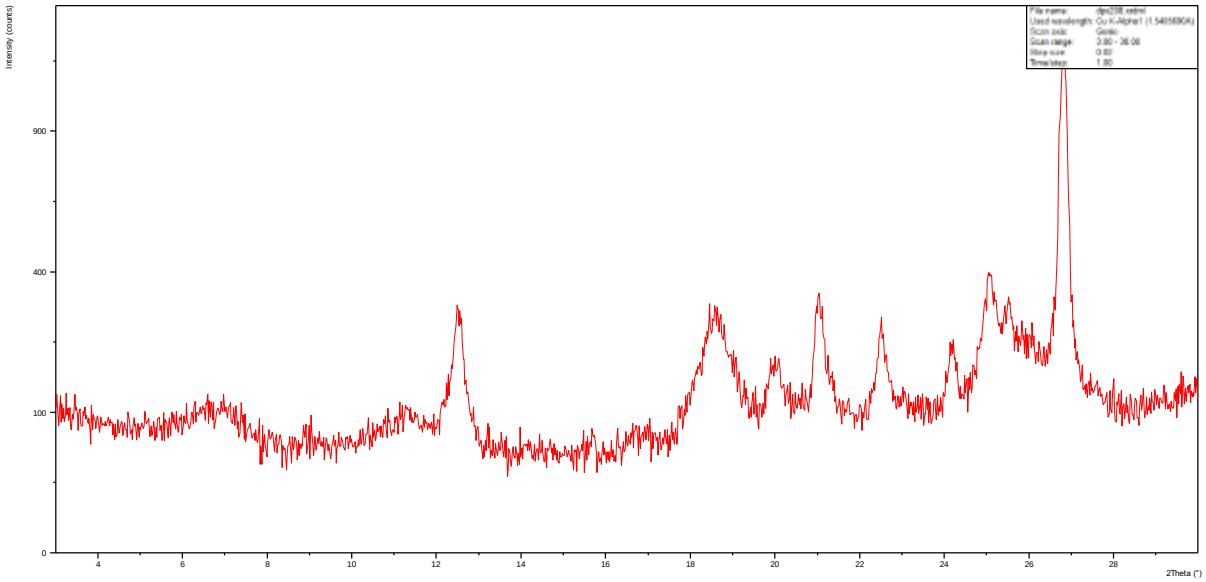

DPX210

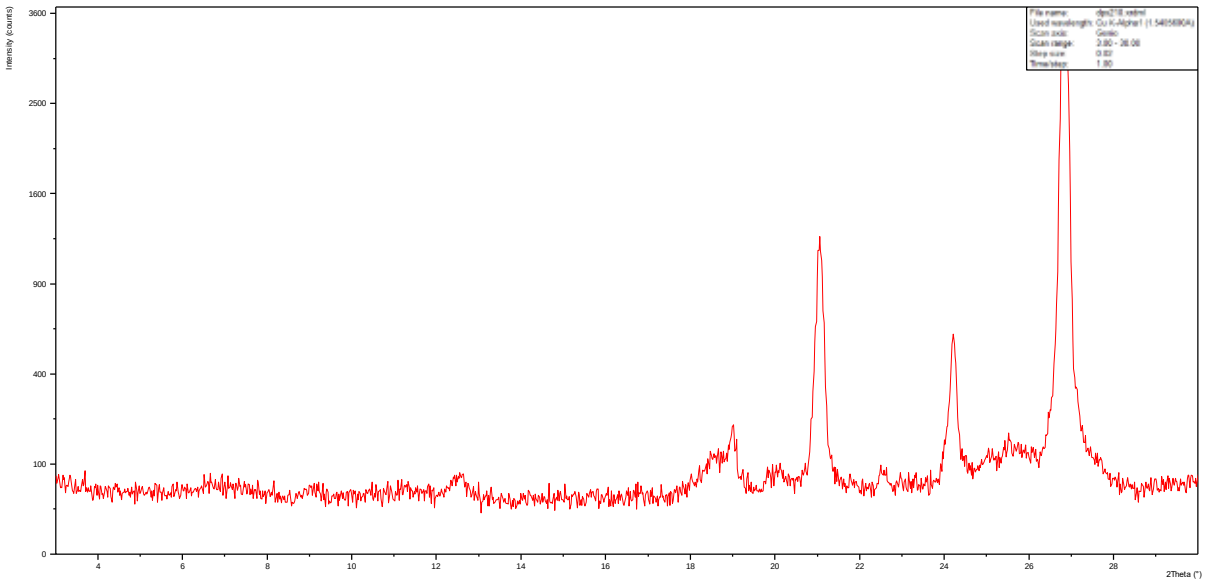

DPX221

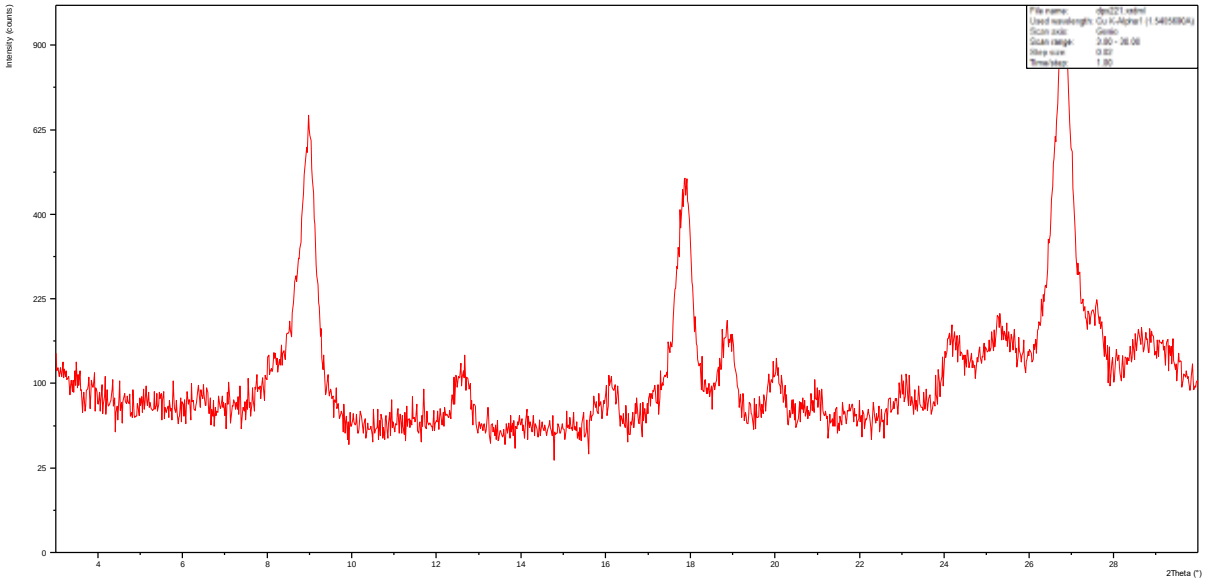

DPX250

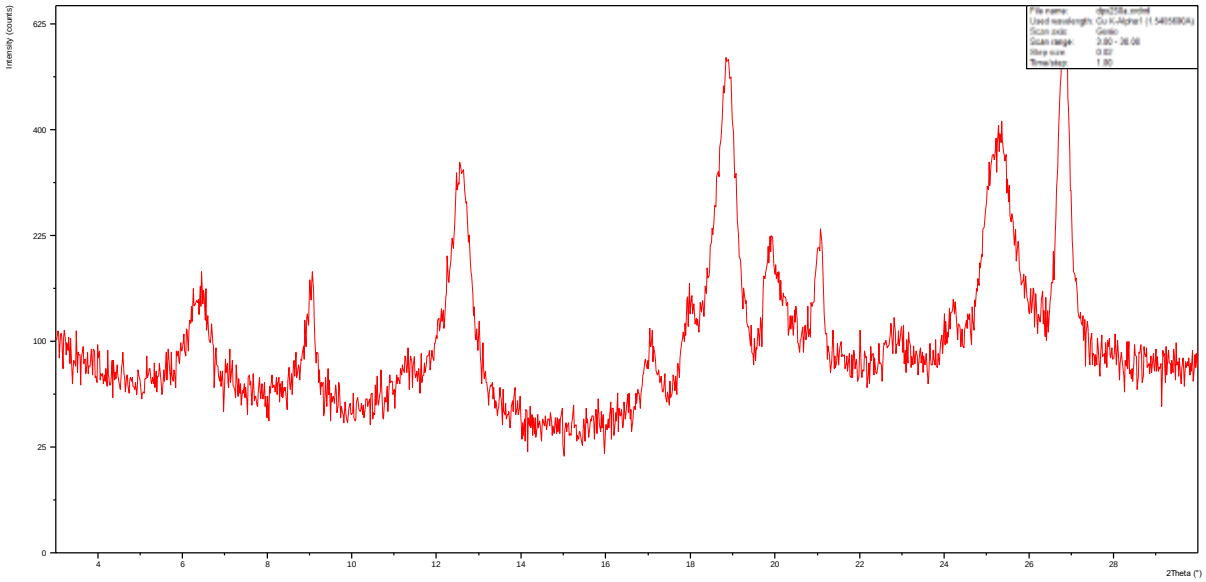

DPX256

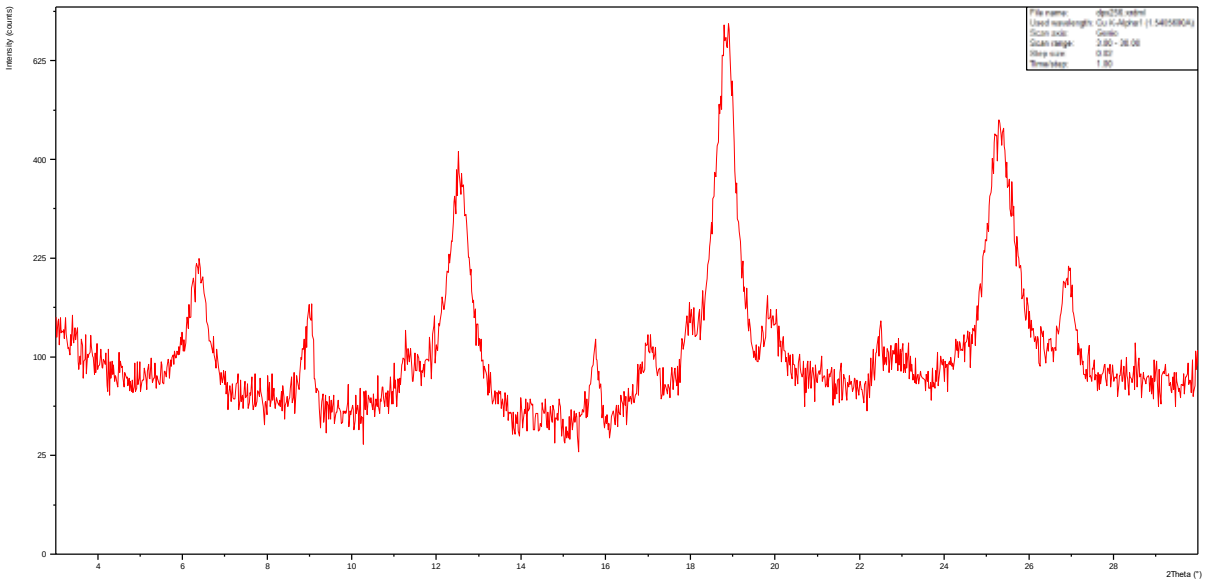

DPX257

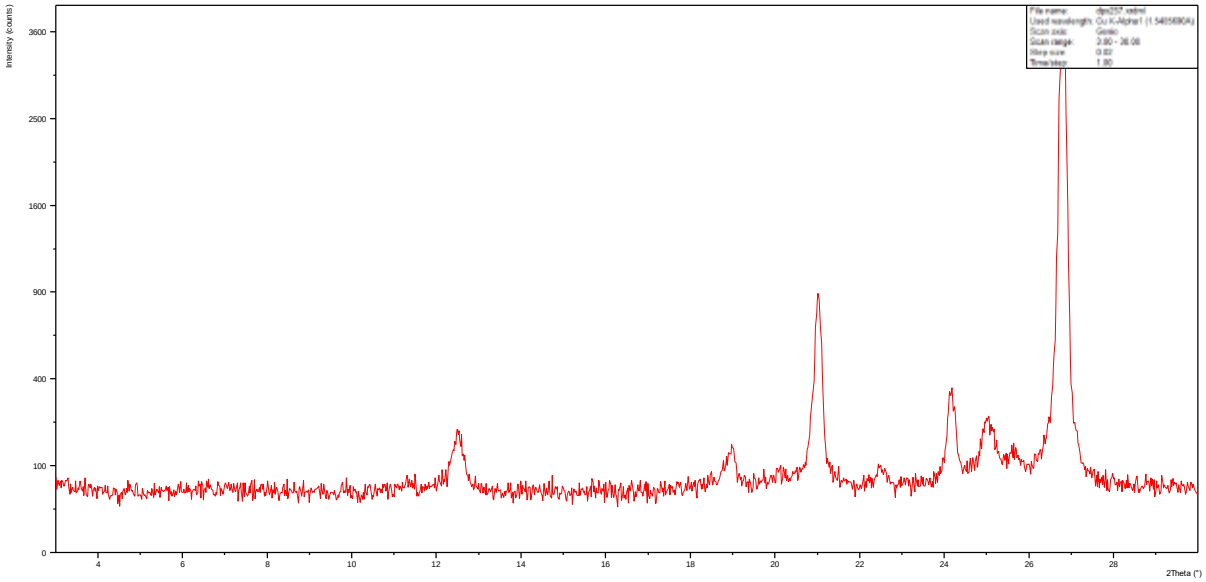

DPX265

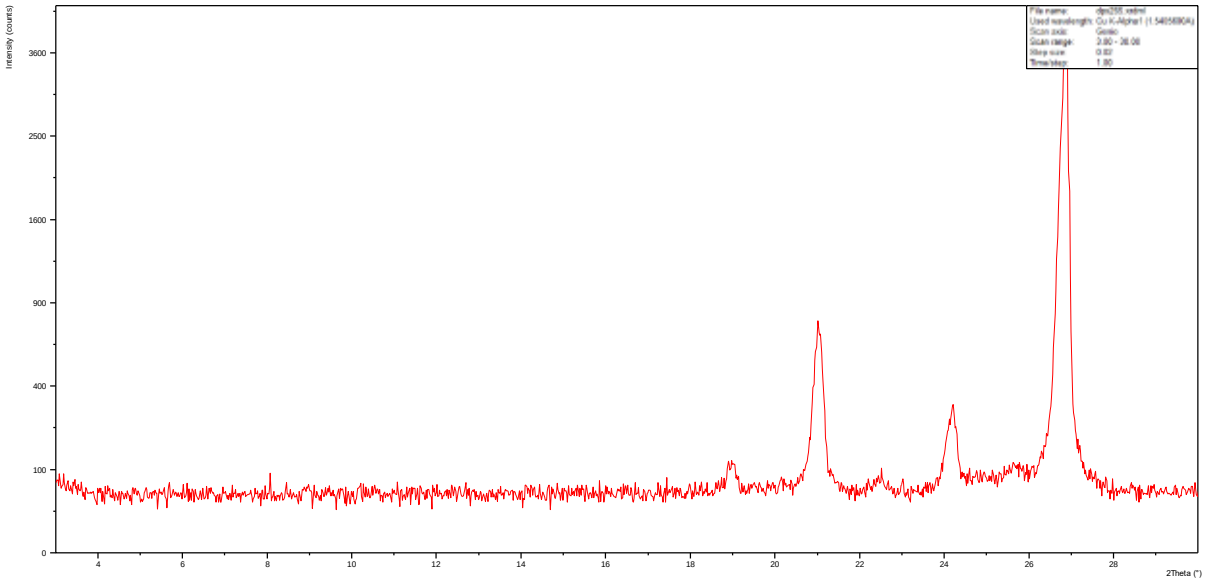

DPX269

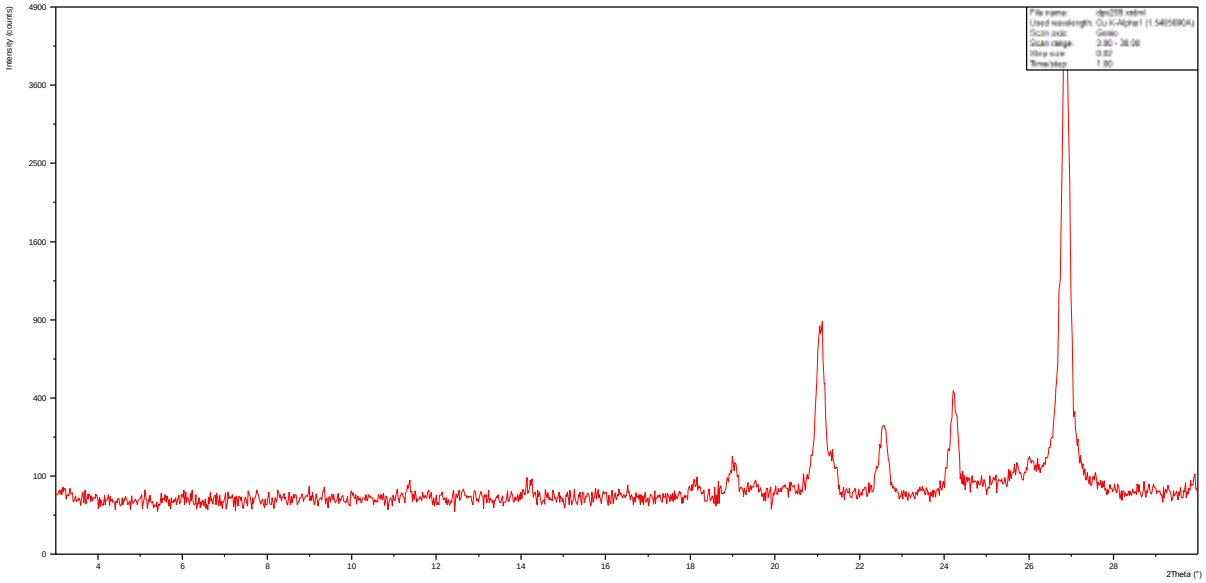

DPX280

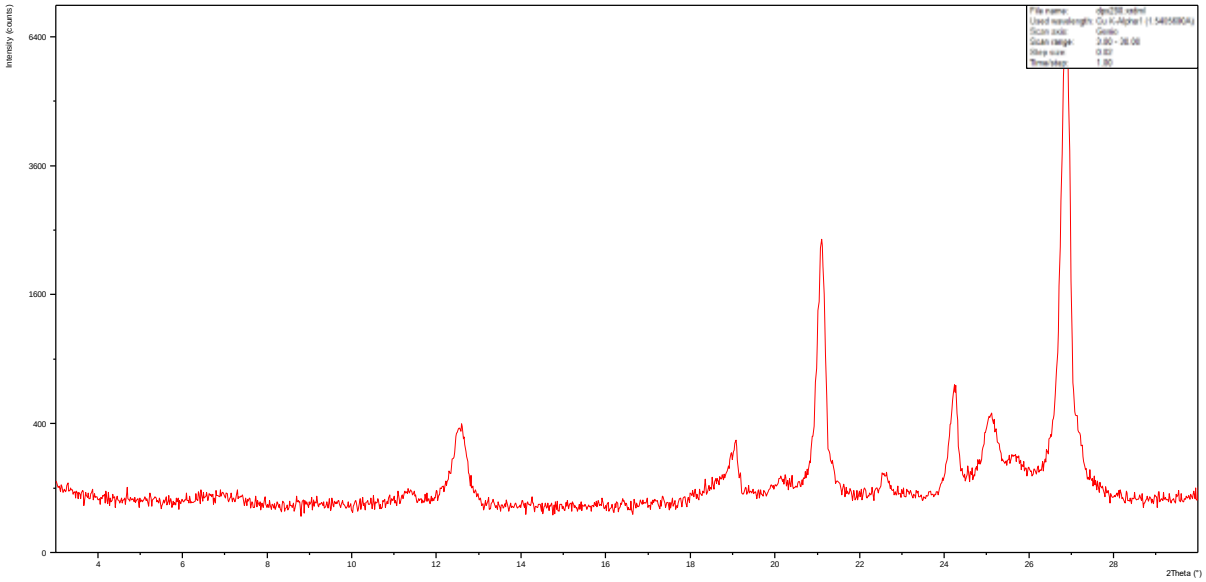
Intensity (counts)
6400
3600
1600
400
0
4
6
8
10
12
14
16
18
20
22
24
26
28
2Theta (°)

Samples from the WS Shear

WR256-A

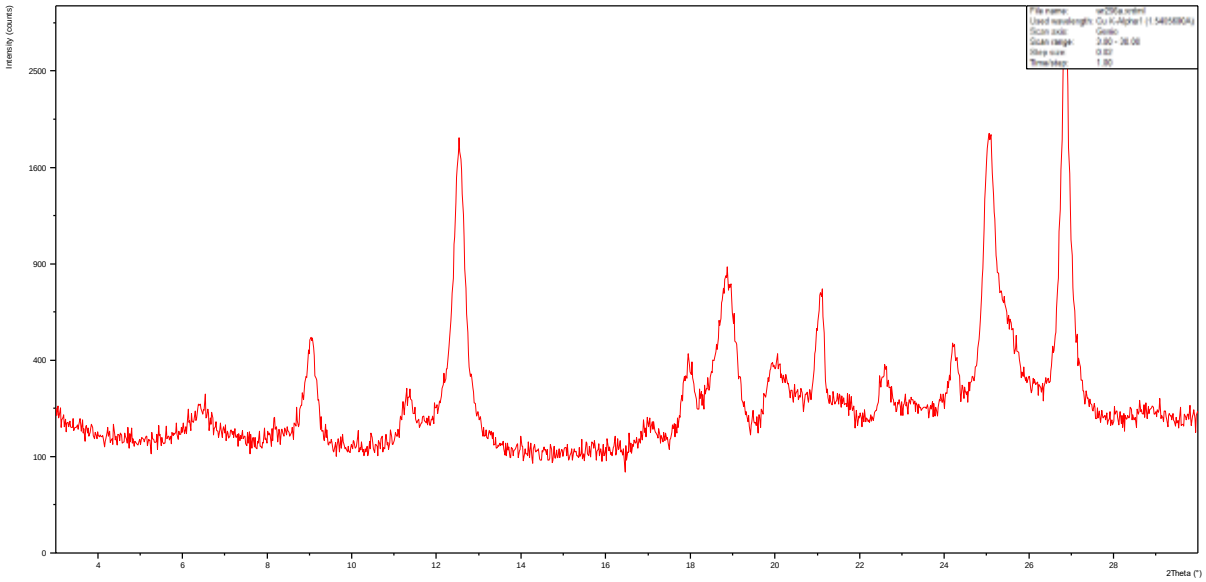

WR256-B

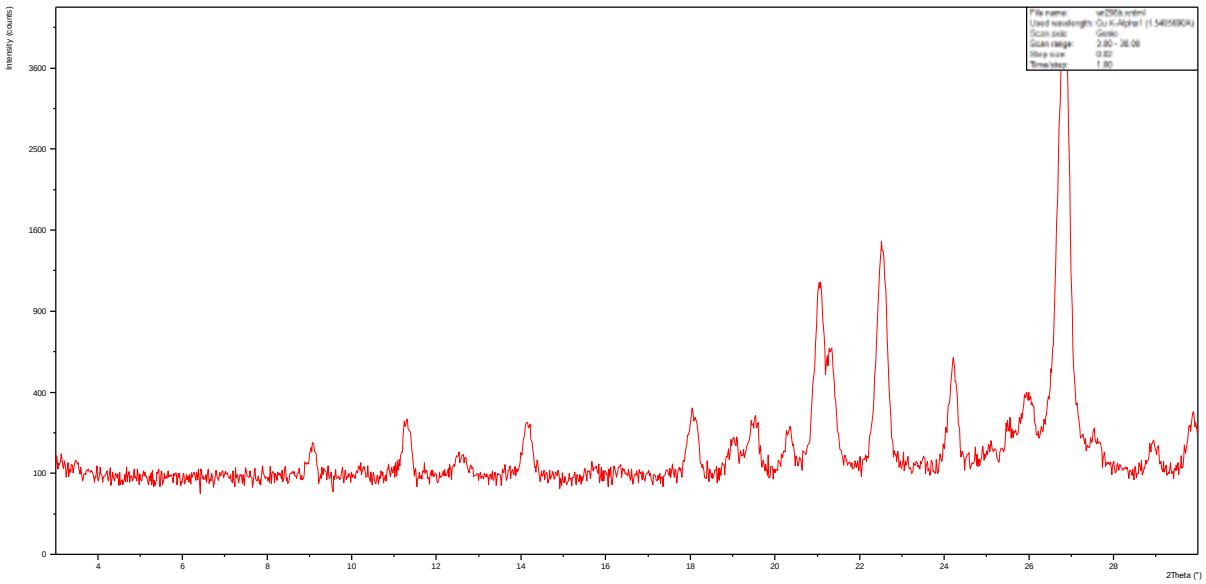

WR282-A

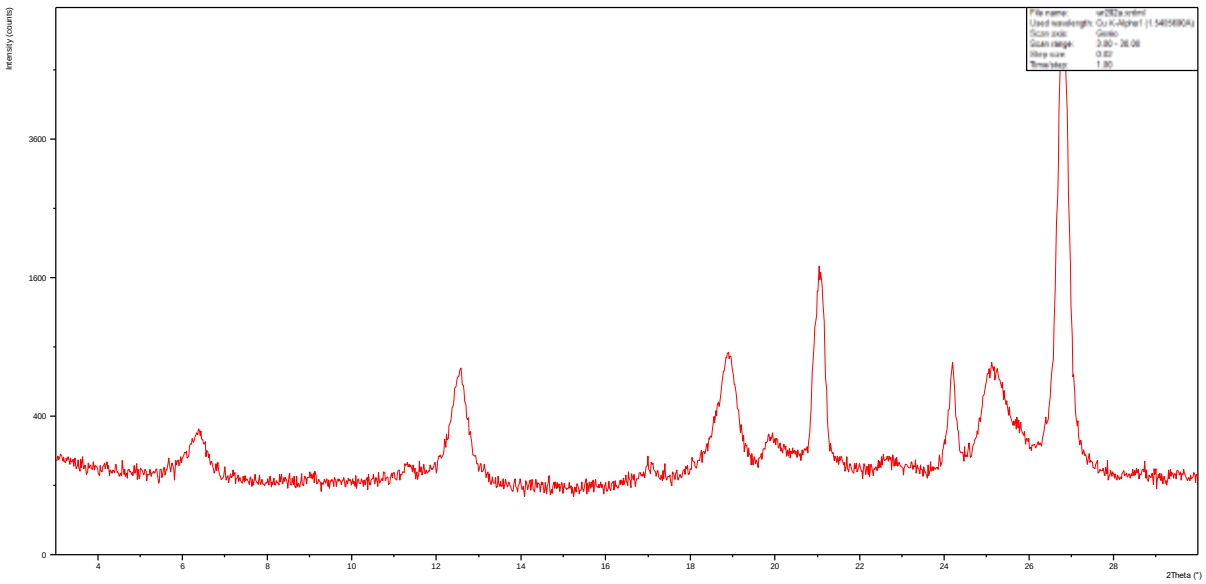

WR293-A

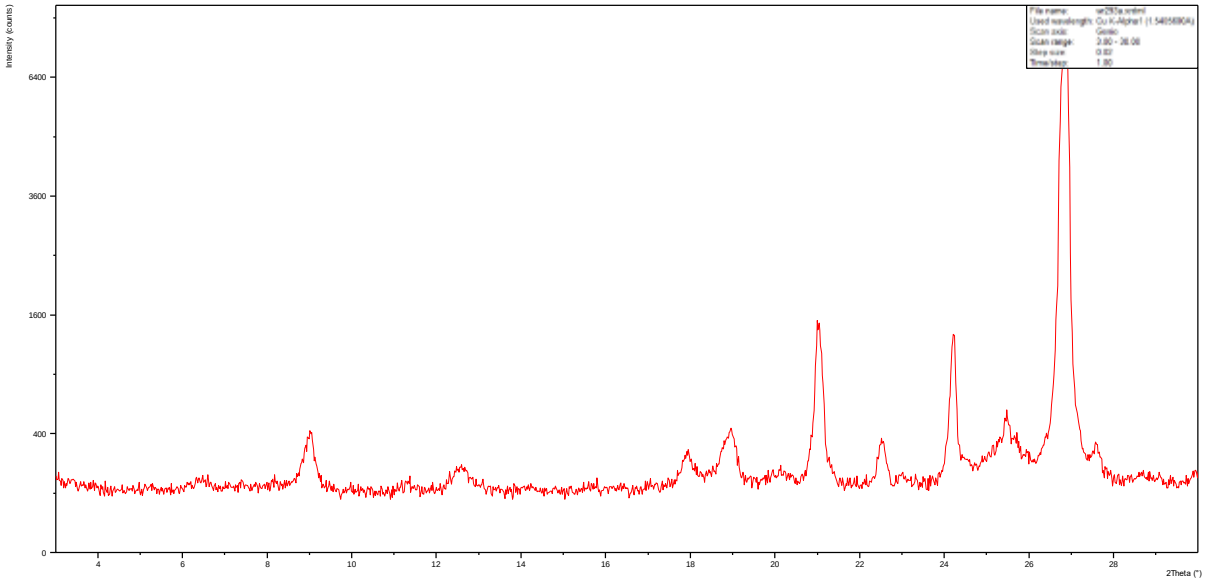

WR293-B

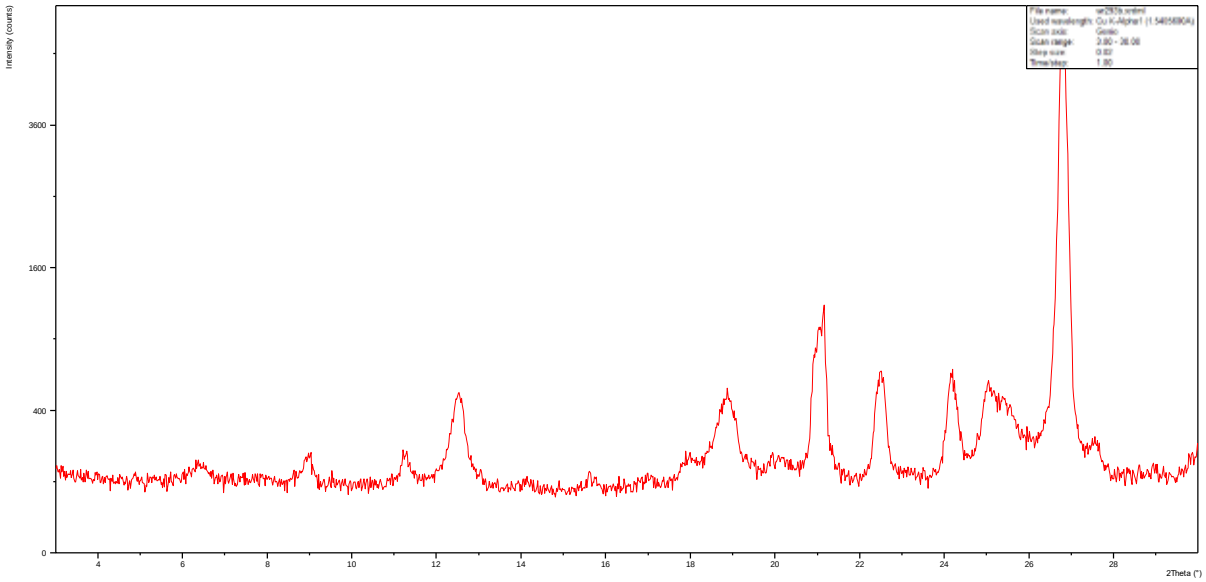

WR301-A

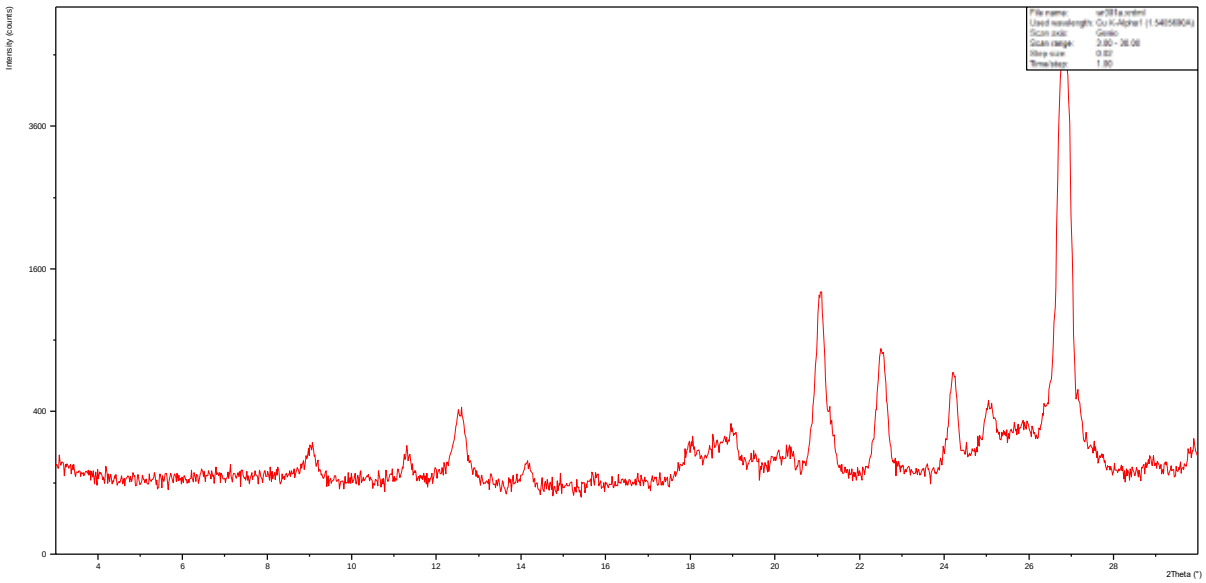

WR301-B

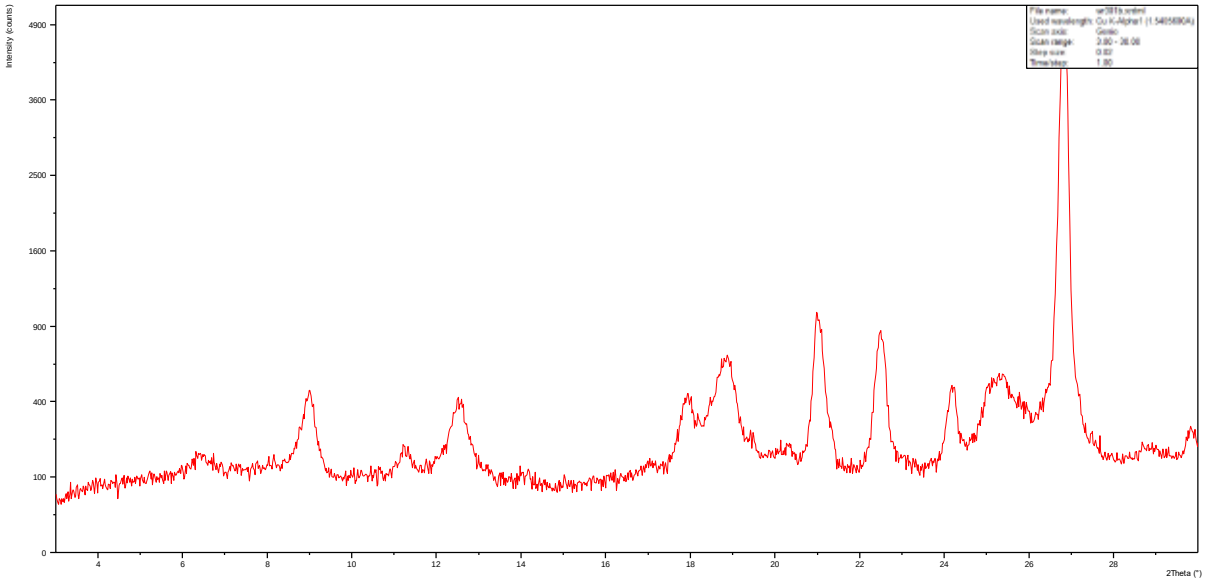

WR315-A

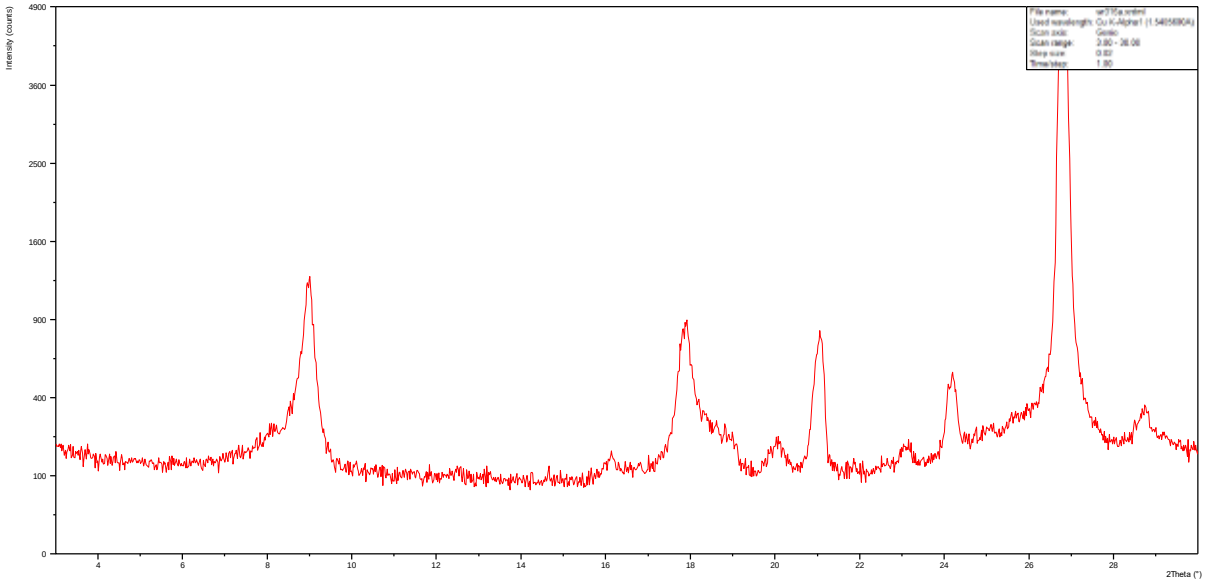

WR315-B

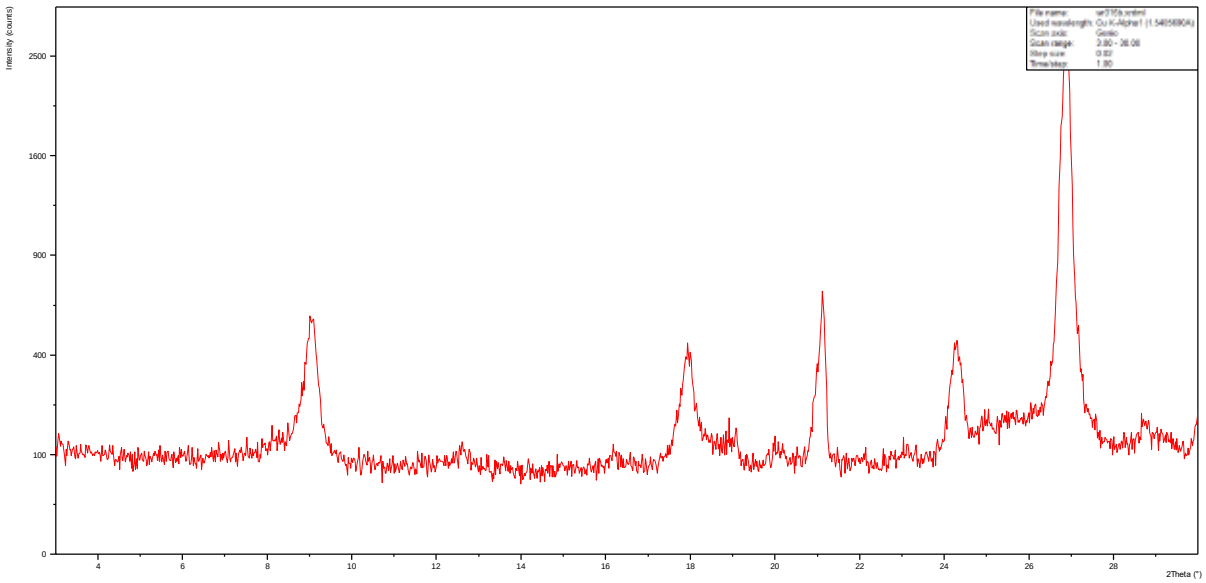

WR352A

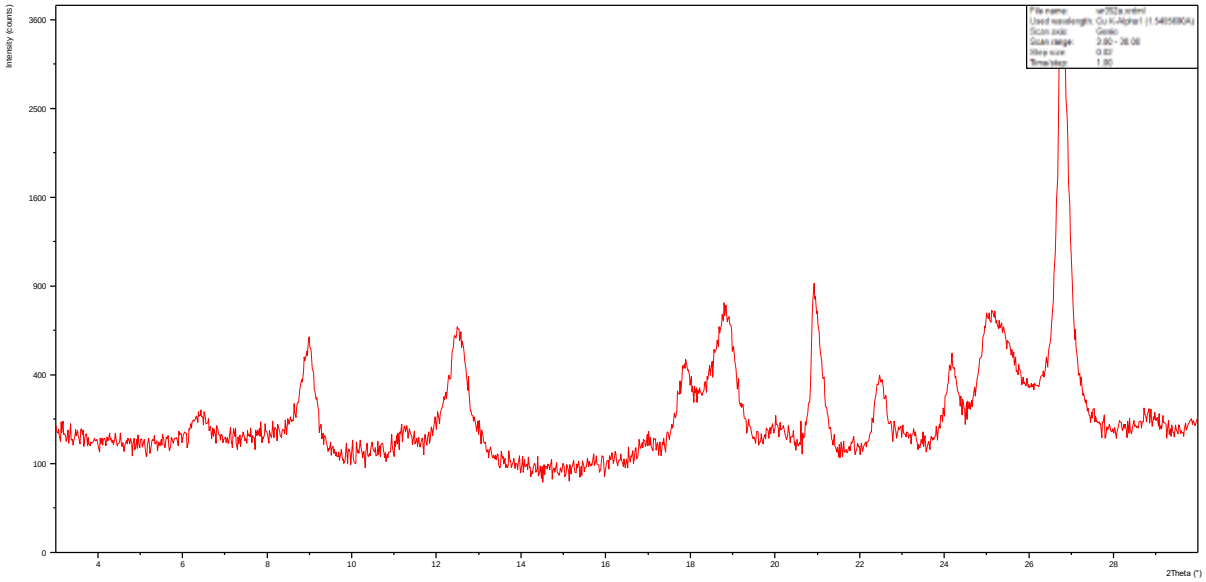

WR352-B

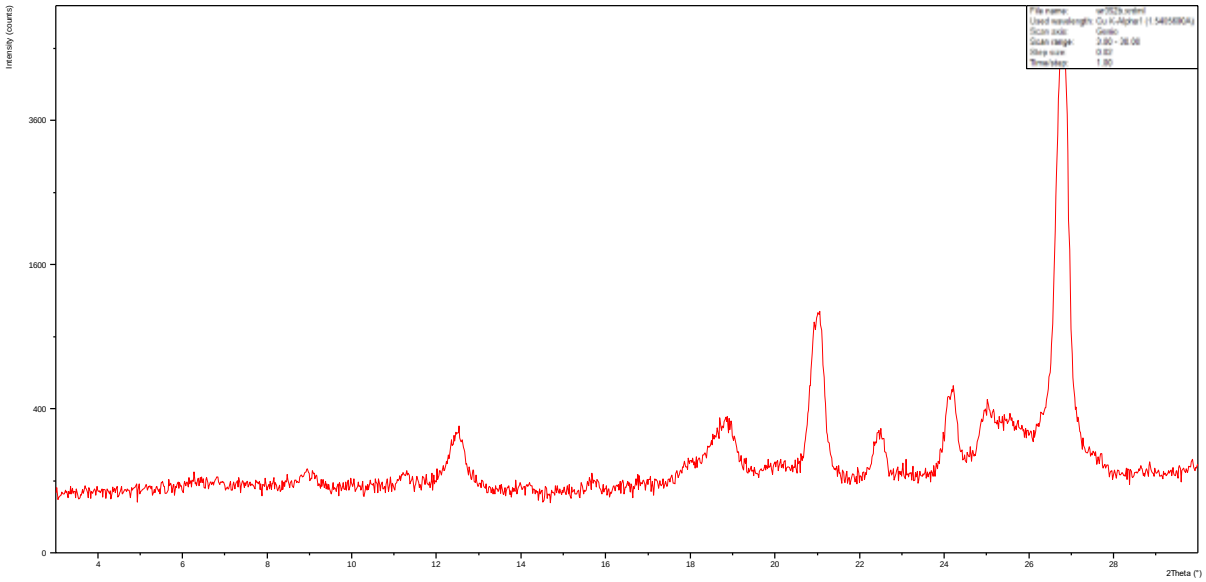

WR404

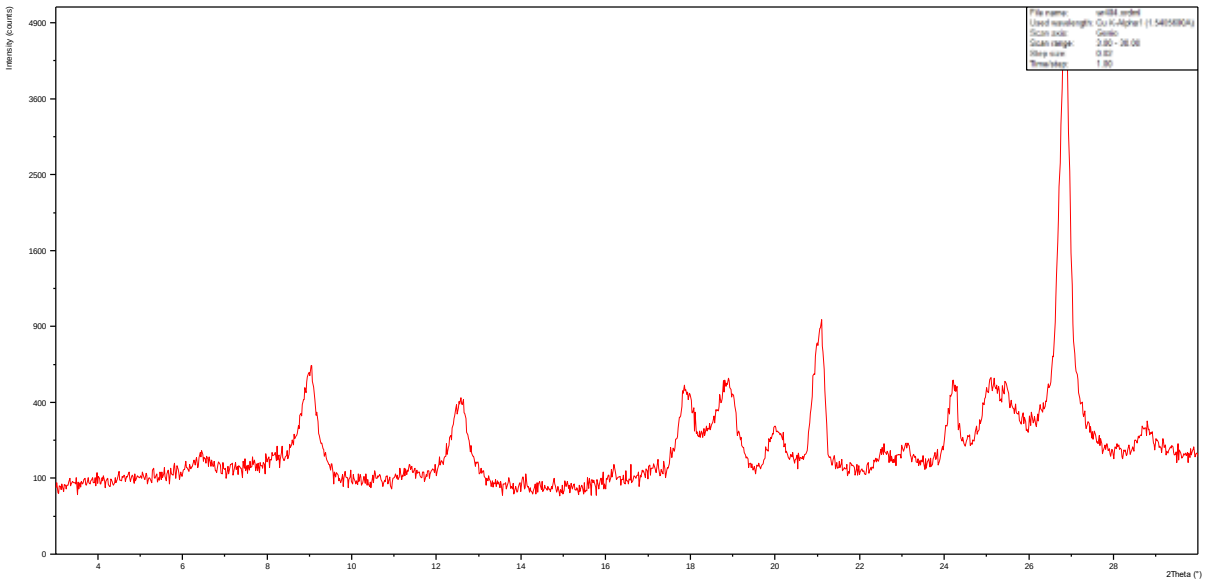

WR409-A

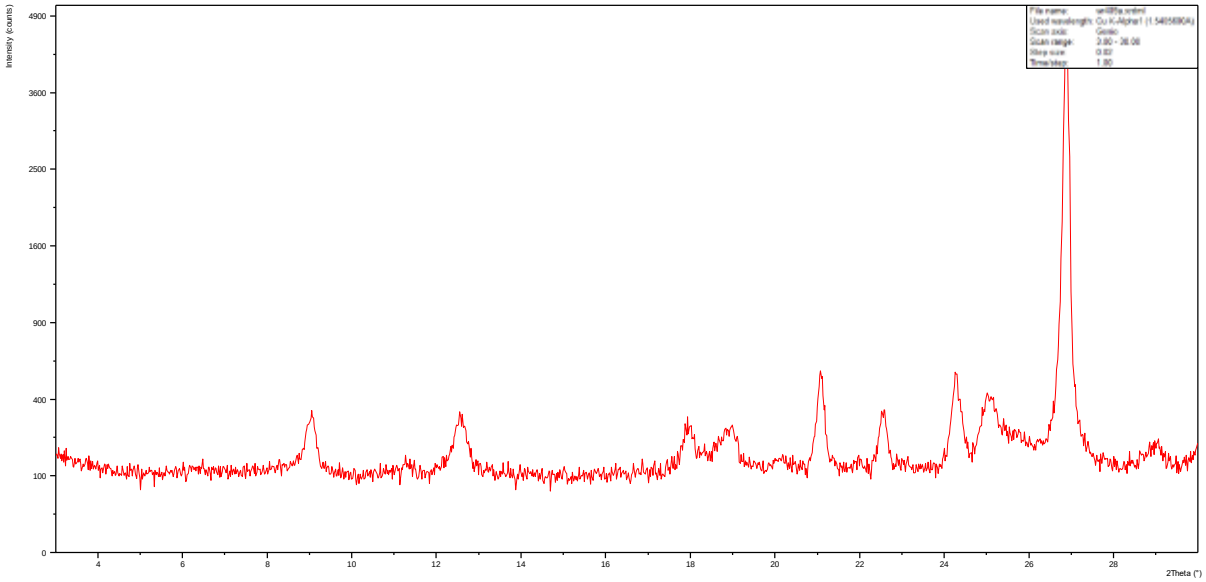
Intensity (counts)
4900
3600
2500
1600
900
400
100
0
4
6
8
10
12
14
16
18
20
22
24
26
28
2Theta (°)